Green Chemistry and Sustainable Technology

Aims and Scope

The series *Green Chemistry and Sustainable Technology* aims to present cutting-edge research and important advances in green chemistry, green chemical engineering and sustainable industrial technology. The scope of coverage includes (but is not limited to):

- Environmentally benign chemical synthesis and processes (green catalysis, green solvents and reagents, atom-economy synthetic methods etc.)
- Green chemicals and energy produced from renewable resources (biomass, carbon dioxide etc.)
- Novel materials and technologies for energy production and storage (bio-fuels and bioenergies, hydrogen, fuel cells, solar cells, lithium-ion batteries etc.)
- Green chemical engineering processes (process integration, materials diversity, energy saving, waste minimization, efficient separation processes etc.)
- Green technologies for environmental sustainability (carbon dioxide capture, waste and harmful chemicals treatment, pollution prevention, environmental redemption etc.)

The series *Green Chemistry and Sustainable Technology* is intended to provide an accessible reference resource for postgraduate students, academic researchers and industrial professionals who are interested in green chemistry and technologies for sustainable development.

More information about this series at http://www.springer.com/series/11661

Haining Tian · Gerrit Boschloo
Anders Hagfeldt
Editors

Molecular Devices for Solar Energy Conversion and Storage

Springer

Editors
Haining Tian
Department of Chemistry—Ångström Laboratory
Uppsala University
Uppsala
Sweden

Gerrit Boschloo
Department of Chemistry—Ångström Laboratory
Uppsala University
Uppsala
Sweden

Anders Hagfeldt
École Polytechnique Fédérale de Lausanne
Lausanne
Switzerland

ISSN 2196-6982 ISSN 2196-6990 (electronic)
Green Chemistry and Sustainable Technology
ISBN 978-981-10-5923-0 ISBN 978-981-10-5924-7 (eBook)
https://doi.org/10.1007/978-981-10-5924-7

Library of Congress Control Number: 2017947030

Printed on acid-free paper

This Springer imprint is published by Springer Nature
The registered company is Springer Nature Singapore Pte Ltd.
The registered company address is: 152 Beach Road, #21-01/04 Gateway East, Singapore 189721, Singapore

Foreword

This outstanding and timely book on solar energy acquisition, conversion, and storage covers a broad range of actual hot topics, starting from organic solar cells, polymer cells, dye sensitized solar cells, via light-driven water splitting devices, and carbon dioxide reduction devices up to perovskite solar cells.

In the spirit of lifelong learning, some perceptive or thinking why and how important it is that we should learn or develop molecule-based solar conversion devices will become perfectly clear after having studied this most inspiring book.

Modern versions of spectroscopic techniques in molecular devices are also presented by world renowned scientists in the fields of:

- X-Ray-photoelectron spectroscopy
- Transient absorption spectroscopy
- Electrochemical impedance spectroscopy

The editors Haining Tian (Uppsala), Gerrit Boschloo (Uppsala), and Anders Hagfeldt (Lausanne) have thoughtfully arranged a collection of altogether thirteen contributions, prepared by leading experts.

The perspectives of this book are far-reaching visions contributing to the scientific debate on planetary boundaries and responsible care for environmental changes. The discussion, in terms of global crisis, encompasses our limited energy resources, global water pollution, and climate change to mention but a few. Therefore, it will be fruitful and rewarding for students, researchers, officials, politicians, and engineers to have this book at their shelf.

Berlin K. Rademann

Preface

With increasing demand of energy in our society, exploring and developing renewable energy is therefore becoming more and more desirable. “Affordable and Clean Energy” is listed as the 7th of 17 goals proposed from the United Nations to transform our world with sustainable development. With the background, the motivation to edit this book is further triggered from recently rapid development and broad application of functional molecules in renewable energy conversion fields. The chemical, physical, electrochemical, and photochemical properties of molecules can be well tuned by reasonable structural modification, making them show broad applications in different solar energy conversion and storage devices, such as solar cells, solar fuels, solar batteries/capacitors, and solar-to-thermal conversion devices. This book “Molecular Devices in Solar Energy Conversion and Storage” aims to give pedagogical overview of how different functional molecules are designed for various devices, what the working principles of these devices are, and how to characterize them and further improve the performance of the devices. The book consists of 13 chapters written by scientists who are experts in their own field. I give my great thanks to these authors and colleagues who kindly accepted to contribute the chapters. The contents of this book are briefly introduced as below:

Chapters 1 and 2 give an introduction of organic solar cells and the application of polymers and small molecules in this type of solar cells.

Chapters 3 and 4 serve as reviews of molecular components used in both liquid and solid state dye sensitized solar cells.

Chapter 5 discusses the organic/inorganic hybrid solar cells with a focus on perovskite solar cells.

Chapters 6 and 7 focus on light-driven water splitting and CO_2 reduction devices using molecular photosensitizer and catalysts to convert and store solar energy into fuels.

Chapter 8 introduces working principles of both photobatteries and photocapacitors systems with the various processes at and between the electrodes reactions presented in detail.

Chapter 9 presents the molecular design and functional devices for molecular solar thermal conversion and storage.

Chapters 10–12 are devoted to the application of X-ray Photoelectron Spectroscopy, Transient Absorption Spectroscopy, and Electrochemical Impedance Spectroscopy in the characterization of molecular devices.

Chapter 13 discusses perovskite solar cells concerning stability issue.

The invaluable insights and knowledge provided in this book are relevant for a wide readership, and are particularly useful for students, researchers, and industrial professionals who are working on molecular devices for solar energy utilization.

I am honored to have Prof. Gerrit Boschloo from Uppsala University and Prof. Anders Hagfeldt from EPFL as co-editors. This book will never be finished without their works and supports. I am also grateful to Prof. Klaus Rademann from Humboldt University of Berlin for writing the foreword of this book. At the end, I will give my gratitude to June Tang and Heather Feng from Springer Beijing for their kind invitation to edit this book and helpful assistance during the edition.

Uppsala, Sweden Haining Tian
May 2017

Contents

Contributors

Leila Alibabaei Department of Chemistry, University of North Carolina, Chapel Hill, NC, USA

Takeo Arai Toyota Central Research and Development Labs., Inc., Nagakute, Aichi, Japan

Eva M. Barea Institute of Advanced Materials (INAM), Universitat Jaume I, Castelló de la Plana, Spain

Gerrit Boschloo Department of Chemistry—Ångström Laboratory, Physical Chemistry, Uppsala University, Uppsala, Sweden

M. Kyle Brennaman Department of Chemistry, University of North Carolina, Chapel Hill, NC, USA

Juan Bisquert Institute of Advanced Materials (INAM), Universitat Jaume I, Castelló de la Plana, Spain

Ute B. Cappel Department of Physics and Astronomy, Uppsala University, Uppsala, Sweden

Pavel Chábera Division of Chemical Physics, Lund University, Lund, Sweden

Tomas Edvinsson Department of Engineering Sciences, Uppsala University, Uppsala, Sweden

Francisco Fabregat-Santiago Institute of Advanced Materials (INAM), Universitat Jaume I, Castelló de la Plana, Spain

Azhar Fakharuddin Department of Physics, University of Konstanz, Konstanz, Germany

Marina Freitag Department of Chemistry—Ångström Laboratory, Physical Chemistry, Uppsala University, Uppsala, Sweden

Sixto Giménez Institute of Advanced Materials (INAM), Universitat Jaume I, Castelló de la Plana, Spain

Anders Hagfeldt Department of Chemistry—Ångström Laboratory, Physical Chemistry, Uppsala University, Uppsala, Sweden; École Polytechnique Fédérale de Lausanne, Laboratory of Photomolecular Science, EPFL SB ISIC LSPM, Lausanne, Switzerland; Laboratory of Photomolecular Science, Institute of Chemical Sciences and Engineering, Swiss Federal Institute of Technology in Lausanne (EPFL), Lausanne, Switzerland

Leif Hammarström Department of Chemistry—Ångström Laboratory, Uppsala University, Uppsala, Sweden

Youyu Jiang Wuhan National Laboratory for Optoelectronics, and School of Optical and Electronic Information, Huazhong University of Science and Technology, Wuhan, China

Erik M.J. Johansson Department of Chemistry—Ångström, Uppsala University, Uppsala, Sweden

Lars Kloo School of Chemical Science and Engineering, Applied Physical Chemistry, KTH Royal Institute of Technology, Stockholm, Sweden

Christian Koerner Dresden Integrated Center for Applied Physics and Photonic Materials (IAPP), TU Dresden, Dresden, Germany

Valeria Lanzilotto Department of Physics and Astronomy, Uppsala University, Uppsala, Sweden

Anders Lennartson Department of Chemistry and Chemical Engineering, Chalmers University of Technology, Gothenburg, Sweden

Karl Leo Dresden Integrated Center for Applied Physics and Photonic Materials (IAPP), TU Dresden, Dresden, Germany

Yaowen Li Laboratory of Advanced Optoelectronic Materials, College of Chemistry, Chemical Engineering and Materials Science, Soochow University, Suzhou, China

Mónica Lira-Cantú Nanostructured Materials for Photovoltaic Energy Group, Catalan Institute of Nanoscience and Nanotechnology (ICN2), CSIC and Barcelona Institute of Science and Technology (BIST), Barcelona, Spain

Reiner Lomoth Department of Chemistry—Ångström Laboratory, Uppsala University, Uppsala, Sweden

Lin Mao Wuhan National Laboratory for Optoelectronics, and School of Optical and Electronic Information, Huazhong University of Science and Technology, Wuhan, China

Thomas J. Meyer Department of Chemistry, University of North Carolina, Chapel Hill, NC, USA

Alba Mingorance Nanostructured Materials for Photovoltaic Energy Group, Catalan Institute of Nanoscience and Nanotechnology (ICN2), CSIC and Barcelona Institute of Science and Technology (BIST), Barcelona, Spain

Tobias Moench Dresden Integrated Center for Applied Physics and Photonic Materials (IAPP), TU Dresden, Dresden, Germany; Robert Bosch GmbH, Car Multimedia, Optics Development, Leonberg, Germany

Takeshi Morikawa Toyota Central Research and Development Labs., Inc., Nagakute, Aichi, Japan

Kasper Moth-Poulsen Department of Chemistry and Chemical Engineering, Chalmers University of Technology, Gothenburg, Sweden

Caroline Murawski School of Physics and Astronomy, University of St. Andrews, St Andrews, UK

Jan Murawski School of Physics and Astronomy, University of St. Andrews, St Andrews, UK

Vasileios Christos Nikolis Dresden Integrated Center for Applied Physics and Photonic Materials (IAPP), TU Dresden, Dresden, Germany

Amador Pérez-Tomás Nanostructured Materials for Photovoltaic Energy Group, Catalan Institute of Nanoscience and Nanotechnology (ICN2), CSIC and Barcelona Institute of Science and Technology (BIST), Barcelona, Spain

Carlito S. Ponseca Jr. Division of Chemical Physics, Lund University, Lund, Sweden

Håkan Rensmo Department of Physics and Astronomy, Uppsala University, Uppsala, Sweden

Yegraf Reyna Nanostructured Materials for Photovoltaic Energy Group, Catalan Institute of Nanoscience and Nanotechnology (ICN2), CSIC and Barcelona Institute of Science and Technology (BIST), Barcelona, Spain

Shunsuke Sato Toyota Central Research and Development Labs., Inc., Nagakute, Aichi, Japan

Lukas Schmidt-Mende Department of Physics, University of Konstanz, Konstanz, Germany

Villy Sundström Division of Chemical Physics, Lund University, Lund, Sweden

Haining Tian Department of Chemistry—Ångström Laboratory, Physical Chemistry, Uppsala University, Uppsala, Sweden

Jinhui Tong Wuhan National Laboratory for Optoelectronics, and School of Optical and Electronic Information, Huazhong University of Science and Technology, Wuhan, China

Jens Uhlig Division of Chemical Physics, Lund University, Lund, Sweden

Koen Vandewal Dresden Integrated Center for Applied Physics and Photonic Materials (IAPP), TU Dresden, Dresden, Germany

Nick Vlachopoulos Laboratory of Photomolecular Science, Institute of Chemical Sciences and Engineering, Swiss Federal Institute of Technology in Lausanne (EPFL), Lausanne, Switzerland

Fengling Zhang Biomolecular and Organic Electronics, Department of Physics, Chemistry and Biology (IFM), Linkoping University, Linkoping, Sweden

Jinbao Zhang Department of Chemistry—Ångström Laboratory, Physical Chemistry, Uppsala University, Uppsala, Sweden

Yinhua Zhou Wuhan National Laboratory for Optoelectronics, and School of Optical and Electronic Information, Huazhong University of Science and Technology, Wuhan, China

Chapter 1
Small Molecule Solar Cells

Tobias Moench, Christian Koerner, Caroline Murawski, Jan Murawski, Vasileios Christos Nikolis, Koen Vandewal and Karl Leo

Abstract In the last years, organic photovoltaics have moved from a lab curiosity to a commercially viable technology. In this chapter, we consider organic photovoltaics based on oligomers ("small molecules") which are deposited by vacuum sublimation. While the physics of the small molecule materials is in many ways very similar to those of polymer organic materials, there are significant differences in materials synthesis, processing, and device concepts. We review a few classes of small molecule solar cell materials and discuss their properties in devices. We discuss device concepts for small molecule organic solar cells, in particular pin devices based on doped transport layers and cascade designs. We point out the points where devices can be improved and describe paths to higher efficiencies, including multi-junction devices which can be very well realized with small molecule organic semiconductors.

Keywords Organic semiconductors · Solar cells · Oligomers · Small molecules · Doping · Mulitjunction

1.1 Introduction

There is no renewable energy technology, which comes even close to the potential of solar energy: The sun needs only 1 h to deliver what humankind needs in a year. The most elegant way to harvest this source is to directly convert sunlight into

T. Moench · C. Koerner · V.C. Nikolis · K. Vandewal · K. Leo (✉)
Dresden Integrated Center for Applied Physics and Photonic Materials (IAPP), TU Dresden, 01062 Dresden, Germany
e-mail: leo@iapp.de

T. Moench
Robert Bosch GmbH, Car Multimedia, Optics Development, 71226 Leonberg, Germany

C. Murawski · J. Murawski
School of Physics and Astronomy, University of St. Andrews, North Haugh, St Andrews KY16 9SS, UK

H. Tian et al. (eds.), *Molecular Devices for Solar Energy Conversion and Storage*, Green Chemistry and Sustainable Technology,
https://doi.org/10.1007/978-981-10-5924-7_1

entropy-free electrical energy using the photovoltaic effect. Solar cells based on that effect have seen a dramatic development in the past few years, mainly in cost reduction which has brought electrical energy generation prices well below grid prices.

This development is mainly based on silicon solar cells, a technology with so many disadvantages that its success may surprise. Silicon solar cells are rigid wafer-based cells produced at high temperatures with environmentally less benign materials. Furthermore, about half of the high-purity silicon is wasted when sawing the ingot into wafers.

Imagine in contrast an all-carbon technology, using 200 times less material, produced in highly efficient roll-to-roll tools at room temperature. Features like transparency and low weight are possible as well. Organic photovoltaics (OPV) is such a technology and could reduce energy prices by another order of magnitude and allows many applications not easily accessible for silicon, e.g., building integrated PV, in particular for windows where homogeneous transparency is required.

To make this dream come true, however, this all-carbon technology must meet the three criteria for photovoltaics, which are a sufficiently high efficiency, a long lifetime, and low cost. Currently, OPV fails in all three criteria. In this chapter, we discuss the technology, which is closest to meeting these criteria: organic photovoltaics based on oligomers ("small molecules") which are deposited by vacuum sublimation. The first reasonably efficient organic solar cells [1] were based on this principle and efficiencies have increased since then from around 1–13%.

In this chapter, we discuss the opportunities and challenges of this technology. In particular, we try to derive the main roadblocks on the way to higher efficiency, which turns out to be the most difficult hurdle to overcome.

In this introduction, we want to briefly review two issues: first, the key steps which led to efficiency improvements up to now and second, the reasons for choosing oligomers instead of polymers and for choosing vacuum processing versus liquid processing techniques.

We start with the second issue, being less a scientific subject but still important if one wants to direct research towards commercial application: Most of the original research on organic semiconductors was initially performed on highly doped metallic-like materials. Key breakthroughs in vapor-deposited small molecule technology were the papers by Tang et al. on organic solar cells [1] and light-emitting diodes [2]. Although polymer OLEDs were discovered a few years later [3] and initially researched much more intensively, this technology never achieved the commercial breakthrough. There are a few simple reasons why the technology path chosen by Tang became mainstream and being used today in many mobile phone displays and might even replace liquid crystal displays in television sets:

- Highly efficient and stable OLEDs are multilayer devices, with each layer serving a single function (electron and hole transport, emission, etc.). Multilayer devices can be easily prepared by vapor deposition, in contrast to liquid processing where sequential layer deposition is difficult and imposes restrictions on materials and processes.

- Small molecules are defined materials. There are no issues with polydispersity, as in polymers [4].
- Small molecules can be easily purified by physical methods such as sublimation.
- Structuring red, green and blue pixels by shadow mask evaporation is a simple technology which turned out to be reliable for not too large substrates.
- Disposal of solvents is in industrialized countries expensive and difficult.

For those reasons, research on polymer OLED has also almost disappeared. There are attempts to coat some of the small molecule OLED layers by wet processing, which might replace vacuum processing step-by-step.

Quite surprisingly, polymer solar cells drew the larger crowd again, till today. In terms of laboratory efficiency, both vacuum- and solution-processing based technologies are almost on par. The reasons why the vacuum-deposited small molecule solar cells do not outperform polymer solar cells as the case in OLED, are subtle but deserve at least some brief comments:

- In contrast to OLED, good transport is important in solar cells since recombination losses and series resistance affect the overall power conversion efficiency substantially. Polymers tend to have better transport properties in disordered films, allowing much thicker absorber layers, resulting in a higher absorption and thus higher currents.
- Recently, a number of well-performing, polymer near-infrared absorbers have been developed. For unknown reasons, such developments were not as successful for small molecule materials, up to date.
- Finally, another practical reason: vacuum coating requires more expensive tools, at least on the lab scale.

Despite these differences in processing, the key innovations which brought OPV from 1% to more than 10% were very similar and are described in the following:

- The breakthrough of Tang [1] was based on the donor–acceptor heterojunction, which allows to separate the tightly bound excitons in organic materials.
- Nevertheless, a planar heterojunction does not help much simply because excitons do not diffuse more than about 10 nm [5], much less than the absorption depth. A key invention was made by Hiramoto introducing the *bulk heterojunction* [6], where donor and acceptor are more or less intimately mixed. If the exciton does not reach the junction, bring the junction to the exciton. This allowed to harvest excitons from a much thicker layer which resulted in much higher photocurrents.
- Finally, new materials and structures were developed which covered a greater spectral range or moved the absorption edge closer to the thermodynamic optimum (which is at approx. 1.6 eV) [7]. In polymer cells, this was mostly achieved by developing efficient near-infrared absorbing materials [8], in small molecule solar cells, two or more cells were combined which is particularly easy if pin cells [9] are evaporated on top of each other.

All in all, these developments have led by now to photoconversion efficiencies of 10–13%. While this progress is impressive, it is not sufficient: there is a rule of thumb in thin-film photovoltaics that up-scaling will cause losses which reduce efficiency by a factor of 2/3 to 3/4, i.e. even 13% results in module efficiencies below 10% which is neither competitive with inorganic thin film, crystalline silicon, and the new photovoltaics shooting star: Organic–inorganic perovskites have reached efficiencies beyond 22% within an extremely short time span.

In the following review, we focus on vacuum processed small molecule devices, and discuss promising absorber material classes, morphology control, and device architectures. Since easy fabrication of multi-junction devices is a large advantage of vacuum processing over solution-processing, we discuss this particular device architecture in more detail. We further provide a physical understanding of the operating mechanisms of OPV, and of the efficiency limiting processes, and conclude with directions towards further efficiency increase.

1.2 Materials, Morphologies and Processing of Active Layers

1.2.1 Basic Principles of Organic Solar Cell Absorber Materials

To understand the peculiarities of small molecule organic solar cells, we briefly introduce the principles of how to assemble an organic molecular solid from isolated molecules in a bottom-up approach. Then, we proceed to explain the different organic solar cell architectures comprised of these molecular solids, such as the widely used bulk heterojunction and their operation, give an overview of different methods to influence the morphology, and present commonly used materials in organic solar cells.

Small molecule materials used in organic solar cells contain carbon atoms as an essential building block and have a molecular weight of usually less than 1000 amu [10]. Thus, small molecule materials contain approximately 100 atoms and are inherently more complex than atomic materials. Take for instance a molecule with 100 atoms comprised of four different elements. Even in this simple case a chemist can theoretically synthesize already 4 million different molecules. Based on the most important force between neutral organic molecules, the van der Waals force, one can form organic molecular solid crystal, associated with significant shifts in the energy levels, represented by the highest occupied molecular orbital (HOMO) and lowest occupied molecular orbital (LUMO). The evolution of this process is shown simplified in the energy diagram depicted in Fig. 1.1a.

The van der Waals forces that lead to the formation of a solid are characterized by a subtle interplay between intra- and intermolecular forces on different length scales [11–13]. Generally, these van der Waals forces are significantly weaker than

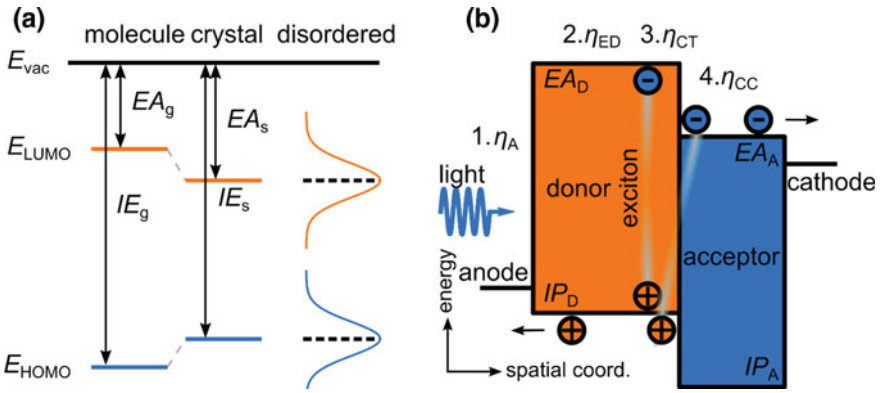

Fig. 1.1 Part **a** shows a simplified energy diagram of a molecule in gas phase (g), an organic molecular crystal, and a disordered organic material in solid state (s). The quantities EA and IP denote electron affinity and ionization potential as they are obtained from photoelectron spectroscopy. Part **b** shows the four step model explaining the overall efficiency of a donor/acceptor (D/A) heterojunction in terms of light absorption, photoexcitation, exciton dissociation, and charge extraction

metallic or ionic forces and lead to the formation of localized states on individual molecules rather than delocalized states as observed in inorganic semiconductors. Moreover, the comparably weak forces between organic molecules in combination with their inherent complexity have important consequences on order and disorder in the solid and as a consequence on the mechanical, optical, and electrical properties of organic solar cells. Here, we denote order as the existence of a single, stable conformation of a molecule which translates into a crystal lattice describing the entire solid without defects. However, as such a material may very well exist only theoretically, we want to briefly discuss the various origins of defects in organic molecular solids giving rise to disorder which have important consequences for the charge carrier transport [12, 14, 15].

Order at the molecular level is dominated by the symmetry, rigidity, and size of the molecule, by the regularity in monomer orientation, and by functional groups added to its backbone [16]. Due to the low symmetry of the molecules as building blocks of organic solid, molecular crystals tend to form lattices with the lowest symmetry, such as monoclinic and triclinic lattices. Furthermore, many organic materials show polymorphism, i.e., the coexistence of several lattice types which form in dependence of the preparation conditions. The energetic differences between these subforms are small, making it hard to predict the morphology from theoretical calculations.

Variations in rigidity, orientation, molecular conformation, and size of the molecule, as well as the steric hindrance of side groups in conjunction with local chemical variations result in disorder [17, 18]. Those defects combined with the relatively weak forces between molecules affect the packing in the organic solid and alter their optoelectronic properties as illustrated in Fig. 1.1a [19].

Organic solar cells are formed by sandwiching two different organic materials between two electrodes in a flat heterojunction (FHJ) as shown in Fig. 1.2 to form an organic solar cell which can convert photons into electrons [1].

In this configuration, the main light-absorbing material is usually the electron donor, whereas the other material acts as the electron acceptor. As shown in Fig. 1.1b, the acceptor material is characterized by a lower electron affinity (EA) and ionization energy (IP) compared to the donor material. To understand the process from light absorption to the extraction of charge carriers at electrodes, we discuss a 4-step efficiency model as shown Fig. 1.1b [20]. These steps are:

1. Illumination and absorption of photons by the materials of the heterojunction. The efficiency of this process is dependent on the wavelength (λ) and described by the absorption efficiency $\eta_A(\lambda)$.
2. Following the initial photon absorption, a strongly bound photoexcitation binding energy $E_{\mathrm{B;exc}} = 0.1–1$ eV is created on the donor molecule. In its lifetime ($\sim$ps to ns) the (Frenkel-)excition can diffuse to a heterointerface [21–23]. The exciton diffusion efficiency of this process can be described as $\eta_{Exc}(\lambda)$.

At an interface, the exciton may dissociate by the formation of a charge-transfer (CT) state at the donor–cceptor interface with efficiency $\eta_{CT}(T)$, where V denotes an externally applied voltage and T the system temperature. Here, the energy level offsets shown in Fig. 1.1b between the two materials provide a driving force to separate the CT state and, thus, justify the heterojunction architecture of the OSC. The dissociation of the CT state is usually explained by the Onsager–Braun theory, which gives the probability of charge carrier separation in an electric field as a function of their mutual separation and orientation of the electric field [20, 24].

3. Separation of charge carriers and transport to their respective electrodes takes place with the efficiency $\eta_{CC}(V,T)$. Note that charge carriers polarize the surrounding highly conjugated molecules forming a so-called polaron.

The product of all these efficiencies defines the external quantum efficiency EQE_{PV} of an organic solar cell:

$$EQE_{PV} = \eta_A(\lambda)\eta_{Exc}(\lambda)\eta_{CT}(T)\eta_{CC}(T,V),$$

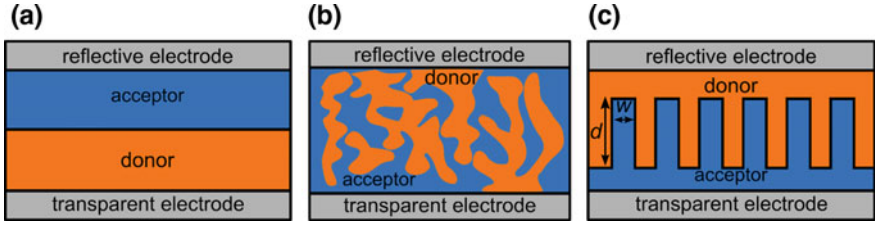

Fig. 1.2 Different geometries of organic solar cells. Part **a** show the flat heterojunction geometry, **b** the usually used bulk heterojunction, and **c** the ideal structured mixed heterojunction with the pillar width w and the diameter d

$$EQE_{PV} = \eta_A(\lambda) IQE_{PV}(\lambda, T, V),$$

$$EQE_{PV} = \frac{number\ of\ extracted\ electrons}{number\ of\ incident\ photons},$$

where IQE_{PV} is the internal quantum efficiency of the photovoltaic system, describing the ratio of the number of extracted electrons to the number of *absorbed* photons.

A major drawback of the flat heterojunction architecture is the low exciton diffusion length ($L_{\mathrm{D;exc}}$ is typically 10–40 nm), which provides an upper thickness limit for the two materials. One solution to compensate for the low exciton diffusion length is to co-deposit the materials to form a bulk heterojunction (BHJ) as shown in Fig. 1.2b instead of the sequential deposition that defines the flat heterojunction (FHJ). A major advantage of the bulk heterojunction architecture is its increased EQE_{PV} and thus overall power conversion efficiency compared to a FHJ OSC. However, major drawbacks of bulk heterojunction OSC are an increased technical effort during their manufacturing and lower control over the thin-film morphology due to the complex thermodynamics that are involved in its formation [25]: as the material growth in a BHJ is self-organized, it is completely ruled by thermodynamics and material specific properties such as their mutual wettability or steric compatibility. In practice, this results in different phase sizes, polymorphism (one famous example being carbon, that can either crystallize in graphite, diamond, or graphene), phase segregation, phase crystallinities, molecular orientations, etc., all of which results in energetic and structural disorder of the BHJ OSC that affects the overall device performance [5, 14, 24, 26–28]. However, the co-deposition of donor and acceptor materials ideally balances a plethora of challenges simultaneously such as

- maximizing the donor–acceptor interfacial area to separate all excitons.
- providing closed transport paths for the charge carriers to their respective electrodes.
- utilizing materials with broad, complementary absorption to harvest all photons.
- mean free charge carrier length in the range of the absorption length of the material to collect all charge carriers before they recombine.
- utilizing cheap, isotropic, and defect free/high purity materials available in large amounts.

A possible theoretical realization of this wish list is shown in Fig. 1.2c. Practically, methods like glancing angle deposition (GLAD), templating structures (epitaxy), evaporation rate tuning, liquid additives, donor–acceptor mixing ratio adjustments, and other specifically adapted vacuum deposition techniques are readily available to influence the morphology of the active, light-absorbing layer over a wide range of length scales from molecular orientation to chessboard-like arrays of nanopillars [29–32]. Available methods are:

- Substrate heating during co-deposition of the blend layer is one possibility to tune the morphology. Typical substrate temperatures are in the range of T_{sub} = 30–200 °C, attempting to increase the kinetic energy of the incoming vapor molecules on the surface without re-evaporation (desorption) from the surface. As a result, molecules of the active layer start to demix if deposited simultaneously, crystallize, tending to growth in larger aggregates and thus help to improve the OSC performance by increasing the donor–acceptor interface area [33–35].
- GLAD utilizes a tilted substrate where the substrate is not perpendicular to the incident vapor flux. Evaporation on a tilted substrate results in the nucleation of material on the surface where the growth nuclei on the surface act as a shadow masks and the region behind the nucleii will not receive any vapor. Thus, nanopillar-like structures start to grow at the nuclei [36]. With this technique, efficiency improvements around 30–40% have been achieved in comparison to the standard perpendicular geometry [37].
- Templating is a method to adjust the thin-film morphology of the active layer by inserting a suitable 1–2 ML thin organic or inorganic layer on the polycrystalline substrate (e.g. ITO) before depositing the active layer [38]. Ideally, a templating layer assists in controlling the morphology of the active layer in the OSC due to the strong interaction of the active layer materials with the template layer. Hence, the molecules should lay down on the template layer to enhance e.g. the transport and absorption perpendicular to the substrate by π–π-stacking. Typical template materials are CuI, PTCDA, graphene(-oxide), multithiophenes, etc. [39].
- Recently, co-evaporants have attracted attention as they facilitate increased active layer thicknesses, by increasing their crystallinity [40, 41]. Here, a third crucible with the co-evaporant is evaporated in addition to the active layer materials. Although a detailed understanding of the co-evaporant effect on the active layer morphology is still missing, this technique might be helpful in increasing the crystallinity of OSC processed on flexible substrates that might be otherwise susceptible to damage by substrate heating at too high temperatures.
- Solvent vapor annealing (SVA) utilizes solvent vapor to modify the active layer of OSCs without direct contact between the liquid solvent and the organic material. SVA utilizes the relatively low boiling point of organic solvents and the weak van der Waals force between the molecules of the thin film, which enables the vapor to reorganize the thin-film molecules by the diffusion into the layer [30]. Finally, SVA can assist the crystallization of organic thin films and thus improve efficiency of OSCs [42, 43]. In conclusion, SVA allows to change the thin-film morphology with relatively low effort and excellent suitability for large area processing. Moreover, the principles of SVA may be applicable to explain degradation of OSCs or the processes in related techniques such as the earlier mentioned co-evaporant approach.

Besides the various preparation options, it is clear that a thorough characterization of the donor–acceptor morphology, including their interfaces, surfaces,

and bulk structure, with various techniques is necessary to understand its impact on the OSC performance. Sensibly employed, the various characterization techniques shed light on specific relationships between the molecular structure, the active layer morphology and their processing conditions, as well as the OSC performance.

1.2.2 Materials Used for Small Molecule Solar Cells: An Overview

Small molecule OSCs processed in vacuum or from solution are used in the best-performing organic solar cells, reaching efficiencies up to 13.2% [44, 45]. Small molecules have significant advantages over their polymeric counterparts due to their well-defined molecular structure, high purity, well-defined molecular weight, and, thus, better morphological control [46]. However, the optoelectronic properties of small molecules strongly depend on their orientation relative to the substrate, which can for example significantly change energy levels of the organic molecules or the absorption of the films and thus affects the OSC performance [47].

During the last decades, a large number of small molecules with suitable absorption, energy levels, energy gap, etc. have been synthesized. However, the focus of research is on electron donating small molecules, since the electron-accepting molecule C_{60} has already shown outstanding electrical properties. Recently, sub-phtalocyanine based acceptor molecules in combination with multiple absorbers (cascades) reach efficiencies up to 8.4% [48]. In the following paragraphs, we briefly introduce a few commonly used donor molecules in organic solar cells.

1.2.2.1 Merocyanines

Merocyanines (MCs) are a material class with relatively high absorption, polarizability, and dipole moment that can be processed in vacuum or from solution depending on their functionalization [49]. Moreover, the MC structure is synthetically easily accessible which results in various molecular variations to shift energy levels and absorption [49, 50]. An extensive collection of different MC compounds used in OSCs can be found in Table 1.1 [50]. The molecule shown in Fig. 1.3 showed the highest reported *PCE* comprising a MC in the active layer with around 6.1% [51] when prepared in vacuum and 2:5% if the active layer is processed from solution with PCBM as acceptor instead of C_{60}. The efficiency differences mainly originate from higher short-circuit currents in the vacuum processed device which in turn originate from a more suitable morphology in the vacuum processed device [49]. However, this comparison shows that MCs exhibit high thermal stability and high solubility.

Table 1.1 Overview on HB194 electrical and photophysical properties

Physical quantity	HB194 (vacuum)	HB194 (solution)
$E_{HOMO;CV}$	−5:75 eV [49, 52]	
$E_{LUMO;CV}$	−3.6 eV [49, 52]	
$\lambda_{\vert,\vert max}$	616 nm [49, 52]	
$\varepsilon at \lambda_{\vert,\vert max}$	60300 $Lmol^{-1}\,cm^{-1}$ [49, 52]	
$\mu_{h,OFET}$	$5 \times 10^{-5}\,cm^2\,V^{-1}\,s^{-1}$ [49, 52]	
V_{oc}	0.96 V [51]	0.97 V [49, 50]
J_{sc}	12.647 mA cm^{-2} [51]	6.947 mA cm^{-2} [49, 50]
FF	0.47 [51]	0.32 [49, 50]
PCE	6.1% [51]	2.5% [49, 50]
I	100 mW m^{-2} [51]	88 mW m^{-2} [49, 50]

The BHJ OSCs are processed in vacuum and from solution

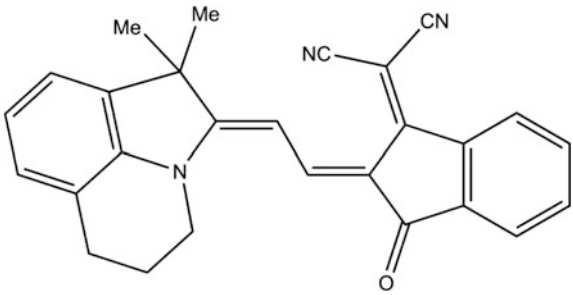

Fig. 1.3 Chemical structure of the donor MC derivative HB194, which is solution- and vacuum processable

1.2.2.2 Phtalocyanines (Pcs)

Metal phtalocyanines (MPcs see Fig. 1.4 M = (Zn, Co, Cu, Ni, Sn, Pb, Al, Fe, Mn, Mg, etc) and metal-free phtalocyanines have attracted much attention to organic electronics due to their high thermal stability and their synthetic versatility. Additionally, the more than 90 different Pcs are available in large quantities making them ideal candidates for low-cost organic electronics [53]. Their applications range from inks, infrared filters in (car) windows, OSCs, OFETs to spintronics [1, 54–56]. For vacuum processed OSCs, the most popular MPcs are ZnPc and CuPc due to their high absorption and their excellent thermal stability [34, 57, 58]. Due to their chemical versatility, few phtalocyanines can be processed from solution reaching efficiencies around 0:5% [59]. However, a limiting factor of MPc based OSCs are the relatively low V_{oc} as shown in Table 1.2 [60]. Increasing V_{oc} is achieved by fluorination of ZnPc, which lowers the *IP* [61, 62].

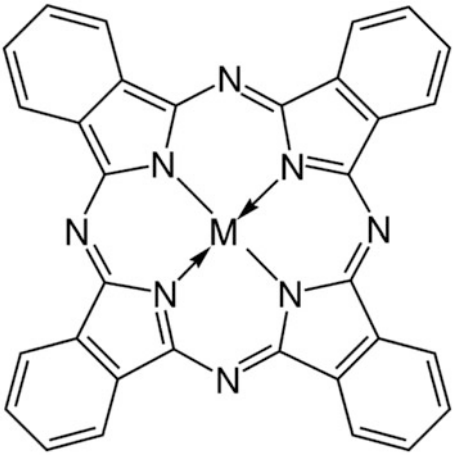

Fig. 1.4 Chemical structure of metal phtalocyanine

Table 1.2 Overview on photophysical and electrical material parameters of CuPc and ZnPc and their performance in BHJ OSC

Physical quantity	CuPc	ZnPc
$E_{HOMO;UPS}$	5:2 eV	5:0 eV to 5:4 eV [63, 64]
$E_{LUMO;IPES}$	3.5 eV	3.3 eV [65]
$\lambda_{\vert,\vert max}$	670 nm [66]	701 nm
$\varepsilon at \lambda_{\vert,\vert max}$	1.3×10^5 Lmol^{-1} cm^{-1} [66]	2.7×10^5 Lmol^{-1} cm^{-1} [66]
$\mu_{h,OFET}$		0.32 cm^2 V^{-1} s^{-1}
V_{oc}	0.58 V [18]	0.52 V [34]
j_{sc}	18.8 mA cm^{-2} [18]	10.3 mA cm^{-2} [34]
FF	0.85 [18]	0.57 [34]
PCE	3.6% [18]	3.0% [34]
I	150 mW m^{-2} [18]	100 mW m^{-2} [34]

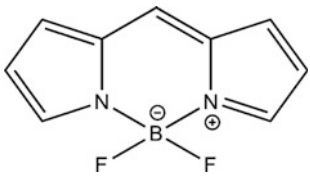

Fig. 1.5 The BODIPY core. A starting point for manifold functionalizations

1.2.2.3 Borondipyrromethenes (BODIPYs) and Derivatives

Borondipyrromethene (hereafter abbreviated as BODIPY) dyes have gained great interest in OSCs during the last years because of their high absorption coefficients, delocalized molecular orbitals and their excellent chemical and photostability as shown in [67]. As shown in Fig. 1.5, the tetrahedral boron atom of the BODIPY molecule is a starting node for functionalizations such as aza-BODIPY and

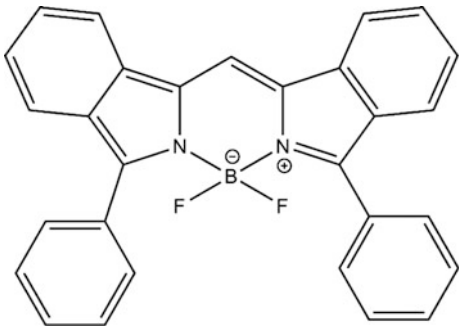

Fig. 1.6 Chemical structure of the IR absorber aza-BODIPY derivative Ph2-benz-BODIPY

Table 1.3 Overview on photophysical and electrical material parameters of aza-BODIPY and BDTT-BODIPY and their performance in BHJ OSC

Physical quantity	Ph2-benz-BODIPY	BDTT-BODIPY
$E_{HOMO;CV}$	−5:23 eV [71, 73]	−5.23 eV [72]
$E_{LUMO;CV}$	−3.65 eV [71, 73]	−3.72 eV [72]
$\lambda_{\vert,\vert max}$	715 nm [71, 73]	641 nm [72]
$\varepsilon at \lambda_{\vert,\vert max}$	106000 $Lmol^{-1}$ cm^{-1} [71, 73]	82000 $Lmol^{-1}$ cm^{-1} [72]
V_{oc}	0.81 V [71, 73]	0.98 V [72]
j_{sc}	8.0 mA cm^{-2}	10.55 mA cm^{-2} [72]
FF	0.85 [71, 73]	0.47 [72]
PCE	3.8%	4.75% [72]
I	100 mW m^{-2}	100 mW m^{-2} [72]

Note that the aza-BODIPY OSC is processed in vacuum, whereas the BDTT-BODIPY OSC is processed from solution with PC71BM instead of C60 for the vacuum device

BDTT-BODIPY [68]. Aza-BODIPYs compounds are promising BODIPY derivatives, absorbing in the NIR range to harvest photons at the low energy range of the solar spectrum, which makes them suitable for tandem devices [69–71].

The chemical structure of the vacuum processable BODIPY derivative Ph2-benz-BODIPY is shown in Fig. 1.6 (vacuum processed). A solution processable BODIPY derivative is BDTT-BODIPY that has reached efficiencies around 4.75% in BHJ OSC with PC71BM [72]. A comparison of their photophysical parameters and their efficiencies in BHJ OSC can be found in Table 1.3 (Fig. 1.7).

1.2.2.4 Diindenoperylene (DIP) and Derivatives

Diindenoperylene (DIP, see Fig. 1.8) and its derivatives belong to the family of perylenes and have gained attention in organic electronic devices like OLEDs due to their simple chemical structure and high charge carrier mobility. A major drawback of DIP is the low extinction coefficient and hence low photocurrent in OSC.

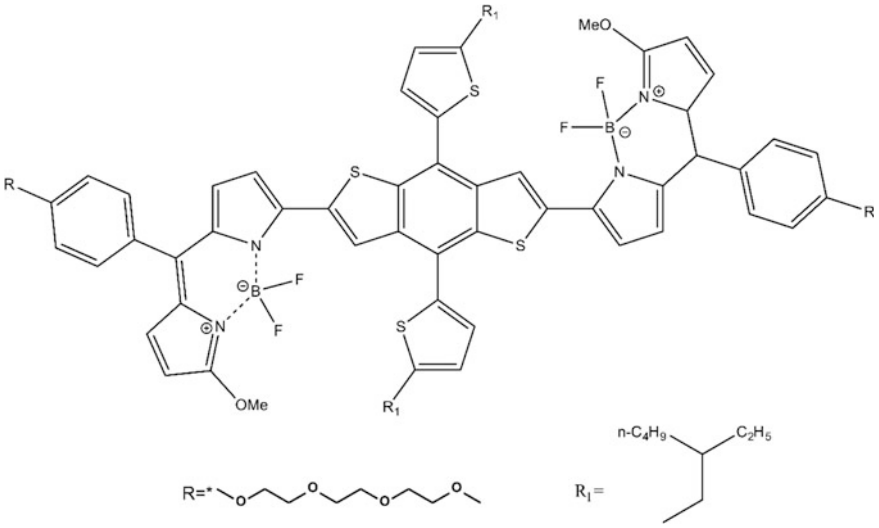

Fig. 1.7 Chemical structure of the solution processable donor molecule BDTT-BODIPY

Fig. 1.8 Chemical structure of the donor molecule DIP

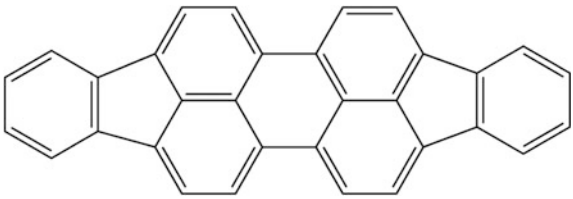

Due to the well-defined thin-film growth of DIP, it exhibits an exceptionally high excition diffusion length and charge carrier mobility as summarized in Table 1.4 [74, 75]. However, all those parameters are strongly dependent on the specific orientation of DIP on the substrate surface which in turn depends on the molecule–substrate interaction [74]. Thus, a dominating standing orientation (σ phase) of DIP molecules is observed on inert SiO_2 substrates if deposited at room temperature and elevated substrate temperatures, which is disadvantageous for OSC due to the weaker absorption of the upright as compared to the λ phase [74, 76].

A promising DIP derivative leading to PCEs around 7.9% with C70 as acceptor is the donor molecule tetraphenyl dibenzoperiflanthene (DBP) shown in Fig. 1.9 [77]. The higher PCE of DBP OSCs over DIP OSCs can be partly attributed to the significantly stronger absorption of DBP [78]. The increased absorption and, thus, PCE of DBP OSCs can be attributed to the rotatable phenyl side groups that facilitate in a horizontal orientation on the substrate surface. Hence, relatively thin OSCs can be processed, balancing the low exciton diffusion length as summarized in Table 1.4.

Table 1.4 Overview on photophysical and electrical material parameters of DIP and DBP and their footprint in BHJ OSC

Physical quantity	DIP	DBP
$E_{HOMO;UPS}$	−5.35 eV [79]	−5.4 to −5.33 eV [80, 81]
$E_{LUMO;IPES}$	−2.8 eV [79]	−3.15 eV [73]
$\lambda_{\vert,\vert max}$	555 nm [76]	
$\varepsilon at \lambda_{\vert,\vert max}$	65400 $Lmol^{-1}$ cm^{-1} [82, 83]	
$\mu_{h,OFET}$	1×10^{-2} cm^2 V^{-1} s^{-1} [83]	1×10^{-4} cm^2 V^{-1} s^{-1} [80, 84]
$\mu_{e,OFET}$	1×10^{-1} cm^2 V^{-1} s^{-1} [83]	
$L_{D,exc}$	100 nm [38]	9 nm [72]
V_{oc}	0.91 V [75]	0.92 V [77]
j_{sc}	8.4 mA cm^{-2} [75]	13.6 mA cm^{-2} [77]
FF	0.52 [75]	0.63 [77]
PCE	4.1% [75]	7.9% [77]
I	100 mW m^{-2} [75]	100 mW m^{-2} [77]

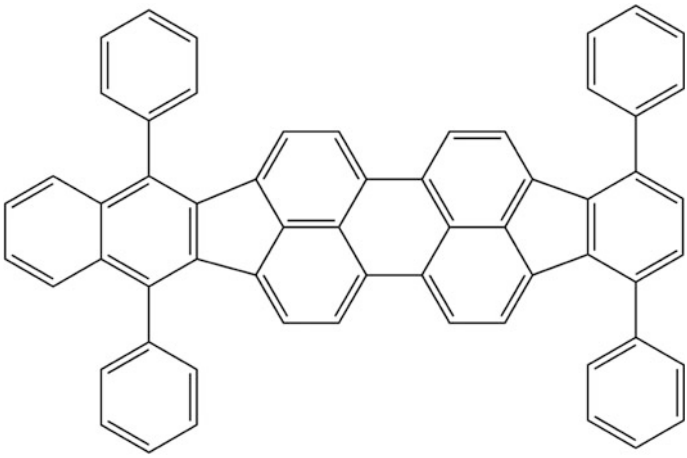

Fig. 1.9 Chemical structure of the DIP derivative DBP

1.2.2.5 Oligothiophenes

Many of the best-performing donor materials for OPV contain at least one thiophene ring. For a long time, poly-3-hexylthiophene (P3HT) was the working horse of polymer OPV research. The fame of oligo- and polythiophene materials originates in part from their previous application in thin-film transistors, yielding high hole mobilities, which is believed to be an essential part for high FF in OPV devices. Although the archetypical sexithiophene molecule a-6T has been used as donor, the efficiencies were not convincing. The problem lies in the weak

absorption due to the upright standing orientation and the strong crystallinity of the film causing extreme roughness [85]. The effect is used in previously developed cascade structures (see Sect. 1.3.3), but first measurements show that the intrinsic stability of α-6T morphology is critical to device lifetime [86].

In 2006, the first efficient small molecule oligothiophene-based OPV device that was substituted at both ends with a dicyanovinylene acceptor moiety was published. Through this electron-accepting substitution, the LUMO is shifted closer to the LUMO of C_{60}, enabling green to red absorber materials with little electron transfer losses. Furthermore, the A-D-A architecture allowed to separately modifying the HOMO and the LUMO to achieve high V_{oc} at low losses. The first material, DCV5T-Bu, showed an efficiency of 3.4%, which was outstanding at that time [87]. In the following, subtle variations to the backbone with varying length and alkyl substitution were performed to develop structure–property relationships for more directed synthesis of superior molecules. For vacuum deposition, all variations must consider the thermal stability of the molecules for later processing. For the backbone length, for example, this requirement limits the number of thiophene units to n = 1…6. The next leap in efficiencies was obtained in 2010 with a 4.9% efficient sexithiophene derivative [88] and 2011 with a 5.2% efficient DCV5T derivative [89]. Finally, the efficiency could be increased to 8.3% with a methyl-substituted DCV5T derivative [90, 91]. The EQE of this record device is shown in Fig. 1.10, demonstrating its photon-to-electron conversion efficiency over a large part of the solar spectrum. Table 1.5 exemplarily lists the important physical parameters of DCV6T-Bu and DCV5T-Me. One impressive fact for small molecules in general, but for those DCVnT materials in particular, is their strong absorptivity. The extinction coefficient of DCV5T-Me (k = 1.5) [92, 93] (see Fig. 1.10) is one of the highest ever reported for OPV donor materials. The abovementioned device contains only 26 nm of donor material in total, which is sufficient to absorb nearly 90% of the light in the absorption maximum. However, these thin absorber layers also illuminate the main weakness of these compounds: If the absorber layers are made thicker, the fill factors are suffering. This points to the fact that the transport properties of the material in the bulk heterojunction are still insufficient. If the mobilities could be significantly increased, absorber layers of approximately 100 nm could be realized and would allow significantly higher photocurrents, bringing the efficiency to values of 12% or above. It seems that it is significantly more difficult to produce layers with excellent transport properties by vacuum deposition than by solution-processing.

In contrast to those longer derivatives, compounds with three or four thiophene units in combination with C_{60} as acceptor were consistently inferior despite higher V_{oc} values. The reasons were extensively studied and are related to the competition of charge carrier generation with geminate recombination to strongly bound donor triplet excitons [94–97] or even energy-transfer to the acceptor instead of electron transfer [96, 98, 99]. Alkyl substitution always played the crucial role in determining the thin-film morphology. For three DCV4T derivatives, the highest efficiency was obtained for a regular two-dimensional brick wall-like stacking being superior to perfect one-dimensional pillars [100, 101]. Alkyl chains also turned out

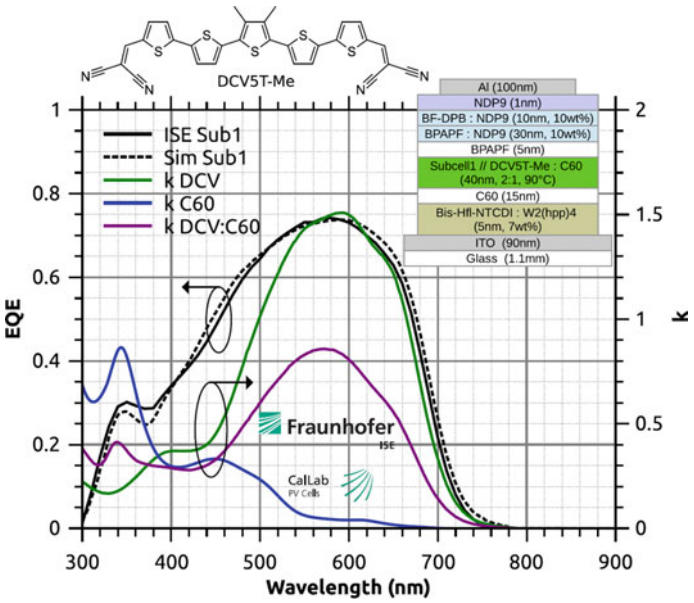

Fig. 1.10 Molecular structure of the donor material DCV5T-Me, EQE data of the optically optimized device (stack shown on the *top right*) in comparison to experimental data (certification by Fraunhofer ISE), and the extinction coefficients of the donor, the acceptor, and the blend (*right scale*). Reprinted with permission from Ref. [69]. Copyright 2016, American Institute of Physics

Table 1.5 Overview on photophysical and electrical material parameters of DCV5T-Me and DCV6T-Bu and their footprint in BHJ OSC

	DCV5T-Me	DCV6T-Bu
$E_{HOMO;CV}$	−5.66 eV	−5.25 eV
$E_{LUMO;CV}$	−3.75 eV	−3.58 eV
$\lambda_{abs,max}$	524 nm	513 nm
ϵ at $\lambda_{abs,max}$	63300 $Lmol^{-1}cm^{-1}$	
$\mu_{h,OFET}$	6.8×10^{-5} cm^2 V^{-1} s^{-1}	2.4×10^{-5} cm^2 V^{-1} s^{-1}
V_{oc}	0.96 V	0.88 V
j_{sc}	13.2 mA/cm^2	11.6 mA/cm^2
FF	0.66	0.57
PCE	8.3%	4.9%
I	100 mW/cm^2	118 mW/cm^2

to be an important means to prevent overly strong crystallization of the donor similar to α-6T. In the special case of DCV4T, strong phase separation and crystallization was observed in form of worm-like structures on the film surface upon film deposition on heated substrates [33], which is unfavorable for efficient devices. In contrast, such negative effects are weakened (shifted to higher substrate temperatures) [97, 102] or even absent in the case of alkyl chains. Substrate heating

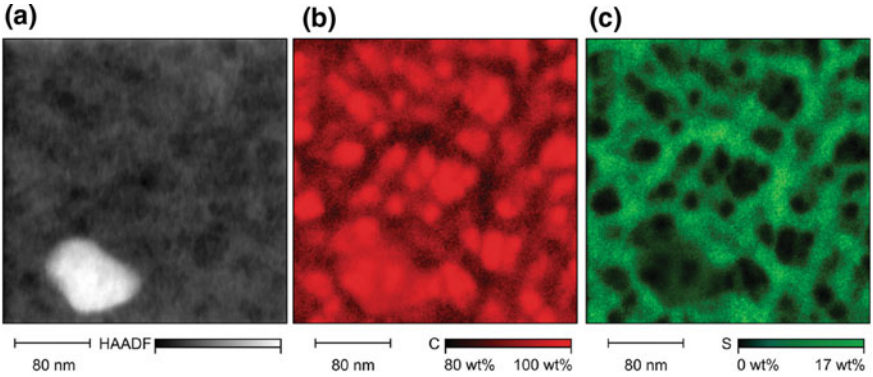

Fig. 1.11 STEM images of DCV5T-Me:C60 deposited at a substrate temperature of 80 °C. The STEM-HAADF image **a** is indicating an overall homogeneous sample thickness. The STEM-EDX images depicted in (**b**) and **c** show small C60 rich domains in a well-connected DCV5T-Me enriched network. Reproduced from Ref. [31] by permission of John Wiley & Sons Ltd.

usually leads to a moderate phase separation still allowing for efficient charge separation and extraction, giving higher j_{sc} and FF compared to non-heated devices [88, 97, 103, 104]. For the high-efficiency material DCV5T-Me, Moench et al. used electron microscopy methods with elemental contrast to reveal the nanoscale morphology of DCV5T-Me:C60 blend layers, consisting of a continuous network of both donor and acceptor phases with an ideal extension of 20–60 nm for the optimum substrate temperature (see Fig. 1.11). Higher temperatures are disadvantageous due to strong molecular aggregation and phase separation [31, 105].

In the meantime, a large variety of compounds has been synthesized and tested in devices also including variations of the acceptor moiety [106–110] and further variations on the oligothiophene backbone [107, 109, 111]. Similar compounds and variations were also tested with solution-processing, achieving up to 10.1% efficiency [44, 112–116]. However, the main difference arises from the combination with the stronger absorbing fullerene PC71BM, giving strong increase in the photocurrent in contrast to the much cheaper fullerene C_{60}. Extended information on the DCVnT materials is given in [92, 97]. A broad overview of oligothiophene and other small molecule materials is given in [117, 118].

1.2.2.6 Summary

To summarize the materials section, one should point out that the number of small molecule materials suitable for vacuum deposition which have been investigated in the past years is still rather small, in particular if one compares to the research on polymer compounds. While many of the materials achieve excellent properties in one of a few aspects, it has been difficult to create materials which excel in all photovoltaic parameters and combine this with qualities like stability or easy synthesis.

So far, the best results have been achieved by the thiophene compound class, which is also the basis for the commercial exploitation of small molecule solar cells by Heliatek. However, these substances still lack in transport properties in the bulk heterojunction, which leads to absorber layers which are much too thin. This is discussed in detail in Sect. 1.4.

1.3 Device Architectures

1.3.1 p-*i*-n *Solar Cells*

Although in principle a single absorber layer, containing a donor–acceptor interface in itself, is already sufficient for converting light into an electric current, there are several drawbacks to this minimalistic approach. Firstly, the exciton diffusion length in organic materials is usually limited to 5–30 nm [119]. This implies that an absorber layer with a thickness exceeding the exciton diffusion length to both sides of the donor–acceptor interface contains regions where the photogenerated excitons recombine before they reach the interface at which they can be separated. Secondly, if the absorber layer is in direct contact with metallic electrodes, excitons can be quenched at the semiconductor–metal interface. Furthermore, the deposition of the metal contact at high temperatures can lead to metal diffusion into the organic semiconductor or introduce unwanted trap states close to the interface [119, 120]. Lastly, absorption layers with an optical thickness smaller than quarter the absorption wavelength fail to benefit from constructive interference in the optical maximum [121].

Recombination may be avoided by assuring that all photogenerated excitons reach the donor–acceptor interface within their exciton diffusion length. However, this typically requires rather small absorber layer thicknesses, which may conflict with the optical requirements. To solve this problem, spacing layers may be introduced that serve the purpose of transporting charge carriers away from the absorption region. Thus, the absorber layer can be placed in the optical maximum, and the number of collected photons increases. The same solution ameliorates also the adverse effects of metallic electrodes on adjacent absorber layers.

Despite the many advantages that come with transport layers, the low mobility usually associated with organic semiconductors introduces significant Ohmic resistance in those layers and limits their practical thickness to little more than the exciton diffusion length [122]. Here, selectively doping the transport layers can easily extend their thickness to hundreds of nanometres.

1.3.2 How Does Doping Work?

Doping of organic semiconductors is comparable to doping in inorganic semiconductors in that a dopant is mixed into a host at a low concentration. This dopant can then either donate (*n*-doping) or accept (*p*-doping) an electron, thus increasing the host's charge carrier density by orders of magnitude.

The doping principle is illustrated in Fig. 1.12a. For *p*-doping, the dopant needs to provide a LUMO energy that is lower than the HOMO of the host, which enables electrons from the HOMO of the host to transfer to the dopant leaving a hole on the host. For *n*-doping, the reverse principle applies: the dopant provides a HOMO energy higher than the LUMO of the host so electrons can transfer from the HOMO of the dopant to the LUMO of the host.

The doping process itself takes two steps: First, the dopant transfers a charge carrier to the host (or vice versa) causing an ionization of the dopant. Second, the charge pair, which is still strongly bound by electrostatic forces, dissociates creating a free charge carrier on the host [123]. In contrast to their inorganic counterpart, doping concentrations of up to 10 wt% are employed in organic semiconductors. The doping efficiency—defined as ratio of free charge carriers to charged acceptor/donor ions—however is typically rather low.

The formation of space charge regions at the interface to the electrodes causes band bending [124]. This leads to efficient extraction of charge carriers from the device without a loss in voltage. Furthermore, the Fermi level in doped transport layers, which depends on the concentration of free charge carriers, is pinned to the respective transport level (i.e., HOMO for *p*-dopants and LUMO for *n*-dopants) [125, 126]. In the dark, the Fermi level is the same throughout the whole device. This causes a potential drop over the intrinsic layer, which gives rise to a built-in

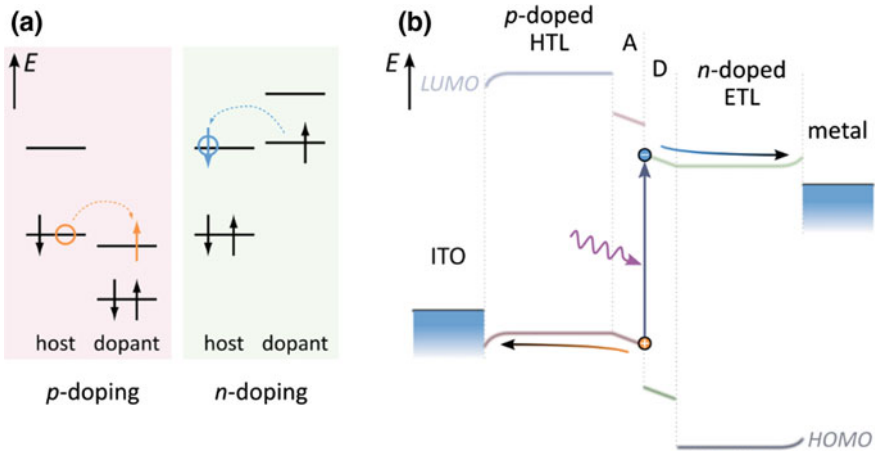

Fig. 1.12 **a** Sketch of the doping principle. **b** Band diagram of a p-i-n solar cell under forward bias

field. Besides its effects on the energy levels, doping increases the film conductivity by several orders of magnitude into the range of 10^{-3} S/cm, both for *p*- and *n*-doping [127, 128]. This makes extending the transport layer thicknesses to several 100 nm possible without adversely affecting charge carrier transport [121]. Finally, stacking the intrinsic absorber layer between a *p*- and an *n*-doped layer yields a so-called *p*-i-*n* solar cell (i.e., *p*-doped, intrinsic, *n*-doped), for which the band diagram is depicted in Fig. 1.12b.

1.3.2.1 Material Properties

Transport Materials

Transport materials need to simultaneously satisfy a number of demands. First, transport materials should feature a sufficiently high conductivity in order to minimize Ohmic losses. It is important to point out that due to the thin layers employed in organic solar cells, already small conductivities (in the range of 10^{-5} S/cm) suffice to generate only a negligible voltage drop across the transport layers [129]. Thus, already small doping concentrations can compensate for the comparably low mobility of charge carriers in organic materials.

Secondly, transport materials should avoid interfering with light collection; hence, materials with a band gap that is significantly wider than the absorption gap are required. Next, to ensure efficient transport of charge carriers away from the absorption region, the transport levels should align with the relevant energy levels of the absorber material (LUMO for electron and HOMO for hole transport). Furthermore, in order to maintain a high IQE, the interface between absorber and transport layers should block excitons from leaving the absorber; this is implicitly ensured when using transport materials with a wide band gap. Moreover, a high glass transition temperature of transport layers not only facilitates long operation hours but also allows for sufficiently high evaporation temperatures of the following layers and post-annealing without influencing the layer morphology. Lastly, if smooth film growth is of concern, it is paramount that transport layers themselves end with a smooth surface that remains invariant to heat or illumination since roughness translates into the following layers with detrimental effects such as short-circuits.

Commonly used hole transport materials are N,N,N′,N′-tetrakis (4-methoxyphenyl)-benzidine (MeO-TPD), N,N′-bis(9,9-dimethyl-fluoren-2-yl)-N, N′-diphenyl-benzidine (BF-DPB), and N,N′-diphenyl-N,N′-bis(4′-[N,N-bis(naphth-1-yl)-amino]-biphenyl-4-yl)-benzidine (Di-NPB) [130, 131]. For electron transport, *n*-doped C_{60} is often employed with the caveat of significant absorption in the ETL [132]. Transparent alternatives are for instance 1,4,5,8-naphthalenetetacarboxylic dianhydride (NTCDA) and 2,3,8,9,14,15-hexachloro-5,6,11,12,17,18-hexaaza-trinaphthylene (HATNA-Cl_6) [133, 134].

Dopants

Doped transport layers are typically formed by co-deposition of the host material with a dopant. Here, we distinguish two classes of dopants: molecular organic materials and metallic materials. Typical molecular organic *p*-dopants are tetracyano-quinodimethane (TCNQ) [135], its fluorinated version F_4-TCNQ [136], and the fluorinated Buckminster fullerene $C_{60}F_{36}$ [137]. Commonly used metallic complexes are metal halides such as $FeCl_3$ or CuI [138, 139], and metal oxides such as MoO_3 and WO_3 [140, 141].

Using photoelectron spectroscopy, Tietze et al. found doping efficiencies up to 36% for the *p*-dopant $C_{60}F_{36}$ in MeO-TPD at very low doping concentrations (<0.001 molar ratio), whereas commonly used concentrations lead to doping efficiencies below 10% [142]. This is explained by the presence of deep intragap states in the host, which need to be filled before free charge carriers can contribute to charge transport. On the other hand, doping concentrations of 4 mol% may already be sufficient to align the Fermi level of the doped organic layer with the electrode independent of the underlying substrate [126].

Compared to *p*-dopants, the number of known *n*-dopants is still rather limited because materials with very high energy levels tend to suffer from instability caused by oxidation [128]. Examples for materials used as *n*-dopants are alkali metals such as Li or Cs [143, 144], molecular materials such as bis(ethylenedithio)-tetrathiafulvalene (BEDT-TTF) or $W_2(hpp)_4$ and $Mo_2(hpp)_4$, where (hpp) is the anion of 1,3,4,6,7,8-hexahydro-2H-pyrimido[1,2-a]pyrimidine [145, 146], and precursor-type materials like pyronin B, 2-(2-Methoxyphenyl)-1,3-dimethyl-1H-benzoimidazol-3-ium iodide (o-MeO-DMBI-I), and 3,6-bis(dimethylamino)acridine (AOB), which can be handled in air and form the dopant only during layer deposition [147–149].

In the case of atomic dopants, an alternative fabrication process to co-deposition is the subsequent deposition of the dopant on top of the host. This technique is possible due to the strong diffusion of atomic dopants into the underlying layer. In the case of lithium as dopant, this results in effective doping of the host up to a thickness of 70 nm [144]. However, this diffusion property of the dopant through the underlying layers typically leads to a reduced device stability, roughens the surface, and deteriorates accurate doping concentrations [126, 128, 140]. As diffusion depends on size, molecular dopants are usually preferred over atomic dopants to minimize the aforementioned effects. Lastly, compared to organic compounds, metallic materials require much higher evaporation temperatures, which are more difficult to precisely control and can damage underlying layers.

Besides instability problems, both organic and inorganic dopants often introduce parasitic absorption. For instance, the absorption maximum of MoO_3 is located at around 480 nm [140], F4-TCNQ at 400 nm, and 1,3,4,5,7,8-Hexafluorotetracyanonaphthoquinodimethane (F6-TNAP) at 475 nm [150]. In order to avoid large absorption losses from those layers, the doping concentration should be kept as small as possible [151].

1.3.2.2 Maximizing Absorption with Thin-Film Optics

With the thickness of organic solar cells in the range of the absorption wavelength, thin-film optics needs to be considered to maximize efficiency. While thin transparent transport layers have long been used to position the absorber layer in the maximum of the electromagnetic field [119, 152], the thickness of those intrinsic layers is typically rather limited due to their low conductivity. Here, doped charge transport layers allow for adjusting layer thicknesses without introducing electrical losses. The strongest influence is the distance between the absorber and the reflecting metal electrode due to interference [132].

Figure 1.13 illustrates the influence of the short circuit current J_{sc} on the distance between absorber and reflective metal electrode. Varying the thickness of the transparent *n*-doped ETL HATNA-Cl_6, a variation in J_{sc} between 2 mA/cm^2 at 0 nm up to 8.5 mA/cm^2 at 50 nm thickness was observed [128]. Optical modeling using a transfer matrix method validates that the origin of this change indeed lies in the modified absorption. In addition, the solar cell efficiency was found to follow the trend of J_{sc} [133]. Note that the optical effect is even stronger when using transport layers that produce parasitic absorption. Therefore, not only widegap transport layers should be selected but also dopants with low absorption in the visible regime.

1.3.2.3 Application of Doped Transport Layers in Other Device Structures

Doped transport layers are not only applied in *p*-i-*n* solar cells but are also encountered in different configurations, such as *n*-i-*p*, M-i-*p*, M-i-*n*, and M-i-i (where M stands for metal) [132, 153]. One key advantage of doped transport layers is the possibility to stack two or more *p*-i-*n*-structures on top of each other

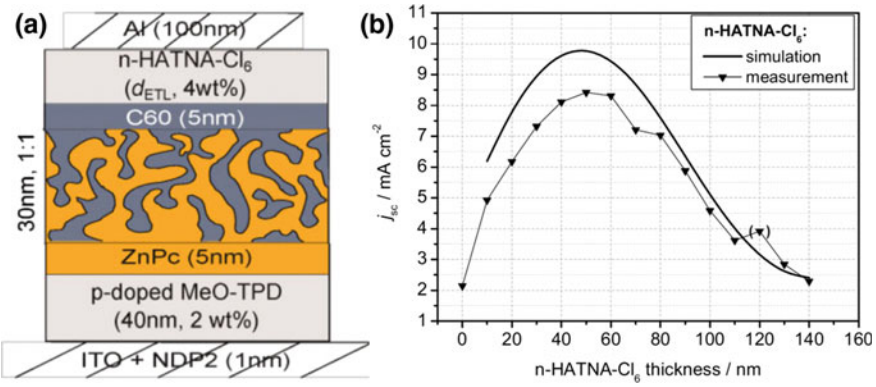

Fig. 1.13 Influence of distance between absorber layer and reflective electrode on the short circuit current J_{sc}. **a** Layer stack used for the investigation comprising an absorbing layer of ZnPc:C_{60} and a transparent n-doped ETL using HATNA-Cl_6 doped with the Novaled dopant NDN1. **b** J_{sc} as a function of the ETL thickness. Reproduced from Ref. [128] by permission of John Wiley & Sons Ltd.

(so-called tandem devices), which allows for stronger absorption and, thus, higher efficiency. Here, the high conductivity of the doped layers is necessary to avoid electrical losses upon charge extraction. In addition, the *pn* junction between two stacked devices enables efficient charge recombination, which is a key requirement for high efficiency in this configuration [154]. Although efficient charge recombination between two sub-cells may also be achieved using ultra-thin metal layers [155], the efficiency of the used metals depends on the specific organic layers. In addition, optical optimization of the layer thicknesses becomes even more important in tandem devices, where the position of two absorber layers needs to be fine-tuned. Here, doped transport layers bear a key advantage.

1.3.3 Cascade Designs

Using the donor–acceptor concept, organic solar cells traditionally employ two materials in their absorber layer. Ideally, these materials should absorb strongly, over a broad wavelength range and complementarily in order to harvest as many photons from the sun as possible. These requirements are not always easily fulfilled in standard bulk heterojunction pin devices, using donors combined with C_{60} as acceptor.

A simple solution is to incorporate additional photoactive materials in the absorber layer of the device, which contribute to the photocurrent either by charge-transfer or by intermolecular exciton energy-transfer. This type of organic solar cells is called cascade organic solar cells and in their simplest form, their absorber part comprises three sequentially deposited photoactive materials.

Besides broadening the spectral absorption range of the absorber stack, increasing the photocurrent, such layered cascades have an additional advantage, in the sense that recombination can be reduced and also the photo-voltage can be enhanced, given an appropriate choice of the stack sequence [156] (Fig. 1.14).

In principle, the energy levels of the materials must decrease monotonically towards the contacts in order to favor an unhindered and continuous charge transport. Considering the system as a standard donor–acceptor system, and depending on the way which the additional material (inserted as interlayer) arranges energetically, we can distinguish two basic cascade architectures: the energy-transfer cascade (ET-cascade), or the charge-transfer cascade (CT-cascade) [48, 157].

In charge-transfer cascade organic solar cells (CT-cascades), the addition of an interlayer between an electron donor and electron acceptor layer results the formation of two new charge generating heterojunctions. The material in the center position serves as acceptor to the outer donor material and as donor to the outer acceptor material, and therefore must be able to transport both electrons and holes efficiently. In this architecture, multiple charge generating-recombination interfaces exist and the open-circuit voltage is mainly determined by the interface with the lowest effective gap. If the outer layers of the tri-layer cascade are no more in

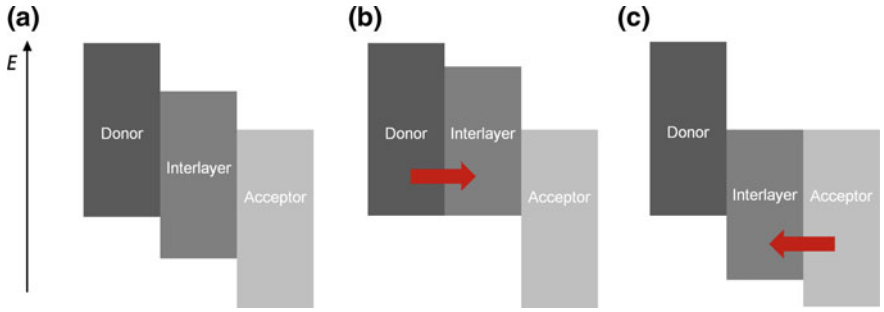

Fig. 1.14 Basic architectures for cascade organic solar cells consisting of 3 photoactive materials. **a** Charge-transfer cascade. **b** Donor-energy-transfer cascade. **c** Acceptor-energy-transfer cascade. The *red arrows* represent energy-transfer, and their direction follows the direction of the occurring energy-transfer mechanism

contact, the effective gap will exceed that of the outer layers [158]. In this way CT-cascades provide, apart from the absorption spectrum broadening, an increased open-circuit voltage.

In energy-transfer cascade organic solar cells (ET-cascades), a material with an aligned HOMO (or LUMO) with the donor (or the acceptor) material is added to the D–A stack. In contrast to the CT-cascade, the addition of the interlayer does not create an additional, electron donor–acceptor junction, and the open-circuit voltage of the device therefore remains unaffected. Instead, Förster resonant energy-transfer [48, 159] is exploited at either the donor or the acceptor side of the heterojunction (b and c), hereby funneling excitations to a single, efficient charge generating interface. For this process to be efficient, an overlap of the emission and the absorption spectra of the energy donating and accepting molecules is required [160].

Using the latter device architecture, Cnops et al. achieved in 2014 an efficiency of 8.4% [48], at the time the highest power conversion efficiency for a fullerene free device. The absorber consists of sequentially deposited alpha-sexithiophene, chloroboron subnaphthalocyanine (SubNc) and chloroboron subphthalocyanine (SubPc) layers, with energy-transfer taking place between SubPc and SubNc. This effectively broadens the exciton harvesting window in the region between 450 and 650 nm (Fig. 1.15).

Unfortunately, the lifetime of the α-6T/SubNc/SubPc cascade is with 330 h under glass–glass encapsulation extremely short, with α-6T the main degrading component. With commercial applications in mind, this short device lifetime necessitates the search for more stable materials suitable for cascade device architectures [86].

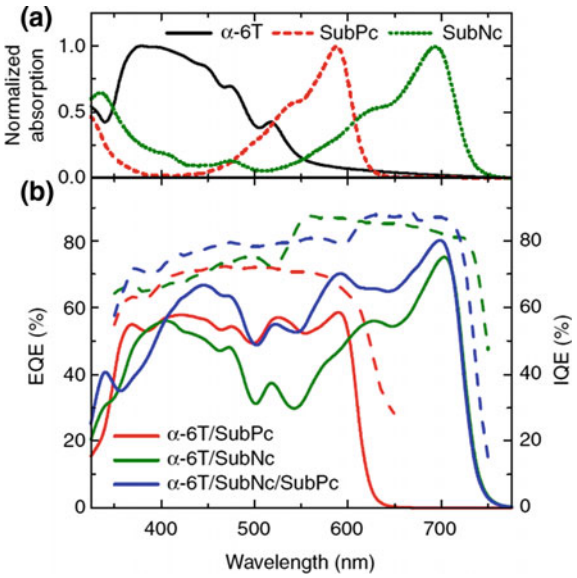

Fig. 1.15 Spectral response of the α-6T/SubNc/SubPc devices. **a** The absorption spectra of the three absorbers are complementary. **b** The EQE (*solid lines*) and IQE (*dashed lines*) spectra show efficient photocurrent generation by all three absorbing materials. As compared to the bilayers, photon harvesting in the tri-layer is significantly enhanced. Reprinted by permission from Macmillan Publishers Ltd.: Ref. [48]. Copyright 2014

1.4 Device Optimization

1.4.1 Optimizing Photocurrent

Once an exciton has reached the donor–acceptor interface, charge-transfer occurs and a CT state is formed [161, 162]. Ideally, CT states dissociate into free carriers, but CT state decay to the ground-state can still occur. The latter process is called geminate recombination, and is virtually absent in the best organic solar cells, where CT state dissociation is much faster than CT state decay [163].

The molecular and microstructural factors responsible for a fast dissociation process, avoiding geminate recombination are currently still under investigation. Charge delocalization over multiple donor or acceptor molecules packed in nano-crystallites or aggregates has been proposed to play an important role [164]. Furthermore the energy landscape at the donor–acceptor interface has been shown to be severely affected by the presence of donor–acceptor mixed amorphous phases in between aggregated phases of neat donor and acceptor, providing the energy gradients to drive charge separation [165, 166]. In both scenarios, aggregation of at least one blend component is crucial to avoid geminate recombination. However, such neat materials aggregates should be small enough (<10 nm) to ensure that excitons reach the charge generating donor–acceptor interfaces.

Once the photo-excitations are converted into free carriers, they have to reach the electrodes before recombining with a carrier of opposite sign. Next to losses due to geminate recombination, the photocurrent is thus determined by such non-geminate losses as well, i.e., the competition between free carrier transport and free carrier

recombination. Small film thicknesses ensure that carriers can reach the electrodes without recombining. However, for thin films, less photons are absorbed, hence an optimum film thickness exists, depending on the extinction coefficient of the absorber material, the carrier mobilities and the recombination rate.

Recently, Neher et al. derived an analytical expression for the current–voltage curves of pin photovoltaic devices under illumination and proposed a figure of merit [167].

$$\alpha = \frac{\sqrt{q}}{2k_B T} \frac{\sqrt{k}\sqrt{d^3}}{\mu} \sqrt{J_G} \tag{1.1}$$

Hereby is q the elementary charge, k_B the Boltzmann constant and T the temperature of the photovoltaic device. JG is the photocurrent when no recombination would take place, i.e., the photocurrent at large negative bias voltages, sweeping out all photogenerated free carriers. The balance between free charge recombination and extraction through is expressed through the dependence on the absorber thickness d, the bimolecular recombination rate constant k and the effective mobility $\mu = \sqrt{\mu_n \mu_p}$, i.e., the geometric mean of the electron mobility μ_n and hole mobility μ_p.

When α is smaller than 1, the photovoltaic device is no more transport-limited, and given no field-dependent geminate recombination, the fill factor (FF) will be high (Fig. 1.16).

For a certain donor–acceptor thin film, the requirement that α should be smaller than 1 to avoid transport limitations sets a maximum film thickness. For example, for rather common values [168] for the effective mobility $\mu = 10^{-4}$ cm^2 V^{-1} s^{-1} and a bimolecular recombination rate constant k = 10^{-11} cm^3 s^{-1} transport limitations under solar illumination are expected to already set in at a film thickness of about 30 nm. This thickness is in most cases not sufficiently high to absorb all above gap photons.

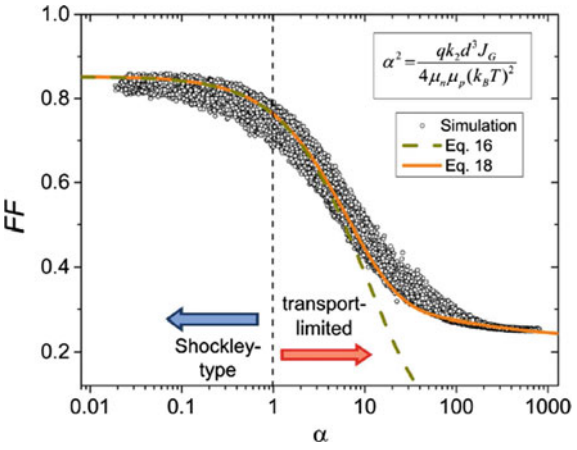

Fig. 1.16 Fill factor (FF) as a function of the dimensionless figure of merit α. *Open circles* are obtained via simulated JV-curves for devices with open-circuit voltages between 0.7 and 0.9 V. Photocurrents will become strongly transport-limited for α larger than 1, resulting in a progressive decrease of the FF when α increases beyond one

One of the currently best-performing polymer solar cells does absorb all solar photons above its gap and achieves a *FF* of 0.76 for 300 nm thick devices. This material has a mobility of 2×10^{-2} cm^2/V s. For strongly absorbing vacuum processed thin films, a thickness of 60 nm would be sufficiently high for a complete photon harvesting. Equation (1.1) allows us to estimate that, given an equal recombination rate, moderately high hole mobilities around 2×10^{-3} cm^2/V s would be needed to get a similarly high *FF* as for the best polymer solar cells, for a 60 nm small molecule absorber layer thickness.

While the in vacuum processed organic photovoltaics most commonly used acceptor C_{60} certainly has an electron mobility higher than this value, the hole mobility of vacuum-deposited donor: C_{60} blends material is often lower than this value [169]. Future work on manipulating the molecular packing or orientation by using substrate heating or molecular templating layers may increase the hole mobilities to these required values.

However, low mobility materials can in principle also overcome the transport limitation for optically thick devices, if the recombination rate constant k can be reduced. Since electron–hole recombination takes place at the donor–acceptor interface, a reduction of these recombination sites can for example be used to decrease k [170]. Equation (1.1) teaches us that a decrease in k by a factor 100 would allow a 10 times lower mobility. Hence, bilayer and cascade architectures with a reduced donor–acceptor contact area may have advantages in this respect, given sufficiently high exciton diffusion lengths.

1.4.2 Optimizing Photo-voltage

The low open-circuit voltage of OPV is one of its largest efficiency limiting factors. For example, DCV5T-Me:C_{60} a rather high V_{oc} material system (for small molecule OPV), yields power conversion efficiencies of up to 8.3%. Under solar illumination, it has a V_{oc} of 0.95 V, losing at least 0.7 eV of energy per incident photon. Crystalline Si on the other hand has an optical gap 1.1 eV, with a V_{oc} under solar illumination of 0.75 V, corresponding to less than half the voltage loss of OPV. Solving the voltage loss problem is a requirement for OPV to ever reach power conversion efficiencies close to those of their inorganic competitors.

At V_{oc}, all charge carriers recombine, and V_{oc} is therefore crucially determined by the properties of the recombining electronic state, which in the case of OPV is a CT state. A significant body of work links V_{oc} to interfacial or CT state properties, see [171–174]. Analytical expression for V_{oc} usually has the following form:

$$V_{oc} = E_g - \Delta_{CT} - \Delta_r^{rec} - \Delta_{nr}^{rec} \tag{1.2}$$

Hereby, E_g is the absorption onset of the blend component with the lowest optical gap. Δ_{CT} represents losses due to electron transfer from donor to acceptor or hole transfer from acceptor to donor. V_{oc} is further reduced by recombination losses,

and, as in inorganics, often distinction is made between losses due to radiative recombination Δ_r^{rec} and non-radiative losses Δ_{nr}^{rec}.

The charge-transfer losses Δ_{CT} constitute a loss mechanism inherent to OPV as they are not present in inorganic PV. A low Δ_{CT} requires a small energetic difference between the CT state and lowest excited state of the neat donor or acceptor material. Besides the frontier energy levels of donor and acceptor materials, also the crystallinity of the materials, as well as the dielectric environment affect the CT state energy [161].

Most donor–acceptor material systems for OPV have significant charge-transfer losses. However, careful tuning of the energy levels has recently yielded solution processed OPV with Δ_{CT} values of $\sim$0.1 eV and below [175–178]. Even more encouraging is that for some of these systems, a high free carrier yield is maintained despite the absence of a significant driving force for charge-transfer.

These findings make the recombination losses currently the limiting factor of the V_{oc} of OPV. These recombination losses depend linearly on the temperature T [173]. At room temperature, and under solar illumination, the experimentally determined recombination losses add up to about 0.6 eV for many donor: fullerene photovoltaic devices, with the non-radiative losses Δ_{nr}^{rec} constituting about 0.35 V [161]. The dominant non-radiative recombination pathways are currently unidentified, but the fact that they always result in a similar voltage loss for many material systems indicates that there might be an underlying mechanism, intrinsic to organic semiconductors responsible for this loss.

The radiative recombination losses Δ_{nr}^{rec} via CT states can however be decreased rather easily. Recently it has been shown that the amount of donor–acceptor contacts reduces this part of the voltage losses [170, 179]. Indeed, a reduction of sites available for recombination will increase the lifetime of the photo-induced charge carriers and thus their chemical potential, i.e., the photo-voltage. Therefore, the interface area between donor and acceptor materials should be large enough for all excitons reach the interface, but small enough to reduce free carrier recombination, hereby increasing V_{oc}.

1.4.3 Multi-junction Devices

Multi-junction devices are a promising concept to increase the efficiency of OSCs. These stacked devices circumvent the problem that the overall active layer thickness is limited by the relatively poor charge carrier transport and that only photons with energy larger than the energy gap can be absorbed. Thus, only a small fraction of the impinging light can be absorbed. The key idea of multi-junction devices is to compensate for the relatively poor charge carrier transport properties and their narrow but strong absorption bands, as compared to inorganic solar cells, by combining them into a multi-junction device to absorb the entire impinging sunlight and increase the overall device efficiency.

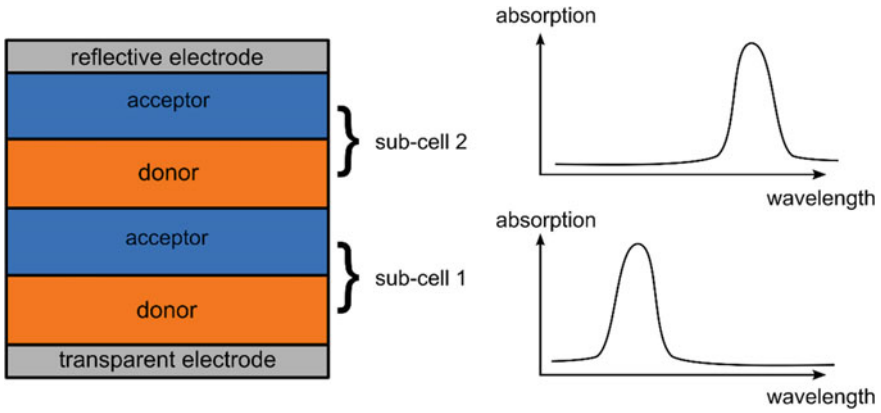

Fig. 1.17 Schematic structure of a (serial connected) multi-junction organic solar cell consisting of two sub-cells and their absorption spectra. The complementary absorption spectra enables the multi-junction to harvest more photons than the individual ones

As shown schematically in Fig. 1.17, a multi-junction OSC contains at least two sub-cells that should exhibit non-overlapping absorption bands to maximize absorption [180]. Technologically, the processing of multi-junction devices from vacuum deposition is highly attractive as the sub-cells can be directly processed on top of each other [181]. Electrically, the sub-cells are either connected in series (two terminal device) or parallel (three terminal device) as shown in Fig. 1.18. For both devices, the JV curve can be calculated by Kirchhoff's circuit laws.

Figure 1.18a shows a serially connected multi-junction device (pin-pin or nip-nip) with a recombination contact between the different sub-cells and two terminals.

The JV curve of a serially connected multi-junction device is shown in Fig. 1.19. As illustrated, to obtain the JV curve of the multi-junction device, the voltages of the sub-cells are added up at same short-circuit current. Moreover, as illustrated by the black line in Fig. 1.19, the short-circuit current of the multi-junction device is calculated by Kichhoffs first law. Thus, at short-circuit current condition of the multi-junction OSC sub-cell 1 is operated in backward direction, while sub-cell 2 is at forward bias. An example for a serial multi-junction device where an individual sub-cell current optimization is performed can be found in [91]. The JV and EQE sub-cell curves of an outdoor tested 10.4% serial multi-junction OSC are shown in Fig. 1.20. Since single DCV5T-Me OSC (J_{sc} = 13.2 mA/cm^2, V_{oc} = 0.96 V, FF = 66%), are very efficient in contrast to near-infrared absorbing single Tol2-benz-BODIPY (J_{sc} = 7.0 mA/cm^2, V_{oc} = 0.71 V, FF = 55%) or Ph2-benz-BODIPY (J_{sc} = 8.0 mA/cm^2, V_{oc} = 0.81 V, FF = 59%) OSC, it is necessary to match the currents between the serially connected sub-cells [69]. Hence, the authors distribute the current from the green absorbing DCV5T-Me sub-cell over three sub-cells as shown in Fig. 1.20a. To optimize the light-incoupling, the authors deposit a 130 nm layer of MgF_2 on the front side of the ITO-coated glass substrate.

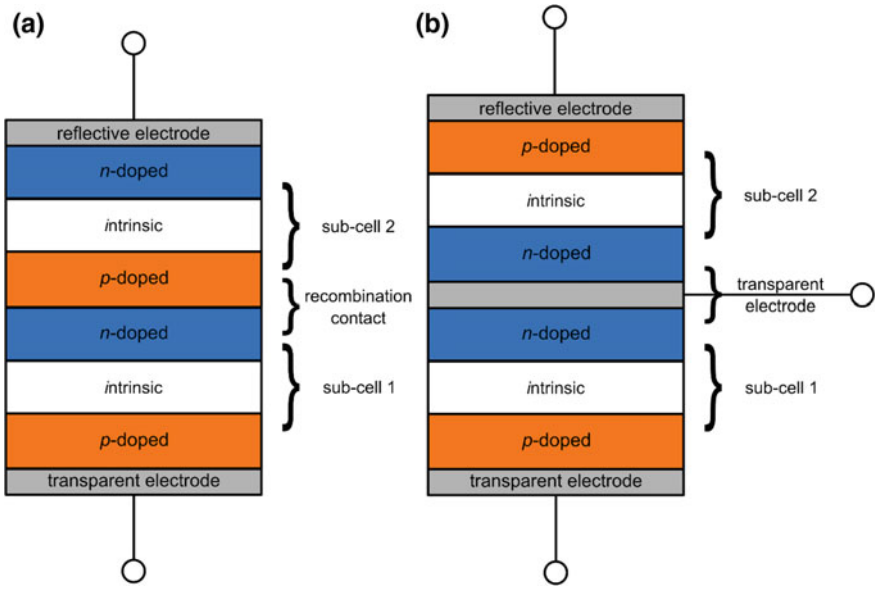

Fig. 1.18 Electrical connection of multi-junction OSC. Part **a** shows a serial connection of two pin OSC with a recombination contact in between. Part **b** shows a parallel device with a transparent electrode in between the two sub-cells (pin-nip)

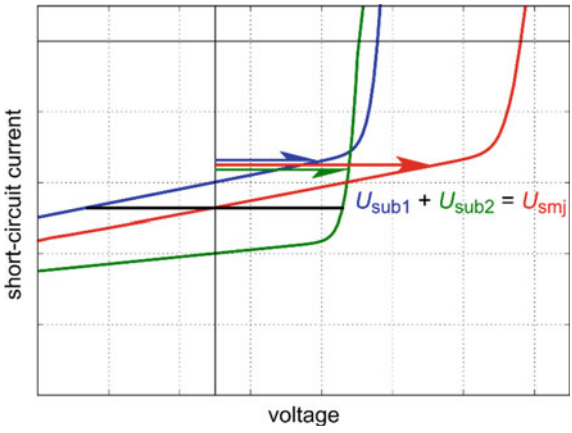

Fig. 1.19 A serial combination of the two sub-cells leads to a multi-junction solar cell. The *blue* and *green arrow* illustrates schematically how the voltages of the sub-cells (U_{sub1} and U_{sub2}) add up to the voltage of the serial multi-junction device (U_{smj}) at same short-circuit current

Moreover, they optimized the thicknesses of the doped transport layers and the sub-cells by a matrix transfer algorithm. As a result, the first sub-cell is located in the first optical field maximum and both other sub-cells in the second optical field maximum.

In view of practical applications, the multi-junction OSC are also tested under realistic outdoor condition where the sun light intensity varies from 5 to 100 mW/cm^2. In this configuration, the best multi-junction with Ph2-benz-BODIPY

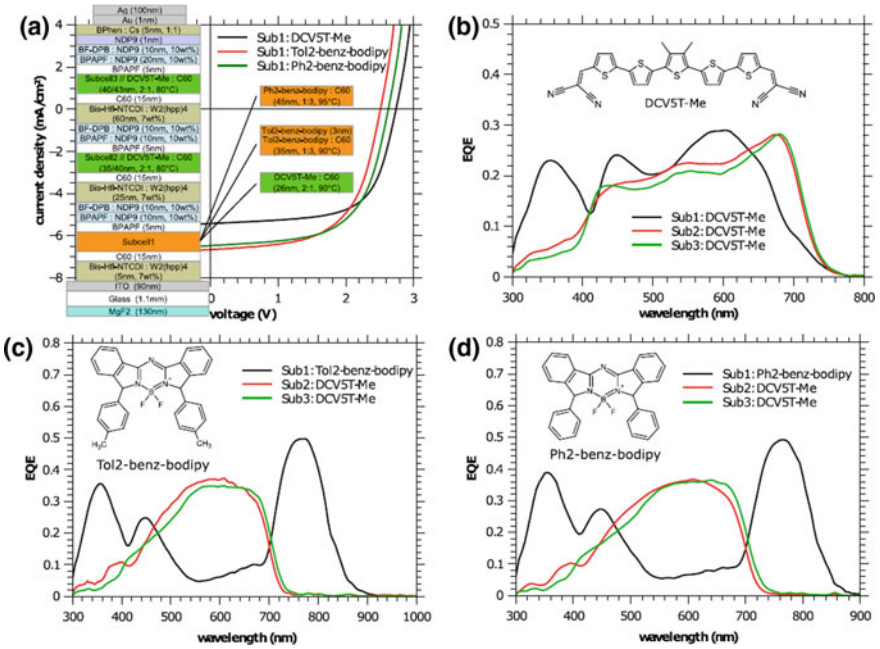

Fig. 1.20 **a** Shows the JV curve of three different material stacks used as sub-cell 1 to optimize the performance of a serial multi-junction OSC and the entire stack of the multi-junction. The sub-cell EQE of the DCV5T-Me OSC is shown in plot (**b**). The sub-cell EQE showing the OSC containing the BODIPY derivatives Tol2-benz-BODIPY and Ph2-benz-BODIPY are shown in (**c**) and (**d**). Reprinted with permission from Ref. [69]. Copyright 2016, American Institute of Physics

reaches 10.9% at low-light conditions around 10–20 mW/cm^2 in the lab and 11.2% in the outdoor test at similar illumination conditions. This superior low-light behavior demonstrates the practical applicability of multi-junction OSC as most countries are illuminated by average sun light intensities significantly lower than 100 mW/cm^2.

Figure 1.18b shows the schematic stack of parallel connected multi-junction device (pin-nip or nip-pin), where a third terminal is inserted between two sub-cells. This contact should have a high transmittivity to reduce parasitic absorptance and a high transverse conductance to maximize the extracted current. As illustrated in Fig. 1.21, the JV curve of a parallel multi-junction device is obtained by adding up the currents of the sub-cells under identical voltage conditions. At open-circuit voltage of the parallel multi-junction device opposing currents a flowing in the individual sub-cells. However, in contrast to serial multi-junction devices, parallel multi-junction devices are limited by their individual sub-cell voltages and not by current.

In conclusion, the multi-junction concept provides an elegant pathway to bypass material class specific weaknesses such as low mobility and narrow absorption

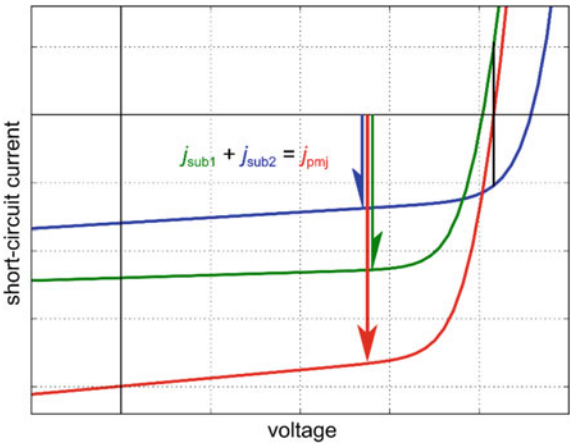

Fig. 1.21 Parallel connection of two sub-cells. The *blue* and *green arrow* illustrates schematically how the currents of the sub-cells (j_{sub1} and j_{sub2}) add up at same voltage to the overall multi-junction current (j_{mpj}). The *black line* indicates how the open-circuit voltage of the sub-cells add up to the open-circuit voltage of the multi-junction device

bands. A more detailed analysis of multi-junction devices and their proper characterization can be found in [180, 182, 183]. It should be mentioned that the easy realization of multilayer-stacks is a significant advantage for vacuum-deposited organic solar cells. Accordingly, the pilot products on the market are using this concept.

1.5 Conclusion

In this chapter, we have given a brief overview of recent developments in the field of organic solar cells using oligomers or the so-called small molecules. While the physics of the small molecule materials is in many ways very similar to those of polymer organic materials, there are significant differences in materials synthesis, processing, and device concepts.

- In synthesis, small molecule solar cells offer two main advantages: First, they allow to produce materials with defined molecular weight, a parameter which is less defined in polymers and can influence the morphology and thus the device properties significantly. Second, the small molecules can be easily purified by physical processes such as sublimation, allowing to reach high better defined purity levels.
- In processing, the main difference is that small molecule materials can usually be processed either by solution or by vapor deposition.
- In terms of device concepts, with small molecules and using vacuum deposition, it is very easy to produce even complex multilayer systems with arbitrary thickness and material sequence.

Whether these differences to polymers are overall an advantage or disadvantage is a matter of taste: The advantages of easier purification and defined deposition

even in multilayers have to be balanced against the additional cost caused by the more involved instrumentation needed for vacuum processing. One can learn from OLED industry that at least in the first wave of commercialization, the advantages of small molecule vacuum technology were overwhelming.

Interestingly, the large majority of academic research on organic solar cells has concentrated on polymer materials. As we have discussed, the variety of small molecule materials is rather limited, compared to the huge number of polymers which have been synthesized in the past few years. Nevertheless, the most efficient organic solar cells at the time of the writing (13.2% efficiency) are based on small molecule materials, it is not because individual cells are superior, but because multi-junction approaches work better than for polymer solar cells.

There are the challenges for the future: Simply said, a solar cell is current, voltage, and fill factor, and in all three parameters, small molecule solar cells are not where we would like them to have:

- Currents are too low, mainly because the active layer thickness is limited due to diffusion length and carrier transport problems. Results with solution processed small molecules show that the materials have the potential for layers sufficiently thick to absorb almost all sunlight, but in vacuum deposition, attempts to reach such large thicknesses (well above 100 nm) have failed so far. Unfortunately, there is no easy recipe to overcome this problem. Thus, research should explore many more materials classes and establish a better understand between molecular structure, thin-film morphology, and electronic properties. Unfortunately, directed research is difficult here since the relation between those quantities is complex.
- Voltages are too low as well: Currently, the best materials available lose about 0.6 V compared to the gap. Of those 0.6 V, about 0.3 V are basic thermodynamics and half of the voltages loss, related to non-radiative recombination, could in principle be avoided. Again, the key is in better understanding the factors controlling voltages, like discussed in this chapter.
- The fill factors of organic solar cells are also too low, mainly because of transport and recombination issues related to the first two points. However, compared to current and voltage, the fill factor losses are smaller and should be almost insignificant when the losses in current and voltage are reduced.

Acknowledgements We thank the many people who have been involved in the work which is presented in this Chapter. In particular, we thank Peter Bäuerle and his coworkers (University of Ulm) for preparation of the thiophene compounds. At IAPP, we thank Johannes Benduhn, Janine Fischer, Felix Holzmüller, Rico Meerheim, Moritz Riede, Reinhgard Scholz, Johannes Widmer, Max Tietze, and many more which cannot be named all here. We thank the Deutsche Forschungsgemeinschaft for their support in the framework of SPP 1355 “Organic Photovoltaics” and the BMBF for support in the “Innoprofile” framework.

References

1. Tang CW (1986) Two-layer organic photovoltaic cell. Appl Phys Lett 48:183. doi:10.1063/1.96937
2. Tang CW, VanSlyke SA (1987) Organic electroluminescent diodes. Appl Phys Lett 51:913
3. Burroughes JH, Bradley DDC, Brown AR, Marks RN, Mackay K, Friend RH, Burns PL, Holmes AB (1990) Light-emitting diodes based on conjugated polymers. Nature 347:539–541. doi:10.1038/347539a0
4. Himmelberger S, Vandewal K, Fei Z, Heeney M, Salleo A (2014) Role of molecular weight distribution on charge transport in semiconducting polymers. Macromolecules 47:7151–7157. doi:10.1021/ma501508j
5. Lunt RR, Giebink NC, Belak AA, Benziger JB, Forrest SR (2009) Exciton diffusion lengths of organic semiconductor thin films measured by spectrally resolved photoluminescence quenching. J Appl Phys 105:53711. doi:10.1063/1.3079797
6. Hiramoto M, Fujiwara H, Yokoyama M (1992) p-i-n like behavior in three-layered organic solar cells having a co-deposited interlayer of pigments. J Appl Phys 72:3781. doi:10.1063/1.352274
7. Würfel P (2009) Physics of solar cells: from basic principles to advanced concepts. Wiley-VCH
8. Zhao J, Li Y, Yang G, Jiang K, Lin H, Ade H, Ma W, Yan H (2016) Efficient organic solar cells processed from hydrocarbon solvents. Nat Energy 1:15027. doi:10.1038/nenergy.2015.27
9. Drechsel J, Männig B, Kozlowski F, Gebeyehu D, Werner A, Koch M, Leo K, Pfeiffer M (2004) High efficiency organic solar cells based on single or multiple PIN structures. Thin Solid Films 451–452:515–517. doi:10.1016/j.tsf.2003.11.044
10. (2004) Organic thin-film photodiodes
11. Israelachvili JN (2011) Intermolecular and surface forces. Academic Press, San Diego, Calif
12. Pope M (1999) Electronic processes in organic crystals and polymers, 2nd edn. Oxford University Press, New York
13. Silinsh E (1994) Organic molecular crystals: interaction, localization, and transport phenomena. American Institute of Physics, New York
14. Street R, Northrup J, Salleo A (2005) Transport in polycrystalline polymer thin-film transistors. Phys Rev B. doi:10.1103/PhysRevB.71.165202
15. Anderson PW (1958) Absence of diffusion in certain random lattices. Phys Rev 109:1492–1505. doi:10.1103/PhysRev.109.1492
16. Brédas J-L, Calbert JP, da Silva Filho DA, Cornil J (2002) Organic semiconductors: a theoretical characterization of the basic parameters governing charge transport. Proc Natl Acad Sci 99:5804–5809
17. Rivnay J, Mannsfeld SCB, Miller CE, Salleo A, Toney MF (2012) Determination of organic semiconductor microstructure from the molecular to device scale. Chem Rev 112:5488
18. Peumans P, Forrest SR (2001) Very-high-efficiency double-heterostructure copper phthalocyanine/C[sub 60] photovoltaic cells. Appl Phys Lett 79:126. doi:10.1063/1.1384001
19. Noriega-Manez RJ (2012) Chain conformation and disorder in high mobility semiconducting polymers: understanding charge transport in complex microstructures. Stanford University
20. Peumans P, Forrest SR (2004) Separation of geminate charge-pairs at donor–acceptor interfaces in disordered solids. Chem Phys Lett 398:27–31. doi:10.1016/j.cplett.2004.09.030
21. Gregg BA (2003) Excitonic solar cells. J Phys Chem B 107:4688–4698. doi:10.1021/jp022507x
22. Bässler H, Köhler A (2011) Charge transport in organic semiconductors. In: Metzger RM (ed) Unimolecular supramol. Electron. I. Springer, Berlin, Heidelberg, pp 1–65
23. Zhu X-Y, Yang Q, Muntwiler M (2009) Charge-transfer excitons at organic semiconductor surfaces and interfaces. Acc Chem Res 42:1779–1787. doi:10.1021/ar800269u

24. Braun CL (1984) Electric field assisted dissociation of charge transfer states as a mechanism of photocarrier production. J Chem Phys 80:4157. doi:10.1063/1.447243
25. Hinderhofer A, Schreiber F (2012) Organic-organic heterostructures: concepts and applications. ChemPhysChem 13:628–643. doi:10.1002/cphc.201100737
26. Bernstein J (2002) Polymorphism in molecular crystals. Oxford University Press, Oxford Clarendon Press, New York
27. Forrest SR (1997) Ultrathin organic films grown by organic molecular beam deposition and related techniques. Chem Rev 97:1793–1896. doi:10.1021/cr941014o
28. Kadish KM, Smith KM, Guilard R (2000) The porphyrin handbook. Academic Press, San Diego
29. Robbie K, Sit JC, Brett MJ (1998) Advanced techniques for glancing angle deposition. J Vac Sci Technol B 16:1115–1122
30. Rand BP, Cheyns D, Vasseur K, Giebink NC, Mothy S, Yi Y, Coropceanu V, Beljonne D, Cornil J, Brédas J-L, Genoe J (2012) The impact of molecular orientation on the photovoltaic properties of a phthalocyanine/fullerene heterojunction. Adv Funct Mater 22:2987–2995. doi:10.1002/adfm.201200512
31. Moench T, Friederich P, Holzmueller F, Rutkowski B, Benduhn J, Strunk T, Koerner C, Vandewal K, Czyrska-Filemonowicz A, Wenzel W, Leo K (2015) Influence of meso and nanoscale structure on the properties of highly efficient small molecule solar cells. Adv Energy Mater. doi:10.1002/aenm.201501280
32. Zhang Y, Diao Y, Lee H, Mirabito TJ, Johnson RW, Puodziukynaite E, John J, Carter KR, Emrick T, Mannsfeld SCB, Briseno AL (2014) Intrinsic and extrinsic parameters for controlling the growth of organic single-crystalline nanopillars in photovoltaics. Nano Lett 5547–5554. doi:10.1021/nl501933q
33. Koerner C, Elschner C, Miller NC, Fitzner R, Selzer F, Reinold E, Bäuerle P, Toney MF, McGehee MD, Leo K, Riede M (2012) Probing the effect of substrate heating during deposition of DCV4T:C_{60} blend layers for organic solar cells. Org Electron 13:623–631. doi:10.1016/j.orgel.2011.12.017
34. Pfuetzner S, Mickel C, Jankowski J, Hein M, Meiss J, Schuenemann C, Elschner C, Levin AA, Rellinghaus B, Leo K, Riede M (2011) The influence of substrate heating on morphology and layer growth in C60:ZnPc bulk heterojunction solar cells. Org Electron 12:435. doi:10.1016/j.orgel.2010.12.007
35. Schünemann C, Wynands D, Wilde L, Hein M, Pfützner S, Elschner C, Eichhorn K-J, Leo K, Riede M (2012) Phase separation analysis of bulk heterojunctions in small-molecule organic solar cells using zinc-phthalocyanine and C_{60}. Phys Rev B. doi:10.1103/PhysRevB.85.245314
36. Hawkeye MM, Brett MJ (2007) Glancing angle deposition: Fabrication, properties, and applications of micro- and nanostructured thin films. J Vac Sci Technol Vac Surf Film 25:1317. doi:10.1116/1.2764082
37. Li N, Forrest SR (2009) Tilted bulk heterojunction organic photovoltaic cells grown by oblique angle deposition. Appl Phys Lett 95:123309. doi:10.1063/1.3236838
38. Kurrle D, Pflaum J (2008) Exciton diffusion length in the organic semiconductor diindenoperylene. Appl Phys Lett 92:133306. doi:10.1063/1.2896654
39. Yang J, Yan D, Jones TS (2015) Molecular template growth and its applications in organic electronics and optoelectronics. Chem Rev 115:5570–5603. doi:10.1021/acs.chemrev.5b00142
40. Kaji T, Zhang M, Nakao S, Iketaki K, Yokoyama K, Tang CW, Hiramoto M (2011) Co-evaporant induced crystalline donor: acceptor blends in organic solar cells. Adv Mater 23:3320–3325. doi:10.1002/adma.201101305
41. Holzmueller F, Wilde L, Wölzl F, Koerner C, Vandewal K, Leo K (2015) Co-evaporant induced crystallization of zinc phthalocyanine:C60 blends for solar cells. Org Electron 27:133–136. doi:10.1016/j.orgel.2015.08.031

42. André MBJCWCCJJ (1997) Effects of solvent on the morphology and crystalline structure of lithium phthalocyanine thin films and powders. Thin Solid Films. doi:10.1016/s0040-6090(96)09087-6
43. Zimmerman JD, Xiao X, Renshaw CK, Wang S, Diev VV, Thompson ME, Forrest SR (2012) Independent control of bulk and interfacial morphologies of small molecular weight organic heterojunction solar cells. Nano Lett 12:4366–4371. doi:10.1021/nl302172w
44. Kan B, Li M, Zhang Q, Liu F, Wan X, Wang Y, Ni W, Long G, Yang X, Feng H, Zuo Y, Zhang M, Huang F, Cao Y, Russell TP, Chen Y (2015) A series of simple oligomer-like small molecules based on oligothiophenes for solution-processed solar cells with high efficiency. J Am Chem Soc 137:3886–3893. doi:10.1021/jacs.5b00305
45. Heliatek sets new organic photovoltaic world record efficiency of 13.2%
46. Lin Y, Li Y, Zhan X (2012) Small molecule semiconductors for high-efficiency organic photovoltaics. Chem Soc Rev 41:4245. doi:10.1039/c2cs15313k
47. Chen W, Huang H, Chen S, Huang YL, Gao XY, Wee ATS (2008) Molecular orientation-dependent ionization potential of organic thin films. Chem Mater 20:7017–7021. doi:10.1021/cm8016352
48. Cnops K, Rand BP, Cheyns D, Verreet B, Empl MA, Heremans P (2014) 8.4% efficient fullerene-free organic solar cells exploiting long-range exciton energy transfer. Nat Commun. doi:10.1038/ncomms4406
49. Kronenberg NM, Steinmann V, Bürckstümmer H, Hwang J, Hertel D, Würthner F, Meerholz K (2010) Direct comparison of highly efficient solution- and vacuum-processed organic solar cells based on merocyanine dyes. Adv Mater 22:4193–4197. doi:10.1002/adma.201000800
50. Kronenberg NM (2010) Organic bulk heterojunction solar cells based on merocyanine colorants. Universität zu Köln
51. Steinmann V, Kronenberg NM, Lenze MR, Graf SM, Hertel D, Meerholz K, Bürckstümmer H, Tulyakova EV, Würthner F (2011) Simple, highly efficient vacuum-processed bulk heterojunction solar cells based on merocyanine dyes. Adv Energy Mater 1:888–893. doi:10.1002/aenm.201100283
52. Bürckstümmer H, Kronenberg NM, Gsänger M, Stolte M, Meerholz K, Würthner F (2010) Tailored merocyaninedyes for solution-processed BHJ solar cells. J Mater Chem 20:240–243. doi:10.1039/B916181C
53. McKeown NB. Phthalocyanine materials: synthesis, structure and function. Cambridge University Press
54. Bao Z, Lovinger AJ, Dodabalapur A (1997) Highly ordered vacuum-deposited thin films of metallophthalocyanines and their applications in field-effect transistors. Adv Mater 9:42–44
55. Faulkner EB, Schwartz RJ (2009) High performance pigments. Wiley
56. Warner M, Din S, Tupitsyn IS, Morley GW, Stoneham AM, Gardener JA, Wu Z, Fisher AJ, Heutz S, Kay CWM, Aeppli G (2013) Potential for spin-based information processing in a thin-film molecular semiconductor. Nature 503:504–508. doi:10.1038/nature12597
57. Schünemann C, Elschner C, Levin AA, Levichkova M, Leo K, Riede M (2011) Zinc phthalocyanine—influence of substrate temperature, film thickness, and kind of substrate on the morphology. Thin Solid Films 519:3939–3945. doi:10.1016/j.tsf.2011.01.356
58. Tress W, Leo K, Riede M (2013) Dominating recombination mechanisms in organic solar cells based on ZnPc and C60. Appl Phys Lett 102:163901. doi:10.1063/1.4802276
59. Petritsch K, Friend RH, Lux A, Rozenberg G, Moratti SC, Holmes AB (1999) Liquid crystalline phthalocyanines in organic solar cells. Synth Met 102:1776–1777
60. Tietze ML, Tress W, Pfützner S, Schünemann C, Burtone L, Riede M, Leo K, Vandewal K, Olthof S, Schulz P, Kahn A (2013) Correlation of open-circuit voltage and energy levels in zinc-phthalocyanine: C_{60} bulk heterojunction solar cells with varied mixing ratio. Phys Rev B. doi:10.1103/PhysRevB.88.085119

61. Meiss J, Merten A, Hein M, Schuenemann C, Schäfer S, Tietze M, Uhrich C, Pfeiffer M, Leo K, Riede M (2012) Fluorinated zinc phthalocyanine as donor for efficient vacuum-deposited organic solar cells. Adv Funct Mater 22:405–414. doi:10.1002/adfm.201101799
62. Brendel M, Krause S, Steindamm A, Topczak AK, Sundarraj S, Erk P, Höhla S, Fruehauf N, Koch N, Pflaum J (2015) The effect of gradual fluorination on the properties of F_nZnPc thin films and F_nZnPc/C_{60} bilayer photovoltaic cells. Adv Funct Mater 25:1565–1573. doi:10.1002/adfm.201404434
63. Hein C, Mankel E, Mayer T, Jaegermann W (2010) Engineering the electronic structure of the ZnPc/C_{60} heterojunction by temperature treatment. Sol Energy Mater Sol Cells 94:662–667. doi:10.1016/j.solmat.2009.10.022
64. Tietze ML (2014) Molecular doping processes in organic semiconductors investigated by photoelectron spectroscopy. TU Dresden
65. Gao W, Kahn A (2002) Electronic structure and current injection in zinc phthalocyanine doped with tetrafluorotetracyanoquinodimethane: interface versus bulk effects. Org Electron 3:53–63
66. Ghani F, Kristen J, Riegler H (2012) Solubility properties of unsubstituted metal phthalocyanines in different types of solvents. J Chem Eng Data 57:439–449. doi:10.1021/je2010215
67. Loudet A, Burgess K (2007) BODIPY dyes and their derivatives: syntheses and spectroscopic properties. Chem Rev 107:4891–4932. doi:10.1021/cr078381n
68. Rousseau T, Cravino A, Bura T, Ulrich G, Ziessel R, Roncali J (2009) BODIPY derivatives as donor materials for bulk heterojunction solar cells. Chem Commun 1673. doi:10.1039/b822770e
69. Meerheim R, Körner C, Oesen B, Leo K (2016) 10.4% efficient triple organic solar cells containing near infrared absorbers. Appl Phys Lett. doi:10.1063/1.4943653
70. Mueller T, Gresser R, Leo K, Riede M (2012) Organic solar cells based on a novel infrared absorbing aza-bodipy dye. Sol Energy Mater Sol Cells 99:176–181. doi:10.1016/j.solmat.2011.11.006
71. Gresser R, Hummert M, Hartmann H, Leo K, Riede M (2011) Synthesis and characterization of near-infrared absorbing benzannulated Aza-BODIPY dyes. Chem Eur J 17:2939–2947. doi:10.1002/chem.201002941
72. Xiao L, Wang H, Gao K, Li L, Liu C, Peng X, Wong W-Y, Wong W-K, Zhu X (2015) A-D-A type small molecules based on boron dipyrromethene for solution-processed organic solar cells. Chem Asian J 10:1513–1518. doi:10.1002/asia.201500382
73. Kraner S, Widmer J, Benduhn J, Hieckmann E, Jägeler-Hoheisel T, Ullbrich S, Schütze D, Sebastian Radke K, Cuniberti G, Ortmann F, Lorenz-Rothe M, Meerheim R, Spoltore D, Vandewal K, Koerner C, Leo K (2015) Influence of side groups on the performance of infrared absorbing aza-BODIPY organic solar cells: performance of IR absorbing aza-BODIPY organic solar cells. Phys Status Solidi 212:2747–2753. doi:10.1002/pssa.201532385
74. Dürr AC, Nickel B, Sharma V, Täffner U, Dosch H (2006) Observation of competing modes in the growth of diindenoperylene on SiO_2. Thin Solid Films 503:127–132. doi:10.1016/j.tsf.2005.11.115
75. Wagner J, Gruber M, Hinderhofer A, Wilke A, Bröker B, Frisch J, Amsalem P, Vollmer A, Opitz A, Koch N, Schreiber F, Brütting W (2010) High fill factor and open circuit voltage in organic photovoltaic cells with diindenoperylene as donor material. Adv Funct Mater 20:4295–4303. doi:10.1002/adfm.201001028
76. Schünemann C (2012) Organic small molecules: correlation between molecular structure, thin film growth, and solar cell performance. Technische Universität Dresden
77. Griffith OL, Liu X, Amonoo JA, Djurovich PI, Thompson ME, Green PF, Forrest SR (2015) Charge transport and exciton dissociation in organic solar cells consisting of dipolar donors mixed with C 70. Phys Rev B. doi:10.1103/PhysRevB.92.085404
78. Grob S (2016) Effect of morphology on molecular organic solar cells. PhD thesis

79. Yokoyama D, Qiang Wang Z, Pu Y-J, Kobayashi K, Kido J, Hong Z (2012) High-efficiency simple planar heterojunction organic thin-film photovoltaics with horizontally oriented amorphous donors. Sol Energy Mater Sol Cells 98:472–475. doi:10.1016/j.solmat.2011.10.014
80. Hirade M, Adachi C (2011) Small molecular organic photovoltaic cells with exciton blocking layer at anode interface for improved device performance. Appl Phys Lett 99:153302. doi:10.1063/1.3650472
81. New material concepts for organic solar cells
82. Karl N (2003) Charge carrier transport in organic semiconductors. doi:10.1016/s0379-6779(02)00398-3
83. Horlet M, Kraus M, Brütting W, Opitz A (2011) Diindenoperylene as ambipolar semiconductor: Influence of electrode materials and mobility asymmetry in organic field-effect transistors. Appl Phys Lett 98:233304. doi:10.1063/1.3598423
84. Boukhili W, Mahdouani M, Bourguiga R, Puigdollers J (2016) Temperature dependence of the electrical properties of organic thin-film transistors based on tetraphenyldibenzoperiflanthene deposited at different substrate temperatures: experiment and modeling. Microelectron Eng 150:47–56. doi:10.1016/j.mee.2015.11.006
85. Sakai J, Taima T, Saito K (2008) Efficient oligothiophene:fullerene bulk heterojunction organic photovoltaic cells. Org Electron 9:582–590. doi:10.1016/j.orgel.2008.03.008
86. Bormann L, Nehm F, Weiß N, Nikolis VC, Selzer F, Eychmüller A, Müller-Meskamp L, Vandewal K, Leo K (2016) Degradation of sexithiophene cascade organic solar cells. Adv Energy Mater 6:1502432. doi:10.1002/aenm.201502432
87. Schulze K, Uhrich C, Schüppel R, Leo K, Pfeiffer M, Brier E, Reinold E, Bäuerle P (2006) Efficient vacuum-deposited organic solar cells based on a new low-bandgap oligothiophene and fullerene C60. Adv Mater 18:2872–2875. doi:10.1002/adma.200600658
88. Wynands D, Levichkova M, Leo K, Uhrich C, Schwartz G, Hildebrandt D, Pfeiffer M, Riede M (2010) Increase in internal quantum efficiency in small molecular oligothiophene:C [sub 60] mixed heterojunction solar cells by substrate heating. Appl Phys Lett 97:73503. doi:10.1063/1.3475766
89. Fitzner R, Reinold E, Mishra A, Mena-Osteritz E, Ziehlke H, Körner C, Leo K, Riede M, Weil M, Tsaryova O, Weiß A, Uhrich C, Pfeiffer M, Bäuerle P (2011) Dicyanovinyl-substituted oligothiophenes: structure-property relationships and application in vacuum-processed small molecule organic solar cells. Adv Funct Mater 21:897–910. doi:10.1002/adfm.201001639
90. Fitzner R, Mena-Osteritz E, Mishra A, Schulz G, Reinold E, Weil M, Körner C, Ziehlke H, Elschner C, Leo K, Riede M, Pfeiffer M, Uhrich C, Bäuerle P (2012) Correlation of π-conjugated oligomer structure with film morphology and organic solar cell performance. J Am Chem Soc 134:11064–11067. doi:10.1021/ja302320c
91. Meerheim R, Körner C, Leo K (2014) Highly efficient organic multi-junction solar cells with a thiophene based donor material. Appl Phys Lett 105:63306. doi:10.1063/1.4893012
92. Körner C (2013) Oligothiophene materials for organic solar cells—photophysics and device properties. TU Dresden
93. Meerheim R, Körner C, Leo K (2014) Highly efficient organic multi-junction solar cells with a thiophene based donor material. Appl Phys Lett 105:63306. doi:10.1063/1.4893012
94. Koerner C, Ziehlke H, Gresser R, Fitzner R, Reinold E, Bäuerle P, Leo K, Riede M (2012) Temperature activation of the photoinduced charge carrier generation efficiency in quaterthiophene: C 60 mixed films. J Phys Chem C 116:25097–25105. doi:10.1021/jp307582a
95. Koerner C, Hein MP, Kažukauskas V, Sakavičius A, Janonis V, Fitzner R, Bäuerle P, Leo K, Riede M (2014) Correlation between temperature activation of charge-carrier generation efficiency and hole mobility in small-molecule donor materials. ChemPhysChem 15:1049–1055. doi:10.1002/cphc.201400030

96. Schueppel R, Schmidt K, Uhrich C, Schulze K, Wynands D, Brédas JL, Brier E, Reinold E, Bu H-B, Baeuerle P, Maennig B, Pfeiffer M, Leo K (2008) Optimizing organic photovoltaics using tailored heterojunctions: a photoinduced absorption study of oligothiophenes with low band gaps. Phys Rev B 77:85311. doi:10.1103/PhysRevB.77.085311
97. Koerner C, Ziehlke H, Fitzner R, Riede M, Mishra A, Bäuerle P, Leo K (2017) Dicyanovinylene-substituted oligothiophenes for organic solar cells. In: Leo K (ed) Elementary processes in organic photovoltaics. Springer International Publishing, pp 51–75
98. Schueppel R, Uhrich C, Pfeiffer M, Leo K, Brier E, Reinold E, Baeuerle P (2007) Enhanced photogeneration of triplet excitons in an oligothiophene-fullerene blend. ChemPhysChem 8:1497–1503. doi:10.1002/cphc.200700306
99. Ziehlke H, Fitzner R, Koerner C, Gresser R, Reinold E, Bäuerle P, Leo K, Riede MK (2011) Side chain variations on a series of dicyanovinyl-terthiophenes: a photoinduced absorption study. J Phys Chem A 115:8437–8446. doi:10.1021/jp203420m
100. Fitzner R, Elschner C, Weil M, Uhrich C, Körner C, Riede M, Leo K, Pfeiffer M, Reinold E, Mena-Osteritz E, Bäuerle P (2012) Interrelation between crystal packing and small-molecule organic solar cell performance. Adv Mater 24:675–680. doi:10.1002/adma.201104439
101. Schrader M, Fitzner R, Hein M, Elschner C, Baumeier B, Leo K, Riede M, Bäuerle P, Andrienko D (2012) Comparative study of microscopic charge dynamics in crystalline acceptor-substituted oligothiophenes. J Am Chem Soc 134:6052–6056. doi:10.1021/ja300851q
102. Levichkova M, Wynands D, Levin AA, Walzer K, Hildebrandt D, Pfeiffer M, Janonis V, Pranaitis M, Kažukauskas V, Leo K, Riede M (2011) Dicyanovinyl sexithiophene as donor material in organic planar heterojunction solar cells: Morphological, optical, and electrical properties. Org Electron 12:2243–2252. doi:10.1016/j.orgel.2011.09.022
103. Wynands D, Levichkova M, Riede M, Pfeiffer M, Baeuerle P, Rentenberger R, Denner P, Leo K (2010) Correlation between morphology and performance of low bandgap oligothiophene:C60 mixed heterojunctions in organic solar cells. J Appl Phys 107:14517. doi:10.1063/1.3271407
104. Ziehlke H, Burtone L, Koerner C, Fitzner R, Reinold E, Bäuerle P, Leo K, Riede M (2011) Increase of charge carrier lifetime in dicyanovinyl–quinquethiophene: fullerene blends upon deposition on heated substrates. Org Electron 12:2258–2267. doi:10.1016/j.orgel.2011.09.015
105. Mönch T (2015) Exploring nanoscale properties of organic solar cells. TU Dresden
106. Steinberger S, Mishra A, Reinold E, Levichkov J, Uhrich C, Pfeiffer M, Bäuerle P (2011) Vacuum-processed small molecule solar cells based on terminal acceptor-substituted low-band gap oligothiophenes. Chem Commun 47:1982. doi:10.1039/c0cc04541a
107. Steinberger S, Mishra A, Reinold E, Mena-Osteritz E, Müller H, Uhrich C, Pfeiffer M, Bäuerle P (2012) Synthesis and characterizations of red/near-IR absorbing A-D-A-D-A-type oligothiophenes containing thienothiadiazole and thienopyrazine central units. J Mater Chem 22:2701–2712. doi:10.1039/C2JM13285K
108. Mishra A, Uhrich C, Reinold E, Pfeiffer M, Bäuerle P (2011) Synthesis and characterization of acceptor-substituted oligothiophenes for solar cell applications. Adv Energy Mater 1:265–273. doi:10.1002/aenm.201100026
109. Steinberger S, Mishra A, Reinold E, Müller CM, Uhrich C, Pfeiffer M, Bäuerle P (2011) A-D-A-D-A-type oligothiophenes for vacuum-deposited organic solar cells. Org Lett 13:90–93. doi:10.1021/ol102603n
110. Fitzner R, Mena-Osteritz E, Walzer K, Pfeiffer M, Bäuerle P (2015) A-D-A-Type oligothiophenes for small molecule organic solar cells: extending the π-system by introduction of ring-locked double bonds. Adv Funct Mater 25:1845–1856. doi:10.1002/adfm.201404210
111. Löbert M, Mishra A, Uhrich C, Pfeiffer M, Bäuerle P (2014) Synthesis and characterization of benzo- and naphtho[2,1-b:3,4-b′]dithiophene-containing oligomers for photovoltaic applications. J Mater Chem C 2:4879. doi:10.1039/c4tc00335g

112. Yin B, Yang L, Liu Y, Chen Y, Qi Q, Zhang F, Yin S (2010) Solution-processed bulk heterojunction organic solar cells based on an oligothiophene derivative. Appl Phys Lett 97:23303. doi:10.1063/1.3460911
113. Weidelener M, Wessendorf CD, Hanisch J, Ahlswede E, Götz G, Lindén M, Schulz G, Mena-Osteritz E, Mishra A, Bäuerle P (2013) Dithienopyrrole-based oligothiophenes for solution-processed organic solar cells. Chem Commun 49:10865. doi:10.1039/c3cc46066e
114. Wessendorf CD, Schulz GL, Mishra A, Kar P, Ata I, Weidelener M, Urdanpilleta M, Hanisch J, Mena-Osteritz E, Lindén M, Ahlswede E, Bäuerle P (2014) Efficiency improvement of solution-processed dithienopyrrole-based A-D-A oligothiophene bulk-heterojunction solar cells by solvent vapor annealing. Adv Energy Mater 4:1400266. doi:10.1002/aenm.201400266
115. Schulz GL, Urdanpilleta M, Fitzner R, Brier E, Mena-Osteritz E, Reinold E, Bäuerle P (2013) Optimization of solution-processed oligothiophene:fullerene based organic solar cells by using solvent additives. Beilstein J Nanotechnol 4:680–689. doi:10.3762/bjnano.4.77
116. Schulz GL, Löbert M, Ata I, Urdanpilleta M, Lindén M, Mishra A, Bäuerle P (2015) Functional tuning of A-D-A oligothiophenes: the effect of solvent vapor annealing on blend morphology and solar cell performance. J Mater Chem A 3:13738–13748. doi:10.1039/C5TA02877A
117. Chen Y, Wan X, Long G (2013) High performance photovoltaic applications using solution-processed small molecules. Acc Chem Res 46:2645–2655. doi:10.1021/ar400088c
118. Malytskyi V, Simon J-J, Patrone L, Raimundo J-M (2015) Thiophene-based push–pull chromophores for small molecule organic solar cells (SMOSCs). RSC Adv 5:354–397. doi:10.1039/C4RA11664J
119. Peumans P, Yakimov A, Forrest SR (2003) Small molecular weight organic thin-film photodetectors and solar cells. J Appl Phys 93:3693–3723. doi:10.1063/1.1534621
120. Owens DW, Aldao CM, Poirier DM, Weaver JH (1995) Charge transfer, doping, and interface morphologies for Al-C60. Phys Rev B 51:17068–17072. doi:10.1103/PhysRevB.51.17068
121. Furno M, Meerheim R, Hofmann S, Lüssem B, Leo K (2012) Efficiency and rate of spontaneous emission in organic electroluminescent devices. Phys Rev B 85:115205. doi:10.1103/PhysRevB.85.115205
122. Peumans P, Uchida S, Forrest SR (2003) Efficient bulk heterojunction photovoltaic cells using small-molecular-weight organic thin films. Nature 425:158. doi:10.1038/nature01949
123. Pahner P, Kleemann H, Burtone L, Tietze ML, Fischer J, Leo K, Lüssem B (2013) Pentacene Schottky diodes studied by impedance spectroscopy: doping properties and trap response. Phys Rev B 88:195205. doi:10.1103/PhysRevB.88.195205
124. Blochwitz J, Fritz T, Pfeiffer M, Leo K, Alloway DM, Lee PA, Armstrong NR (2001) Interface electronic structure of organic semiconductors with controlled doping levels. Org Electron 2:97–104. doi:10.1016/S1566-1199(01)00016-7
125. Pfeiffer M, Leo K, Zhou X, Huang JS, Hofmann M, Werner A, Blochwitz-Nimoth J (2003) Doped organic semiconductors: Physics and application in light emitting diodes. Org Electron 4:89–103. doi:10.1016/j.orgel.2003.08.004
126. Olthof S, Tress W, Meerheim R, Lüssem B, Leo K (2009) Photoelectron spectroscopy study of systematically varied doping concentrations in an organic semiconductor layer using a molecular p-dopant. J Appl Phys 106:103711. doi:10.1063/1.3259436
127. Maennig B, Pfeiffer M, Nollau A, Zhou X, Leo K, Simon P (2001) Controlled p-type doping of polycrystalline and amorphous organic layers: self-consistent description of conductivity and field-effect mobility by a microscopic percolation model. Phys Rev B 64:195208. doi:10.1103/PhysRevB.64.195208
128. Lüssem B, Riede M, Leo K (2012) Doping of organic semiconductors. Phys Status Solidi A 210:9. doi:10.1002/pssa.201228310
129. Falkenberg C (2011) Optimizing organic solar cells transparent electron transport materials for improving the device performance. Technische Universität Dresden

130. Pfuetzner S, Petrich A, Malbrich C, Meiss J, Koch M, Riede MK, Pfeiffer M, Leo K (2008) Characterisation of different hole transport materials as used in organic p-i-n solar cells. In: Heremans PL, Muccini M, Meulenkamp EA (eds) Proceedings of the SPIE, p 69991M
131. Menke T, Ray D, Kleemann H, Hein MP, Leo K, Riede M (2014) Highly efficient p-dopants in amorphous hosts. Org Electron 15:365. doi:10.1016/j.orgel.2013.11.033
132. Maennig B, Drechsel J, Gebeyehu D, Simon P, Kozlowski F, Werner A, Li F, Grundmann S, Sonntag S, Koch M, Leo K, Pfeiffer M, Hoppe H, Meissner D, Sariciftci NS, Riedel I, Dyakonov V, Parisi J (2004) Organic p-i-n solar cells. Appl Phys A Mater Sci Process 79:1–14. doi:10.1007/s00339-003-2494-9
133. Falkenberg C, Leo K, Riede MK (2011) Improved photocurrent by using n-doped 2,3,8,9,14,15-hexachloro-5,6,11,12,17,18-hexaazatrinaphthylene as optical spacer layer in p-i-n type organic solar cells. J Appl Phys 110:124509. doi:10.1063/1.3664828
134. Falkenberg C, Uhrich C, Olthof S, Maennig B, Riede MK, Leo K (2008) Efficient p-i-n type organic solar cells incorporating 1,4,5,8-naphthalenetetracarboxylic dianhydride as transparent electron transport material. J Appl Phys 104:34506. doi:10.1063/1.2963992
135. El-Khatib N, Boudjema B, Guillaud G, Maitrot M, Chermette H (1988) Theoretical and experimental doping of molecular materials: P and N doping of zinc phthalocyanine. J Less Common Met 143:101–112. doi:10.1016/0022-5088(88)90035-5
136. Zhou X, Blochwitz J, Pfeiffer M, Nollau A, Fritz T, Leo K (2001) Enhanced hole injection into amorphous hole-transport layers of organic light-emitting diodes using controlled p-type doping. Adv Funct Mater 11:310
137. Meerheim R, Olthof S, Hermenau M, Scholz S, Petrich A, Tessler N, Solomeshch O, Lüssem B, Riede M, Leo K (2011) Investigation of C60F36 as low-volatility p-dopant in organic optoelectronic devices. J Appl Phys 109:103102. doi:10.1063/1.3590142
138. Romero DB, Schaer M, Zuppiroli L, Cesar B, François B (1995) Effects of doping in polymer light-emitting diodes. Appl Phys Lett 67:1659. doi:10.1063/1.115048
139. Lee J-H, Leem D-S, Kim J-J (2008) High performance top-emitting organic light-emitting diodes with copper iodide-doped hole injection layer. Org Electron 9:805–808. doi:10.1016/j.orgel.2008.05.011
140. Gao C-H, Zhu X-Z, Zhang L, Zhou D-Y, Wang Z-K, Liao L-S (2013) Comparative studies on the inorganic and organic p-type dopants in organic light-emitting diodes with enhanced hole injection. Appl Phys Lett 102:153301. doi:10.1063/1.4802081
141. Chang C-C, Hsieh M-T, Chen J-F, Hwang S-W, Chen CH (2006) Highly power efficient organic light-emitting diodes with a p-doping layer. Appl Phys Lett 89:253504. doi:10.1063/1.2405856
142. Tietze ML, Burtone L, Riede M, Lüssem B, Leo K (2012) Fermi level shift and doping efficiency in p-doped small molecule organic semiconductors: a photoelectron spectroscopy and theoretical study. Phys Rev B 86:35320. doi:10.1103/PhysRevB.86.035320
143. Kido J, Matsumoto T (1998) Bright organic electroluminescent devices having a metal-doped electron-injecting layer. Appl Phys Lett 73:2866–2868. doi:10.1063/1.122612
144. Parthasarathy G, Shen C, Kahn A, Forrest SR (2001) Lithium doping of semiconducting organic charge transport materials. J Appl Phys 89:4986–4992. doi:10.1063/1.1359161
145. Nollau A, Pfeiffer M, Fritz T, Leo K (2000) Controlled n-type doping of a molecular organic semiconductor: Naphthalenetetracarboxylic dianhydride (NTCDA) doped with bis(ethylenedithio)-tetrathiafulvalene (BEDT-TTF). J Appl Phys 87:4340. doi:10.1063/1.373413
146. Cotton FA, Gruhn NE, Gu J, Huang P, Lichtenberger DL, Murillo CA, Van Dorn LO, Wilkinson CC (2002) Closed-shell molecules that ionize more readily than cesium. Science 298:1971–1974. doi:10.1126/science.1078721
147. Wei P, Menke T, Naab BD, Leo K, Riede M, Bao Z (2012) 2-(2-Methoxyphenyl)-1,3-dimethyl-1 H -benzoimidazol-3-ium iodide as a new air-stable n-type dopant for vacuum-processed organic semiconductor thin films. J Am Chem Soc 134:3999–4002. doi:10.1021/ja211382x
148. Menke T, Wei P, Ray D, Kleemann H, Naab BD, Bao Z, Leo K, Riede M (2012) A comparison of two air-stable molecular n-dopants for C60. Org Electron 13:3319–3325. doi:10.1016/j.orgel.2012.09.024

149. Werner AG, Li F, Harada K, Pfeiffer M, Fritz T, Leo K (2003) Pyronin B as a donor for n-type doping of organic thin films. Appl Phys Lett 82:4495. doi:10.1063/1.1583872
150. Koech PK, Padmaperuma AB, Wang L, Swensen JS, Polikarpov E, Darsell JT, Rainbolt JE, Gaspar DJ (2010) Synthesis and application of 1,3,4,5,7,8-hexafluorotetracyanonaphthoquinodimethane (F6-TNAP): a conductivity dopant for organic light-emitting devices. Chem Mater 22:3926. doi:10.1021/cm1002737
151. Murawski C, Fuchs C, Hofmann S, Leo K, Gather MC (2014) Alternative p-doped hole transport material for low operating voltage and high efficiency organic light-emitting diodes. Appl Phys Lett 105:113303. doi:10.1063/1.4896127
152. Peumans P, Bulović V, Forrest SR (2000) Efficient photon harvesting at high optical intensities in ultrathin organic double-heterostructure photovoltaic diodes. Appl Phys Lett 76:2650. doi:10.1063/1.126433
153. Walzer K, Maennig B, Pfeiffer M, Leo K (2007) Highly efficient organic devices based on electrically doped transport layers. Chem Rev 107:1233–1271. doi:10.1021/cr050156n
154. Timmreck R, Olthof S, Leo K, Riede MK (2010) Highly doped layers as efficient electron–hole recombination contacts for tandem organic solar cells. J Appl Phys 108:33108. doi:10.1063/1.3467786
155. Hiramoto M, Suezaki M, Yokoyama M (1990) Effect of thin gold interstitial-layer on the photovoltaic properties of tandem organic solar cell. Chem Lett 19:327–330. doi:10.1246/cl.1990.327
156. Schlenker CW, Barlier VS, Chin SW, Whited MT, McAnally RE, Forrest SR, Thompson ME (2011) Cascade organic solar cells. Chem Mater 23:4132–4140. doi:10.1021/cm200525h
157. Barito A, Sykes ME, Huang B, Bilby D, Frieberg B, Kim J, Green PF, Shtein M (2014) Universal design principles for cascade heterojunction solar cells with high fill factors and internal quantum efficiencies approaching 100%. Adv Energy Mater 4:1400216. doi:10.1002/aenm.201400216
158. Stevens MA, Arango AC (2016) Open-circuit voltage exceeding the outermost HOMO-LUMO offset in cascade organic solar cells. Org Electron 37:80–84. doi:10.1016/j.orgel.2016.06.008
159. Ichikawa M, Suto E, Jeon H-G, Taniguchi Y (2010) Sensitization of organic photovoltaic cells based on interlayer excitation energy transfer. Org Electron 11:700–704. doi:10.1016/j.orgel.2009.12.023
160. Feron K, Belcher W, Fell C, Dastoor P (2012) Organic solar cells: understanding the role of Förster resonance energy transfer. Int J Mol Sci 13:17019–17047. doi:10.3390/ijms131217019
161. Vandewal K (2016) Interfacial charge transfer states in condensed phase systems. Annu Rev Phys Chem 67:113–133. doi:10.1146/annurev-physchem-040215-112144
162. Deibel C, Strobel T, Dyakonov V (2010) Role of the charge transfer state in organic donor-acceptor solar cells. Adv Mater 22:4097–4111. doi:10.1002/adma.201000376
163. Vandewal K, Albrecht S, Hoke ET, Graham KR, Widmer J, Douglas JD, Schubert M, Mateker WR, Bloking JT, Burkhard GF, Sellinger A, Fréchet JMJ, Amassian A, Riede MK, McGehee MD, Neher D, Salleo A (2013) Efficient charge generation by relaxed charge-transfer states at organic interfaces. Nat Mater 13:63–68. doi:10.1038/nmat3807
164. Gelinas S, Rao A, Kumar A, Smith SL, Chin AW, Clark J, van der Poll TS, Bazan GC, Friend RH (2014) Ultrafast long-range charge separation in organic semiconductor photovoltaic diodes. Science (80–)343:512–516. doi:10.1126/science.1246249
165. Jamieson FC, Domingo EB, McCarthy-Ward T, Heeney M, Stingelin N, Durrant JR (2012) Fullerenecrystallisation as a key driver of charge separation in polymer/fullerene bulk heterojunction solar cells. Chem Sci 3:485–492. doi:10.1039/C1SC00674F
166. Sweetnam S, Graham KR, Ngongang Ndjawa GO, Heumüller T, Bartelt JA, Burke TM, Li W, You W, Amassian A, McGehee MD (2014) Characterization of the polymer energy landscape in polymer: fullerene bulk heterojunctions with pure and mixed phases. J Am Chem Soc 136:14078–14088. doi:10.1021/ja505463r

167. Neher D, Kniepert J, Elimelech A, Koster LJA (2016) A new figure of merit for organic solar cells with transport-limited photocurrents. Sci Rep 6:24861. doi:10.1038/srep24861
168. Kniepert J, Lange I, Heidbrink J, Kurpiers J, Brenner TJK, Koster LJA, Neher D (2015) Effect of solvent additive on generation, recombination, and extraction in PTB7:PCBM solar cells: a conclusive experimental and numerical simulation study. J Phys Chem C 119:8310–8320. doi:10.1021/jp512721e
169. Fischer J, Widmer J, Kleemann H, Tress W, Koerner C, Riede M, Vandewal K, Leo K (2015) A charge carrier transport model for donor-acceptor blend layers. J Appl Phys 117:45501. doi:10.1063/1.4906561
170. Vandewal K, Widmer J, Heumueller T, Brabec CJ, McGehee MD, Leo K, Riede M, Salleo A (2014) Increased open-circuit voltage of organic solar cells by reduced donor-acceptor interface area. Adv Mater 26:3839–3843. doi:10.1002/adma.201400114
171. Burke TM, Sweetnam S, Vandewal K, McGehee MD (2015) Beyond Langevin recombination: how equilibrium between free carriers and charge transfer states determines the open-circuit voltage of organic solar cells. Adv Energy Mater 5:1500123. doi:10.1002/aenm.201500123
172. Graham KR, Erwin P, Nordlund D, Vandewal K, Li R, Ngongang Ndjawa GO, Hoke ET, Salleo A, Thompson ME, McGehee MD, Amassian A (2013) Re-evaluating the role of sterics and electronic coupling in determining the open-circuit voltage of organic solar cells. Adv Mater 25:6076–6082. doi:10.1002/adma.201301319
173. Vandewal K, Tvingstedt K, Gadisa A, Inganäs O, Manca JV (2010) Relating the open-circuit voltage to interface molecular properties of donor:acceptor bulk heterojunction solar cells. Phys Rev B 81:125204. doi:10.1103/PhysRevB.81.125204
174. Widmer J, Tietze M, Leo K, Riede M (2013) Open-circuit voltage and effective gap of organic solar cells. Adv Funct Mater 23:5814–5821. doi:10.1002/adfm.201301048
175. Liu J, Chen S, Qian D, Gautam B, Yang G, Zhao J, Bergqvist J, Zhang F, Ma W, Ade H, Inganäs O, Gundogdu K, Gao F, Yan H (2016) Fast charge separation in a non-fullerene organic solar cell with a small driving force. Nat Energy 1:16089. doi:10.1038/nenergy.2016.89
176. Ran NA, Love JA, Takacs CJ, Sadhanala A, Beavers JK, Collins SD, Huang Y, Wang M, Friend RH, Bazan GC, Nguyen T-Q (2016) Harvesting the full potential of photons with organic solar cells. Adv Mater 28:1482–1488. doi:10.1002/adma.201504417
177. Wang C, Xu X, Zhang W, Bergqvist J, Xia Y, Meng X, Bini K, Ma W, Yartsev A, Vandewal K, Andersson MR, Inganäs O, Fahlman M, Wang E (2016) Low band gap polymer solar cells with minimal voltage losses. Adv Energy Mater 6:1600148. doi:10.1002/aenm.201600148
178. Tuladhar SM, Azzouzi M, Delval F, Yao J, Guilbert AAY, Kirchartz T, Montcada NF, Dominguez R, Langa F, Palomares E, Nelson J (2016) Low open-circuit voltage loss in solution-processed small-molecule organic solar cells. ACS Energy Lett 1:302–308. doi:10.1021/acsenergylett.6b00162
179. Sulas DB, Yao K, Intemann JJ, Williams ST, Li C-Z, Chueh C-C, Richards JJ, Xi Y, Pozzo LD, Schlenker CW, Jen AK-Y, Ginger DS (2015) Open-circuit voltage losses in selenium-substituted organic photovoltaic devices from increased density of charge-transfer states. Chem Mater 27:6583–6591. doi:10.1021/acs.chemmater.5b02133
180. Ameri T, Dennler G, Lungenschmied C, Brabec CJ (2009) Organic tandem solar cells: a review. Energy Environ Sci 2:347. doi:10.1039/b817952b
181. Riede M, Mueller T, Tress W, Schueppel R, Leo K (2008) Small-molecule solar cells—status and perspectives. Nanotechnology 19:424001. doi:10.1088/0957-4484/19/42/424001
182. Hadipour A, de Boer B, Blom PWM (2008) Device operation of organic tandem solar cells. Org Electron 9:617–624. doi:10.1016/j.orgel.2008.03.009
183. Timmreck R, Meyer T, Gilot J, Seifert H, Mueller T, Furlan A, Wienk MM, Wynands D, Hohl-Ebinger J, Warta W (2015) Characterization of tandem organic solar cells. Nat Photonics 9:478–479

Chapter 2
Polymer Solar Cells

Youyu Jiang, Yaowen Li, Jinhui Tong, Lin Mao, Yinhua Zhou and Fengling Zhang

Abstract Polymer solar cells are typically based on bulk-heterojunction active layers containing polymers and fullerene or other molecules, which are solution-processable. The easy processing is the biggest difference comparing to the small molecule-based solar cells. Tremendous efforts have been devoted to developing high-efficient materials, novel architectures and explore the underlying physical mechanism. The power conversion efficiency of polymer solar cells has been progressively improved to 12% for both single- and multijunction cells, which indicates a remarkable advance toward marketable production. This chapter will provide a comprehensive overview of the polymer solar cells. The content includes: a brief description of polymer solar cells, active layer materials, interfacial layer materials, electrodes, morphology of active layers, multi-function cells, as well as large-area solar modules.

Keywords Polymer solar cells · Bulk-heterojunction · Polymer · Fullerene acceptors · Non-fullerene acceptors · Solution-processable · Morphology of active layers

Y. Jiang · J. Tong · L. Mao · Y. Zhou
Wuhan National Laboratory for Optoelectronics, and School of Optical and Electronic Information, Huazhong University of Science and Technology, Wuhan 430074, China

Y. Li
Laboratory of Advanced Optoelectronic Materials, College of Chemistry, Chemical Engineering and Materials Science, Soochow University, Suzhou 215123, China

F. Zhang (✉)
Biomolecular and Organic Electronics, Department of Physics, Chemistry and Biology (IFM), Linkoping University, 581 83 Linkoping, Sweden
e-mail: fengling.zhang@liu.se

H. Tian et al. (eds.), *Molecular Devices for Solar Energy Conversion and Storage*, Green Chemistry and Sustainable Technology,
https://doi.org/10.1007/978-981-10-5924-7_2

2.1 Introduction

Recent years, a new kind of solar cells composed of polymers has been developed. These solution-processed bulk-heterojunction (BHJ) polymer solar cells (PSCs) possess many unique advantages, such as easy manufacture and up scaling, light-weight, big material library, and excellent mechanical flexibility. In 1992, conjugated polymers under illumination transferring their electrons to buckminsterfullerene were observed [1, 2], which suggested the potential application in solar cells. However, the efficiency of the solar cells based on bilayers of polymer and buckminsterfullerene was very low due to the electron transfer or charge generation only happened at the interfaces between the polymer and buckminsterfullerene layers. With the availability of a soluble fullerene derivative ($PC_{61}BM$), bulk polymer fullerene heterojunction PSCs were fabricated by mixing polymer (donor) and $PC_{61}BM$ (acceptor) in organic solvents, which demonstrated significant enhanced energy conversion efficiency because of enlarged interfaces between the donor and acceptor [3]. Since then, the bulk-heterojunction PSCs based on blends of semiconducting polymers and fullerene derivatives underwent a revolutionary growth in the last decade [4, 5]. Nowadays, power conversion efficiencies (PCEs) of 11% [6] are achieved in single-heterojunction PSCs based on both fullerene and non-fullerene acceptors with active area <1 cm^2.

2.1.1 Device Structure

A simple PSC with a layer structure by sandwiching an active layer (absorber) between two electrodes (cathode and anode) is shown in Fig. 2.1. The active layer usually composes of two different materials: one tends to lose electrons named electron donor, the other tends to capture electrons called electron acceptor. Two electrodes need to have different work functions to form an internal electric field for free charge carrier generation and transportation to corresponding electrodes. In addition, at least one of two electrodes should be transparent to allow photons incident into active layers for absorption. To have a better performance PSC, two interfacial layers are needed, that is, a hole transport or extracting layer (HTL or HEL) and an electron transport or extracting layer (ETL or EEL). The HEL and EEL are critical for selectively extracting holes and electrons from the active layer, respectively. A PSC can be built up from an anode to a cathode or from a cathode to an anode. For a conventional PSC, HEL, active layers, and EEL are continuously deposited on an anode. A PSC with reverse order of layers, that is, EEL, active layers, and HEL continuously deposited on a cathode, is named as an inverted PSC.

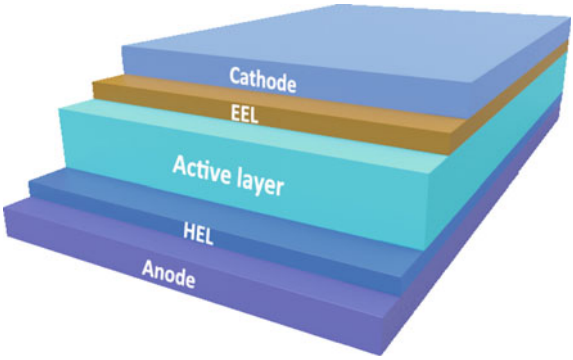

Fig. 2.1 The device structure of a conventional polymer solar cell

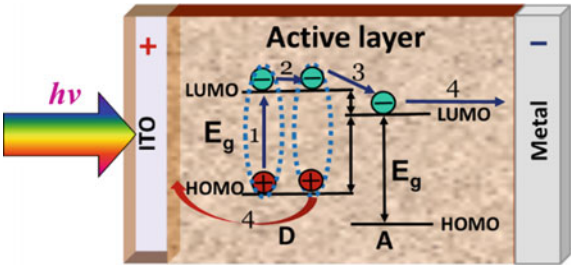

Fig. 2.2 A schematic outline of the conversion from photons to electrons in a PSC

2.1.2 Working Principle

The conversion from photons to electrons in PSCs can be divided into four main steps (shown in Fig. 2.2), which is similar to small molecular solar cells in Chap. 1. When a PSC is illuminated with the Sun or other light sources, some photons will be reflected by the surface of the electrode, only the photons pass through a transparent electrode (commonly is Indium-tin-oxide, ITO) with energy bigger than the band gap (E_g) of materials of the active layer can be absorbed. The photons with energy smaller than the band gap of active materials will pass through the active layer of the PSC without absorption. The absorbed photons can excite electrons in absorbers from ground states to excited states and form excitons (bound electron-hole pairs) (step 1 in Fig. 2.2). The excitons will diffuse in the active layer (step 2). During diffusion, some excitons may recombine and release the energy to surrounding (nonradiative recombination) and some may recombine and emit photons (radiative recombination, which is not useful for PSCs). The others may dissociated to free electrons and holes at the interfaces between donor and acceptor when electrons transfer from donor (D) to acceptor (A) (step 3) due to the lowest unoccupied molecular orbitals (LUMOs) offset between D and A as well as a strong internal electric field formed by the work function difference between two electrodes. If excitons are also generated in acceptor phase by absorbing photons, free electrons and holes can be also formed through holes transfer from A to D due to

the highest occupied molecular orbitals (HOMOs) offsets and a strong internal electric field. Finally, free charge carriers (electrons and holes) are drifted by the internal electric field toward the corresponding electrodes (step 4) and collected at two electrodes.

The optical bandgaps of a polymer ($E_{g,D}$) and acceptor ($E_{g,A}$) of a PSC define the ranges of the photons absorbed by the active layers. Most photons from the Sun are in the range of 600–800 nm. Selecting materials with absorption spectra maximum overlapping with the solar spectrum is prerequisite to obtain a high photo-induced current. The relative positions of the LUMOs and the HOMOs of D and A govern the free charge carrier generation and photovoltage. The less energy losses in this initial electron transfer, the higher photovoltage will be obtained [7].

2.1.3 Evaluation of PSCs

PSCs are evaluated in the same way as described in Chap. 1. The output electrical power is the product of photo-induced current (I) and voltage (V). The PCE is the ratio of the maximum electrical power density produced by the device and the incident light power density. For the lab standard, an AM1.5 solar spectrum (Fig. 2.3a) is reproduced and the input power density P_{in} is set to 100 mW/cm^2. For determining the electric output power density, current density-voltage (J-V) curves are measured. At a certain voltage (V_{max}), corresponding to a certain current density (J_{max}), the output power density reaches a maximum (P_{max}) (Fig. 2.3b). The PCE is equal to P_{max}/P_{in}.

$$PCE_{\max} = \frac{P_{\max}}{P_{in}} = \frac{(JV)_{\max}}{P_{in}} = FF\frac{J_{sc}V_{oc}}{P_{in}} \tag{2.1}$$

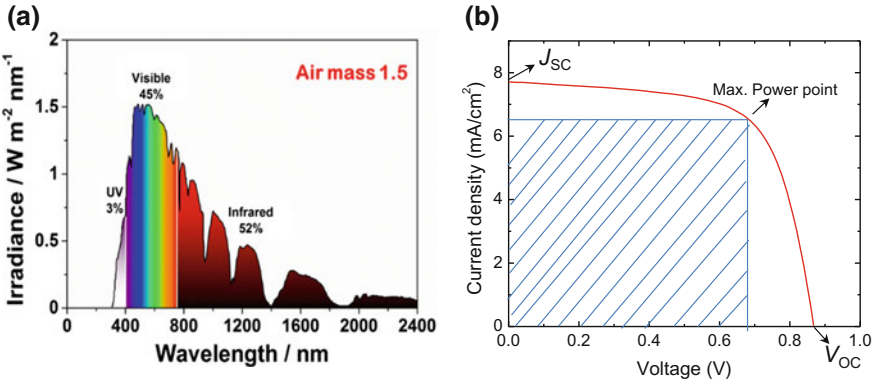

Fig. 2.3 **a** Solar spectrum (http://rredc.nrel.gov/solar/spectra/am1.5) and **b** typical J-V characteristics of a PSC

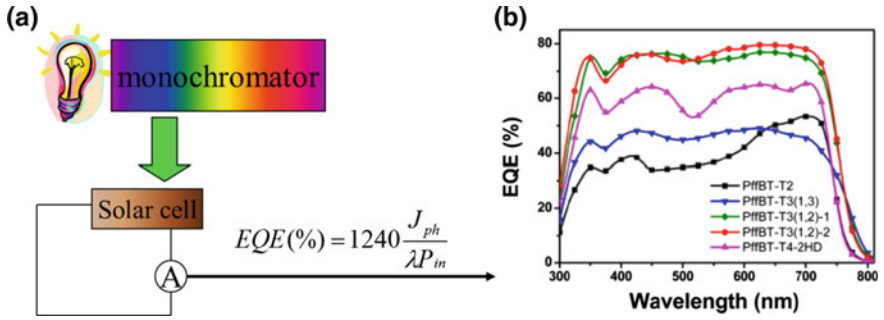

Fig. 2.4 **a** A schematic diagram of EQE measurement, calculation and **b** 5 EQE profiles, Reprinted with permission from Ref. [6]. Copyright 2015 by American Chemical Society

where J_{sc} is the current density flowing out of the device at short circuit, V_{oc} is the voltage at open circuit, the ratio $P_{max}/J_{sc}V_{oc}$ is called the fill factor (FF) and reflects how "square" the J-V curve looks. For a high PCE, a high J_{sc}, V_{oc} and FF are needed [8].

In addition, to know details of photon to electron conversion at each wavelength, two quantum efficiencies, internal quantum efficiency (IQE) and external quantum efficiency (EQE) are concerned. IQE is defined as the number of extracted electrons (n_e) from a PSC illuminated with a monochromatic light divided by the number of absorbed photons (n_{abs}) by the PSC (Eq. (2.2)).

$$IQE = \frac{n_e}{n_{abs}} \tag{2.2}$$

EQE is defined as the number of extracted electrons (n_e) from a PSC illuminated with a monochromatic light divided by the number of incident photons (n_{in}) to the PSC (Eq. (2.3)) where the J_{ph} is photo-induced current density, λ is a wavelength of the monochromatic light and P_{in} is input power density of the monochromatic light. A schematic layout of a setup for measuring photocurrent under monochromatic light to calculate EQE and examples of EQE profile is illustrated in Fig. 2.4. Integrating all current density J_{ph} for all wavelengths will get a short circuit current density J_{sc} of a PSC under white light.

$$EQE(\%) = \frac{n_e}{n_{in}} = 1240\frac{J_{ph}}{\lambda P_{in}} \tag{2.3}$$

2.2 Active Layer Materials

Optoelectric properties of materials used in active layers are crucial for the performance of PSCs. Typically, the active materials of BHJ PSCs consist of p-type semiconducting polymers (D) and n-type semiconductors (A), classically fullerene

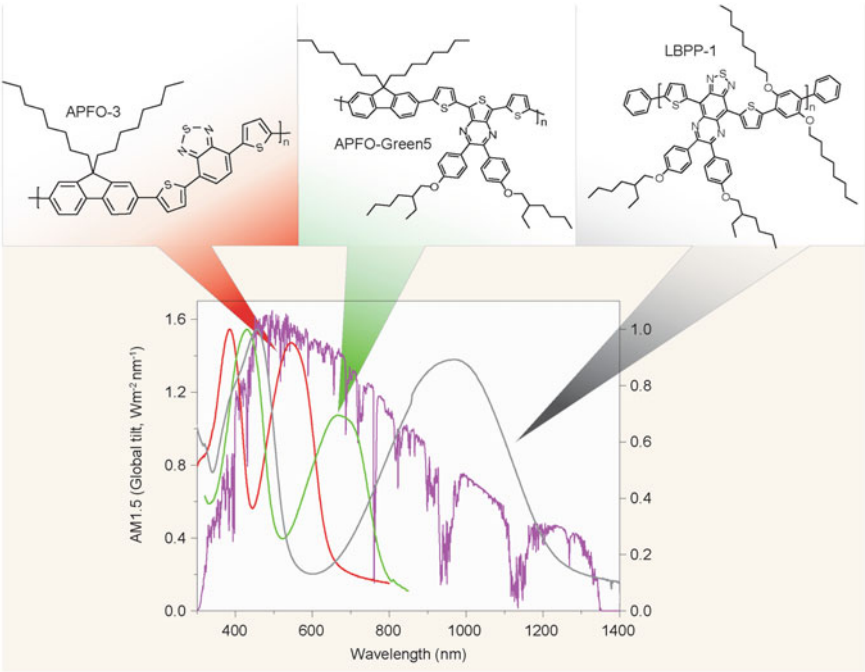

Fig. 2.5 The absorption spectra and molecular structures of three representative polymers with different optical bandgaps. Reprinted with permission from Ref. [8]. Copyright 2016 by Oxford Journals

derivatives, but recently non-fullerene acceptors are very rapidly developed. To efficiently harvest the photon energy, the absorption spectra of PSCs should have large overlaps with the solar spectrum in the visible and near-infrared region. The absorption spectra and molecular structures of three representative polymers with different optical bandgaps are shown in Fig. 2.5. As shown in Fig. 2.3a, roughly 70% of the solar energy is distributed in the wavelength region from 380 to 900 nm; hence, in theory, the donor polymer (the main light absorber in PSCs) with lower optical bandgap would show higher J_{sc}. Since LUMO of the donor polymer should be at least 0.3 eV higher than the LUMO of the acceptor (Fig. 2.2) to enable efficient exciton splitting to free charge at the D/A interface, further narrowing the bandgap of a polymer would require an lift up of the HOMO level of the polymer. However, increasing the HOMO level of the polymer will lead to a decrease in the V_{oc}, which is generally believed to tightly correlate with the energy level difference between the HOMO of the donor and the LUMO of the acceptor in BHJ PSCs. Therefore, it is very important to balance the optical bandgaps and the HOMO/LUMO energy offsets of the active materials. In addition, other properties of active materials are also highly desired for a high-performance PSCs, including: (1) good solubility and miscibility between donor and acceptor; (2) high and

balanced hole/electron carrier mobilities to enhance charge transport; (3) optimal morphology to promote charge separation and favorable transport. All these properties are not independent of each other. Therefore, efficient active materials should be rationally designed to compromise these requirements by molecular engineering. During the past decades an extensive development of active materials has been undertaken. A great number of donors and acceptors have been synthesized. This section, from a molecular structure of active materials (D and A) viewpoint, will introduce typical donor polymers, fullerene and non-fullerene acceptors.

2.2.1 Donor Materials

Conjugated polymers with high molecular weight can be processed from high viscosity solutions in organic solvents, which are easy to form high-quality films using wet-processing techniques. Meanwhile, the flexible natures of polymers are more suitable for roll-to-roll manufacturing on flexible substrates to get robust, light-weight PSCs.

2.2.1.1 Polythiophene Derivatives

In the past decade, a great many conjugated polymers have been designed, synthesized, and applied as donors in PSCs. Among these polymers, polythiophene (PT) derivatives are one of the most important types of donor materials, the most prominent of them is regioregular poly(3-hexylthiophene) (P3HT). With regard to the 3-hexylthiophene unit, as shown in Fig. 2.6, the positions 2 and 5 are named as head and tail, respectively. Coupling each thiophene unit in a consecutive head-to-tail manner during the polymerization yields a regioregular P3HT. The regioregularity, molecular weight, and polydispersity of P3HT have been shown to significantly affect the performances of PSCs. Friend et al. demonstrated that increasing the regioregularity of P3HT will be beneficial for obtaining P3HT with a

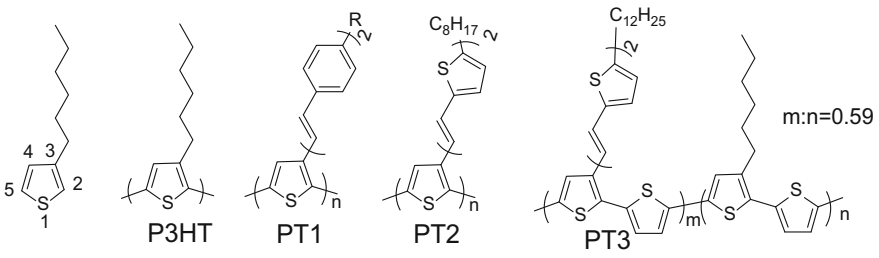

Fig. 2.6 The molecular structures of P3HT and its analogous polymers

coplanar conformation, reducing bandgap as well as higher charge carrier mobility (up to 0.2 $cm^2/(V\ s)$) [9]. The PCEs of corresponding PSCs remained relatively constant at ~3.6% for P3HT with a molecular weight (M_W) = 43.7 and 72.8 kDa, but decreased at higher Mw [10]. Upon optimization of the active layer morphology via thermal or solvent annealing, an impressive PCE of 5% was achieved [11, 12]. Unfortunately, the high HOMO (−5.1 eV) energy level and large bandgap (~2.0 eV) of P3HT restrict the V_{oc} to ~0.6 V and J_{sc} with $PC_{61}BM$ as the acceptor, which consequently limits the overall efficiency.

Much efforts are devoted to designing PT derivatives to realize higher efficiency in PSCs, that is, to explore PT derivatives with better photovoltaic properties than P3HT. As shown in Fig. 2.6, Li's group synthesized a series of two-dimensional (2D) PT derivatives containing conjugated side chains [13, 14]. They demonstrated that incorporation of conjugated side chain such as bi(phenylenevinylene) (PT2) or bi(thienylenevinylene) (PT3) on PT main chain can effectively extend conjugation degree, and hence the absorption spectra of conjugated polymers in UV region are enhanced and red-shifted. By controlling the ratio between the thiophene units in the main chain and the conjugated side chains, the absorption region of PT3 can be further enhanced and red-shifted, delivering a strong and broad absorption spectrum in the range of 300–680 nm. Meanwhile, the HOMO energy level of the PTs with bi(thienylenevinylene) conjugated side chains dropped by *ca.* 0.2 eV in comparison with that of P3HT, which could lead to a higher V_{oc} when used as a donor in cells. The PSC based on PT3:$PC_{61}BM$ delivers a PCE of 3.18%.

After intensively studying the P3HT based active layers, several important molecular structure related factors governing device performance were discovered, such as the stacking model of P3HT chain, HOMO energy level and miscibility with PCBM. Yang et al. developed a PT derivative (P3HDTTT in Fig. 2.7) with alternating thiophene attaching long alkyl chain and 2,2′-bithiophene by a simple synthesis process [15]. It is interesting to find that the P3HDTTT with less electron-donating alkyl chain shows an almost same absorption spectrum compared to that of P3HT, while the HOMO energy level down shifted 0.4 eV (−4.9 eV as for P3HT to −5.3 eV as for P3HDTTT). Therefore, the device based on P3HDTTT:

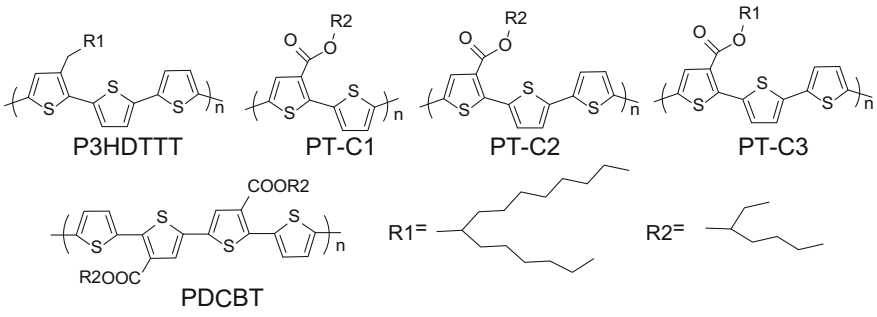

Fig. 2.7 The molecular structure of polythiophene derivatives with side chain engineering

$PC_{61}BM$ without annealing process showed a significantly improved V_{oc} from 0.64 to 0.82 V, delivering a PCE of 3.4%. Li [16] and Chen [17], respectively, investigated the effect of an electron-withdrawing moiety in the substituent of PT derivatives on the photovoltaic performance by incorporating carboxylate side chain (PT-C1, PT-C2, and PT-C3). They demonstrated that the electron-accepting carboxylate can effectively reduce the HOMO energy level of PTs by 0.2–0.3 eV compared to that of P3HT, but no effect on their bandgap. The device based on PT-C3:$PC_{61}BM$ showed a V_{oc} of 0.78 V and PCE of 3.87%. Recently, Hou et al. [18]. further developed the carboxylate side chain attached PT(PDCBT), where a more symmetric polymer main chain was designed. PDCBT presents higher absorption coefficient, highly crystalline and compact π-π stacking with a smaller separation than P3HT. The PSCs based on PDCBT:$PC_{71}BM$ exhibit a PCE of 7.2% with V_{oc} = 0.91 V, J_{sc} = 11.0 mA/cm^2, and fill factor FF = 72.0%. Moreover, the performance of PSCs based on PDCBT is insensitive to variations of active layer thickness and processing conditions such as additives and thermal treatment, which indicate that PDCBT has great potential in large-scale manufacturing of low-cost, high-performance PSCs.

In order to further expand the conjugation and enhance electron delocalization ability of PTs, fused thiophene derivatives were used to replace thiophene units in polymers, which can effectively increase hole mobility, decrease bandgap as well as enhance the coplanarity of polymers. There are several star moieties such as thieno[3,2-b]thiophene, thieno[3,4-b]thiophene (TT), benzo[1,2-b:6,5-b′]dithiophene (BDT), indacenodithiophene (IDT) and dithieno[3,2-b:2′,3′-d]thiophene (shown in Fig. 2.8), that play important roles in constructing high-performance donor materials. Especially for the BDT and TT moieties based donor materials, when blended with $PC_{71}BM$, the corresponding PSCs generally give high PCE in the range of

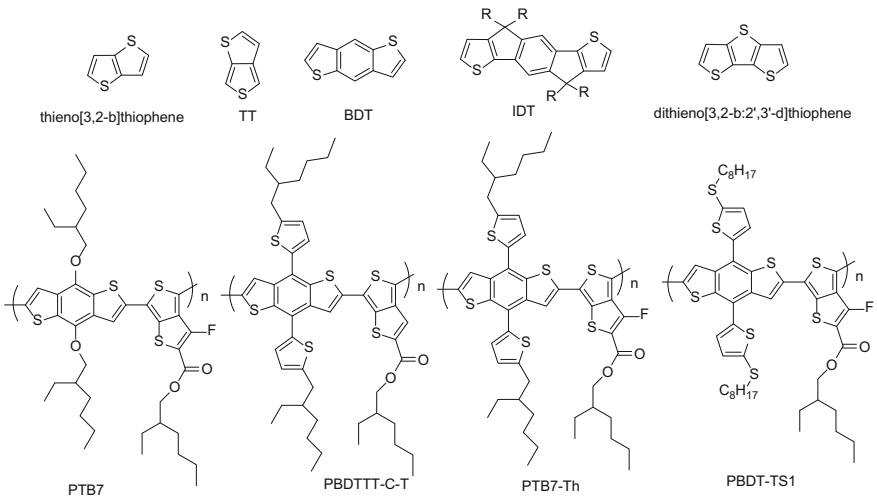

Fig. 2.8 The molecular structures of fused thiophene-based polythiophene derivatives

7–9%. Yu et al. developed the ester-substituted TT unit to copolymerize with alkoxyl-substituted BDT units, thus preparing a series of copolymers based on BDT and TT [19, 20]. Incorporating fluorine atom on TT units can further improve the performance of photovoltaic device. PTB7 became one of the most investigated donor materials since 2010. Because it has a strong absorption from 550 to 750 nm, and a decreased HOMO and LUMO to −5.15 and −3.31 eV, respectively [21, 22]. The device with an ITO/PEDOT:PSS/PTB7:$PC_{71}BM$/Ca/Al structure and CB/DIO as a processing solvent yielded an impressive PCE of 7.4% with a V_{oc} of 0.74 V, a J_{sc} of 14.50 mA/cm^2, and an FF of 68.97% [21, 22]. Furthermore, Wu et al. improved the PCE of the PTB7-based device to 9.2% by applying an inverted device structure and new interface material [23]. In addition to PTB7, the combination of BDT and TT units yielded several high-performance copolymers, such as PBDTTT-C-T [24], PBDT-TS1 [25], PTB7-Th [26], etc. For instance, when the alkoxyl side chains on BDT were replaced by the conjugated thienyl side chains, the resulting polymer PTB7-Th (also named as PCE-10) showed very impressive photovoltaic performance by delivering a PCE of 9.35%, and became one of the most studied polymers.

2.2.1.2 Poly(*p*-Phenylenevinylene) Derivatives

In the early stage, poly(*p*-phenylenevinylene)s (PPVs) attracted considerable interest for photovoltaic applications. In order to obtain high-quality PPVs films by solution process, PPVs with better solubility and high molecular weights are needed, which can be achieved by the widely developed Gilch route. The solution-processable poly (2-methoxy-5-((2′-ethylhexyl)oxy)-1,4-phenylenevinylene) (MEH-PPV) and poly (2-methoxy-5-((3′,7′-dimethyloctyl)oxy)-1,4-phenylenevinylene) (MDMO-PPV) with high molecular weights are successfully synthesized and shown in Fig. 2.9. A PSC using MEH-PPV/$PC_{61}BM$ as the active layer has been fabricated and showed PCE values in the range 1.1–1.3% [27]. PCE as high as 3.3% was achieved in MDMO-based PSC with $PC_{61}BM$ as the acceptor material, mainly through the application of chlorinated solvents to tune active layer morphologies [28, 29]. A high V_{oc} up to 0.82 V was obtained as a result of the relatively low HOMO energy level of −5.4 eV of MDMO-PPV; however, the large bandgap of MDMO-PPV limited the J_{sc} to 5–6 mA/cm^2. In addition to introducing functional groups on the phenylene ring, the molecular orbital energy levels of PPV derivatives can also be tuned by incorporating electronic substituents into the conjugated vinylene bridges. Compared to MEH-PPV, the replacement of vinylene linkages with cyanovinylene linkages in CN-PPV lowers both the LUMO and HOMO levels by $\sim$0.5 eV, with little effect on the magnitude of the bandgap. Additionally, CN-PPV displays high electron affinities and electron transport properties as a result of the electron-withdrawing effect of the cyano side group and a low-lying LUMO level so that it can function as a suitable electron acceptor in photovoltaic devices in either a bilayer or bulk-heterojunction configuration [30, 31]. A number of PPV derivatives containing alternating arylene-ethynylene units were synthesized to evaluate their

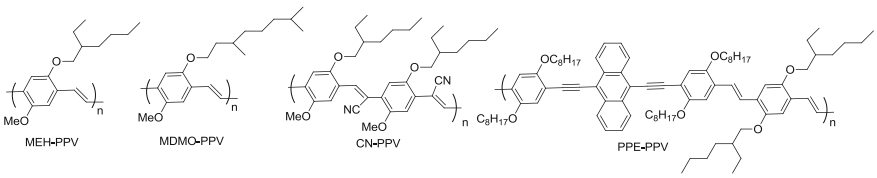

Fig. 2.9 The molecular structures of Poly(*p*-phenylenevinylene) derivatives

photovoltaic properties. The coplanar and rigid nature of the acetylene moiety in the polymer chain may have the potential to obtain a higher degree of packing and thus improve the photovoltaic performance of such devices. PPE-PPV as shown in Fig. 2.9 containing coplanar electron-rich anthracene units and triple bond bridges exhibits broader absorption, a lower HOMO level, and a smaller optical bandgap of 1.9 eV, compared to that of MDMO-PPV [32]. A device with the configuration of ITO/PEDOT/PPE-PPV:$PC_{61}BM$ (1:2, w/w)/LiF/Al, yielded a PCE value of up to 2% with a high V_{oc} of 0.81 V.

2.2.1.3 D-A Conjugated Polymers

Low bandgap polymers with tunable energy levels can be easily achieved by constructing a donor–acceptor (D-A) structure polymers. The D-A structure polymers with internal charge transfer (ICT) intrinsic property leads to more desirable double bond characteristic between repeating units. Moreover, a more planar conjugated backbone will facilitate the π-electrons delocalization along the conjugated backbone, leading to a smaller bandgap [33]. These features offer important advantages of individually tuning the bandgap and energy levels of the conjugated polymer. The ideal conjugated polymer for a BHJ PSC should have a low-lying HOMO energy level to ensure a high V_{oc} and a narrow bandgap to maximize the J_{sc}. In addition, the charge mobility, molecular interaction, and stability of a conjugated polymer can also be optimized by appropriate backbone design. In 2003, Andersson and coworkers reported an alternating copolymer based on benzothiadiazole and fluorene, which exhibited a considerable PCE of 2.2% [34]. Afterward, numerous photovoltaic polymers with D-A structures were designed and applied in PSCs and some of the D-A copolymers achieved milestone PCEs in the development of PSCs.

Fluorene is one of the most popular donor units used in D-A polymers for PSCs due to their notable features of the polyfluorenes, such as good thermal and chemical stability, high charge carrier mobility, and high absorption coefficients. Moreover, both the central fused five-membered ring structure and alkyl chains anchored on the 9-position of the fluorene eliminate the severe steric hindrance of adjacent benzene units. Most fluorene-based conjugated polymers have low HOMO levels around −5.5 eV due to the weak electron donor ability of fluorene unit. As a result, V_{oc} of polyfluorene-based BHJ PSCs are generally around 1 V. However,

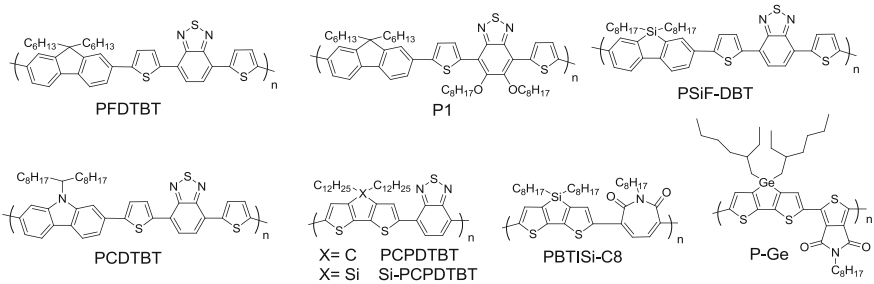

Fig. 2.10 The molecular structures of fluorene and its analog-based D-A copolymers

these polymers usually have relatively large bandgaps, which are not ideal for efficient light harvesting. The copolymer PFDTBT (Fig. 2.10) with alternating fluorine and di-2-thienyl-2,1,3-benzothiazole presents a J_{sc} of 4.66 mA/cm^2, a V_{oc} of 1.04 V, a *FF* of 0.46, giving a PCE of 2.2% [34]. After incorporating octyloxy chains on benzothiadiazole rings, the P1 with high molecular weight and solution processibility showed an improved PCE of 3.1% [35]. Further changing the bridging atom of the fluorene from carbon to silicon has a strong effect on the electron-donating ability and energy levels of related polymers (PFDTBT *vs.* PSiF-DBT, Fig. 2.10) [36]. Furthermore, silafluorene-based polymers have higher electroluminescent efficiency, thermal stability, and slightly larger hole mobility [37]. Therefore, a larger J_{sc} has been demonstrated with a little drop on V_{oc}, and a PCE over 5% was realized for a silafluorene-based polymer. When substituting the center carbon in the fluorene unit with a nitrogen (i.e., converting the fluorene into the carbazole), the carbazole-based polymers show an increased HOMO energy level and more excellent p-type transporting ability. Heeger et al. synthesized a carbazole-based polymer (PCDTBT), as shown in Fig. 2.10, has been demonstrated with a V_{oc} of 0.88 V, a J_{sc} of 10.6 mA/cm^2, and an impressive *FF* around 66%, leading to an overall PCE over 6% in its BHJ cells [38].

To address this bandgap challenge, the thiophene analog of the fluorene, cyclopentadithiophene (CPT), and silol dithiophene donor units by fusing two thiophenes were developed. The PSC based on PCPDTBT with alternating CPT donor unit and benzothiadiazole acceptor unit (Fig. 2.10) and $PC_{71}BM$ shows a significantly increased J_{sc} up to $\sim$11 mA/cm^2 by optimizing the morphology [39]. In comparison with CPT unit, the silol dithiophene donor unit shows a similar electron-donating ability, hence the silol dithiophene-based polymer (Si-PCPDTBT, Fig. 2.10) giving a nearly identical HOMO levels and bandgaps with those of PCPDTBT. Moreover, Si-PCPDTBT allows a better stacking of the polymer backbone. This helps improve hole and electron mobility of Si-PCPDTBT/$PC_{71}BM$ blend, a factor of 2–3 higher than those of the PCPDTBT/$PC_{71}BM$ blend. Thus, a pronounced increases on both the V_{oc} (from 0.37 to 0.57 V) and the J_{sc} (from 15.5 to 17.3 mA/cm^2) under the same processing condition, with a PCE of 5.9% achieved for Si-PCPDTBT (vs. 2.7% for

PCPDTBT) [40]. Marks and co-workers further utilize silol dithiophene donor unit to copolymerize with imide-functionalized acceptor unit (bithiopheneimide, BTI), giving a copolymer PBTISi-C8 (Fig. 2.10) with more ordered and closer π–π stacking molecular arrangement, This feature is expected to enhance intermolecular charge transport perpendicular to the substrate, leading to a considerable J_{sc} of 12.8 mA/cm^2 [41]. Dithienogermole with Ge as the bridging atom was also reported by Reynolds et al. [42]. The polymer P-Ge exhibits decent photovoltaic properties with enhanced PCEs over 7% in inverted BHJ solar cells with $PC_{71}BM$ as the acceptor.

BDT derivatives are another popular class of donor units in constructing D-A copolymers, especially for the copolymers incorporating varied benzothiadiazole (BT) derivatives acceptor units owing to their strong electron-withdrawing and coplanarity properties. In 2011, You and co-workers prepared PBnDT-DTBT and PBnDT-DTffBT (Fig. 2.11), and applied them in PSCs [43]. In comparison, the fluorinated polymer PBnDT-DTffBT indicated an enhanced absorption coefficient and a downshifted HOMO level compared to PBnDT-DTBT without fluorine. In the PSCs, PBnDT-DTffBT exhibited a high PCE of 7.2% (V_{oc} = 0.91 V, J_{sc} = 12.9 mA/cm^2, and FF = 61%) using $PC_{61}BM$ as the acceptor. When the alkoxy-modified benzodithiophene replaced the alkyl-substituted benzodithiophene to construct the $PBDT_{HDO}$-DT_HBTff copolymer (Fig. 2.11), the PSC achieved a high PCE of 8.30% in Jiang's group [44]. Wang et al. developed a series of polymers with different π-bridges of furan, thiophene, and thienothiophene, and investigated their influence on the photovoltaic properties. The theoretical calculations indicated that the polymer structures gradually changed from z-shaped to an almost straight line when the π-bridges varied from furan to thiophene and then to thienothiophene, and the absorption bandgaps of the polymers ranged from 1.96 to 1.78 eV when the HOMO levels changed from −5.44 to −5.21 eV, which result in an increased J_{sc} but decreased V_{oc} [45].

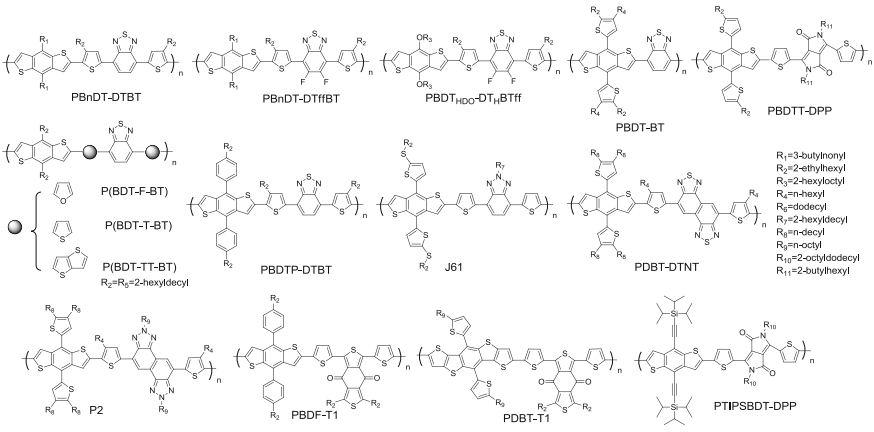

Fig. 2.11 The molecular structures of BDT-based D-A copolymers

Two-dimensional side chain groups, such as furan, thiophene, selenophene, or benzene, were frequently introduced on BDT to modify the properties of polymers (Fig. 2.11), and some very impressive photovoltaic results were obtained. For example, PBDT-BT could yield PCE of 9.4% in the PSCs [46]. Yang et al. from UCLA synthesized a low bandgap polymer PBDTT-DPP with a backbone of the diketopyrrolopyrrole (DPP) and BDT units, specifically for tandem solar cells. Single BHJ solar cells fabricated from PBDTT-DPP and $PC_{71}BM$ exhibited PCEs of more than 6%. The inverted tandem solar cells with P3HT:$IC_{60}BA$ as front cell materials and PBDTT-DPP:$PC_{71}BM$ as rear cell materials were successfully fabricated, which showed a certified PCE of 8.62% [47]. Janssen et al. designed a series of DPP-based polymers by incorporating different electron-donating units in the main chain to tailor the electronic structure and solubility of the polymers, which can effectively tune the morphology of active layer as well as improve the device performance [48]. Hou's group developed a PBDTP-DTBT. A maximum PCE of 8.07% was achieved with a V_{oc} of 0.88 V for the PSC by introducing 0.5% of DIO in the blend film [49]. Li et al. incorporated alkylthio-substituted BDT and more electron-rich "N" atom made BTz (a slighter weaker acceptor unit) into the polymer and synthesized J61, and a very impressive PCE of 9.53% was recorded by using a non-fullerene acceptor [50]. Cao et al. applied naphtho[1,2-c:5,6-c]bis[1,2,5]-thiadiazole (NT) as acceptor unit when designing highly efficient D-A copolymers. The PBDT-DTNT polymer containing NT demonstrated a pronounced red-shifted absorption spectrum and high hole mobility while maintaining a suitable energy level. PBDT-DTNT exhibited a promising photovoltaic performance with a PCE of 6% [51]. Furthermore, they developed naphtho[1,2-c:5,6-c]bis(2-octyl-[1-3]triazole) (TZNT) to enlarge the π-conjugated area of the BT-containing polymers [52]. After optimization of the alkyl side chains, P2 exhibited a PCE of 7.11% with a high V_{oc} of 0.92 V. Additionally, benzo-[1,2-c:4,5-c′] dithiophene-4,8-dione (BDD) acceptor units were widely used when designing photovoltaic conjugated polymers. Sun and co-workers developed a PBDF-T1 copolymer based on alkylphenyl-BDT and BDD, which indicated an optical bandgap of 1.82 eV and a HOMO level of 5.32 eV [53]. The PBDF-T1-based PSC device achieved a high PCE of 8.12%. Diketopyrrolopyrrole (DPP) possessed a strong electron-deficient amide group and a planar conjugated backbone. The DPP-based molecules showed excellent transport properties for both the electron and the hole. Hwang et al. synthesized PTIPSBDT-DPP by incorporating TIPS-substituted BDT and DPP, which achieved a low bandgap of 1.44 eV [54]. As a result, PTIPSBDT-DPP showed an OFET hole mobility up to 0.12 $cm^2\ V^{-1}\ s^{-1}$, and an extraordinary PCE of 8.0% with a V_{oc} of 0.76 V for the PSCs. To extend the π-conjugated system of BDT, dithienobenzodithiophene (DTBDT) was designed and applied by researchers when preparing photovoltaic polymers. Sun et al. prepared the PDBT-T1 copolymer, which possessed a wide optical bandgap of 1.85 eV and a low-lying HOMO level of −5.36 eV [55]. The PSC achieved a high PCE of 9.74% with an impressive *FF* of 75%, which was the highest PCE value for

the PSCs constructed with DTBDT-based polymers, thus suggesting that DTBDT had significant potential in designing highly efficient conjugated molecules for PSCs.

2.2.2 Acceptors

2.2.2.1 Fullerene Derivatives

Fullerenes are the predominant acceptor materials for PSCs because of their high electron mobility and efficient charge transfer from polymer donors to the fullerenes. The simple model fullerene is C_{60}. But it has limited solubility in organic solvents (chloroform, chlorobenzene, etc.) that hinders its application in PSCs. An ideal functional fullerene should exhibit good solubility in common organic solvents and suitable energy levels which match with donor materials to maximize V_{oc} of the devices. Based on this, research conducted on fullerene acceptor materials to date is mainly focused on the up-shifting LUMO levels by means of chemical functionalization.

Nowadays, soluble fullerene derivatives based on $PC_{61}BM$ and its analog $PC_{71}BM$ are considered the most advanced acceptor materials and widely used for BHJ PSCs. $PC_{61}BM$ (Fig. 2.12) was first synthesized for applications to physics and biology by Wudl et al. in 1995 [56]. The solubility of $PC_{61}BM$ in toluene is 35 mg/mL, which higher than that of C_{60} (2.15 mg/mL in toluene) [57, 58]. The crystallization temperature and melting point of $PC_{61}BM$ are 195 and 290 °C, respectively [59], indicating its good thermal stability for the application as an acceptor in PSCs. The electron mobility of $PC_{61}BM$ is *ca.* 2×10^{-3} cm^2 V^{-1}, which was measured by the space-charge-limited-current (SCLC) method [60]. The LUMO and HOMO levels of $PC_{61}BM$ reported by Li et al. are −3.91 and −5.93 eV, respectively, which was measured by the cyclic voltammetry with a three-electrode system in a mixed solution of *o*-dichlorobenzene/acetonitrile (5:1) with $PC_{61}BM$ and 0.1 mol L^{-1} $[Bu_4N]PF_6$ [58]. The PCE of PSCs based on the most representative active layer, P3HT/$PC_{61}BM$, reached 4.37% with the V_{oc} of 0.61 V [61]. Considering the fact that C_{70} exhibits significantly extended absorption than C_{60} in the visible part of the spectrum, Janssen and co-workers developed a $PC_{61}BM$ analog (namely $PC_{71}BM$, Fig. 2.12) to improve the light absorption in the visible region [62]. The synthetic procedure of $PC_{71}BM$ is similar to that of $PC_{61}BM$. Due to the asymmetric shape of C_{70}, unlike $PC_{61}BM$ is one single isomer, $PC_{71}BM$ is a mixture of three isomers: one chiral a-type isomer and two achiral b-type isomers, with the weight of 7:85:8 [62]. The solubility of $PC_{71}BM$ in chlorobenzene is 80 mg/mL, which is better than that of $PC_{61}BM$ [63]. The LUMO and HOMO levels of $PC_{71}BM$ are −3.91 and −5.87 eV, respectively [58]. So far, the PCEs of single-junction PSCs based on $PC_{71}BM$ as an acceptor has broken the 10% efficiency barrier [64–67].

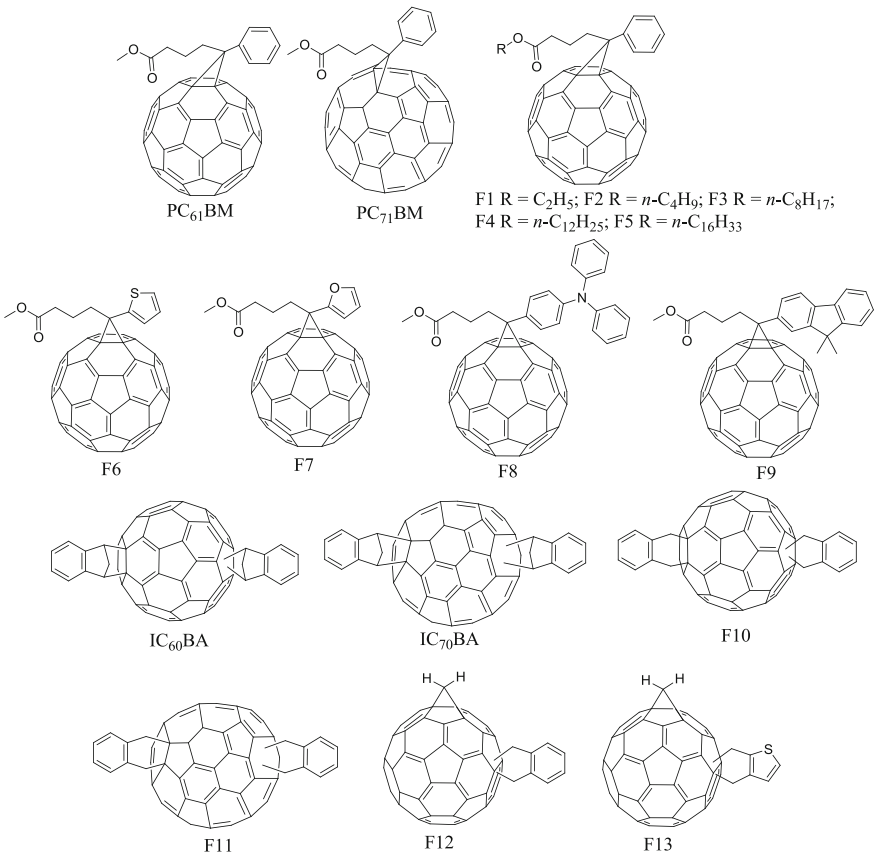

Fig. 2.12 The molecular structures of different fullerene derivative acceptors

The substituents on C_{60} in $PC_{61}BM$ can be generally divided as aromatic part and the non-aromatic part. Much effort has been devoted to understanding the relationship between the substituents of $PC_{61}BM$ and their photovoltaic properties. Replacing the methyl end group of $PC_{61}BM$ by different lengths alkyl chain (F1–F5, Fig. 2.12) showed little effect on their LUMO levels and UV-visible absorption spectroscopy, while influences the solubility of the derivatives [63, 68, 69]. Troshin et al. demonstrated that the solubility of fullerene derivatives affect the nanomorphology of their blend film with P3HT [63]. The solubility of F1 (19 mg/mL in chlorobenzene) which bears an ethyl group (Fig. 2.12) is poorer than that of $PC_{61}BM$ (50 mg/mL in chlorobenzene), and lower PCE of 2.7% was obtained when compared to the PCE of $PC_{61}BM$ (3.7%) based devices. Cao et al. synthesized four $PC_{60}BM$-like derivatives (F2, F3, F4, and F5, as shown in Fig. 2.12) with a longer alkyl chain end-capped group [68]. They found that F2 with butyl end group showed higher PCE than that of $PC_{61}BM$ when employing MEH-PPV as donor materials to fabricate the BHJ devices. Nevertheless, F3–F5 which have longer end group led to

poorer photovoltaic performance than $PC_{61}BM$ and F2, indicating that high carrier mobility and good compatibility with donor materials are also important besides the solubility when designing fullerene derivative acceptors.

In comparison with $PC_{61}BM$, replacing phenyl group by thienylene ring on $PC_{61}BM$ (F6, Fig. 2.12) led to a poorer solubility than $PC_{61}BM$, but has little effect on the photovoltaic performance [63]. Jen et al. reported the synthesis and photovoltaic application of triphenylamine and dimethylfluorene-substituted $PC_{61}BM$s (F8 and F9, Fig. 2.12) for PSCs [70]. By replacing the phenylene ring in the side chain of $PC_{61}BM$ with triphenylamine or dimethylfluorene unit, the thermal stability of the corresponding devices is remarkably enhanced by suppressing the destructive phase segregation between the polymer and fullerene due to amorphous nature and high glass-transition temperature of F8 and F9. The two acceptors show comparable PCE ($\sim$4%) to $PC_{61}BM$, especially, there is no significant degradation in morphology or solar cell performance even after 10 h annealing at 150 °C, indicating the attractive application for improving the long-term stability of PSCs [70].

Because the second functionalization on the core structure of the mono-substituted fullerene could further reduce the π-conjugation and electron delocalization in the cage, bisadduct fullerene derivatives have large electrochemical reduction potentials and, thus, high lying LUMO levels. Indene-C_{60} bisadduct ($IC_{60}BA$, Fig. 2.12) with a higher LUMO level (0.17 eV up-shifted than that of $PC_{60}BM$) was reported by Li et al. as an acceptor material to further improve the photovoltaic performance of P3HT [71]. $IC_{60}BA$ has easier synthesized route and purification in comparison to $PC_{61}BM$. Benefited from the up-shifted LUMO level of $IC_{60}BA$, the device based on P3HT: $IC_{60}BA$ achieved an encouraging PCE of 5.44% and a high V_{oc} of 0.84 V, which is 0.26 V higher than that of P3HT:$PC_{61}BM$ based device [71]. Indene-C_{70} bisadduct ($IC_{70}BA$, Fig. 2.12) possesses 0.19 eV higher LUMO than that of $PC_{71}BM$, which lead to a promising PCE of 5.79% in the PSCs based on P3HT: $IC_{70}BA$ [72]. By further optimizing the device based on P3HT: $IC_{70}BA$ with 3% 1-chloronaphthalene and pre-thermal annealing at 150 °C for 10 min, a remarkable PCE of 7.40% was obtained, which is the highest value reported in the literature for P3HT-based PSCs [73]. Obviously, $IC_{60}BA$ and $IC_{70}BA$ have been emerged as the most successful acceptors when blending with P3HT for PSCs. Some bisadduct fullerene derivatives with different functional groups were explored as acceptors for PSCs (Fig. 2.12). Wang et al. reported a dihydronapthyl-based C_{60} bisadduct derivative (F10, Fig. 2.12), which is synthesized in high yield at mild temperature [74]. The high LUMO level of F10 resulting in a high V_{oc} of 0.82 V when blending with P3HT as active layer for PSCs, leading to a PCE of 5.73% [74]. The dihydronaphthyl-based C_{70} fullerene bisadduct derivative (F11, Fig. 2.12) has improved absorption and high lying LUMO level, resulting in a higher PCE of 5.95% [75]. Ding et al. developed two 56 π-electron methanofullerene derivatives (F12 and F13, as shown in Fig. 2.12) [76]. The combination with high LUMO levels and sterically small addends of F12 and F13 feature their outstanding performance when blending with P3HT to fabricate devices. Most fullerene bisadducts enable for higher V_{oc} in the PSCs (compared with $PC_{61}BM$ based devices) due to their increased LUMO levels. However, these bisadducts derivatives are usually mixtures of different isomers with different LUMO levels,

resulting in films with lower electron mobility in comparison with $PC_{61}BM$. Such energy level distribution is not only detrimental to charge transport, but possibly also to electron transfer. It remains, therefore, challenging to produce PSCs with higher V_{oc} than that of $PC_{61}BM$, but without decreasing in *FF* and J_{sc} values.

2.2.2.2 Non-fullerene Acceptors

Fullerene derivatives ($PC_{61}BM$ and $PC_{71}BM$) are the most common and successful acceptor materials used in highly efficient PSCs. However, the fullerene-based PSCs suffer relatively large energy loss (generally over 0.6 eV) and thus limit its further improvement [77, 78]. What is more, fullerene-based materials have some other drawbacks such as poor absorption properties (Fig. 2.13), and costly preparation [79]. To address these problems, more and more efforts have been devoted to designing and synthesizing non-fullerene acceptor materials, and the PCE of fullerene-free PSCs has been improved to over 12%, almost approaching the best results of its fullerene counterparts. Over the past several years, many types of small molecule and polymer acceptors were developed and applied in PSCs, and some of them achieved very impressive results. The rapid development of non-fullerene PSCs has opened a new avenue for the fundamental study of organic photovoltaics.

Small molecule non-fullerene acceptors

The most widely investigated non-fullerene small molecules to date have been based on the perylene diimide (PDI) core unit, which has shown to possess many desirable design features as electron acceptors for PSCs, such as high electron mobility and high electron affinity (EA; *ca.* 3.9 eV for the unmodified PDI, which is similar to widely used fullerene acceptors). However, PDIs are easy to form micrometer-sized crystallites during solution process due to their strong π–π stacking tendency. The large crystallites can prevent a sufficiently large donor–acceptor interfacial area for efficient exciton splitting. A PDI dimer (TP, Fig. 2.14) using hydrazine as a linker in the imide position, allowing twisting of the dimer and

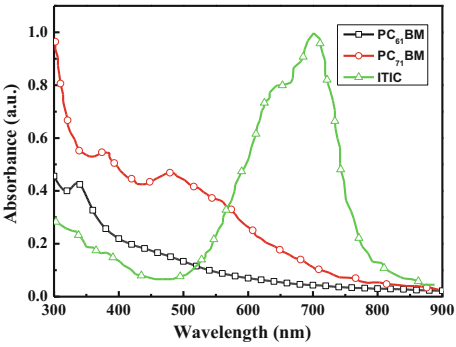

Fig. 2.13 The absorbance of the fullerene acceptors $PC_{61}BM$, $PC_{71}BM$ and non-fullerene acceptor ITIC (the molecular structure shown in the following part)

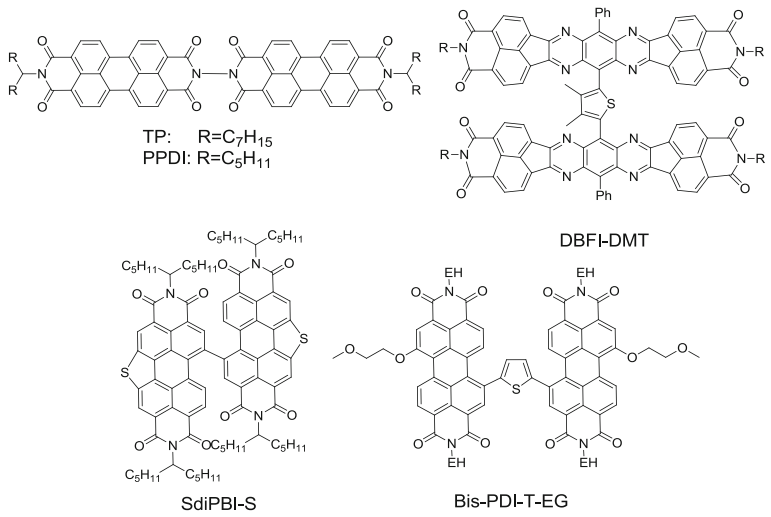

Fig. 2.14 The molecular structures of PDI-based non-fullerene acceptor materials

thus suppression of crystallinity [80]. An average domain size of about 10 nm was observed for the blend of PBDTTT-C-T/TP (1:1), which resulted in a PCE of 3.2% with a high J_{sc} of 9.0 mA/cm^2. Judicious optimization of both the acceptor and the polymer donor recently resulted in an improved PCE of 5.45% for PPDI [81]. Twisted PDI dimer structures have been continually exploited as an efficient strategy for their use in BHJ PSCs. A closely related PDI dimer (SdiPBI-S, Fig. 2.14) with sulfur bridges in the bay positions had a more twisted molecular configuration, a slightly lower electron affinity, and a blue-shifted absorption profile providing better spectral complementarity with narrow bandgap donor polymers [82]. Consequently, a high PCE of 7.16% was achieved with the PDBT-T1 donor polymer owing to a high V_{oc}, as well as large J_{sc} and *FF* values. Further optimizing the structure of PDI dimer, SdiPBI-Se (Fig. 2.14) with Se bridges was synthesized. With a well-established wide-bandgap polymer (PDBT-T1) as the donor, a high efficiency of 8.4% with an unprecedented high *FF* of 70.2% is achieved for solution-processed PDBT-T1:SdiPBI-Se based PSCs [83]. Moreover, a thienyl-bridged PDI dimer, Bis-PDI-T-EG (Fig. 2.14), which has a dihedral angle of 50°–60° between the two PDI-thienyl planes, showed significant reduction of the aggregation compared with its monomeric counterpart in BHJ blends [84]. Compound Bis-PDI-T-EG yielded small phase domains with a size of ~30 nm, which results in a corresponding PCE of up to 4.03%, while its monomeric counterpart produced crystalline domains on the order of hundreds of nanometers with a PCE of only 0.13%. Further fine-tuning of the film-forming process by solvent additives and solvent vapor annealing also improved the PCE to 6.1% [85].

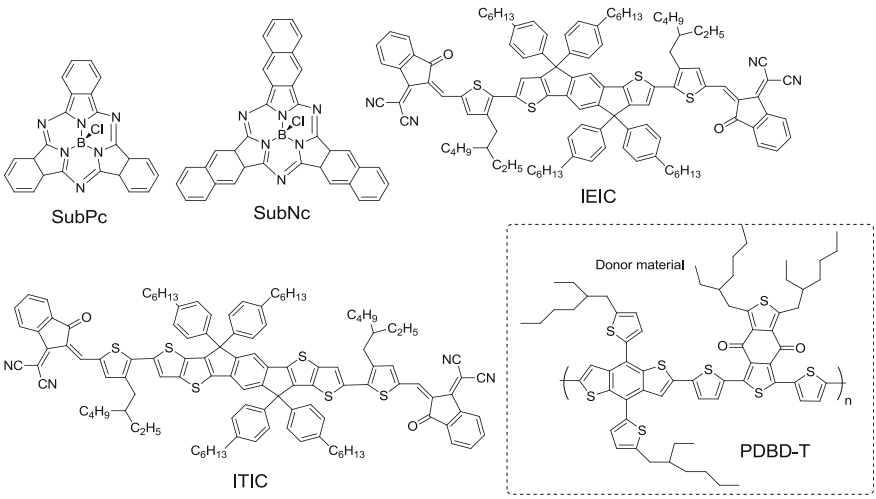

Fig. 2.15 The molecular structures of other non-fullerene acceptor materials

Linking two tetraazabenzodifluoranthenes (BFIs) units in the central tetraazaanthracene position with thiophene promotes a nonplanar 3D molecule, DBFI-DMT (Fig. 2.14), which showed an improved performance over the $PC_{61}BM$ in blends with PSEHTT donor polymer, demonstrating a maximum PCE of 6.4% in inverted BHJ structures ascribed to more efficient molecular packing and improved isotropic charge transport due to a more twisted molecular conformation [86].

Subphthalocyanines (SubPcs, Fig. 2.15), and in particular boron SubPc chlorides, are another class of rotationally symmetric molecules that have shown great promise in PSC applications. Bilayer devices using either SubPc or SubNc as the acceptor material with an α-sexithiophene donor afforded high PCEs of 4.69% and 6.02%, respectively [87]. Moreover, efficiencies as high as 8.40% were achieved with a three-layer device architecture employing both SubPc and SubNc due to a high V_{oc} of 0.96 V, a J_{sc} of 14.55 mA/cm^2, and a FF of 61% [87]. The three photoactive materials have complementary optical absorption profiles. Both IQE and EQE spectra importantly show efficient photocurrent generation by all three absorbing materials. Over the past 2 years, small acceptor molecules based on indacenodithiophenes (IDT) units have been explored and showed great potential in achieving outstanding photovoltaic performance. In 2015, Zhan et al. reported the synthesis of IEIC (Fig. 2.15), which showed a low bandgap of 1.57 eV and an appropriate LUMO level of −3.82 eV [88]. PSCs based on IEIC:PTB7-Th showed high PCE of 6.31%. Then they designed and synthesized a series of non-fullerene acceptors containing indacenodithieno[3,2-b]-thiophene with different side chains to further optimize their photovoltaic performance [89–91]. ITIC with phenyl side chains (Fig. 2.15) was developed in 2015 and exhibited initial PCE of 6.8% when PTB7-Th was used as donor [89]. By applying novel polymer donor materials based on benzodithiophene and fluorobenzotriazole, further improved PCE was

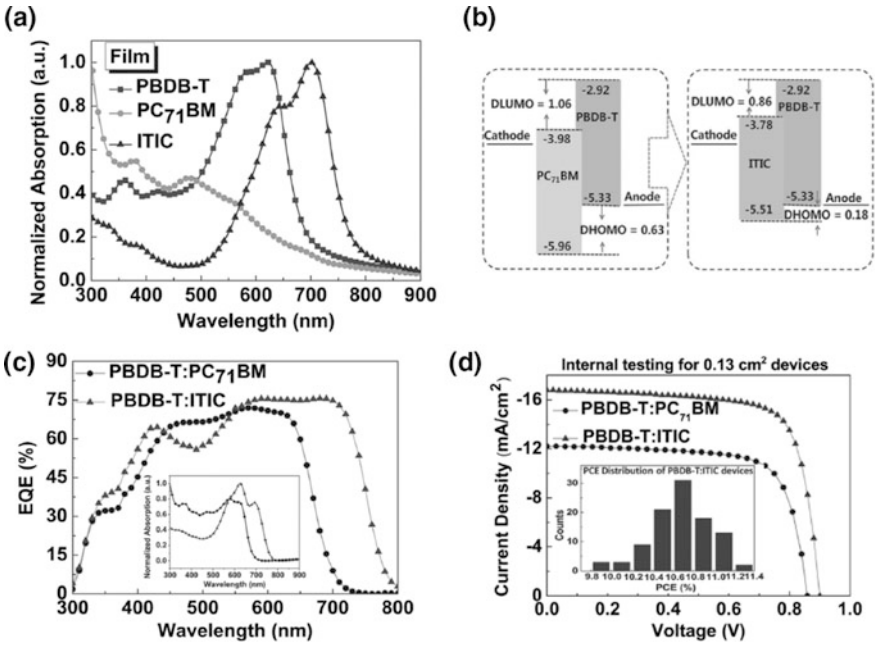

Fig. 2.16 **a** The absorption spectra of donor polymer PBDB-T, fullerene acceptor $PC_{71}BM$ and non-fullerene acceptor ITIC; **b** molecular energy level alignments in the devices based on PBDB-T:$PC_{71}BM$ and PBDB-T:ITIC; **c** EQE curves and absorption spectra of PBDB-T:$PC_{71}BM$ and PBDB-T:ITIC blend film; and **d** *J-V* curves of $PC_{71}BM$-baseed and ITIC-based cells. Reprinted with permission from Ref. [92]. Copyright 2016 by WILEY-VCH Verlag GmbH Co. KGaA, Weinheim

obtained for ITIC -based PSCs by Li and co-workers [50]. For instance, a high PCE of 9.53% was obtained when J61 was used as a donor in PSCs. Recently, Hou and co-workers reported a breakthrough PCE of 11.21% in thermal stable PSCs based on PBDB-T and ITIC [92]. As shown in Fig. 2.16, the absorption spectrum of the PBDB-T film substantially overlaps that of the $PC_{71}BM$ in the visible range but is complementary with that of ITIC; therefore, the PBDB-T:ITIC blend film has a more favorable optical absorption than fullerene $PC_{71}BM$-based blend film, thus for broader EQE photo response and higher photo-induced current.

Polymer non-fullerene acceptors

Polymer/polymer blend BHJ PSCs (all-PSCs) that utilize conjugated polymers as both electron donor and acceptor have recently attracted much attention because they have numerous potential advantages over conventional BHJ polymer/fullerene solar cells. The PCE of polymer/polymer BHJ solar cells was limited to around 2% until 2012 [93], it has steeply increased owing to the development of low bandgap polymer acceptors, which show both high electron mobility and high electron affinity similar to those of fullerenes [94]. Very recently, PCE of 8.27% [95] was reported.

Among the variety of the n-type polymers, the naphthalene diimide (NDI)-based copolymers have been the most successful polymer acceptors. In particular, the NDI-bithiophene (NDI-T2) based n-type polymer P(NDI2OD-T2), which also is known as Polyera Activeink N2200 (Fig. 2.17), has been most extensively used in all-PSCs, because of its high electron mobility, high electron affinity, and broad light absorption [96]. By developing new polymer donor and morphology control, the PCE of the all-PSCs with N2200 as acceptor has been steadily improved up to 8% in the last few years [97–100]. For example, Kim and co-workers fabricated all-PSCs with a fluorine substituted polymer as donor (PPDT2FBTH) and N2200 as acceptor, delivering a PCE of 5.0% [99]. Ito et al. efficiently improved the charge carrier generation and collection by utilizing conventional PTB7-Th as donor and N2200 as acceptor, finally leading to a PCE of 5.7% [98]. Hou et al. highlighted for the first time the importance of donor/acceptor molecular interactions and orientation correlations in governing the device performance of all-PSCs. They replace the anisotropic polymeric donor PBDTBDD with its 2D-conjugated version PBDTBDD-T. The efficiency of all-PSCs featuring the anisotropic polymer acceptor N2200 was drastically boosted to 5.8% [101]. It is noted that N2200 mainly absorb the light at ~400 nm and in the wavelength range of 600–800 nm with very weak absorption in the visible region from 430 to 600 nm, therefore a medium bandgap polymer donor with main peak absorption in the visible region can efficiently complement to that of N2200, hence giving higher performance all-PSCs. Ito et al. have demonstrated that the PCE of low bandgap PBDTTT-EFT/N2200 binary BHJ solar cells can be improved by introducing medium bandgap PCDTBT to complement the weak absorption at visible wavelengths. For the ternary blend all-PSCs containing 10 wt% PCDTBT, the EQEs at visible wavelengths was successfully increased to 65–70%, and a PCE as high as 6.65% was obtained [102]. More recently, Li et al. selected a medium fluorinated bandgap benzodithiophene-alt-benzotriazole copolymers (J51, bandgap of 1.91 eV) to be used as donor polymers for developing high-efficiency all-PSCs with N2200. The polymer donor and acceptor possess matching electronic energy levels, complementary absorption in the vis-NIR region of 300–850 nm, as well as appropriate nanoscale phase-separated D/A interpenetrating network, which delivered the best PCE (8.27%) in all-PSCs up to date [95]. Regarding other NDI-based copolymers acceptors, replacement of bithiophene unit in the backbone of N2200 with biselenophene resulted in PNDIBS (Fig. 2.17), giving a high field-effect electron mobility (0.07 $cm^2/(V\ s)$) and broad visible-near-infrared absorption band with an optical bandgap of 1.4 eV. All-PSCs comprised of PNDIBS acceptor and P3HT donor has a PCE of 0.9%. Further modification of N2200 is the fluorination of bithiophene unit. This approach can effectively improve its electron-withdrawing ability, crystallinity, and electron transport of the resulting polymers P(NDI2DT-F2T) (Fig. 2.17). As a result, a PCE as high as 6.71% was obtained from the P(NDI2DT-F2T)/PBDTT-TT-F-based all-PSC, which was a remarkable enhancement in comparison with the reference device with N2200 as the acceptor. PNDIT-HD is composed of NID and one thiophene (Fig. 2.17). When it was blended with PTB7 as donor to fabricate a PSC, a PCE of 5.96% was obtained.

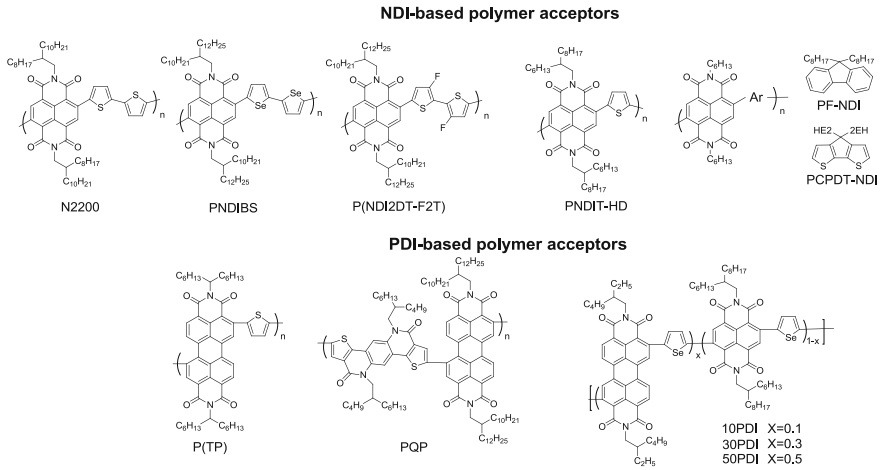

Fig. 2.17 The molecular structures of NDI or PDI-based polymer acceptors

[103] Some fused conjugated units were copolymerized with NDI as well such as fluorine and cyclopentadithiophene resulting in polymers PF-NDI and PCPDT-NDI (Fig. 2.17). A PCE of 1.63% was achieved from the PF-NDI/P3HT-based an all-PSC [104], while a PCE of 1.12% can be obtained from the PCPDT-NDI/PTB7 blending device [105].

Perylene diimides (PDIs) and its derivatives exhibit excellent thermal, chemical, and photochemical stability as well as strong electron-withdrawing ability and absorption in the visible and near-infrared region. These features make PDI-based materials suitable as electron acceptors in the field of BHJ solar cells. A comprehensive study was performed on a series of PDI-based polymers with different comonomers. P(TP), as shown in Fig. 2.17, containing PDI unit and thiophene comonomers in the PDI polymer backbones was investigated as the acceptor in all-PSCs, where P(TP) was used as a model system for phase separation control during solution printing. This solution printing method was designed to use a microstructured printing blade, which can induce polymer crystallization by fluid flow. As a result, the highest PCE of 3.2% was obtained, which is the best cell efficiency for solution printed an all-PSCs so far [106]. A novel acceptor polymers PQP (Fig. 2.17) composed of dual electron-withdrawing units were recently reported. The morphology of blended films between the acceptor PQP and the PTB7 donor polymer can be finely tuned by adding chloronaphthalene co-solvent. A face-on arrangement and favorable phase separation in the blend was observed, leading to a high PCE of 3.52% achieved from the PTB7/PQP blend film based all-PSC [107]. Jenekhe et al. use dual-acceptor (NDI and PDI) strategy to synthesize the random copolymer containing selenophene unit. By changing the ratio of compolymerization, it is easy to optimize the crystallinity of blend film between PBDTTT-CT donor and random polymer acceptor. The 30PDI (Fig. 2.17) presents

an optimal crystallinity (crystalline domain size of 5.11 nm) provided a compatible blend with PBDTTT-CT. The all-PSC based on 30PDI as the acceptor component afforded a PCE of 6.3% with high J_{sc} of 18.6 mA/cm^2 and EQE of 91% [108].

2.3 Morphology

While the aforementioned tremendous design and synthetic endeavors that focus on photoactive materials to optimize their optoelectronic properties, morphology tuning of the BHJ blend structures demonstrates also critical importance for rationally improving device performance. The morphology of BHJ affects the probability of photo-induced excitons diffusing to the donor–acceptor interface, exciton dissociation efficiency to generate free charge carriers and charge transport channels for collecting the electrons and holes, all of which are the key steps in the photo-electric conversion process of BHJ PSCs. In particular, too large a domain of high purity would negatively impact the exciton dissociation, while too small a domain with the excellent mixing of donor and acceptor would impede the charge transport and increase probability for free carrier recombination. Given the intrinsically limited diffusion length (about 10 nm) of the Frenkel excitons in organic materials, a desirable morphology of BHJ films should include pure donor-rich and acceptor-rich domains of 10–20 nm length scale, connected through a bi-continuous interpenetration network [2, 109–111]. Furthermore, both crystalline regions and amorphous regions are also important. In the past decade, considerable efforts have been conducted to study how to precisely characterize and control the nanomorphology of the BHJ blends, and consequently contributing to maximize the PCE of PSCs [5, 112–117].

2.3.1 Morphology Characterization Techniques

Characterizing the morphology of the blend films with high chemical specificity and spatial resolution is a challenging. Full characterization of morphology involves surface features, structural order (i.e., the crystallinity and molecular packing orientation), and the domain size and purity, etc., thus requiring the use of complementary techniques.

One of the most common tools in this filed is atomic force microscopy (AFM). Since the surface phase shift and undulation are highly sensitive to tip-sample force interactions, it thus probes the surface properties of the samples. The tapping mode as a combination of noncontact and contact modes are commonly used for organic semiconducting films. The obtained topographical images reveal the surface features, for example, roughness on the surface of the blends by height images, and donor–acceptor phase separation structured domain size of various length scales by phase images [28]. Other useful techniques include the conductive AFM (c-AFM),

photoconductive AFM (pc-AFM) and scanning electron microscopy (SEM). Noncontact scanning Kelvin probe microscopy (SKPM) has also been incorporated to provide supplemental surface information (e.g., distribution of each component) based on the surface electronic states [118–122]. These characterizations reveal detailed information about the surfaces of layers but limited in detecting the bulk nanostructure within mixed films.

Transmission electron microscopy (TEM) is able to visualize bulk structure with very high-resolution (1 nm or less). TEM is typically operated in the bright-field (BF) imaging mode, in which the scattering contrast depends on the mass of the atoms, density, and region thickness. For example, thick regions or regions with heavier atoms of the sample appear darker, while samples with thinner regions or no sample appear brighter. As indicated, the variation of the chemical and/or the electronic structures of the donor and acceptor bear the possibility to distinguish the different D/A phase, and thus reveal the nanostructures in the BHJ blends [123, 124]. A further increase of TEM contrast is enabled by adopting energy-filtered TEM (EF-TEM) [125, 126] and scanning TEM (STEM) [127] via detecting the transmitted electrons with an energy loss feature of a specific atomic core level and the average atomic number (z) of the component material, respectively.

X-ray scattering is another powerful tool to probe the nanostructure information such as the crystallite sizes, the crystalline lattice spacing, and molecular packing orientations [117]. In this approach, X-rays impinge on the sample at a small grazing angle and the scattered X-rays at different angles are detected for imaging. Compared to the microscopy techniques, X-ray scattering also affords in situ measurement of the sample, which is particularly suited to investigate the time-resolved structure evolution during the film drying or annealing for BHJ blends [128, 129]. Because most of the organic semiconducting materials have weak crystallinity, two-dimensional grazing incident wide-angle X-ray scattering (2D GIWAXS) using a synchrotron beamline with a high X-ray photon flux and beam collimation has recently been widely used to investigate accurate structural information within BHJ blends. Figure 2.18 shows the schematic representation of the typical 2D GIWAXS setup. 2D GIWAXS characterization provides detail information on the preferential orientation (i.e., edge-on or face-on), the lattice spacing of the molecular stacking, and domain size in the BHJ blends [130–132]. 2D grazing incident small-angle X-ray scattering (2D GISAXS) also gives some insight into the morphology (e.g., the average domain size, shape, and inter-domain correlation of the BHJ components) [133]. To gain a complete picture of bulk morphology, the dominant domain size, and the distributions of domain spacing of either donor-to-donor or acceptor-to-acceptor phases, relative domain purities, and the donor–acceptor interface are evaluated with resonant soft X-ray scattering (R-SoXS) [134–137]. Hence, the morphology parameters extracted from these X-ray scattering techniques allows deep understanding of the relationship between morphology structure and the device performance.

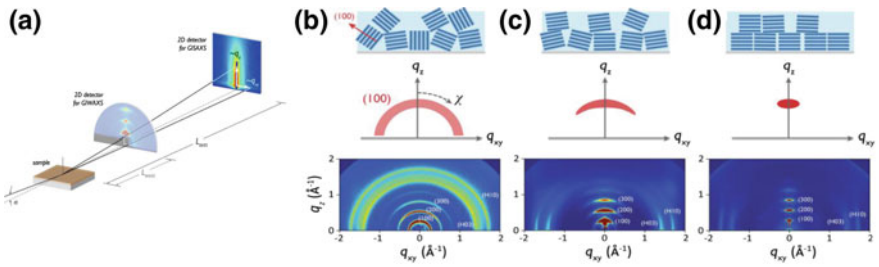

Fig. 2.18 **a** Schematic representations of the typical 2D GIWAXS and GISAXS setup: q_z and q_{xy} denote X-ray scattering in the out-of-plane and in-plane directions, respectively. **b** Randomly oriented arrangements of crystallites, with no preference for a specific crystallographic orientation (100) with respect to the substrate normal produce rings in the diffraction patterns. **c** Textured or oriented films with a distribution of crystallite orientations produce arcs of diffracted intensity. **d** Highly oriented films produce spots or ellipses. Reprinted with permission from Ref. [117]. Copyright 2012 by American Chemical Society

2.3.2 Morphology Engineering

There has been intensive research on developing approaches to tune the morphology, commonly including physical methods and chemical modification. The molecular structure of the photoactive materials including the conjugated backbones, the side chains, and the molecular weights mainly decides its solubility in the solvent and their miscibility in solution as well as film structures. Different materials mentioned above display variation in morphology. In this section, physical methods to manipulate the morphology of active layers will be introduced.

2.3.2.1 Processing Solvents and Solvent Annealing

Processing solvents can influence the morphology of the BHJ blends by largely determining the solubility and miscibility of donor and acceptor materials, as well as the rate of film formation. Thus, the choices of solvents and methods of film deposition play critical roles in optimizing morphology for improving device performance.

In most cases, high boiling solvent such as chlorobenzene (CB), dichlorobenzene (DCB), and trichlorobenzene (TCB) bears higher performance than low boiling solvents like chloroform (CF) mainly due to their better solubility for photoactive materials and/or slow film drying for structure reorganization. In 2001, Shaheen et al. first reported the improved PCE of the MDMO-PPV:$PC_{61}BM$ based PSCs from 0.9 to 2.5% by changing the processing solvent from toluene to chlorobenzene, which was attributed to chlorobenzene effectively reducing the phase segregation of the active layers, resulting in an increase of the charge dissociation efficiency and charge carrier mobility for both holes and electrons [28]. Ruderer et al. probed the impact of the solvent with different boiling points on the

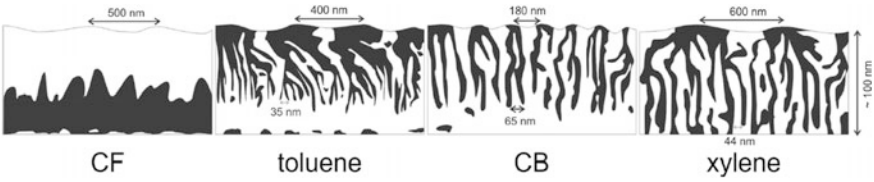

Fig. 2.19 *Black* and *white* schematic morphology of P3HT:$PC_{61}BM$ films made using CF, toluene, CB, and xylene solutions, as reconstructed from the results of AFM, XRR, and GISAXS investigations. *Black areas* correspond to pure $PC_{61}BM$ phases and *white* to pure P3HT phases. Reprinted with permission from Ref. [138]. Copyright 2011 by WILEY-VCH Verlag GmbH Co. KGaA, Weinheim

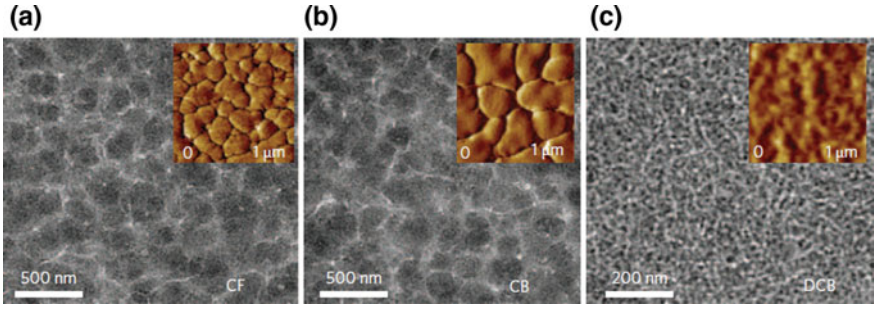

Fig. 2.20 TEM images of PCDTBT:$PC_{71}BM$ films spin-cast from CF (**a**), CB (**b**) and DCB (**c**) solvents. The *insets* show the surface phase images measured by atomic force microscopy (AFM). Reprinted with permission from Ref. [38]. Copyright 2009 by Nature Publishing Group

morphology of P3HT:$PC_{61}BM$ blends [138]. A combination of AFM, X-ray reflectivity (XRR), and GISAXS investigations demonstrated changes in vertical and lateral phase separation, where toluene, CB, and xylene showed a $PC_{61}BM$-riched top layer compared to a P3HT-rich top layer for chloroform (Fig. 2.19). The PSCs made from toluene, CB, and xylene solutions showed higher efficiencies of almost 2.6% than efficiency of 0.4% for CF-fabricated PSCs. The above-mentioned rational solvent choice has been adopted to optimize the morphology of donor–acceptor (D-A) polymer based BHJ blends. Park et al. reported that DCB-processed PCDTBT:$PC_{71}BM$ blend showed much smaller domains as compared to the CB- and CF-processed blends (Fig. 2.20), which is beneficial for reducing charge carrier recombination, thus improving efficiency up to 6.1% [38]. In some cases, low boiling CF also demonstrated efficient in achieving high device performance. Mori et al. reported the low boiling solvent CF gave a well-mixed blend morphology consisting of nanoscale phase-separated domains as compared to micrometer-scaled phase-separated structures for CB- and DCB-processed polymer/polymer blends P3HT:PF12TBT, resulting in significant increases of efficiency from 0.54% (DCB-processed) and 0.80% (CB-processed) to 2.0% (CF-processed) [139]. Recently, Chen's group developed a series of benzo

[1,2-b:4,5-b′]dithiophene-based and oligothiophenes-based small molecules based solar cells with high PCEs when using CF as the processing solvent. Combining with further chloroform-solvent annealing and/or thermal annealing treatment gives outstanding PCEs around 10% [140–142].

Mixed solvents, on the other hand, also enable well-tuning of the BHJ morphology by rationally determining both the solubility and the rate of the film drying. This approach was pioneered by Zhang et al., where they showed the photocurrent density of the devices prepared from a mixed solvent of CF:CB (80:1, v/v) was almost double those of CF-, CF:toluene-, and CF:xylene-processed PSCs [143]. Such enhancement was attributed to a finer and more uniform distribution of domains in CF:CB-processed APFO-3:$PC_{61}BM$ blend films, which is associated with the increase in free charge carrier generation. Since then, this strategy has been developed to improve device performance, and also seems promising for the large-scale production of organic solar cells. For instance, Ye et al., exhibited increased device performance from 4.87 to 5.38% when using DCB:CF (4:1, v/v) to replace pure DCB as the processing solvent for PDPP3T:$PC_{71}BM$ based devices [136]. Detailed measurements of AFM, 2D GIWAXS, and R-SoXS showed that addition of CF to DCB resulted in a marked improvement in domain purity and reduced domain size with sharper donor/acceptor interface, leading to similar J_{sc} and V_{oc} but higher *FF* (from 0.59 to 0.70). Intensive works of this approach for large-scale manufacturing have been made by Brabec group [144–146]. As one of such examples, DCB:mesitylene mixed solvent results in a reliable printed firing with optimum wetting, spreading, and drying rate of the formulation on the substrate, thus offering increased PCE from 1.3 to 2.9% for inkjet-printed P3HT:$PC_{61}BM$ blends as compared to pristine solvents commonly used [144].

With the rapid progress in PCEs, developing halogen-free solvents to replace predominately used halogenated solvents for PSC process becomes an urgent work for applications [147–150], due to the halogenated solvents may induce environmental issues like acid rain and depletion of the ozone layer. Chueh et al. used two non-chlorinated solvents, o-xylene, 1,2,4-trimethylbenzene and small amounts of 1,2-dimethylnaphthalene as additives to prepare BHJ films, and realized comparable device performance with the highest efficiency up to 7.26% to that of 7.22% for pristine DCB-processed devices [151]. Other halogen-free solvents including N-methylpyrrolidone (NMP) and 2-methylterahydrofuran have also been incorporated to replace the chlorinated processing solvents. Recently, Zhang et al. reported 2-methylanisole (MA) as the single processing solvent to realize a PCE of 9.67% for PBDT-TS1:$PC_{71}BM$ based solar cells without using any additives or post-treatment. They found MA-, xylene:NMP-, and DCB:DIO-processed BHJ films exhibited similar surface roughness imaged with AFM and almost same phase separation in TEM images (Fig. 2.21), thus indicating MA can replace conventional solvents in well-tuning the morphology within PBDT-TS1:$PC_{71}BM$ films [152].

Solvent annealing is another effective way to modulate the morphology of the active layers in PSCs by controlling the film-structural evolution process [61]. In 1994, Inganäs group obtained POPT films with highly ordered molecular packing after exposing the film to CF vapor [153]. Afterward, similar solvent annealing

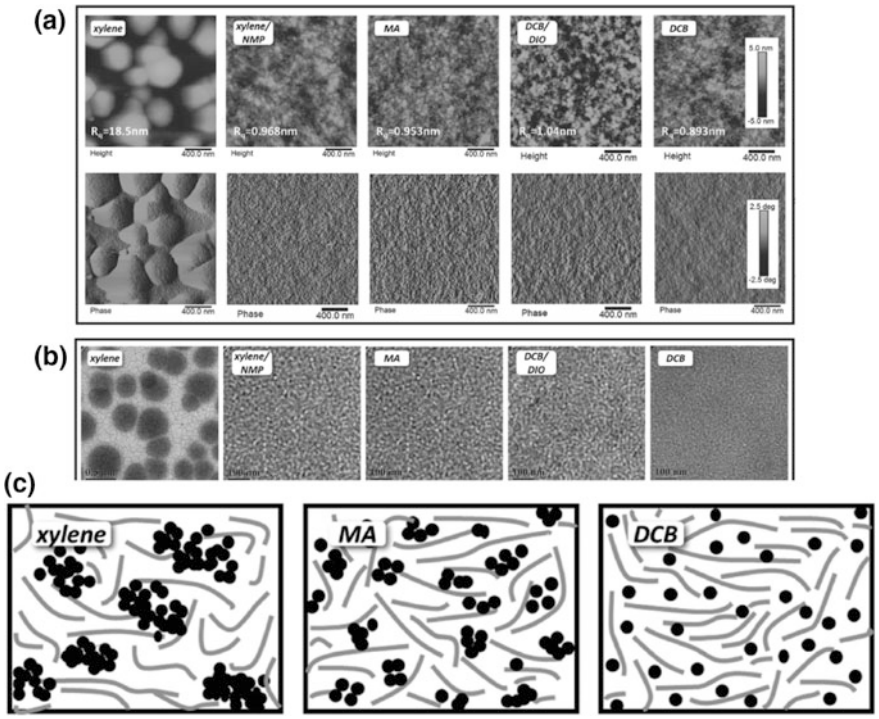

Fig. 2.21 **a** AFM and **b** TEM images of blend films processed by various solvent systems, **c** the morphology schema of the blend films prepared by different single solvents (the *dots* and *lines* refer to PC_{71} BM and polymers, respectively). Reprinted with permission from Ref. [152]. Copyright 2016 by WILEY-VCH Verlag GmbH Co. KGaA, Weinheim

approaches have been explored for BHJ blends. In this way, the as-cast films were generally treated with solvents or solvent vapors in a partially closed container like a petri dish. Such treatment can slow the film drying, thus providing more opportunities to structure evolution such as the phase separation and the crystallization within the BHJ blends. Mihailetchi et al. found the hole mobility of P3HT in the P3HT:PC_{61}BM blend improved by 33-fold up to 5.0×10^{-7} m^2 V^{-1} s^{-1} via solvent annealing, and the resulting devices showed higher efficiency of 3.7% than 3.1% for fast-drying processed devices [154]. Shrotriya et al. also revealed increase both in exciton generation rate and electron-hole pair dissociation upon slow growth of the P3HT:PC_{61}BM films [155]. Hegde et al. reported a detailed crystallinity evolution of P3HT in P3HT:PC_{61}BM blends during CS_2-solvent annealing (Fig. 2.22). Upon solvent annealing, BHJ film was swollen and partial PCBM diffused away from the P3HT domains, thereby increasing P3HT crystallization and facilitating the phase separation within the P3HT:PC_{61}BM film [156]. As despite applicable of solvent annealing approach to morphology tuning for novel BHJ systems, a combination of thermal annealing treatment (descried in the following part) have been found necessary to improve device performance in most cases [61, 140].

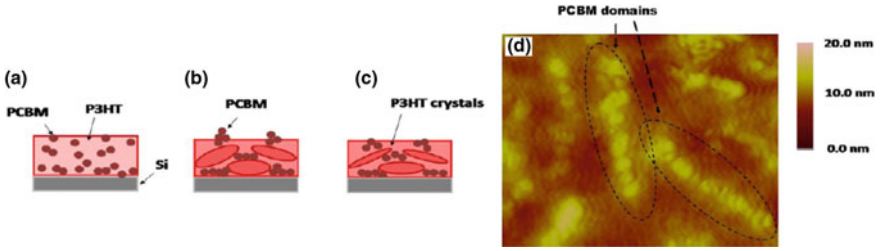

Fig. 2.22 Schematic of a model for the morphology evolution during solvent vapor annealing, **a** as-cast P3HT:PCBM with relatively mixed state of P3HT:PCBM, **b** crystallization of P3HT which induces phase separation of PCBM, **c** Diffusion of PCBM in the layer at longer solvent exposure promoted by the dissolution of P3HT crystals and **d** AFM height image of solvent annealed thin-film at $L/L_0 = 0.5$ for 5 s which shows long needle shaped domains of PCBM. Reprinted with permission from Ref. [156]. Copyright 2012 by Elsevier

2.3.2.2 Solvent Additives

The use of solvent additives brings a breakthrough in achieving high-performance PSCs and is becoming the primary approach to optimize device performance. In 2006, Bazan's group first revealed a modification of the P3HT aggregation and P3HT/$PC_{61}BM$ phase separation through blending alkanethiols into toluene solution [157]. Later, the same group reported PCPDTBT:$PC_{71}BM$ based devices with the addition of 1% 1,8-octanedithiol as the processing additive displayed a significant increase in PCE from 2.8 to 5.6% [158]. Further studies of a class of 1,8-di(R)octanes with various functional groups (R) revealed criteria of additives used in the fabrication of BHJ PSCs: (1) selective solubility of the fullerene component; and (2) higher boiling point than the host solvent [159]. This approach provides longer time for polymer and fullerene blend film drying, and allows better control of both crystallinities of the polymer and phase separation within the blends (Fig. 2.23). More detailed studies have been focused on the role of solvent additives in controlling morphology. Su et al. elucidated the precise morphology with GIWAXS/GISAXS and TEM analyses (Fig. 2.24) [130]. Compared to the film processed without additives, 1,6-diiodohexane (DIH) with suitable alkyl chain length not only induced 2.4 and 3.6 times higher polymer crystallinity in the out-of-plane and in-plane directions, respectively, but also decreased the average size of the aggregated fractal-like $PC_{71}BM$ clusters from 150 nm to 30 nm by removing their grain boundaries. The DIH processed PSCs thus showed higher efficiency up to 7.3% than 5.0% for additive-free processed PSCs.

To date, various high boiling point solvents including 1,8-diiodooctane (DIO), 1-chloronaphthalene (CN) [160], diphenyl ether [161, 162], and N-methyl-2-pyrrolidone (NMP) [163], have been employed as processing additives to improve device performance and understand the correlation between molecular structures and device performance. Among these, DIO was proved to be the most successful universal additive in most BHJ systems. In the last decade, intensive and

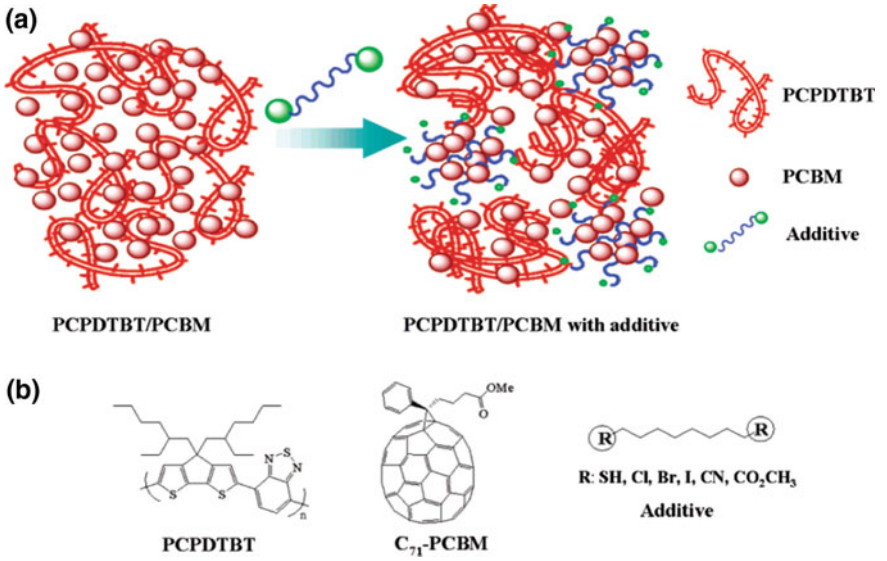

Fig. 2.23 **a** Schematic depiction of the role of the processing additive in the self-assembly of bulk-heterojunction blend materials. **b** Structures of PCPDTBT, $PC_{71}CBM$ and additives. Reprinted with permission from Ref. [159]. Copyright 2008 by American Chemical Society

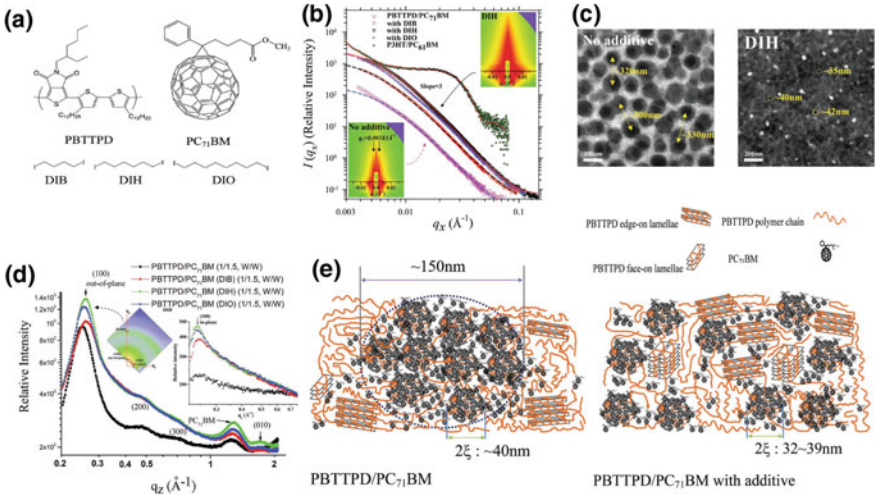

Fig. 2.24 **a** Molecular structures of PBTTPD, $PC_{71}BM$, and the solvent additives. **b** In-plane GISAXS profiles of the PBTTPD/$PC_{71}BM$ films processed with different solvents. **c** TEM images of PBTTPD/$PC_{71}BM$ films prepared without and with additive DIH. **d** Out-of-plane GIWAXS profiles of the lamellar peaks and the π–π stacking of PBTTPD and the halo of $P_{71}BM$ aggregation. **e** Schematic representations of mesograins in PBTTPD/$PC_{71}BM$ films processed without and with additive DIH. Reprinted with permission from Su et al. [130]. Copyright 2011 by WILEY-VCH Verlag GmbH Co. KGaA, Weinheim

systematic studies have been focused on the effects of DIO in PTB7-based BHJ blends [21], which yielded significant improvement the PCEs of PSCs up to 7% with DIO. For instance, TEM images showed that DIO resulted in much more uniform surface morphology without large phase separation [21]. Further studies of EF-TEM precisely demonstrated phase separation with 20–40 nm domain sizes [164], which contributed to improved exciton generation and reduced charge recombination. SAXS investigations revealed that DIO addition to a CB solution completely dissolves the $PC_{71}BM$ aggregates and induces strong coupling between partial negative charges on iodine and electron-deficient $PC_{71}BM$ [165], thus facilitating the integration of the $PC_{71}BM$ molecules into the PTB7 aggregates and promoting the formation of smaller domains and greater donor–acceptor interpenetration. Combining three X-ray techniques, Collins et al. found the domain composition and crystallinity essentially unchanged with the addition of DIO into the casting solution, while the domain size dramatically decreased from 177 nm to 34 nm that consists well with the EF-TEM results [135]. Meanwhile, low crystallinity of PTB7 in BHJ films is observed, leading to limited hole mobility of $\sim 6 \times 10^{-4}$ cm^2 V^{-1} s^{-1}, which partially explains the relative low performance of PTB7 based thick-film PSCs.

Recently, with optimized morphology upon DIO as a solvent additive, several novel single-junction PSCs like PffBT4T-2OD:$PC_{71}BM$ and PBDB-T:ICIT displayed outstanding PCEs around 11%. Though considerable improvements in device performance induced by DIO additive, sometimes poor reproducibility (i.e., batch-to-batch variation of device performance) was observed. Since DIO has low saturated vapor pressure (about 1×10^{-2} Pa) at room temperature, DIO could not be fully dried under ambient temperature and pressure, and the residual DIO may affect the stability of the morphology [166]. To remove the residual DIO for stabilizing morphology, subsequent handling with high vacuum and alcohol treatment have been introduced and proved. Methanol treatment inducing favorable interfacial ohmic contact, smooth morphology and optimal component distribution on the top surface of active layers, thus leading to higher PCEs and better reproducibility PSCs was reported [167].

2.3.2.3 Thermal Annealing

Thermal annealing is another alternative method to modulate the morphology of active layers for optimizing PSCs performance. Thermal treatment was first successfully utilized in P3HT based PSCs. In 2000, Dittmer et al. found increased crystallinity of P3HT within the P3HT:EP-PTC blends after thermal annealing at 80 °C for 1 h [168]. The better molecular packing provided increased charge transport, and the resulting PSCs displayed enlarged EQE over the whole wavelength region. On basis of this observation, Padinger et al. presented a high-efficiency (3.5%) P3HT:$PC_{61}BM$ based PSCs achieved by a thermal treatment after deposition of electrode, denotes as post-annealing [169]. In 2005, Yang group reported that upon previous treatment with P3HT:$PC_{61}BM$ film annealing at 110 °

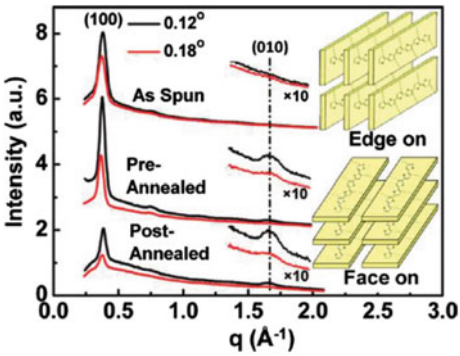

Fig. 2.25 Grazing incident X-ray diffraction (GIXRD) spectra of P3HT:$PC_{61}BM$ blend films as spun; pre-annealed 30 min; post-annealed 30 min. The *insets* represent the schemes of edge-on and face-on of P3HT chains. Reprinted with permission from Ref. [171]. Copyright 2011 by American Chemical Society

C, the absorption of the BHJ films red-shifted and shoulder peaking at 545 nm and 600 nm emerged, implying an increased degree of self-organization and crystallinity of P3HT in the P3HT:$PC_{61}BM$ blends [61]. Along with a better balance charge transport, the resulting PSCs displayed a very high FF of 67.4% and thus PCE up to 4.4%. Later, Ma et al. investigated the effects of the post-annealing temperature, and exhibited a further increase in PCE up to 5% after 150 °C post-thermal treatment [170]. Further studies using TEM revealed that thermal annealing produced a nanoscale interpenetrating network with long, thin fibrillar crystals of P3HT in a homogeneous nanocrystalline $PC_{61}BM$ layer [124]. Using X-ray diffraction, Chen et al. observed post-annealing treatment induced P3HT chains preferentially oriented face-on packing with respect to the substrate (Fig. 2.25) [171]. Additionally, post-annealing treatment can give increased contact between active layers and electrodes. The thermally annealing induced morphology modification thus contributed to the higher efficiency of P3HT:$PC_{61}BM$ based PSCs.

2.3.2.4 Ternary Blends

Ternary blends comprise three components in the blend films: the dominating D:A system and the third material, which can be a nanometal, an oxide, a carbon material, a polymer or a small molecule. The presence of such components is designed to introduce potentially beneficial optoelectronic properties and modulate the BHJ morphology, thus maximizing the device performance.

Direct mixing of metal nanoparticles of Ag [172], Pt [173], and Au [174], etc., in an active layer has been proved as an alternative approach to improve device performance. For example, Wang et al. reported blending truncated octahedral Au nanoparticles with large size of 70 nm into a BHJ solution, displayed enhancement in PCE from 3.54 to 4.36% (P3HT:$PC_{71}BM$), from 5.77 to 6.45% (PCDTBT:$PC_{71}BM$), and from 3.92 to 4.54% (Si-PCPDTBT:$PC_{71}BM$) [175]. Such improvement was primarily attributed to a combination of enhanced light

absorption caused by the light scattering of Au nanoparticles, and reduced series resistances of PSCs.

Carbon nanotubes, as one of the carbon materials, have also been incorporated into the active layers of PSCs due to their superior charge carrier mobility. Lu et al. reported a considerable increase the PCE of PSCs up to 8.6% by adding N-doped multiwall carbon nanotubes (N-MCNTs) into the PTB7:PC71BM [176]. They found that incorporating N-MCNTs may serve as nucleus centers and increased crystallinity of both PTB7 and $PC_{71}BM$ and decreased domain size, thus leading to a better phase-separated nanomorphology, which facilitated exciton dissociation and charge transport.

Compared to inorganic additives, organic compounds including both polymers and small molecules have more compatibility and have been widely used as a third component to further tune the morphology and improve device performance and stability [177–180]. Lee et al. reported that the crystallinity of P3HT and PCE of the PSC was enhanced to 2.5% by adding a diblock polymer P3HT-*b*-C_{60} as a compatibilizer into the P3HT:$PC_{61}BM$ blend film [181]. More interestingly, they demonstrated that P3HT-*b*-C_{60} also suppressed thermal nanophase separation, due to the preferential location of the diblock copolymer at the interface between P3HT and $PC_{61}BM$ resulted in reduction of phase sizes of the P3HT:$PC_{61}BM$ blend with uniform distribution, thus improving the long-term stability of the PSCs. Besides efficient morphology modification and improved device stability was obtained in the PSCs by adding the block polymers, cross-linking compounds involving thiophene-based (e.g., P3HNT, P3HT-Br) [182, 183] and fullerene-based (e.g., PCBSD, PCBG) derivatives [184, 185] have also been added to the active layers. Poly(dimethylsiloxane) PDMS has been adopted to modulate the morphology [186]. Chen group reported a series of BDT-based small molecules based solar cells exhibited improved efficiencies with the addition of PDMS into the casting solution. They found PDMS processed films displayed slightly increased domain size but smaller roughness, which contributed to increased PCEs with the highest value up to 8% [141].

Recently, blending another donor or acceptor with the common binary D:A system has been developed as an emerging candidate to tune morphology and overcome the PCE bottleneck for binary BHJ PSCs [187–190]. For example, Lu et al. reported that a ternary PSC with 10% PID2 addition into a PTB7:$PC_{71}BM$ host blend demonstrated the highest PCE up to 8.22% [191]. The authors found ternary blend films at optimized ratios showed fibrous features detected by TEM, but no such structure was observed in the PTB7:$PC_{71}BM$ or PID2:$PC_{71}BM$ devices. Furthermore, 2D GIWAXS and R-SoXS studies indicated that PID2 had little influence on the crystalline structures of both conjugated polymers and $PC_{71}BM$ but inducing the formation of smaller phase-separated domains. Thus the improved light harvesting, energy level cascading, and the optimized morphology contributed to improved device performance. Fang et al. showed hierarchical phase separation formed in the ternary blend film revealed by a combination of TEM, 2D GIWAXS and R-SoXS analysis (Fig. 2.26), where the high crystallinity of small molecule BDT-3T-CNCOO provided the driving force of polymer PBDTTT-C-T to self-assemble to a fibrous structure with larger crystal size and greater purity

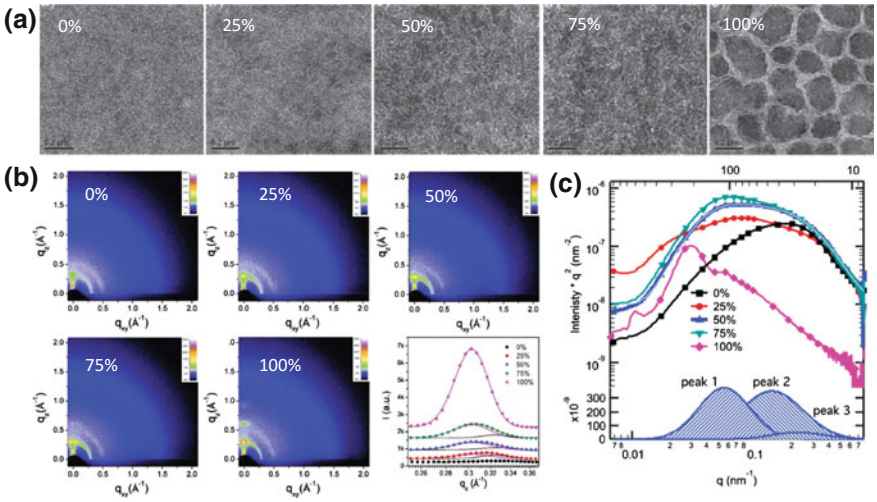

Fig. 2.26 **a** TEM images, **b** 2D GIWAXS images, and **c** R-SoXS scattering profiles of PBDTTT-C-T:$PC_{71}BM$ active layers with different BDT-3T-CNCOO weight ratios. Reprinted with permission from Ref. [192]. Copyright 2015 by WILEY-VCH Verlag GmbH Co. KGaA, Weinheim

domains and the long-chain PBDTTT-C-T possibly restrains unfavorable aggregation of small molecule/fullerene domains [192]. The formed hierarchical phase separation balances the charge separation and transport, leading to high FF over 70% and PCE up to 8.58%.

In summary, several common and efficient processing methods including solvents, solvent additives, solvent and thermal annealing, and ternary blends have been developed to tune morphology of the active layers of PSCs for optimizing performance. Advances in morphology characterization techniques including AFM, TEM, and X-ray provide a deep understanding of the structure-property relationship between the morphology modification and device performance. These developments have and will continuously inspire novel photoactive material synthesis and more effective device process toward even high-performance PSCs.

2.4 Interface Engineering

As shown in the device structure (Fig. 2.1), the HEL and EEL play an important role for solar cell efficiency. Particularly, the work functions of the interfaces (EEL and HEL) determine V_{oc} and the charge extraction efficiency. Furthermore, the surface energy of the interfaces also affect the film quality and phase segregation of the layers deposited on top of them [193].

2.4.1 HEL

Among various HELs used in PSCs, conducting polymer poly (3,4-ethylenedioxythiophene): poly(styrene sulfonate) (PEDOT:PSS) is the most widely used one [194, 195]. First, PEDOT:PSS is an aqueous solution, which is environment-friendly and easily forming smooth films with different techniques, such as spin coating, blade coating, spray or others. Second, PEDOT:PSS has a higher work function (5.0 eV) than commonly used anode ITO (4.7 eV), which enlarge the internal electric fields for exciton dissociation and free charge carrier collection. Third, PEDOT:PSS dispersion is commercially available and affordable. Fourth, PEDOT:PSS films are reproducible and stable in air. Fifth, PEDOT:PSS films are highly transparent and do not affect the transmittance of anodes. Sixth, the conductivity of PEDOT:PSS can be modified to meet different requirements. All above merits of PEDOT:PSS make it a most effective universal HEL for PSCs to block electrons and extract holes from active layers of conventional PSCs with the configuration of bottom electrode/HEL/active layer/EEL/top electrode. The configuration of inverted PSCs is bottom electrode/EEL/active layer/HEL/top electrode. It is a bit of a challenge to deposit aqueous PEDOT:PSS dispersion onto active layers as the HEL due to the hydrophobicity of most active layers used in PSCs. Current strategies are adding a small amount of surfactant (<1 wt%) into the PEDOT:PSS dispersion [196, 197] or turning the surface of the active layer to hydrophilicity by air or oxygen plasma treatment or UV-Ozone treatment [198]. In addition, commercially available formulation PEDOT:PSS CPP containing surfactant can also wet well the hydrophobic active layers of PSCs [6, 199, 200],

In addition, semiconducting oxides such as MoO_3, WO_3, NiO_x, and V_2O_5, can be used as HELs [201–204]. These oxides can be prepared by either vacuum deposition or solution processing. The current status of the HEL in PSCs is: PEDOT:PSS is widely used in conventional PSCs by directly coating PEDOT:PSS onto the ITO; MoO_3 is widely employed in inverted PSCs by vacuum deposition on top of active layers together with the top metal electrodes. Obviously, for industrialization of PSCs with printing technologies, vacuum deposited oxides will be ruled out.

2.4.2 EEL

To achieve good performance PSCs, EELs are surely very important and more challenging than HELs due to their poor air stability. In conventional PSCs, the popular EEL is low work function metals such as calcium (Ca) or magnesium (Mg), which needs to be deposited in vacuum prior to top metal electrodes, mostly Al. Generally, PSCs need to be characterized in an inert atmosphere or a good encapsulation because the low work function metals are very reactive and easily oxidized in air by oxygen or humidity.

Semiconducting oxides such as ZnO and TiO_x have been used as EELs in PSCs. The oxide films are mainly processed from solutions, nanoparticle dispersions or precursors followed by thermal annealing [205, 206]. Commonly, the oxides are employed in inverted PSCs to lower the work function of ITO. The functionalities of ZnO or TiO_x as EELs strongly depend on the oxides' quality and the surface states. Moreover, the conductivity of the oxides is sensitive to ultraviolet (UV) illumination. So far, the oxides are the most popular EELs in PSCs.

In addition, insulators are another type of important EELs. Lithium fluoride (LiF) is a representative insulating EEL [29]. A vacuum deposited thin layer ($\sim$0.6 nm) of LiF prior to Al deposition as EEL can significantly enhance the performance of PSCs due to the formation of surface dipoles, which pronouncedly lower the work function of electrodes [207]. However, vacuum process LiF EEL is not compatible with printing PSCs. In 2007, Zhang et al. first introduced solution-processed polyethylene oxide (PEO) (shown in Fig. 2.27) as EEL in the PSCs based on a polyfluorene copolymer LBPF3 and $PC_{60}BM$ [208]. Comparable performance with LiF was achieved. The fact that V_{oc} could be increased up to 200 mV by simply inserting a thin PEO layer between active layers and Al proved the simplicity of replacing LiF by polymer EEL. Polymer modifiers with good film-forming ability could be universal modifiers as EELs. In 2009, by employing PEO converting ITO from a hole collection electrode into an electron collection electrode, Zhou et al. were the first to realize inverted vacuum free semitransparent PSCs with the structure of ITO/PEO/active layer/PEDOT [209]. PEO reduced the work function of ITO up to 0.5 eV was confirmed by Ultraviolet photoemission spectroscopy (UPS) measurement. This is the first demonstration of inverted PSCs with ITO as a cathode modified by a polymer EEL. Inefficient active materials, low conductivity of PEDOT:PSS electrode and semi-transparency of the device with uncompleted photon absorption limit the PCE of the PSCs. Later on, other polymers have also been demonstrated as modifiers to lower the work function of ITO or metal electrode for efficient electron collection in PSCs [23, 210–213]. For example, a record PCE of 9.2% was demonstrated in inverted PSCs by reducing the work function of ITO from 4.7 to 4.1 eV with thin layer of poly [(9,9-bis(3′-(N,N-dimethylamino)propyl)-2,7-fluorene)-alt-2,7-(9,9–dioctyl-fluorene)] (PFN, Fig. 2.27) [23]. Self-assembled (SAM) monolayers APTES and F2BPA (Fig. 2.27) that chemically bind onto the ITO or other oxides were also found to be able to reduce the work functions of the surfaces they modified [214, 215]. However, these SAM layers are chemically bound to the surface requiring a particular surface chemistry.

Effort to searching better EELs for PSCs made Zhou et al. notice polyethylenimine (PEI) and polyethylenimine ethoxylated (PEIE) (Fig. 2.27) [216]. Extensive study confirmed that these two polymers could universally reduce the work functions of most conductors, including metals, metal oxides, conducting polymers, graphene, and ITO by about 1 eV. Investigation revealed that the polymer modifiers

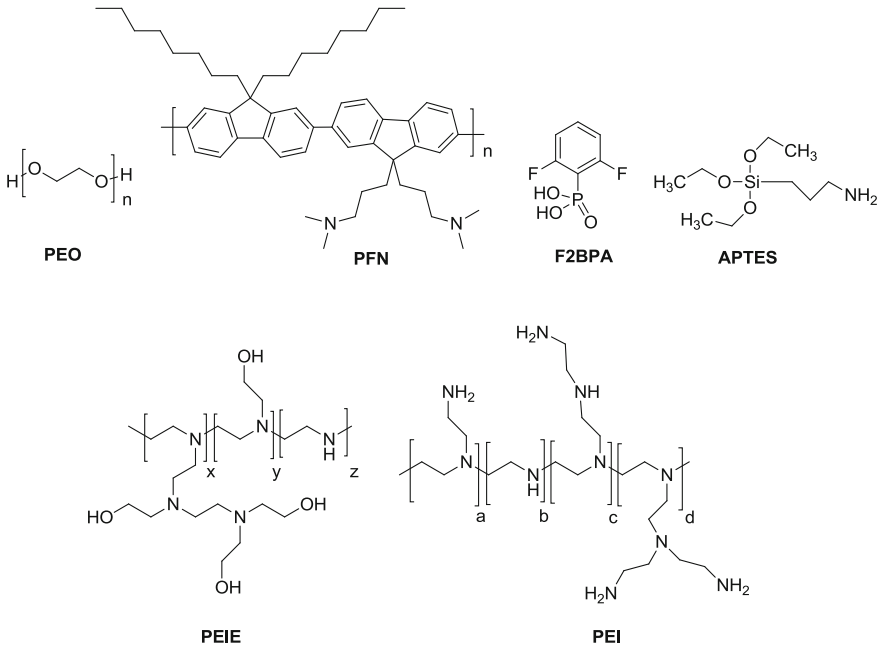

Fig. 2.27 The chemical structures of molecules and polymers for lowering the work function of ITO

are physically adsorbed onto the conductors, independent on the surface chemistry. The low work function modification can be easily done by spin coating, printing or even immersing the conductors into the solution. The produced low work function interfaces exhibit good air stability. Nowadays, PEI or PEIE is extensively used as EELs not only in organic solar cells [216–218], but also organic LEDs [219], organic field-effect transistors [220, 221], organic photodetectors [222, 223], perovskite solar cells [224], perovskite LEDs [225], and inorganic quantum dot LEDs [226].

Another important application of PEIE is to realize a low work function conducting polymer. For example, the work function of conducting polymer PEDOT:PSS could be decreased from 5.0 eV to about 3.6 eV after modification by PEI or PEIE, which enables the possibility of fabricating all-plastic solar cells by employing high conducting PEDOT:PSS as both anodes and cathodes for hole and electron collections fully solution-processed on highly flexible low-cost plastic substrates [216, 227].

2.5 Electrodes

As shown in Fig. 2.1, PSCs consist of two electrodes (the top one and the bottom one). At least one of them has to be transparent for light illumination through and then to the active layers. Typically, ITO is widely used as the transparent electrode due to its high conductivity and high optical transmittance. Vacuum deposited metals (such as Al, Ag, Au) are generally used as top electrodes. Conventionally, glass substrates are commonly used for PSCs because they are highly transparent and very smooth with high temperature and organic solvent tolerance. However, glass substrates are rigid and fragile, which restrict their applications in flexible PSCs. Transparent polyethylene terephthalate (PET), polyethylene naphthalate (PEN) and polyethersulfone (PES) are typically used as substrates for flexible PSCs.

In the past years, the community has been searching for the replacement for ITO transparent electrode and top metal electrodes. ITO electrode needs to be replaced due to their poor mechanical flexibility and high cost resulted from scarcity of the materials. The vacuum deposition of top metal electrodes is high energy-consuming and requires expensive deposition facilities with high-cost maintenance, and is thus incompatible with up-scale production with printing equipment. In 2002, Zhang et al. demonstrated the PSCs using doped high conducting PEDOT:PSS as an electrode to replace ITO [228]. Later, more higher conductivity formulations of PEDOT:PSS [229, 230], silver nanowires, carbon nanotubes and graphene have been studied as the replacement for ITO. For PEDOT:PSS in particular, different strategies, such as adding high boiling polar solvents (dimethyl sulfone, ethylene glycol), post-treatment with acid (sulfuric acid, phosphoric acid, or organic acids) or polar solvents have been used for enhancing its conductivity. The conductivity of PH1000 is about 500–2000 S/cm when processed from the formulation with the addition of the polar solvent [231, 232]. The PSCs with appropriately processed PEDOT:PSS bottom electrodes exhibit similar performance to the PSCs with ITO electrodes.

To replace top metal electrodes, solution-processable PEDOT:PSS is also the main candidate. PEDOT:PSS as the top electrode has been only used in inverted solar cells because of its high work function. Employing PEDOT:PSS as a top electrode in conventional PSCs by inserting a low work function interfacial layer (or EEL) between PEDOT:PSS and active layers were also explored. However, most of the EELs such as the above-mentioned ZnO or PEI are acid sensitive, which is not compatible with an acidic PEDOT:PSS dispersion with a pH value of about 1.5–2.5. Tuning the pH value of PEDOT:PSS making it compatible with the EELs is a possible way to build PSCs in conventional structure with PEDOT:PSS films as top electrodes [233]. So far, all-solution-processed PSCs with PEDOT:PSS top electrode in the conventional structure are still challenging.

Used as the electrodes, accurately pattering the solution-processed PEDOT:PSS is important. The metal electrodes are generally patterned via shadow masking. However, PEDOT:PSS films are generally prepared by spin coating, which makes

fine scale patterning difficult [234]. Film transfer printing (or transfer lamination) has been shown to be an effective technique to pattern PEDOT:PSS electrode [235–238]. PEDOT:PSS is first deposited on the transfer medium (such as polydimethylsiloxane) and then transferred onto the target surface. Before transfer printing, the PEDOT:PSS films are cut into the desired shape and size. The interplay between the adhesion of the film to the transfer medium and target surface is the key for the success of transfer printing. The yield of the transfer printing onto the hydrophilic surface is high because of the hydrophilic nature of the PEDOT:PSS. Therefore, mildly treating the surface of the active layer with oxygen plasma before transfer printing, turning the surface hydrophilic, can enhance the transfer yield of PEDOT:PSS films. Another advantage of the transfer printing technique is that the PEDOT:PSS is deposited dry onto the target surface alleviating damage to the active layer or interfaces by water [6].

Due to the fact that PEDOT:PSS electrodes are solution-processable, vacuum-free, with tunable work function, optically transparent and can be patterned with the transfer printing technique, both ITO electrode and metal electrode can be replaced by PEDOT:PSS films. Vacuum-free inverted PSCs including all-plastic solar cells with an architecture: plastic substrates/PEDOT:PSS/PEI/active layer/PEDOT:PSS can be fabricated (Fig. 2.28) [227]. Krebs and coworkers [239–241] reported large-area polymer solar modules by roll-to-roll printing using vacuum-free processing and at potentially very low manufacturing cost [6].

On the other hand, several nanoscale materials including nanoscale forms of carbon, as well as metallic nanowires and grids are also showing great promise as electrodes for PSCs. In 1999, Ago et al. initially demonstrated the use of the multiwalled carbon nanotubes (MWNTs) as an opaque hole-collecting electrode to fabricate the photovoltaic device, which showed higher quantum efficiency than that of controlled ITO device [242]. Later, Pasquier et al. reported a single-walled carbon nanotube film with ~45% transparency in the visible and ~282 Ω/square resistivity displayed a higher efficiency of 0.99% for P3HT:PC_{61}BM based PSCs than 0.69% of the ITO referenced device [243]. Since then, many efforts have been devoted to developing higher transparent and conducting carbon nanotube

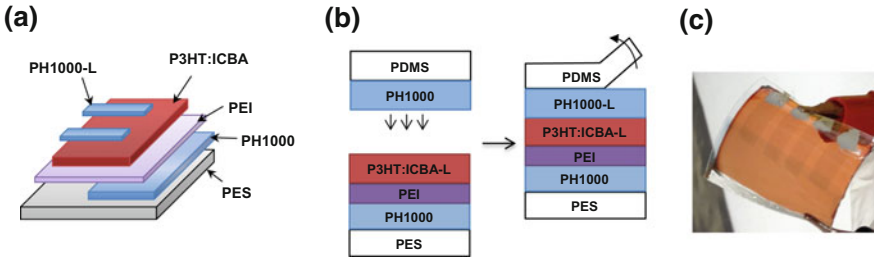

Fig. 2.28 **a** Device structure of an all-plastic solar cell; **b** transfer printing of PEDOT:PSS PH1000 electrode; **c** photography picture of a fabricated all-plastic solar cell. Reprinted with permission from Ref. [227]. Copyright 2014 by The Royal Society of Chemistry

electrodes for solar cells. Chemical treatments have been proven to have a dramatic role in modifying both transparency and conductivity. For example, several studies showed oxidized carbon nanotubes (*o*-CNTs) with the transparency of 70–90% and remarkable conductivity up to 7700 S cm^{-1} (ITO is 4400 S cm^{-1}), which led to the corresponding devices displaying comparable efficiency with the ITO referenced devices [244, 245]. Recently, Jeon et al. reported direct and dry deposited carbon nanotube film doped with MoO_x serving as an electron-blocking transparent electrode showed high efficiency up to 6.04% for PTB7:PC_{71}BM device, which is 83% of the leading ITO-based device performance (7.48%) [246]. Another alternative choice is hybrid carbon nanotubes. Hu et al. showed that the PEDOT:PSS:CNTs hybrid film as electrode achieved similar efficiency of 7.47% with 7.69% of the ITO controlled device, and also displayed promising application of the PEDOT:PSS:CNTs ink in the roll-to-roll process for larger scale flexible electronics [247].

Graphene, as one emerging carbon nanomaterial, has recently attracted much attention in transparent electrodes [248–250], due to its fascinating properties, including high carrier mobility, good optical transparency, and low resistivity as well as excellent mechanical flexibility. Wang et al. showed increasing the thickness of the pristine graphene film induced decreased sheet resistance from 1350 to 210 Ω/square but the loss of transparency from 91 to 72%, and the resulting devices displayed an efficiency of 0.21% [251]. Furthermore, doped graphene aiming to improve conductivity has been developed as transparent electrode [252–255]. Liu et al. used doped graphene transparent electrodes as both cathode and anode to fabricate semitransparent organic solar cells, which can absorb light from both sides with the power conversion efficiency up to 3.4%.

Another efficient emerging electrode is metallic nanowires and grids [256, 257]. Several studies reported solution-processed silver nanowires (Ag NWs) had a sheet resistance and transmittance similar to those of ITO (10–20 Ω/square with 80% transmittance), together with a relatively high work function around 4.5 eV [258–261]. These promising characteristics enable its successful use as electrodes in PSCs. Recently, Guo et al. reported efficient, fully printed tandem PSCs using silver nanowires as the transparent top electrode, which showed efficiencies of 5.81% (on glass) and 4.85% (on flexible substrate) without V_{oc} losses [262].

In summary, emerging electrodes including conducting polymers, carbon nanomaterials, as well as metallic nanowires and grids have exhibited promising application in PSCs. Although considerable potential advantages, these electrodes are still limited by lower device performance than those PSCs based on regular ITO or metal in most cases. The development of electrodes that combines high transparency, low sheet resistance, robust chemical stability, low-cost, and effective charge collecting ability is still challenging, and will attract broad attention in various fields to further push it forward.

2.6 Tandem Solar Cells

Building tandem solar cells is an effective way to increase PCE of PSCs because a broader spectrum of solar radiation can be harvested by stacked junctions. The thermalization loss of photon energy can also be minimized. Typical structure of a tandem solar cell is shown in Fig. 2.29. The double-junction tandem structure consists of a front cell with a high-bandgap junction, an interconnecting layer, and a rear cell with a low bandgap (LBG) junction.

2.6.1 Interconnecting Layer

In tandem PSCs, interconnecting layer (ICL), also known as charge recombination layer (CRL), is a critical component for realizing high device performance. The ICLs generally consist of a p-type hole transporting layer (HTL) and a n-type electron transporting layer (ETL), which functions as the charge recombination zone and simultaneously serve to shift the vacuum levels. The latter is driven by the alignment of Fermi levels of the HTL and ETL. An ideal ICL must have the characteristics: (1) high optical transmittance to minimize light absorption losses; (2) large work function contrast to efficiently collect electrons from one sub-cell and holes from the other sub-cell, respectively; (3) sufficient electrical contact between the ETL and the HTL within the ICL to enable efficient recombination of the holes and electrons; (4) robust impermeability to protect the underlying layers of bottom cell from dissolution by the processing solvents of the top cell.

In 2006, Dennler et al. [263]. for the first time stacked a vacuum deposited ZnPc/C_{60} based cell on the top of a solution-processed P3HT:PCBM layer using a 1 nm thick Au intermediate recombination layer (Fig. 2.30). Such tandem devices comprising active materials with complementary absorption spectra exhibit a short circuit current I_{sc} of 4.8 mA cm^{-2}, an open circuit voltage V_{oc} of 1020 mV, and a fill factor of 0.45. Spectral photocurrent response region was effectively extended from about 650 nm (P3HT:PCBM) to about 800 nm contributed by the ZnPc/C_{60} junction.

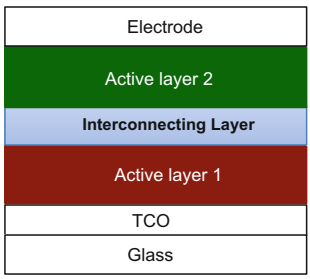

Fig. 2.29 Device structure of an organic tandem solar cell

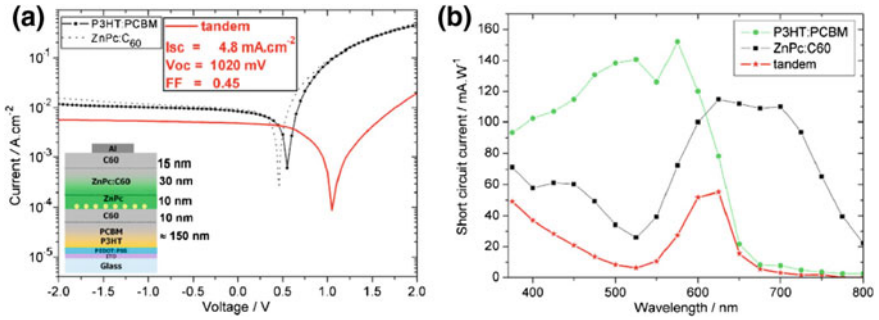

Fig. 2.30 **a** The J-V characteristics of single-junction and double-junction solar cells as well as the structure of organic tandem solar cells with junctions of P3HT:PCBM and ZnPc:C60 (*inset*); **b** current at short circuit condition versus wavelength of the incident monochromatic light for single cells and tandem cells. Reprinted with permission from Ref. [263]. Copyright 2006 by American Institute of Physics

So far, the above-mentioned ICLs are vacuum-evaporated nanometer-scale metals. These ICLs did not yield high-performance tandem cells and these ICLs are processed via high vacuum deposition. In 2007, Gilot et al. [233]. reported solution-processed ZnO/PEDOT as the ICL. The ZnO film was prepared by spin coating its nanoparticles in acetone and the PEDOT film was prepared by spin coating from neutral *p*H water dispersion. The V_{oc}s for double and triple-junction solar cells are close to the sum of the V_{oc} of individual cells. However, the efficiency of the tandem devices is just about 2%, which mainly attributed to the overlapping absorption of each sub-cell. UV illumination was found able to enhance the V_{oc} and PCE of the tandem cells. Later on, subcells with complementary absorption region were adopted to enhance the light harvest of the tandem cells and therefore improve their efficiency. In 2007, Kim et al. [264]. reported tandem cells with P3HT:PC_{70}BM and PCPDTBT:PCBM that have spectrally complementary absorption and achieved a high PCE of 6.5% (Fig. 2.31). It was record-high at that time. Particularly, a solution-processed ICL TiO_x/PEDOT:PSS was used in the tandem cells that simplified the fabrication of the tandem PSCs. Since then, solution-processed ZnO/PEDOT:PSS and TiO_x/PEDOT:PSS ICLs were widely studied and applied in tandem PSCs.

With the development of inverted single junction PSCs due to their better air stability than conventional PSCs, inverted tandem solar cells were also widely studied. The polarity of the ICL has to be reversed for efficient charge carrier collection because the polarity of the subcells was switched. Then, the PEDOT:PSS/ZnO and PEDOT:PSS/TiO_x were also employed for inverted polymer tandem cells. In 2012, Dou et al. [265] demonstrated a PCE of 8.6% in inverted tandem PSCs with PEDOT:PSS/ZnO as ICL.

Another important ICL is PEDOT:PSS/PEI or PEDOT:PSS/PEIE (Fig. 2.32) [266]. This ICL is developed based on the finding of the surface modification function of the PEIE or PEI by Zhou et al. [216]. The polymer surface modifier

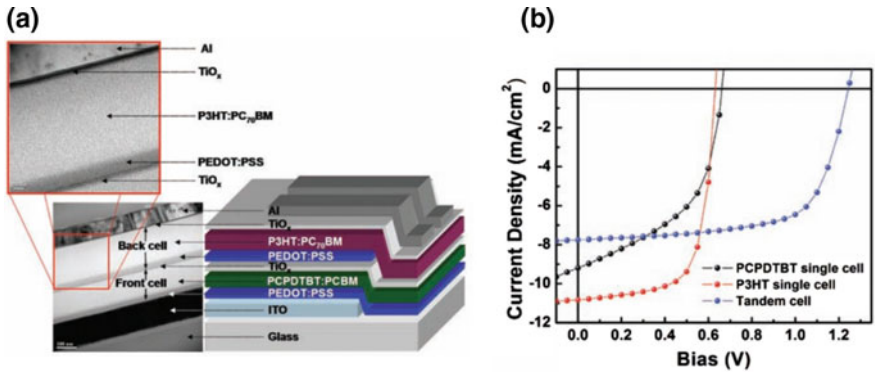

Fig. 2.31 **a** Structure of organic tandem solar cells and **b** the *J-V* characteristics. Reprinted with permission from Ref. [264]. Copyright 2007, Science

PEIE or PEI which containing simple aliphatic amine groups can substantially reduce the work function of conductors including metals, transparent conductive metal oxides, conducting polymers, and graphene. They used this polymer modifier to develop an all-polymer ICL PEDTO:PSS/PEIE. This ICL shows very low optical absorption, high electrical conductivity, and a large work function contrast of 1.3 eV between its top and bottom interfaces. Its use yields tandem cells in which the open circuit voltage is the sum of that of individual cells. Its simple polymeric composition and its unprecedented performance make it a promising component for emerging organic photovoltaic technologies. Recently, Tong et al. [267] further optimized the conductivity of the ICL via modifying the PEDOT: PSS formulation and selecting the processing solvent of the polyethylenimine to avoid the patterning and shorts. And based on the optimized ICL, they demonstrated the first all-solution-processed multijunction (up to 7-junction, 22 layers, Fig. 2.32) all-plastic solar cells with high yield. These cells with high photovoltage (5.37 V for 7 junctions) have been shown to meet the requirements to power liquid-crystal displays and full-color light emitting diodes under low-intensity light conditions. They could become very low-cost solutions for powering various portable and wearable electronic devices, including wireless sensors for the internet of things applications.

Based on this PEDOT:PSS/PEI ICL, Kang et al. [268]. demonstrated a new fabrication strategy and device structure of tandem solar cells. The PEI has mixed the active layer for film spin coating. The PEI modification moved to the PEDOT: PSS surface and lowered its work function to form the efficient ICL. The constructed tandem structure achieved a PCE about 11%.

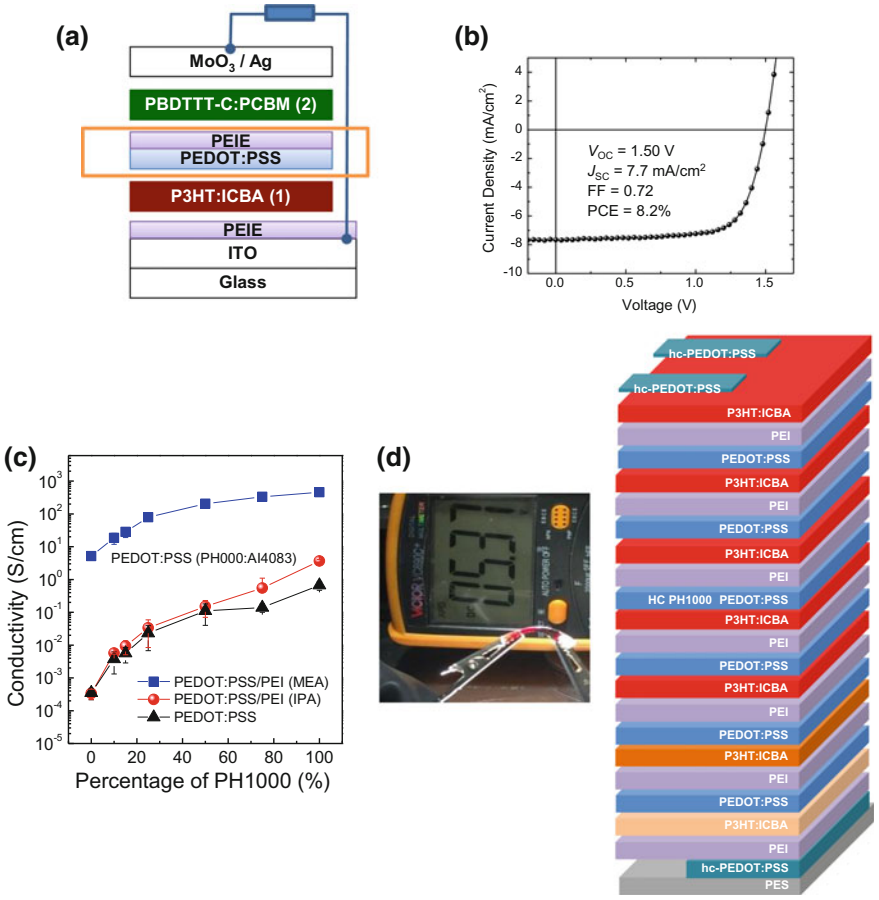

Fig. 2.32 **a**, **b** Tandem solar cells with PEDOT:PSS/PEIE as the ICL and the *J-V* characteristics; Reprinted with permission from Ref. [266]. Copyright 2012 by The Royal Society of Chemistry. **c** Conductivity tuning of the PEDOT:PSS/PEI ICL; **d** all-solution-processed all-plastic multijunction (7-junction, 22 layers) cells displayed V_{oc} of 5.37 V. Reprinted with permission from Ref. [267]. Copyright 2016 by The Royal Society of Chemistry

2.6.2 *Low Bandgap Polymer Sub-cell*

As mentioned, the advantage of the tandem solar cells is to extend the light harvest in a broad spectral region by stacking different junctions with different bandgaps. The typically used large bandgap junctions are P3HT:ICBA and PCDTBT:PCBM which has a bandgap of about 2 eV. The two large bandgap junctions could deliver J_{SC} about 10 mA cm^{-2}, and high EQE about 70% from 400 to about 680 nm. It was challenging that obtains high-performance low bandgap junctions that have highly complementary spectral absorption region to the large bandgap ones.

Efficient polymers that absorbs toward 850 nm (~1.46 eV), 900 nm (~1.38 eV) or longer wavelength are desired to build efficient polymer tandem solar cells.

In recent years, progress has been made in the development of novel high-efficiency low bandgap polymers and enabled PCE enhancement of polymer tandem solar cells. In 2012, You et al. [269]. introduced strong electron-withdrawing fluoroine atoms on the benzothiadiazole (BT) unit to form the difluorobenzothiadiazole (DFBT) unit to lower the highest occupied molecular orbital (HOMO) level (Fig. 2.33). Further, they inserted a strong electron-donating oxygen atom into the cyclopentadithiophene unit to form the dithienopyran (DTP) unit. The DTP electron-donating moiety and the DFBT electron-withdrawing moiety construct the low bandgap D-A type polymers: poly[2,7-(5,5-bis-(3,7-dimethyl octyl)-5H-dithieno [3,2-b:20,30-d]pyran)-alt-4,7-(5,6-difluoro-2,1,3-benzothiadiazole)] (PDTP-DFBT). The bandgap of the PDTP-DFBT is as low as 1.38 eV, which also shows a high hole mobility and deep HOMO level. Single-junction devices based on PDTP-DFBT show high quantum efficiency of >60% from 710 to 820 nm and the spectral response extends to 900 nm and a PCE of 7.9%. With the combination of P3HT:ICBA as the large bandgap junction and PDTP-DFBT:PCBM as the low bandgap junction, polymer tandem solar cells with a certified PCE of 10.6% has been achieved.

In 2013, Li et al. reported the design and synthesis of a new low bandgap semiconducting polymer, poly[[2,5-bis(2-hexyldecyl-2,3,5,6-tetrahydro-3,6-dioxopyrrolo[3,4-c]pyrrole-1,4-diyl]-alt-[3′,3″-dimethyl-2,2′:5′,2″-terthiophene]-5,5″-diyl] (PMDPP3T, Fig. 2.33) that absorbs until 950–1000 nm. Subcells of

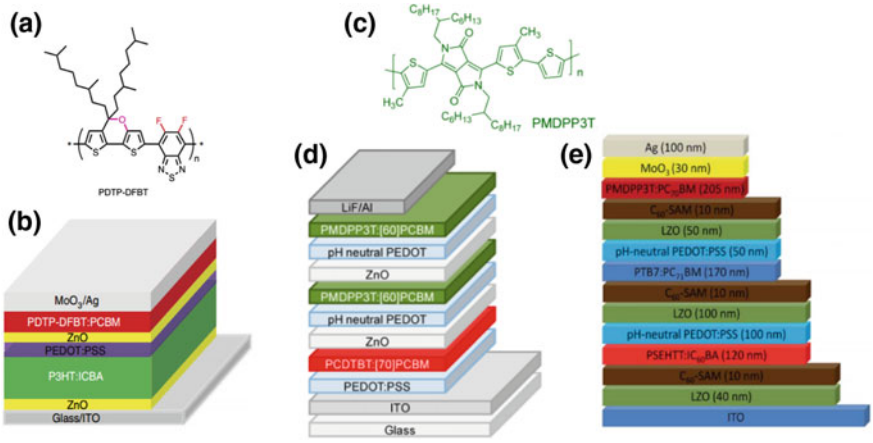

Fig. 2.33 **a** Chemical structure of low bandgap polymer PDTP-DFBT; **b** Tandem cell structure based on the PDTP-DFBT:PCBM junction; Reprinted with permission from Ref. [269]. Copyright 2013 by Macmillan Publishers Limited: Nature Communications. **c** Chemical structure of low bandgap polymer PMDPP3T; **d** structure of tripe-junction tandem cell based on the PMDPP3T:PCBM junction; Reprinted with permission from Ref. [270]. Copyright 2013 by American Chemical Society. **e** Structure of tripe-junction tandem cell with the PMDPP3T:PCBM junction; All the three junctions absorb different spectral region. Reprinted with permission from Ref. [271]. Copyright 2015 by The Royal Society of Chemistry

PMDPP3T with [6]-phenyl-C61-butyric acid methyl ester ([60] PCBM) enabled very efficient two-junction and triple-junction cells with broad spectral response and PCEs of 8.9 and 9.6% when combined with a wide bandgap sub-cell (PCDTBT:PCBM) as shown in Fig. 2.33 [270]. The high complementarity of the absorption spectra of the active layers enabled high photocurrents in tandem and triple configurations. Later on, in 2015 Yusoff et al. also used PMDPP3T:$PC_{70}BM$ to build a triple-junction polymer tandem solar cell with three distinct subcells with minimal absorption spectral overlap (Fig. 2.33). Accordingly, a high power conversion efficiency of 11.83% was obtained for the triple-junction cells [271].

2.7 Solar Modules, Production, and Applications

Like other types of solar cells, producing large-area cells and modules is important to provide enough power for applications. High module efficiency is still the main target of the current research. In addition, high-resolution patterning technique and new module architecture are studied to obtain high geometric fill factor (active area/total module area). In this section, we introduce current status and challenges of polymer solar module (PSM) including the new concept of module design; the module application and economic assessment.

2.7.1 Solar Modules

Different from silicon wafer based solar modules that are manufactured as a series of individual cells and then assembled together, thin-film PSCs are typically fabricated with bottom-up solution processing and the module is formed by individual cells with the stripe geometry that the cell contact to the next cell by overlapping the top electrode of one cell stripe with the bottom electrode of the next cell stripe, as show in Fig. 2.34 [272]. This interconnection part does not contribute to the current generation, leading to noneffective area, and therefore efficiency loss of the solar module. As the example, the area loss of the module in Fig. 2.34 is about 1/3. This will lead to a big loss of the efficiency of the module.

In order to reduce the area loss in the module, patterning methods with high precision are required. So far, the techniques for creating patterned films such as inkjet-printing, screen printing, flexography-printing, and gravure-printing have been proved to possess broad application for their high throughput and roll-to-roll compatibility [273–278].

Particularly, the laser ablation technique has been demonstrated as an effective method to produce high-precision patterns and yields small interconnecting area loss [278–280]. The typical patterns via laser ablation technique are shown in

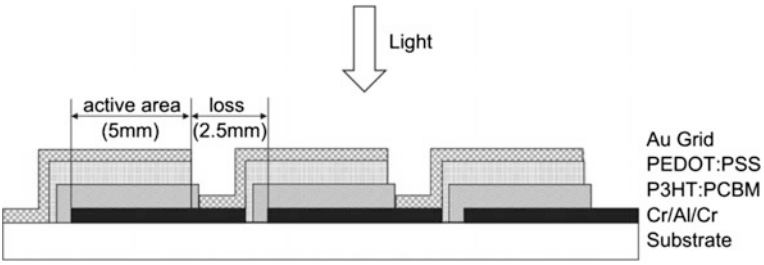

Fig. 2.34 Schematic drawing of the monolithic series circuitry. Reprinted with permission from Ref. [272]. Copyright 2011 by Elsevier

Fig. 2.35. High geometric fill factor above 90% was achieved (up to 98.5%) with interconnection widths less than 100 μm [280, 281]. For example, the Brabec's group fabricated solution-processed semitransparent modules with high geometric fill factor exceeding 95%, respectively [282]. Yang's group demonstrated the solar module with the device geometric fill factor of 90% [279]. Hanisch et al. reported polymer tandem modules patterned with the laser ablation exhibiting geometric fill factor of 95% [278].

Besides the laser ablation technique, new solar module structure has also been developed to increase the geometric fill factor and also enhance the ease of module fabrication. Lee's group has published several works figuring out ways to simplify the traditional post-patterning processing and obtain less area loss. They developed a conceptual polymer solar module using self-aligned dual charge-selecting interfacial layers (PEI and MoO_3) to alternate the polarity of serial subcells, as shown in Fig. 2.36. The feature of this design is that the electrical contact of adjacent cells is connected in the same panel; the whole organic active layer does not need to be broken to expose the bottom electrode for serial connection. Average PCE of the module cell (4.24%) reaching 82% relative to the small-sized lab-cell (5.19%) is achieved through high geometric fill factor of 96% [283]. Kang et al. also have dramatically reduced both ohmic and aperture loss through fabricating the main active layers without any pattern formation. By adding silver nanoparticles and applying a reverse bias voltage, the serial connection region became electrically contacted. The module efficiency is 5.6% with a high geometric fill factor of 90% [284]. Hong et al. reported a series connection method that facilitates module fabrication without the aid of additional and complicated post-patterning of charge transport layers. With the successive deposition of component layers using slot-die and doctor-blade printing techniques, module efficiency reaching 7.5% is achieved with an area of 4.15 cm^2 [285].

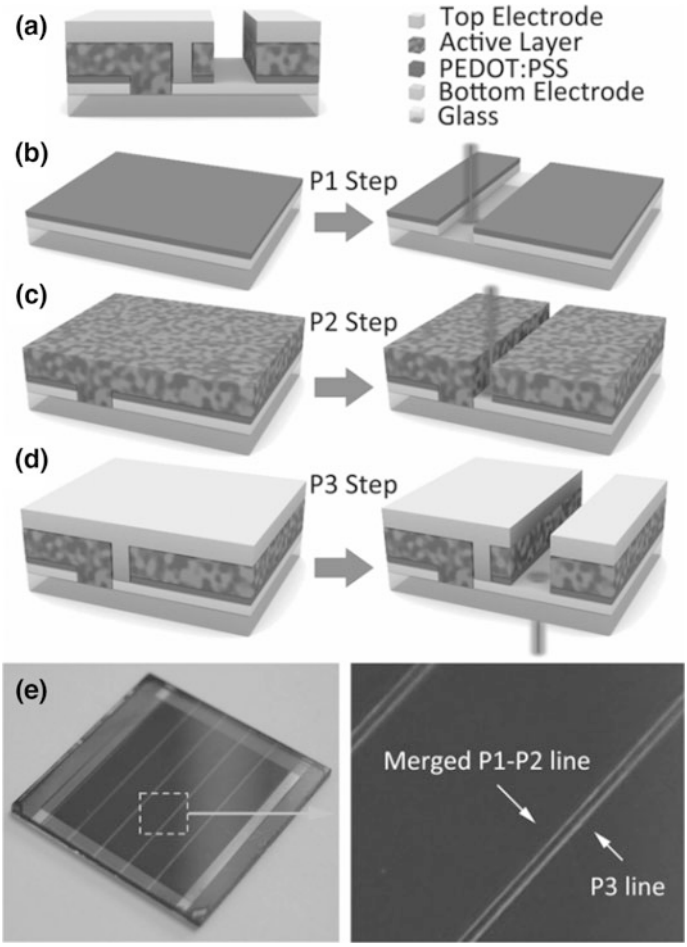

Fig. 2.35 **a** Schematic illustration of the module configuration with the patterns; and **b–d** procedures for photovoltaic module fabrication. **e** The photographic image of a sample module device. Reprinted with permission from Ref. [279]. Copyright 2015 by WILEY-VCH Verlag GmbH Co. KGaA, Weinheim

2.7.2 Productions and Applications

PSCs are solution-processed, highly flexible. The whole processing does not need high temperature. These features enable the fabrication of the polymer solar cells to well suit the roll-to-roll production. The Krebs group has done pioneer work on large-area polymer solar modules via roll-to-roll coating. Figure 2.37 shows the photograph of the coating of the active layers of the polymer solar cells [239].

The infinite PV, a Danish company, has marketed a variety of organic solar products prepared via roll-to-roll printing fabrication. One of the representative products: HeLi-on (Fig. 2.38), it is a portable compact solar charger including the

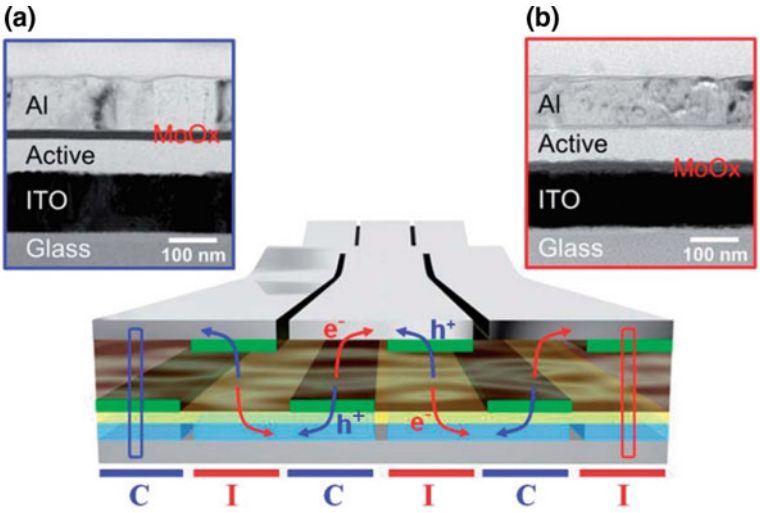

Fig. 2.36 A schematic illustration of new-conceptual module cell architecture. Reprinted with permission from Ref. [283]. Copyright 2013 by The Royal Society of Chemistry

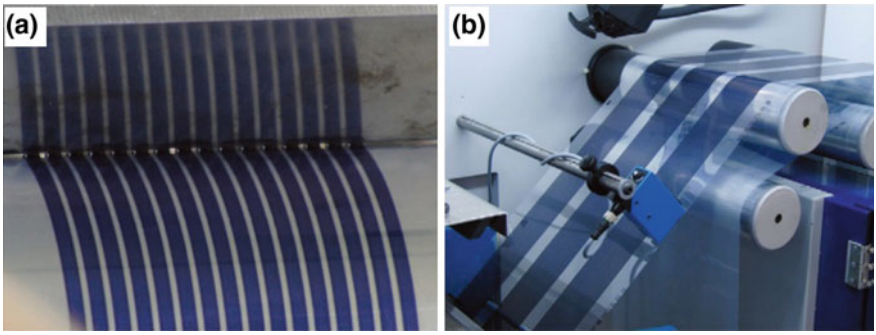

Fig. 2.37 **a** Photograph of the standing meniscus during slot-die coating of the active layer of the PSC comprising many very tightly spaced stripes. **b** A total of 48 stripes (3 mm wide spaced by 1 mm) are coated simultaneously). Reprinted with permission from Ref. [239]. Copyright 2012 by Elsevier

polymer solar panel and energy storage battery bank. When sunlight is on, one can charge an external device by simply unrolling the solar panel under sunlight; when the Sun is down there is still internal energy storage battery to provide the power. The internal battery can be charged either with the solar panel or with any USB charger. HeLi-on measures 11.3 × 3.6 × 2.8 cm and weighs 105 g. The solar cells parts are less than 2 μm thick, encapsulated in a protective foil on both sides. The total thickness of the solar panel to less than 1 mm, which is a representative application of the thin-film solar cells.

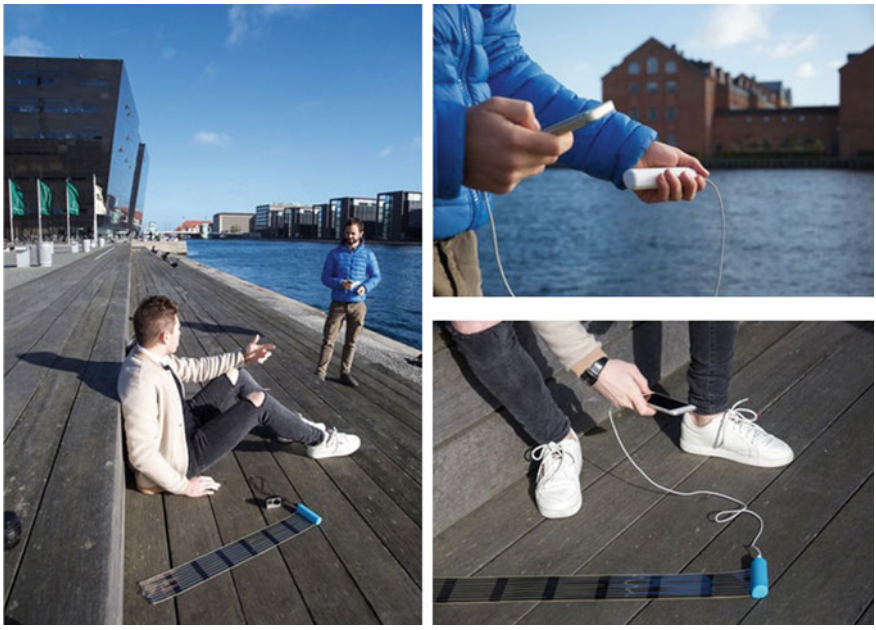

Fig. 2.38 Charging smartphones using printed organic solar cells (infinitePV, Denmark)

Fig. 2.39 The BIOPV array at the African Union building contains 445 Belectric PSC solar modules

Recently, PSCs for building-integration has been demonstrated at the African Union building by BELECTRIC OPV GmbH (shown in Fig. 2.39). The PSC array includes 445 flexible, transparent organic solar modules created by the company. The 25 × 20 m installation is translucent, enabling 75% light transmission across

the overall roof surface, and generating sufficient solar energy to power the building's LED light system

References

1. Sariciftci N, Smilowitz L, Heeger AJ et al (1992) Photoinduced electron transfer from a conducting polymer to buckminsterfullerene. Science 258:1474–1476
2. Morita S, Zakhidov AA, Yoshino K (1992) Doping effect of buckminsterfullerene in conducting polymer: change of absorption spectrum and quenching of luminescene. Solid State Commun 82:249–252
3. Yu G, Gao J, Hummelen JC et al (1995) Polymer photovoltaic cells: enhanced efficiencies via a network of internal donor-acceptor heterojunctions. Sci-AAAS-Wkly Paper Ed 270:1789–1790
4. Lu L, Zheng T, Wu Q et al (2015) Recent advances in bulk heterojunction polymer solar cells. Chem Rev 115:12666–12731
5. Dou L, You J, Hong Z et al (2013) 25th anniversary article: a decade of organic/polymeric photovoltaic research. Adv Mater 25:6642–6671
6. Hu HW, Jiang K, Yang GF et al (2015) Terthiophene-based D-A polymer with an asymmetric arrangement of alkyl chains that enables efficient polymer solar cells. J Am Chem Soc 137:14149–14157
7. Scharber MC, Mühlbacher D, Koppe M et al (2006) Design rules for donors in bulk-heterojunction solar cells-Towards 10% energy-conversion efficiency. Adv Mater 18:789–794
8. Zhang F, Inganäs O, Zhou Y et al (2016) The development of polymer-fullerene solar cells. Nat Sci Rev 3:222–239
9. Sirringhaus H, Tessler N, Friend RH (1998) Integrated optoelectronic devices based on conjugated polymers. Science 280:1741–1744
10. Koppe M, Brabec CJ, Heiml S et al (2009) Influence of molecular weight distribution on the gelation of P3HT and its impact on the photovoltaic performance. Macromolecules 42:4661–4666
11. Dennler G, Scharber MC, Brabec CJ (2009) Polymer-fullerene bulk-heterojunction solar cells. Adv Mater 21:1323–1338
12. Kim Y, Cook S, Tuladhar SM et al (2006) A strong regioregularity effect in self-organizing conjugated polymer films and high-efficiency polythiophene:fullerene solar cells. Nat Mater 5:197–203
13. Hou J, Huo L, He C et al (2005) Synthesis and absorption spectra of poly(3-(phenylenevinyl)thiophene)s with conjugated side chains. Macromolecules 39:594–603
14. Hou J, Tan ZA, Yan Y et al (2006) Synthesis and photovoltaic properties of two-dimensional conjugated polythiophenes with bi(thienylenevinylene) side chains. J Am Chem Soc 128:4911–4916
15. Hou J, Chen TL, Zhang S et al (2009) An easy and effective method to modulate molecular energy level of poly(3-alkylthiophene) for high-voc polymer solar cells. Macromolecules 42:9217–9219
16. Zhang M, Guo X, Yang Y et al (2011) Downwards tuning the HOMO level of polythiophene by carboxylate substitution for high open-circuit-voltage polymer solar cells. Poly Chem 2:2900–2906
17. Hu X, Shi M, Chen J et al (2011) Synthesis and photovoltaic properties of ester group functionalized polythiophene derivatives. Macromol Rapid Commun 32:506–511
18. Zhang M, Guo X, Ma W et al (2014) A polythiophene derivative with superior properties for practical application in polymer solar cells. Adv Mater 26:5880–5885

19. Liang Y, Wu Y, Feng D et al (2009) Development of new semiconducting polymers for high performance solar cells. J Am Chem Soc 131:56–57
20. Liang Y, Feng D, Wu Y et al (2009) Highly efficient solar cell polymers developed via fine-tuning of structural and electronic properties. J Am Chem Soc 131:7792–7799
21. Liang Y, Xu Z, Xia J et al (2010) For the bright future—bulk heterojunction polymer solar cells with power conversion efficiency of 7.4%. Adv Mater 22:E135–E138
22. Lu L, Yu L (2014) Understanding low bandgap polymer PTB7 and optimizing polymer solar cells based on it. Adv Mater 26:4413–4430
23. He Z, Zhong C, Su S et al (2012) Enhanced power-conversion efficiency in polymer solar cells using an inverted device structure. Nat Photonics 6:591–595
24. Huo L, Zhang S, Guo X et al (2011) Replacing alkoxy groups with alkylthienyl groups: a feasible approach to improve the properties of photovoltaic polymers. Angew Chem Int Ed 123:9871–9876
25. Ye L, Zhang S, Zhao W et al (2014) Highly efficient 2D-conjugated benzodithiophene-based photovoltaic polymer with linear alkylthio side chain. Chem Mater 26:3603–3605
26. Liao S-H, Jhuo H-J, Cheng Y-S et al (2013) Fullerene derivative-doped zinc oxide nanofilm as the cathode of inverted polymer solar cells with low-bandgap polymer (PTB7-Th) for high performance. Adv Mater 25:4766–4771
27. Shrotriya V, Wu EH-E, Li G et al (2006) Efficient light harvesting in multiple-device stacked structure for polymer solar cells. Appl Phys Lett 88:064104
28. Shaheen SE, Brabec CJ, Sariciftci NS et al (2001) 2.5% efficient organic plastic solar cells. Appl Phys Lett 78:841–843
29. Brabec CJ, Shaheen SE, Winder C et al (2002) Effect of LiF/metal electrodes on the performance of plastic solar cells. Appl Phys Lett 80:1288–1290
30. Granstrom M, Petritsch K, Arias AC et al (1998) Laminated fabrication of polymeric photovoltaic diodes. Nature 395:257–260
31. Gupta D, Kabra D, Kolishetti N et al (2007) An efficient bulk-heterojunction photovoltaic cell based on energy transfer in graded-bandgap polymers. Adv Funct Mater 17:226–232
32. Hoppe H, Egbe DAM, Muhlbacher D et al (2004) Photovoltaic action of conjugated polymer/fullerene bulk heterojunction solar cells using novel PPE-PPV copolymers. J Mater Chem 14:3462–3467
33. Brédas J-L, Norton JE, Cornil J et al (2009) Molecular understanding of organic solar cells: the challenges. Acc Chem Res 42:1691–1699
34. Svensson M, Zhang F, Veenstra SC et al (2003) High-performance polymer solar cells of an alternating polyfluorene copolymer and a fullerene derivative. Adv Mater 15:988–991
35. Li W, Qin R, Zhou Y et al (2010) Tailoring side chains of low band gap polymers for high efficiency polymer solar cells. Polymer 51:3031–3038
36. Wang E, Wang L, Lan L et al (2008) High-performance polymer heterojunction solar cells of a polysilafluorene derivative. Appl Phys Lett 92:033307
37. Boudreault P-LT, Michaud A, Leclerc M (2007) A new poly(2,7-dibenzosilole) derivative in polymer solar cells. Macromol Rapid Commun 28:2176–2179
38. Park SH, Roy A, Beaupre S et al (2009) Bulk heterojunction solar cells with internal quantum efficiency approaching 100%. Nat Photonics 3:297–302
39. Mühlbacher D, Scharber M, Morana M et al (2006) High photovoltaic performance of a low-bandgap polymer. Adv Mater 18:2884–2889
40. Coffin RC, Peet J, Rogers J et al (2009) Streamlined microwave-assisted preparation of narrow-bandgap conjugated polymers for high-performance bulk heterojunction solar cells. Nat Chem 1:657–661
41. Guo X, Zhou N, Lou SJ et al (2012) Bithiopheneimide–dithienosilole/dithienogermole copolymers for efficient solar cells: information from structure–property–device performance correlations and comparison to Thieno[3,4-c]pyrrole-4,6-dione analogues. J Am Chem Soc 134:18427–18439
42. Amb CM, Chen S, Graham KR et al (2011) Dithienogermole as a fused electron donor in bulk heterojunction solar cells. J Am Chem Soc 133:10062–10065

43. Zhou H, Yang L, Stuart AC et al (2011) Development of fluorinated benzothiadiazole as a structural unit for a polymer solar cell of 7% efficiency. Angew Chem Int Ed 50:2995–2998
44. Wang N, Chen Z, Wei W et al (2013) Fluorinated benzothiadiazole-based conjugated polymers for high-performance polymer solar cells without any processing additives or post-treatments. J Am Chem Soc 135:17060–17068
45. Wang X, Sun Y, Chen S et al (2012) Effects of π-conjugated bridges on photovoltaic properties of donor-π-acceptor conjugated copolymers. Macromolecules 45:1208–1216
46. Subbiah J, Purushothaman B, Chen M et al (2015) Organic solar cells using a high-molecular-weight benzodithiophene-benzothiadiazole copolymer with an efficiency of 9.4%. Adv Mater 27:702–705
47. Dou L, You J, Yang J et al (2012) Tandem polymer solar cells featuring a spectrally matched low-bandgap polymer. Nat Photon 6:180–185
48. Li W, Hendriks KH, Furlan A et al (2013) Universal correlation between fibril width and quantum efficiency in diketopyrrolopyrrole-based polymer solar cells. J Am Chem Soc 135:18942–18948
49. Zhang M, Gu Y, Guo X et al (2013) Efficient polymer solar cells based on benzothiadiazole and alkylphenyl substituted benzodithiophene with a power conversion efficiency over 8%. Adv Mater 25:4944–4949
50. Bin H, Zhang ZG, Gao L et al (2016) Non-fullerene polymer solar cells based on alkylthio and fluorine substituted 2D-conjugated polymers reach 9.5% efficiency. J Am Chem Soc 138:4657–4664
51. Wang M, Hu X, Liu P et al (2011) Donor-acceptor conjugated polymer based on Naphtho [1,2-c:5,6-c]bis[1, 2, 5]thiadiazole for high-performance polymer solar cells. J Am Chem Soc 133:9638–9641
52. Dong Y, Hu X, Duan C et al (2013) A series of new medium-bandgap conjugated polymers based on Naphtho[1,2-c:5,6-c]bis(2-octyl-[1–3]triazole) for high-performance polymer solar cells. Adv Mater 25:3683–3688
53. Huo L, Liu T, Fan B et al (2015) Organic solar cells based on a 2D Benzo[1,2-b:4,5-b′] difuran-conjugated polymer with high-power conversion efficiency. Adv Mater 27:6969–6975
54. Kim J-H, Lee M, Yang H et al (2014) A high molecular weight triisopropylsilylethynyl (TIPS)-benzodithiophene and diketopyrrolopyrrole-based copolymer for high performance organic photovoltaic cells. J Mater Chem A 2:6348–6352
55. Huo L, Liu T, Sun X et al (2015) Single-junction organic solar cells based on a novel wide-bandgap polymer with efficiency of 9.7%. Adv Mater 27:2938–2944
56. Hummelen JC, Knight BW, LePeq F et al (1995) Preparation and characterization of fulleroid and methanofullerene derivatives. J Org Chem 60:532–538
57. Sivaraman N, Dhamodaran R, Kaliappan I et al (1992) Solubility of C60 in organic solvents. J Org Chem 57:6077–6079
58. He Y, Li Y (2011) Fullerene derivative acceptors for high performance polymer solar cells. Phys Chem Chem Phys 13:1970–1983
59. Matsuo Y, Sato Y, Niinomi T et al (2009) Columnar structure in bulk heterojunction in solution-processable three-layered p-i-n organic photovoltaic devices using tetrabenzoporphyrin precursor and silylmethyl[60]fullerene. J Am Chem Soc 131:16048–16050
60. Mihailetchi VD, van Duren JKJ, Blom PWM et al (2003) Electron transport in a methanofullerene. Adv Funct Mater 13:43–46
61. Li G, Shrotriya V, Huang J et al (2005) High-efficiency solution processable polymer photovoltaic cells by self-organization of polymer blends. Nat Mater 4:864–868
62. Wienk MM, Kroon JM, Verhees WJH et al (2003) Efficient methano[70] fullerene/MDMO-PPV bulk heterojunction photovoltaic cells. Angew Chem Int Ed 42:3371–3375
63. Troshin PA, Hoppe H, Renz J et al (2009) Material solubility-photovoltaic performance relationship in the design of novel fullerene derivatives for bulk heterojunction solar cells. Adv Funct Mater 19:779–788

64. Chen J-D, Cui C, Li Y-Q et al (2014) Single-junction polymer solar cells exceeding 10% power conversion efficiency. Adv Mater 27:1035–1041
65. Zhang S, Ye L, Zhao W et al (2015) Realizing over 10% efficiency in polymer solar cell by device optimization. Sci China Chem 58:1–9
66. Liu Y, Zhao J, Li Z et al (2014) Aggregation and morphology control enables multiple cases of high-efficiency polymer solar cells. Nat Commun 5:5293
67. Zhao J, Li Y, Yang G et al (2016) Efficient organic solar cells processed from hydrocarbon solvents. Nat Energy 1:15027
68. Zheng L, Zhou Q, Deng X et al (2004) Methanofullerenes used as electron acceptors in polymer photovoltaic devices. J Phys Chem B 108:11921–11926
69. Mayorova JY, Nikitenko SL, Troshin PA et al (2007) Synthesis and investigation of fullerene-based acceptor materials. Mendeleev Commun 17:175–177
70. Zhang Y, Yip H-L, Acton O et al (2009) A simple and effective way of achieving highly efficient and thermally stable bulk-heterojunction polymer solar cells using amorphous fullerene derivatives as electron acceptor. Chem Mater 21:2598–2600
71. He Y, Chen H-Y, Hou J et al (2010) Indene-C60 bisadduct: a new acceptor for high-performance polymer solar cells. J Am Chem Soc 132:1377–1382
72. He Y, Zhao G, Peng B et al (2010) High-yield synthesis and electrochemical and photovoltaic properties of indene-C70 bisadduct. Adv Funct Mater 20:3383–3389
73. Guo X, Cui C, Zhang M et al (2012) High efficiency polymer solar cells based on poly (3-hexylthiophene)/indene-C70 bisadduct with solvent additive. Energy Environ Sci 5:7943–7949
74. Meng X, Zhang W, Tan ZA et al (2012) Dihydronaphthyl-based [60]fullerene bisadducts for efficient and stable polymer solar cells. Chem Commun 48:425–427
75. Meng X, Zhang W, Tan ZA et al (2012) Highly efficient and thermally stable polymer solar cells with dihydronaphthyl-based [70]fullerene bisadduct derivative as the acceptor. Adv Funct Mater 22:2187–2193
76. Ye G, Chen S, Xiao Z et al (2012) o-Quinodimethane-methano[60]fullerene and thieno-o-quinodimethane-methano[60]fullerene as efficient acceptor materials for polymer solar cells. J Mater Chem 22:22374–22377
77. Li W, Hendriks KH, Furlan A et al (2015) High quantum efficiencies in polymer solar cells at energy losses below 0.6 eV. J Am Chem Soc 137:2231–2234
78. Scharber MC (2016) On the efficiency limit of conjugated polymer:fullerene-based bulk heterojunction solar cells. Adv Mater 28:1994–2001
79. Eftaiha AAF, Sun J-P, Hill IG et al (2014) Recent advances of non-fullerene, small molecular acceptors for solution processed bulk heterojunction solar cells. J Mater Chem A 2:1201–1213
80. Shivanna R, Shoaee S, Dimitrov S et al (2014) Charge generation and transport in efficient organic bulk heterojunction solar cells with a perylene acceptor. Energy Environ Sci 7:435–441
81. Ye L, Sun K, Jiang W et al (2015) Enhanced efficiency in fullerene-free polymer solar cell by incorporating fine-designed donor and acceptor materials. ACS Appl Mater Interfaces 7:9274–9280
82. Sun D, Meng D, Cai Y et al (2015) Non-fullerene-acceptor-based bulk-heterojunction organic solar cells with efficiency over 7%. J Am Chem Soc 137:11156–11162
83. Meng D, Sun D, Zhong C et al (2016) High-performance solution-processed non-fullerene organic solar cells based on selenophene-containing perylene bisimide acceptor. J Am Chem Soc 138:375–380
84. Zhang X, Lu Z, Ye L et al (2013) A potential perylene diimide dimer-based acceptor material for highly efficient solution-processed non-fullerene organic solar cells with 4.03% efficiency. Adv Mater 25:5791–5797
85. Zhang X, Zhan C, Yao J (2015) Non-fullerene organic solar cells with 6.1% efficiency through fine-tuning parameters of the film-forming process. Chem Mater 27:166–173

86. Li H, Hwang Y-J, Courtright BAE et al (2015) Fine-tuning the 3D structure of nonfullerene electron acceptors toward high-performance polymer solar cells. Adv Mater 27:3266–3272
87. Cnops K, Rand BP, Cheyns Det al (2014) 8.4% efficient fullerene-free organic solar cells exploiting long-range exciton energy transfer. Nat Commun 5:3406
88. Lin Y, Zhang Z-G, Bai H et al (2015) High-performance fullerene-free polymer solar cells with 6.31% efficiency. Energy Environ Sci 8:610–616
89. Lin Y, Wang J, Zhang Z-G et al (2015) An electron acceptor challenging fullerenes for efficient polymer solar cells. Adv Mater 27:1170–1174
90. Lin Y, He Q, Zhao F et al (2016) A facile planar fused-ring electron acceptor for as-cast polymer solar cells with 8.71% efficiency. J Am Chem Soc 138:2973–2976
91. Lin Y, Zhao F, He Q et al (2016) High-performance electron acceptor with thienyl side chains for organic photovoltaics. J Am Chem Soc 138:4955–4961
92. Zhao W, Qian D, Zhang S et al (2016) Fullerene-free polymer solar cells with over 11% efficiency and excellent thermal stability. Adv Mater 28:4734–4739
93. Facchetti A (2013) Polymer donor–polymer acceptor (all-polymer) solar cells. Mater Today 16:123–132
94. Zhao X, Zhan X (2011) Electron transporting semiconducting polymers in organic electronics. Chem Soc Rev 40:3728–3743
95. Gao L, Zhang Z-G, Xue L et al (2016) All-polymer solar cells based on absorption-complementary polymer donor and acceptor with high power conversion efficiency of 8.27%. Adv Mater 28:1884–1890
96. Yan H, Chen Z, Zheng Y et al (2009) A high-mobility electron-transporting polymer for printed transistors. Nature 457:679–686
97. Deshmukh KD, Qin T, Gallaher JK et al (2015) Performance, morphology and photophysics of high open-circuit voltage, low band gap all-polymer solar cells. Energy Environ Sci 8:332–342
98. Mori D, Benten H, Okada I et al (2014) Highly efficient charge-carrier generation and collection in polymer/polymer blend solar cells with a power conversion efficiency of 5.7%. Energy Environ Sci 7:2939–2943
99. Kang H, Uddin MA, Lee C et al (2015) Determining the role of polymer molecular weight for high-performance all-polymer solar cells: its effect on polymer aggregation and phase separation. J Am Chem Soc 137:2359–2365
100. Mu C, Liu P, Ma W et al (2014) High-efficiency all-polymer solar cells based on a pair of crystalline low-bandgap polymers. Adv Mater 26:7224–7230
101. Ye L, Jiao X, Zhou M et al (2015) Manipulating aggregation and molecular orientation in all-polymer photovoltaic cells. Adv Mater 27:6046–6054
102. Benten H, Nishida T, Mori D et al (2016) High-performance ternary blend all-polymer solar cells with complementary absorption bands from visible to near-infrared wavelengths. Energy Environ Sci 9:135–140
103. Lee C, Kang H, Lee W et al (2015) High-performance all-polymer solar cells via side-chain engineering of the polymer acceptor: the importance of the polymer packing structure and the nanoscale blend morphology. Adv Mater 27:2466–2471
104. Zhou E, Cong J, Zhao M et al (2012) Synthesis and application of poly (fluorene-alt-naphthalene diimide) as an n-type polymer for all-polymer solar cells. Chem Commun 48:5283–5285
105. Xiao B, Ding G, Tan ZA et al (2015) A comparison of n-type copolymers based on cyclopentadithiophene and naphthalene diimide/perylene diimides for all-polymer solar cell applications. Poly Chem 6:7594–7602
106. Diao Y, Zhou Y, Kurosawa T et al (2015) Flow-enhanced solution printing of all-polymer solar cells. Nat Commun 6:7955
107. Jung IH, Zhao D, Jang J et al (2015) Development and structure/property relationship of new electron accepting polymers based on thieno[2′,3′:4,5]pyrido[2,3-g]thieno[3,2-c] quinoline-4,10-dione for all-polymer solar cells. Chem Mater 27:5941–5948

108. Hwang Y-J, Earmme T, Courtright BAE et al (2015) n-Type semiconducting naphthalene diimide-perylene diimide copolymers: controlling crystallinity, blend morphology, and compatibility toward high-performance all-polymer solar cells. J Am Chem Soc 137:4424–4434
109. Yu G, Gao J, Hummelen JC et al (1995) Polymer photovoltaic cells: enhanced efficiencies via a network of internal donor-acceptor heterojunctions. Science 270:1789–1791
110. Clarke TM, Durrant JR (2010) Charge photogeneration in organic solar cells. Chem Rev 110:6736–6767
111. Heeger AJ (2014) 25th anniversary article: bulk heterojunction solar cells: understanding the mechanism of operation. Adv Mater 26:10–28
112. Benanti TL, Venkataraman D (2006) Organic solar cells: an overview focusing on active layer morphology. Photosynth Res 87:73–81
113. Huang Y, Kramer EJ, Heeger AJ et al (2014) Bulk heterojunction solar cells: morphology and performance relationships. Chem Rev 114:7006–7043
114. Dang MT, Hirsch L, Wantz G et al (2013) Controlling the morphology and performance of bulk heterojunctions in solar cells. lessons learned from the benchmark poly (3-hexylthiophene):[6, 6]-phenyl-c61-butyric acid methyl ester system. Chem Rev 113:3734–3765
115. Lu L, Zheng T, Wu Q et al (2015) Recent advances in bulk heterojunction polymer solar cells. Chem Rev 115:12666–12731
116. McNeill CR (2012) Morphology of all-polymer solar cells. Energy Environ Sci 5:5653–5667
117. Rivnay J, Mannsfeld SCB, Miller CE et al (2012) Quantitative determination of organic semiconductor microstructure from the molecular to device scale. Chem Rev 112:5488–5519
118. Pingree LSC, Reid OG, Ginger DS (2009) Electrical scanning probe microscopy on active organic electronic devices. Adv Mater 21:19–28
119. Pingree LSC, MacLeod BA, Ginger DS (2008) The changing face of PEDOT:PSS films: substrate, bias, and processing effects on vertical charge transport. J Phys Chem C 112:7922–7927
120. Reid OG, Munechika K, Ginger DS (2008) Space charge limited current measurements on conjugated polymer films using conductive atomic force microscopy. Nano Lett 8:1602–1609
121. Coffey DC, Reid OG, Rodovsky DB et al (2007) Mapping local photocurrents in polymer/fullerene solar cells with photoconductive atomic force microscopy. Nano Lett 7:738–744
122. Lin L-Y, Chen Y-H, Huang Z-Y et al (2011) A low-energy-gap organic dye for high-performance small-molecule organic solar cells. J Am Chem Soc 133:15822–15825
123. Moon JS, Lee JK, Cho S et al (2009) "Columnlike" structure of the cross-sectional morphology of bulk heterojunction materials. Nano Lett 9:230–234
124. Yang X, Loos J, Veenstra SC et al (2005) Nanoscale morphology of high-performance polymer solar cells. Nano Lett 5:579–583
125. Kozub DR, Vakhshouri K, Orme LM et al (2011) Polymer crystallization of partially miscible polythiophene/fullerene mixtures controls morphology. Macromolecules 44:5722–5726
126. Loos J, Yang X, Koetse MM et al (2005) Morphology determination of functional poly [2-methoxy-5-(3,7-dimethyloctyloxy)-1,4-phenylenevinylene]/poly[oxa-1,4-phenylene-1,2-(1-cyanovinylene)-2-methoxy,5-(3,7-dimethyloctyloxy)-1,4-phenylene-1,2-(2-cyanovinylene)-1,4-phenylene] blends as used for all-polymer solar cells. J Appl Polym Sci 97:1001–1007
127. Klein MFG, Pfaff M, Müller E et al (2012) Poly(3-hexylselenophene) solar cells: correlating the optoelectronic device performance and nanomorphology imaged by low-energy scanning transmission electron microscopy. J Polym Sci B Polym Phys 50:198–206

128. Rogers JT, Schmidt K, Toney MF et al (2012) Time-resolved structural evolution of additive-processed bulk heterojunction solar cells. J Am Chem Soc 134:2884–2887
129. Buss F, Schmidt-Hansberg B, Sanyal M et al (2016) Gaining further insight into the solvent additive-driven crystallization of bulk-heterojunction solar cells by in situ X-ray scattering and optical reflectometry. Macromolecules 49:4867–4874
130. Su M-S, Kuo C-Y, Yuan M-C et al (2011) Improving device efficiency of polymer/fullerene bulk heterojunction solar cells through enhanced crystallinity and reduced grain boundaries induced by solvent additives. Adv Mater 23:3315–3319
131. Zhou H, Chen Q, Li G et al (2014) Science 345:542
132. Lu X, Hlaing H, Germack DS et al (2012) Bilayer order in a polycarbazole-conjugated polymer. Nat Commun 3:795
133. Huang Y, Liu F, Guo X et al (2013) Manipulating backbone structure to enhance low band gap polymer photovoltaic performance. Adv Energy Mater 3:930–937
134. Swaraj S, Wang C, Yan H et al (2010) Nanomorphology of bulk heterojunction photovoltaic thin films probed with resonant soft X-ray scattering. Nano Lett 10:2863–2869
135. Collins BA, Li Z, Tumbleston JR et al (2013) Absolute measurement of domain composition and nanoscale size distribution explains performance in PTB7:PC71BM solar cells. Adv Energy Mater 3:65–74
136. Ye L, Zhang S, Ma W et al (2012) From binary to ternary solvent: morphology fine-tuning of D/A blends in PDPP3T-based polymer solar cells. Adv Mater 24:6335–6341
137. Carpenter JH, Hunt A, Ade H (2015) Characterizing morphology in organic systems with resonant soft X-ray scattering. J Electron Spectrosc Relat Phenom 200:2–14
138. Ruderer MA, Guo S, Meier R et al (2011) Solvent-induced morphology in polymer-based systems for organic photovoltaics. Adv Funct Mater 21:3382–3391
139. Mori D, Benten H, Ohkita H et al (2012) Polymer/polymer blend solar cells improved by using high-molecular-weight fluorene-based copolymer as electron acceptor. ACS Appl Mater Interfaces 4:3325–3329
140. Kan B, Zhang Q, Li M et al (2014) Solution-processed organic solar cells based on dialkylthiol-substituted benzodithiophene unit with efficiency near 10%. J Am Chem Soc 136:15529–15532
141. Zhou J, Zuo Y, Wan X et al (2013) Solution-processed and high-performance organic solar cells using small molecules with a benzodithiophene unit. J Am Chem Soc 135:8484–8487
142. Kan B, Li M, Zhang Q et al (2015) A series of simple oligomer-like small molecules based on oligothiophenes for solution-processed solar cells with high efficiency. J Am Chem Soc 137:3886–3893
143. Zhang F, Jespersen KG, Björström C et al (2006) Influence of solvent mixing on the morphology and performance of solar cells based on polyfluorene copolymer/fullerene blends. Adv Funct Mater 16:667–674
144. Hoth CN, Choulis SA, Schilinsky P et al (2007) High photovoltaic performance of inkjet printed polymer: fullerene blends. Adv Mater 19:3973–3978
145. Hoth CN, Steim R, Schilinsky P et al (2009) Topographical and morphological aspects of spray coated organic photovoltaics. Org Electron 10:587–593
146. Hoth CN, Schilinsky P, Choulis SA et al (2008) Printing highly efficient organic solar cells. Nano Lett 8:2806–2813
147. Zhao W, Ye L, Zhang S et al (2015) A universal halogen-free solvent system for highly efficient polymer solar cells. J Mater Chem A 3:12723–12729
148. Chen K-S, Yip H-L, Schlenker CW et al (2012) Halogen-free solvent processing for sustainable development of high efficiency organic solar cells. Org Electron 13:2870–2878
149. Duan C, Cai W, Hsu BBY et al (2013) Toward green solvent processable photovoltaic materials for polymer solar cells: the role of highly polar pendant groups in charge carrier transport and photovoltaic behavior. Energy Environ Sci 6:3022–3034
150. Chang J-H, Wang H-F, Lin W-C et al (2014) Efficient inverted quasi-bilayer organic solar cells fabricated by using non-halogenated solvent processes. J Mater Chem A 2:13398–13406

151. Chueh C-C, Yao K, Yip H-L et al (2013) Non-halogenated solvents for environmentally friendly processing of high-performance bulk-heterojunction polymer solar cells. Energy Environ Sci 6:3241–3248
152. Zhang H, Yao H, Zhao W et al (2016) High-Efficiency Polymer Solar Cells Enabled by Environment-Friendly Single-Solvent Processing. Adv. Energy Mater. 6:1502177
153. Berggren M, Gustafsson G, Inganäs O et al (1994) Thermal control of near-infrared and visible electroluminescence in alkyl-phenyl substituted polythiophenes. Appl Phys Lett 65:1489–1491
154. Mihailetchi VD, Xie H, de Boer B et al (2006) Origin of the enhanced performance in poly (3-hexylthiophene): [6, 6]-phenyl C61-butyric acid methyl ester solar cells upon slow drying of the active layer. Appl Phys Lett 89:012107
155. Shrotriya V, Yao Y, Li G et al (2006) Effect of self-organization in polymer/fullerene bulk heterojunctions on solar cell performance. Appl Phys Lett 89:063505
156. Hegde R, Henry N, Whittle B et al (2012) The impact of controlled solvent exposure on the morphology, structure and function of bulk heterojunction solar cells. Sol Energy Mater Sol Cells 107:112–124
157. Peet J, Soci C, Coffin RC et al (2006) Method for increasing the photoconductive response in conjugated polymer/fullerene composites. Appl Phys Lett 89:252105
158. Peet J, Kim JY, Coates NE et al (2007) Efficiency enhancement in low-bandgap polymer solar cells by processing with alkane dithiols. Nat Mater 6:497–500
159. Lee JK, Ma WL, Brabec CJ et al (2008) Processing additives for improved efficiency from bulk heterojunction solar cells. J Am Chem Soc 130:3619–3623
160. Hoven CV, Dang X-D, Coffin RC et al (2010) Improved performance of polymer bulk heterojunction solar cells through the reduction of phase separation via solvent additives. Adv Mater 22:E63–E66
161. Nguyen TL, Choi H, Ko SJ et al (2014) Semi-crystalline photovoltaic polymers with efficiency exceeding 9% in a [similar]300 nm thick conventional single-cell device. Energy Environ Sci 7:3040–3051
162. Choi H, Ko S-J, Kim T et al (2015) Small-bandgap polymer solar cells with unprecedented short-circuit current density and high fill factor. Adv Mater 27:3318–3324
163. Yao Y, Hou J, Xu Z et al (2008) Effects of solvent mixtures on the nanoscale phase separation in polymer solar cells. Adv Funct Mater 18:1783–1789
164. Hammond MR, Kline RJ, Herzing AA et al (2011) Molecular order in high-efficiency polymer/fullerene bulk heterojunction solar cells. ACS Nano 5:8248–8257
165. Lou SJ, Szarko JM, Xu T et al (2011) Effects of additives on the morphology of solution phase aggregates formed by active layer components of high-efficiency organic solar cells. J Am Chem Soc 133:20661–20663
166. Chang L, Lademann HWA, Bonekamp J-B et al (2011) Effect of trace solvent on the morphology of P3HT:PCBM bulk heterojunction solar cells. Adv Funct Mater 21:1779–1787
167. Ye L, Jing Y, Guo X et al (2013) Remove the residual additives toward enhanced efficiency with higher reproducibility in polymer solar cells. J Phys Chem C 117:14920–14928
168. Dittmer JJ, Marseglia EA, Friend RH (2000) Electron trapping in dye/polymer blend photovoltaic cells. Adv Mater 12:1270–1274
169. Padinger F, Rittberger RS, Sariciftci NS (2003) Effects of postproduction treatment on plastic solar cells. Adv Funct Mater 13:85–88
170. Ma W, Yang C, Gong X et al (2005) Thermally stable, efficient polymer solar cells with nanoscale control of the interpenetrating network morphology. Adv Funct Mater 15:1617–1622
171. Chen D, Nakahara A, Wei D et al (2011) P3HT/PCBM bulk heterojunction organic photovoltaics: correlating efficiency and morphology. Nano Lett 11:561–567
172. Kim K, Carroll DL (2005) Roles of Au and Ag nanoparticles in efficiency enhancement of poly(3-octylthiophene)/C60 bulk heterojunction photovoltaic devices. Appl Phys Lett 87:203113

173. Chang M-Y, Chen Y-F, Tsai Y-S et al (2009) Blending platinum nanoparticles into poly (3-hexylthiophene):[6, 6]-phenyl-c61-butyric acid methyl ester enhances the efficiency of polymer solar cells. J Electrochem Soc 156:B234–B237
174. Topp K, Borchert H, Johnen F et al (2010) Impact of the incorporation of Au nanoparticles into polymer/fullerene solar cells. J Phys Chem A 114:3981–3989
175. Wang DH, Kim DY, Choi KW et al (2011) Enhancement of donor-acceptor polymer bulk heterojunction solar cell power conversion efficiencies by addition of Au nanoparticles. Angew Chem Int Ed 50:5519–5523
176. Lu L, Xu T, Chen W et al (2013) The role of N-doped multiwall carbon nanotubes in achieving highly efficient polymer bulk heterojunction solar cells. Nano Lett 13:2365–2369
177. Sivula K, Ball ZT, Watanabe N et al (2006) Amphiphilic diblock copolymer compatibilizers and their effect on the morphology and performance of polythiophene: fullerene solar cells. Adv Mater 18:206–210
178. Tsai J-H, Lai Y-C, Higashihara T et al (2010) Enhancement of P3HT/PCBM photovoltaic efficiency using the surfactant of triblock copolymer containing poly(3-hexylthiophene) and poly(4-vinyltriphenylamine) segments. Macromolecules 43:6085–6091
179. Bechara R, Leclerc N, Lévêque P et al (2008) Efficiency enhancement of polymer photovoltaic devices using thieno-thiophene-based copolymers as nucleating agents for polythiophene crystallization. Appl Phys Lett 93:013306
180. Burke KB, Belcher WJ, Thomsen L et al (2009) Role of solvent trapping effects in determining the structure and morphology of ternary blend organic devices. Macromolecules 42:3098–3103
181. Jea Uk L, Jae Woong J, Todd E et al (2010) Morphology control of a polythiophene–fullerene bulk heterojunction for enhancement of the high-temperature stability of solar cell performance by a new donor–acceptor diblock copolymer. Nanotechnology 21:105201
182. Miyanishi S, Tajima K, Hashimoto K (2009) Morphological stabilization of polymer photovoltaic cells by using cross-linkable poly(3-(5-hexenyl)thiophene). Macromolecules 42:1610–1618
183. Kim BJ, Miyamoto Y, Ma B et al (2009) Photocrosslinkable polythiophenes for efficient, thermally stable, organic photovoltaics. Adv Funct Mater 19:2273–2281
184. Cheng Y-J, Hsieh C-H, Li P-J et al (2011) Morphological stabilization by in situ polymerization of fullerene derivatives leading to efficient, thermally stable organic photovoltaics. Adv Funct Mater 21:1723–1732
185. Drees M, Hoppe H, Winder C et al (2005) Stabilization of the nanomorphology of polymer-fullerene "bulk heterojunction" blends using a novel polymerizable fullerene derivative. J Mater Chem 15:5158–5163
186. Graham KR, Mei J, Stalder R et al (2011) Polydimethylsiloxane as a macromolecular additive for enhanced performance of molecular bulk heterojunction organic solar cells. ACS Appl Mater Interfaces 3:1210–1215
187. Yang L, Yan L, You W (2013) Organic solar cells beyond one pair of donor–acceptor: ternary blends and more. J Phys Chem Lett 4:1802–1810
188. An Q, Zhang F, Zhang J et al (2016) Versatile ternary organic solar cells: a critical review. Energy Environ Sci 9:281–322
189. Ameri T, Khoram P, Min J et al (2013) Organic ternary solar cells: a review. Adv Mater 25:4245–4266
190. Lu L, Kelly MA, You W et al (2015) Status and prospects for ternary organic photovoltaics. Nat Photon 9:491–500
191. Lu L, Xu T, Chen W et al (2014) Ternary blend polymer solar cells with enhanced power conversion efficiency. Nat Photon 8:716–722
192. Fang J, Wang Z, Zhang J et al (2015) Understanding the impact of hierarchical nanostructure in ternary organic solar cells. Adv Sci 2:1500250
193. Ma H, Yip H-L, Huang F et al (2010) Interface engineering for organic electronics. Adv Funct Mater 20:1371–1388

194. Zhang F, Gadisa A, Inganäs O et al (2004) Influence of buffer layers on the performance of polymer solar cells. Appl Phys Lett 84:3906–3908
195. Roman L, Berggren M, Inganäs O (1999) Polymer diodes with high rectification. Appl Phys Lett 75:3557–3559
196. Savva A, Neophytou M, Koutsides C et al (2013) Synergistic effects of buffer layer processing additives for enhanced hole carrier selectivity in inverted organic photovoltaics. Org Electron 14:3123–3130
197. Lin Q, Armin A, Nagiri RCR et al (2015) Electro-optics of perovskite solar cells. Nat Photon 9:106–112
198. Baierl D, Fabel B, Gabos P et al (2010) Solution-processable inverted organic photodetectors using oxygen plasma treatment. Org Electron 11:1199–1206
199. Glatthaar M, Niggemann M, Zimmermann B et al (2005) Organic solar cells using inverted layer sequence. Thin Solid Films 491:298–300
200. Zhou Y, Cheun H, Choi S et al (2011) Optimization of a polymer top electrode for inverted semitransparent organic solar cells. Org Electron 12:827–831
201. Tao C, Ruan S, Xie G et al (2009) Role of tungsten oxide in inverted polymer solar cells. Appl Phys Lett 94:043311
202. Ratcliff EL, Meyer J, Steirer KX et al (2012) Energy level alignment in PCDTBT:PC70BM solar cells: solution processed NiOx for improved hole collection and efficiency. Org Electron 13:744–749
203. Teran-Escobar G, Pampel J, Caicedo JM et al (2013) Low-temperature, solution-processed, layered V2O5 hydrate as the hole-transport layer for stable organic solar cells. Energy Environ Sci 6:3088–3098
204. Bai S, Cao M, Jin Y et al (2014) Low-temperature combustion-synthesized nickel oxide thin films as hole-transport interlayers for solution-processed optoelectronic devices. Adv. Energy Mater. 4:1301460
205. Beek WJE, Wienk MM, Kemerink M et al (2005) Hybrid zinc oxide conjugated polymer bulk heterojunction solar cells. J Phys Chem B 109:9505–9516
206. White MS, Olson DC, Shaheen SE et al (2006) Inverted bulk-heterojunction organic photovoltaic device using a solution-derived ZnO underlayer. Appl Phys Lett 89:143517
207. Jönsson S, Carlegrim E, Zhang F et al (2005) Photoelectron spectroscopy of the contact between the cathode and the active layers in plastic solar cells: the role of LiF. Jpn J Appl Phys 44:3695
208. Zhang F, Ceder M, Inganas O (2007) Enhancing the photovoltage of polymer solar cells by using a modified cathode. Adv Mater 19:1835
209. Zhou Y, Li F, Barrau S et al (2009) Inverted and transparent polymer solar cells prepared with vacuum-free processing. Sol Energy Mater Sol Cells 93:497–500
210. Luo J, Wu H, He C et al (2009) Enhanced open-circuit voltage in polymer solar cells. Appl Phys Lett 95:043301
211. He C, Zhong C, Wu H et al (2010) Origin of the enhanced open-circuit voltage in polymer solar cells via interfacial modification using conjugated polyelectrolytes. J Mater Chem 20:2617–2622
212. Zheng L, Ma Y, Chu S et al (2014) Nanoscale 6:8171
213. Tang Z, Andersson LM, George Z et al (2012) Interlayer for modified cathode in highly efficient inverted ITO-free organic solar cells. Adv Mater 24:554–558
214. Sharma A, Hotchkiss PJ, Marder SR et al (2009) Tailoring the work function of indium tin oxide electrodes in electrophosphorescent organic light-emitting diodes. J Appl Phys 105:084507
215. Bulliard X, Ihn S-G, Yun S et al (2010) Enhanced performance in polymer solar cells by surface energy control. Adv Funct Mater 20:4381–4387
216. Zhou Y, Fuentes-Hernandez C, Shim J et al (2012) A universal method to produce low-work function electrodes for organic electronics. Science 336:327–332
217. Kyaw AKK, Wang DH, Gupta V et al (2013) Efficient solution-processed small-molecule solar cells with inverted structure. Adv Mater 25:2397–2402

218. O'Connor TF, Zaretski AV, Shiravi BA et al (2014) Stretching and conformal bonding of organic solar cells to hemispherical surfaces. Energy Environ Sci 7:370–378
219. Höfle S, Schienle A, Bernhard C et al (2014) Solution processed, white emitting tandem organic light-emitting diodes with inverted device architecture. Adv Mater 26:5155–5159
220. Weber C, Oberberg M, Weber D et al (2014) Improved morphology and performance of solution-processed metal-oxide thin-film transistors due to a polymer based interface modifier. Adv Mater Interfaces 1:1400137
221. Głowacki ED, Romanazzi G, Yumusak C et al (2015) Epindolidiones—versatile and stable hydrogen-bonded pigments for organic field-effect transistors and light-emitting diodes. Adv Funct Mater 25:776–787
222. Azzellino G, Grimoldi A, Binda M et al (2013) Fully inkjet-printed organic photodetectors with high quantum yield. Adv Mater 25:6829–6833
223. Saracco E, Bouthinon B, Verilhac JM et al (2013) Work function tuning for high-performance solution-processed organic photodetectors with inverted structure. Adv Mater 25:6534–6538
224. Zhou H, Chen Q, Li G et al (2014) Interface engineering of highly efficient perovskite solar cells. Science 345:542–546
225. Wang J, Wang N, Jin Y et al (2015) Interfacial control toward efficient and low-voltage perovskite light-emitting diodes. Adv Mater 27:2311–2316
226. Kim HH, Park S, Yi Y et al (2015) Inverted quantum dot light emitting diodes using polyethylenimine ethoxylated modified ZnO. Sci Rep 5:8968
227. Zhou Y, Khan TM, Shim JW et al (2014) All-plastic solar cells with a high photovoltaic dynamic range. J Mater Chem A 2:3492–3497
228. Zhang FL, Johansson M, Andersson MR et al (2002) Polymer photovoltaic cells with conducting polymer anodes. Adv Mater 14:662–665
229. Admassie S, Zhang FL, Manoj AG et al (2006) A polymer photodiode using vapour-phase polymerized PEDOT as an anode. Sol Energy Mater Sol Cells 90:133–141
230. Zhou Y, Zhang F, Tvingstedt K et al (2008) Investigation on polymer anode design for flexible polymer solar cells. Appl Phys Lett 92:233308
231. Kim N, Kee S, Lee SH et al (2014) Highly conductive PEDOT:PSS nanofibrils induced by solution-processed crystallization. Adv Mater 26(2268–72):2109
232. Xia Y, Sun K, Ouyang J (2012) Solution-processed metallic conducting polymer films as transparent electrode of optoelectronic devices. Adv Mater 24:2436–2440
233. Gilot J, Wienk MM, Janssen RAJ (2007) Double and triple junction polymer solar cells processed from solution. Appl Phys Lett 90:143512
234. Granlund T, Nyberg T, Stolz Roman L et al (2000) Patterning of polymer light-emitting diodes with soft lithography. Adv Mater 12:269–273
235. Gupta D, Wienk MM, Janssen RA (2013) Efficient polymer solar cells on opaque substrates with a laminated PEDOT: PSS top electrode. Adv Energy Mater 3:782–787
236. Wang X, Ishwara T, Gong W et al (2012) High-performance metal-free solar cells using stamp transfer printed vapor phase polymerized poly(3,4-ethylenedioxythiophene) top anodes. Adv Funct Mater 22:1454–1460
237. Yin LY, Zhao ZX, Jiang FY et al (2014) PEDOT:PSS top electrode prepared by transfer lamination using plastic wrap as the transfer medium for organic solar cells. Org Electron 15:2593–2598
238. Docampo P, Hanusch FC, Stranks SD et al (2014) Adv Energy Mater 4:1400355
239. Søndergaard R, Hösel M, Angmo D et al (2012) Roll-to-roll fabrication of polymer solar cells. Mater Today 15:36–49
240. Angmo D, Dam HF, Andersen TR et al (2014) All-solution-processed, ambient method for ITO-free, roll-coated tandem polymer solar cells using solution-processed metal films. Energy Technology 2:651–659
241. Andersen TR, Dam HF, Hosel M et al (2014) Scalable, ambient atmosphere roll-to-roll manufacture of encapsulated large area, flexible organic tandem solar cell modules. Energy Environ Sci 7:2925–2933

242. Ago H, Petritsch K, Shaffer MSP et al (1999) Composites of carbon nanotubes and conjugated polymers for photovoltaic devices. Adv Mater 11:1281–1285
243. Pasquier AD, Unalan HE, Kanwal A et al (2005) Conducting and transparent single-wall carbon nanotube electrodes for polymer-fullerene solar cells. Appl Phys Lett 87:203511
244. Feng Y, Ju X, Feng W et al (2009) Organic solar cells using few-walled carbon nanotubes electrode controlled by the balance between sheet resistance and the transparency. Appl Phys Lett 94:123302
245. Kim S, Yim J, Wang X et al (2010) Spin- and spray-deposited single-walled carbon-nanotube electrodes for organic solar cells. Adv Funct Mater 20:2310–2316
246. Jeon I, Cui K, Chiba T et al (2015) Direct and dry deposited single-walled carbon nanotube films doped with MoOx as electron-blocking transparent electrodes for flexible organic solar cells. J Am Chem Soc 137:7982–7985
247. Mei A, Li X, Liu L et al (2014) Science 345:295
248. Wang X, Zhi L, Tsao N et al (2008) Transparent carbon films as electrodes in organic solar cells. Angew Chem 120:3032–3034
249. Gomez De Arco L, Zhang Y, Schlenker CW et al (2010) Continuous, highly flexible, and transparent graphene films by chemical vapor deposition for organic photovoltaics. ACS Nano 4:2865–2873
250. Yang Z, Ren J, Zhang Z et al (2015) Recent advancement of nanostructured carbon for energy applications. Chem Rev 115:5159–5223
251. Wang Y, Chen X, Zhong Y et al (2009) Large area, continuous, few-layered graphene as anodes in organic photovoltaic devices. Appl Phys Lett 95:063302
252. Hyesung P, Jill AR, Ki Kang K et al (2010) Doped graphene electrodes for organic solar cells. Nanotechnology 21:505204
253. Shi Y, Kim KK, Reina A et al (2010) Work function engineering of graphene electrode via chemical doping. ACS Nano 4:2689–2694
254. Liu Z, Li J, Sun Z-H et al (2012) The application of highly doped single-layer graphene as the top electrodes of semitransparent organic solar cells. ACS Nano 6:810–818
255. Chang J-K, Lin W-H, Taur J-I et al (2015) Graphene anodes and cathodes: tuning the work function of graphene by nearly 2 eV with an aqueous intercalation process. ACS Appl Mater Interfaces 7:17155–17161
256. Wu H, Hu L, Rowell MW et al (2010) Electrospun metal nanofiber webs as high-performance transparent electrode. Nano Lett 10:4242–4248
257. Tvingstedt K, Inganäs O (2007) Electrode grids for ITO free organic photovoltaic devices. Adv Mater 19:2893–2897
258. Lee J-Y, Connor ST, Cui Y et al (2008) Solution-processed metal nanowire mesh transparent electrodes. Nano Lett 8:689–692
259. De S, Higgins TM, Lyons PE et al (2009) Silver nanowire networks as flexible, transparent, conducting films: extremely high DC to optical conductivity ratios. ACS Nano 3:1767–1774
260. Lim J-W, Cho D-Y, Eun K et al (2012) Mechanical integrity of flexible Ag nanowire network electrodes coated on colorless PI substrates for flexible organic solar cells. Sol Energy Mater Sol Cells 105:69–76
261. Han B, Pei K, Huang Y et al (2014) Uniform self-forming metallic network as a high-performance transparent conductive electrode. Adv Mater 26:873–877
262. Guo F, Li N, Radmilovic VV et al (2015) Fully printed organic tandem solar cells using solution-processed silver nanowires and opaque silver as charge collecting electrodes. Energy Environ Sci 8:1690–1697
263. Dennler G, Prall H-JR, Koeppe R et al (2006) Enhanced spectral coverage in tandem organic solar cells. Appl Phys Lett 89:073502
264. Kim JY, Lee K, Coates NE et al (2007) Efficient tandem polymer solar cells fabricated by all-solution processing. Science 317:222–225
265. Dou L, You J, Yang J et al (2012) Tandem polymer solar cells featuring a spectrally matched low-bandgap polymer. Nat Photonics 6:180–185

266. Zhou Y, Fuentes-Hernandez C, Shim JW et al (2012) High performance polymeric charge recombination layer for organic tandem solar cells. Energy Environ Sci 5:9827–9832
267. Tong J, Xiong S, Zhou Y et al (2016) Flexible all-solution-processed all-plastic multijunction solar cells for powering electronic devices. Mater Horiz 452–459
268. Kang H, Kee S, Yu K et al (2014) Simplified tandem polymer solar cells with an ideal self-organized recombination layer. Adv Mater 27:1408–1413
269. You J, Dou L, Yoshimura K et al (2013) A polymer tandem solar cell with 10.6% power conversion efficiency. Nat Commun 4:1446
270. Li W, Furlan A, Hendriks KH et al (2013) Efficient tandem and triple-junction polymer solar cells. J Am Chem Soc 135:5529–5532
271. Bin Mohd Yusoff AR, Kim D, Kim HP et al (2015) A high efficiency solution processed polymer inverted triple-junction solar cell exhibiting a power conversion efficiency of 11.83%. Energy Environ Sci 8:303–316
272. Zimmermann B, Schleiermacher HF, Niggemann M et al (2011) ITO-free flexible inverted organic solar cell modules with high fill factor prepared by slot die coating. Sol Energy Mater Sol Cells 95:1587–1589
273. Krebs FC, Spanggard H, Kjær T et al (2007) Large area plastic solar cell modules. Mater Sci Eng, B 138:106–111
274. Lungenschmied C, Dennler G, Neugebauer H et al (2007) Flexible, long-lived, large-area, organic solar cells. Sol Energy Mater Sol Cells 91:379–384
275. Zimmermann B, Glatthaar M, Niggemann M et al (2007) ITO-free wrap through organic solar cells-A module concept for cost-efficient reel-to-reel production. Sol Energy Mater Sol Cells 91:374–378
276. Eggenhuisen TM, Galagan Y, Coenen EWC et al (2015) Digital fabrication of organic solar cells by Inkjet printing using non-halogenated solvents. Sol Energy Mater Sol Cells 134:364–372
277. Kaduwal D, Schleiermacher H-F, Schulz-Gericke J et al (2015) Layout flexibility for sheet-to-sheet produced flexible ITO-free organic solar modules with organic functional layers slot die coated under ambient atmospheric conditions. Sol Energy Mater Sol Cells 136:200–205
278. Hanisch J, Wahl T, Wessendorf CD et al (2016) Efficient polymer tandem modules and solar cells by doctor blading. J Mater Chem A 4:4771–4775
279. Ye F, Chen Z, Zhao X et al (2015) "Layer-filter threshold" technique for near-infrared laser ablation in organic semiconductor device processing. Adv Funct Mater 25:4453–4461
280. Lucera L, Machui F, Kubis P et al (2016) Highly efficient, large area, roll coated flexible and rigid OPV modules with geometric fill factors up to 98.5% processed with commercially available materials. Energy Environ Sci 9:89–94
281. Spyropoulos GD, Kubis P, Li N et al (2014) Flexible organic tandem solar modules with 6% efficiency: combining roll-to-roll compatible processing with high geometric fill factors. Energy Environ Sci 7:3284–3290
282. Guo F, Kubis P, Przybilla T et al (2015) Nanowire interconnects for printed large-area semitransparent organic photovoltaic modules. Adv Energy Mater 5:1401779
283. Lee J, Back H, Kong J et al (2013) Seamless polymer solar cell module architecture built upon self-aligned alternating interfacial layers. Energy Environ Sci 6:1152–1157
284. Kang H, Hong S, Back H et al (2014) A new architecture for printable photovoltaics overcoming conventional module limits. Adv Mater 26:1602–1606
285. Hong S, Kang H, Kim G et al (2016) A series connection architecture for large-area organic photovoltaic modules with a 7.5% module efficiency. Nat Commun 7:10279

Chapter 3
Liquid Dye-Sensitized Solar Cells

Haining Tian and Lars Kloo

Abstract Dye-sensitized solar cells represent a type of device which converts solar energy into electricity based on molecular components. This is an attractive alternative for solar energy conversion because such devices can be made as low-cost, colorful, and transparent solar cell in contrast to the traditional semiconductor-based solar cells. In this chapter, we will give an overview of all molecule-based components in this kind of solar cell and also comment on its working principle, the dye design, the dye arrangement, the electrolyte composition, as well as the counter electrode materials. The standard types of dye-sensitized solar cells are regarded as n-type, but at the end, p-type and tandem dye-sensitized solar cells will also be introduced.

Keywords Dye-sensitized solar cells · Liquid · Dye · Redox couple · Counter electrode · p-Type · Tandem solar cell

3.1 Introduction

The development of dye-sensitized solar cells (DSSCs), or photoelectrochemical solar cells, clearly emerged from the study of photoinduced reactions at semiconductor electrodes in electrochemical cells. Much fundamental work was reported by Gerischer, Memming, and others during the 1950s and 1960s [1–3]. It was early realized that the systems studied potentially could be used for harvesting solar energy; and then, primarily by splitting of the classical solvent, water. Those ideas

H. Tian (✉)
Department of Chemistry—Ångström Laboratory, Physical Chemistry, Uppsala University, 751 20 Uppsala, Sweden
e-mail: haining.tian@kemi.uu.se

L. Kloo (✉)
School of Chemical Science and Engineering, Applied Physical Chemistry, KTH Royal Institute of Technology, Teknikringen 30, 100 44 Stockholm, Sweden
e-mail: larsa@kth.se

H. Tian et al. (eds.), *Molecular Devices for Solar Energy Conversion and Storage*, Green Chemistry and Sustainable Technology,
https://doi.org/10.1007/978-981-10-5924-7_3

can be traced back to the exciting work by Moser and others more than 100 years earlier, where dye sensitization was the main concept introduced and exploited for more than 100 years in photography before the charge-coupled device (CCD) chip revolutionized the instant and digital photography [4]. It is an interesting phenomenon that the semiconductor-based CCD devices out-competed dye-sensitized photography, whereas dye-sensitized solar cells very well may out-compete semiconductor-based solar cells in the future.

Going back to the early days of investigation of photoinduced redox reactions, molecules at the semiconductor electrodes were studied including dye molecules, such as erythrosine and related compounds. However, the main focus was on the photoelectrode rather than a fully operational and regenerative device. It was not until Grätzel and coworkers started to systematically study the DSSCs in the middle of the 1980s that the DSSC emerged as a photelectrochemical solar cell, where the development of the liquid electrolyte was an essential step. The seminal nature paper by Grätzel and O'Regan in 1991 is often taken as the start of the DSSC era, where the introduction of a TiO_2-based nanostructured electrode was the keep advancement to boost conversion efficiencies from about 1% to a daunting 7–8% [5]. Indeed, this was a major achievement in one step promoting the DSSC from an academic research interest in a future solar cell technology. In retrospect, this major improvement builds on the systematic work performed in the EPFL lab the preceding years and maybe some papers published around 1985 could equally well be regarded as the real start of the DSSC era [6].

The initial DSSC devices relying on electron-conducting (n-type) substrates made from wide band gap semiconductor materials are typically referred to as 'n-type' DSSCs. As will be described in more detail below, the key step in light harvesting in such devices is the injection of energy-rich electrons from a sensitizing dye into the wide band gap electrode material, where the next step is electron transport in the conduction band (CB) of this n-type semiconductor; therefrom the denotation 'n-type' DSSC (n-DSSC). The inverted configuration of solar cell using a p-type semiconductor, such as NiO, instead of an n-type semiconductor is therefore recognized as 'p-type' DSSC (p-DSSC). The combination of both types of photoelectrodes is a strategy to fabricate the tandem DSSCs.

3.2 Liquid n-Type Dye-Sensitized Solar Cell

Titanium oxide (TiO_2) is used as n-type semiconductor in a classic dye-sensitized solar cell (DSSC) [5, 7]. The band gap energy of anatase TiO_2 is 3.2 eV, which gives a threshold of its ground-state UV–vis absorption spectrum at 385 nm. Other large band gap semiconductors, such as ZnO and SnO_2, have also been used as alternatives to TiO_2 in DSSCs [8, 9]. Dye sensitization of large band gap semiconductor is an effective strategy to extend the light response into the visible light region and even into the near infrared (IR) region. By sintering the mesoporous semiconductor material on a conducting substrate, preferably a transparent substrate

with a thin also transparent conductive metal oxide layer, such as fluorine-doped tin oxide (FTO) glass and subsequently sensitizing it by photosensitizer (dye), a photoanode has been fabricated. Besides of the photoanode, also an electrolyte and a counter electrode (CE) are needed to assemble the sandwich structure of the electrochemical device, the DSSC. Figure 3.1 shows a schematic drawing of the configuration of a DSSC. The electrolyte consists of redox couple (R/R^+), additives, and suitable liquid mediator (organic solvent, ionic liquid, etc.). Alternative CE materials to the ubiquitous platinized FTO have been well investigated, including metal sulfide/oxide/nitride materials and organic polymers (see Chap. 4).

Figure 3.2 shows the working principle described by several charge transfer and transport processes in the DSSC. Upon light illumination, the dye molecule (S) absorbed on the semiconductor surface is transferred to the excited state (S*) (2), which gives it the driving force to inject the energy-rich electron into the CB of the semiconductor (2), forming the dye oxidized state (S^+). The reduction of the oxidized dye is mediated by the reductant in the electrolyte to regenerate the dye allowing further light absorption (3); simultaneously, the injected electron in the semiconductor diffuses to the conducting layer of the glass substrate, such as FTO glass [10] (4). The electron can then be extracted to the external circuit and when drained of it energy led to the CE, reducing the oxidized species in redox couple at the electrode surface (5). Apart from the relaxation of the excited state of the dye (6), there are two further electron recombination loss processes significantly influencing the obtained efficiency of a DSSC, namely the recombination of the injected electron with either the oxidized dye (7) or with the oxidant in the electrolyte (8).

The energy levels of the excited state ($E_{S*/S+}$) and the oxidized ground state ($E_{S/S+}$) of a dye, as estimated through oxidation/reduction potentials, are two important parameters influencing the performance of the DSSC as a device. $E_{S/S+}$ is commonly estimated from the first oxidation potential measured by cyclic voltammetry (CV) of the dye dissolved in a suitable solvent. $E_{S*/S+}$ can be obtained by Eq. 3.1 combining spectroscopic and electrochemical data:

$$E_{S*/S+} = E_{S/S+} - \Delta E_{0-0}. \tag{3.1}$$

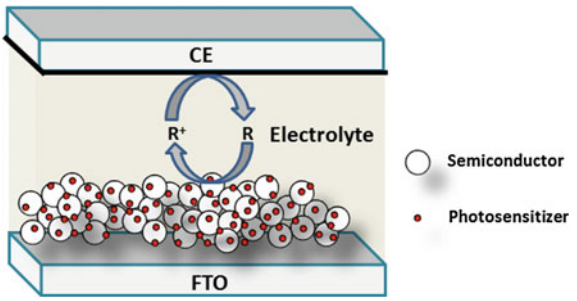

Fig. 3.1 Schematic drawing of the DSSC components

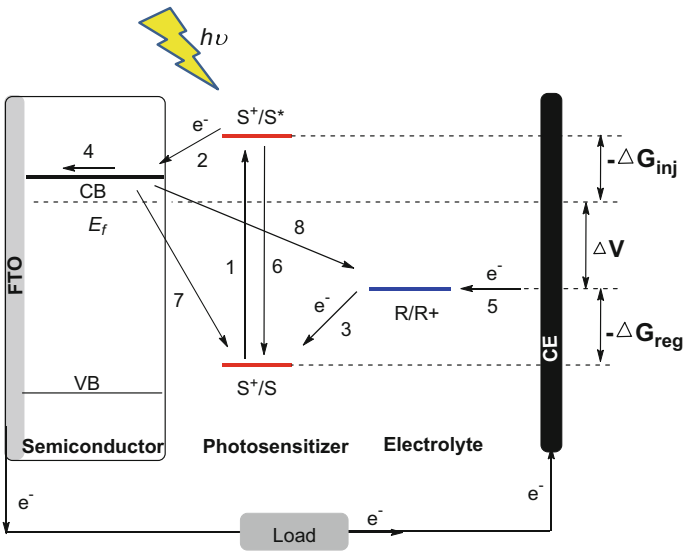

Fig. 3.2 The central charge transfer processes in a DSSC

The energy levels $E_{S/S+}$ and $E_{S*/S+}$ are typically taken as approximate values of the Highest Occupied Molecular Orbital (HOMO) level and the Lowest Unoccupied Molecular Orbital (LUMO) level in many publications. Sometimes, the energy level of the reduced state ($E_{S/S-}$) of the dye is regarded as an estimate of the dye LUMO level. Since the electron injection represents the energy-generating and most central process in an n-type DSSC, the $E_{S/S+}$ and $E_{S*/S+}$ are most commonly used. $E_{S/S-}$ and the corresponding energy level of the excited state ($E_{S*/S-}$) of the dye are commonly used in p-type DSSCs, where hole injection is regarded as the central process. $E_{S*/S-}$ can be obtained from Eq. 3.2:

$$E_{S*/S-} = E_{S/S-} + \Delta E_{0-0}. \tag{3.2}$$

The energy of the 0–0 transition (ΔE_{0-0}) is the difference between the HOMO and the LUMO, which can be experimentally estimated from the intersection of the absorption and photoluminescence (PL) spectra *or* simply taken as the onset of PL *or* offset of absorption.

For a solar cell, the overall light-to-electricity conversion efficiency, η, can be derived by the short-circuit photocurrent (J_{SC}), the open-circuit voltage (V_{OC}), the fill factor (FF) compared to the intensity of the incident light (P_{in}), shown in Eq. 3.3:

$$\eta = \frac{J_{SC} \times V_{OC} \times FF}{P_{in}}, \tag{3.3}$$

in which FF is defined by the ratio of the maximum power output (P_{max}) from the solar cell per unit area divided by J_{SC} and V_{OC} (Eq. 3.4). The value of FF is between 0 and less than 1:

$$FF = \frac{P_{max}}{J_{SC} \times V_{OC}}. \tag{3.4}$$

J_{SC} is determined by the value and spectrum of incident photon-to-current conversion efficiency (IPCE) of the solar cell. V_{oc} in a DSSC is given by the difference between the quasi-Fermi Level of the semiconductor ($E_{f,n}$) and the energy level (redox potential) of the electrolyte redox couple ($E_{R/R+}$).

The external quantum efficiency (EQE), also known as IPCE in DSSCs, offers information about how efficiently a device converts photons to electrical current at a given wavelength. This parameter can be calculated by dividing the $J_{SC}(\lambda)$ of solar cell generated in the external circuit under monochromatic irradiation by the photon flux (Φ_λ) that reaches to the solar cell. It can be expressed like in Eq. 3.5:

$$\text{IPCE } (\lambda) = \frac{J_{SC}(\lambda)}{e\Phi_\lambda} = 1240 \frac{J_{SC}(\lambda)(\text{A cm}^{-2})}{\lambda(\text{nm})P_{in}(\lambda)(\text{W cm}^{-2})}, \tag{3.5}$$

where e is the elementary charge and P_{in} is the power of incident light.

The IPCE can also be expressed as Eq. 3.6, which allows partition into the main primary processes that contribute to the overall efficiency of a solar cell:

$$\text{IPCE } (\lambda) = \eta_A \eta_{inj} \eta_{reg} \eta_{col}, \tag{3.6}$$

where η_A is the light harvesting efficiency at a given wavelength. It can be written as $(1–10^{-A})$, in which A is the absorbance at a particular wavelength. Sometimes, the absorbance is related to the oscillator strength obtained from theoretical calculations. η_{inj} is the electron injection efficiency, η_{reg} is the dye regeneration efficiency, and η_{col} is the charge collection efficiency of electrons from the semiconductor to the external circuit mainly influenced by electron recombination irreversible trapping and electron transport in the semiconductor.

In a DSSC, the absorbance of solar cell, A, is determined by the dye-sensitized semiconductor electrode. In principle, a dye-sensitized semiconductor electrode with large enough internal surface area or/and sufficiently thick layer can increase the A to infinity. Disregarding the influence of light management, thus reflection, transmission, and scattering, it is possible to generate a η_A close to 100%. However, a large internal surface area and a thick layer at the same time increase the probability of recombination processes generating an electron transport issue in the electrode, thus decreasing η_{col}. An optimal electrode configuration is therefore required. With a suitable semiconductor electrode, tuning the properties of the dye is an effective strategy to improve the η_A. A certain amount of dye with a high molar extinction coefficient adsorbed to the electrode is always favorable for light

harvesting at a given absorption region. Ideally, such a dye with a broad absorption spectrum will generate a broad IPCE spectrum contributing to a high J_{SC}.

From the kinetic aspect, the electron injection efficiency, η_{inj}, depends on the rate constant of electron injection (k_{inj}) and the excited state relaxation rate (k_{s*}) of the dye, as shown in Eq. 3.7:

$$\eta_{inj} = \frac{k_{inj}}{k_{inj} + k_{s*}}. \tag{3.7}$$

Apparently, an optimal η_{inj} can be achieved by accelerating electron injection process and prolonging the lifetime of the dye's excited state as much as possible. η_{inj} can be extracted from photoluminescence quenching and/or transient absorption (TA) experiments. Experimentally, the electron injection from excited dye to the semiconductor CB takes place at the femtosecond (fs) to picosecond (ps) timescale [11–13]. The electron injection is affected by the free energy difference ($-\Delta G_{inj}$) between $E_{S*/S+}$ and the energy of the CB edge (E_{CB}) of the semiconductor. With respect to a certain semiconductor, the $-\Delta G_{inj}$ is solely determined by dye. Katoh and coworkers have systematically studied and analyzed the relationship between η_{inj} and $-\Delta G_{inj}$ in DSSCs, concluding that a driving force corresponding to a $-\Delta G_{inj} > 0.2$ eV is required in order to generate a high enough η_{inj} [14]. The relaxation rate of the excited state of the dye is greatly influenced by the molecular structure and structural changes induced by the excitation process. An efficient dye usually shows a lifetime of its excited state at the nanosecond (ns) scale, which is rather common for most excited singlet states [15].

The dye regeneration efficiency, η_{reg}, is used to evaluate the probability of the dye to become regenerated by reduction of the oxidized dye by the redox-active electrolyte in competition with the electron recombination loss reaction between the oxidized dye and the injected electrons in the semiconductor (Eq. 3.8):

$$\eta_{reg} = \frac{k_{reg}}{k_{reg} + k_{rec}}, \tag{3.8}$$

where k_{reg} and k_{rec} are the rate constants of regeneration and recombination, respectively. The dye regeneration is related to the free energy difference ($-\Delta G_{reg}$) between $E_{S/S+}$ and $E_{R/R+}$. TA spectroscopy (Chap. 11) is an effective technique to evaluate the η_{reg}. For the commonly used iodide/triiodide (I^-/I_3^-) redox system, the dye regeneration takes place in the microsecond domain and a $-\Delta G_{reg}$ value of 0.75 eV is required to obtain close to 100% in η_{reg} for Ru-based complex dyes in DSSCs [16]. Spiccia and coworkers systematically investigated the dye regeneration between a series of organic dyes and ferrocene derivatives, revealing that a $-\Delta G_{reg} > 0.3$ eV is sufficient to render close to an ideal η_{reg} [17]. A similar conclusion from cobalt redox couples was reported by Hagfeldt and coworkers [18].

Charge collection efficiency, η_{col}, is widely expressed by the followed equation (Eq. 3.9):

$$\eta_{\mathrm{col}} = 1 - \frac{\tau_{tr}}{\tau_{rec}}, \tag{3.9}$$

where τ_{tr} is the electron transport time and τ_{rec} is the charge recombination time, which can be obtained by Intensity-Modulated Photovoltage Spectroscopy (IMVS) and Intensity-Modulated Photocurrent Spectroscopy (IMPS), respectively. Also, Impedance Spectroscopy can be also used to extract η_{col} by extracting the recombination resistance (R_{rec}) and transport resistant (R_{tr}). As mentioned above, the thickness and material of electrode and also the photosensitizer can determine η_{col}, since they influence the τ_{tr} (R_{tr}) and τ_{rec} (R_{rec}). On the other hand, the mass/charge transport limitation in the electrolytes can also influence η_{col} by affecting τ_{rec} (R_{rec}).

From the aforementioned working principle, we can conclude that every component in DSSCs plays a crucial role in the electron transfer and transport processes, which is directly responsible for the obtainable efficiency of the device.

3.2.1 Dyes

3.2.1.1 Molecular Photosensitizers

Molecular photosensitizers, normally referred to as the "Dye", represent a crucial component that affects the light harvesting and electron generation in a DSSC. An ideal dye should have the following properties:

(i) Broad light absorption spectrum capturing photons in as large as possible spectral range or the solar spectrum.
(ii) Suitable LUMO and HOMO energy levels to allow both efficient electron injection and dye regeneration.
(iii) Excellent blocking effect to suppress the rates of the unwanted electron recombination loss processes at the semiconductor/dye/electrolyte interface.
(iv) Good stability for long-term use.
(v) Facile and environmentally friendly synthetic route with high yields allowing straightforward up-scaling.

Ruthenium (Ru) bipyridine complexes, initially introduced by Grätzel and coworkers [19], have been successful dyes for DSSCs. Figure 3.3 shows a selection of representative Ru-based dyes. Carboxylic acid functionalized bipyridine ligands are used as the electron acceptor and as anchoring group to attach the dye to the semiconductor surface. The thiocyanate ligands are beneficial for broadening the absorption spectra due to its electron-donating ability. In principle, this kind of dye has two metal-to-ligand charge transfer (MLCT) bands, mainly located in the visible light region. Also, the long-lived excited state (20–60 ns) typically observed for the Ru-based dyes [19, 20] allows an efficient electron injection. N3 is the prototype Ru-based dye. With this dye as a platform, many analogous dyes have been developed. The most classical one is N719, in which two of carboxylic acid

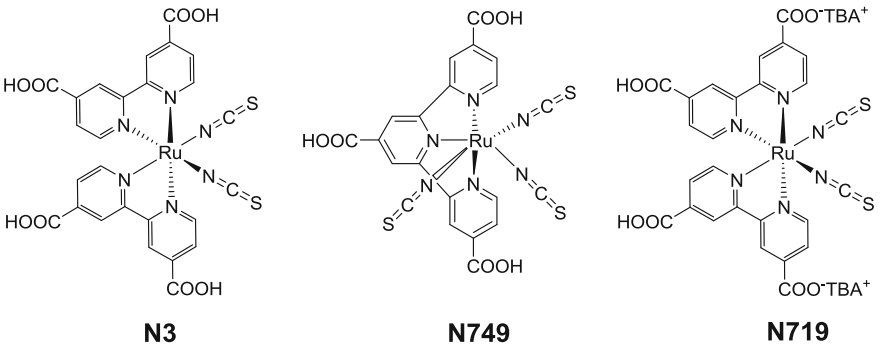

Fig. 3.3 Three representative Ru complex dyes used in DSSCs

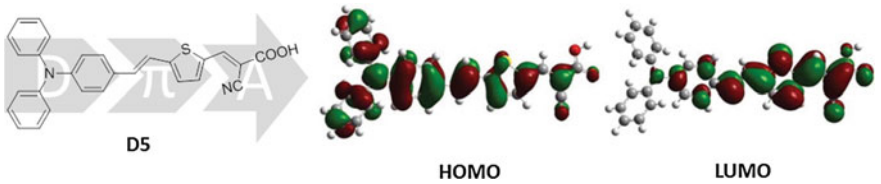

Fig. 3.4 Molecular structure and calculated spatial distribution of the HOMO and LUMO of the dye D5. The pictures of HOMO and LUMO are reproduced from Ref. [22] by permission of The Royal Society of Chemistry

groups of N3 have been deprotonated and replaced by tetrabutylammonium counter ions. The deprotonation of the carboxylic acid groups in N719 affected both redox potential and excited state lifetime improving the device efficiency to 10% [19]. By replacing the bipyridine with a tris-pyridine ligand, the resulting N749 dye shows an extended light harvesting region into near IR and even IR region, which renders an impressive J_{SC} of ca. 20 mA cm^{-2} and an efficiency of 10% [21]. Molecular engineering by modifying the ligands of the metal complex allows effective tuning of the dye energy levels, as well as absorption spectrum.

Organic dyes were developed alongside the investigation of Ru-based dyes. The main driving force toward organic dyes is that they can be made more environmentally friendly and at much lower cost. The band gap of organic dye can easily be tuned. The general design of an organic dye involves three parts: electron donor (D), conjugated linker (π), and electron acceptor (A). Light absorption pumps the electron from the donor unit to the acceptor unit via the π linker. The electrons of the dye HOMO and LUMO are expected to be located in donor part and acceptor part, respectively. The anchoring group is usually placed on the electron acceptor group, where the electrons can easily inject into the semiconductor CB.

Figure 3.4 shows an efficient and classic D-π-A-type organic dye (named D5) based on a simple synthetic route and invented by Sun and coworkers in 2006 [22] to be used primarily in DSSCs. In this dye, the triphenylamine unit acts as the D, the thiophene vinyl linker is employed as the π unit and the cyanoacrylic acid

constitutes A, as well as serving as the anchoring group. The molecule is characterized by an efficient intramolecular charge transfer from the donor part to the acceptor part via the HOMO to LUMO transition. DSSCs based on the D5 dye showed a promising efficiency of 6%. By tuning the different moieties, the physical properties of descendant dyes can be significantly changed.

As shown in Fig. 3.5, using the same linker and acceptor groups, the dyes TH208 and C1–1 based on the stronger electron-donating units, phenoxazine, and tetrahydroquinoline instead of triphenylamine, respectively, can be designed and synthesized. These dyes show more negative HOMO energies than the D5 dye [23]. Moreover, the structure of the donor moiety influences the dye behavior on the semiconductor surface. In the C1–1 dye, the tetrahydroquinoline unit has a more flat structure than the other dye donor groups, resulting in more serious dye aggregation than observed for the others. In TH208, the phenoxazine unit typical has a butterfly structure, which in principle unfavorable should prevent dye aggregation on the surface; moreover, the butyl chain in this dye is expected to suppressing aggregation as well. Dye aggregation will be further discussed in Sect. 3.2.1.4. Chenodeoxycholic acid (CDCA) is a conventional aggregation inhibitor used as co-adsorbent to inhibit dye aggregation on the semiconductor surface. The working principle of CDCA is based on its large molecular structure, and therefore cosensitization using CDCA is expected to prevent direct dye contact each other minimizing dye aggregation. Normally, evaluation of device performance before and after the addition of CDCA to a dye bath is an efficient method to detect if dye aggregation takes place. Table 3.1 shows the photovoltaic performance of the devices based on TH208, D5, and C1–1 with and without CDCA. TH208 dye shows the smallest improvement of photocurrent in the presence of CDCA, which probably can be attributed to its donor butterfly structure and alkyl chain as mentioned above.

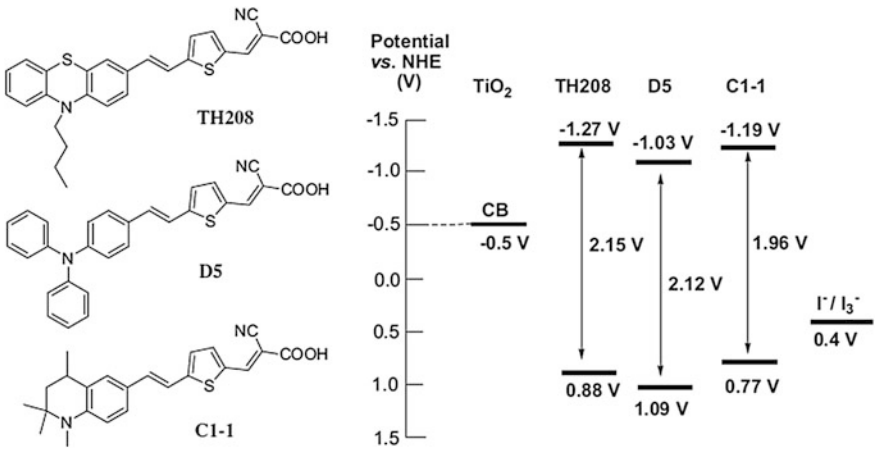

Fig. 3.5 Molecular structures and energy levels of the related organic dyes TH208, D5, and C1–1 only differing in the donor groups. Reprinted from Ref. [23], Copyright 2010, with permission from Elsevier

Table 3.1 Photovoltaic properties of DSSCs based on TH208, D5, and C1–1 with/without CDCA as co-adsorbent

Dye	J_{SC} (mA cm^{-2})	V_{OC} (mV)	ff	η (%)
TH208[a]	13.4	685	0.70	6.4
TH208[b]	12.2	638	0.72	5.6
D5[a]	12.4	665	0.73	6.0
D5[b]	10.7	615	0.73	4.8
C1–1[a]	14.5	661	0.68	6.4
C1–1[b]	10.4	583	0.72	4.4

Irritation: AM 1.5G (100 mW cm^{-2}); Working area: 0.159 cm^2; Electrolyte: 0.6 M 1,2-dimethyl-3-n-propylimidazolium iodide (DMPII)/0.06 M LiI/0.04 M I_2/0.4 M 4-tert-butylpyridine (TBP) in acetonitrile

[a]Dye bath: CH_2Cl_2 solution (2×10^{-4} M) with saturated CDCA, 2 h

[b]Dye bath: CH_2Cl_2 solution (2×10^{-4} M), 2 h

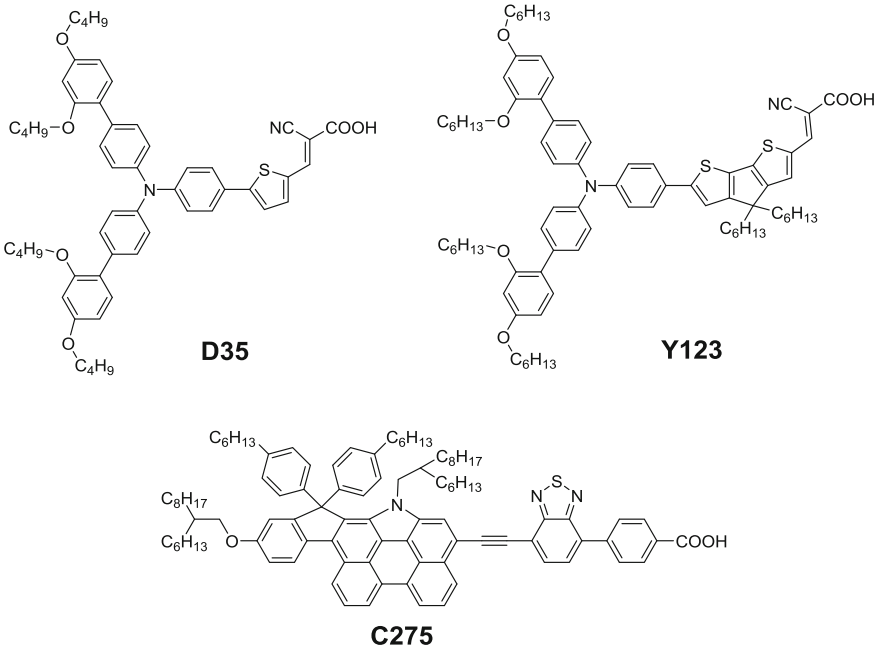

Fig. 3.6 Molecular structures of the organic D35, Y123, and C275 dyes

For a set electron donor unit and linker moiety, the introduction of bulky alkyl chains is a well-known and effective method to minimize aggregation in otherwise unfavorable dyes [24]. Moreover, a bulky alkyl chain structure also is presumed to block the redox couple to reach the electrode surface, therefore retarding the recombination rates between injected electrons and the oxidized species in the electrolyte. Figure 3.6 shows three representative alkyl chain decorated organic dyes showing good performance in dye-sensitized solar cells. The D35 dye is a

good example of such a dye, which has displayed 7% DSSC efficiency in combination with cobalt(III/II) tris(2,2′-bipyridine) ($Co^{3+/2+}$ $(bpy)_3$) as redox couple [25]. Besides of inhibition of dye aggregation, the butoxyl units also show an efficient blocking effect with respect to $Co^{3+/2+}$ $(bpy)_3$ as compared to non-bulky analogues. Also, the replacement of the vinyl thiophene unit in D5 with the single thiophene unit in D35 has some good effects. Although the vinyl unit extends the π- conjugated system of the dye to narrow E_{0-0} red-shifting the dye light absorption, it can easily be isomerized and subsequently influence the device performance [26–28]. Therefore, a rigid π-conjugated system is required to formulate a stable dye. Thiophene or fused thiophene units have become more popular linkers in organic dyes, due to their rigid conjugated systems. By using alkyl chain functionalized cyclopentadithiophene (CPDT), instead of a single thiophene as linker, the Y123 dye shows enhanced photovoltaic performance with a DSSC efficiency of 10% [29]. After systematic structural optimization, the perylene-based dye C275 is the best performing organic DSSC dye so far, rendering a device efficiency up to 12.5% in a single dye-based DSSC [30].

Changing the chromophore is always a method to seek new molecular photosensitizer for DSSCs. Porphyrin dyes have also been intensely investigated for DSSCs, since porphyrin is a good chromophore platform to develop panchromatic dyes. The porphyrin chromophore intrinsically displays light absorption in the Soret and Q bands [31]. However, the light absorption in the Q band is very weak, and there is also lack of light absorption between the Soret and Q bands. Along with the emergence of D-π-A structures, the introduction of electron donor and π-conjugated linker groups in porphyrin-based dyes also became a significant strategy to improve the light absorption ability. Also, the introduction of long alkyl chains greatly increased the solubility making purification more convenient also solving the serious aggregation issue observed for the simpler porphyrin dyes. The performance of porphyrin-based devices has therefore rapidly improved. Figure 3.7 shows two highly efficient porphyrin dyes for DSSCs. SM315-based devices have shown an impressive efficiency of 13% in the combination with cobalt-based redox couples [31].

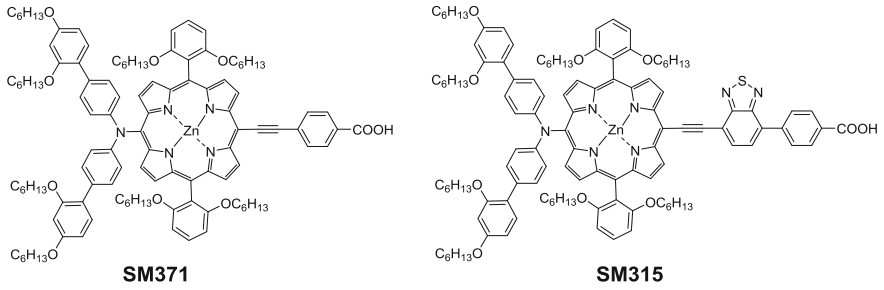

Fig. 3.7 Molecular structures of the SM371 and SM315 porphyrin dyes

3.2.1.2 Cosensitization

In most cases, an individual dye shows a limited light absorption. Cosensitization of the semiconductor using more than one dye may be an effective strategy to improve the light harvesting exploiting complementary light absorption or electron injection between different dyes [32–35].

A representative example is cosensitization of the porphyrin dye YD2-o-C8 (Fig. 3.8) and the organic dye Y123 (Fig. 3.6) [32]. As mentioned above, the porphyrin dye has an absorption gap between the Soret and Q bands, normally leading to a concave shape in the resulting IPCE spectrum from 480 to 630 nm. The Y123 dye has a complementary IPCE response located in that exact region. The cosensitization of YD2-o-C8 and Y123 in DSSCs fills this gap, giving a prominent J_{SC} of 17.7 mA cm^{-2} and a device efficiency of 12.3% under 99.5 mW cm^{-2} light illumination.

Another strategy for improving electron injection from the dye to the TiO_2 CB is cosensitization of the two organic dyes ADEKA-1 and LEG4 (see Fig. 3.9a) [34]. These two dyes have similar absorption spectra, but distinctly different HOMO and LUMO levels. Using cosensitization, the IPCE values are greatly improved, as shown in Fig. 3.9b. From Density Functional Theory (DFT) calculations, the electrons in the ADEKA-1 LUMO are mainly located on the phenyl unit. However, the electrons in the excited LEG4 are mainly concentrated on the cyanoacrylic acid unit. Theoretically, LEG4 should show more efficient electron injection than ADEKA-1. From experimental data, we know that the LUMO level of LEG4 is more positive than that of ASEKA-1. The electron transfer from excited ASEKA-1 to LEG4 is therefore thermodynamically feasible, which is further proved by complete emission quenching of ASEKA-1 in the presence of LEG4 when adsorbed on Al_2O_3. As a consequence, the enhanced IPCE of cosensitization should be caused by efficient electron transfer from ADEKA-1 to LEG4; the latter then efficiently injects the electrons into the TiO_2 CB. The proposed electron transfer processes in ADEKA-1 and LEG4 are shown in Fig. 3.9c. The co-sensitized system

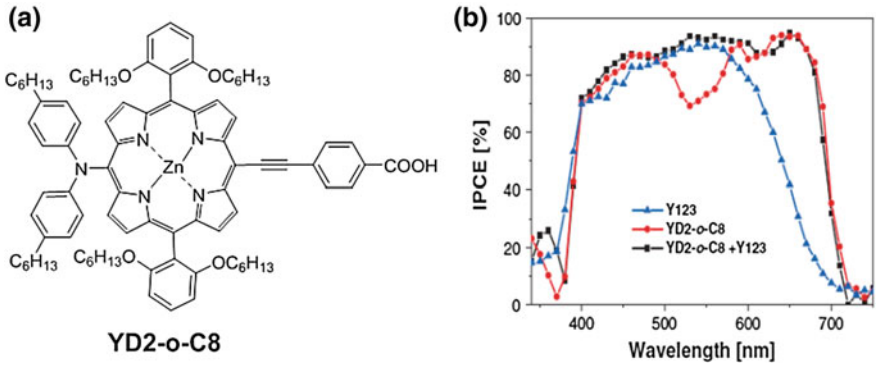

Fig. 3.8 YD2-o-C8 dye (**a**) and the IPCE spectra (**b**) of devices based on different mono- and co-sensitized systems. From [32]. Reprinted with permission from AAAS

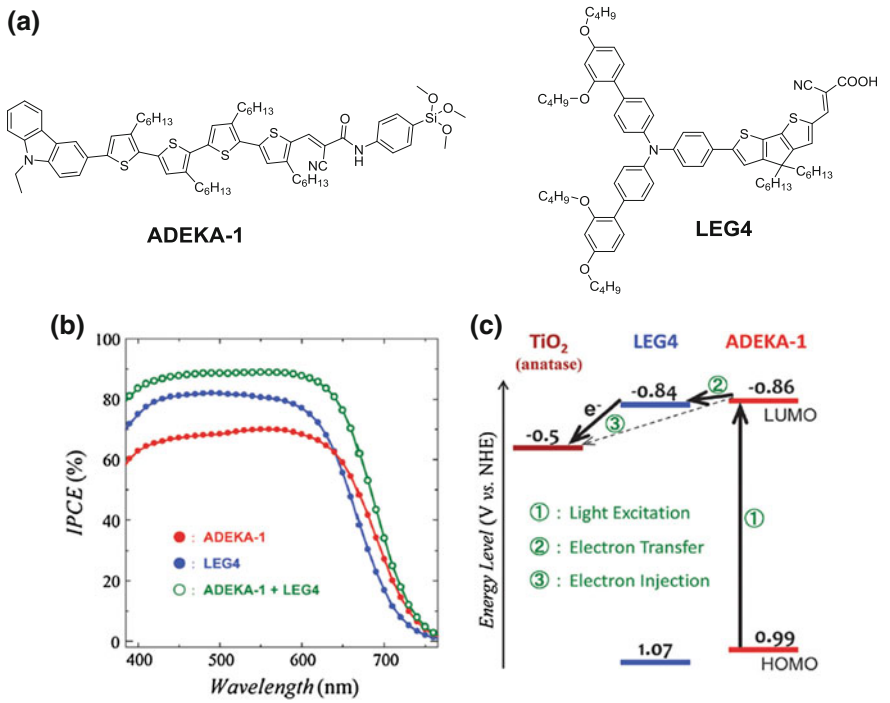

Fig. 3.9 Molecular structures of the ADEKA-1 and LEG4 dyes (**a**), IPCE spectra of DSSCs based on mono- and co-sensitized devices (**b**) and electron transfer processes in LEG4 and ADEKA-1 co-sensitized DSSCs. Reproduced from Ref. [34] by permission of the Royal Society of Chemistry

gave an efficiency of 14% under 100 mW cm^{-2} light illumination. Therefore, cosensitization is a wise represention of a successful method to boost DSSC efficiency by the strategic arrangement of different dyes on the electrode surface.

3.2.1.3 Anchoring Groups

The anchoring group plays a crucial role with respect to the stability of a dye bound to the semiconductor. The carboxylic acid is the most common anchoring group used in dyes for DSSCs, irrespective of type, and it easily forms ester bond with metal oxide materials, such as TiO_2, ZnO, and NiO. Normally, if the anchoring group itself is not a strong electron acceptor, it should be complemented by an electron acceptor group in order to make electron injection efficient. The cyanoacrylic acid is a classic group integrating a strong electron acceptor, the cyano unit, and an anchoring group, the carboxylic acid. This combination has been broadly applied in dyes due to its strong electron accepting ability in combination with the synthetic simplicity by which it is linked with essentially any dye. Although there are some reports showing that the dyes containing the cyanoacrylic

acid unit can show good stability in DSSCs [36–39], degradation and isomerization studies related to the acrylic acid indicate that it may not be the ideal anchoring group candidate for long-term stability [28, 40]. Many alternative anchoring groups have therefore been developed [41].

Pyridyl represents one of the anchoring group alternatives. Harima and coworkers compared a dye with a carboxylic acid (NI1, Fig. 3.10a) and a dye with a pyridyl unit (NI3, Fig. 3.10b) in DSSCs [42]. From the FTIR data in Fig. 3.10c, the NI3-sensitized TiO_2 shows a new peak around 1615 cm^{-1}, implying the formation of coordination bond between the nitrogen atom in the pyridine unit and the Lewis acidic sites on the TiO_2 surface; this may lead to efficient electron injection. Subsequently, Tian, Sun, and coworkers further developed this kind of acceptor, using the dipicolinic acid instead of the simple pyridine, in the organic dye PD2, shown in Fig. 3.11a. Also, in order to harvest photons as efficiently as possible, the structure of PD2 was designed with a larger conjugated linker than that in Nl3. The presence of two carboxylic acid units makes the nitrogen atom less important as anchoring site to the TiO_2 surface according to DFT calculations. However, the two carboxylic acid units allow the PD2 dye bind strongly to TiO_2, making PD2-based DSSCs promisingly stable in combination with cobalt electrolytes. Moreover, PD2 dye-based DSSCs show quite broad IPCE spectra (up to 900 nm, Fig. 3.11b) in comparison to the analogous cyanoacrylic acid dye LEG1-based devices. The addition of TBP to the electrolyte changed this effect, and it was suggested that the protonation of pyridine on TiO_2 in the TBP-free electrolyte is responsible for the broadening the light harvesting region of PD2 dye.

Another acceptor worth mentioning is 2-(1,1-dicyanomethylene)rhodanine (DCRD) without a carboxylic acid group in its framework [43]. The dye RD-II containing the DCRD group also has a tautomer, as shown in Fig. 3.12, in which a hydroxyl unit is present. The strong electron-withdrawing ability of DCRD is

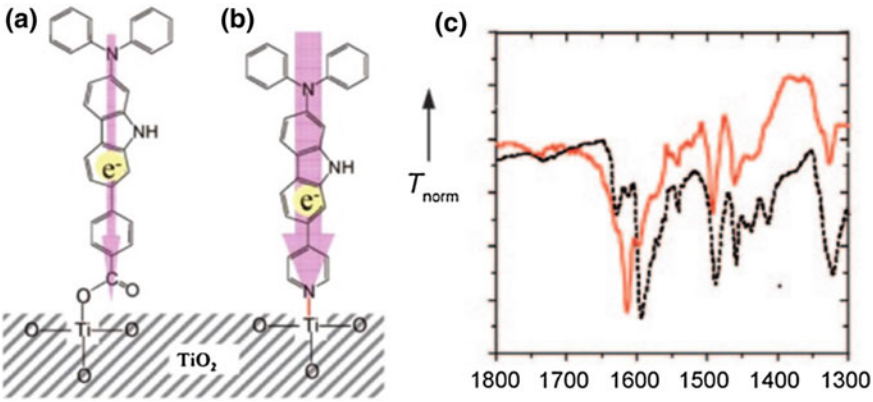

Fig. 3.10 **a** A carboxylic acid-based dye NI1 and **b** the analogous pyridyl-based dye NI3 adsorbed on a TiO_2 surface and **c** the IR spectra of NI3 before (*black line*) and after (*red line*) sensitizing the TiO_2. Reproduced from Ref. [42] by permission of John Wiley & Sons Ltd.

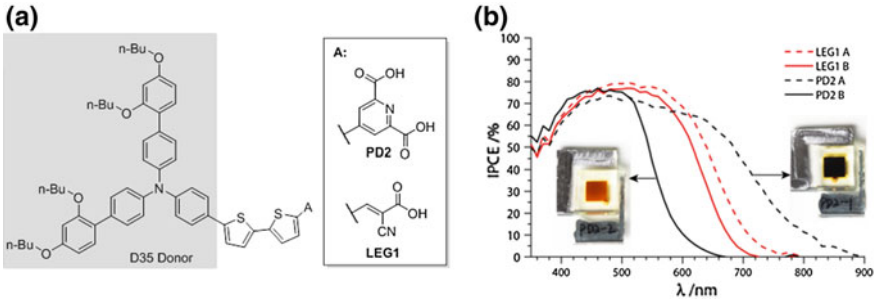

Fig. 3.11 Molecular structures of the PD2 and LEG 1 dyes (**a**) and IPCE spectra of DSSCs based on the dyes in combination with different electrolytes (*A* without TBP; *B* with TBP). Reproduced from Ref. [43] by permission of The Royal Society of Chemistry

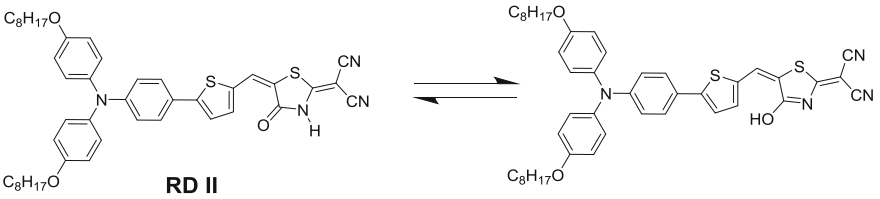

Fig. 3.12 Molecular structure of the RD-II dye and its resonance form. Reproduced from Ref. [43] by permission of John Wiley & Sons Ltd.

beneficial for broad light absorption. The ring hydroxyl group and nitrogen atom provide a novel coordination mode with TiO_2, enhancing the stability of the dye. The RD-II has shown remarkable stability under long-term (1000 h) light illumination.

3.2.1.4 Dye Arrangement on Surface

The dye arrangement strongly influences the electron injection and recombination, as well as regeneration, thus determining the final performance of the DSSCs. Reviewing the DSSC literature, we note that remarkably little is known about the dye organization of the semiconductor surface. Dye load has been investigated, as well as suggestions for binding modes, but much less is known about how dyes are arranged on the semiconductor surface; the degree of aggregation, adsorption into monolayers or multilayers, if the dye molecules are standing like in most cartoons on dye adsorption, or rather lying down, etc. These are central scientific questions are raised along with the development of DSSCs; not the least considering the design of new dye systems.

There are many studies on the capacity of the mesoporous electrode to adsorb dye molecules, and estimates of the so-called dye load have led to the hypothesis of

a self-assembled monolayer (SAM) being formed on the metal oxide surface. Detailed studies based on indirect methods (such as the classical liquid dye-depletion method) clearly indicate a behavior well described by a Langmuir isotherm [44, 45]. This has been taken as an indirect evidence for the formation of a SAM. However, the formal basis for a Langmuir behavior only presumes a finite number of adsorption sites and a single type of adsorbent. Thus, an experimentally obtained Langmuir isotherm is not a sufficient evidence for the formation of a SAM, and in spite of this the SAM is presumed in essentially every DSSC article published; not the least in spectroscopic studies of adsorbed dye molecules.

Direct studies of dye adsorption of the more commonly used metal-organic dyes N719 and Z907 onto TiO_2 surfaces of various morphologies, including the classical mesoporous DSSC electrode surfaces, based on adsorption from solution mimicking the methods typically used when making DSSC devices, show a completely different adsorption pattern. The adsorption isotherms are fully Langmuiric, but the direct measurements show the formation of multilayer islands of aggregated dye molecules. This phenomenon appears already at low coverage levels and persists up to a formal 100% coverage level according to the Langmuir model. Furthermore, at the maximum coverage level it is clear that a substantial fraction of the substrate surface is not covered by dye molecules [46, 47]. This has some implications for the formulation of the DSSC electrolyte, viz., the necessity for addition of Lewis bases blocking recombination losses from the exposed metal oxide surface. With this in mind, spectroscopic and theoretical studies presuming a SAM should probably be regarded with some reservation, although it is likely that even if the dye molecule are adsorbed in aggregated clusters, the application of a SAM model may provide useful insights. The postulated effects of coadsorbents, such as CDCA and various organic phosphor-oxide compounds, in reducing aggregation of dye molecules still need to be investigated by direct methods.

One may ponder if multilayer formation on the mesoporous semiconductor surface is a general phenomenon, also exhibited by organic and porphyrin-type of dyes. Very recent direct studies on a simple organic dye, L0, slightly modified by replacing the acceptor –CN group by a bromine atom (denoted L0Br) to enhance X-ray contrast and spectroscopic signals surprisingly indicate that the D-π-A-type of organic dyes in fact appears to adsorb in a SAM-like fashion and with a close to 100% surface coverage [48].

Andersson and coworkers adopted the depth profiling technique neutral impact collision ion scattering spectroscopy (NICISS) to study the N719 arrangement on TiO_2. From the study (see Fig. 3.13), it showed that the dye layer on TiO_2 surface is inhomogeneous in thickness. There should be a mixture of monolayer and multilayers.

O'Shea and coworkers studied the geometric and chemical interaction of zinc protoporphyrin on rutile TiO_2 by synchrotron radiation based X-ray absorption and photoemission techniques. Their results suggest that zinc protoporphyrin forms monolayers on TiO_2 [49]. Using high-resolution atomic force microscopy (AFM), quartz microbalance with dissipation technique (QCMD), and molecular dynamics (MD) simulations, Harms and coworkers got insight into the arrangement of an

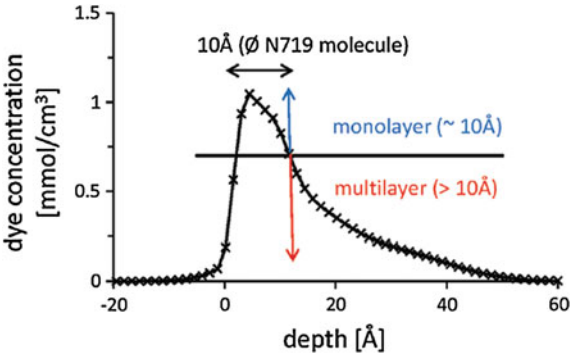

Fig. 3.13 NICISS data showing the formation of N719 multilayers on TiO_2. Reproduced from Ref. [46] by permission of The Royal Society of Chemistry

amphiphilic Ru dye, Z907, on electrode, also suggesting the formation of dye monolayer [50]. These results are in contrast with previous AFM and NICISS studied both showing a pronounced tendency by Z907 to form bilayers in dye islands [47, 51].

The comparison of absorption spectra of a dye in solution and on film is a conventional way to judge if there is aggregation and what type aggregation it displays; since J aggregation shows bathochromic shift and H aggregation a hypochromic shift, as compared to the monomeric dye [52]. However, the deprotonation of dyes on the semiconductor surface can also make the dye absorption shift to the blue; therefore, it is quite difficult to distinguish whether the hypochromic shift observed for a dye adsorbed on an electrode surface is caused by H aggregation or deprotonation. It is also notable that similar spectral effects originating from a Stark shift from the electrical field generated by the injected electrons and cations in the electrolyte can be observed [53, 54]

Dye structure, such as organic/inorganic, with/without long alkyl chains and with/without a large π-conjugated system, is definitely a vital factor influencing dye adsorption on an electrode surface. X-ray photoelectron spectroscopy (XPS) is a powerful and sensitive technique to extract more details of different dyes on a surface. The detailed application of photoelectron spectroscopy in DSSCs to investigate the dye arrangement on surfaces will be discussed in Chap. 12.

3.2.2 Electrolyte

As briefly described in the introductory parts, the initial studies of photoelectrochemical cells were very focused on the photoelectrodes and the electrolyte can be described as a simple necessity to connect a counter electrode, thus essentially only consisting of a solvent and a supporting dissolved salt (electrolyte). As the DSSC emerged as a fully operational device, also the electrolyte complexity has increased where different additives have been observed to give an overall improvement of performance, reproducibility, or stability. Below, a short overview of the

background of the most commonly used electrolyte compositions used today is given through a semi-historical journey. Many electrolyte components have been covered in recent reviews [7, 55, 56], and this overview therefore aims at the conceptual improvements of the electrolyte composition evolving over time, rather than a comprehensive review of everything published in the area.

3.2.2.1 Solvents

In the early days of photoelectrochemistry water was the natural choice as electrolyte solvent, not the least since photodecomposition of water itself into oxygen and in particular hydrogen was of central interest [57]. Since then, many solvents have been investigated and these were recently reviewed. Water as solvent has obtained renewed interest, since the solvent represents the ultimate 'green' solvent [58–60].

In the process of DSSC development, it was realized that dye regeneration by the presence of a suitable reducing agent in the electrolyte was a necessary requirement. Reducing agents investigated involved organic radicals, as well as charged metal complexes and other charged species. The charged redox species appeared most useful, and thus the ability to dissolve suitable salts became a central prerequisite for the solvent to be used. This emphasizes that polar solvents, protic or non-protic, are preferred. Water, of course, belongs to this group, as well as alcohols and related solvents. Water as a solvent for DSSC electrolytes typically is made slightly acidic in order to facilitate dye adsorption on the photoelectrode. In spite of this, protons, in particular under illumination, tend to induce unwanted side reactions leading to dye desorption and decomposition [61, 62]. In general, acid–base chemistry in DSSCs is difficult to control and certainly influences both performance and long-term stability. This has made protic solvents less popular in DSSCs, at least when aiming for sustainable performance. The general advice tends to be to minimize the presence of water in DSSC electrolytes, although a recent study has highlighted that up to as much as 40% water in a water/acetonitrile mixture does not detrimentally affect the performance [63]. Also, the use of water-soluble redox systems has re-introduced water as an interesting 'green' alternative as DSSC solvent, although long-term stability still remains an issue. Possibly, the choice of suitable combinations of materials will open for stable water-based DSSCs in the future. In this context, it should also be mentioned that the most commonly used nanomaterial in the mesoporous photoelectrodes is anatase TiO_2. Many alternatives have been investigated, but few can compete with TiO_2 and one of the main reasons is that many electronically favorable alternative materials tend to be far too soluble in the presence of a polar solvent and simply dissolve; the metal oxides are essentially salts more or less prone to dissolution in polar solvents.

Matching of energy levels between the different components and materials used in a DSSC is essential for high performance. One preferable parameter to vary is the redox potential of the redox system to properly match in particular the HOMO level of the dye. This will allow efficient dye regeneration under working conditions,

as mentioned in previous sections. One way to massage the redox potential (E_{redox}) of a particular redox system is to vary the concentrations and relative amounts of the reduced and oxidized components in a specific redox system (exploiting the predictions of the Nernst equation, as shown in Eq. 3.10):

$$E_{\text{redox}} = E^0 - \frac{RT}{nF} ln \frac{a_{red}}{a_{ox}}, \tag{3.10}$$

where E^0 is the standard electrode potential, R is the ideal gas constant, T is the absolute temperature, n is the number of electrons involved in the redox reaction, F is the Faraday constant, and a_i represents the activities (of the reduced and oxidized forms of the redox system used). At room temperature and for a one-electron system, a change of a factor of 10 in the ratio between the reduced and oxidized components of the redox system would correspond to a change in redox potential of about 60 mV. This, for practical reasons, allows the adjustment of the redox potential to about 100 mV up or down. Of course, and as will be discussed in more detail below, in a DSSC device other materials or unwanted side reactions may limit the available compositional degrees of freedom. Another option to modify the electrochemical properties of a redox system is to select a redox system with organic subcomponents, which are available for chemical modification through the introduction of electron-withdrawing or electron-donating functional groups. Synthetic design will then become the essential tool. This strategy has successfully been used for both purely organic and metal-organic complex redox systems [18, 64]. An increasing organic character of the redox system components limits the number of suitable solvents, and polar, non-protic, organic solvents stand out as the best candidates as DSSC electrolyte solvents. Highly useful solvents classes involve organic nitriles and carbonates. This selection of solvents is further emphasized by the use of electrolyte additives that either enhances performance or long-term stability, or both, of the DSSC devices. Such additives tend to be both inorganic salts and organic molecules. The polar organic solvents are typically good solvents for dissolution of the two very different types of solutes.

In addition to the above-described desired properties of a good DSSC electrolyte solvent, also other properties must be considered, such as melting point (it should not freeze under operating conditions), viscosity (high viscosity will influence mobilities and thus transport properties), light absorption (possibly shadowing the sensitizing dye), selective solubility (it preferably should not dissolve the metal oxide substrate, the device sealing material and other materials), high boiling point (to minimize evaporation problems), etc. [56]. As we will note, these combined requirements represent a formidable challenge and the optimal DSSC solvent still remains to be identified.

A serious concern since the early days of DSSC devices, accentuated by the potential application for small- or large-scale energy production, is the evaporation of the typically rather volatile organic solvents that offer the best device performance. One strategy has been to turn to solvents of the same chemical family but with considerably higher boiling points; from acetonitrile to methoxy propionitrile,

or from ethylene/propylene carbonate to γ-butyrolactone and similar changes. Typically, long-term stability in such devices is considerably enhanced, which can be linked to the slower evaporation rates representing a lower stress to the sealing materials, which always tend to be too permeable. On the other hand, the price paid is in lower performance, typically 1–2% lower conversion efficiencies at higher illumination levels. The weaker performance can be directly linked to the viscosity in the high-boiling solvents, which in turn leads lower ion mobility and charge/mass-transport problems. The bottleneck of limited charge transport is less problematic at lower light levels, and thus the combination of viscous, high-boiling solvents and quite stable DSSCs appear attractive for indoor applications. In particular, in the cases, high boiling points also are associated with high melting points.

Another strategy to minimize the evaporation problems of the volatile organic solvents is to add a gelling component. Many different materials have been used for this purpose, and the overall effect appears very similar to the previously described one. Gelation typically forms some sort of micrometer-scale networks, and one would expect that such a, from a molecular perspective, large structure would not affect transport properties in the solvent/gel system. However, it is clear that the necessary chemical compatibility between the gel-forming materials and the solvent molecules and/or electrolyte solutes retards charge/mass transport with an overall device performance loss in the range of one or a few percent [7]. Though, the stability issue appears to be properly addressed.

Following the rationales given above, ionic liquids emerged as interesting alternatives as electrolyte solvents in DSSCs. Figure 3.14 shows some typical ionic liquid used in solar cells. The main advantages on paper are their typically exceptionally low vapor pressure in combination with very high chemical and electrochemical stability, as well as they being intrinsic electrolytes. Ionic liquids can be described as low-melting salts, where the cation or anion typically is organic; most commonly the cation. This opens for synthetic design, and the number of available ionic liquids designed for particular purposes is huge. Ionic liquids were tested early in the DSSC history, but more suitable ionic liquids have been more systematically studied later. In this context, it should be emphasized that 'ionic liquids' denotes a single type of solvent no more than the denotation 'organic solvents'; the versatility is vast and has been successfully exploited in many areas through systematic substitutions in and of the ionic components. As solvents, mainly because of their combined ionic and organic character, the ionic liquids are

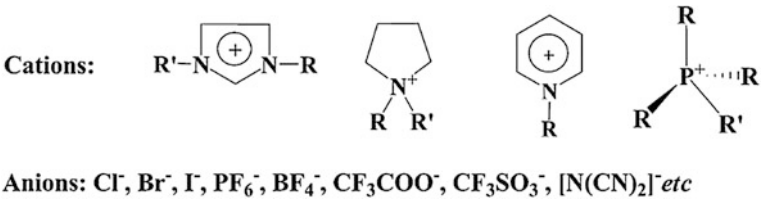

Fig. 3.14 Typical ionic liquid compositions. Reproduced from Ref. [65] by permission of The Royal Society of Chemistry

typically good solvents for both salts and organic substances, the most clear exception being highly fluorinated ionic liquids. Ionic liquids have been used to make quite stable DSSCs, but the main drawback of ionic liquids is the high viscosity. Even so-called low-viscous ionic liquids are by the standards of molecular solvents quite viscous. This directly affects solute mobilities with the same consequences as discussed above for high-boiling molecular solvents [65]. Recent approaches to mitigate this problem involve deep-eutectic ionic liquids and mixtures with organic solvents [66, 67]. Both strategies look promising but although both offer less mass-transport problems they also re-introduce 'old' sources of potential problems associated with acid–base reactions and solvent evaporation. Recent efforts also involve the use of liquid-crystalline electrolytes in combination with ionic liquids to enhance ion mobility through directed charge transport. Such cells also show good performance at high temperatures [68–70].

3.2.2.2 Redox Couples

In the process of formulating working DSSCs, it was early realized that the addition of a suitable reducing agent to the electrolyte would enhance the efficiency through reduction/regeneration of the sensitizing dye used. It is clear from literature that a search period involved many different reducing agents, ranging from organic radicals to metal-organic complexes, and where the halides, in particular iodide and bromide, stood out as attractive alternatives. Under operation, when the overall regenerative process is in operation a steady-state will emerge, where the oxidized counterpart of the added reducing agent will form as a natural consequence of device operation. It was soon realized that there were clear advantages of adding also the oxidized component to the electrolyte, since it allows both better stability and control of the redox potential of the system as a whole. However, typically the oxidized form of a redox system is added at lower concentrations than the reduced form, since a high concentration of the former tends to enhance recombination losses in the DSSC and there is a crossing point, where higher concentrations lead to worse performance. In relation to the discussion about solvents and the use of more viscous solvents in the DSSC devices, the lower ion mobility in such media can obviously be counteracted by increasing the redox system concentrations and in line with the above observation lower photovoltage as a consequence of more severe recombination losses is the typical penalty paid. In the seminal 1991 DSSC paper, the redox system I^-/I_3^- was employed and it became the reference system to match new alternative and survived in that role essentially 20 years [5]. In spite of the fact that the I^-/I_3^- system shows several less optimal properties, such as light absorption, relatively low photovoltages (lower than expected when only looking at redox potentials of the I^-/I_3^- system) and significant chemical and photochemical reactivity, it brings together also a combination of the DSSC essential properties when it comes to high conversion efficiency, and less so when it comes to long-term stability. The main advantages involve low recombination losses and efficient charge transport in liquid electrolytes. The I^-/I_3^- system can be regarded as a

2-electron redox system, and, as will be discussed more in detail below, this has both good and bad effects with respect to DSSC performance. The less than optimal properties have triggered a search for alternative redox systems, and those efforts have been recently reviewed. Some of the main steps in development will be discussed below. For references consult Ref. [55], although the order of redox systems in that review is different from the chronological one.

A logical strategy in the search for alternative redox systems to the I^-/I_3^- one was to investigate very similar halide- and pseudohalide systems. Thus, a selection of systems based on for instance Br^-/Br_3^-, $SCN^-/(SCN)_3^-$ and variations thereof including interhalogen systems have been reported. None of these outperform the standard I^-/I_3^- system; mainly because of less well-matched redox potentials with respect to the best performing sensitizing dyes or because of chemical instability. Interesting analogous 2-electron systems can be found in sulfur chemistry, viz., the S^{2-}/S_x^{2-} systems, where the polysulfide species not always are fully characterized. The redox potential of such systems has been observed to be best suited for quantum-dot-sensitized solar cells analogous to the DSSC. The study of organic analogues, involving the 2-electron transition between a thiolate anion and a disulfide species, has allowed more efficient application in DSSCs. However, although scientifically interesting none has been shown to be better than the standard I^-/I_3^- system. A report by Boschloo and Hagfeldt showing the inherent weakness of the I^-/I_3^- system in particular, and the 2-electron systems in general, triggered a renewed search for efficient 1-electron systems [71]. The main message of their report was that the 2-electron process in fact consists of two 1-electron processes, where it is the total oxidation from I_3^- to I^- that determines the photovoltage and thus inevitably causes a loss of up to 0.5 V (Fig. 3.15). More recent attempts to mitigate this problem have been to use tandem systems showing some progress [72].

In parallel to the investigation of 2-electron systems, also metal-complex-based, 1-electron systems were studied. Metal-organic iron systems are known for fast redox reactions and both hexacyanoferrate- and ferrocenium-based electrolyte systems gave working DSSCs. Overall conversion efficiencies were typically low, and albeit efficient in sensitizer regeneration they were equally prone to accept the

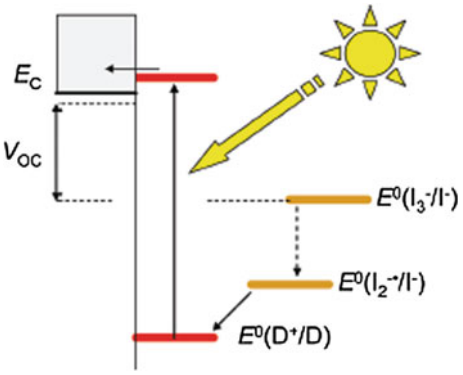

Fig. 3.15 The 0.5 V loss in I^-/I_3^- redox systems. Reprinted with the permission from Ref. [73]. Copyright 2009 American Chemical Society

injected, energy-rich electrons from the photoelectrode causing severe recombination losses. The use of metal-organic systems opens for chemical modification of the ligands of the metal complexes studied. The groups of Grätzel and Bignozzi most successfully applied this to cobalt complexes, where bulky side groups were added to the ligands to retard the unwanted recombination reactions, see Fig. 3.16. The strategy was partly successful, since recombination losses could be reduced. However, a DSSC represents a complex system of multi-interdependent processes and the already diffusively sluggish cobalt complexes became even less mobile giving low overall conversion efficiencies at reasonable illumination levels. This caused a temporary halt to the progress in 1-electron systems.

In 2011, the use of 1-electron systems obtained a boost in both performance and research interest. Since the previous studies 10 years earlier, organic sensitizers of D-π-A-type had emerged as highly competitive dye systems, and they also opened for a straightforward modification of dye design. The Hagfeldt and Sun groups revived the idea of introducing bulky side chains to retard recombination from the photoelectrode to the oxidized components of a Co-based redox system, but now by including the bulky side chains in the dye rather than in the metal complex ligands [25]. This had the desired effect on the recombination losses and at the same time less serious effects on charge transport limitations. The main advantage of the new 1-electron systems is a high DSSC photovoltage of about 1 V. A simple estimate shows that this in principle, with reasonable photocurrents and fill factors, should be able to generate DSSCs with 15–18% conversion efficiencies. The new strategy involving porphyrin dyes and/or cosensitization has shown 14% efficient DSSCs [74, 75], but there are still challenges that have to be met in order to improve also the photocurrents and fill factors. Nevertheless, the combination of a bulky dye and a metal-organic, 1-electron redox system pushed the standard so far, the I^-/I_3^- redox system, to second place.

The best performing DSSCs based on 1-electron systems involve metal-organic complexes of the Co^{II}/Co^{III} system. The main problems of the cobalt complexes involve slow diffusion and the risk of decomposition through ligand exchange;

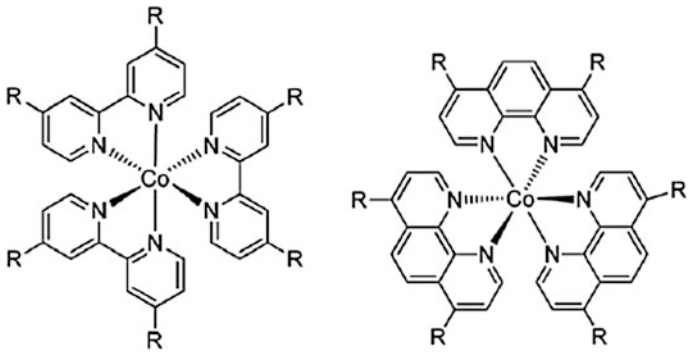

Fig. 3.16 Examples of cobalt(II/III) complexes whose redox properties can be modified using different substituents, R

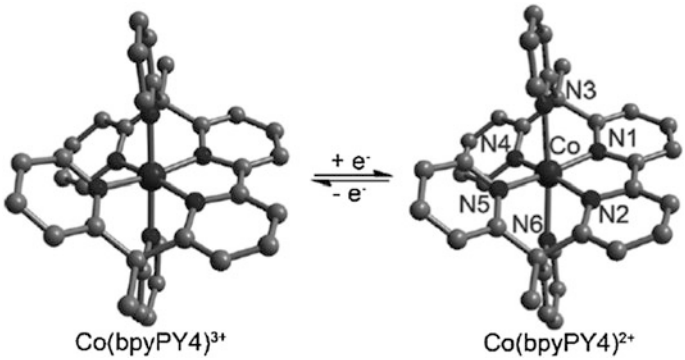

Fig. 3.17 The hexadentate ligand reported by the Bach and Long groups. Reproduced from Ref. [77] by permission of John Wiley & Sons Ltd.

the latter not the least in the presence of different electrolyte additives (see Fig. 3.17). The former problem concerns cell performance and the latter cell stability. Bach and Long showed that the exchange of the typically used bidentate ligands for 5- or 6-dentate ones appear to reduce ligand-exchange problems, although the transport problems remain [76, 77]. Different strategies have been employed to improve the mobilities of the cobalt complexes, such as addition of polymers promoting ion-pair dissociation and the inclusion of tandem redox pairs [78–80]. These strategies have only partially solved the transport problem.

It is likely that most redox systems based on metal complexes will display transport problems in liquids electrolytes, unless self-exchange can be exploited. Self-exchange reactions were shown to have significant effect on the transport properties in organic hydroquinone-based systems, and looking for metal complex systems with similar properties quickly identified Cu^{I}/Cu^{II} as an interesting alternative [81]. The main advantage of such systems is that diffusion problems are partly decoupled by the relay effect of self-exchange reactions in the electrolyte. Peng and coworkers showed promising results based on a substitute Cu(I/II) phenantroline system [82]. More recent and promising studies involve with close to 10% conversion efficiencies [83]. It is clear that the transport problems of the Co-based systems have been mitigated, but the very labile Cu-based systems pose some questions regarding long-term stability in the light of ligand-exchange effects [83, 84]. Nevertheless, to every challenge there is a solution and the current limbo of the liquid solar cells will be resolved when a system is identified that minimizes negative effects and enhances positive ones.

3.2.2.3 Additives

In the ambition to optimize DSSC performance, various additives to the electrolyte have been investigated. Typically, good effects are determined by effects on overall PV performance and they are interpreted in terms of a hypothesis on the molecular

level. In general, the DSSC research field is in desperate need for in situ/in operando techniques; it can offer information at a molecular level, and thus help to identify the exact molecular effects of the additives rendering better device performance. Today, such insights are lacking and the effects observed and postulated reasons must be categorized as phenomenological [85].

Different types of additives have been used. Most of them are based on intrinsic chemistry knowledge and expected effects. For instance, fundamental thermodynamics tell that adsorbed sensitizer molecules to some extent must desorb in the presence of the electrolyte (there is no dye present from the start). It is likely that an equilibrium is established between adsorbed and electrolyte dye molecules, and preferably dye desorption should be kept to a minimum in order to not affect the light absorption and electron injection efficiencies. Attempts to add dye molecules do not seem to have mitigated the fundamental problem [86]. Light absorption efficiencies tend to be reduced because of competing for absorption by non-injecting dissolved dye molecules, and furthermore dissolved dye molecules tend to be much more sensitive to light-induced decomposition. Also the addition of excess ligand to either metal-organic dyes or redox systems has been investigated, as well as polymers/nanoparticles to enhance electrolyte ion transport. Typically, the beneficial effects of such additions tend to not be fully met.

Today liquid, and also many solid-state DSSCs, typically contains two standard types of additives. First, a Lewis-base is added, most commonly a nitrogen-donating organic molecule, and most commonly explicitly either tert-butyl pyridine or alkylbenzimidazoles, and salts of polarizable cations. Microscopic studies on tert-butyl pyridine evaporated onto flat TiO_2 surfaces show the nitrogen atoms of the molecule to bind to defects in the surface structure (Fig. 3.18) [87]. This is in coherence with the expected effect of this additive, where a direct interaction with the metal oxide surface is thought to both affect the energy levels (most importantly of the conduction band) of TiO_2 pushing them closer to the vacuum level and to block the metal oxide surface minimizing recombination losses directly to the electrolyte. Both are plausible explanations to the macroscopic effects observed, although nobody really knows. A large number of similar compounds have also been investigated, but none seem to outperform the standard additive mentioned above [88]. In order to further improve the performance of DSSCs,

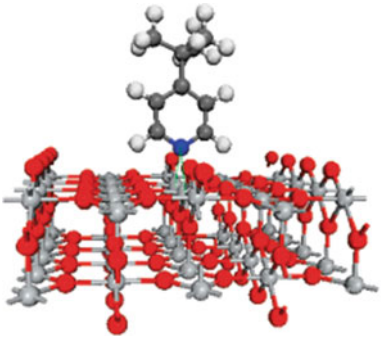

Fig. 3.18 The proposed TiO_2 adsorption mode of tert-butylpyridine. Reprinted with the permission from Ref. [87]. Copyright 2010 American Chemical Society

a molecular understanding of the effects is essential. Without that, we will rely on trial and error.

Another major class of additives, with equal limited molecular understanding, is salts of highly polarizable cations. Most commonly, salts of lithium ions are added, but also salts of magnesium and the organic guanidinium ions show similar macroscopic effects in many DSSC systems. It is clear that the main effects originate from interactions in the TiO_2/dye/electrolyte interface. Just as for the Lewis-base additives the exact nature at a molecular level is unknown. It has been speculated that both interactions with the dye molecules, adsorption on the TiO_2 surface or intercalation into the TiO_2 materials may affect device performance [88]. It seems clear that TiO_2 energy levels are affected, in an opposite way than by Lewis bases, and that the distribution of sub-band gap trap states as well is affected.

Although additives macroscopically offer better performance of the DSSC devices, it is clear that the additives not represent innocent spectators to the chemistry in the electrolytes and that these significantly affect mainly long-term stability. Again, both types of additive can be regarded from an acid–base perspective. Recent studies clearly show that the added Lewis bases certainly affect both dye adsorption and the integrity of the redox systems in solution, both regarding iodine- and metal-oxide-based systems [83, 84, 89, 90]. It is also clear that the presence of lithium ions enhances initial DSSC efficiencies but through dye desorption effects (it is a Lewis acid of nonnegligible strength) contribute to fast device degradation under illumination [90, 91]. One may thus ponder on how necessary the additives really are for long-term good DSSC performance [92]. And, again, the identification of systems combining the short-term and long-term beneficial effects will rely on a molecular understanding of the fundamental chemistry in the DSSC electrolyte and at the electrode interfaces.

3.2.2.4 Counter Electrode

A platinized FTO glass sheet is the most commonly used CE in DSSCs, particularly for I^-/I_3^--based devices, since platinum nanoparticles formed are excellent catalysts for the reduction of triiodide to iodide ions. However, the high cost of Pt is a drawback considering any large-scale production of DSSC CEs. Carbon materials, metal oxides, carbides, sulfides and nitrides have all been investigated as replacements to Pt, and some of these alternatives have shown comparable performance [93]. Molecular polymer CEs, such as poly(3,4-ethylenedioxythiophene) (PEDOT) [94, 95], polypyrrole (PPy) [96, 97] and polyaniline (PANI) [98, 99], have also attracted attention due to their low-cost and large catalytic area. The large surface area of polymer CEs are particularly good for some iodine-free redox couples, such as thiolate/disulfide as well as metal complexes [95]. Swelling and defoliation of the electrode surface after exposure to liquid electrolytes are the main stability issues of such polymer CEs which limit the practical application of this kind of CEs in liquid devices.

3.3 Liquid p-Type Dye-Sensitized Solar Cells

p-type dye-sensitized solar cells (p-DSSCs) can be regarded as an inverted device in comparison to the conventional DSSCs, and such devices were proposed and fabricated for the first time by Lindquist, Hagfeldt, and coworkers in 1999 [100]. A p-DSSC consists of a p-type semiconductor, a photosensitizer, a redox electrolyte, and a CE. NiO is the most popular semiconductor used in this type of system due to its large band gap (3.4 eV), suitable valence band (VB) energy (−0.5 V vs. Normal Hydrogen Electrode, *NHE*) [100], facile preparation, and good stability. Figure 3.19 shows the structure of a p-DSSC, as well as its working principle mirroring that of an n-DSSC. Just as for an n-DSSC, the central process is the light-induced excitation of the photosensitizer, but that instead injects a hole into the VB of the p-type semiconductor and subsequently the reduced dye will reduce the oxidant species in the redox electrolyte in the regeneration step. Thereafter, the reductant species will be oxidized at the CE by the hole provided via the external circuit from the photocathode. The theoretical maximum photovoltage in the p-DSSC is determined by the energy difference (ΔV) between the quasi-Fermi level (of holes) in the p-type semiconductor and the potential (energy level) of the electrolyte redox couple. Of course, also in this type of device there are unwanted charge recombination loss processes, such as the recombination between injected holes and the reduced dye. The development and study of p-DSSCs are primarily aiming to the fabrication of tandem DSSCs (t-DSSCs), where the p-DSSC photoelectrode is combined with a conventional n-DSSC photoelectrode. p-DSSCs have also gained interest in the research on solar fuels.

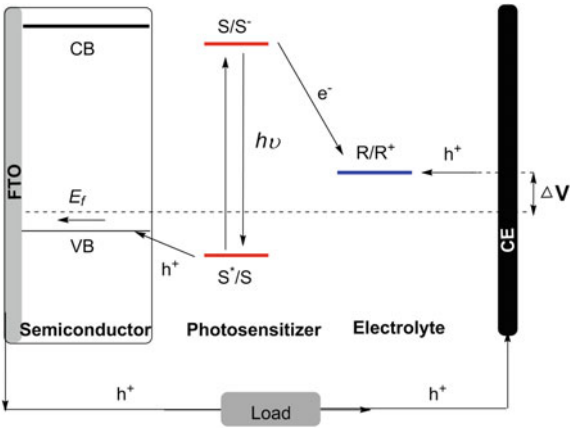

Fig. 3.19 The schematics of the structure and charge transfer/transport processes in a p-DSSC

3.3.1 Dyes

Although the conventional dyes for p-DSSCs still adhere to the D-π-A structure known from n-type devices, the anchoring group is now instead attached to the donor unit in dyes for p-DSSCs. Such an arrangement places the acceptor group far away from the semiconductor surface. Such a design is favorable for hole injection and extension of the charge recombination process between the injected holes and the reduced dyes, since the electron in the reduced dye molecule is expected to be concentrated on the A unit. Figure 3.20 shows the molecular structure of a representative dye for p-DSSCs, P1, and its spatial electron distribution in the HOMO and LUMO.

The efficiency of P1-based p-DSSCs is 0.15% with a J_{SC} of 5.48 mA cm^{-2}, a V_{OC} of 84 mV and an FF of 0.34 [102]. The lifetime of the reduced P1 on the NiO surface is very short, ca. 200 ps, due to the fast recombination of injected holes and the reduced dye molecules. Consequently, this affects the dye regeneration by the redox couple limiting the photocurrent. Using longer linker unit to push the reduced dye electron further away from the NiO surface and thus prolong the lifetime of the reduced dye is a strategy for improving the efficiency. Exploiting this idea, Bach and co-authors developed a series of oligothiophene-based dyes for p-DSSCs and also studied the effect of different linker lengths on the charge separation, as well as on the device performance (Fig. 3.21) [103]. With the increment of the number of thiophene units, 2, 4, and 6, the lifetime of the reduced dye $\tau_1(\tau_2)$ could be increased from 0.17 μs (1.34 μs) to 1.22 μs (12.17 μs), then to 2.54 μs (13.56 μs) extracted from a double exponential model. Along with the increment of charge separation time, the device performance was also improved. The best efficiency of 0.41% with a J_{SC} of 5.35 mA cm^{-2}, a V_{OC} of 218 mV and an FF of 0.35 was obtained from the dye **3** (**PMI-6T-TPA**) containing six thiophene units in the linker part (Fig. 3.21).

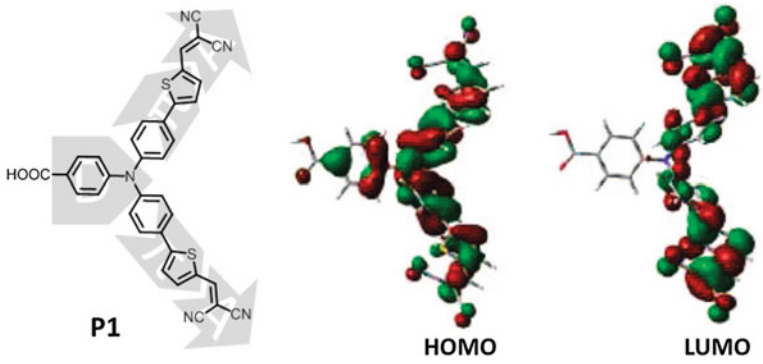

Fig. 3.20 Molecular structure, and the calculated HOMO and LUMO of the P1 dye. HOMO and LUMO pictures are reprinted with the permission from Ref. [101]. Copyright 2010 American Chemical Society

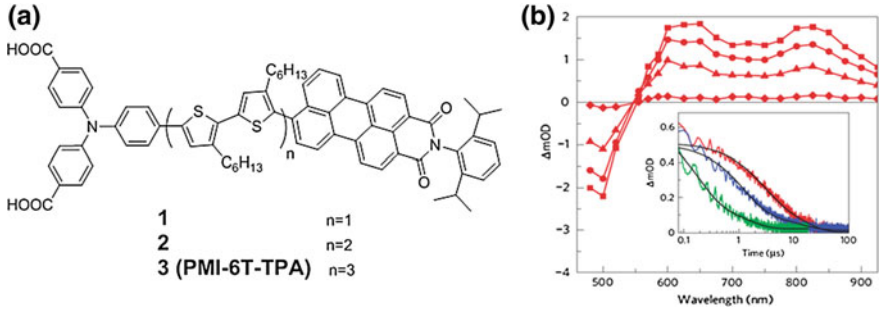

Fig. 3.21 **a** Molecular structures of oligomer thiophene-based dyes, **b** Transient absorption decay signals of NiO films sensitized with 1 (*green*), 2 (*blue*) and 3 (*red*). Observation wavelength: 700 nm, laser intensity 70 μJ cm^{-2} per pulse for 1 and 2 and 35 μJ cm^{-2} for 3. Reproduced by permission from Macmillan Publisher Ltd.: Ref. [103]. Copyright 2009

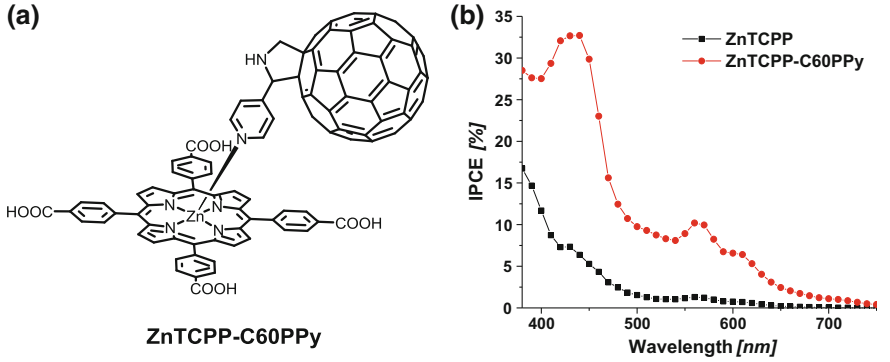

Fig. 3.22 **a** The molecular structure of the ZnTCPP–C60PPy aggregate and **b** IPCE spectra of the p-DSSCs based on ZnTCPP alone and the supramolecular system ZnTCPP–C60PPy. Reproduced by permission from the author of Ref. [104]

Following the successful application of porphyrin dyes in n-DSSCs, porphyrin dyes have also been investigated in p-DSSCs. The initial attempt with the simple porphyrin dye meso-tetra(carboxyphenyl) porphyrin (TCPP) in p-DSSCs offered very performance [100], since the lifetime of the intramolecular charge separation of the porphyrin dye is quite short. This limits the hole injection process. Subsequently, Tian and coworkers used a zinc-coordinated TCPP (ZnTCPP) dye to sensitize NiO and later adopted a pyridine-modified fullerene (C60PPy) to form a supramolecule with ZnTCPP adsorbed to NiO in situ [104]. The supramolecular dye aggregate is shown in Fig. 3.22a. The linked C60PPy acts as a strong electron acceptor and the energy match between the porphyrin dye and the fullerene is appropriate for fast electron transfer and extended charge separation, expected to improve the porphyrin dye regeneration and to suppress the hole recombination loss reaction rates. Furthermore, since the C60PPy is expected to be positioned far away

from the NiO surface, the charge recombination is expected to be suppressed. As a consequence, the supramolecular system ZnTCPP-C60PPy rendered an efficiency of 0.09%. In absence of the fullerene, the single-component ZnTCPP-based device showed an efficiency of 0.02%. The photocurrent is greatly improved from in 0.5 to 1.5 mA cm^{-2} by simply adding C60PPy as an acceptor. As noted in Fig. 3.22b, the IPCE of the ZnTCPP–C60PPy-based devices increase by a factor of 10 in comparison with the p-DSSCs based on ZnTCPP alone. These results suggest that the fullerene should be an ideal acceptor to develop more efficient dyes for p-DSSCs.

Besides these dyes mentioned above, other types of molecular photosensitizers, such as boron-dipyrromethenes (BODIPY) [105], diketopyrrolopyrroles (DPP) [106, 107], carbazoles [108], polymers [109], and Ru/Ir complexes [110–112] have been developed for p-DSSCs. A BODIPY dye has shown the highest photocurrent, 8 mA cm^{-2}, among these dyes in p-DSSCs [105], due to its broad light response region. Also for p-DSSCs, the rational design of dyes is the best strategy to obtain enhanced performance.

3.3.2 Redox Couples

I^-/I_3^- emerged as the conventional redox couple also for p-DSSCs. However, the energy difference between the redox potential of I^-/I_3^- and the pseudo-Fermi level of NiO is very small, ca. 0.1–0.3 V, depending on which kind of NiO material is used. Therefore, the theoretical photovoltage of devices based on the combination of NiO and I^-/I_3^- is less than 0.3 V, which seriously limits the obtainable efficiency of the resulting p-DSSCs. In order to increase the photovoltage, you can either choose a semiconductor with a more positive pseudo-Fermi level than NiO or select a redox couple with more negative redox potential than the I^-/I_3^- system. New inorganic p-type semiconductor materials for p-DSSCs will not be discussed in this chapter. There are several successful examples from changing the redox couple to improve the photovoltage, thus rendering improved efficiencies [104, 113–116]. Figure 3.23 depicts two representative redox couples replacing I^-/I_3^- for high photovoltages in p-DSSC devices.

Tris(1,2-diaminoethane)cobalt(II/III) complexes ($\mathbf{[Co(en)_3]^{2+/3+}}$) [115] and tris (acetylacetonato)iron(III)/(II) complexes ($\mathbf{[Fe(acac)_3]^{0/1-}}$) [116] show redox potentials of −0.025 and −0.20 V versus NHE, respectively. Both systems show more negative potentials than I^-/I_3^- (−0.3 V vs. NHE). Table 3.2 collects the

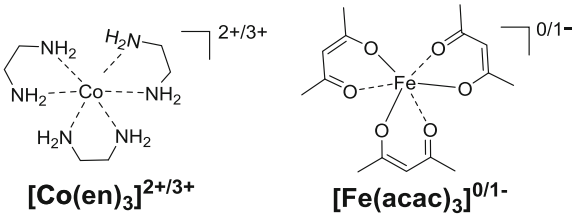

Fig. 3.23 Molecular structures of $[Co(en)_3]^{2+/3+}$ and $[Fe(acac)_3]^{0/1-}$

Table 3.2 Photovoltaic data of **PMI-6T-TPA**-based p-DSSCs with different redox couples

Redox couple	J_{SC} (mA cm^{-2})	V_{OC} (mV)	ff	η (%)
I^-/I_3^-	6.26	243	0.39	0.6
$[Co(en)_3]^{2+/3+}$	4.11	724	0.4	1.2
$[Fe(acac)_3]^{0/1-}$	6.45	765	0.51	2.5

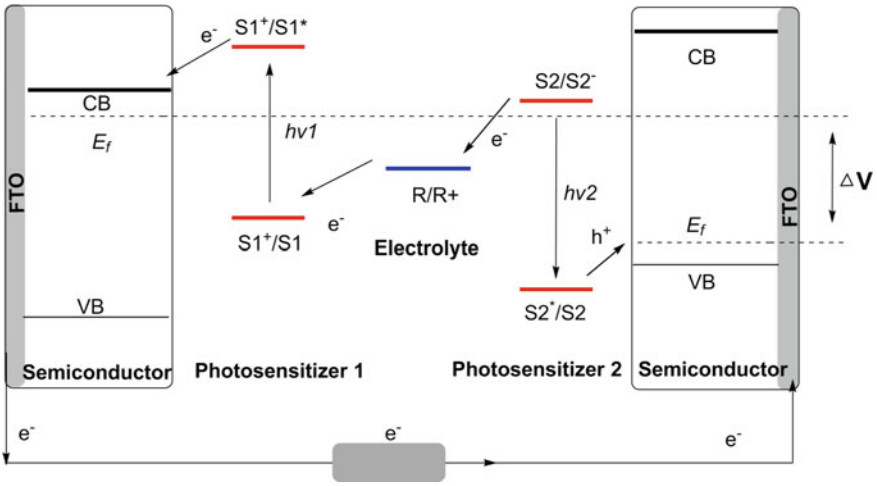

Fig. 3.24 Configuration and working principle of t-DSSCs

photovoltaic parameters of **PMI-6T-TPA** sensitized p-DSSCs based on the redox couples. **$[Fe(acac)_3]^{0/1-}$** and **$[Co(en)_3]^{2+/3+}$**-based devices show impressive V_{OC}'s of 645 mV and 724 mV, respectively. This without scarifying the photocurrent leading to improved efficiencies. Eventually, **$[Fe(acac)_3]^{0/1-}$**-based p-DSSCs render the highest efficiency of 2.5% with a J_{SC} of 7.65 mA cm^{-2}, a V_{OC} of 645 mV, and *an FF* of 0.51. However, both **$[Fe(acac)_3]^{1-}$** and **$[Co(en)_3]^{2+}$** are very sensitive to oxygen making the solar cell fabrication process complicated. The use of electron transport material instead of liquid redox electrolytes will be addressed in Chap. 4.

3.4 p-n Tandem Dye-Sensitized Solar Cells

In order to overcome the so-called Shockley–Queisser limit, setting an efficiency ceiling of 33% for single-junction solar cells, a tandem solar cell (multi-junction) cell would be one way to break through this ceiling. The configuration and working principle of tandem dye-sensitized solar cells (t-DSSCs) is shown in Fig. 3.24.

The ideal t-DSSCs should have at least one dye attached to each photoelectrode and the dyes on the different electrodes should have complementary light absorption characteristics. The photoanode and photocathode are assembled in a sandwich structure and share the same redox electrolyte. The working principle of tandem

Table 3.3 Photovoltaic data of n, p, and p–n tandem DSSCs based on different dyes and redox couples

Redox couple	Type	Dye	J_{SC} (mA cm^{-2})	V_{OC} (mV)	ff	η (%)	Refs.
$Co^{II/III}(dtbpy)_3$	**n**	N719	1.64	660	0.57	0.61	[113]
	p	PINDI	1.66	350	0.34	0.20	
	t	N719/PINDI	0.91	970	0.62	0.55	
I^-/I_3^-	**n**	N719	2.74	905	0.72	1.79	[103]
	p	PMI-6T-TPA	4.64	186	0.35	0.30	
	t	N719/PMI-6T-TPA	2.40	1079	0.74	1.91	
Thiolate/Disulfide	**n**	SQ2	2.60	595	0.64	1.00	[117]
	p	PMI-6T-TPA	5.30	285	0.34	0.51	
	t	SQ2/PMI-6T-TPA	2.50	814	0.65	1.33	

n: n-type; **p**: p-type; **t**: tandem; the illumination of t-DSSCs is from n-type side (photoanode)

solar cells is essentially the sum of conventional n-DSSCs and p-DSSCs. The theoretical photovoltage is in a t-DSSC, and however, is independent of the redox system and is instead determined by the difference between the quasi-Fermi level of (electrons in) the n-type semiconductor substrate and the pseudo-Fermi level of (holes in) the p-type semiconductor substrate. Table 3.3 lists the photovoltaic parameters of several representative t-DSSCs based on different redox couples.

From the working principle, the redox couple ideally should have no effect on the obtained photovoltage. However, the redox couple significantly influences the dye regeneration and charge recombination rates on at both photoelectrodes, and thus indirectly the redox electrolyte will affect the shift of the pseudo-Fermi levels of the semiconductor materials used. An ideal redox couple for t-DSSCs should be good enough in enhancing the dye regeneration and minimizing the charge recombination on both of photoelectrodes. The main challenge with t-DSSCs is current matching, where the tandem cell tends to be controlled by the worst photoelectrode (typically the p-type electrode) rather than the best.

Acknowledgements We greatly thank Dr. Nick Vlachopoulos at École polytechnique fédérale de Lausanne (EPFL) for kindly discussion on DSSCs historical part. We also gratefully acknowledge financial support from The Knut and Alice Wallenberg Foundation and The Swedish Energy Agency.

Appendix—Abbreviations

DSSCs	Dye-sensitized solar cells
n-DSSCs	n-type dye-sensitized solar cells
p-DSSCs	p-type dye-sensitized solar cells
t-DSSCs	Tandem dye-sensitized solar cells

(continued)

(continued)

CCD	Charge-coupled device
CB	Conduction band
IR	Infrared
FTO	Fluorine-doped tin oxide
CE	Counter electrode
R/R	Redox couple
S	Ground state dye
S*	Excited state dye
$E_{S^*/S^+}/E_{S^*/S^-}$	Energy level of the excited state dye
E_{S/S^+}	Energy level of the oxidized ground state
E_{S/S^-}	Energy level of the reduced state
CV	Cyclic voltammetry
HOMO	The Highest Occupied Molecular Orbital
LUMO	The Lowest Unoccupied Molecular Orbital
ΔE_{0-0}	Energy of the 0–0 transition
PL	Photoluminescence
η	The overall light-to-electricity conversion efficiency
J_{SC}	Short-circuit photocurrent
V_{OC}	Open-circuit voltage
FF	Fill factor
P_{in}	Intensity of the incident light
P_{max}	Maximum power output
IPCE	Incident photon-to-current conversion efficiency
$E_{R/R+}/E_{redox}$	Energy level (redox potential) of the electrolyte redox couple
EQE	External quantum efficiency
$J_{SC}(\lambda)$	Short-circuit current generated under monochromatic light
Φ_λ	Photon flux
λ	Light wavelength
e	Elementary charge
η_A	Light harvesting efficiency
η_{inj}	Electron injection efficiency
η_{reg}	Dye regeneration efficiency
η_{col}	Charge collection efficiency
k_{inj}	Rate constant of electron injection
k_{s^*}	Rate constant of excited state relaxation rate
TA	Transient absorption
fs	Femtosecond
ps	Picosecond
E_{CB}	Energy of the CB edge
$-\Delta G_{inj}$	Free energy difference between E_{S^*/S^+} and E_{CB}

(continued)

(continued)

k_{reg}	Rate constants of regeneration
k_{rec}	Rate constants of recombination
$-\Delta G_{reg}$)	Free energy difference between $E_{S/S+}$ and $E_{R/R+}$
τ_{tr}	Electron transport time
τ_{rec}	Charge recombination time
IMVS	Intensity-Modulated Photovoltage Spectroscopy
IMPS	Intensity-Modulated Photocurrent Spectroscopy
R_{rec}	Recombination resistance
R_{tr}	Transport resistant
MLCT	Metal-to-ligand charge transfer
D	Electron donor
π	Conjugated linker
A	Electron acceptor
CDCA	Chenodeoxycholic acid
DMPII	1,2-dimethyl-3-n-propylimidazolium iodide
TBP	4-tert-butylpyridine
$Co^{3+/2+}$ $(bpy)_3$	Cobalt(III/II) tris(2,2′-bipyridine)
CPDT	Cyclopentadithiophene
DCRD	2-(1,1-dicyanomethylene)rhodanine
SAM	Self-assembled monolayer
AFM	Atomic force microscopy
QCMD	Quartz microbalance with dissipation technique
MD	Molecular dynamics
NICISS	Neutral impact collision ion scattering spectroscopy
XPS	X-ray photoelectron spectroscopy (XPS)
E^O	Standard electrode potential
R	Ideal gas constant
T	Absolute temperature
n	Number of electrons
F	Faraday constant
a_i	Represents the activities
PEDOT	Poly(3,4-Ethylenedioxythiophene)
PPy	polypyrrole
PANI	Polyaniline
VB	Valence band
NHE	Normal Hydrogen Electrode
ΔV	Theoretical maximum photovoltage

References

1. Gerischer H (1978) Electrochemistry of the excited electronic state. J Electrochem Soc 125:218C–226C
2. Gerischer H, Willig F (1976) Reaction of excited dye molecules at electrodes. In: Topics in current chemistry, no 61, vol 61. Springer, pp 31–84
3. Memming R (1984) Electron transfer process with excited molecules at semiconductor electrodes. Prog Surf Sci 17:7–74
4. Moser J (1887) Notiz über Verstärkung photoelektrischer Ströme dursch optische Sensibilisirung. Monatsh Chem 8:373
5. O'Regan B, Gratzel M (1991) A low-cost, high-efficiency solar cell based on dye-sensitized colloidal TiO_2 films. Nature 353(6346):737–740
6. Desilvestro J, Grätzel M, Kavan L, Moser J (1985) Highly efficient sensitization of titanium dioxide. J Am Chem Soc 107:2988–2990
7. Hagfeldt A, Boschloo G, Sun L, Kloo L, Pettersson H (2010) Dye-sensitized solar cells. Chem Rev 110(11):6595–6663. doi:10.1021/cr900356p
8. Jose R, Thavasi V, Ramakrishna S (2009) Metal oxides for dye-sensitized solar cells. J Am Ceram Soc 92(2):289–301. doi:10.1111/j.1551-2916.2008.02870.x
9. Birkel A, Lee Y-G, Koll D, Meerbeek XV, Frank S, Choi MJ, Kang YS, Char K, Tremel W (2012) Highly efficient and stable dye-sensitized solar cells based on SnO_2 nanocrystals prepared by microwave-assisted synthesis. Energy Environ Sci 5(1):5392–5400. doi:10.1039/C1EE02115J
10. Bisquert J (2007) Hopping transport of electrons in dye-sensitized solar cells. J Phys Chem C 111(46):17163–17168. doi:10.1021/jp077419x
11. Asbury JB, Ellingson RJ, Ghosh HN, Ferrere S, Nozik AJ, Lian T (1999) Femtosecond IR study of excited-state relaxation and electron-injection dynamics of Ru(dcbpy)2(NCS)2 in solution and on nanocrystalline TiO_2 and Al_2O_3 thin films. J Phys Chem B 103(16):3110–3119. doi:10.1021/jp983915x
12. Benkö G, Kallioinen J, Korppi-Tommola JEI, Yartsev AP, Sundström V (2002) Photoinduced ultrafast dye-to-semiconductor electron injection from nonthermalized and thermalized donor states. J Am Chem Soc 124(3):489–493. doi:10.1021/ja016561n
13. Koops SE, O'Regan BC, Barnes PRF, Durrant JR (2009) Parameters influencing the efficiency of electron injection in dye-sensitized solar cells. J Am Chem Soc 131(13):4808–4818. doi:10.1021/ja8091278
14. Katoh R, Furube A (2014) Electron injection efficiency in dye-sensitized solar cells. J Photochem Photobiol C: Photochem Rev 20:1–16. doi:10.1016/j.jphotochemrev.2014.02.001
15. Hagfeldt A, Grätzel M (2000) Molecular photovoltaics. Acc Chem Res 33(5):269–277. doi:10.1021/ar980112j
16. Clifford JN, Palomares E, Nazeeruddin MK, Grätzel M, Durrant JR (2007) Dye dependent regeneration dynamics in dye sensitized nanocrystalline solar cells: evidence for the formation of a ruthenium bipyridyl cation/iodide intermediate. J Phys Chem C 111(17):6561–6567. doi:10.1021/jp067458t
17. Daeneke T, Mozer AJ, Uemura Y, Makuta S, Fekete M, Tachibana Y, Koumura N, Bach U, Spiccia L (2012) Dye regeneration kinetics in dye-sensitized solar cells. J Am Chem Soc 134(41):16925–16928. doi:10.1021/ja3054578
18. Feldt SM, Lohse PW, Kessler F, Nazeeruddin MK, Gratzel M, Boschloo G, Hagfeldt A (2013) Regeneration and recombination kinetics in cobalt polypyridine based dye-sensitized solar cells, explained using Marcus theory. Phys Chem Chem Phys 15(19):7087–7097. doi:10.1039/C3CP50997D

19. Nazeeruddin MK, Kay A, Rodicio I, Humphry-Baker R, Mueller E, Liska P, Vlachopoulos N, Graetzel M (1993) Conversion of light to electricity by cis-X2bis(2,2′-bipyridyl-4,4′-dicarboxylate)ruthenium(II) charge-transfer sensitizers (X = Cl-, Br-, I-, CN-, and SCN-) on nanocrystalline titanium dioxide electrodes. J Am Chem Soc 115(14):6382–6390. doi:10.1021/ja00067a063
20. Nazeeruddin MK, Zakeeruddin SM, Humphry-Baker R, Jirousek M, Liska P, Vlachopoulos N, Shklover V, Fischer C-H, Grätzel M (1999) Acid-base equilibria of (2,2′-Bipyridyl-4,4′-dicarboxylic acid)ruthenium(II) complexes and the effect of protonation on charge-transfer sensitization of nanocrystalline titania. Inorg Chem 38(26):6298–6305. doi:10.1021/ic990916a
21. Ozawa H, Shimizu R, Arakawa H (2012) Significant improvement in the conversion efficiency of black-dye-based dye-sensitized solar cells by cosensitization with organic dye. RSC Adv 2(8):3198–3200. doi:10.1039/C2RA01257J
22. Hagberg DP, Edvinsson T, Marinado T, Boschloo G, Hagfeldt A, Sun L (2006) A novel organic chromophore for dye-sensitized nanostructured solar cells. Chem Commun 21:2245–2247. doi:10.1039/B603002E
23. Tian H, Yang X, Cong J, Chen R, Teng C, Liu J, Hao Y, Wang L, Sun L (2010) Effect of different electron donating groups on the performance of dye-sensitized solar cells. Dyes Pigments 84(1):62–68. doi:10.1016/j.dyepig.2009.06.014
24. Gabrielsson E, Ellis H, Feldt S, Tian H, Boschloo G, Hagfeldt A, Sun L (2013) Convergent/Divergent synthesis of a linker-varied series of dyes for dye-sensitized solar cells based on the D35 donor. Adv Energy Mater 3(12):1647–1656. doi:10.1002/aenm.201300367
25. Feldt SM, Gibson EA, Gabrielsson E, Sun L, Boschloo G, Hagfeldt A (2010) Design of organic dyes and cobalt polypyridine redox mediators for high-efficiency dye-sensitized solar cells. J Am Chem Soc 132(46):16714–16724. doi:10.1021/ja1088869
26. El-Zohry A, Orthaber A, Zietz B (2012) Isomerization and aggregation of the solar cell dye D149. J Phys Chem C 116(50):26144–26153. doi:10.1021/jp306636w
27. Hong J, Lai H, Liu Y, Yuan C, Li Y, Liu P, Fang Q (2013) New organic dyes containing E- or Z-trifluoromethyl acrylic acid as the electron acceptors for dye-sensitized solar cell applications: an investigation of the effect of molecular configuration on the power conversion efficiency of the cells. RSC Adv 3(4):1069–1072. doi:10.1039/C2RA22195K
28. Zietz B, Gabrielsson E, Johansson V, El-Zohry AM, Sun L, Kloo L (2014) Photoisomerization of the cyanoacrylic acid acceptor group—a potential problem for organic dyes in solar cells. Phys Chem Chem Phys 16(6):2251–2255. doi:10.1039/C3CP54048K
29. Yum J-H, Baranoff E, Kessler F, Moehl T, Ahmad S, Bessho T, Marchioro A, Ghadiri E, Moser J-E, Yi C, Nazeeruddin MK, Grätzel M (2012) A cobalt complex redox shuttle for dye-sensitized solar cells with high open-circuit potentials. Nat Commun 3:631. doi:http://www.nature.com/ncomms/journal/v3/n1/suppinfo/ncomms1655_S1.html
30. Yao Z, Zhang M, Wu H, Yang L, Li R, Wang P (2015) Donor/acceptor indenoperylene dye for highly efficient organic dye-sensitized solar cells. J Am Chem Soc 137(11):3799–3802. doi:10.1021/jacs.5b01537
31. Mathew S, Yella A, Gao P, Humphry-Baker R, CurchodBasile FE, Ashari-Astani N, Tavernelli I, Rothlisberger U, NazeeruddinMd K, Grätzel M (2014) Dye-sensitized solar cells with 13% efficiency achieved through the molecular engineering of porphyrin sensitizers. Nat Chem 6(3):242–247. doi:10.1038/nchem.1861 http://www.nature.com/nchem/journal/v6/n3/abs/nchem.1861.html#supplementary-information
32. Yella A, Lee H-W, Tsao HN, Yi C, Chandiran AK, Nazeeruddin MK, Diau EW-G, Yeh C-Y, Zakeeruddin SM, Grätzel M (2011) Porphyrin-sensitized solar cells with cobalt (II/III)-based redox electrolyte exceed 12 percent efficiency. Science 334(6056):629–634. doi:10.1126/science.1209688
33. Lan C-M, Wu H-P, Pan T-Y, Chang C-W, Chao W-S, Chen C-T, Wang C-L, Lin C-Y, Diau EW-G (2012) Enhanced photovoltaic performance with co-sensitization of porphyrin and an organic dye in dye-sensitized solar cells. Energy Environ Sci 5(4):6460–6464. doi:10.1039/C2EE21104A

34. Kakiage K, Aoyama Y, Yano T, Oya K, J-i Fujisawa, Hanaya M (2015) Highly-efficient dye-sensitized solar cells with collaborative sensitization by silyl-anchor and carboxy-anchor dyes. Chem Commun 51(88):15894–15897. doi:10.1039/C5CC06759F
35. Qin C, Numata Y, Zhang S, Islam A, Yang X, Sodeyama K, Tateyama Y, Han L (2013) A near-infrared cis-configured squaraine co-sensitizer for high-efficiency dye-sensitized solar cells. Adv Funct Mater 23(30):3782–3789. doi:10.1002/adfm.201203384
36. Joly D, Pellejà L, Narbey S, Oswald F, Chiron J, Clifford JN, Palomares E, Demadrille R (2014) A robust organic dye for dye sensitized solar cells based on iodine/iodide electrolytes combining high efficiency and outstanding stability. Sci Rep 4:4033. doi:10.1038/srep04033
37. Hara K, Wang Z-S, Cui Y, Furube A, Koumura N (2009) Long-term stability of organic-dye-sensitized solar cells based on an alkyl-functionalized carbazole dye. Energy Environ Sci 2(10):1109–1114. doi:10.1039/B907486D
38. Shi D, Cao Y, Pootrakulchote N, Yi Z, Xu M, Zakeeruddin SM, Grätzel M, Wang P (2008) New organic sensitizer for stable dye-sensitized solar cells with solvent-free ionic liquid electrolytes. J Phys Chem C 112(44):17478–17485. doi:10.1021/jp807191w
39. Kuang D, Comte P, Zakeeruddin SM, Hagberg DP, Karlsson KM, Sun L, Nazeeruddin MK, Grätzel M (2011) Stable dye-sensitized solar cells based on organic chromophores and ionic liquid electrolyte. SoEn 85(6):1189–1194. doi:10.1016/j.solener.2011.02.025
40. Chen C, Yang X, Cheng M, Zhang F, Sun L (2013) Degradation of cyanoacrylic acid-based organic sensitizers in dye-sensitized solar cells. Chemsuschem 6(7):1270–1275. doi:10.1002/cssc.201200949
41. Zhang L, Cole JM (2015) Anchoring groups for dye-sensitized solar cells. ACS Appl Mater Interfaces 7(6):3427–3455. doi:10.1021/am507334m
42. Ooyama Y, Inoue S, Nagano T, Kushimoto K, Ohshita J, Imae I, Komaguchi K, Harima Y (2011) Dye-sensitized solar cells based on donor-acceptor π-conjugated fluorescent dyes with a pyridine ring as an electron-withdrawing anchoring group. Angew Chem 123 (32):7567–7571. doi:10.1002/ange.201102552
43. Mao J, He N, Ning Z, Zhang Q, Guo F, Chen L, Wu W, Hua J, Tian H (2012) Stable dyes containing double acceptors without COOH as anchors for highly efficient dye-sensitized solar cells. Angew Chem Int Ed 51(39):9873–9876. doi:10.1002/anie.201204948
44. Robert D, Victor Weber J (2000) Study of the adsorption if dicarboxylic acids on titanium dioxide in aqueous solution. Adsor 6:175–178
45. Lim J, Kwon YS, Park S-H, Song IY, Choi J, Park T (2011) Thermodynamic control over the competitive anchoring of N719 dye on nanocrystalline TiO_2 for improving photoinduced electron generation. Langmuir 27:14647–14653
46. Ellis-Gibbings L, Johansson V, Walsh RB, Kloo L, Quinton JS, AG G (2012) Formation of N719 dye multilayers on dye sensitized solar cell photoelectrode surfaces investigated by direct determination of element concentration depth profiles. Langmuir 28:9431–9439
47. Johansson V, Ellis-Gibbings L, Clarke T, Gorlov M, Andersson GG, Kloo L (2014) On the correlation between dye coverage and photoelectrochemical performance in dye-sensitized solar cells. PCCP 16:711–718
48. Liu P, Johansson V, Triksilana H, Rosdahl J, Andersson G, Kloo L (2016) EXAFS and NICIS spectroscopy studies on the dye-sensitised sensitized solar cell photoelectrode interface
49. Rienzo A, Mayor LC, Magnano G, Satterley CJ, Ataman E, Schnadt J, Schulte K, O'Shea JN (2010) X-ray absorption and photoemission spectroscopy of zinc protoporphyrin adsorbed on rutile TiO2(110) prepared by in situ electrospray deposition. J Chem Phys 132 (8):084703. doi:10.1063/1.3336747
50. Voïtchovsky K, Ashari-Astani N, Tavernelli I, Tétreault N, Rothlisberger U, Stellacci F, Grätzel M, Harms HA (2015) In situ mapping of the molecular arrangement of amphiphilic dye molecules at the TiO_2 surface of dye-sensitized solar cells. ACS Appl Mater Interfaces 7 (20):10834–10842. doi:10.1021/acsami.5b01638

51. Ni J-S, Hung C-Y, Liu K-Y, Chang Y-H, Ho K-C, Lin K-F (2012) Effects of tethering alkyl chains for amphiphilic ruthenium complex dyes on their adsorption to titanium oxide and photovoltaic properties. J Colloid Interface Sci 386(1):359–365. doi:10.1016/j.jcis.2012.07.019
52. Deng Y, Yuan W, Jia Z, Liu G (2014) H- and J-aggregation of fluorene-based chromophores. J Phys Chem B 118(49):14536–14545. doi:10.1021/jp510520m
53. Cappel UB, Feldt SM, Schöneboom J, Hagfeldt A, Boschloo G (2010) The influence of local electric fields on photoinduced absorption in dye-sensitized solar cells. J Am Chem Soc 132(26):9096–9101. doi:10.1021/ja102334h
54. Ardo S, Sun Y, Staniszewski A, Castellano FN, Meyer GJ (2010) Stark effects after excited-state interfacial electron transfer at sensitized TiO_2 nanocrystallites. J Am Chem Soc 132(19):6696–6709. doi:10.1021/ja909781g
55. Cong J, Yang X, Kloo L, Sun L (2012) Iodine/iodide-free redox shuttles for liquid electrolyte-based dye-sensitized solar cells. Energy Environ Sci 5(11):9180. doi:10.1039/c2ee22095d
56. Yu Z, Vlachopoulos N, Gorlov M, Kloo L (2011) Liquid electrolytes for dye-sensitized solar cells. Dalton Trans 40(40):10289–10303. doi:10.1039/c1dt11023c
57. Fujishima A, Honda A (1972) Electrochemical photolysis of water at a semiconductor electrode. Nature 238:37–38
58. Tian H, Gabrielsson E, Lohse PW, Vlachopoulos N, Kloo L, Hagfeldt A, Sun L (2012) Development of an organic redox couple and organic dyes for aqueous dye-sensitized solar cells. Energy Environ Sci 5:9752–9755
59. Daeneke T, Uemura Y, Duffy NW, Mozer AJ, Koumura N, Bach U, Spiccia L (2012) Aqueous dye-sensitized solar cell electrolytes based on the ferricyanide-ferrocyanide redox couple. Adv Mater 24:1222–1225
60. Yang W, Soderberg M, Eriksson AIK, Boschloo G (2015) Efficient aqueous dye-sensitized solar cell electrolytes based on a TEMPO/TEMPO + redox couple. RSC Adv 5:26706–26709
61. Chen C, Yang X, Cheng M, Zhang F, Sun L (2013) Degradation of cyanoacrylic acid-based organic sensitizers in dye-sensitized solar cells. Chemsuschem 6:1270–1275
62. Agrell HG, Lindgren J, Hagfeldt A (2003) Degradation mechanisms in a dye-sensitized solar cell studied by UV–VIS and IR spectroscopy. SoEn 75:169–180
63. Law C, Pathirana SC, Li X, Anderson AY, Barnes PRF, Listorti A, Ghaddar TH, O'Regan BC (2010) Water-based electrolytes for dye-sensitized solar cells. Adv Mater 22:4505–4509
64. Tian H, Yu Z, Hagfeldt A, Kloo L, Sun L (2011) Organic redox couples and organic counter electrode for efficient organic dye-sensitized solar cells. J Am Chem Soc 133:9413–9422
65. Gorlov M, Kloo L (2008) Ionic liquid electrolytes for dye-sensitized solar cells. DTr:2655-2666
66. Jhong H-R, Wonga DS-H, Wana C-C, Wang Y-Y, Wei T-C (2009) A novel deep eutectic solvent-based ionic liquid used as electrolyte for dye-sensitized solar cells. Electrochem Commun 11:209–211
67. Yu Z, Vlachopoulos N, Hagfeldt A, Kloo L (2013) Incompletely solvated ionic liquid mixtures as electrolyte solvents for highly stable dye-sensitized solar cells. RSC Adv 3:1896–1901
68. Yamanaka N, Kawano R, Kubo W, Kitamura T, Wada Y, Watanabe M, Yanagida S (2005) Ionic liquid crystal as a hole transport layer of dye-sensitized solar cells. Chem Commun 740–742
69. Högberg D, Soberats B, Uchida S, Yoshio M, Kloo L, Segawa H, Kato T (2014) Nanostructured two-component liquid-crystalline electrolytes for high-temperature dye-sensitized solar cells. Chem Mater 26:6496–6502
70. Högberg D, Soberats B, Yatagai R, Uchida S, Yoshio M, Kloo L, Segawa H, Kato T (2016) Liquid-crystalline dye-sensitized solar cells: design of two-dimensional molecular assemblies for efficient ion transport and thermal stability. Chem Mater 28:6493–6500

71. Boschloo G, Gibson EA, Hagfeldt A (2011) Photomodulated voltammetry of iodide/triiodide redox electrolytes and its relevance to dye-sensitized solar cells. J Phys Chem Lett 2:3016–3020
72. Cong J, Yang X, Hao Y, Kloo L, Sun L (2012) A highly efficient colourless sulfur/iodide-based hybrid electrolyte for dye-sensitized solar cells. RSC Adv 2:3625–3629
73. Boschloo G, Hagfeldt A (2009) Characteristics of the iodide/triiodide redox mediator in dye-sensitized solar cells. Acc Chem Res 42:1819–1826
74. Yella A, Lee H-W, Tsao HN, Yi C, Chandiran AK, Nazeeruddin MK, Diau EW-G, Yeh C-Y, Zakeeruddin SM, Grätzel M (2011) Porphyrin-sensitized solar cells with cobalt (II/III)-based redox electrolyte exceed 12 percent efficiency. Science 334:629–634
75. Kakiage K, Aoyama Y, Yano T, Oya K, J-i Fujisawa, Hanaya M (2015) Highly-efficient dye-sensitized solar cells with collaborative sensitization by silyl-anchor and carboxy-anchor dyes. Chem Commun 51:15894–15897
76. Kashif MK, Axelson JC, Duffy NW, Forsyth CM, Chang CJ, Long JR, Spiccia L, Bach U (2012) A new direction in dye-sensitized solar cells redox mediator development. In situ fine-tuning of the cobalt(II)/(III) redox potential through lewis base interactions. J Am Chem Soc 134:16646–16653
77. Kashif MK, Nippe M, Duffy NW, Forsyth CM, Chang CJ, Long JR, Spiccia L, Bach U (2013) Stable dye-sensitized solar cell electrolytes based on cobalt(II)/(III) complexes of a hexadentate pyridyl ligand. Angew Chem Int Ed 52:5527–5531
78. Achari MB, Elumalai V, Vlachopoulos N, Safdari M, Gao J, Gardner JM, Kloo L (2013) A quasi-liquid polymer-based cobalt redox mediator electrolyte for dye-sensitized solar cells. PCCP 15:17419–17425
79. Xiang W, Huang W, Bach U, Spiccia L (2013) Stable high efficiency dye-sensitized solar cells based on a cobalt polymer gel electrolyte. Chem Commun 49:8997–8999
80. Cong J, Hao Y, Boschloo G, Kloo L (2015) Electrolytes based on TEMPO-Co tandem redoxx systems outperform single redox systems in dye-sensitized solar cells. Chemsuschem 8:264–268
81. Cheng M, Yang X, Zhang F, Zhao J, Sun L (2012) Efficient dye-sensitized solar cells based on hydroquinone/benzoquinone as a bioinspired redox couple. Angew Chem Int Ed 51:9896–9899
82. Bai Y, Yu Q, Cai N, Wang Y, Zhang M, Wang P (2011) High-efficiency organic dye-sensitized mesoscopic solar cells with a copper redox shuttle. Chem Commun 47:4376–4378
83. Cong J, Kinschel D, Daniel Q, Safdari M, Gabrielsson E, Chen H, Svensson PH, Sun L, Kloo L (2016) Bis(1,1-bis(2-pyridyl)ethane)copper(I/II) as an efficient redox couple for liquid dye-sensitized solar cells. J Mater Chem A 4:14550–14554
84. Hoffeditz WL, Katz MJ, Deria P, Cutsail GE III, Pellin MJ, Farha OK, Hupp JT (2016) One electron changes everything. A multispecies copper redox shuttle for dye-sensitized solar cells. J Phys Chem C 120:3731–3740
85. Abe R, Higashi M, Domen K (2011) Overall water splitting under visible light through a two-step photoexcitation between TaON and WO_3 in the presence of an iodate-iodide shuttle redox mediator. Chemsuschem 4(2):228–237. doi:10.1002/cssc.201000333
86. Heo N, Jun Y, Park JH (2013) Dye molecules in electrolytes: new approach for suppression of dye-desorption in dye-sensitized solar cells. Sci Rep 3 Article number 1712
87. Yu S, Ahmadi S, Sun C, Palmgren P, Hennies F, Zuleta M, Göthelid M (2010) 4-tert-butyl pyridine bond site and band bending on TiO_2(110). J Phys Chem C 114:2315–2320
88. Hagfeldt A, Boschloo G, Sun L, Kloo L, Pettersson H (2010) Dye-sensitized solar cells. Chem Rev 110:6595–6663
89. Yu Z, Gorlov M, Nissfolk J, Boschloo G, Kloo L (2010) Investigation of Iodine Concentration Effects in Electrolytes for Dye-Sensitized Solar Cells. J Phys Chem C 114:10612–10620
90. Gao J (2016) Electrolyte-based dynamics: fundamental studies for stable liquid dye-sensitized solar cells. KTH Royal Institute of Technology

91. Gao J, Yang W, Pazoki M, Boschloo G, Kloo L (2015) Cation-dependent photostability of Co(II/III)-mediated dye-sensitized solar cells. J Phys Chem C 119:24704–24713
92. Gao J, Achari MB, Kloo L (2014) Long-term stability for cobalt-based dyesensitized solar cells obtained by electrolyte optimization. Chem Commun 50:6249–6251
93. Wu M, Ma T (2014) Recent progress of counter electrode catalysts in dye-sensitized solar cells. J Phys Chem C 118(30):16727–16742. doi:10.1021/jp412713h
94. Burschka J, Brault V, Ahmad S, Breau L, Nazeeruddin MK, Marsan B, Zakeeruddin SM, Gratzel M (2012) Influence of the counter electrode on the photovoltaic performance of dye-sensitized solar cells using a disulfide/thiolate redox electrolyte. Energy Environ Sci 5 (3):6089–6097. doi:10.1039/C2EE03005E
95. Tian H, Yu Z, Hagfeldt A, Kloo L, Sun L (2011) Organic redox couples and organic counter electrode for efficient organic dye-sensitized solar cells. J Am Chem Soc 133(24):9413–9422
96. Wu J, Li Q, Fan L, Lan Z, Li P, Lin J, Hao S (2008) High-performance polypyrrole nanoparticles counter electrode for dye-sensitized solar cells. J Power Sour 181(1):172–176. doi:10.1016/j.jpowsour.2008.03.029
97. Xia J, Chen L, Yanagida S (2011) Application of polypyrrole as a counter electrode for a dye-sensitized solar cell. J Mater Chem 21(12):4644–4649. doi:10.1039/C0JM04116E
98. Tai Q, Chen B, Guo F, Xu S, Hu H, Sebo B, Zhao X-Z (2011) In situ prepared transparent polyaniline electrode and its application in bifacial dye-sensitized solar cells. ACS Nano 5 (5):3795–3799. doi:10.1021/nn200133g
99. Li Z, Ye B, Hu X, Ma X, Zhang X, Deng Y (2009) Facile electropolymerized-PANI as counter electrode for low cost dye-sensitized solar cell. Electrochem Commun 11(9):1768–1771. doi:10.1016/j.elecom.2009.07.018
100. He J, Lindström H, Hagfeldt A, Lindquist S-E (1999) Dye-sensitized nanostructured p-type nickel oxide film as a photocathode for a solar cell. J Phys Chem B 103(42):8940–8943. doi:10.1021/jp991681r
101. Qin P, Wiberg J, Gibson EA, Linder M, Li L, Brinck T, Hagfeldt A, Albinsson B, Sun L (2010) Synthesis and mechanistic studies of organic chromophores with different energy levels for p-type dye-sensitized solar cells. J Phys Chem C 114(10):4738–4748. doi:10.1021/jp911091n
102. Li L, Gibson EA, Qin P, Boschloo G, Gorlov M, Hagfeldt A, Sun L (2010) Double-layered NiO photocathodes for p-type DSSCs with record IPCE. Adv Mater 22(15):1759–1762. doi:10.1002/adma.200903151
103. Nattestad A, Mozer AJ, Fischer MKR, Cheng YB, Mishra A, Bauerle P, Bach U (2010) Highly efficient photocathodes for dye-sensitized tandem solar cells. Nat Mater 9(1):31–35. http://www.nature.com/nmat/journal/v9/n1/suppinfo/nmat2588_S1.html
104. Tian H, Oscarsson J, Gabrielsson E, Eriksson SK, Lindblad R, Xu B, Hao Y, Boschloo G, Johansson EMJ, Gardner JM, Hagfeldt A, Rensmo H, Sun L (2014) Enhancement of p-type dye-sensitized solar cell performance by supramolecular assembly of electron donor and acceptor. Sci Rep 4:4282. doi:10.1038/srep04282. http://www.nature.com/srep/2014/140307/srep04282/abs/srep04282.html#supplementary-information
105. Wood CJ, Summers GH, Gibson EA (2015) Increased photocurrent in a tandem dye-sensitized solar cell by modifications in push-pull dye-design. Chem Commun 51 (18):3915–3918. doi:10.1039/C4CC10230D
106. Farré Y, Zhang L, Pellegrin Y, Planchat A, Blart E, Boujtita M, Hammarström L, Jacquemin D, Odobel F (2016) Second generation of diketopyrrolopyrrole dyes for NiO-based dye-sensitized solar cells. J Phys Chem C 120(15):7923–7940. doi:10.1021/acs.jpcc.5b12489
107. Favereau L, Warnan J, Pellegrin Y, Blart E, Boujtita M, Jacquemin D, Odobel F (2013) Diketopyrrolopyrrole derivatives for efficient NiO-based dye-sensitized solar cells. Chem Commun 49(73):8018–8020. doi:10.1039/C3CC44232B
108. Park JY, Jang BY, Lee CH, Yun HJ, Kim JH (2014) Influence of the anchoring number in a carbazole-based photosensitizer on the photovoltaic performance of p-type NiO dye sensitized solar cells. RSC Adv 4(106):61248–61255. doi:10.1039/C4RA08271K

109. Shao Z, Pan X, Chen H, Tao L, Wang W, Ding Y, Pan B, Yang S, Dai S (2014) Polymer based photocathodes for panchromatic tandem dye-sensitized solar cells. Energy Environ Sci. doi:10.1039/C4EE01315H
110. Gennari M, Légalité F, Zhang L, Pellegrin Y, Blart E, Fortage J, Brown AM, Deronzier A, Collomb M-N, Boujtita M, Jacquemin D, Hammarström L, Odobel F (2014) Long-lived charge separated state in NiO-based p-type dye-sensitized solar cells with simple cyclometalated iridium complexes. J Phys Chem Lett 5(13):2254–2258. doi:10.1021/jz5009714
111. Ji Z, Natu G, Huang Z, Kokhan O, Zhang X, Wu Y (2012) Synthesis, photophysics, and photovoltaic studies of ruthenium cyclometalated complexes as sensitizers for p-type NiO dye-sensitized solar cells. J Phys Chem C 116(32):16854–16863. doi:10.1021/jp303909x
112. Ji Z, Natu G, Wu Y (2013) Cyclometalated ruthenium sensitizers bearing a triphenylamino group for p-type NiO dye-sensitized solar cells. ACS Appl Mater Interfaces 5(17):8641–8648. doi:10.1021/am402263q
113. Gibson EA, Smeigh AL, Le Pleux L, Fortage J, Boschloo G, Blart E, Pellegrin Y, Odobel F, Hagfeldt A, Hammarström L (2009) A p-type NiO-based dye-sensitized solar cell with an open-circuit voltage of 0.35 V. Angew Chem Int Ed 48(24):4402–4405. doi:10.1002/anie.200900423
114. Xu X, Zhang B, Cui J, Xiong D, Shen Y, Chen W, Sun L, Cheng Y, Wang M (2013) Efficient p-type dye-sensitized solar cells based on disulfide/thiolate electrolytes. Nanoscale 5(17):7963–7969. doi:10.1039/C3NR02169F
115. Powar S, Daeneke T, Ma MT, Fu D, Duffy NW, Götz G, Weidelener M, Mishra A, Bäuerle P, Spiccia L, Bach U (2013) Highly efficient p-type dye-sensitized solar cells based on Tris(1,2-diaminoethane)Cobalt(II)/(III) electrolytes. Angew Chem Int Ed 52(2):602–605. doi:10.1002/anie.201206219
116. Perera IR, Daeneke T, Makuta S, Yu Z, Tachibana Y, Mishra A, Bäuerle P, Ohlin CA, Bach U, Spiccia L (2015) Application of the tris(acetylacetonato)iron(III)/(II) redox couple in p-type dye-sensitized solar cells. Angew Chem Int Ed 54(12):3758–3762. doi:10.1002/anie.201409877
117. Powar S, Bhargava R, Daeneke T, Götz G, Bäuerle P, Geiger T, Kuster S, Nüesch FA, Spiccia L, Bach U. Thiolate/disulfide based electrolytes for p-type and tandem dye-sensitized solar cells. Electrochim Acta. doi:10.1016/j.electacta.2015.09.026

Chapter 4
Solid-State Dye-Sensitized Solar Cells

Jinbao Zhang, Marina Freitag, Anders Hagfeldt and Gerrit Boschloo

Abstract The conventional liquid dye-sensitized solar cell (l-DSC) is a photoelectrochemical system with a liquid redox electrolyte. Replacement of the liquid electrolyte with a solid-state hole transporting material (HTM) has several advantages: dye desorption is prevented, liquid leakage or evaporation cannot occur, and, finally, a solid-state device is made, which is easier to encapsulate and to series-connect. Thus far, solid-state dye-sensitized solar cell (ssDSC) are lagging behind in terms of power conversion efficiencies compared to the l-DSC, but recent advances in dyes and hole conducting materials, leading to ssDSC with 11% efficiency, suggest that this gap will soon be closed.

Keywords Hybrid photovoltaics · Mesoporous semiconductor films · Dye-sensitization · Electron transfer kinetics · Hole transporting materials · Conducting polymers

List of Abbreviations

FTO	Fluorine-doped tinoxide
FF	Fill factor
HOMO	Highest occupied molecular orbital
HTM	Hole-transporting material
IPCE	Incident photon-to-current efficiency
l-DSC	Dye-sensitized solar cell with liquid electrolyte
J_{SC}	Short-circuit current density
PCE	Power conversion efficiency
PEDOT	Poly(3,4-ethylenedioxythiophene)

J. Zhang · M. Freitag · A. Hagfeldt · G. Boschloo (✉)
Department of Chemistry—Ångström Laboratory, Physical Chemistry,
Uppsala University, 523, 751 20 Uppsala, Sweden
e-mail: gerrit.boschloo@kemi.uu.se

A. Hagfeldt
École Polytechnique Fédérale de Lausanne, Laboratory of Photomolecular Science,
EPFL SB ISIC LSPM, CH G1 523, Chemin des Alambics,
Station 6, 1015 Lausanne, Switzerland

H. Tian et al. (eds.), *Molecular Devices for Solar Energy Conversion and Storage*, Green Chemistry and Sustainable Technology,
https://doi.org/10.1007/978-981-10-5924-7_4

PEP	Photoelectrochemical polymerization
P3HT	Poly(3-hexylthiophene)
spiro-OMeTAD	(2,2′(,7,7′(-tetrakis-(N, N-di-*p*-methoxyphenylamine) 9,9′(-spirobifluorene)
ssDSC	Dye-sensitized solar cell with solid-state hole transporting material
TCO	Transparent conductive oxide
T_g	Glass transition temperature
TPA	Triphenylamine
V_{OC}	Open-circuit potential

4.1 Introduction

In the solid-state dye-sensitized solar cell (ssDSC), the liquid redox electrolyte of the dye-sensitized solar cell (l-DSC) is replaced by a solid-state hole transporting material (HTM). After photoinduced electron from the excited dye to conduction band of the mesoporous semiconductor, the HTM reduces the oxidized dye and the hole (positive charge) that is created in the HTM moves away from the sensitized electrode by means of charge hopping to a metal contact. In contrast, in conventional l-DSC diffusion of redox species is responsible for hole transport to the counter electrode. DSC with gelled redox electrolytes are thus not considered to be ssDSC. Different types of materials can serve as HTM in a ssDSC, ranging from a molecular organic hole conductors, such as spiro-OMeTAD (2,2′(,7,7′(-tetrakis-(N, N-di-*p*-methoxyphenylamine)9,9′(-spirobifluorene) [1], via conducting polymers, such as PEDOT [2], to inorganic p-type semiconductors, such as CuI [3].

There are several very strong arguments why ssDSC is potentially more attractive and/or better than conventional l-DSC:

- No liquid is present: this avoids dye desorption, a detrimental process in l-DSCs, as well as solvent evaporation. Eventually, this should lead to improved stability
- Solid device structures are easier to interconnect in series and to encapsulate compared to l-DSC
- ssDSC are easier to apply in tandem device structures

The progress in ssDSC has been relatively slow, but in recent years good progress has been made, especially in the development of HTMs.

Several small molecules HTMs have been developed that can match the benchmark, spiro-OMeTAD, in performance at a much lower cost. An interesting new development is the copper complex-based HTM, which has led to a breakthrough in ssDSC performance with power conversion efficiencies (PCE) up to 11%.

With the reduction of cost for the HTM as well as high power output under indoor light conditions, ssDSC has also become very attractive for consumer applications.

Little research has been devoted to long-term stability studies of ssDSC. The expectation is, however, that with the development of new HTMs with improved doping methods, the current stability issues that have been reported can be overcome.

4.2 Basic Principles of Solid-State Dye-Sensitized Solar Cells

A schematic drawing of a typical ssDSC device structure is shown in Fig. 4.1a. Onto a conducting glass substrate, usually glass coated with fluorine-doped tinoxide (FTO), first a thin dense compact layer of TiO_2 is deposited, followed by a mesoporous layer of TiO_2 For the conventionally used spiro-OMeTAD as HTM the mesoporous layer is relatively thin (1–3 μm). The dense TiO_2 layer prevents direct contact between the FTO and the HTM, which could lead to losses due to shunting (holes in the HTM and electrons in the FTO could recombine). Dye molecules are adsorbed onto the TiO_2 surface. Next, the HTM is infiltrated into the porous structure, while also a thin overstanding layer of the HTM is formed. Finally, a metal contact is evaporated on top of the HTM. Direct contact between metal and TiO_2 could also lead to shunting.

The working mechanism of a ssDSC is similar to that of a l-DSC and is displayed in Fig. 4.1b. The dye molecules absorb photons and the resulting excited molecules can inject an electron into the conduction band of TiO_2. The oxidized dye receives an electron from the hole transport material (dye regeneration). After these initial charge separation processes, electron transport is proceeded in the

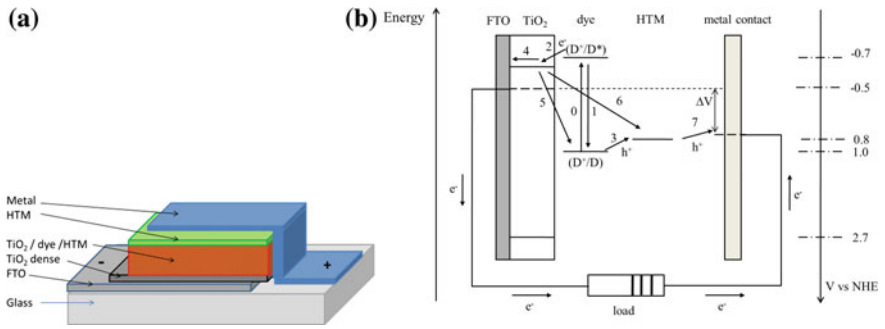

Fig. 4.1 **a** Schematic structure of a solid-state dye-sensitized solar cell. **b** Energy-level diagram for a ssDSC. The basic electron transfer processes are indicated by numbers (1–7). The potentials for an ssDSC based on LEG4 dye and spiro-OMeTAD HTM are shown

mesoporous TiO_2 film to the FTO substrate and hole transport in the HTM layer to the metal contact. The kinetics of these processes, as well as the recombination processes will now be discussed first.

The electron injection from the excited dye to the TiO_2 conduction band is very fast for suitable dyes and occurs on a time scale of 50 fs to ps in both l-DSC and ssDSC [4]. In ssDSC dye regeneration can also be ultrafast. Bach et al. reported 50% hole injection within 900 ps for oxidized N3 in contact with spiro-OMeTAD [5]. Fast regeneration (<1 μs) was also reported for other small organic HTMs by Durrant and co-workers [6, 7]. In fact, dye reduction (or hole injection to the HTM) may occur before electron injection into TiO_2. Cappel and co-workers found that in the TiO_2/ID176 (a perylene dye)/spiro-OMeTAD system electron injection and dye regeneration were complete after 1 ps, based on the observation of the Stark effect, a spectral shift of the dye spectrum caused by the electric field between the electron in TiO_2 and the hole in the HTM [8]. Remarkably, much slower (millisecond) regeneration kinetics were reported for PEDOT as a polymeric HTM [9]. Haque et al. found that a driving force of about 0.2 eV is needed for efficient (>85%) dye regeneration by the HTM [7].

The electron lifetime and electron transport time of the mesoporous TiO_2 electrode of the ssDSC has been analyzed in several studies [10–15]. The electron lifetime is significantly shorter by 2–3 orders of magnitude compared to l-DSC with the conventional iodide/triiodide redox mediator [11, 13–15]. As a result, the electron diffusion length in ssDSC is considerably shorter than in l-DSC with liquid I^-/I_3^- electrolytes, by about one order of magnitude ($\sim$1 μm vs. $\sim$10 μm) [10, 11, 15]. Interestingly, the electron transport, as measured by small-modulation photocurrent transients, was found to be significantly faster than in l-DCS with same film thickness and at the same photocurrent density [13, 14], see Fig. 4.2. The origin for this is not clear yet.

In ssDSC, the mobility of the holes in the HTM (e.g., spiro-OMeTAD) is typically higher than the electron mobility in the mesoporous TiO_2 [16]. Nevertheless,

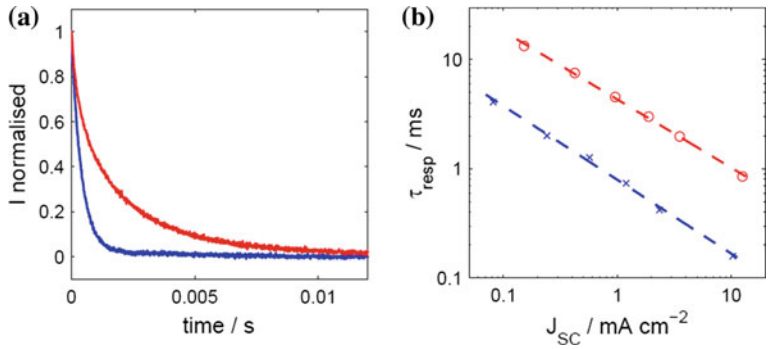

Fig. 4.2 **a** Photocurrent response from a ssDSC (*blue*) and a l-DSC (*red*) with equal mesoporous TiO_2 thickness. **b** Photocurrent response time as function of short-circuit photocurrent (Reproduced from Ref. [14] with permission of the author)

it is very important that the overstanding HTM layer is thin in order to avoid additional series resistance in the solar cell. If the layer is too thin pinholes could appear resulting in contact of the metal contact with the mesoporous TiO_2 film, which could result in shunting losses.

The energy levels involved in the ssDSC are essentially the same as in conventional l-DSC, see Fig. 4.1b. The liquid redox electrolyte is replaced with a solid hole conductor with a Fermi-level being rather difficult to determine. A major difference between l-DSC and ssDSC is the absence of a liquid in the latter. This will in principle affect the energy levels of all the components. In l-DSC, most relevant energy levels can be determined using electrochemistry, where the redox levels of the dye are preferably determined for molecules that are adsorbed on mesoporous TiO_2. The interaction between solvent and components results in changes and broadening of the energy levels. Fluctuations of the orientation of the solvent molecules results in small variations in the energy levels, which leads to a Gaussian distribution. In contrast, in the solid state such interactions and changes in orientation are largely absent. The molecules in a solid matrix will therefore have significantly lower reorganization energies. Techniques such as photoelectron spectroscopies (UPS, XPS) are appropriate to analyze the energy levels of solid systems, see Chap. 12.

In ssDSCs with organic HTM, commonly a salt is added to the HTM. This will give increase the conductivity of the HTM layer. Although no fundamental studies have been done on this topic, it is believed that this is needed for compensation of the electronic charge in the TiO_2. Specifically, in liquid DSC it is well established that electrons in mesoporous TiO_2 are charge-compensated by ions in the electrolyte [17]. Doping of the HTM is also important to increase the conductivity. This can be done by redox complexes with high redox potential but conveniently also by oxygen from air. The latter is often used for doping of spiro-OMeTAD and the addition of lithium ions is also believed to facilitate this process.

4.3 Components of the ssDSC

4.3.1 Blocking Layer on Conducting Glass

The blocking layer is an electron-selective contact between the transparent conductive oxide (TCO) layer and the HTM. It physically separates them and impedes the recombination of electrons in the TCO with holes in the HTM. The blocking layer should not absorb visible light; high band gap semiconductors are therefore suitable. The conduction band of this semiconductor should be well matched with the mesoporous oxide so that electron injection can take place. It is important that there are no pinholes or cracks in this layer to avoid direct contact of TCO with the HTM, while the layer should be as thin as possible to minimize resistance losses.

The commonly used compact layer in ssDSCs is TiO_2 [1]. The requirement of the compact layer depends on the nature of the hole transport medium. For example, no compact layer is needed for the efficient operation in the case of I^-/I_3^- as the redox mediator in l-DSCs because of the slow reduction kinetics of I_3^- at the TCO. In the ssDSC with solid-state HTMs such as spiro-OMeTAD or PEDOT, a much faster charge recombination between the electrons in TCO and holes in HTM takes place, and a suitable blocking layer on the TCO is required for good solar cell performance.

The preparation method determines the density of the compact TiO_2 layer and thus the required thickness. Many different methods have been reported for the preparation of the TiO_2 compact layer, including spray pyrolysis [1, 18], spin coating [19], sputtering [20], and atomic layer deposition [21]. Among them, the most commonly employed method is spray pyrolysis because of its easy operation, cheap precursors, and availability to obtain high-density compact layer. Specifically, this process is attained by spraying a titanium isopropoxide/acetylacetone precursor solution on top of the TCO glass, such as FTO, at high temperature ($\sim$500 °C). The thickness of the compact TiO_2 can be tuned by controlling the spray cycles or the concentration of the titanium precursors. The influence of the underlayer thickness has been previously studied, and an optimal thickness of 100 nm (compact TiO_2) was reported for the ssDSCs based on small-molecular HTMs [18]. The spray pyrolysis method generally requires high-temperature annealing to obtain high crystallinity. This limits its compatibility with the plastic conductive substrate if pursuing flexible devices. In this respect, it would be interesting to explore some alternative low-temperature approaches for making metal oxide underlayer or other alternative materials, such as polymers.

The blocking effect of the compact underlayer on TCO can be assessed using electrochemical methods, usually by measuring the current through the underlayer under a certain bias potential, corresponding to the electron transfer to a solution-based redox-active species, such as $K_4Fe(CN)_6$ [22].

4.3.2 Mesoporous Semiconductor Layer

TiO_2 is by far the most studied material for the mesoporous semiconductor in ssDSC. Anatase is the preferred crystal form of TiO_2 in dye-sensitized solar cells [17]. It was quickly understood that the thickness of the mesoporous TiO_2 layer must be much less ($\sim$2 μm) [23] than the optimal thickness for equivalent liquid electrolyte-based DSCs ($\sim$10 μm). This is because of the poor infiltration of HTM in thicker films, as well as because of the fast electron–hole recombination kinetics, which limits the electron diffusion length.

The size of the TiO_2 nanocrystals has a profound effect on its properties in ssDSC. Docampo et al. found that small crystal size results in electrodes with a relatively large surface area and high dye-coverage, but with relatively long electron transport times, while large crystals result in faster transport (but lower

dye-coverage) [12]. The porosity of the mesoporous layer is another important parameter. An increased performance was found in solid-state dye-sensitized solar cells having mesoporous TiO_2 films with some increased porosity, which was attributed to better pore filling with the HTM [24].

Other TiO_2 nanostructures have also been studied for ssDSC. TiO_2 nanotubes have the rutile crystal structure and are grown by electrochemical methods. They have been introduced with some success in ssDSC, reaching efficiencies of 1.67% with the organic dye C203 [25] and later 2.9% with the ruthenium dye C106 [26]. Ramakrishna and co-workers investigated TiO_2 nanofibers and mesoporous nanofibers in ssDSC, employing D131 as the sensitizer and P3HT as the hole transporting material [27]. By making the electrospun nanofibers mesoporous, the PCE improved from 0.42 to 1.82%, due to increased dye adsorption. The electron transport and collection was not much affected by increased porosity.

More ordered mesoporous TiO_2 structures have been developed by the Steiner and Snaith groups using block co-polymer as templates [28]. This allowed them to make oriented one-dimensional (1D) columnar structures as well as three-dimensional (3D) bicontinuous gyroid structures. For a 400 nm thick film sensitized with D149 a PCE of 1.7% was found. Docampo et al. further optimized this system and obtained a PCE of 3.4% [29].

Even higher ordering of the porous structure was achieved by Crossland et al., who developed mesoporous single crystals of TiO_2 anatase, which displayed one order of magnitude higher electron mobility at the same charge density compared to conventional mesoporous TiO_2 layers [30]. In ssDSC device they obtained a PCE of 3.1% using the D102 dye, for which a reported record value of 4.1% is reported (see Table 4.1).

Modification of the mesoporous TiO_2 by an ultrathin layer of Al_2O_3 was reported for ssDSC with CuI [31], CUSCN [32] and later also for spiro-OMeTAD as HTM [33]. The general trend found is that Al_2O_3 improves voltages by slowing

Table 4.1 Photovoltaic parameters of ssDSC devices based on the spiro-OMeTAD hole conductor with different additives and different dyes[a]

Year	Dye	Additives in HTM	*PCE* (%)	V_{OC} (V)	J_{SC} (mA cm^{-2})	*FF*	References
1998	N3	Sb, Li	0.7[b]	0.34[b]	0.3[b]	0.62[b]	[1]
2001	N719	Sb, Li, TBP	2.6	0.91	5.1	0.57	[39]
2005	Z907	Sb, Li, TBP	4.0	0.75	8.3	0.64	[23]
2005	D102	Sb, Li, TBP	4.1	0.87	7.7	0.62	[50]
2007	K68	Li, TBP	5.1	0.86	11.0	0.68	[42]
2011	C106	Li, TBP	5.0	0.85	8.3	0.71	[56]
2011	Y123	Co, Li, TBP	7.2	0.986	9.5	0.76	[58]
2015	LEG4	TeCA, Li, TBP	7.7	0.90	11.65	0.73	[64]
2016	XY2	FK209, Li, TBP	7.51	0.902	10.96	0.764	[61]

[a]Measured at 1 sun (100 mW cm^{-2} simulated sunlight with AM1.5G spectral distribution). [b]Light intensity: 9.4 mW cm^{-2}

down the electron (in TiO_2) to hole (in HTM) recombination, but it decreases the photocurrent density.

Relatively few studies have been performed on alternative metal oxide semiconductors in ssDSC. O'Regan et al. developed in the year 2000 a method for electrodeposition of a columnar ZnO structure, which was dye-sensitized and filled by CuSCN using again electrodeposition [34]. A solar cell performance of 1.5% was obtained. Plank et al. reported on ssDSCs based on ZnO nanowires grown using hydrothermal methods, resulting in ssDSC devices with 0.7% efficiency when an ultrathin MgO or ZrO_2 shell was applied [35]. Di Gao and co-workers developed TiO_2-coated ZnO nanowires, grown in a sequential fashion to achieve 50 micron length. In combination with the Z907 dye and a multistep HTM filling they reached a PCE 5.65% [36].

Tennakone et al. reported in 2001 on mesoporous SnO_2 with an ultrathin Al_2O_3 layers sensitized by a ruthenium dye [37]. In combination with CuI as hole conductor they obtained a photocurrent density of 1.7 mA cm^{-2} and an open-circuit voltage of 0.35 V. Docampo et al. reported an SnO_2-based ssDSC in combination with spiro-OMeTAD as HTM with an efficiency of 1.26% [38]. Important part of this work was the problem of contact between the SnO_2 electrode and the top Ag-contact, which could be avoided by an additional mesoporous Al_2O_3 layer on top the SnO_2 mesoporous film.

4.3.3 Dyes for ssDSC

There are several basic requirements for the sensitizing dyes in ssDSCs: (a) the excited state energy level of the dye molecule should appropriately match with the conduction band of the mesoporous oxide for efficient electron injection; (b) light excitation should accompany a fast and efficient electron transfer from the light harvesting moiety of the dye structure to the semiconductor oxide nanoparticle; (c) the dye should have a high extinction coefficient, since the mesoporous semiconductor layer is typically only 2 μm thick in ssDSC; (d) the highest occupied molecular orbitals (HOMO) of the dye should be sufficiently low so as to be efficiently regenerated by accepting electrons from the HTM; (e) the dye surface coverage should be high enough to physically isolate the HTM and the oxide in order to impede the electron recombination in the device; (f) dye molecules should be stable in the presence of light and air and at elevated temperatures.

4.3.3.1 Metal Coordination Complexes

Ruthenium complex-based dyes were commonly used in the beginning of the development of ssDSCs because of their widespread use in liquid electrolyte DSCs. They generally have a broad absorption spectrum, but low extinction coefficient. In one of the first report of ssDSCs, Bach et al. used the Ru-dye N3 (see Fig. 4.3) in

combination with the organic HTM spiro-OMeTAD and a PCE of 0.74% was obtained at an intensity of 9.4 $mWcm^{-2}$ [1]. Later, the partially deprotonated form of N3, namely N719 was used. By careful optimization of the additive *tert*-butylpyridine (TBP) a certified PCE of 2.56% was obtained for a solar cell device with an active area of 1.07 cm^2 [39]. The additive TBP plays a crucial role in the inhibition of the interfacial electron recombination. In 2005 the amphiphilic dye Z907 with hydrophobic tails was introduced in ssDSCs and a PCE of 4.0% was obtained [23]. The enhanced photovoltaic performance of ssDSCs was attributed to the dense packing of dyes on the surface of TiO_2 as well as the hydrophobic isolating chains which block the direct contact between spiro-OMeTAD and TiO_2. Inspired by this, the effect of the hydrocarbon chain lengths on the Ru-dye was systematically investigated, and it was confirmed that the hydrophobic chains act as insulating barrier between TiO_2 and HTM, and can efficiently suppress the interfacial electron recombination, as demonstrated by detailed studies via transient absorption results [40].

An ion-coordinating dye K51 was developed by Grätzel and co-workers by grafting triethylene oxide methyl ether on the bipyridine ligand (see Fig. 4.3) [41]. It is known that the conduction band of TiO_2 can be positively shifted by lithium ions physisorbed at the surface, which can cause a drop of open-circuit voltage of the devices. In the case of ion-coordinating dye, the ethylene oxide can form coordinative bonds with lithium ions to avoid its surface adsorption on TiO_2. By comparing with the reference dye Z907, the K51-sensitized ssDSCs showed a 20% increase in PCE (3.8%). K51 dye was further modified to K68 by adding heptyl groups to the ethylene oxide chains in order to enhance its hydrophobic properties [42]. By effective combination of the functions of ion coordination and hydrophobicity, the electron recombination in the devices based on K68 dye was significantly reduced and the open-circuit voltage was highly improved.

A thiophene group was added to the bipyridine ligand by Peng Wang and co-workers in order to increase the extinction coefficient of Z907, resulting in C101 with an enhanced performance of 4.5% compared to 2.9% for Z907 [43]. In CYC-B11 bithiophene groups were added (see Fig. 4.3), resulting in a good molar extinction coefficient ($2.42 \times 10^4\ M^{-1}cm^{-1}$ at 554 nm) and a high PCE for ssDSCs of 4.7% [44].

A different concept is to add an auxiliary electron donor to the Ru-dye molecule. This donor leads to fast intramolecular dye regeneration after electron injection, but may also improve light absorption of the complex. Thelakkat and co-workers developed the Ru-TPA-NCS dye and studied the intermolecular charge transfer steps [45, 46]. They found the induced spatial separation of the dye cation and electrons in TiO_2 after dye excitation retarded the electron recombination. The introduction of multifunctional electron–donor antenna groups on the dyes is a potentially interesting way to improve the performance of ssDSCs.

Zinc porphyrins are very promising for ssDSCs due to their very high extinction coefficients, broad spectral response and their ease of chemical modification. In 2005, Schmidt-Mende et al. achieved 3.0% efficiency using a zinc porphyrin dye [47]. In 2014, using a zinc porphyrin dye modified with both donor and accept

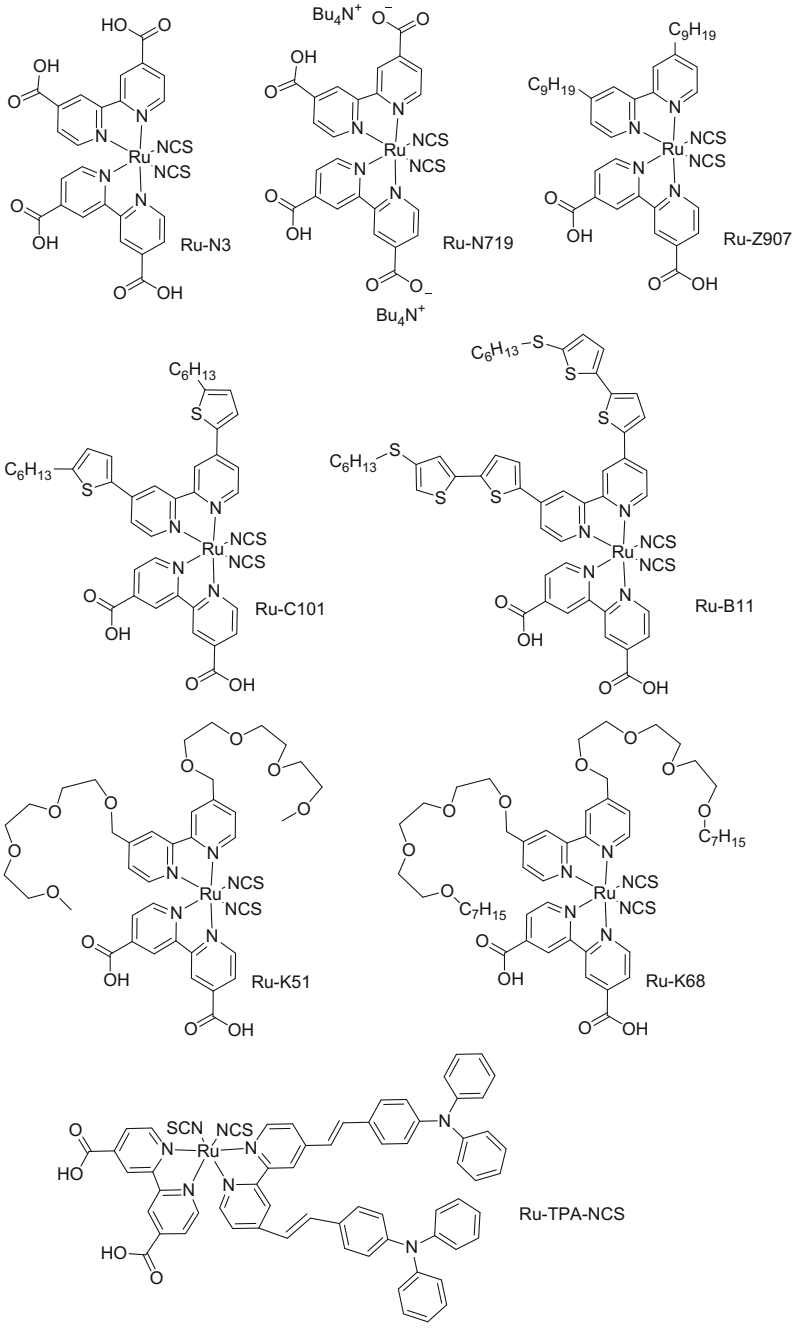

Fig. 4.3 Ruthenium-based sensitizers tested in ssDSC

moieties and appropriate alkoxy chains (Y350), a high PCE of 4.8% was reached in a ssDSC device using spiro-OMeTAD [48]. The performance was further improved to 6.4% by co-sensitization with the organic dye Y123. Nazeeruddin and co-workers developed new porphyrin dyes with a triaza-truxene donor for ssDSCs [49]. This donor exhibited a strong push–pull effect and an excellent light harvesting ability was obtained (extinction coefficient of 60,000 M^{-1} cm^{-1} at 650 nm). A high PCE of 5.1% was obtained by optimizing the coadsorber CDCA in the dye bath, compared to 1.6% without CDCA.

4.3.3.2 Organic Metal-Free Dyes

The majority of the organic dyes have higher molar extinction coefficients than the Ru-complexes. Organic dyes can be easily modified to tune their electronic properties. Many types of organic dye structures have been proposed and tested in ssDSCs. The indoline dye D102 (Fig. 4.4) was the first efficient organic sensitizer investigated for ssDSC in 2005. It exhibits a high extinction coefficient of 56,000 $M^{-1}cm^{-1}$ at 490 nm. A PCE of 4.1% was obtained by Schmidt-Mende et al. [50]. Another indoline dye, D149, was used as sensitizer in ssDSCs with CuI as HTM, exhibiting a PCE of 4.2% [51].

Hagfeldt and co-workers investigated a perylene dye ID176 for ssDSCs [52]. This dye showed a good absorption coefficient (25000 M^{-1} cm^{-1} at 590 nm) as well as a broad absorption spectrum. The devices with good performance, high photocurrent of 9 mA cm^{-2} and PCE of 3.2%, were obtained. An interesting fact of this dye is that it worked well in ssDSCs but not in liquid DSCs. By detailed time-resolved absorption spectroscopy measurements it was found that (a) the dye ID176 regeneration by solid-state spiro-OMeTAD was ultrafast, enabling the possibility of reductive quenching prior to injection of electrons to the TiO_2, and (b) lithium ions are very necessary for efficient electron injection in the device [53].

Triphenylamine (TPA)-based dyes are among the most popular dyes for dye-sensitized solar cells. They are generally used in Donor-π conjugated linker-Acceptor (D-π-A) dyes. In D-π-A dyes, the donor part usually consists of electron-rich groups; the π part contains a conjugated structure; the acceptor is generally an electron deficient moiety, and has an anchor group for binding on the surface of TiO_2. The electron density of the highest occupied molecular orbital (HOMO) of the dye molecule is mainly located in the donor part, whereas the density of the lowest unoccupied molecular orbital (LUMO) of the dye molecule is mostly located on the acceptor part. After the photoexcitation of the dye, the electrons subsequently transfer from the donor to the acceptor through the π-bridge. By this design, the electrons and holes are spatially separated in the dye molecule after light excitation, which could favor charge injection and dye regeneration. The properties of D-π-A dyes can be tuned by suitable combination of these three parts. TPA is the most popular donor group, while cyanoacetic acid is the most popular acceptor.

Sun, Nazeeruddin and co-workers developed a series of donor–linker–acceptor types of dyes, in order to study the effects of the alkyl chains in the donor part on ssDSCs performance [54]. The device based on D21L6 ($-OC_6H_{13}$ chains) and D25L6 ($-OC_{12}H_{25}$ chains) dyes demonstrated relatively high PCE of 4.5% and 4.0%, respectively, compared to a PCE of 3.3% for D5L6-sensitized ssDSCs. They found that the alkoxy chains have some influence on the light absorption, but a large effect on the recombination kinetics in the device. Hagfeldt and co-workers developed and investigated D35 with two bulky *o*, *p*-dibutoxyphenyl groups on the TPA moiety. The D35-based devices showed a promising PCE of 4.5%, due to improved electron lifetime in the device [55] (Fig. 4.5). Inclusion of a 4,4′-didodecyl-4H-cyclopenta[2,1-b:3,4-b′]dithiophene (CPDT) conjugated linker improves the absorption spectrum of TPA-dyes. Using such a modified dye a certified PCE of 6.1% was achieved by Cai et al [56]. Dualeh et al. systematically studied the influence of the donor of D-π-A dyes on the V_{oc} of the ssDSCs. Depending on dye design significant shifts in the conduction band edge and recombination kinetics could be found, which directly affect the V_{OC} of the device. A PCE 6.9% was achieved for Y123 [57]. Later, the PCE for this dye was improved to 7.2% [58].

Sellinger and co-workers developed a series of TPA-based D-π-A dyes with different types of alkyl chains on the dye for ssDSCs [59]. They obtained a PCE of 6.3% in ssDSCs based on dye WN3.1 and concluded from this work that the alkyl chains are key factors in the suppression of electron recombination in the devices. Interestingly, Abate et al. reported a "donor-free" organic dye, cyanoacrylic end-functionalized oligo (3-hexylthiophene) (oligo-3HT), on basis of a reference D-π-A dye MK2 (see Fig. 4.5) [60]. The V_{oc} and PCE were both enhanced in the device based on the donor-free dye oligo-3HT. They summarized that the enhancement was mainly attributed to long-lived dye cations for oligo-3HT dye. Very recently, Y. Zhang et al. developed a series of dyes featuring a benzothiadiazole (BTZ) auxiliary acceptor with the overall structure D-A-π-A. For the XY2

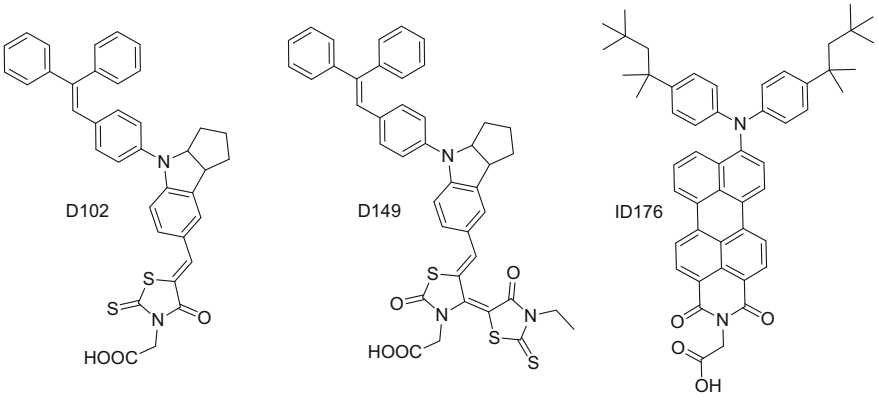

Fig. 4.4 Indoline sensitizers (D102, D149) and perylene dye (ID176) tested in ssDSC

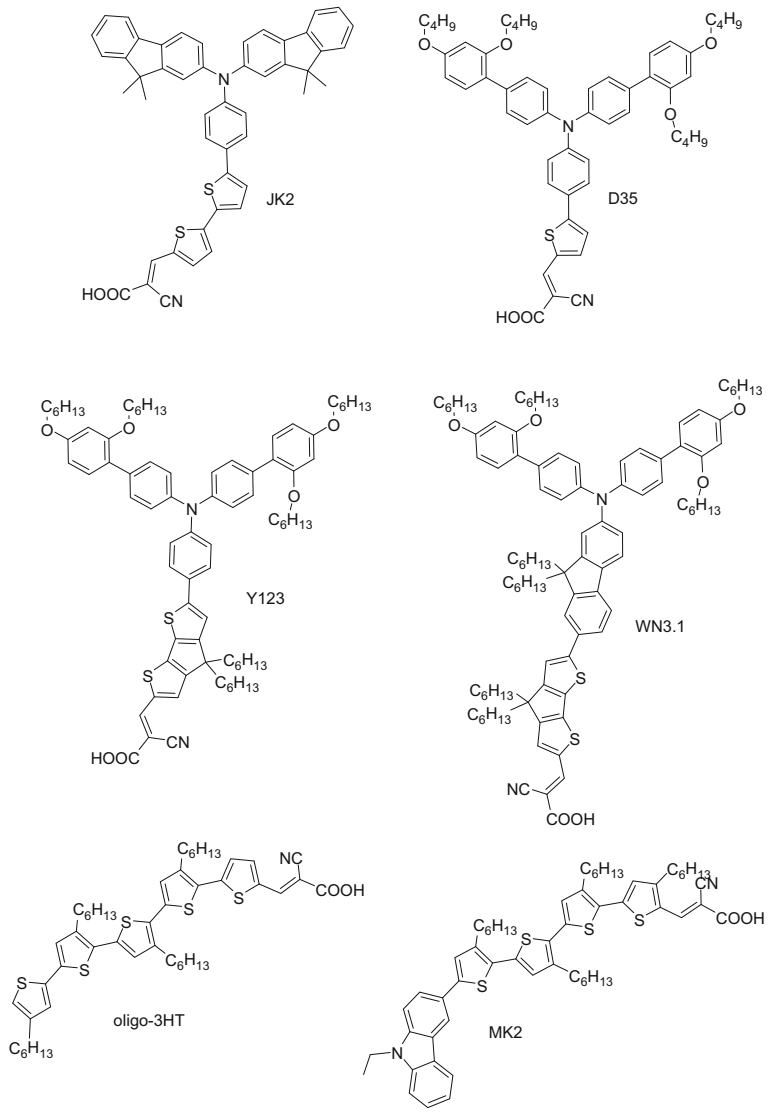

Fig. 4.5 Organic sensitizers for ssDSC with cyanoacrylic acid binding group

dye, having a high extinction coefficient of 6.66×10^4 $M^{-1}cm^{-1}$, and spiro-OMeTAD as HTM a high PCE of 7.5% was obtained [61].

Organic metal-free dyes with red or near-infrared (near-IR) absorption have also been employed in ssDSCs. For example, Grätzel and co-workers reported a near-IR absorbing squaraine dye, JD10, with strong absorption (672 nm, 250,000 M^{-1} cm^{-1}). By effectively reducing the dye aggregation via adding the coadsorber chenodeoxycholic acid (CDCA) in the dye bath, an efficiency of 3.2% was obtained [62].

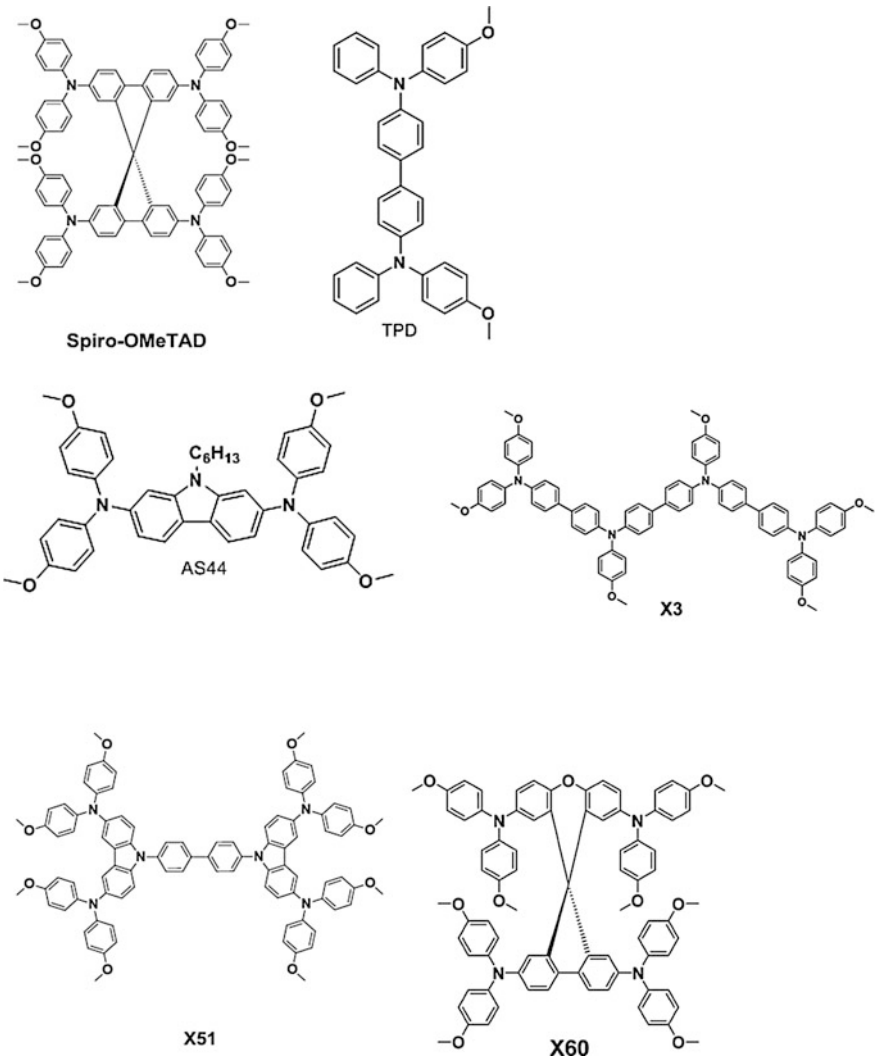

Fig. 4.6 Molecular structure of some small-molecular HTMs tested in ssDSC

Akkaya et al. developed a series of boron-dipyrromethene (BODIPY)-based molecules as red and near-IR sensitizers for ssDSCs [63]. The devices with these dyes exhibited relatively low incident photon-to-current efficiency (IPCE) in spite of their broad absorption spectra. Further study on the kinetics of the charge transfer at the interfaces is needed in order to further improve their performance. It should be noted that the red or near-IR absorbing dyes provide more choices of the colors in the solar cell (such as visibly colorless) and are important to broaden the overall absorption spectrum in co-sensitized systems.

4.3.4 Hole Transporting Materials

The hole transporting material transport the holes in the ssDSC device after the charge separation. There are several basic requirements for HTM to meet in order to perform efficiently in ssDSCs: (a) the HOMO energy level of the HTM should be located appropriately higher with respect to the dye in order to drive the hole transfer process; usually at least 200 mV potential difference between the dye and HTM is needed for efficient hole transfer; (b) the HTM is preferred to be transparent in order to avoid the light loss caused by the absorption of the HTM; (c) the HTM is expected to be amorphous so that it does not crystallize and thus hinder its pore infiltration; the glass transition temperature of HTM is a key factor which influences its thermal and photochemical stability; (d) the HTM should possess high hole mobility and conductivity in order to transport the charges efficiently. Based on these requirements, different types of HTMs have been developed, such as organic materials, metal-complexes, and inorganic materials.

4.3.4.1 Small Organic Molecular HTM

In the first report of ssDSCs, Haarer and co-workers developed a novel device concept with Ru-dye and an organic triphenyldiamine-based HTM TPD [65], (see Fig. 4.6) for molecular structure. The as-obtained device showed a PCE of 0.2%. However, its low glass transition temperature (T_g) of 62 °C could promote ease of crystallization and thus impair the pore filling. The low pore filling resulted in a poor contact between the HTM and dyes, which could be the reason for its low performance. In this respect, Bach et al. for the first time introduced Spiro-OMeTAD as HTM in ssDSC and the device showed much enhanced performance (PCE = 0.74%, at 9.4 $mWcm^{-2}$) [1]. This improved performance could be mainly attributed to its high T_g (120 °C) and good hole conductivity by chemical doping. After that, Thelakkat and co-workers synthesized a series of TPD-based molecules to study the influence of their hole mobilities on the solar cell performance [66]. They concluded that the effective mobility of the pristine HTM is the determining factor for the transport properties. Durrant et al. designed a series of triarylamine-based oligomers with different molecular weight and mobility as HTMs for ssDSCs [6]. They concluded that there was little correlation between the hole mobility and device performance. However, it was found that the photocurrent was directly dependent on the hole transfer yield, which was influenced by the pore filling fraction and the energy difference (thermodynamic driving force) for the interfacial hole transfer. The device based on a trimer of TPD gave a high PCE of over 2%. For the sake of increasing the range of amorphous small-molecule organic molecules available for the realization of ssDSCs, Chevrot and collaborators synthesized two hydrazine derivatives, 2CzMPH and 3TDPH, with biscarbazole and terthiophene groups, respectively [67]. Their relatively high glass transition temperatures at 80 °C for 3TDPH and 93 °C for 2CzMPH, and the observed high thermal stability make them

promising to be used in ssDSCs. The as-obtained device with the HTM 2CzMPH gave a V_{oc} of 500 mV and a J_{sc} of 0.42 mA cm^{-2}. Sellinger and co-workers developed a series of HTMs with varied glass transition temperature, molecular size, solubility, and melting point [68]. They exhibited relatively low melting points, making them possible to use with a melting infiltration method for the deposition in TiO_2 films. It is worth noting that the obtained device based on HTM AS44 outperformed spiro-OMeTAD-based ones, which could be mainly attributed to the high solubility of AS44 and thus high pore filling property.

Yang et al. found that a light soaking treatment was essential for the HTM MeO-TPD (N,N,N′,N′-tetrakis(4-methoxyphenyl)benzidine) to achieve the high efficiency ssDSC. Before light soaking PCE was 1.1% for LEG4-sensitized devices, but this increased with illumination time to 4.9%, matching the performance of similar devices with spiro-OMeTAD [69]. The electron lifetime for the light-soaked devices improved, and a mechanism based on Li^+ ion migration was proposed to explain this effect.

The Licheng Sun group has designed a series of triphenylamine-based HTMs to further improve the photovoltaic characteristics of ssDSCs. First, they synthesized simple triphenylamine-based oligomer X3, which gave high PCEs of 5.8% under 1 sun and 7.1% under 0.46 sun, respectively, in combination with the LEG4 dye [70]. Later, they synthesized a series of triphenylamine analogues in order to systematically study the influences of the molecular size, HOMO level and charge carrier mobility on the solar cell performance. By effective integration of the organic dye LEG4 and the HTMs, a PCE of 6% was obtained using X51 [71]. It was found that a minor change in the conjugation length and molecular configuration had a great impact on the molecular solubility, mobility, and T_g. These properties in turn affected the photovoltaic parameters of ssDSCs. Further improvement was achieved with X60 that comprises a low-cost spiro[fluorene-9, 90-xanthene] core to replace the expensive spiro-OMeTAD. Its performance matches that of spiro-OMeTAD and an impressive PCE of 7.3% was obtained [72] (Table 4.2).

Bouclé, Grazulevicius and co-workers presented a star-shape triphenylamine HTM, which demonstrated an excellent thermal stability (degradation temperature:

Table 4.2 Performance of ssDSCs devices based on small-molecule HTMs other than spiro-OMeTAD

Year	HTM	$\sigma \times 10^4$ S cm^{-1}	Dye	Dopant	*PCE* (%)	References
2004	AS44	0.2	Z907	TBPA, Li, TBP	2.26	[68]
2013	Carbazole2b	–	D102	Li, TBP	3.53	[74]
2013	MeO-TPD	–	LEG4	Li, TBP	4.9	[69]
2013	X3	1.99	LEG4	Li, TBP	5.8	[70]
2014	X51	1.05	LEG4	Li, TBP	6.0	[71]
2016	X60	1.1	LEG4	FK209, Li, TBP	7.3	[72]

510 °C) and high transparency [73]. However, this HTM exhibited a quite low PCE (PCE = 0.74%). The reason for this poor performance needs further study. Later, they presented a carbazole-based HTM for which they obtained a PCE of 3.5% using D102 dye, matching the performance of spiro-OMeTAD in their devices [74]. Robertson and co-workers developed a series of diacetylene-bridged triphenylamines with different functional side groups as HTMs for ssDSCs [75]. They found the difference in the electron-donating strength of functional groups had large influences on their electronic properties, such as the energy levels (HOMOs) and hole mobility, and thus the dye-HTM interactions. The key finding in this work was that the photocurrent generation was likely exponentially dependent on the dye-HTM energy offset, and the energy offset could affect the dye regeneration kinetics.

The relatively low hole conductivity is a potential limitation of the organic molecular HTM. Chemical doping is thus widely used to increase the hole conductivity of HTMs. In the first report of spiro-OMeTAD from Bach et al., a dopant $N(PhBr)_3SbCl_6$ was used to oxidize spiro-OMeTAD and increase the hole density in the HTM matrix [1]. Snaith et al. found that doping with lithium improves the hole mobility and conductivity of spiro-OMeTAD significantly [76]. Cappel et al. demonstrated the importance of oxygen in case of Li-doping, which was enhanced under illumination [77, 78]. The following mechanism was proposed by Abate et al. [78]:

$$\text{spiro-OMeTAD} + O_2 \leftrightarrow \text{spiro-OMeTAD}^{\cdot+} O_2^{\cdot-} \tag{4.1}$$

$$\text{spiro-OMeTAD}^{\cdot+} O_2^{\cdot-} + \text{LiTFSI} \rightarrow \text{spiro-OMeTAD}^{\cdot+} \text{TFSI}^{-} + Li_xO_y \tag{4.2}$$

where Li_xO_y stands for lithium oxide complexes. In the absence of LiTFSI, the concentration of oxidized spiro-OMeTAD was found to be negligible.

Burschka et al. developed a new dopant based on a cobalt (III) complex (FK102) for ssDSC [58]. The conductivity of spiro-OMeTAD could be well tuned by controlling the molar ratio of the dopant: the conductivity increased from 4.4×10^{-5} to 5.3×10^{-4} S cm^{-1} by addition of 1.0% FK102. By optimizing the doping concentration a very high PCE of 7.2% was reached [58]. Later, they synthesized several new cobalt complexes and studied the relationship between the structure of dopants and their properties. The redox potential could be adjusted by changing the ligands, while the solubility depends on the counter ions [79]. McGehee and co-workers found that doping by the doubly oxidized spiro-OMeTAD$(TFSI)_2$ salt was efficient [80]. There was no need for either oxygen or lithium salt addition, and PCE-values up to 4.7% using the WN3.1 dye. Xu et al. developed a photochemical doping method, where 1,1,2,2-tetrachloroethane (TeCA) was added to the spiro-OMeTAD spin coating solution, which was subsequently irradiated using 400 nm light [64]. This resulted in very effective doping, giving ssDSC devices with efficiencies up to 7.7% (Table 4.1).

4.3.4.2 Conducting Polymers as HTM

There are two types of ssDSCs based on polymer HTMs: These are either based on the deposition of polymers by solution casting or on in situ formation of the polymer, usually by photoelectrochemical polymerization (PEP). At first, the solution-casting type of polymer HTMs will be discussed. In the early 2000s, poly (thiophene)-based polymers have been widely studied by several groups. For example, the Sariciftci group applied the soluble poly(3-octylthiophene) (P3OT) as HTM in ssDSCs with N719 dye [81]. There was no underlayer used in that device, so the device suffered from the loss of photogenerated charges through fast recombination. Therefore, poor photovoltaic performance was observed with low PCE of <1%. Poly(3-hexylthiophene) (P3HT) became a popular solution-processed HTM since it has good solubility in organic solvent and outstanding hole conductivity. With P3HT enhanced PCE-values as high as 3–4% were achieved in combination with organic dyes, e.g., D131 [82]. However, the high molecular weight and large size create a pore filling problem for P3HT, especially in the case of thick TiO_2 films. The poor infiltration fraction decreases the dye regeneration yield and the extracted photocurrent. In this context, Johansson and co-workers combined P3HT and small-molecule TPAA together to form mixed HTMs for ssDSCs [83]. They found the dye regeneration kinetics to be significantly improved by this effective combination. Moreover, the hole conductivity in the HTM matrix was improved and the charge recombination within it was reduced, as evidenced by laser spectroscopy and transient photovoltage measurements.

The second type in situ techniques consist of solid-state polymerization (SSP) and photoelectrochemical polymerization. In SSP, a dibromo-monomer was first synthesized on the basis of the monomer by bromination reaction. Then the dibromo-monomer was spin coated on the dye-TiO_2 films, followed by a self-coupling reaction under a heating process. There is no need of additives during SSP. The formed polymer has a high conductivity due to the self-doping by Br anions during the SSP process. Kim et al. employed SSP to prepare PEDOT HTM and a PCE of over 5% was achieved in ssDSCs based on Ru-N719 dye [84]. Compared to PEP, the SSP method is relatively simple but it is difficult to control the reaction parameters. It is also usually a time-consuming process to prepare the required amount of polymer HTM.

The photoelectrochemical polymerization (PEP) method was first reported by the Yanagida group in Japan in 1997 [85]. They synthesized polypyrrole as HTM in situ in the mesoporous TiO_2 of an ssDSC with N3 as sensitizer, and obtained a PCE of 0.1%. The scheme of the PEP process is shown in Fig. 4.7. Generally, PEP can be used to polymerize the small monomers in the solution with the assistance of light and applied electrochemical potential. The process can be summarized as follows: (a) the incident light induces the dye excitation, which is followed by the charge separation at the interfaces; (b) the photoinduced electrons are injected into

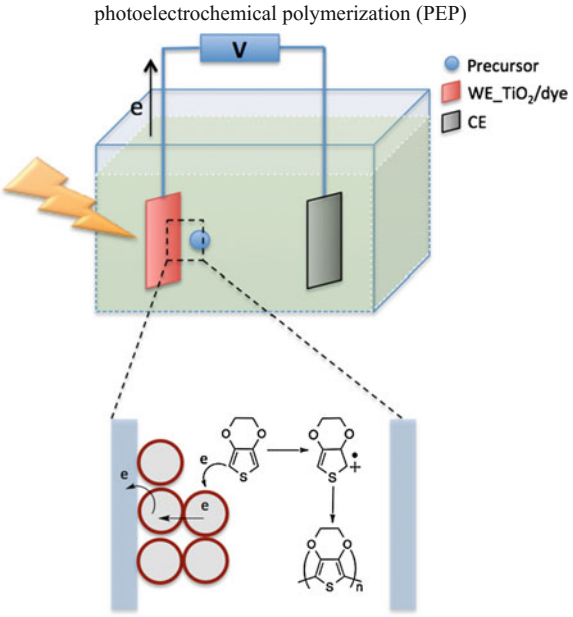

Fig. 4.7 Principle of photoelectrochemical polymerization for deposition of HTM in ssDSC

TiO_2 from the LUMO level of the excited dye; meanwhile the holes are transferred to the precursors in the solution from the HOMO of dye; (c) the precursors in the solution are oxidized by accepting the holes from the dyes and precursor radicals are formed; (d) the oligomers and polymers are generated by coupling reactions of the radicals. By using PEP, the polymer can be uniformly and homogeneously generated in the pores. The formed polymer is doped electrochemically and has high conductivity (Fig. 4.7).

Later, Yanagida and co-workers used the dimer bis-EDOT and trimer (tri-EDOT) as precursors to form the rather transparent polymer PEDOT [2, 86]. They investigated the effects of the additives (lithium salt and *tert*-butyl-pyridine) on the photovoltaic performance of the device, as learned from spiro-OMeTAD based ssDSCs [87]. The device based on PEP with LiTFSI showed a high PCE of 2.85%. The Bin Liu and co-workers used PEP with organic metal-free dyes, such as D149 and obtained a PCE of 6.1% [88]. Later, they obtained 7.1% using D102. This was achieved by selecting 670 nm light for the PEP procedure, leading to homogeneous excitation and PEDOT formation in the film [89].

The Hagfeldt and Jouini groups started to explore the aqueous PEP to prepare the polymer HTM instead of acetonitrile-based PEP as done before. In order to prepare bis-EDOT solution in water, Triton X-100 as a supporting colloidal medium was added in the water to improve the solubility of bis-EDOT. By using the aqueous PEP of bis-EDOT and organic dyes LEG4, a PCE of 5.2% was obtained, which is comparable with a PCE of 5.6% with organic PEP under similar conditions [90]. By further optimization a PCE of 7.1% was obtained for a LEG4-sensitized

Table 4.3 Efficiencies of ssDSCs devices based on conducting polymers prepared by photoelectrochemical polymerization

Year	Precursor of PEP	Dye	*PCE* (%)	CE	Electrolyte added	References
1998	Pyrrole	N3	0.1	Au	No	[85]
2003	bisEDOT	N719	0.53	Au/FTO	Yes	[84]
2007	bisEDOT	Z907	2.85	Au/FTO	Yes	[87]
2010	bisEDOT	D149	6.1	Au/FTO	Yes	[88]
2012	bisEDOT	D205	7.1	Au/FTO	Yes	[89]
2014	EDOP	D35	4.3	Ag	Yes	[92]
2015	bisEDOT(aq)	LEG4	5.2	Ag	Yes	[90]
2016	bisEDOT	LEG4	7.1	Ag	Yes	[91]

ssDSC [91]. The TiO_2 film thickness was about 6 μm, which is about 3 times larger than the optimum thickness for ssDSC with spiro-OMeTAD as HTM. Poly(3, 4-ethylenedioxypyrrole) (PEDOP) was also successfully applied by PEP, giving a PCE of 4.3% in combination with the D35 dye [92] (Table 4.3).

4.3.4.3 Inorganic Hole Conductors as HTM

Several solid inorganic materials have been tested as hole conductors in ssDSC. In 1995 Tennakone reported the very first ssDSC using CuI as a solid hole conductor [3]. CuI is a wide-band gap p-type semiconductor (E_g = 3.1 eV), with very high conductivities of about 1 S cm^{-1} and hole mobilities of 1 cm^2V^{-1} s^{-1} in spin coated films [93]. This is orders of magnitude higher than these parameters in organic HTMs. CuI can be deposited onto a dye-sensitized mesoporous TiO_2 using drop coating. It has, however, a problem in its tendency to form larger crystals over time, which degrades the contact with the dye molecules. A possible solution was addition of some ionic liquid additive, which reduces the CuI crystal size to about 10 nm [94]. Efficiencies of 3.0% were obtained using the N3 dye as sensitizer [94], and 4.2% using the D149 dye [51].

Tennakone et al. developed a new p-type semiconductor 4CuBr $3S(C_4H_9)_2$ and explored it as HTM for ssDSC [95]. They found this HTM, which has a polymeric nature, to be more stable than CuI, and obtained a J_{SC} of 4.3 mA cm^{-2} and a V_{OC} of 0.40 V in devices based on N3-sensitized TiO_2.

O'Regan and co-workers explored the p-type semiconductor CuSCN (E_g = 3.1 eV) as a hole conductor in ssDSC. In initial work CuSCN was deposited using electrodeposition [96, 97], while in later work solution deposition from n-propyl sulfide was used [98, 99]. Efficiencies reached about 2% using the N3 dye [99]. Later, Premalal et al. improved doping of CuSCN by introducing trimethylamine and obtained PCE of 3.4% using N719 dye [100].

Table 4.4 Record ssDSCs devices based on inorganic and metal complex hole transport materials

HTM	Dye	*PCE* (%)	V_{OC} (V)	J_{SC} (mA cm^{-2})	*FF*	References
CuI	D149	4.2	0.551	14.1	0.54	[51]
CuSCN	N719	3.39	0.578	10.52	0.556	[100]
$CsSnI_3$	N719	8.51	0.723	15.9	0.739	[102]
Cs_2SnI_6	N719, YD2-o-C8, RLC5	7.80	0.618	18.6	0.680	[104]
$Cu(dmp)_2$	LEG4	8.0	1.01	13.8	0.59	[105]
$Cu(tmbpy)_2$	Y123	11.3	1.08	13.87	0.75	[106]
Co (bpyPY4)	Y123	5.8	0.77	12.1	0.62	[107]

NiO has also been tested as a p-type semiconductor for ssDSC. Mesoporous TiO_2 was first covered with NiO and subsequently sensitized using N3 dye. Resulting ssDSCs gave a J_{SC} of 0.15 mA cm^{-2} and a V_{OC} of 480 mV [101].

Kanatzidis and co-workers reported the use of $CsSnI_3$ perovskite as HTM in ssDSC [102]. This material is a highly absorbing small band gap p-type semiconductor (E_g = 1.3 eV). They obtained devices with efficiencies up to 8.5%. It is, however doubtful, if $CsSnI_3$ is only acting as HTM is this case, since later work has demonstrated that solar cells in which $CsSnI_3$ was in direct contact with mesoporous TiO_2 gave high photocurrents [103]. The more stable Cs_2SnI_6 material also can act as HTM, and efficiencies of 7.8% were reported [104]. This too is a black semiconductor material (Table 4.4).

4.3.4.4 Metal Complexes as HTM

Recently, metal complexes have been introduced as a new type of HTM. They are based on earth abundant and very stable copper or cobalt complexes in solid-state DSC, resulting in record-breaking efficiencies for ssDSC, see Fig. 4.8. Especially copper complexes showed fast electron self-exchange rate for copper bipyridyl and phenanthroline based complexes. The copper dimethyl phenanthroline $[Cu(dmp)_2]^{2+/+}$ molecules were the first complexes to be used as HTM for ssDSCs. Freitag et al. prepared so-called zombie ssDSCs by evaporating the electrolyte in ambient conditions [105]. The resulting ssDSC showed a high short-circuit photocurrent (J_{SC}) of 13.8 mA cm^{-2}, exceeding the J_{SC} of a liquid electrolyte-based DSC (9.4 mA cm^{-2}) under the same conditions (1000 W m^{-2} AM1.5G irradiation) (Fig. 4.9). Very recently, further improvements were achieved with copper tetramethylbipyridyl complexes that gave zombie cells with PCE of 11.3%, J_{SC} of 13.87 mA cm^{-2} and V_{OC} of 1.08 V [106]. This is the first time that ssDSC have broken the important 10% limit. The copper complex-based HTMs have a bright red/orange color. Bach and co-workers found that some cobalt polypyridine

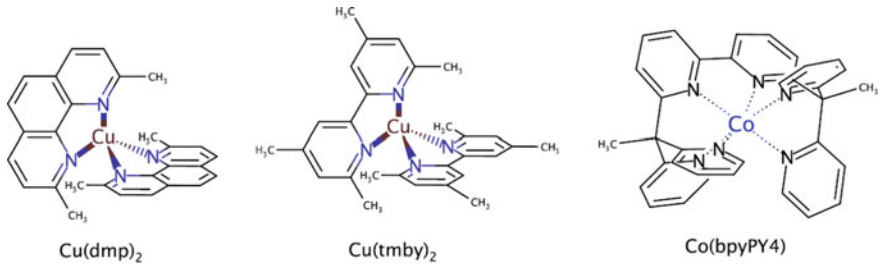

Fig. 4.8 Chemical structures of the transition metal-based HTMs for ssDSCs

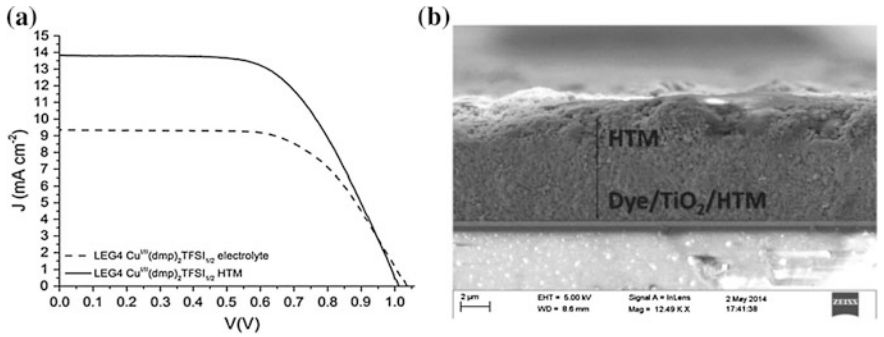

Fig. 4.9 **a** J–V characteristics of ssDSCs and DSCs employing $Cu(dmp)_2$ HTM or redox mediator to show the increase in photocurrent from liquid electrolyte to HTM. **b** Cross section by SEM of a representative working electrode with copper based HTM without PEDOT-coated FTO counter electrode (Reproduced from Ref. [105] with permission from The Royal Society of Chemistry)

complexes can also act as efficient HTMs [107]. A cobalt complex with hexadentate ligand Co(bpyPY4) yielded up to 5.8% efficiency in ssDSC with Y123 as dye, while the standard $Co(bpy)_3$ yielded only 0.2%. While photocurrent was good, 12.1 mA cm^{-2}, the voltage of 0.77 V was clearly lower than that of the copper complex-based HTMs. An advantage of the cobalt-based HTM is its low absorption in the visible range.

The preparation method for ssDSC with metal complex as HTM differs from other small-molecule HTM: it is based on the slow evaporation of a relatively large volume of solution inside a FTO-glass sandwich device structure, which sometimes needs to be repeated. More practical deposition methods for this HTM need to be developed.

4.3.5 Metal Electrode

The final part of the ssDSC is the metal electrode, which normally is deposited on top of the HTM layer by vacuum evaporation. Gold and silver are typically used,

where silver is preferred because of its better reflectivity and lower cost, whereas gold is preferred for better chemical stability. Gold has also the advantage that a contact through pinholes in the HTM layer are not very detrimental for the solar cell performance, while in case of silver stronger shunting is found.

Some alternatives to these metals have been explored. Single wall carbon nanotubes (SWCNT) have been transferred on top ssDSC with PEDOT as HTM by means of film transfer, pressing and solvent densification method [108]. The performance was good (PCE 4.8%), but slightly lower than comparative solar cell with evaporated Ag (5.2%).

Chiang et al. used sputtered ITO [109] electrodes in bifacial transparent ssDSC devices. A very thin gold layer (1 nm) was needed on top of the spiro-OMeTAD to present sputtering damage. Illumination from the ITO side led to somewhat lower PCE (1.5%) compared to FTO-side illumination (2.0%). A transparent electrode allows the ssDSC to be used in tandem solar cells [110].

Margulis et al. developed a transparent electrode for ssDSC based on PEDOT:PSS conducting polymer and Ag-nanowires, which were deposited by spray coating [111]. The PEDOT interfacial layer was needed to create an ohmic contact with the spiro-OMeTAD. The resulting electrode is highly transparent (transmittance 92%), has a low sheet resistance (18 Ω per square) and did not damage the underlying ssDSC. PCE-values of 3.6% were reached using D35 dye, only 0.1% less than that with evaporated Ag electrode.

Pressed graphite powder [99] or gold-coated FTO-glass [94] have been used in research, but do not provide a practical contact for actual solar cells.

4.4 Pore Filling with HTM and Its Effect on SsDSC Performance

Pore filling in ssDSC is a critical issue. Complete filling of the pores inside the sensitized mesoporous films with a solid HTM is not an easy task. Several studies were aimed at determining the degree of pore filling in ssDSC, using a range of different methods. Snaith et al. estimated the degree of pore filling by spiro-OMeTAD from comparison of the thicknesses of overstanding HTM layers on substrates either with or without mesoporous film (both with a dense underlayer of dye-sensitized TiO_2). They calculated a pore filling fractions of 0.85 and 0.44 for 2 μm and 5.7 μm thick mesoporous films (with 60% porosity), respectively, when spin coated using the same conditions (15vol.% HTM in spin coating solution) [11]. Ding et al. quantified pore filling of spiro-OMeTAD in mesoporous TiO_2 films using XPS depth profiling and UV–vis absorption [112]. XPS profiling demonstrated that spiro-OMeTAD was uniformly distributed within the mesoporous film. All the spiro-OMeTAD in the mesoporous film with overstanding layer

(with thicknesses determined by SEM) was dissolved in a fixed amount of solvent and its concentration was determined by UV-vis. From this, the HTM pore filling fraction was calculated to be 60–65% under optimal conditions.

Docampo et al. developed an optical method to determine the degree of pore filling of mesoporous films with HTM. This method is based on the observation of interference fringes in the transmission spectra in the visible and near-infrared region, from which an effective refractive index can be determined, which is directly related to the pore filling fraction [113]. For an optimized film they determined the following volume fractions: TiO_2 52%, dye 4%, spiro-OMeTAD 33%, and air 10%.

Cappel et al. used photoinduced absorption spectroscopy to determine whether dye molecules were regenerated by the HTM in mesoporous TiO_2 films with different thicknesses and using different concentrations of HTM in the spin coating solution [114]. Their observation was that in all cases no signal of the oxidized dye could be found, indicating good dye regeneration. The conclusion was that HTM was well coated onto the dye monolayer, even when the pores were only filled to a small fraction.

An alternative, potentially very suitable method to achieve good HTM infiltration in the mesoporous films is melt-infiltration [115–117]. This has, however, to date not led to very high device efficiencies. Fredin et al. used thermally melted (at 255 °C) TPD-based HTM into dye/TiO_2 films and accomplished good pore filling as evidenced by SEM images [116]. However, the temperature used was high, probably exceeding the degradation temperatures of the dyes. The same group tested 4-((diethyl-amino)benzaldehyde-1,1)-diphenyl-hydrazone as HTM with a lower melting point (<100 °C). A 35% increase in maximum IPCE was obtained in comparison to the earlier work. One reason is the relatively high temperature needed for this procedure for conventional organic HTM such as spiro-OMeTAD, can cause damage to the system. Baker and co-workers designed a TPD-based HTM with a very low T_g of 20 °C for ssDSCs [118]. They applied a heat-assisted method after the spin coating of HTM solution. It was found that the performance of the devices was dramatically improved after the heat treatment. This great enhancement was attributed to the increased pore filling fraction and thus improved dye regeneration yield. Bailie et al. obtained 100% infiltration of spiro-OMeTAD in mesoporous TiO_2 by conventional spin coating of the spiro solution, followed by heating to 150 °C, which is above the glass transition temperature [115]. They found that the dye was intact, but that the additive *tert*-butylpyridine had evaporated, which led to poor solar cell results.

The most important factor for HTM pore filling is that all dye molecules are contacted by the HTM and that the HTM forms a continuous network. Melas-Kyriazi et al. determined solar cell parameters, recombination kinetics and hole injection efficiency as function of spiro-OMeTAD pore filling fraction (PFF) [119]. The hole injection efficiency to spiro-OMeTAD (i.e., the dye regeneration efficiency) ranged from 57 to 94% for a PFF from 26 and 65%. At the same

time the electron/hole recombination lifetime increased almost linearly from 1.7 to 10 ms. The calculated carrier diffusion length increase from 2 to 7 μm for the same PFF range.

4.5 Variations of the SsDSC

P-type ssDSC P-type alternatives to the standard ssDSC have been developed by using a dye-sensitized NiO p-type electrode in combination with an organic electron transporting material. Tian and co-workers [120] used NiO sensitized by the organic triphenylamine-based P1 dye and phenyl-C61-butyric acid methyl ester (PCBM) as electron transported, and obtained devices with a good open-circuit voltage (0.62 V), but with a very low photocurrent of 50 μA cm^{-2}. This was attributed to the short lifetime of the reduced P1 dye after hole injection into the NiO, or slow dye regeneration by the PCBM. Very recently, Pham et al. obtained significantly improved photocurrent of 0.45 mA cm^{-2} in a similar system, but using diketopyrrolopyrrole (DPP)-based dyes [121].

Excitonic enhancement by light absorption in the HTM In order to improve light absorption in the relatively thin sensitized mesoporous TiO_2 film of the ssDSC, light absorbers can be added to the HTM matrix. Mor et al. added a pyran dye in the spiro-OMeTAD matrix that was infiltrated into a squaraine (SQ) dye-sensitized TiO_2 nanotube array electrode [122]. They demonstrated a significant enhancement in the light harvesting and photocurrent generation of solid-state dye-sensitized solar cells due to Förster resonance energy transfer (FRET) from the pyran dye to the SQ dye. The IPCE at 480 nm was about 25% in the optimized cells, compared to 3% in devices without the energy accepting SQ dye. The PCE was 1.6% at best.

Unger et al. used a light-absorbing HTM tris(thienyl-vinyl-thienyl)triphenylamine (TVT) that could transfer excitation energy to a squaraine dye bound to TiO_2. They determined that of the IPCE of 35% at 430 nm 6% was due to exciton transfer to SQ dye, while the remaining 29% was due to direct electron injection from TVT into TiO_2 [123]. Moon et al. used the polymer P3HT as the light-absorbing HTM in combination with the porphyrin dye YD2 [124]. They obtained a very high photocurrent of 12.1 mA cm^{-2}, compared to only 2.56 mA cm^{-2} when spiro-OMeTAD was used as HTM. A large part of the photocurrent was attributed to FRET form P3HT to YD2 dye.

Tandem ssDSC Bruder et al. fabricated tandem solar cell combining a solid-state dye-sensitized cell with bulk heterojunction solar cell, achieving 6.0% efficiency [125]. The ssDSC top cell had 900 nm mesoporous TiO_2 and was sensitized using D102, while the bulk heterojunction was composed of ZnPc/C60 prepared by vacuum deposition. A recombination layer of 2 nm Ag was located in between the two cells. Both individual cells gave about 4% efficiency. A tandem solar cell using 2 stacked ssDSC devices was prepared by Chiang et al. [110]. The top cell was sensitized using Z907, while the bottom cell was sensitized using the

squaraine dye B1. Both cells had a sputtered ITO counter electrode and were connected in parallel, resulting in a PCE of 3.1%, which was close to the sum of PCE of the individual cells (2.6% for Z907 and 0.58% for B1).

4.6 Future Outlook

The practical advantages of ssDSC compared to the liquid analogues are obvious given the simplifications of encapsulation both externally (avoiding leakage of a volatile solvent) and internally (no need to protect electrical interconnects for large scale modules). However, other problems arise such as creating a strong contact between the HTM and the dye for efficient regeneration of the oxidized (or excited dye in a reductive quenching mechanism) and efficient filling of the mesoporous electrode with the HTM to allow efficient hole transport to the cathode. The former problem has been elegantly solved by in situ photopolymerization of monomers in an electrolyte solution by the dye-sensitized photoelectrode. The oxidation of the monomer forming the polymer is made by the photooxidized dye automatically forming an intimate dye/polymer connection. So far mainly PEDOT has been studied, but with the development of with large variations of redox potentials and with the possibility to include monomer units as functional groups of the dye this development of ssDSC is definitely interesting to pursue. The latter problem of pore filling, which leads to the use of relatively thin mesoporous films, can at least partly find solutions by the use of dyes with high extinction coefficients and the development of different nanostructures of the oxide films such as nanorods and tubes that can efficiently facilitate the pore filling process.

An intriguing opportunity for ssDSC is to minimize the driving force for the regeneration of the oxidized dyes. Thus, HTMs with relatively high electrochemical potential (high work function) can be used resulting in a high photovoltage. The fundamental underlying principles are the one-electron transfer process as compared to two electrons for the I^-/I_3^- redox systems for liquid DSCs avoiding potential losses to form intermediates, and a low reorganization energy. Thus, fast regeneration and high photovoltages have, for example, been obtained with spiro-OMeTAD as HTM. With the very rapid development of HTMs for perovskite solar cells there will also be a plethora of compounds to explore for ssDSCs with the potential to improve for example photovoltage by identifying HTMs with optimized structures and work functions for dye regeneration.

Recently, Cu phenanthroline complexes were applied in the solid phase as efficient molecular hole transporting material for ssDSC. The copper complexes have a distorted tetragonal geometry, in which the structural change in confirmation between the copper (I) and copper (II) complex is minimized. It has a high self-exchange rate for electron transfer, which makes the required driving force for dye regeneration low and an efficient charge transfer has been obtained at only 0.2 V. This new copper complex-based HTM devices have superseded the

performance of spiro-OMeTAD as HTM. The demonstration of a 11.3% efficient ssDSC has broken the psychologically important 10% limit. This opens up a new avenue to develop solid-state DSSC by new molecularly engineering of high hole mobility transition metal complexes. The redox energy of these HTMs can be easily tuned by varying the electron density of the substituents on the 2,2′-bipyridine or 1,10-phenanthroline ligands. Finally, the Cu complex-based ssDSC, as well as liquid DSC, show excellent power output at indoor light conditions. In comparison with GaAs solar cells under indoor light, the DSCs give higher power output indicating the potential that Cu complex based DSCs can be the premium technology for consumer electronic applications.

References

1. Bach U, Lupo D, Comte P, Moser JE, Weissortel F, Salbeck J, Spreitzer H, Grätzel M (1998) Solid-state dye-sensitized mesoporous TiO_2 solar cells with high photon-to-electron conversion efficiencies. Nature 395(6702):583–585
2. Saito Y, Kitamura T, Wada Y, Yanagida S (2002) Poly(3, 4-ethylenedioxythiophene) as a hole conductor in solid state dye sensitized solar cells. Synth Metals 131(1–3):185–187. doi:10.1016/s0379-6779(02)00198-4
3. Tennakone K, Kumara G, Kumarasinghe AR, Wijayantha KGU, Sirimanne PM (1995) A dye-sensitized nano-porous solid-state photovoltaic cell. Semicond Sci Technol 10 (12):1689–1693. doi:10.1088/0268-1242/10/12/020
4. Listorti A, O'Regan B, Durrant JR (2011) Electron transfer dynamics in dye-sensitized solar cells. Chem Mater 23(15):3381–3399. doi:10.1021/cm200651e
5. Bach U, Tachibana Y, Moser JE, Haque SA, Durrant JR, Grätzel M, Klug DR (1999) Charge separation in solid-state dye-sensitized heterojunction solar cells. J Am Chem Soc 121 (32):7445–7446
6. Kroeze JE, Hirata N, Schmidt-Mende L, Orizu C, Ogier SD, Carr K, Gratzel M, Durrant JR (2006) Parameters influencing charge separation in solid-state dye-sensitized solar cells using novel hole conductors. Adv Funct Mater 16(14):1832–1838. doi:10.1002/adfm.200500748
7. Haque SA, Park T, Holmes AB, Durrant JR (2003) Transient optical studies of interfacial energetic disorder at nanostructured dye-sensitised inorganic/organic semiconductor heterojunctions. ChemPhysChem 4(1):89. doi:10.1002/cphc.200390014
8. Cappel UB, Feldt SM, Schoneboom J, Hagfeldt A, Boschloo G (2010) The influence of local electric fields on photoinduced absorption in dye-sensitized solar cells. J Am Chem Soc 132 (26):9096–9101
9. Mozer AJ, Panda DK, Gambhir S, Winther-Jensen B, Wallace GG (2010) Microsecond dye regeneration kinetics in efficient solid state dye-sensitized solar cells using a photoelectrochemically deposited PEDOT hole conductor. J Am Chem Soc 132(28):9543–9545. doi:10.1021/ja1026453
10. Kruger J, Plass R, Grätzel M, Cameron PJ, Peter LM (2003) Charge transport and back reaction in solid-state dye-sensitized solar cells: a study using intensity-modulated photovoltage and photocurrent spectroscopy. J Phys Chem B 107(31):7536–7539
11. Snaith HJ, Humphry-Baker R, Chen P, Cesar I, Zakeeruddin SM, Grätzel M (2008) Charge collection and pore filling in solid-state dye-sensitized solar cells. Nanotechnology 19 (42):424003

12. Docampo P, Guldin S, Steiner U, Snaith HJ (2013) Charge transport limitations in self-assembled TiO_2 photoanodes for dye-sensitized solar cells. J Phys Chem Lett 4(5):698–703. doi:10.1021/jz400084n
13. Boschloo G, Marinado T, Nonomura K, Edvinsson T, Agrios AG, Hagberg DP, Sun L, Quintana M, Karthikeyan CS, Thelakkat M, Hagfeldt A (2008) A comparative study of a polyene-diphenylaniline dye and Ru(dcbpy)(2)(NCS)(2) in electrolyte-based and solid-state dye-sensitized solar cells. Thin Solid Films 516(20):7214–7217
14. Cappel U (2011) Characterisation of organic dyes for solid state dye-sensitized solar cells. PhD thesis Uppsala University, Sweden
15. Fabregat-Santiago F, Bisquert J, Cevey L, Chen P, Wang M, Zakeeruddin SM, Grätzel M (2008) Electron transport and recombination in solid-state dye solar cell with spiro-OMeTAD as hole conductor. J Am Chem Soc 131(2):558
16. Snaith HJ, Grätzel M (2007) Electron and hole transport through mesoporous TiO_2 infiltrated with spiro-MeOTAD. Adv Mater 19(21):3643–3647
17. Hagfeldt A, Boschloo G, Sun L, Kloo L, Pettersson H (2010) Dye-sensitized solar cells. Chem Rev 110(11):6595
18. Peng B, Jungmann G, Jäger C, Haarer D, Schmidt H-W, Thelakkat M (2004) Systematic investigation of the role of compact TiO_2 layer in solid state dye-sensitized TiO_2 solar cells. Coord Chem Rev 248:1479–1489
19. Lellig P, Niedermeier MA, Rawolle M, Meister M, Laquai F, Muller-Buschbaum P, Gutmann JS (2012) Comparative study of conventional and hybrid blocking layers for solid-state dye-sensitized solar cells. Phys Chem Chem Phys 14(5):1607–1613. doi:10.1039/c2cp23026g
20. Fang YL, Wang XM, Ai XL, Huang JG, Wang Q, Wu T (2014) Sputtered TiOx thin film as compact layer for solid-state dye sensitized solar cells. Ceram Int 40(10):15941–15949. doi:10.1016/j.ceramint.2014.07.122
21. Jiang CY, Koh WL, Leung MY, Chiam SY, Wu JS, Zhang J (2012) Low temperature processing solid-state dye sensitized solar cells. Appl Phys Lett 100(11). doi:10.1063/1.3693399
22. Kavan L, Tetreault N, Moehl T, Gratzel M (2014) Electrochemical characterization of TiO_2 blocking layers for dye-sensitized solar cells. J Phys Chem C 118(30):16408–16418. doi:10.1021/jp4103614
23. Schmidt-Mende L, Zakeeruddin SM, Gratzel M (2005) Efficiency improvement in solid-state-dye-sensitized photovoltaics with an amphiphilic Ruthenium-dye. Appl Phys Lett 86(1). doi:10.1063/1.1844032
24. Fang YL, Wang Q, Huang JG, Wu T (2015) Enhanced pore filling of spiro-OMeTAD by enlarging the porosity of TiO_2 films and its effects on the photovoltaic performance of ss-DSCs. Appl Phys a-Mater Sci Processing 118(4):1339–1346. doi:10.1007/s00339-014-8883-4
25. Chen P, Brillet J, Bala H, Wang P, Zakeeruddin SM, Gratzel M (2009) Solid-state dye-sensitized solar cells using TiO_2 nanotube arrays on FTO glass. J Mater Chem 19(30):5325–5328. doi:10.1039/b905196a
26. Wang MK, Bai J, Le Formal F, Moon SJ, Cevey-Ha L, Humphry-Baker R, Gratzel C, Zakeeruddin SM, Gratzel M (2012) Solid-state dye-sensitized solar cells using ordered TiO_2 nanorods on transparent conductive oxide as photoanodes. J Phys Chem C 116(5):3266–3273. doi:10.1021/jp209130x
27. Zhang W, Zhu R, Ke L, Liu XZ, Liu B, Ramakrishna S (2010) Anatase mesoporous TiO_2 nanofibers with high surface area for solid-state dye-sensitized solar cells. Small 6(19):2176–2182. doi:10.1002/smll.201000759
28. Crossland EJW, Kamperman M, Nedelcu M, Ducati C, Wiesner U, Smilgies DM, Toombes GES, Hillmyer MA, Ludwigs S, Steiner U, Snaith HJ (2009) A bicontinuous double gyroid hybrid solar cell. Nano Lett 9(8):2807–2812. doi:10.1021/nl803174p

29. Docampo P, Guldin S, Stefik M, Tiwana P, Orilall MC, Huttner S, Sai H, Wiesner U, Steiner U, Snaith HJ (2010) Control of solid-state dye-sensitized solar cell performance by block-copolymer-directed TiO_2 synthesis. Adv Funct Mater 20(11):1787–1796. doi:10.1002/adfm.200902089
30. Crossland EJW, Noel N, Sivaram V, Leijtens T, Alexander-Webber JA, Snaith HJ (2013) Mesoporous TiO_2 single crystals delivering enhanced mobility and optoelectronic device performance. Nature 495(7440):215–219. doi:10.1038/nature11936
31. Zhang XT, Liu HW, Taguchi T, Meng QB, Sato O, Fujishima A (2004) Slow interfacial charge recombination in solid-state dye-sensitized solar cell using Al_2O_3-coated nanoporous TiO_2 films. Solar Energy Mater Solar Cells 81(2):197–203. doi:10.1016/j.solmat.2003.11.005
32. O'Regan BC, Scully S, Mayer AC, Palomares E, Durrant J (2005) The effect of Al_2O_3 barrier layers in TiO_2/Dye/CuSCN photovoltaic cells explored by recombination and DOS characterization using transient photovoltage measurements. J Phys Chem B 109(10):4616–4623. doi:10.1021/jp0468049
33. Brennan TP, Bakke JR, Ding IK, Hardin BE, Nguyen WH, Mondal R, Bailie CD, Margulis GY, Hoke ET, Sellinger A, McGehee MD, Bent SF (2012) The importance of dye chemistry and $TiCl_4$ surface treatment in the behavior of Al_2O_3 recombination barrier layers deposited by atomic layer deposition in solid-state dye-sensitized solar cells. Phys Chem Chem Phys 14(35):12130–12140. doi:10.1039/c2cp42388j
34. O'Regan B, Schwartz Daniel T, Zakeeruddin SM, Grätzel M (2000) Electrodeposited nanocomposite n-p heterojunctions for solid-state dye-sensitized photovoltaics. Adv Mater 12(17):1263–1267
35. Plank NOV, Howard I, Rao A, Wilson MWB, Ducati C, Mane RS, Bendall JS, Louca RRM, Greenham NC, Miura H, Friend RH, Snaith HJ, Welland ME (2009) Efficient ZnO nanowire solid-state dye-sensitized solar cells using organic dyes and core-shell nanostructures. J Phys Chem C 113(43):18515–18522. doi:10.1021/jp904919r
36. Xu CK, Wu JM, Desai UV, Gao D (2012) High-efficiency solid-state dye-sensitized solar cells based on TiO_2-coated ZnO nanowire arrays. Nano Lett 12(5):2420–2424. doi:10.1021/nl3004144
37. Tennakone K, Perera VPS, Kottegoda IRM, De Silva LAA, Kumara G, Konno A (2001) Dye-sensitized solid-state photovoltaic cells: Suppression of electron-hole recombination by deposition of the dye on a thin insulating film in contact with a semiconductor. J Electron Mater 30(8):992–996. doi:10.1007/bf02657723
38. Docampo P, Snaith HJ (2011) Obviating the requirement for oxygen in SnO_2-based solid-state dye-sensitized solar cells. Nanotechnology 22(22). doi:10.1088/0957-4484/22/22/225403
39. Krüger J, Plass R, Cevey L, Piccirelli M, Grätzel M (2001) High efficiency solid-state photovoltaic device due to inhibition of interface charge recombination. Appl Phys Lett 79(13):2085–2087
40. Schmidt-Mende L, Kroeze JE, Durrant JR, Nazeeruddin MK, Gratzel M (2005) Effect of hydrocarbon chain length of amphiphilic ruthenium dyes on solid-state dye-sensitized photovoltaics. Nano Lett 5(7):1315–1320. doi:10.1021/nl050555y
41. Kuang DB, Wang P, Ito S, Zakeeruddin SM, Gratzel M (2006) Stable mesoscopic dye-sensitized solar cells based on tetracyanoborate ionic liquid electrolyte. J Am Chem Soc 128(24):7732–7733
42. Kuang D, Klein C, Snaith HJ, Humphry-Baker R, Zakeeruddin SM, Gratzel M (2008) A new ion-coordinating ruthenium sensitizer for mesoscopic dye-sensitized solar cells. Inorg Chim Acta 361(3):699–706. doi:10.1016/j.ica.2007.05.031
43. Wang MK, Moon SJ, Zhou DF, Le Formal F, Cevey-Ha NL, Humphry-Baker R, Gratzel C, Wang P, Zakeeruddin SM, Gratzel M (2010) Enhanced-light-harvesting amphiphilic ruthenium dye for efficient solid-state dye-sensitized solar cells. Adv Funct Mater 20(11):1821–1826. doi:10.1002/adfm.200902396

44. Chen CY, Wang MK, Li JY, Pootrakulchote N, Alibabaei L, Ngoc-le CH, Decoppet JD, Tsai JH, Gratzel C, Wu CG, Zakeeruddin SM, Gratzel M (2009) Highly efficient light-harvesting ruthenium sensitizer for thin-film dye-sensitized solar cells. ACS Nano 3 (10):3103–3109. doi:10.1021/nn900756s
45. Handa S, Wietasch H, Thelakkat M, Durrant JR, Haque SA (2007) Reducing charge recombination losses in solid state dye sensitized solar cells: the use of donor-acceptor sensitizer dyes. Chem Commun 17:1725–1727. doi:10.1039/b618700e
46. Karthikeyan CS, Wietasch H, Thelakkat M (2007) Highly efficient solid-state dye-sensitized TiO_2 solar cells using donor-antenna dyes capable of multistep charge-transfer cascades. Adv Mater 19(8):1091–1095. doi:10.1002/adma.200601872
47. Schmidt-Mende L, Campbell WM, Wang Q, Jolley KW, Officer DL, Nazeeruddin MK, Grätzel M (2005) Zn-porphyrin-sensitized nanocrystalline TiO_2 heterojunction photovoltaic cells. ChemPhysChem 6(7):1253–1258. doi:10.1002/cphc.200500147
48. Yi C, Giordano F, Cevey-Ha N-L, Tsao HN, Zakeeruddin SM, Grätzel M (2014) Influence of structural variations in push-pull zinc porphyrins on photovoltaic performance of dye-sensitized solar cells. Chemsuschem 7(4):1107–1113. doi:10.1002/cssc.201301271
49. Qin P, Sanghyun P, Dar MI, Rakstys K, ElBatal H, Al-Muhtaseb SA, Ludwig C, Nazeeruddin MK (2016) Weakly conjugated hybrid zinc porphyrin sensitizers for solid-state dye-sensitized solar cells. Adv Funct Mater 26(30):5550–5559. doi:10.1002/adfm.201601120
50. Schmidt-Mende L, Bach U, Humphry-Baker R, Horiuchi T, Miura H, Ito S, Uchida S, Gratzel M (2005) Organic dye for highly efficient solid-state dye-sensitized solar cells. Adv Mater 17(7):813
51. Konno A, Kumara GRA, Kaneko S, Onwona-Agyeman B, Tennakone K (2007) Solid-state solar cells sensitized with indoline dye. Chem Lett 36(6):716–717. doi:10.1246/cl.2007.716
52. Cappel UB, Karlsson MH, Pschirer NG, Eickemeyer F, Schöneboom J, Erk P, Boschloo G, Hagfeldt A (2009) A broadly absorbing perylene dye for solid-state dye-sensitized solar cells. J Phys Chem C 113(33):14595
53. Cappel UB, Smeigh AL, Plogmaker S, Johansson EMJ, Rensmo H, Hammarström L, Hagfeldt A, Boschloo G (2011) Characterization of the interface properties and processes in solid state dye-sensitized solar cells employing a perylene sensitizer. J Phys Chem C 115 (10):4345–4358
54. Moon SJ, Yum JH, Humphry-Baker R, Karlsson KM, Hagberg DP, Marinado T, Hagfeldt A, Sun LC, Gratzel M, Nazeeruddin MK (2009) Highly efficient organic sensitizers for solid-state dye-sensitized solar cells. J Phys Chem C 113(38):16816–16820. doi:10.1021/jp9033722
55. Jiang X, Karlsson KM, Gabrielsson E, Johansson EMJ, Quintana M, Karlsson M, Sun L, Boschloo G, Hagfeldt A (2011) Highly efficient solid-state dye-sensitized solar cells based on triphenylamine dyes. Adv Funct Mater 21(15):2944–2952
56. Cai N, Moon SJ, Cevey-Ha L, Moehl T, Humphry-Baker R, Wang P, Zakeeruddin SM, Gratzel M (2011) An organic D-pi-A dye for record efficiency solid-state sensitized heterojunction solar cells. Nano Lett 11(4):1452–1456. doi:10.1021/nl104034e
57. Dualeh A, De Angelis F, Fantacci S, Moehl T, Yi CY, Kessler F, Baranoff E, Nazeeruddin MK, Gratzel M (2012) Influence of donor groups of organic D-pi-A dyes on open-circuit voltage in solid-state dye-sensitized solar cells. J Phys Chem C 116(1):1572–1578. doi:10.1021/jp209691e
58. Burschka J, Dualeh A, Kessler F, Baranoff E, Cevey-Ha N-L, Yi C, Nazeeruddin MK, Grätzel M (2011) Tris(2-(1H-pyrazol-1-yl)pyridine)cobalt(III) as p-type dopant for organic semiconductors and its application in highly efficient solid-state dye-sensitized solar cells. J Am Chem Soc 133(45):18042–18045
59. Nguyen WH, Bailie CD, Burschka J, Moehl T, Gratzel M, McGehee MD, Sellinger A (2013) Molecular engineering of organic dyes for improved recombination lifetime in solid-state dye-sensitized solar cells. Chem Mater 25(9):1519–1525. doi:10.1021/cm3036357

60. Abate A, Planells M, Hollman DJ, Stranks SD, Petrozza A, Kandada ARS, Vaynzof Y, Pathak SK, Robertson N, Snaith HJ (2014) An organic "donor-free" dye with enhanced open-circuit voltage in solid-state sensitized solar cells. Adv Energy Mater 4(13). doi:10.1002/aenm.201400166
61. Zhang XY, Xu YY, Giordano F, Schreier M, Pellet N, Hu Y, Yi CY, Robertson N, Hua JL, Zakeeruddin SM, Tian H, Gratzel M (2016) Molecular engineering of potent sensitizers for very efficient light harvesting in thin-film solid-state dye-sensitized solar cells. J Am Chem Soc 138(34):10742–10745. doi:10.1021/jacs.6b05281
62. Dualeh A, Delcamp JH, Nazeeruddin MK, Gratzel M (2012) Near-infrared sensitization of solid-state dye-sensitized solar cells with a squaraine dye. Appl Phys Lett 100(17). doi:10.1063/1.4707374
63. Kolemen S, Cakmak Y, Erten-Ela S, Altay Y, Brendel J, Thelakkat M, Akkaya EU (2010) Solid-state dye-sensitized solar cells using red and near-IR absorbing bodipy sensitizers. Org Lett 12(17):3812–3815. doi:10.1021/ol1014762
64. Xu B, Gabrielsson E, Safdari M, Cheng M, Hua Y, Tian HN, Gardner JM, Kloo L, Sun LC (2015) 1, 1, 2, 2-tetrachloroethane (TeCA) as a solvent additive for organic hole transport materials and its application in highly efficient solid-state dye-sensitized solar cells. Adv Energy Mater 5(10). doi:10.1002/aenm.201402340
65. Hagen J, Schaffrath W, Otschik P, Fink R, Bacher A, Schmidt HW, Haarer D (1997) Novel hybrid solar cells consisting of inorganic nanoparticles and an organic hole transport material. Synth Metals 89(3):215–220. doi:10.1016/s0379-6779(97)81221-0
66. Jager C, Haarer D, Peng B, Thelakkat M (2004) The influence of the time-of-flight mobility on the efficiency of solid-state dye-sensitized TiO_2 solar cells. Appl Phys Lett 85(25):6185–6187. doi:10.1063/1.1834717
67. Aich R, Tran-Van F, Goubard F, Beouch L, Michaleviciute A, Grazulevicius JV, Ratier B, Chevrot C (2008) Hydrazone based molecular glasses for solid-state dye-sensitized solar cells. Thin Solid Films 516(20):7260–7265. doi:10.1016/j.tsf.2007.12.125
68. Leijtens T, Ding IK, Giovenzana T, Bloking JT, McGehee MD, Sellinger A (2012) Hole transport materials with low glass transition temperatures and high solubility for application in solid-state dye-sensitized solar cells. ACS Nano 6(2):1455–1462. doi:10.1021/nn204296b
69. Yang L, Xu B, Bi DQ, Tian HN, Boschloo G, Sun LC, Hagfeldt A, Johansson EMJ (2013) Initial light soaking treatment enables hole transport material to outperform spiro-OMeTAD in solid-state dye-sensitized solar cells. J Am Chem Soc 135(19):7378–7385
70. Xu B, Tian HN, Bi DQ, Gabrielsson E, Johansson EMJ, Boschloo G, Hagfeldt A, Sun LC (2013) Efficient solid state dye-sensitized solar cells based on an oligomer hole transport material and an organic dye. J Mater Chem A 1(46):14467–14470. doi:10.1039/c3ta13646a
71. Xu B, Tian HN, Lin LL, Qian DP, Chen H, Zhang JB, Vlachopoulos N, Boschloo G, Luo Y, Zhang FL, Hagfeldt A, Sun LC (2015) Integrated design of organic hole transport materials for efficient solid-state dye-sensitized solar cells. Adv Energy Mater 5(3). doi:10.1002/aenm.201401185
72. Xu B, Bi D, Hua Y, Liu P, Cheng M, Gratzel M, Kloo L, Hagfeldt A, Sun L (2016) A low-cost spiro[fluorene-9, 9′-xanthene]-based hole transport material for highly efficient solid-state dye-sensitized solar cells and perovskite solar cells. Energy Environ Sci 9(3):873–877. doi:10.1039/C6EE00056H
73. Tomkeviciene A, Puckyte G, Grazulevicius JV, Degbia M, Tran-Van F, Schmaltz B, Jankauskas V, Boucle J (2012) Diphenylamino-substituted derivatives of 9-phenylcarbazole as glass-forming hole-transporting materials for solid state dye sensitized solar cells. Synth Metals 162(23):1997–2004. doi:10.1016/j.synthmet.2012.10.002
74. Puckyte G, Schmaltz B, Tomkeviciene A, Degbia M, Grazulevicius JV, Melhem H, Boucle J, Tran-Van F (2013) Carbazole-based molecular glasses for efficient solid-state dye-sensitized solar cells. J Power Sources 233:86–92. doi:10.1016/j.jpowsour.2013.01.137

75. Planells M, Abate A, Hollman DJ, Stranks SD, Bharti V, Gaur J, Mohanty D, Chand S, Snaith HJ, Robertson N (2013) Diacetylene bridged triphenylamines as hole transport materials for solid state dye sensitized solar cells. J Mater Chem A 1(23):6949–6960. doi:10.1039/c3ta11417a
76. Snaith HJ, Gratzel M (2006) Enhanced charge mobility in a molecular hole transporter via addition of redox inactive ionic dopant: implication to dye-sensitized solar cells. Appl Phys Lett 89(26). doi:10.1063/1.2424552
77. Cappel UB, Daeneke T, Bach U (2012) Oxygen-induced doping of spiro-MeOTAD in solid-state dye-sensitized solar cells and its impact on device performance. Nano Lett 12 (9):4925–4931. doi:10.1021/nl302509q
78. Abate A, Leijtens T, Pathak S, Teuscher J, Avolio R, Errico ME, Kirkpatrik J, Ball JM, Docampo P, McPherson I, Snaith HJ (2013) Lithium salts as "redox active" p-type dopants for organic semiconductors and their impact in solid-state dye-sensitized solar cells. Phys Chem Chem Phys 15(7):2572–2579. doi:10.1039/c2cp44397j
79. Burschka J, Kessler F, Nazeeruddin MK, Gratzel M (2013) Co(III) complexes as p-dopants in solid-state dye-sensitized solar cells. Chem Mater 25(15):2986–2990. doi:10.1021/cm400796u
80. Nguyen WH, Bailie CD, Unger EL, McGehee MD (2014) Enhancing the hole-conductivity of spiro-OMeTAD without oxygen or lithium salts by using spiro(TFSI)(2) in perovskite and dye-sensitized solar cells. J Am Chem Soc 136(31):10996–11001. doi:10.1021/ja504539w
81. Gebeyehu D, Brabec CJ, Padinger F, Fromherz T, Spiekermann S, Vlachopoulos N, Kienberger F, Schindler H, Sariciftci NS (2001) Solid state dye-sensitized TiO_2 solar cells with poly(3-octylthiophene) as hole transport layer. Synth Metals 121(1–3):1549–1550. doi:10.1016/s0379-6779(00)01239-x
82. Zhang W, Zhu R, Li F, Wang Q, Liu B (2011) High-performance solid-state organic dye sensitized solar cells with P3HT as hole transporter. J Phys Chem C 115(14):7038–7043. doi:10.1021/jp1118597
83. Johansson EMJ, Yang L, Gabrielsson E, Lohse PW, Boschloo G, Sun L, Hagfeldt A (2012) Combining a small hole-conductor molecule for efficient dye regeneration and a hole-conducting polymer in a solid-state dye-sensitized solar cell. J Phys Chem C 116 (34):18070
84. Koh JK, Kim J, Kim B, Kim JH, Kim E (2011) Highly efficient, iodine-free dye-sensitized solar cells with solid-state synthesis of conducting polymers. Adv Mater 23 (14):1641. doi:10.1002/adma.201004715
85. Murakoshi K, Kogure R, Wada Y, Yanagida S (1997) Solid state dye-sensitized TiO_2 solar cell with polypyrrole as hole transport layer. Chem Lett 5:471–472. doi:10.1246/cl.1997.471
86. Saito Y, Fukuri N, Senadeera R, Kitamura T, Wada Y, Yanagida S (2004) Solid state dye sensitized solar cells using in situ polymerized PEDOTs as hole conductor. Electrochem Commun 6(1):71–74. doi:10.1016/j.elecom.2003.10.016
87. Xia JB, Masaki N, Lira-Cantu M, Kim Y, Jiang KJ, Yanagida S (2008) Influence of doped anions on poly(3, 4-ethylenedioxythiophene) as hole conductors for iodine-free solid-state dye-sensitized solar cells. J Am Chem Soc 130(4):1258–1263. doi:10.1021/ja075704o
88. Liu XZ, Zhang W, Uchida S, Cai LP, Liu B, Ramakrishna S (2010) An efficient organic-dye-sensitized solar cell with in situ polymerized poly(3, 4-ethylenedioxythiophene) as a hole-transporting material. Adv Mater 22 (20):E150. doi:10.1002/adma.200904168
89. Liu X, Cheng Y, Wang L, Cai L, Liu B (2012) Light controlled assembling of iodine-free dye-sensitized solar cells with poly(3, 4-ethylenedioxythiophene) as a hole conductor reaching 7.1% efficiency. Phys Chem Chem Phys 14(19):7098–7103. doi:10.1039/C2CP40882A
90. Zhang JB, Yang L, Shen Y, Park BW, Hao Y, Johansson EMJ, Boschloo G, Kloo L, Gabrielsson E, Sun LC, Jarboui A, Perruchot C, Jouini M, Vlachopoulos N, Hagfeldt A (2014) Poly(3, 4-ethylenedioxythiophene) hole-transporting material generated by photo-electrochemical polymerization in aqueous and organic medium for all-solid-state dye-sensitized solar cells. J Phys Chem C 118(30):16591–16601. doi:10.1021/jp412504s

91. Zhang JB, Vlachopoulos N, Jouini M, Johansson MB, Zhang XL, Nazeeruddin MK, Boschloo G, Johansson EMJ, Hagfeldt A (2016) Efficient solid-state dye sensitized solar cells: The influence of dye molecular structures for the in-situ photoelectrochemically polymerized PEDOT as hole transporting material. Nano Energy 19:455–470. doi:10.1016/j.nanoen.2015.09.010
92. Zhang J, Haggman L, Jouini M, Jarboui A, Boschloo G, Vlachopoulos N, Hagfeldt A (2014) Solid-state dye-sensitized solar cells based on poly(3, 4 ethylenedioxypyrrole) and metal-free organic dyes. ChemPhysChem 15(6):1043–1047. doi:10.1002/cphc.201301075
93. Inudo S, Miyake M, Hirato T (2013) Electrical properties of CuI films prepared by spin coating. Phys Status Solidi a-Appl Mater Sci 210(11):2395–2398. doi:10.1002/pssa.201329319
94. Kumara GRA, Konno A, Shiratsuchi K, Tsukahara J, Tennakone K (2002) Dye-sensitized solid-state solar cells: Use of crystal growth inhibitors for deposition of the hole collector. Chem Mater 14 (3):954−+. doi:10.1021/cm011595f
95. Tennakone K, Senadeera GKR, De Silva D, Kottegoda IRM (2000) Highly stable dye-sensitized solid-state solar cell with the semiconductor 4CuBr 3S(C4H9)(2) as the hole collector. Appl Phys Lett 77(15):2367–2369. doi:10.1063/1.1312858
96. O'Regan B, Schwartz DT (1996) Efficient dye-sensitized charge separation in a wide-band-gap p-n heterojunction. J Appl Phys 80(8):4749–4754. doi:10.1063/1.363412
97. O'Regan B, Schwartz DT, Zakeeruddin SM, Gratzel M (2000) Electrodeposited nanocomposite n-p heterojunctions for solid-state dye-sensitized photovoltaics. Adv Mater 12 (17):1263−+. doi:10.1002/1521-4095(200009)12:17<1263::aid-adma1263>3.0.co;2-t
98. Kumara G, Konno A, Senadeera GKR, Jayaweera PVV, De Silva D, Tennakone K (2001) Dye-sensitized solar cell with the hole collector p-CuSCN deposited from a solution in n-propyl sulphide. Solar Energy Mater Solar Cells 69(2):195–199. doi:10.1016/s0927-0248(01)00027-7
99. O'Regan B, Lenzmann F, Muis R, Wienke J (2002) A solid-state dye-sensitized solar cell fabricated with pressure-treated P25-TiO_2 and CuSCN: analysis of pore filling and IV characteristics. Chem Mater 14(12):5023–5029
100. Premalal EVA, Kumara G, Rajapakse RMG, Shimomura M, Murakami K, Konno A (2010) Tuning chemistry of CuSCN to enhance the performance of TiO_2/N719/CuSCN all-solid-state dye-sensitized solar cell. Chem Commun 46(19):3360–3362. doi:10.1039/b927336k
101. Bandara J, Weerasinghe H (2005) Solid-state dye-sensitized solar cell with p-type NiO as a hole collector. Solar Energy Mater Solar Cells 85(3):385–390. doi:10.1016/j.solmat.2004.05.010
102. Chung I, Lee B, He J, Chang RPH, Kanatzidis MG (2012) All-solid-state dye-sensitized solar cells with high efficiency. Nature 485(7399):486
103. Kumar MH, Dharani S, Leong WL, Boix PP, Prabhakar RR, Baikie T, Shi C, Ding H, Ramesh R, Asta M, Graetzel M, Mhaisalkar SG, Mathews N (2014) Lead-free halide perovskite solar cells with high photocurrents realized through vacancy modulation. Adv Mater 26(41):7122−+. doi:10.1002/adma.201401991
104. Lee B, Stoumpos CC, Zhou NJ, Hao F, Malliakas C, Yeh CY, Marks TJ, Kanatzidis MG, Chang RPH (2014) Air-stable molecular semiconducting lodosalts for solar cell applications: Cs(2)Snl(6) as a hole conductor. J Am Chem Soc 136(43):15379–15385. doi:10.1021/ja508464w
105. Freitag M, Daniel Q, Pazoki M, Sveinbjornsson K, Zhang J, Sun L, Hagfeldt A, Boschloo G (2015) High-efficiency dye-sensitized solar cells with molecular copper phenanthroline as solid hole conductor. Energy Environ Sci 8(9):2634–2637. doi:10.1039/c5ee01204j
106. Cao YS, Ummadisingu A, Teuscher J, Luo J, Pellet N, Giordano F, Zakeeruddin SM, Moser J-E, Freitag M, Hagfeldt A, Grätzel M (2017) 11% efficiency solid-state dye-sensitized solar cells with copper(ii/i) hole transport materials. Nat Commun 8:15390. doi:10.1038/ncomms15390

107. Kashif MK, Milhuisen RA, Nippe M, Hellerstedt J, Zee DZ, Duffy NW, Halstead B, De Angelis F, Fantacci S, Fuhrer MS, Chang CJ, Cheng Y-B, Long JR, Spiccia L, Bach U (2016) Cobalt polypyridyl complexes as transparent solution-processable solid-state charge transport materials. Adv Energy Mater 6(24):1600874-n/a. doi:10.1002/aenm.201600874
108. Aitola K, Zhang JB, Vlachopoulos N, Halme J, Kaskela A, Nasibulin AG, Kauppinen EI, Boschloo G, Hagfeldt A (2015) Carbon nanotube film replacing silver in high-efficiency solid-state dye solar cells employing polymer hole conductor. J Solid State Electrochem 19 (10):3139–3144. doi:10.1007/s10008-015-2937-1
109. Chiang YF, Tsai CH, Chen P, Guo TF (2012) Bifacial transparent solid-state dye-sensitized solar cell with sputtered indium-tin-oxide counter electrode. Sol Energy 86(6):1967–1972. doi:10.1016/j.solener.2012.03.004
110. Chiang YF, Chen RT, Burke A, Bach U, Chen P, Guo TF (2013) Non-color distortion for visible light transmitted tandem solid state dye-sensitized solar cells. Renew Energy 59:136–140. doi:10.1016/j.renene.2013.03.018
111. Margulis GY, Christoforo MG, Lam D, Beiley ZM, Bowring AR, Bailie CD, Salleo A, McGehee MD (2013) Spray deposition of silver nanowire electrodes for semitransparent solid-state dye-sensitized solar cells. Adv Energy Mater 3(12):1657–1663. doi:10.1002/aenm.201300660
112. Ding IK, Tétreault N, Brillet J, Hardin BE, Smith EH, Rosenthal SJ, Sauvage F, Grätzel M, McGehee MD (2009) Pore-filling of spiro-OMeTAD in solid-state dye sensitized solar cells: quantification, mechanism, and consequences for device performance. Adv Funct Mater 19 (15):2431–2436
113. Docampo P, Hey A, Guldin S, Gunning R, Steiner U, Snaith HJ (2012) Pore filling of spiro-OMeTAD in solid-state dye-sensitized solar cells determined via optical reflectometry. Adv Funct Mater 22(23):5010–5019. doi:10.1002/adfm.201201223
114. Cappel UB, Gibson EA, Hagfeldt A, Boschloo G (2009) Dye regeneration by spiro-MeOTAD in solid state dye-sensitized solar cells studied by photoinduced absorption spectroscopy and spectroelectrochemistry. J Phys Chem C 113(15):6275
115. Bailie CD, Unger EL, Zakeeruddin SM, Gratzel M, McGehee MD (2014) Melt-infiltration of spiro-OMeTAD and thermal instability of solid-state dye-sensitized solar cells. Phys Chem Chem Phys 16(10):4864–4870. doi:10.1039/c4cp00116h
116. Fredin K, Johansson EMJ, Blom T, Hedlund M, Plogmaker S, Siegbahn S, Leifer K, Rensmo H (2009) Using a molten organic conducting material to infiltrate a nanoporous semiconductor film and its use in solid-state dye-sensitized solar cells. Synth Metals 159:166–170
117. Law C, Spence R, O'Regan BC (2013) Brief air heating of TiO_2/dye films, to 120-250 degrees C; the effect on resulting liquid junction dye sensitised solar cells (DSSCs) and melt-processed solid-state DSSCs. J Mater Chem A 1(45):14154–14161. doi:10.1039/c3ta13145a
118. Yuan W, Zhao H, Baker GL (2014) Low glass transition temperature hole transport material in enhanced-performance solid-state dye-sensitized solar cell. Org Electron 15(11):3362–3369. doi:10.1016/j.orgel.2014.09.017
119. Melas-Kyriazi J, Ding IK, Marchioro A, Punzi A, Hardin BE, Burkhard GF, Tetreault N, Gratzel M, Moser JE, McGehee MD (2011) The effect of hole transport material pore filling on photovoltaic performance in solid-state dye-sensitized solar cells. Adv Energy Mater 1 (3):407–414. doi:10.1002/aenm.201100046
120. Zhang L, Boschloo G, Hammarstrom L, Tian HN (2016) Solid state p-type dye-sensitized solar cells: concept, experiment and mechanism. Phys Chem Chem Phys 18(7):5080–5085. doi:10.1039/c5cp05247e
121. Pham TTT, Saha SK, Provost D, Farre Y, Raissi M, Pellegrin Y, Blart E, Vedraine S, Ratier B, Aldakov D, Odobel F, Boucle J (2017) Toward efficient solid-state p-type dye-sensitized solar cells: the dye matters. J Phys Chem C 121(1):129–139. doi:10.1021/acs.jpcc.6b10513

122. Mor GK, Basham J, Paulose M, Kim S, Varghese OK, Vaish A, Yoriya S, Grimes CA (2010) High-efficiency forster resonance energy transfer in solid-state dye sensitized solar cells. Nano Lett 10(7):2387–2394. doi:10.1021/nl100415q
123. Unger EL, Morandeira A, Persson M, Zietz B, Ripaud E, Leriche P, Roncali J, Hagfeldt A, Boschloo G (2011) Contribution from a hole-conducting dye to the photocurrent in solid-state dye-sensitized solar cells. Phys Chem Chem Phys 13(45):20172
124. Moon SJ, Baranoff E, Zakeeruddin SM, Yeh CY, Diau EWG, Gratzel M, Sivula K (2011) Enhanced light harvesting in mesoporous TiO_2/P3HT hybrid solar cells using a porphyrin dye. Chem Commun 47(29):8244–8246. doi:10.1039/c1cc12251g
125. Bruder I, Karlsson M, Eickemeyer F, Hwang J, Erk P, Hagfeldt A, Weis J, Pschirer N (2009) Efficient organic tandem cell combining a solid state dye-sensitized and a vacuum deposited bulk heterojunction solar cell. Solar Energy Mater Solar Cells 93(10):1896–1899. doi:10.1016/j.solmat.2009.05.020

Chapter 5
Hybrid Organic/Inorganic and Perovskite Solar Cells

Azhar Fakharuddin and Lukas Schmidt-Mende

Abstract In this chapter, we describe the various hybrid organic/inorganic solar cells with a focus on perovskite solar cells. We present a brief introduction to the topic of solar cells in general and our definition of hybrid solar cells. As dye-sensitized and solid-state dye-sensitized solar cells are covered in detail in other chapters of this book, we only provide a short description of the fundamental working mechanisms of dye-sensitized, solid-state dye-sensitized and extremely thin absorber solar cells as a necessary background for the other parts of this chapter. We then focus, in detail, on the current understanding of perovskite solar cells such as the crystal structure, the optical and electronic properties of perovskite films, their formation, and current device architectures. Additionally, we look at the specialty of perovskite solar cells: The often-observed hysteresis effect when recording current density–voltage curves. We conclude with technological aspects, such as the preparation of flexible perovskite solar cells, their low-temperature processing, and degradation mechanisms. We finish our chapter with a brief mentioning of hybrid bulk heterojunction solar cells.

Keywords Interfaces · Charge transport and transfer in perovskite solar cells · Hysteresis · Bulk heterojunctions · Stability of perovskite solar cells

Abbreviations

tBP	4-tert-butylpyridien
BI	Building integration
BHJ	Bulk heterojunction solar cell
E_C	Conduction band edge
CE	Counter electrode
L_D	Diffusion length

A. Fakharuddin · L. Schmidt-Mende (✉)
Department of Physics, University of Konstanz, 78457 Konstanz, Germany
e-mail: lukas.schmidt-mende@uni-konstanz.de

H. Tian et al. (eds.), *Molecular Devices for Solar Energy Conversion and Storage*, Green Chemistry and Sustainable Technology,
https://doi.org/10.1007/978-981-10-5924-7_5

DSSC	Dye-sensitized solar cell
ETL	Electron transport layer
EPBT	Energy payback time
ETA	Extremely thin absorber solar cell
E_F	Fermi energy level
FF	Fill factor
f-PSC	Flexible perovskite solar cell
FTO	Fluorine doped tin oxide
FA	Formamidinium
HSC	Hybrid organic/inorganic solar cell
HI	Hydriodic acid
LED	Light emitting diode
MOS	Metal oxide semiconductor
MA	Methylammonium
V_{OC}	Open circuit voltage
OPV	Organic photovoltaic
OSC	Organic solar cell
PSC	Perovskite solar cell
PCE	Photoconversion efficiency
J_{SC}	Photocurrent density
PV	Photovoltaic
P3HT	Poly(3-heylthiophene)
PC	Polycarbonate
PES	Polyethersulfone
PEN	Polyethylene naphthalate
PET	Polyethylene terephthalate
QDSC	Quantum dot solar cell
R2R	Roll-to-roll
SS	Single step
s-DSSC	Solid-state dye-sensitized solar cell
HTL	Solid-state hole transport layer
ToF	Time-of-flight method
ITO	Tin doped indium oxide
TS	Two step
VAVD	Vacuum assisted vapor deposition
E_V	Valence band edge
WE	Working electrode

5.1 Introduction

5.1.1 *Emergence of Solar Cells in Renewable Energy Paradigm*

Energy harvesting is one of the greatest challenges to mankind in the twenty-first century. At present, >80% worldwide energy demand is met by fossil fuel based resources such as coal, oil, and gas that contribute to global warming owing to the emission of greenhouse gases produced when these fuels are burnt to produce energy. On the other hand, these resources are limited and with increasing energy demand, efforts are dedicated to seek energy from alternative resources that are renewable and eliminate the environmental risks associated with the use of fossil fuels. Wind and solar are two such resources that can take up the increasing energy demand challenge. In fact, the energy from the sun alone is several thousand times higher than the total global energy demand of ~17 TW; it requires covering ~0.4% of our earth surface with 15% efficient solar panels. This led to widespread research and development activities in photovoltaic (PV) devices resulting in total PV installation ~178 MW in 2014 up from only ~800 MW in 2000, which is now growing even more rapidly [1, 2].

The PV technology can be divided into three main classes: (i) wafer-based or crystalline silicon PVs that typically employ 100–200 μm thick absorber layer, (ii) thin film solar cells ($CuInGaSe_2$, a-Si:H, CdTe, etc.) employing much thinner films of ~1 μm than (i), and (iii) nanostructured solar cells where molecules or organic/inorganic crystals are employed as absorbers. Examples of (iii) are dye-sensitized solar cells (DSSCs), organic solar cells (OSCs/OPVs), quantum dot solar cells (QDSCs), and emerging perovskite solar cells (PSCs). These solar cells employ a thin absorber layer typically 50–300 nm (except for DSSCs where thickness is 5–20 μm) which is deposited on an electron or hole selective contact (ETL and HTL). In Table 5.1, we compare state-of-the-art photoconversion efficiency (PCE) of various types of solar cells and also their large area modules. Wafer-based and thin film PVs dominate the solar cells' market primarily due to their high PCE (25–26%) [3] and also a device lifetime >20 years; however, it is very recently that PSCs have also demonstrated high PCE of ~20–22% [7, 8], although the devices still have to demonstrate long-term stability. The formers, therefore, accounted for ~99% of the total PV installations worldwide at the end of 2015(~90% for silicon and 9% for thin film PVs) leaving only 1% for all other types of PVs [9]. Furthermore, a drastic reduction in the cost of silicon-based solar cells to ~0.7 $/$W_P$ in 2014 from ~70–75$/$W_P$ in the 1970s and energy payback time (EPBT) of ~2.5–3 years made it very competitive for new PV technologies to directly compete with market dominating silicon solar cells [2].

For any new PV technology to enter the market, it should offer at least three of the four key characteristics shown in Fig. 5.1. The new PV technologies such as OSCs, DSSCs, and PSCs offer added functionalities (transparency, color tuning, flexibility, low-light workability, and building integration (BI)) that silicon and thin

Table 5.1 Photoconversion efficiency (PCE) of various best performing laboratory scale solar cells and their modules on larger areas

PV type	Best cell PCE (%)	Best module PCE (%)	Module area (cm^2)	Commercialization status
Si	25.6 ± 0.5 (Panasonic)	21.2 ± 0.4 (Solexel)	~240	In market
GaAs	28.8 ± 0.9 (Alta devices)			In market
CIGS	21.0 ± 0.6 (Sloibro)	18.7 ± 0.6 (Solibro)	~16	In market
CdTe	21.0 ± 0.4 (First Solar)	11.7	–	In market
DSSC	14.3 (Ref. [5])	10.7 (Sharp)	26.5	In market
OPV	11.2 ± 0.3 (Toshiba)	9.7 ± 0.3 (Toshiba)	~26.1	NA
PSC	22.1 (KRICT/UNIST) Certified by NREL	12.9 (Ref. [6])	40 (aperture area)	Currently not stable
ETA	~5	–	–	NA

The values are taken from NREL best cell efficiency chart [3] and also "solar cell efficiency tables" (version 48) [4], if not stated otherwise

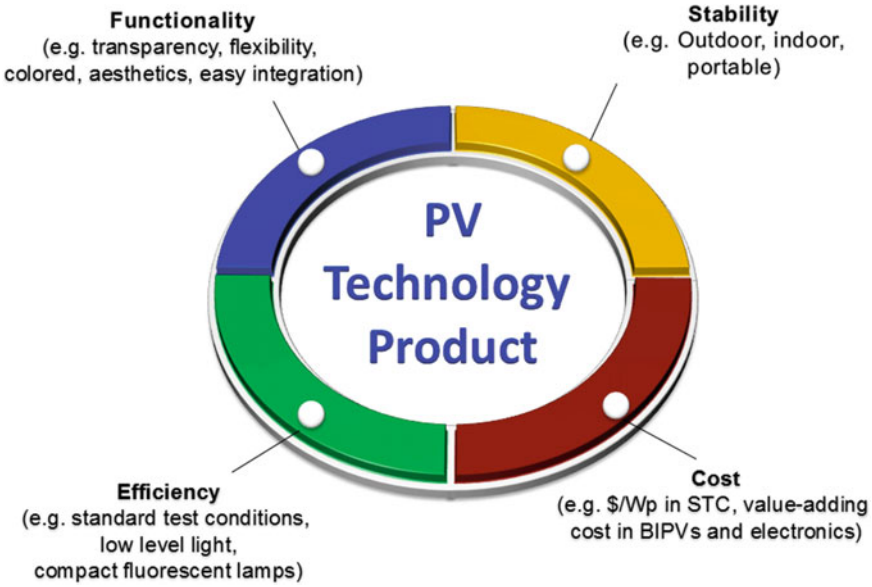

Fig. 5.1 Schematic representing the four key requirements for any new type of solar cells that are to enter energy market where functionality will also play a key part along with PCE, cost and stability. Depending upon the application and market demand, the PVs can be made technologically differently (rigid/flexible substrates, transparent/opaque, materials and device architectures and so forth). Figure adapted with permission from Ref. [1]. Copyright of The Royal Society of Chemistry

film technologies may not. These new technologies are mostly solution processable making device fabrication compatible to roll-to-roll (R2R) production and can be used for building or automobile integrated and portable applications. However, these devices currently suffer from inferior outdoor stability and low PCE (except PSCs where PCE of 21–22% has already been reported) [7, 8].

5.1.2 Hybrid Organic/Inorganic Solar Cells

Hybrid organic/inorganic solar cells (HSCs) utilize both organic and inorganic materials as active component to combine characteristics such as cost-effectiveness, tuning of size and optical properties, high absorption characteristics, and easy processability. The inorganic component is typically semiconducting nanoparticles such as TiO_2, ZnO, CdS, CuI, $CuISn_2$, PbS, etc., sometimes already with high absorption coefficient and a tunable optical bandgap [10–12]. Typically, hybrid solar cells make interface with the inorganic component with that of an organic or polymer counterparts. There are a number of different material combinations and architectures used for hybrid solar cells. Currently, the most investigated systems are: (i) DSSCs employing a liquid electrolyte which provide PCEs of 10–14%, (ii) their solid-state analogue, where the liquid electrolyte is replaced by an organic hole transporter material, such as spiro-OMeTAD, (iii) extremely thin absorber solar cells (ETA), where the dye of DSSCs is replaced by an inorganic thin absorber layer and, (iv) more recently also the PSCs originally resulted from the ETA concept with remarkable PCE $\sim$22.1%. Another class of hybrid devices is bulk heterojunction solar cells (BHJ), where inorganic absorber particles are blended with organic semiconductors to form a hybrid bulk heterojunction solar cell. This concept is based on the BHJs, where in general, the organic acceptor (usually the fullerene derivative PCBM) is replaced by an inorganic acceptor material [13].

In many of these hybrid solar cell devices, a film based on nanoparticles of the inorganic semiconductor is used to form a mesoporous film or network of these particles. For example, TiO_2 is often used to form a mesoporous film as electron transport pathways in DSSCs. However, there exist many examples where this mesoporous film is replaced by more ordered nanostructures of different inorganic semiconductors, such as nanowires, nanotubes, and nanorods leading to more controlled nanostructured hybrid devices.

In this chapter, we will only briefly describe DSSCs and solid-state DSSCs as they are already covered in Chaps. 3 and 4 of this book. Also, we will have only a shortly description the architecture of hybrid bulk heterojunction solar cells at the end of the chapter. The main focus of this chapter will be on PSCs, which are described in more detail as important recently emerging new solar cells architecture.

5.2 Dye-Sensitized Solar Cells Employing a Liquid Electrolyte

DSSCs, also called Grätzel cells, employ a nanostructured porous scaffold ~5–20 μm on a fluorine doped tin oxide (FTO) coated conducting glass substrate also called working electrode (WE) subsequently anchored with an organic or inorganic dye [14–16]. A counter electrode (CE) is also an FTO, coated with a metal catalyst (typically platinum). The WE and CE are sandwiched together with a spacer between them and a redox electrolyte containing inorganic salts is filled in the gap between the two glass plates as shown in the Fig. 5.2. The photoconversion

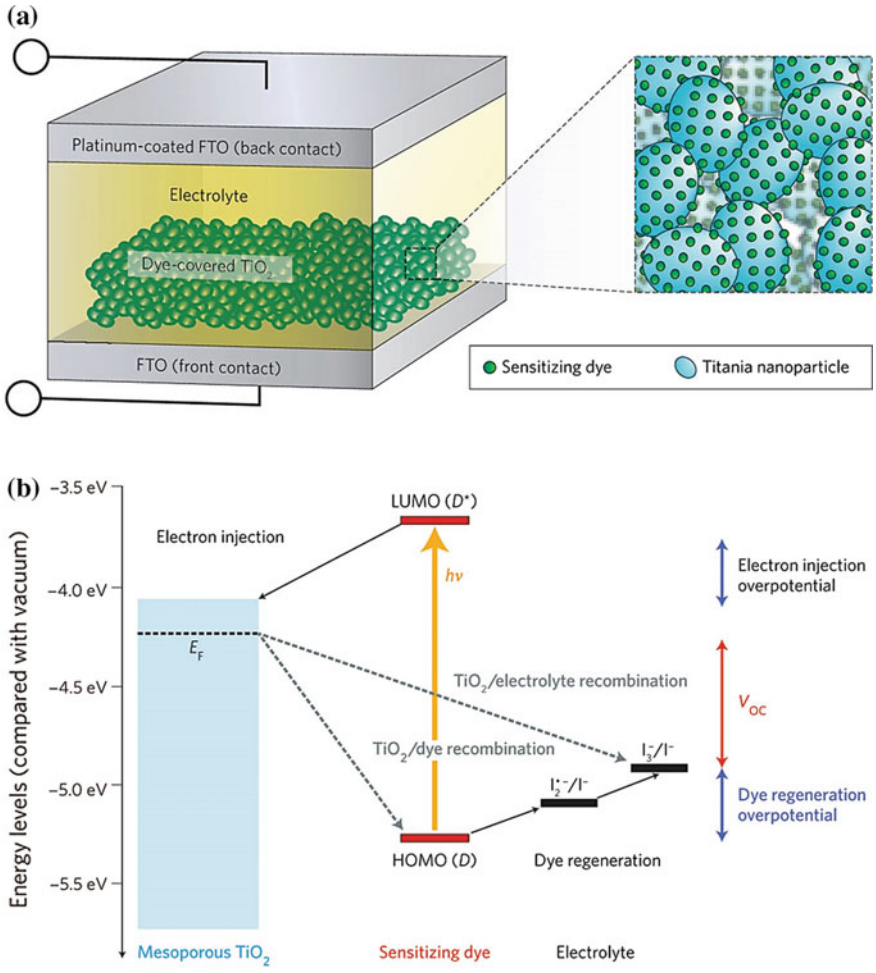

Fig. 5.2 The various components of a dye-sensitized solar cell, their energy level alignment and working mechanism. Figure adapted with permission from Ref. [21]. Copyright of Macmillan Publishers Limited

takes place when the incident sun light is absorbed by the dye molecules attached to a wide bandgap metal oxide semiconductor (MOS, typically TiO_2, ZnO and SnO_2). The photogenerated electrons are injected from dye to the conduction band (CB) of the MOS and are diffused through the porous MOS to the electron transport layer (ETL). The oxidized dye is brought to its neutral state by electron donation from redox electrolyte which is filled within the pores of the MOS. For an efficient photovoltaic operation, the MOS should offer (i) a high surface area to anchor large amount of dye that will, in turn, increase photogenerated electrons, (ii) high electron mobility to extract all photogenerated electrons to the selective contact, and (iii) suitable CB edge so that maximum photogenerated electrons can be injected from dye to the MOS which would otherwise result in loss of photovoltage (over potential) [17–20].

The dyes are the key component to enhance light absorption (absorption coefficient $\varepsilon \sim 15{,}000\ M^{-1}\ cm^{-1}$) in the DSSCs as the MOS employed have low absorption characteristics in the visible range. As shown in Fig. 5.3, two commonly employed dye molecules known as N3 ($RuL_2(NCS)_2$) and black dye ($RuL'(NCS)_3$) extend the absorption characteristics of DSSCs >750 and >900 nm, respectively, from only $\sim$350–400 nm for pristine TiO_2. Ideally, a dye should absorb all light

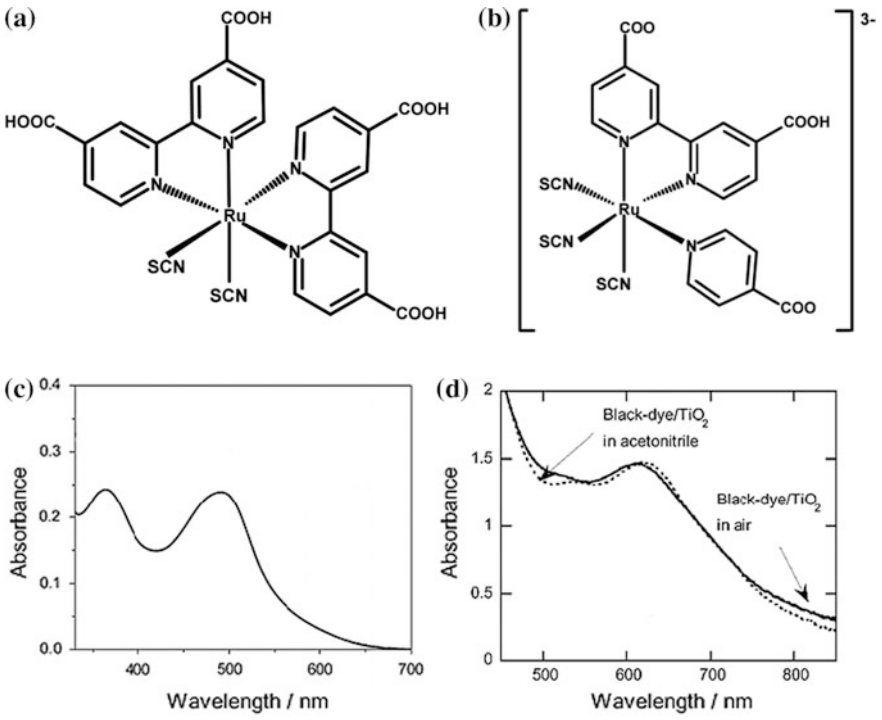

Fig. 5.3 Chemical structure and spectral response of N_3 and black dyes (**a** and **b**), whereas **c** and **d** are absorbance spectra of the same. Figures (**c** and **d**) adapted with permission from Refs. [27] and [28], respectively. Copyright of The Royal Society of Chemistry

below a threshold, inject all photogenerated electrons to the MOS and anchor well with the MOS [22, 23]. Sensitizer employing ruthenium complexes are the most commonly employed and typically result in PCE >10–12% in conjunction with I^-/I_3^- redox electrolyte for best performing DSSCs; however, more recently porphyrins sensitizers have shown PCE ~13% in conjunction with Cobalt (II/III) redox shuttle [24]. The cobalt redox shuttle allows achieving higher open circuit voltages due to its more favorable redox potential. Ferrocene-based electrolytes are also employed to reduce the loss in potential [25, 26]. The record PCE in DSSCs (~14.3%) is achieved via co-sensitization of silyl-anchor and carboxyl-anchor dyes and cobalt-based redox electrolyte as a hole conductor by Kakiage et al. [5]. Various other dyes such as porphyrins, phthalocyanines, transition metal complexes, metal free dyes, and natural extracts from fruits and vegetables are also investigated as light sensitizers; however, the PCE has been far lower than the champion DSSC [22].

The photovoltaic parameters such as open circuit voltage ($\boldsymbol{V_{OC}}$), photocurrent density ($\boldsymbol{J_{SC}}$), and fill factor ($\boldsymbol{FF}$) in the DSSCs are determined by choice of various materials components in addition to the device fabrication. For example, cobalt-based redox shuttle typically results in higher voltage output due to its ~200 mV lower lying redox potential. This is because the $\boldsymbol{V_{OC-}}$ in DSSCs is a difference between $\boldsymbol{E_{RED}}$ and $\boldsymbol{E_{F-}}$ (Fermi energy level of metal oxide semiconductor (MOS)). This resulted in $\boldsymbol{V_{OC}} > 1$ V in the state-of-the-art DSSC (PCE 14.3%), despite the fact that 400–600 mV of potential is lost as over potential at dye-MOS and dye–electrolyte interface (Fig. 5.2b). Similarly, $\boldsymbol{J_{SC}}$ depends on the surface area and charge transport properties of MOS, absorption and electron injection efficiency of the dye molecule, and recombination at the interfaces of the electron and hole transport layers. For more details on DSSCs, we refer the reader to Chap. 3 “Liquid Electrolyte Solar Cells” of this book.

5.3 Solid-State Dye-Sensitized Solar Cells

Solid-state DSSCs (*s*-DSSCs) emerged as an alternative to their liquid counterparts due to leakage and volatility of liquid electrolytes resulting in device instability [29]. The *s*-DSSCs employ an organic (mostly spiro-OMeTAD or P3HT) or inorganic (CuI, CuSCN, CuBr, etc.) counterpart as a replacement to redox electrolyte which is deposited on top of a dye-anchored MOS [30]. The use of solid-state hole transport layer (HTL) often brings a pore-filling issue; i.e., the inferior penetration and coverage of MOS pores with HTL that typically limits the PCE. Therefore, the best performing *s*-DSSCs employ a thinner MOS layer (~2 μm) than their liquid rivals with the highest PCE achieved ~10.2% (without mask) using CuSCN as HTL [31]. The state-of-the-art *s*-DSSCs employing spiro-OMeTAD as a HTL (doped with 4-tert-butylpyridine (tBP) and Li $[CF_3SO_2]_2N$) resulted in PCE ~8% [32]. Whereas the addition of such dopants makes the device moisture sensitive due to hygroscopic nature of Li-salts, the HTL

without it shows lower PCE owing to inferior hole mobility of pristine spiro-OMeTAD [33]. Similarly, polymer conjugated HTLs such as P3HT are also used as HTL in s-DSSCs [34]; however, owing to their higher molecular weight they result in poor penetration into the nanoporous MOS.

The reader is referred to Chap. 4 "Solid-State Dye-Sensitized Solar Cells" of this book for more details.

5.4 Extremely Thin Absorber (ETA) Solar Cells

ETA solar cells, also called semiconductor sensitized solar cells, resemble *s*-DSSCs in device architecture, where a semiconductor absorber film (thickness <50 nm, $1.1 < E_g < 1.8$ eV) is applied between n-type and p-type selective contacts ($E_g > 3$ eV) [35, 36]. Although they adopt the concept of photogenerated charge separation in two different materials as that of the DSSCs, charges are not completely separated at the interfaces leading them to behave differently from the DSSCs. This is due to the high absorber thickness (several tens of nanometers) in them unlike the DSSCs (where only a monolayer of dye covers the TiO_2 surface) which imply transport of photogenerated charges over a short distance of several nanometers in ETA solar cells (Fig. 5.4a). Typical examples of absorber materials used in ETA solar cells are CdS, CdSe, Sb_2S_3, In_2S_3, $CuInS_2$, etc. Table 5.2 depicts a historical timeline notable efficiency of these devices. The inception of ETA solar cells dates back to 1998, where a thin Se layer is employed between mesoporous TiO_2 and CuSCN as n-type and p-type selective contacts, respectively (Table 5.2). Since then, these devices have only evolved to a PCE $\sim$5% which is significantly lower than the *s*-DSSCs.

ETA solar cells solve, to some extent, the limitation of mesoporous DSSCs and thin film planar solar cells. On one hand, the replacement of liquid electrolyte with a solid state HTL eases its commercial production and the mesoporous n-type layer in ETA allows the use of thin absorber layer without compromising absorber volume. On the other hand, the thin absorber layers facilitate the use of materials of low charge mobility and short carrier lifetime that may not be otherwise used in thin film solar cells with thicker absorber layers. In addition, the devices can be potentially fabricated cheaper than thin film solar cells as the thin absorber layer eventually relaxes stringent conditions on the purity. However, the performance of these devices is limited by the energy offset at the interfaces that is required to drive electron injections and interfacial recombination owing to the highly porous structure of n-type layer.

The working mechanism of ETA solar cells is arguably different from DSSCs, especially if the absorber is a flat continuous layer between the selective contacts. Herein, as the width of absorber is typically $\sim$50 nm between heavily doped selective contacts, an electric field is generated and the PV mechanism is similar to p-i-n PVs. In the case of a discontinuous film where no distinct separation exists between electron and hole selective contacts, the PV mechanism may differ, as

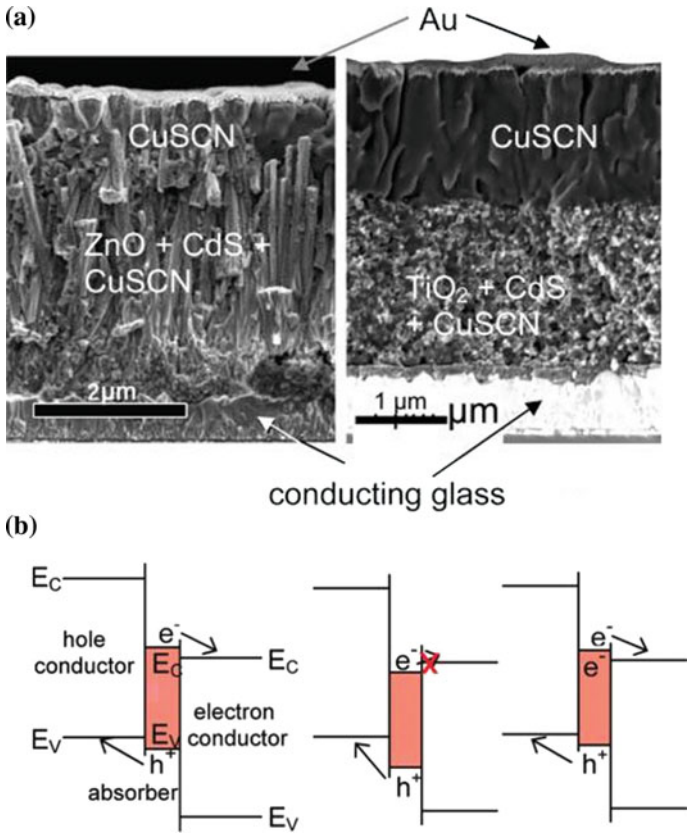

Fig. 5.4 Cross-section view of an ETA solar cell employing **a** ZnO/CdS/CuSCN and **b** TiO_2/CdS/CuSCN cell. These devices also employ a thin compact hole-blocking layer on conducting substrates. A cartoon to explain working mechanism of ETA solar cells. The description can be found in the text. Figures are reproduced with permission from Ref. [35]. Copyright of American Chemical Society

Table 5.2 Timeline of best performing ETA solar cells

Year	Device architecture	Efficiency	References
1998	TiO_2/Se/CuSCN	0.13	Tennakone et al. [37]
2002	TiO_2/PbS/Spiro-OMeTAD	0.49	Robert et al. [38]
2005	TiO_2/CdSe/CuSCN	2.3	Lévy-Clément et al. [39]
2006	TiO_2/CdS/CuSCN	1.3	Larramona et al. [40]
2008	ZnO/In_2S_3/CuSCN	3.4	Belaidi et al. [41]
2009	TiO_2/Sb_2S_3/CuSCN	3.4	Itzhaik et al. [42]
2010	TiO_2/Sb_2S_3/CuSCN	3.7	Shinji et al. [43]
	ZnO_{rod}/In_2S_3/$CuInS_2$	4.2	Krunks et al. [44]
	TiO_2/Sb_2S_3/P3HT	5.1	Chang et al. [45]

Data is reproduced with permission from [35]. Copyright of American Chemical Society

explained by Hodes and Chen [35]. The charge separation at the interfaces could take places if one of the two interfaces, i.e., ETL-absorber and absorber-HTL, energetically favors the charge injection. Figure 5.4c shows a generic model of an ETA solar cell with two possibilities: (i) energy levels at the two interfaces favor electron and hole injection, and (ii) lower conduction band edge (E_C) of absorber inhibits electron injection. Whereas in Fig. 5.4c the charge transfers to conduction band E_C of ETL and valence band E_V of HTL takes place owing to the favorable energy level offset, charge transfer in Fig. 5.4d is not possible. Herein, under illumination holes are transferred to HTL and the excess electrons now available in the absorber shift the E_C of the absorber upwards until electron injections start to take place (Fig. 5.4e). A similar behavior is demonstrated for E_V in the case for hole transport from In_2S_3 to the CuSCN when interfaced with n-type ZnO [46].

Although their performance is not at par with other organic solar cells, the route to further improvement, as suggested by Mora-Seró and Bisquert [47], lies in (i) using absorbers with high extinction coefficients, (ii) optimizing interfacial energy levels to minimize charge transfer losses, and (iii) improving surface of n-type selective contacts to increase light harvesting as well as charge transport properties of the various material components.

It should be mentioned here, that the discovery of PSCs has been made by looking for such an inorganic absorber with high extinction coefficient. First solar cells employing perovskite have initially been prepared in ETA solar cell architecture as thin absorber material on a mesoporous TiO_2 scaffold. From there, it developed quickly further and is now considered as a new class of emerging solar cells, which we discuss in the next section.

5.5 Perovskite Solar Cells

Perovskite solar cells (PSCs), first discovered in 2009 [48], have reached a certified PCE ~22.1% in 2016 [3]. This value is more than double of their first viable solid-state designs report in 2012 with PCE ~9–11% [49, 50]. Although, historically, PSCs are first understood as an extension of the DSSCs and ETA solar cells, where the dyes are replaced with $CH_3NH_3PbX_3$ and $CH_3NH_3PbBr_3$ sensitizers of ~20 times higher absorption coefficient [51, 52] they subsequently evolved as a separate class of solution processable thin film PVs. The PSCs typically employ a thin layer (~300 nm) of an organometallic halide perovskite ($CH_3NH_3PbX_3$, where X = I, Cl and Br) between electron and hole transport layers (ETL and HTL). Figure 5.5 highlights the key achievements in the past 7 years for PSCs toward understanding their PV mechanism, efficiency breakthroughs, and also their upscaling. It shows that PSCs evolved faster than any other class of PVs in history with ~6 times increase in PCE in merely 7 years with notable developments such as ~15.6% efficient flexible PSC on conducting plastic substrates, ~13% efficient

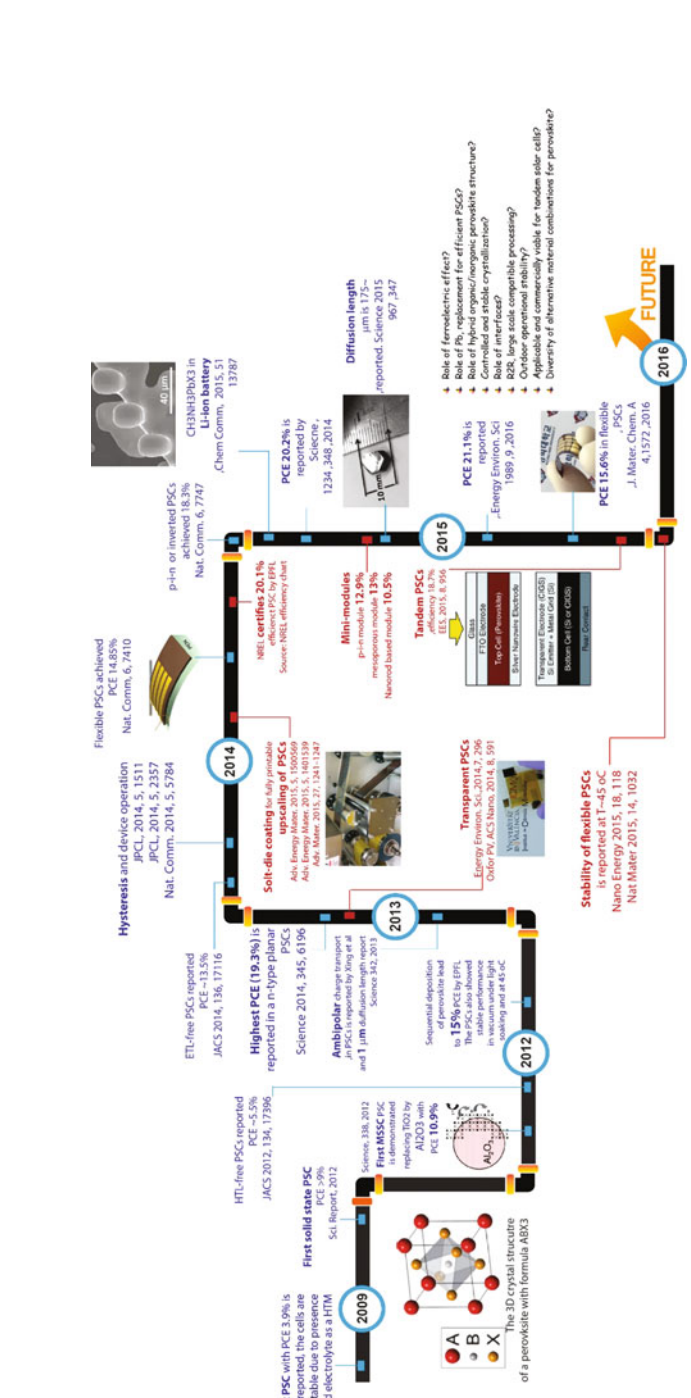

Fig. 5.5 Evolution and major breakthrough in perovskite solar cells since their discovery in 2009. The breakthrough relating PCE improvement and toward understanding its working mechanism are listed above the *black lines* (in *blue text*) whereas the various key developments relating to the stability and large area processing are listed below the *black line* (*red text*). The key issues pertaining to their commercial development are on the right panel (future). Figure is adapted with permission from Ref. [57]. Copyright Wiley-VCH Verlag GmbH & Co. KGaA. Reproduced with permission

large are module, report of $\sim$500 cm^2 large area panel, stable performance for $\sim$1000 h under light soaking, tandem devices with PCE $\sim$20–22%.

Similarly, from a materials perspective, organometallic halide perovskites have also shown remarkable improvements. For example, electron/hole diffusion lengths of 1.2–1.9 μm are reported in their thin films which reach up to $\sim$175 μm in their single crystals. Similarly, the $CH_3NH_3PbX_3$ demonstrated a high absorption coefficient (10^3–10^4 cm^{-1}), tunable bandgap $\sim$1.5–2.5 eV by changing stoichiometric ratio of halide cations, high charge carrier mobility (2–66 cm^2 V^{-1} s^{-1}), low exciton binding energy $\sim$2 meV, low trap state density $\sim 10^{10}$ cm^{-3}, and a charge carrier lifetime of $\sim$270 ns [53, 54]. These properties added with the low-temperature processability (<150 °C) of $CH_3NH_3PbX_3$ make them a desirable material for solar cells, in performance similar to those of inorganic semiconductors. However, PSCs still have to overcome issues, such as toxicity owing to presence of Pb, scalability issues, hysteresis and also degradation as will be elaborated in subsequent sections [55, 56].

5.5.1 Crystal Structure of Halide Perovskites

Perovskites are expressed with a chemical formula ABX_3, where A is typically organic cation such as formamidinium (FA) and methylammonium (MA) or an inorganic cation such as Cs or a mixture of them, B is a divalent metal cation typically Pb^{2+} but Sn^{2+} is also employed to replace toxic lead, and X is a halogen atom (anion), viz. Cl, I, Br or their stoichiometric mixture binding A and B. Ideally a perovskite crystal forms a cubic crystal structure and has a space group $Pm\bar{3}m$. The choice of the various components of a perovskite crystal is crucial for its structural stability which is realized in terms of its tolerance factor (***t***), $t = \frac{R_A + R_X}{\sqrt{2}(R_B + R_X)}$ and octahedral factor (**μ**), where R_A, R_B, R_X are the Goldsmith ionic radii of A, B, and X, respectively [58–60]. Whereas ***t*** is ratio of distances between A-X and B-X for an ideal crystal structure, **μ** is the ratio between ionic radii of B and X. Figure 5.6 shows calculated and estimated ***t*** and **μ** of various common perovskites crystals. The closer the ***t*** value is to unity the more stable the perovskite is due to the cubic structure and a lower ***t*** value will lead to relatively less stable structures (orthorhombic or tetragonal). A stable perovskite crystal thereby requires $R_A > R_B > R_X$. Alternatively, a mismatch in the ionic radii of the three results in a tilt in BX_6 octahedra also causing a displacement of A cation. This induces electrical polarity in perovskite crystals and is a reason of their ferroelectric behavior. A detailed understanding of the typical three-dimensional and lower dimensional organic perovskites and its correlation with its electronic, optical and di-electric properties can be found in a comprehensive review by Saparov and Mitzi et al. [61].

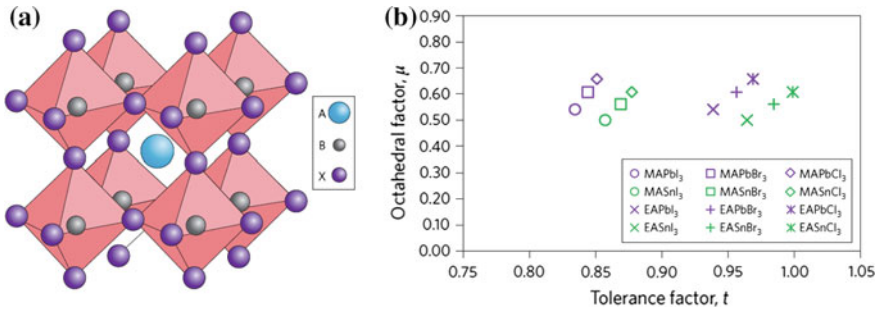

Fig. 5.6 **a** Crystal structure a perovskite with formula ABX_3 and **b** a plot of tolerance and octahedral factors of various organic perovskites. In the inset of (**b**) MA is methylammonium (CH_3NH_3) and EA is ethylammonium ($CH_3CH_2NH_3$). In most state-of-the-art PSCs, MA is mixed with formamidinium (FA; $NH_2CH{=}NH_2$) and also Cesium (Cs). Figure is adapted with permission from Ref. [54]. Copy right of Macmillan Publishers Limited

5.5.2 *Optical Properties of Halide Perovskites*

Organometallic halide perovskites ($CH_3NH_3PbX_3$) are direct bandgap materials with a tunable bandgap ($\boldsymbol{E_G}$) between 1.5 and 2.5 eV. Among the various halide perovskites, $CH_3NH_3PbI_3$ is the most prominent material to achieve a PCE close to the Shockley–Queisser limit of a single junction material ($\sim$33.7% at 1.4 eV). This is due to the bandgap of $CH_3NH_3PbI_3$, i.e., between 1.5 and 1.6 eV [62], which coupled with its higher absorption coefficient can theoretically yield PCE >30%. In fact, its absorption coefficient is notably higher than for crystalline silicon and also comparable or higher than most thin film materials (Fig. 5.7) [63]. Its steep absorption onset at $\sim$800 nm combined with high absorption coefficient enables $\sim$80% of incident light below its $\boldsymbol{E_G}$ to be absorbed by merely $\sim$300 nm thick

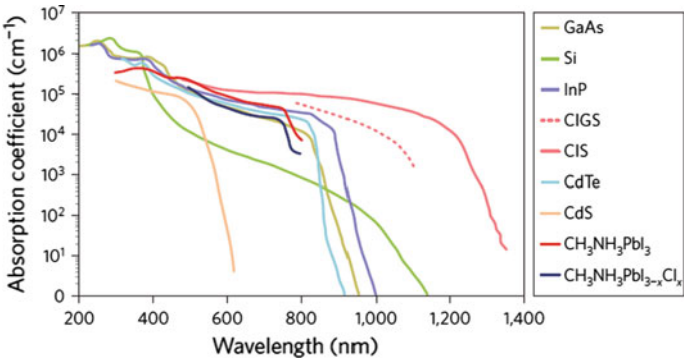

Fig. 5.7 A comparison of absorption coefficients of halide perovskites with those of silicon and most thin films solar cells, respectively. Figure is adapted with permission from Ref. [54]. Copy right of Macmillan Publishers Limited

film. The $CH_3NH_3PbI_3$ shows two distinct transitions at 760 and 480 nm [42−44]. Significant research is devoted to understanding the electronic band structures of halide perovskites. No contribution of methyl ammonium is found in energy band formations as their energy levels fall with the bandgap of perovskite. The valance bands at the two transitions (760 and 480 nm) are made of p-orbitals of **I** mixed with 6p and 6 s orbitals of **Pb** whereas σ-antibonding orbitals of 6p of **Pb** and 5 s of **I** and π-antibonding orbitals of 6p of **Pb** and 5p of **I** contribute to formation of the bottom of the conduction band [24, 45].

The bandgap of $CH_3NH_3PbX_3$ is tunable by changing chemical composition of its different materials constituents such as A, B, and X. Bandgap tuning allows the control over light absorption in PSCs and also enables obtaining higher V_{OC} in these devices according to Shockley–Queisser limit. For example, replacing MA with FA or using a mixture of MA, FA, and Cs has shown redshifted absorbance and also superior electronic transport [64]. It suggests that the size and chemical structure of the cation has a correlation with its optical properties. A phase change from tetragonal to quasi-cubic is observed when MA is replaced with FA due to the larger size of former (∼2.79 Å) than the latter (∼1.81 Å). A mixture of MA and FA, on the other hands, also provides phase instability. In fact, PCEs of 20–22% have already been achieved using mixed perovskites (15% MA and 85% FA or sometimes also including Cs) on glass substrates that are relatively stable when exposed to outdoor conditions [7, 8, 65].

Sutton et al. [66] demonstrated a systematic shift to shorter wavelength for absorbance as well as photoluminescence when Br is incorporated into $CsPbI_3$ (Fig. 5.8). The incorporation of Br resulted in improved stability of the PSCs compared to their pure iodide rivals. A systematic monotonic shift for $CH_3NH_3PbI_{3-x}Br_x$ by varying the Br content and a shift into the center of visible spectrum is demonstrated. Not only the bandgap tuning showed variation in color by chemical management in PSCs, but also the device employing $CH_3NH_3PbI_{3-x}Br_x$ showed superior moisture stability. Furthermore, bandgap tuning in PSCs has also

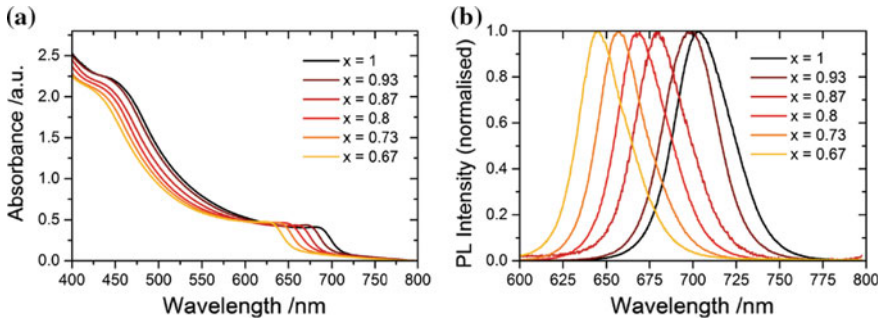

Fig. 5.8 **a** Absorbance and PL spectra for $CsPb(I_xBr_{1-x})_3$ films with varying iodide concentration "x". **b** PL spectra were excited using a tunable pulsed laser at 410 nm with a spot size of ≈0.2 mm^2. Figure is adapted with permission from Ref. [68]. Copyright Wiley-VCH Verlag GmbH & Co. KGaA. Reproduced with permission

demonstrated high V_{OC} of ~1.61 V in $CH_3NH_3PbBr_3$ perovskites; however, the PCE was limited to ~7.5% due to the limited J_{SC}. It is important to note that most high-efficiency PSCs nowadays use mixed halide perovskite as they offer light harvesting over a broader visible spectrum and also due to the fact that lattice distortion in $CH_3NH_3PbI_{3-x}Br_x$ crystals makes it less sensitive to moisture [67].

Likewise, Br which is known to influence structural and optical properties of $CH_3NH_3PbI_3$, the use of Cl has also been investigated. However, there is no evidence that incorporation of Cl leads to any variation in crystal structure or light harvesting properties of resultant perovskite film. Even the chemical analysis such as XRD and XPS typically fails to find a trace of Cl in resultant $CH_3NH_3PbI_{3-x}Cl_x$ films. Nonetheless, Cl-based mixed perovskite has shown several folds higher diffusion length (up to 1 micron) compared to pure $CH_3NH_3PbI_3$ [69]. It has also shown to retard the rapid crystallization of $CH_3NH_3PbI_3$ eventually providing a control over perovskite film morphology, especially when films are deposited using single-step deposition [55, 56]. The state-of-the-art performance of PSCs without a scaffold (19.3%) is reported using $CH_3NH_3PbI_{3-x}Cl_x$ films, where scaffold-less devices are fabricated via solution processing [70].

5.5.3 *Electronic Properties of Halide Perovskites and PV Mechanism*

The great interest in halide perovskites is primarily due to their remarkable electronic properties. For example, recent studies have shown a low exciton binding energy ~2 meV at room temperature asserting the fact that these devices do not require a heterojunction for their operation [71, 72]. This could explain the high efficiency in mono-junction PSCs (those employing only one of the selective contacts).

An important parameter for any type of solar cell is diffusion length (L_D). It is the measure of the path length that charge carriers can travel before they recombine and this determines the film thickness which should be shorter than its L_D so as to collect photogenerated electrons. Halide perovskites demonstrate large L_D which vary from $CH_3NH_3PbI_3$ to mixed halide perovskite such as $CH_3NH_3PbI_{3-x}Cl_x$ (Fig. 5.9). In a comparative study by Stranks et al. [69], pure iodide-based perovskite demonstrated L_D ~129 ± 41 and 105 ± 32 nm whereas their mixed counterpart ($CH_3NH_3PbI_{3-x}Cl_x$) demonstrated L_D 1069 ± 204 and 1213 ± 243 nm, for electrons and holes, respectively. Subsequently, measurements using electron-beam-induced current (EBIC) analysis shows these values to be as high as 1.9 μm for electrons (~1.2 μm for holes) [73]. The electronic properties of $CH_3NH_3PbI_{3-x}Cl_x$ are indeed similar to intrinsic semiconductors, with a carrier density (10^9 cm^{-3}) similar to intrinsic silicon. Perovskite films of high quality demonstrate electron mobility as high as ~60–100 cm^2 V^{-1} s^{-1}) [74]. The mobility also depends on whether a perovskite films are made using pure iodide or is a mixed halide one. Typically, higher electronic properties are reported for mixed halide counterpart ($CH_3NH_3PbI_{3-x}Cl_x$) [75, 76].

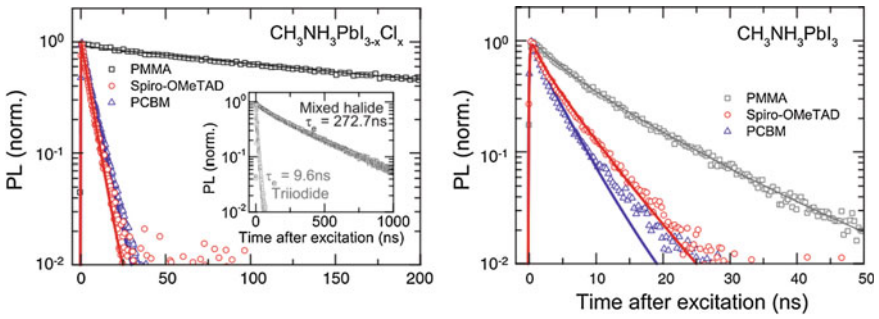

Fig. 5.9 Time-resolved photoluminescence spectra of mixed halide perovskite (*left*) and triiodide perovskite (*right*). The perovskite layer is interfaced with an ETL (PCBM; *blue triangles*) or HTL (Spiro-OMeTAD; *red circles*) quencher layer. The films were excited using a pulsed (0.3–10 MHz) excitation source at 507 nm from on the glass substrate side. Figures adapted with permission from Ref. [69]. Reprinted with permission from AAAS

As thin films are characterized by a larger number of surface defects, they usually demonstrate inferior carrier mobility, larger trap density, and shorter carrier lifetime than their corresponding single crystals. The highest diffusion length for perovskites is also reported in their single crystals of 3 mm in size; i.e., ~175 μm for electron and holes at 100 mW cm^{-2} and exceeds 3 mm at weaker light intensities (Fig. 5.10). In fact, at a radiation intensity of 0.003 mW cm^{-2} , the single crystal demonstrated carrier life time ~2.6 s and L_D ~33 ± 5 mm. Hall effect measurements of the single crystal revealed a low trap density 4.5 × 10^{10} cm^{-3} and electron mobility ~24.8 ± 4.1 cm^2 V^{-1} s^{-1}. The mobility is also verified using time-of-flight method (ToF) which was 24 ± 6.8 cm^2 V^{-1} s^{-1} [77]. A recent theoretical simulation revealed that the traps that are induced due to surface defects in

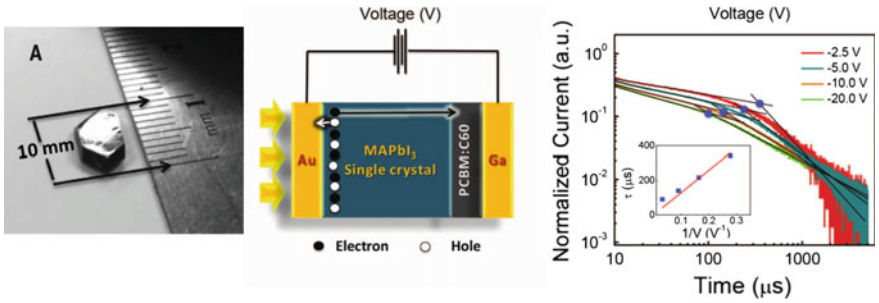

Fig. 5.10 Photograph of an as-prepared $MAPbI_3$ single crystal (*left*), schematic illustration of the cell for the time-of-flight measurement to calculate carrier lifetime and trap density (*middle*), and normalized transient current curves of the cells (*right*). The carrier transit time is determined by the intercept of the pre-transit and post-transit asymptotes of the photocurrent, marked by *solid blue circles*. Inset shows the charge transit time versus the reciprocal of applied voltage; the solid line is shows fitted data. Adapted with permission from Ref. [77]. Reprinted with permission from AAAS

perovskite lie close to the band edges [78]. This could employ that these defects might not be so critical in obtaining high performance in the devices, as they might not induce significant recombination of charge carriers. The lower loss in potential (0.4–0.45) and a high V_{OC} ($\sim$1.1 V) obtained in solution processed PSCs, using the $MAPbI_3$ (E_G $\sim$1.55 eV), could affirm the less critical role of such surface defects as a major recombination center [63]. Such remarkable electronic properties extend the use of halide perovskite material to other electronic devices such as laser and light emitting diodes (LEDs).

An important curiosity about PSCs is their photovoltaic mechanism. From the available literature, it is quite convincing that PSCs are non-excitonic in nature. The reported values of their exciton binding energy ($\leq$5 meV) for most common perovskites, determined experimentally from optical measurements [36] and also by theoretical calculations [30], suggest >98% charge dissociation even at room temperature. Although the charge separation takes place within perovskite film, selective contacts are crucial to selectively transport the photogenerated charge carrier toward respective electrode, without which devices have shown extremely poor performance [57, 79]. A significant important question from structural point of view is the role of MA cation in PV mechanism. As the ionic behaviors of the halide perovskite are well reported, and its volatile nature of that leads to ion migration and also the fact that no contribution of MA cation is found in formation of band structure of $MAPbX_3$ suggests that the MA cation provides an ion conducting pathway [55]. This could also be understood from the low fill factor when MA is replaced with Cs (in $CsPbI_3$ PSCs), as shown in Table 5.3. It hints that a polar and mobile entity at A site in ABX_3 rather that relatively nonvolatile Cs is favorable to obtain high PCE in these devices, as evident from a large difference in the performance of the PSCs made using $MAPbI_3$ and $CsPbI_3$ (Table 5.3).

5.5.4 *Methods for Perovskite Film Formation*

One of the greatest interests in PSCs lies in their solution processability that allows fabrication of high-performance devices using cost-efficient techniques. In a typical procedure, the $CH_3NH_3PbX_3$ film is fabricated at room temperature by mixing an organic component and a metal halide; i.e., $CH_3NH_3I + PbI_2 \rightarrow CH_3NH_3PbI_3$. Although the high-quality films are typically fabricated in situ to avoid their decomposition in presence of moisture and oxygen, the device fabrication at ambient has also yielded a notable performance $\sim$19.3% [70]. Typically, single-step or two-step spin coating is used to fabricate perovskite films. Whereas the single-step fabrication involves spinning of a solution containing both the precursors dissolved in a solvent (e.g., DMF), the two-step fabrication involves coating of the PbX_2 first followed by coating of CH_3NH_3I which can be carried out via spin coating, dip coating, or vacuum-assisted vapor deposition (Fig. 5.11). Crystallization of $CH_3NH_3PbI_3$ films is associated with a color change from yellow to light brown at room temperature, which upon annealing changed to dark brown indicating a

Table 5.3 A comparison of Tolerance factor (TF) and bandgap of various hybrid and inorganic perovskites and their photovoltaic performance when employed as absorber in solar cells

Absorber	Tolerance factor	Bandgap	PV parameters[a]
$CH_3NH_3PbI_3$	0.83	1.55	**17.9%** (21.0, 1.11 V, 0.76 FF) [46][b]
$CH_3NH_3PbI_{3-x}Cl_x$	0.83–0.85	1.85	**19.3%** (22.7, 1.13 V, 0.75 FF) [47]
$CH_3NH_3PbCl_3$	0.85		
$CH_3NH_3PbI_{3-x}Br_x$	0.81–0.83	1.6–2.3	**16.5%** (19.6, 1.1 V, 0.76 FF) [48]
$CH_3NH_3PbBr_{3-x}Cl_x$	0.81–0.85	~2.2	**2.7%** (4, 1.5 V, 0.46 FF) [49]
$CH_3NH_3PbBr_3$	0.81	2.3	**7.5%** (6.04, 1,61 V, 0.77 FF) [50][c] **11.4%** (14.1, 1.11 V, 0.73 FF) [51][d]
$CsPbI_3$	0.81 [28]	1.65	**2.9%** (12, 0.8 V, 0.30 FF) [52]
$FAPbI_3$			
$(FAPbI_3)_{1-x}(MAPbBr3)_x$			**20.8%** (24,6, 1.16 V, 0.73 FF) [53]
$Csx(MA_{0.17}FA_{0.83})_{(100-x)}Pb(I_{0.83}Br_{0.17})_3$			**21.1%** (23.5, 1.15 V, 0.78 FF) [54]
$CH_3NH_3SnI_3$	0.97	1.30	**6.4%** (16.8, 0.88 V, 0.42 FF) [55]

Most devices employ Spiro and TiO_2 as HTL and ETL, respectively, unless stated otherwise. Reproduced with permission from Ref. [55]. Copyright under common creative license

[a]The IV parameters follow the order (PCE (J_{SC}, V_{OC}, and FF)). The units for J_{SC} is mA/cm^2 and not included to shorten the text

[b]A corresponding device employing MAPbBr3 resulted in PCE 4.4% (4.4, 1.3 V, 0.75 FF)

[c]Employs PEDOT:PSS and ICBA as HTL/ETL

[d]PTAA and TiO_2

complete transformation of initial precursors into crystalline perovskite. Although the fabrication of $CH_3NH_3PbI_3$ films seems easy, an understanding of processing parameters and their effect on the underlying reaction chemistry is crucial to obtaining high quality, thin yet pin-hole free films for efficient devices. The perovskite film morphology depends on the type of solvent employed, processing conditions such as annealing and rate of solvent extraction, and the surface properties of underneath layer.

The choice of various methods is to have a control of $CH_3NH_3PbI_3$ morphology, which starts to crystallize rapidly, even at room temperature. For example, two-step method typically yields dense perovskite films with a >200 nm thick over layer of $CH_3NH_3PbI_3$. However, recently modified single-step methods have also started to show high PCE >20%, as will be discussed in the subsequent section.

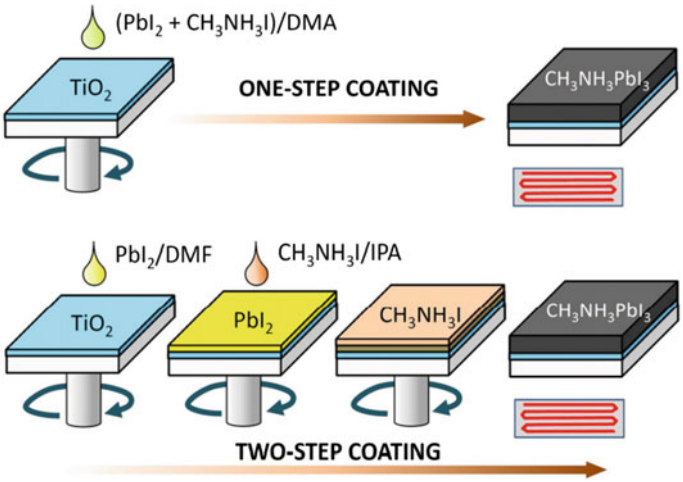

Fig. 5.11 Schematic shows two typically employed deposition methods for perovskite solar cell. Adapted with permission from Ref. [80]. Copyright of American Institute of Physics (AIP)

5.5.4.1 Perovskite Films via a Single-Step Deposition

Single-step (SS) deposition of perovskite is a cost-effective way compared to its two-step counterpart and thereby offers more compatibility to mass production. Herein, the two precursors, viz., PbX_2 and CH_3NH_3X are dissolved in a solvent such as DMF, DMSO and γ-butyrolactone. For laboratory-scale devices, spin coating is the most common method employed; however, doctor balding and slot-die coating—methods compatible with large area processing—are also reported resulting in PCE 10–12% [81]. A complete transformation of spin-coated perovskite film requires annealing at 70–100 °C. Although initially thermal annealing was the only method employed which usually takes an hour, recently photonic curing of perovskite films has been also demonstrated which takes merely a few seconds to fully crystallize [82]. This makes single-step deposition a highly desirable method of choice, particularly for large-scale processing.

The best performing PSCs made via SS demonstrated PCE ~19.3% via interface optimization and modified ITO surface [70] whereas the average efficiency obtained in a device without such cumbersome fabrication process is lower. The simple SS deposition typically results in lower PCE compared to two-step rivals due to difficulty in controlling the crystallization of perovskite films. However, with some modifications, it leads currently to the highest reported efficiencies. The difficulty in formation of a thin pin-hole free and a homogeneous surface via SS leads to morphological defects such as larger number of grain boundaries eventually resulting in charge recombination at such interfaces. The formation of pin-holes is because the solvent evaporates spontaneously and the precursors tend to form large crystallites during spinning. Recently, modified SS deposition has shown high efficient and reproducible PSCs with PCE >20%. For example, solvent dripping

technique, which employs a solvent different from the one used to form perovskite solution has shown PCE of ~19% [83]. This new solvent is dropped over the perovskite film during spin coating for a faster crystallization that helps to obtain perovskite films with large crystals. Chlorobenzene is a common solvent employed to induce such a fast crystallization. Zhu et al. [84] also showed PCE ~18.8% using toluene dripping. The state-of-the-art PCE ~21.1% is obtained using this method, where a perovskite employing triple cation (FA, MA and Cs) and a mixture of halides (I and Br) is fast crystallized via chlorobenzene dripping (Fig. 5.12). This resulted in dense perovskite film over a mesoporous scaffold with additional perovskite capping layer, which is a key to obtain high performance in these devices.

Various other methods to optimize morphology of perovskite film via controlling the crystal growth are introduced such as (i) incorporation of chloride into precursors that results in mix halide perovskite ($CH_3NH_3PbI_{3-x}Cl_x$) (even though no Cl^- has been detected in the film, leading to the assumption that the chloride is

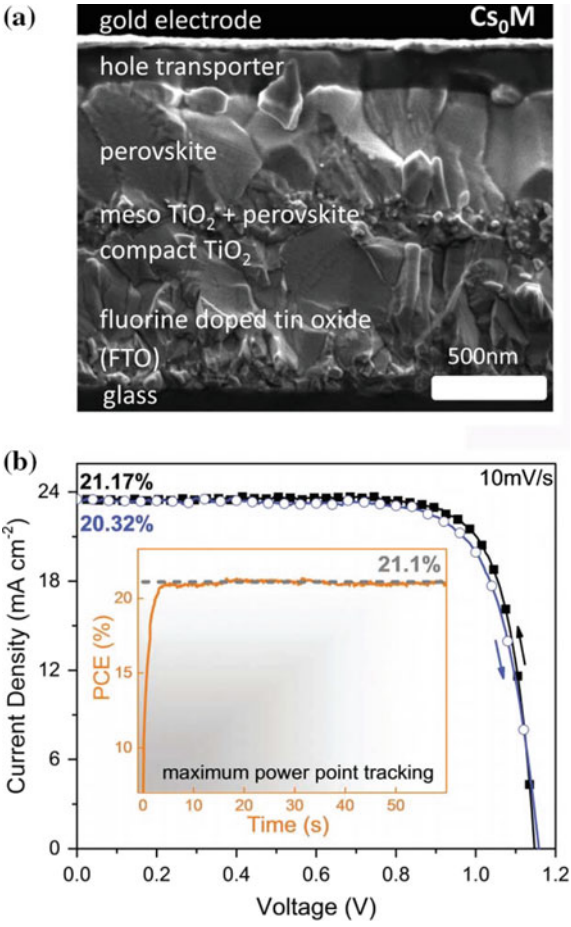

Fig. 5.12 **a** Cross-sectional view of the state-of-the-art (reported) PSC employing a triple cation (MA/FA/Cs) and **b** current–voltage curve of the same, the inset shows stabilized power output of the device. Figure adapted with permission from Ref. [7] Copy right of The Royal Society of Chemistry

only beneficial for the film formation but not included in the perovskite lattice), (ii) use of additives such as hydriodic acid (HI), and (iii) solvent–solvent extraction [85] also demonstrated improvement in film properties [55]. Toward the former, a small amount of HI to perovskite solution helped achieve PCE >18%. Similarly, the solvent–solvent extraction method has reported PCE up to 15.2% by Zhou et al. [85] in planar PSCs. The dual source evaporation [86] which involves evaporating organic and inorganic precursors at low pressure (10^{-5} m bar) can also be termed as a SS deposition method. Although this method yielded ultra-smooth and dense $CH_3NH_3PbI_{3-x}Cl_x$ which resulted in PCE ~15%, the method could offer limitations to cost-effective large-scale fabrication of PSCs.

5.5.4.2 Perovskite Films via Two-Step Deposition

Two-step (TS) deposition also often referred as sequential deposition was first introduced by Burschka et al. [87] who deposited PbI_2 on mesoporous TiO_2 and dried it at 70 °C. The films were then immersed in CH_3NH_3I solution in iso-propanol, which yielded pin-hole free dense perovskite films with PCE ~15%. Since then, TS is employed as a preferred deposition method to obtain not only high performance but also high reproducibility. Sequential deposition solved the limitation of pore-filling of mesoporous TiO_2 films in SS deposition and also typically demonstrates an over layer of perovskite on top of the mesoporous film, called capping layer [88]. The immersion of PbI_2 coated substrates requires ample CH_3NH_3I solution which offers limitation to scalability and also could increase fabrication cost. Alternatives such as spin coating CH_3NH_3I solution (two-step spin coating), and vacuum-assisted vapor deposition (VAVD) have been introduced. The latter involves placing PbI_2-coated substrates in a vacuum surrounded by solid CH_3NH_3I crystals which upon heating evaporate and react with the PbI_2 films (Fig. 5.13). The best PCE using DS deposition method in a mesoporous PSC is ~20% where mixed cations (FA and MA) based perovskite demonstrated a complete pore-filling along with a capping layer over the filled mesoporous TiO_2 layer [89]. However, the PCE for a planar rival is ~16.2% only.

Although both the deposition methods now yield uniform films of desired morphology resulting in device with efficiencies >20% the SS method seems more preferred choice owing to its relatively easier and cost-effective processing than TS deposition, although a direct comparison of the cost involved for large area processing using the two methods has not yet reported.

5.5.5 Device Architectures for Perovskite Solar Cells

One of the unique features PSCs offer is their wide variety of device designs which ranges from mesoporous (employing a scaffold such as TiO_2) to planar (those with a thin flat layer only), and from p-i-n or n-i-p configuration to p-n or n-p

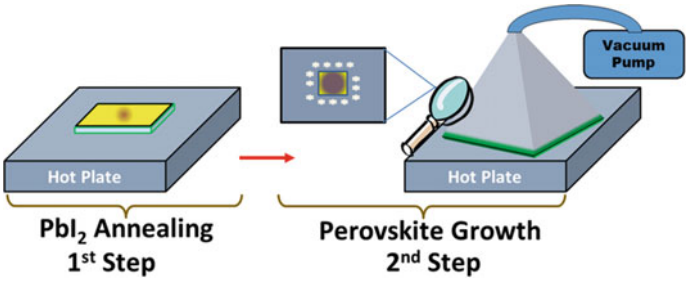

Fig. 5.13 Schematic of double-step deposition via vacuum vapor assisted sequential processing. Figure adapted with permission from the Ref. [90]. Copyright of American Institute of Physics (AIP)

configuration (Fig. 5.14). Although, the first PSCs were merely an advancement of the DSSCs or ETA solar cells, where a perovskite absorber ($CH_3NH_3PbI_3$ or $CH_3NH_3PbBr_3$) with ~20 times higher absorption coefficient replaced the dye [91], it subsequently emerged as a separate class of solution processable thin film PVs. Also, the understanding of their working mechanism led to the optimization of their various material constituents: for example, (i) the thickness of TiO_2 scaffold which was ~10 μm in the first PSCs was systematically dropped to ~500 nm in 2012, (ii) the liquid electrolyte was replaced by a solid state HTL, e.g., 2,2′,7,7′-tetrakis-(N,N-p-dimethoxy-phenylamino)-9,9′-spirobifluorene (spiro-OMETAD) which improved the PCE three times (9.7% in 2012 from an initial 3.9% in 2009) and made the solar cells considerable more stable, and (iii) the perovskite film which was initially conceived to be a thin absorber layer subsequently evolved to a dense semiconducting layer (~300 nm). The developments such as optimization of perovskite film characteristics, energy level alignment at the device interfaces and incorporation of FA and/or Cs along with MA, and also, introducing mixed halide salts such as PbBr and PbI brought PSCs to deliver PCE 22.1% in 2016.

A typical PSC employs a 300–500 nm thick perovskite layer between electron and hole selective contacts. Figure 5.15 shows few common material combinations employed in literature. In fact, a film thickness of ~280 nm has shown to absorb >80% of incident light in the visible spectrum. Upon light absorption, electrons are photoexcited from the valance band to the conduction band of the perovskite absorber. The charge separation that takes place within the perovskite shows that these devices are not excitonic in nature and rather fit well with a free carrier model as usually observed in inorganic solar cells [92]. However, the selective contacts are required for efficient charge extraction. The significant role of these interfaces can also be evidenced from the difference in PV performance of device employing a single selective contact to those employing two charge selective contacts (Fig. 5.14). Although charge generation and separation takes place within perovskite, a poor charge extraction leads to higher recombination within the device, as shown in inferior PV parameters of such devices in literature (Fig. 5.14e and f). This also takes place if the selective contacts are not pin-hole-free or if the

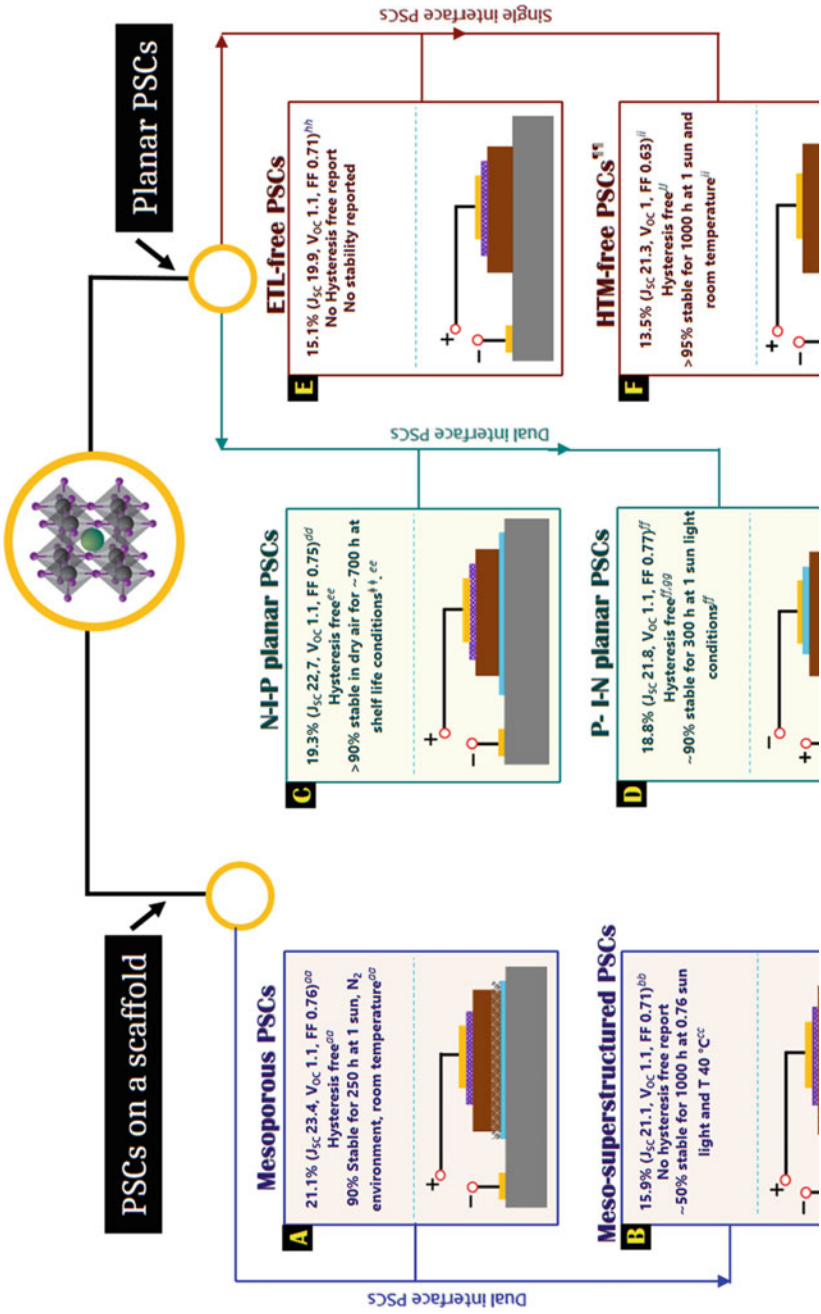
PSCs on a scaffold
Planar PSCs
Mesoporous PSCs
A
21.1% (J_{SC} 23.4, V_{OC} 1.1, FF 0.76)[aa]
Hysteresis free[aa]
90% Stable for 250 h at 1 sun, N_2 environment, room temperature[aa]
Meso-superstructured PSCs
B
15.9% (J_{SC} 21.1, V_{OC} 1.1, FF 0.71)[bb]
No hysteresis free report
~50% stable for 1000 h at 0.76 sun light and T 40 °C[cc]
Dual Interface PSCs
N-I-P planar PSCs
C
19.3% (J_{SC} 22.7, V_{OC} 1.1, FF 0.75)[dd]
Hysteresis free[ee]
>90% stable in dry air for ~700 h at shelf life conditions[ff, ee]
P- I-N planar PSCs
D
18.8% (J_{SC} 21.8, V_{OC} 1.1, FF 0.77)[ff]
Hysteresis free[ff,gg]
~90% stable for 300 h at 1 sun light conditions[ff]
Dual Interface PSCs
ETL-free PSCs
E
15.1% (J_{SC} 19.9, V_{OC} 1.1, FF 0.71)[hh]
No Hysteresis free report
No stability reported
HTM-free PSCs[ii]
F
13.5% (J_{SC} 21.3, V_{OC} 1, FF 0.63)[jj]
Hysteresis free[jj]
>95% stable for 1000 h at 1 sun and room temperature[jj]
Single Interface PSCs

◂**Fig. 5.14** The common device architectures of perovskite solar cells are classified in two major categories: mesoporous, employing a scaffold and planar, employing a thin flat layer. The mesoporous scaffold can be electrically conducting such as TiO_2 and ZnO or insulating such as Al_2O_3 and ZrO_2. The planar PSCs can be divided in two subcategories: (i) dual-interface PSCs, employing a perovskite layer between ETL and HTL and (ii) single-interface PSCs employing only one of the two selective contacts. The inset of each Figure also shows highest performance reported for each architecture and whether or not hysteresis-free and a stable performance is achieved. Figure adapted with permission from Ref. [55]. Copyright under common creative license. ǂ ǂ Room temperature, room light, ¶¶ The device also employing monolithic PSCs (few micron thick carbon back contact is deposited over perovskite), *aa* Saliba et al. [7], *bb* Wojciechowski et al. [93], *cc* Leijtens et al. [94], *dd* Zhou et al. [70], *ee* Baena et al. [95], *ff* Zhu et al. [84], *gg* Bi et al. [96], *hh* Hu et al. [97], *ii* Wei et al. [98], *JJ* Wei et al. [99]

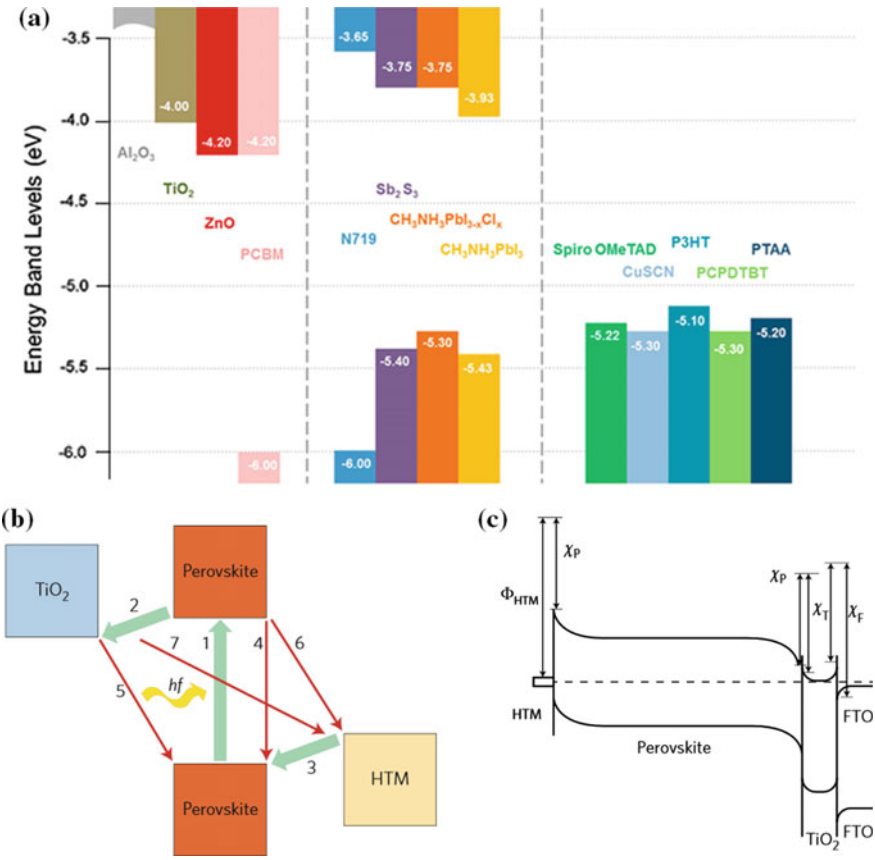

Fig. 5.15 **a** Schematic showing energy levels of commonly employed material components in perovskite solar cells; viz, ETL, perovskite and HTL. Figure adapted with permission from Ref. [62] Copyright of Elsevier. **b** Schematic depicting electron transfer process in PSCs. The *green arrows* show processes related to energy conversion, such as charge separation and transfer, whereas the *red arrows* show various possible recombination paths in a PSC. **c** Energy level diagram showing PV mechanism in PSCs. Herein, χP, χT, and χF are the electron affinities of the perovskite, TiO_2 and the conducting substrate (FTO), respectively, and Φ_{HTM} is the work function of the HTL. Figure is adapted with permission from Ref. [54]. Copyright of Macmillan Publishers Ltd.

perovskite layer is not dense enough which could make a short circuit between ETL and HTL or perovskite-FTO (in the case of ETL-free PSCs). This requires extreme care during fabrication of each of these films, particularly, the perovskite layer, to ensure maximum collected photogenerated electrons.

An interesting feature associated with PSCs is the use of insulating oxides such as Al_2O_3 as a scaffold layer (Fig. 5.14b) on conducting substrates which facilitates perovskite crystallization [50]. These devices are termed as meso-superstructured PSCs (or MSSCs). The charge transport in these devices differs from a conventional p-i-n or n-i-p devices as electron transport to selective contacts is carried by the perovskite layer itself. In the various reports on MSSCs, a systematically higher V_{OC} is observed in these devices than those employing a TiO_2 scaffold, although the J_{SC} is often lower [50, 100]. This could be explained from the origin of V_{OC} in PSCs which is limited by the splitting of quasi-Fermi levels of electrons and holes in perovskite layer. In the case of Al_2O_3-based PSCs, the splitting of Fermi level is determined by perovskite layer itself as the insulating layer does not take part in PV operation whereas, the in the case of TiO_2, the electron injection takes place from perovskite to the conduction band of TiO_2. The presence of sub bandgap states in TiO_2 creates an energy offset at the interface, restricts the Fermi level split, and also results in non-radiative recombination thereby restricting the V_{OC} in these devices [50].

The high absorption coefficient coupled with the high charge carrier mobility (2–66 $cm^2\ V^{-1}\ s^{-1}$) [74] of halide perovskites are the main reasons for high performance in these devices. However, the characteristics of the perovskite layer such as morphology, density, and thickness are key parameters for high performing devices. Furthermore, for efficient devices, the energy level alignments at the device interfaces, viz., ETL-perovskite and HTL-perovskite, charge mobility of ETL and HTL are also crucial and can lead to a potential drop across the interfaces. The state-of-the-art mesoporous PSCs (PCE 19–22%) [7, 8, 65] and planar PSCs (PCE 18–19%) [70, 96] usually demonstrate both, a careful interfacial design and perovskite film optimization.

The planar PSCs employing an n-type or p-type thin flat layer underneath perovskite absorber are of particular interest as these devices are more compatible with mass production. However, although addition of a mesoporous layer which often also require high-temperature sintering hinder roll-to-roll production compatibility of PSCs, the planar devices show often reproducibility issues and are generally less stable, especially if TiO_2 is used as ETL. One must also note that, in most state-of-the-art planar or mesoporous PSCs, a clear distinction is hard to be drawn. This is because both employ a perovskite capping layer and also the mesoporous PSCs also employ a compact TiO_2 layer underneath the meso-TiO_2 [57]. Nevertheless, in both the mesoporous and planar PSCs, various alternative n-type metal oxides to TiO_2 such as ZnO [95], SnO_2 [101, 102], and Zn_2SO_4, are also employed. SnO_2 has shown exceptional performance resulting in a PCE $\sim$16% in n-i-p and $\sim$19% in p-i-n configuration. Not only incorporation of such ETL layers reduced hysteresis—drop in power output under the effect of an electric field—but also, more importantly, improved the stability of PSCs. Similarly, replacement of TiO_2 by fullerene derivative has also shown hysteresis-free performance.

Likewise n-type planar PSCs, their p-type analogues also showed remarkable PCE of 17–19% [84, 103]. These devices are also often termed in literature as inverted PSCs as holes instead of electrons are collected at the conducting substrate. Although initially these devices mostly employed organic selective contacts such as poly(3,4-ethylenedioxythiophene)-poly(styrene sulfonate) (PEDOT:PSS) as HTL and PCBM as an ETL [104], which led to rapid degradation, quite recently they are replaced with inorganic counterparts such as NiO and TiO_2 or SnO_2. Besides high performance, these devices are low-temperature processable which make them compatible with mass production. A general prerequisite in the planar PSCs is a thick enough pin-hole free selective contact on FTO to avoid charge recombination, yet thin enough not to add series resistance of the film. However, despite the remarkable performance made in these architectures, they are often characterized by degradation when exposed to atmospheric stress factors or light soaking.

The working of PSCs, in principle, require only one of the selective interfaces to be present for efficiency charge extraction, owing to the ambipolar charge transport properties of halide perovskites [105, 106]. Figure 5.14 shows two such architectures which employ a HTL only (e) and an ETL only (f). These devices yet have to demonstrate a stable performance. Nonetheless, these devices are much simpler in design and do not employ the expensive materials such as spiro-OMeTAD and gold contacts. Carbon-based PSCs (or monolithic PSCs) often termed as HTL free PSCs, cannot be placed under these categories as carbon derivatives demonstrate hole extraction characteristics. In monolithic PSCs, a thick mesoporous carbon layer (~ 10 μm) is coated on top of a TiO_2 layer and an insulating layer such as ZrO_2 is employed between them. PSCs without an insulating layer are also reported when carbon black is replaced with carbon nanotubes, a material with superior hole mobility. The perovskite solution is inserted through the thick carbon layer that infiltrates through the porous scaffold. These devices have shown one of the most notable stability (1000 h in light soaking) for PSCs [107, 108]. The simplicity, ease of fabrication and also cost-effectiveness make them a promising architecture for large-scale production. This design is particularly interesting after the demonstration that a degraded perovskite solution can be replaced by a fresh one, giving a new life to the device [109].

The wide variety of PSCs designs make their working principle hard to generalize. The origin of V_{OC} and mechanisms of photovoltaic action is still being under investigation. Nevertheless, with the knowledge so far gained about PSCs, it is clear that they are not excitonic and the charge separation takes place inside the perovskite layer, even at room temperature. The V_{OC} which is primarily determined by the splitting of quasi-Fermi levels of electrons and holes in the perovskite layer itself, is influenced by the interfacing materials such as their energy level alignment to perovskite and also their charge mobility [57, 110]. A selection of suitable perovskite and selective contacts have led to V_{OC} as high as 1.61 V. A detailed correlation of PV parameters and the different design architecture can be found in our research update published elsewhere [55].

5.5.6 Hysteresis in Perovskite Solar Cells

The *J–V* curves of PSCs typically show a dependency on the measurement conditions such as scan direction, rate and range, and voltage pretreatment [111–114]. This often leads to difficulty in reporting true performance of the device as the PCE is overestimated when scanning from forward-to-reverse voltage sweep direction. The origin of this anomalous hysteresis is still under debate, the plausible reasons might be, ionic–electronic transport, slow ion migration, the ferroelectric properties of halide perovskites, dynamic trapping and de-trapping of photogenerated charges, and also the charge accumulation at TiO_2-perovskite interface [112, 115–121]. We refer to a comprehensive review for further details on the origin of *J–V* hysteresis and its elimination [122]. The hysteresis also shows its strong dependency on the ETL/HTL, device architecture, processing conditions of perovskite and so forth. For example, replacing TiO_2 with PCBM or C_{60} as an ETL reduced hysteresis significantly [123, 124]. The fact that most high-efficiency PSCs (both the planar and mesoporous) do not show any hysteresis points to the urgent need for optimizing the device architectures and interfacial layers and also the processing conditions, which would lead to efficient and stable PSCs.

As the PCE of a perovskite solar cell can strongly depend on the measurement parameters, it is extremely important to have a reliable measurement protocol, which eliminates such differences [125, 126]. Only then, it is possible to compare published PCE values in literature and get a conclusive idea of, e.g., best preparation parameters [127]. It is suggested by different researchers to measure the solar cell by tracking the maximum power point over time until it has stabilized, which will allow reliable measurement methods. For a detailed explanation of such a tracking algorithm and an example of the technical implementation, we refer the reader to the report by Zimmermann et al. [128].

5.5.7 Flexible and Low-Temperature Perovskite Solar Cells

The commercially available wafer based or thin film solar cells are typically developed on rigid substrates that restrict their application areas to be roof or ground mounted only. One of the added features of organic solar cells is the possibility to manufacture them on flexible substrates, such as transparent conducting plastics and metallic foils. This could widen their application domain from portable and wearable applications to indoor or integrated such as building or automobile integrated photovoltaics. These flexible substrates are also compatible with roll-to-roll (R2R) processing, which, added with the solution processability of PSCs, could lead to achieve grid parity of PV technology (<0.5$/kWh). Toward this, the state-of-the-art PCE of $\sim$15.6% in laboratory scale flexible-PSCs (*f*-PSCs), which is on par with commercial silicon and thin film modules and much higher

than its DSSC (~8%) and OPV (11%) counterparts, makes its case further compelling for commercial deployment [2].

The typical substrates used in *f*-PSCs are: (i) conducting plastic-based polymeric substrates such as polyethylene terephthalate (PET), polyethylene naphthalate (PEN) or polycarbonate (PC), and polyethersulfone (PES), and (ii) metallic substrates such as titanium and nickel foils, and stainless steel. Whereas the former can only withstand a temperature up to 150 °C, the latter allow processing at high temperatures. However, the opacity of metallic substrates requires the metal back contact to be highly transparent to enable maximum incident light reaching the working electrode. Typical examples of (i) are shown in Fig. 5.16. For an in-depth understanding of *f*-PSCs and its comparison with other flexible PVs. we refer to a comprehensive account by Giacomo et al. [2].

In brief, the best performing *f*-PSC (PEN/ITO/ZnO/MAPbI3/PTAA/Au) shows an efficiency ~15.4% (V_{OC} 1.1 V, J_{SC} 18.7 mA cm^{-2}, and FF 0.76) for forward scan and 15.6% for a reverse scan (V_{OC} 1.1 V, J_{SC} 18.7 mA cm^{-2}, and FF 0.76) [129]. These devices built on polymer substrates show negligible hysteresis and a good mechanical stability. The high efficiency in these devices and the hysteresis-free performance is, largely, attributed to ZnO which facilitated faster electron extraction at ETL-perovskite interface than a corresponding TiO_2-based counterpart. The possibility to prepare ZnO films at low temperature and its superior electron conductivity (0.0031 mS cm^{-1}) than the TiO_2 (0.00006 mS cm^{-1}) demonstrates its potential as a leading ETL material in PSCs. One must note that a ZnO film prepared at low temperature typically offers more surface defects which are a source of thermal degradation in ZnO-based PSCs [130]. Similarly, PCEs of ~15.3 and 14.9% are demonstrated in PET-ITO based PSCs employing a TiO_2-based thin layer as ETL [131] and for $ZnSnO_4$ ETL based PSCs on PEN-ITO [132], respectively.

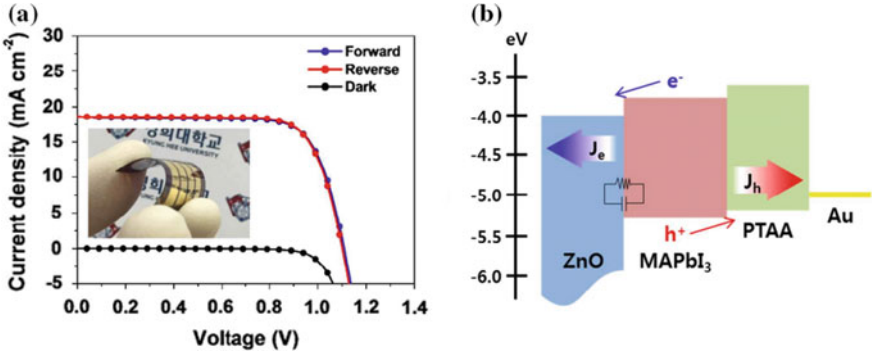

Fig. 5.16 **a** Current density–voltage curves of state-of-the-art flexible perovskite solar cells with device architecture (PEN/ITO/ZnO/MAPbI3/PTAA/Au). A photograph of the device is shown in the inset. **b** Schematic band energy diagram of ZnO electron conductor based MAPbI3 planar perovskite hybrid solar cells. Adapted with permission from Ref. [129]. Copyright of The Royal Society of Chemistry

The *f*-PSCs on metallic substrate (Ti foil) also demonstrated a PCE of 13.1% when TiO_2 nanowires (NWs) are used as ETL which is significantly higher than a TiO_2 NP rival (9.9%) [133]. Herein, the key issue of transparency in the device is solved using PEDOT as HTL and ITO-PEN as back contact. Although the PSCs showed flexibility, mechanical stability and a low sheet resistance, a large hysteresis is observed in these devices (PCE values at reverse and forward scan are 13.1 and 7.3%, respectively).

5.5.8 *Degradation in Perovskite Solar Cells*

For any solar cell, the important thing next to high efficiency is its long-term operational stability. This is particularly important for new PV technologies such as PSCs to enter the market as the commercially available silicon and thin film PVs has a typical lifetime of >20 years. Although intensive initial efficiency driven research has brought PSCs to deliver a PCE 22.1% in merely 4 years since their first viable device (PCE 9.7%), one of the key challenges to be solved is their long-term operation stability [56, 134]. The PSCs have shown to degrade when exposed to external stress factors such as humidity, UV light, light soaking, temperature, and under the effect of an electric field [135–139] and also due to internal factor such as reactive interfaces that leads to decomposition of perovskite with either ETL [19, 57, 66, 140, 141] or metallic contact such as Ag [142, 143]. The instability in these devices arises from the fact that the perovskite crystals are chemically unstable and are subjected to a phase change under the effect of atmospheric factors [49, 144, 145]. Another significant degradation route in these devices is change in current–voltage profile at different scan parameters (scan direction, scan rate, and relaxation time) which is understood due to ion movement of halide ions [125, 146, 147].

Research to improve stability of perovskite can be classified in two types: First is to improve stability of the full device by either using inorganic selective contacts (ETL and HTL), or improving encapsulating strategies to protect the device from external factors whereas in the second type, the focus is to improve stability of perovskite layer itself by incorporation of mixed halide cations (Br incorporation is known to induce more resilient perovskite), or recently, replacement of organic cation (typically MA) with inorganic one (Cs) [56, 134, 136, 139]. Incorporation of perovskite films in hydrophilic polymer matrix has also shown to improve humidity stability of perovskite films, where the moisture absorbed by perovskite is dehydrated by the polymer chains keeping the perovskite films dry [148, 149]. For a detailed overview of various degradation pathways in the PSCs, we refer to comprehensive reviews in literature [139, 145, 150].

Toward the first strategy, in a typical n-i-p architecture, the HTL acts as the first line of defense. The typically employed HTLs such as spiro-OMeTAD and poly (3-hexylthiophene) (P3HT) shows poor protection ability against moisture,

particularly, when incorporated with hygroscopic dopants such as Li-TFSI which is extremely reactive to moisture. This is overcome by incorporating alternative inert dopants to HTL, or humidity resilient dopants and also by incorporating the HTM in an insulating polymer (polycarbonate) shield along with incorporation of single-walled carbon nanotubes [33]. The latter successfully halted humidity creep into the device and showed highly stable performance even when exposed to running water for few minutes. Similarly, moisture ingress into the device can be overcome by cross-linking the hole transporting material. An extreme thermal stability up to 110 °C and a humidity stability up to 30 days at Rel. H 70% is reported when an arylamine derivative (N4,N4′-Di(naphthalen-1-yl)-N4,N4′-bis (4-vinylphenyl)biphenyl-4,4′-diamine) (VNBP) is used at HTL [151]. The VNBP coupled with a thin layer of MoO_3 showed extreme resilience toward polar and nonpolar solvents.

From an ETL perspective, n-type planar PSCs show significant degradation compared to their mesoporous counterparts whereas in mesoporous PSCs, this degradation can be controlled by replacing the common ETLs such as TiO_2 nanoparticles or pristine ZnO with Al_2O_3 or TiO_2 nanorods or doped ZnO nanorods, respectively. The TiO_2 nanoparticles have shown to form a reactive interface with perovskite, which triggers in presence of light (predominantly UV light). Interface modification such as introduction of Sb_2S_3 or CdS thin layer on top of TiO_2 has shown to improve device stability [57]. Similarly, doped TiO_2 such as Al- or Nd-doped has shown to improve device operational stability considerably [57].

In the p-i-n or inverted architecture, poly(3,4-ethylenedioxythiophene) poly (styrenesulphonate) (PEDOT:PSS) and phenyl-C61-butyric acid methyl ester (PCBM) are the typically employed HTL and ETL. Although use of these organic layers eases device fabrication at low temperature (typically ≤ 150 °C), it raises significant concerns about stability. Particularly important is the acidic and hygroscopic nature of PEDOT:PSS. Not only it degrades the perovskite layer at the interface, but also, it can corrode the conducting substrate underneath, as it has shown in organic solar cells. Thin buffer layers such as MoO_3 and $CuAlO_2$ are introduced between perovskite and PEDOT:PSS to minimize interfacial degradation. However, the twofold corrosion effect of PEDEOT:PSS offers challenges toward a stable device using it. An efficient and stable device is reported by completely replacing the organic selective contacts with inorganic ones: viz., NiO_x as HTL and ZnO as ETL in inverted PSCs. The device retained >90% of initial performance after 60 days in air.

5.6 Hybrid Bulk Heterojunction Solar Cells

A typical hybrid bulk heterojunction solar cell is a polymer/metal oxide structure. The device architecture is very similar to fully organic bulk heterojunction solar cells; just that a metal oxide replaces the acceptor material (e.g., a fullerene or other

conjugated acceptor). Metal oxide particles are mixed with a donor polymer in a solution, which is used to prepare a thin film. Most common acceptors are ZnO nanocrystals with diameters of 10–20 nm. Sometimes TiO_2 can also be found as an acceptor; however, it typically leads to lower device performance. As these metal oxides have a wide bandgap energy of around 3 eV, they are transparent in the visible spectrum and therefore the light is absorbed only in the polymer. In bulk heterojunction solar cells, the film morphology plays a dominant role as excitons need to be separated at a donor–acceptor interface and charges need to migrate to the electrodes. Loss mechanisms are very similar as in fully organic bulk heterojunction solar cells: Islands of one material act as recombination center and direct contact of donor and acceptor material to the wrong electrode leads to increased recombination. To ensure sufficient contact between the metal-oxide nanoparticles to form direct pathways for the electrons, common polymer/metal oxide mixing ratios have a high excess of metal oxide in the order of 1:3 wt:wt ratio. ZnO/P3HT cells have been shown to work reasonable with efficiencies of a few percent [152]. One major limitation in theses solar cells seems to be an inefficient charge separation mechanism at the polymer/metal oxide interface. To overcome this problem, molecular modifiers like dye monolayers on the metal oxide have been introduced. They strongly influence the contact between polymer and metal oxide. However, the implementation of the dyes is much simpler in cells, where first a mesoporous metal oxide layer is formed, then covered by the monolayer of day by immersing this layer into a dye bath and finally infiltrate the structure with a polymer. This gives the same type of cell architecture as found in *s*-DSSCs and also has similar device physics. In contrast to a *s*-DSSC, the absorbing polymer layer can additionally contribute to the charge generation, even though in many cases it turned out that it acts just as parasitic absorber as charge and/or energy transfer to the dye/metal oxide surface is inefficient.

Another type of hybrid bulk heterojunction solar cells is based on inorganic absorber materials such as, e.g., CdTe, CdSe, PbS, and PbSe nanoparticles of different shapes blended with a hole transport polymer such as P3HT. Also, here the morphology of these solar cells is key issue for high performance and it turned out that elongated particles form more efficient charge transport networks than spherical particles [153]. Charge separation in these absorber/polymer bulk heterojunctions is observed after photoexcitation of the inorganic absorber and subsequent transport of holes or hole injection into the polymer phase. In optimized systems, these inorganic nanoparticles have led to 7% efficient solar cells [154]. As these nanoparticles have intrinsically a large number of surface traps, it is important for efficient solar cells to passivate these surface traps by the selection of appropriate ligands and surface treatments [155].

References

1. Fakharuddin A, Jose R, Brown TM, Fabregat-Santiago F, Bisquert J (2014) A perspective on the production of dye-sensitized solar modules. Energy Environ Sci 7(12):3952–3981. doi:10.1039/c4ee01724b
2. Di Giacomo F, Fakharuddin A, Jose R, Brown TM (2016) Progress, challenges and perspectives in flexible perovskite solar cells. Energy Environ Sci 9(10):3007–3035. doi:10.1039/C6EE01137C
3. NERL (2016) Best research cell efficiencies (2016). doi:http://www.nrel.gov/ncpv/images/efficiency_chart.jpg
4. Green MA, Emery K, Hishikawa Y, Warta W, Dunlop ED (2016) Solar cell efficiency tables (version 48). Prog Photovolt Res Appl 24(7):905–913. doi:10.1002/pip.2788
5. Kakiage K, Aoyama Y, Yano T, Oya K, J-i Fujisawa, Hanaya M (2015) Highly-efficient dye-sensitized solar cells with collaborative sensitization by silyl-anchor and carboxy-anchor dyes. Chem Commun 51(88):15894–15897. doi:10.1039/C5CC06759F
6. Heo JH, Han HJ, Kim D, Ahn TK, Im SH (2015) Hysteresis-less inverted $CH_3NH_3PbI_3$ planar perovskite hybrid solar cells with 18.1% power conversion efficiency. Energy Environ Sci 8(5):1602–1608. doi:10.1039/c5ee00120j
7. Saliba M, Matsui T, Seo J-Y, Domanski K, Correa-Baena J-P, Nazeeruddin MK, Zakeeruddin SM, Tress W, Abate A, Hagfeldt A, Gratzel M (2016) Cesium-containing triple cation perovskite solar cells: improved stability, reproducibility and high efficiency. Energy Environ Sci. doi:10.1039/C5EE03874J
8. Saliba M, Orlandi S, Matsui T, Aghazada S, Cavazzini M, Correa-Baena J-P, Gao P, Scopelliti R, Mosconi E, Dahmen K-H, De Angelis F, Abate A, Hagfeldt A, Pozzi G, Graetzel M, Nazeeruddin MK (2016) A molecularly engineered hole-transporting material for efficient perovskite solar cells. Nat Energy:15017. doi:10.1038/nenergy.2015.17
9. Olivier Lavagne d'Ortigue AWaSE (2015) Renewable energy capacity statistics 2015
10. Hoppea H, Sariciftci NS (2004) Organic solar cells: an overview. J Mater Res 19(7):1925. doi:10.1557/JMR.2004.0252
11. Dennler G, Lungenschmied C, Neugebauer H, Sariciftci NS, Latrèche M, Czeremuszkin G, Wertheimer MR (2006) A new encapsulation solution for flexible organic solar cells. Thin Solid Films 511–512:349–353. doi:10.1016/j.tsf.2005.12.091
12. Hoppe H, Sariciftci NS (2006) Morphology of polymer/fullerene bulk heterojunction solar cells. J Mater Chem 16(1):45–61. doi:10.1039/B510618B
13. Scharber MC, Sariciftci NS (2013) Efficiency of bulk-heterojunction organic solar cells. Prog Polym Sci 38(12):1929–1940. doi:10.1016/j.progpolymsci.2013.05.001
14. O'Regan B, Gratzel Michael (1991) A low-cost, high-efficiency solar cell based on dye-sensitized colloidal TiO_2 films. Nature 353:737–740. doi:10.1038/353737a0
15. Wu J, Lan Z, Lin J, Huang M, Huang Y, Fan L, Luo G (2015) Electrolytes in dye-sensitized solar cells. Chem Rev 115(5):2136–2173. doi:10.1021/cr400675m
16. Hagfeldt A, Boschloo G, Sun L, Kloo L, Pettersson H (2010) Dye-sensitized solar cells. Chem Rev 110(11):6595–6663. doi:10.1021/cr900356p
17. Jose R, Thavasi V, Ramakrishna S (2009) Metal oxides for dye-sensitized solar cells. J Am Ceram Soc 92(2):289–301
18. Schmidt-Mende L, Zakeeruddin SM, Grätzel M (2005) Efficiency improvement in solid-state-dye-sensitized photovoltaics with an amphiphilic Ruthenium-dye. Appl Phys Lett 86(1):013504-013501–013504-013503. doi:10.1063/1.1844032
19. Wali Q, Fakharuddin A, Jose R (2015) Tin oxide as a photoanode for dye-sensitised solar cells: current progress and future challenges. J Power Sources 293:1039–1052. doi:10.1016/j.jpowsour.2015.06.037
20. Zhang Q, Cao G (2011) Nanostructured photoelectrodes for dye-sensitized solar cells. Nano Today 6(1):91–109. doi:10.1016/j.nantod.2010.12.007

21. Hardin BE, Snaith HJ, McGehee MD (2012) The renaissance of dye-sensitized solar cells. Nat Photon 6(3):162–169. doi:10.1038/nphoton.2012.22
22. Calogero G, Bartolotta A, Di Marco G, Di Carlo A, Bonaccorso F (2015) Vegetable-based dye-sensitized solar cells. Chem Soc Rev 44(10):3244–3294. doi:10.1039/C4CS00309H
23. Robertson N (2006) Optimizing dyes for dye-sensitized solar cells. Angew Chem Int Ed 45 (15):2338–2345. doi:10.1002/anie.200503083
24. Mathew S, Yella A, Gao P, Humphry-Baker R, Curchod BFE, Ashari-Astani N, Tavernelli I, Rothlisberger U, Nazeeruddin MK, Grätzel M (2014) Dye-sensitized solar cells with 13% efficiency achieved through the molecular engineering of porphyrin sensitizers. Nat Chem 6 (3):242–247. doi:10.1038/nchem.1861
25. Daeneke T, Kwon TH, Holmes AB, Duffy NW, Bach U, Spiccia L (2011) High-efficiency dye-sensitized solar cells with ferrocene-based electrolytes. Nat Chem 3(3):211–215. doi:10.1038/nchem.966
26. Powar S, Daeneke T, Ma MT, Fu D, Duffy NW, Götz G, Weidelener M, Mishra A, Bäuerle P, Spiccia L, Bach U (2013) Highly efficient p-type dye-sensitized solar cells based on Tris (1,2-diaminoethane)Cobalt(II)/(III) electrolytes. Angew Chem Int Ed 52(2):602–605. doi:10.1002/anie.201206219
27. Jang S-R, Vittal R, Lee J, Jeong N, Kim K-J (2006) Linkage of N_3 dye to N_3 dye on nanocrystalline TiO_2 through trans-1,2-bis(4-pyridyl)ethylene for enhancement of photocurrent of dye-sensitized solar cells. Chem Commun 1:103–105. doi:10.1039/B510725C
28. Katoh R, Furube A, Kasuya M, Fuke N, Koide N, Han L (2007) Photoinduced electron injection in black dye sensitized nanocrystalline TiO_2 films. J Mater Chem 17(30): 3190–3196. doi:10.1039/B702805A
29. Kalyanasundaram K (2010) Dye-sensitized solar cells, vol 1, 1 edn. CRC press, Switzerland, p 305
30. Bach U, Lupo D, Comte P, Moser JE, Weissörtel F, Salbeck J, Spreitzer H, Grätzel M (1998) Solid-state dye-sensitized mesoporous TiO_2 solar cells with high photon-to-electron conversion efficiencies. Nature 395(6702):583–585
31. Chung I, Lee B, He J, Chang RPH, Kanatzidis MG (2012) All-solid-state dye-sensitized solar cells with high efficiency. Nature 485(7399):486–489
32. Yum J-H, Chen P, Grätzel M, Nazeeruddin MK (2008) Recent developments in solid-state dye-sensitized solar cells. Chemsuschem 1(8–9):699–707. doi:10.1002/cssc.200800084
33. Bakr ZH, Wali Q, Fakharuddin A, Schmidt-Mende L, Brown TM, Jose R (2017) Advances in hole transport materials engineering for stable and efficient perovskite solar cells. Nano Energy 34:271–305. doi:10.1016/j.nanoen.2017.02.025
34. Snaith HJ, Schmidt-Mende L (2007) Advances in liquid-electrolyte and solid-state dye-sensitized solar cells. Adv Mater 19(20):3187–3200
35. Hodes G, Cahen D (2012) All-solid-state, semiconductor-sensitized nanoporous solar cells. Acc Chem Res 45(5):705–713. doi:10.1021/ar200219h
36. Mora-Sero I, Gimenez S, Fabregat-Santiago F, Azaceta E, Tena-Zaera R, Bisquert J (2011) Modeling and characterization of extremely thin absorber (eta) solar cells based on ZnO nanowires. Phys Chem Chem Phys 13(15):7162–7169. doi:10.1039/C1CP20352E
37. Tennakone K, Kumara GRRA, Kottegoda IRM, Perera VPS, Aponsu GMLP (1998) Nanoporous n-##IMG## [http://ej.iop.org/images/0022-3727/31/18/019/toc_img1.gif]/selenium/p-CuCNS photovoltaic cell. J Phys D: Appl Phys 31(18):2326
38. Plass R, Pelet S, Krueger J, Grätzel M, Bach U (2002) Quantum dot sensitization of organic–inorganic hybrid solar cells. J Phys Chem B 106(31):7578–7580. doi:10.1021/jp020453l
39. Lévy-Clément C, Tena-Zaera R, Ryan MA, Katty A, Hodes G (2005) CdSe-sensitized p-CuSCN/nanowire n-ZnO heterojunctions. Adv Mater 17(12):1512–1515. doi:10.1002/adma.200401848
40. Larramona G, Choné C, Jacob A, Sakakura D, Delatouche B, Péré D, Cieren X, Nagino M, Bayón R (2006) Nanostructured photovoltaic cell of the type titanium dioxide, cadmium sulfide thin coating, and copper thiocyanate showing high quantum efficiency. Chem Mater 18(6):1688–1696. doi:10.1021/cm052819n

41. Belaidi A, Dittrich T, Kieven D, Tornow J, Schwarzburg K, Lux-Steiner M (2008) Influence of the local absorber layer thickness on the performance of ZnO nanorod solar cells. Phys Status Solidi (RRL)—Rapid Res Lett 2(4):172–174. doi:10.1002/pssr.200802092
42. Itzhaik Y, Niitsoo O, Page M, Hodes G (2009) Sb_2S_3-sensitized nanoporous TiO_2 solar cells. J Phys Chem C 113(11):4254–4256. doi:10.1021/jp900302b
43. Nezu S, Larramona G, Choné C, Jacob A, Delatouche B, Péré D, Moisan C (2010) Light soaking and gas effect on nanocrystalline TiO_2/Sb_2S_3/CuSCN photovoltaic cells following extremely thin absorber concept. J Phys Chem C 114(14):6854–6859. doi:10.1021/jp100401e
44. Krunks M, Kärber E, Katerski A, Otto K, Oja Acik I, Dedova T, Mere A (2010) Extremely thin absorber layer solar cells on zinc oxide nanorods by chemical spray. Sol Energy Mater Sol Cells 94(7):1191–1195. doi:10.1016/j.solmat.2010.02.036
45. Chang JA, Rhee JH, Im SH, Lee YH, H-j Kim, Seok SI, Nazeeruddin MK, Gratzel M (2010) High-performance nanostructured inorganic–organic heterojunction solar cells. Nano Lett 10 (7):2609–2612. doi:10.1021/nl101322h
46. Tornow J, Schwarzburg K, Belaidi A, Dittrich T, Kunst M, Hannappel T (2010) Charge separation and recombination in radial ZnO/In_2S_3/CuSCN heterojunction structures. J Appl Phys 108(4):044915. doi:10.1063/1.3466776
47. Mora-Seró I, Bisquert J (2010) Breakthroughs in the development of semiconductor-sensitized solar cells. J Phys Chem Lett 1(20):3046–3052. doi:10.1021/jz100863b
48. Ikegami M, Suzuki J, Teshima K, Kawaraya M, Miyasaka T (2009) Improvement in durability of flexible plastic dye-sensitized solar cell modules. Sol Energy Mater Sol Cells 93(6–7):836–839
49. Kim HS, Lee CR, Im JH, Lee KB, Moehl T, Marchioro A, Moon SJ, Humphry-Baker R, Yum JH, Moser JE, Grätzel M, Park NG (2012) Lead iodide perovskite sensitized all-solid-state submicron thin film mesoscopic solar cell with efficiency exceeding 9%. Sci Rep 2. doi:10.1038/srep00591
50. Lee MM, Teuscher J, Miyasaka T, Murakami TN, Snaith HJ (2012) Efficient hybrid solar cells based on meso-superstructured organometal halide perovskites. Science 338 (6107):643–647. doi:10.1126/science.1228604
51. Kim HS, Im SH, Park NG (2014) Organolead halide perovskite: new horizons in solar cell research. J Phys Chem C 118(11):5615–5625. doi:10.1021/jp409025w
52. Kazim S, Nazeeruddin MK, Grätzel M, Ahmad S (2014) Perovskite as light harvester: a game changer in photovoltaics. Angewandte Chemie—Int Ed 53(11):2812–2824. doi:10.1002/anie.201308719
53. Brittman S, Adhyaksa GWP, Garnett EC (2015) The expanding world of hybrid perovskites: materials properties and emerging applications. MRS Commun 5(1):7–26. doi:10.1557/mrc.2015.6
54. Green MA, Ho-Baillie A, Snaith HJ (2014) The emergence of perovskite solar cells. Nat Photonics 8(7):506–514. doi:10.1038/nphoton.2014.134
55. Fakharuddin A, De Rossi F, Watson TM, Schmidt-Mende L, Jose R (2016) Research update: behind the high efficiency of hybrid perovskite solar cells. APL Mater 4(9):091505. doi:10.1063/1.4962143
56. Ito S (2016) Research update: overview of progress about efficiency and stability on perovskite solar cells. APL Mater 4(9):091504. doi:10.1063/1.4961955
57. Fakharuddin A, Schmidt-Mende L, Mora-Sero I, Garcia-Belmonte G, Jose R (2016) Interfaces in perovskite solar cells. Adv Energy Mater (2017) (in press)
58. Yagi T, Mao HK, Bell PM (1978) Structure and crystal chemistry of perovskite-type $MgSiO_3$. Phys Chem Miner 3(2):97–110. doi:10.1007/BF00308114
59. Peña MA, Fierro JLG (2001) Chemical structures and performance of perovskite oxides. Chem Rev 101(7):1981–2017. doi:10.1021/cr980129f
60. Megaw HD (1946) Crystal structure of double oxides of the perovskite type. Proceedings of the Physical Society 58(2):133–152. doi:10.1088/0959-5309/58/2/301

61. Saparov B, Mitzi DB (2016) Organic-inorganic perovskites: structural versatility for functional materials design. Chem Rev 116(7):4558–4596. doi:10.1021/acs.chemrev.5b00715
62. Boix PP, Nonomura K, Mathews N, Mhaisalkar SG (2014) Current progress and future perspectives for organic/inorganic perovskite solar cells. Mater Today 17:16–23
63. Green MA, Ho-Baillie A, Snaith HJ (2014) The emergence of perovskite solar cells. Nat Photonics 8:506–514
64. Amat A, Mosconi E, Ronca E, Quarti C, Umari P, Nazeeruddin MK, Grätzel M, De Angelis F (2014) Cation-induced band-gap tuning in organohalide perovskites: interplay of spin-orbit coupling and octahedra tilting. Nano Lett 14(6):3608–3616. doi:10.1021/nl5012992
65. Bi D, Tress W, Dar MI, Gao P, Luo J, Renevier C, Schenk K, Abate A, Giordano F, Correa Baena J-P, Decoppet J-D, Zakeeruddin SM, Nazeeruddin MK, Grätzel M, Hagfeldt A (2016) Efficient luminescent solar cells based on tailored mixed-cation perovskites. Science Adv 2(1). doi:10.1126/sciadv.1501170
66. Li W, Zhang W, Van Reenen S, Sutton RJ, Fan J, Haghighirad AA, Johnston MB, Wang L, Snaith HJ (2016) Enhanced UV-light stability of planar heterojunction perovskite solar cells with caesium bromide interface modification. Energy Environ Sci 9(2):490–498. doi:10.1039/C5EE03522H
67. Noh JHJH, Im SSH, Heo JHJH, Mandal TNT, Seok SSI (2013) Chemical management for colorful, efficient, and stable inorganic-organic hybrid nanostructured solar cells. Nano Lett 13:1764–1769. doi:10.1021/nl400349b
68. Sutton RJ, Eperon GE, Miranda L, Parrott ES, Kamino BA, Patel JB, Hörantner MT, Johnston MB, Haghighirad AA, Moore DT, Snaith HJ (2016) Bandgap-tunable cesium lead halide perovskites with high thermal stability for efficient solar cells. Adv Energy Mater 6(8):n/a–n/a. doi:10.1002/aenm.201502458
69. Stranks SD, Eperon GE, Grancini G, Menelaou C, Alcocer MJP, Leijtens T, Herz LM, Petrozza A, Snaith HJ (2013) Electron-hole diffusion lengths exceeding 1 micrometer in an organometal trihalide perovskite absorber. Science 342 (6156):341–344. doi:10.1126/science.1243982
70. Zhou H, Chen Q, Li G, Luo S, Song TB, Duan HS, Hong Z, You J, Liu Y, Yang Y (2014) Interface engineering of highly efficient perovskite solar cells. Science 345(6196):542–546. doi:10.1126/science.1254050
71. Lin Q, Armin A, Nagiri RCR, Burn PL, Meredith P (2015) Electro-optics of perovskite solar cells. Nat Photonics 9(2):106–112. doi:10.1038/nphoton.2014.284
72. Miyata A, Mitioglu A, Plochocka P, Portugall O, Wang JTW, Stranks SD, Snaith HJ, Nicholas RJ (2015) Direct measurement of the exciton binding energy and effective masses for charge carriers in organic-inorganic tri-halide perovskites. Nat Phys 11(7):582–587. doi:10.1038/nphys3357
73. Edri E, Kirmayer S, Henning A, Mukhopadhyay S, Gartsman K, Rosenwaks Y, Hodes G, Cahen D (2014) Why lead methylammonium tri-iodide perovskite-based solar cells require a mesoporous electron transporting scaffold (but not necessarily a hole conductor). Nano Lett 14:1000–1004
74. Stoumpos CC, Malliakas CD, Kanatzidis MG (2013) Semiconducting tin and lead iodide perovskites with organic cations: phase transitions, high mobilities, and near-infrared photoluminescent properties. Inorg Chem 52:9019–9038. doi:10.1021/ic401215x
75. Bretschneider SA, Weickert J, Dorman JA, Schmidt-Mende L (2014) Research update: Physical and electrical characteristics of lead halide perovskites for solar cell applications. APL Mater 2(4). doi:10.1063/1.4871795
76. Olthof S (2016) Research update: the electronic structure of hybrid perovskite layers and their energetic alignment in devices. APL Mater 4(9):091502. doi:10.1063/1.4960112
77. Dong Q, Fang Y, Shao Y, Mulligan P, Qiu J, Cao L, Huang J (2015) Electron-hole diffusion lengths >175 m in solution grown $CH_3NH_3PbI_3$ single crystals. Science 347:967–970. doi:10.1126/science.aaa5760

78. Yin W-J, Shi T, Yan Y (2014) Unusual defect physics in $CH_3NH_3PbI_3$ perovskite solar cell absorber. Appl Phys Lett 104(6):063903. doi:10.1063/1.4864778
79. Juarez-Perez EJ, Wußler M, Fabregat-Santiago F, Lakus-Wollny K, Mankel E, Mayer T, Jaegermann W, Mora-Sero I (2014) Role of the selective contacts in the performance of lead halide perovskite solar cells. J Phys Chem Lett 5:680–685. doi:10.1021/jz500059v
80. Im JH, Kim HS, Park NG (2014) Morphology-photovoltaic property correlation in perovskite solar cells: one-step versus two-step deposition of $CH_3NH_3PbI_3$. APL Mater 2(8). doi:10.1063/1.4891275
81. Razza S, Castro-Hermosa S, Di Carlo A, Brown TM (2016) Research update: large-area deposition, coating, printing, and processing techniques for the upscaling of perovskite solar cell technology. APL Mater 4(9):091508. doi:10.1063/1.4962478
82. Troughton J, Carnie MJ, Davies ML, Charbonneau C, Jewell EH, Worsley DA, Watson TM (2016) Photonic flash-annealing of lead halide perovskite solar cells in 1 ms. J Mater Chem A 4(9):3471–3476. doi:10.1039/C5TA09431C
83. Giordano F, Abate A, Correa Baena JP, Saliba M, Matsui T, Im SH, Zakeeruddin SM, Nazeeruddin MK, Hagfeldt A, Graetzel M (2016) Enhanced electronic properties in mesoporous TiO_2 via lithium doping for high-efficiency perovskite solar cells. Nat Commun 7. doi:10.1038/ncomms10379
84. Zhu ZG, Bai Y, Liu X, Chueh C-C, Yang S, Jen AKY (2016) Enhanced efficiency and stability of inverted perovskite solar cells using highly crystalline SnO_2 nanocrystals as the robust electron-transporting layer. Adv Mater n/a–n/a. doi:10.1002/adma.201600619
85. Zhou Y, Yang M, Wu W, Vasiliev AL, Zhu K, Padture NP (2015) Room-temperature crystallization of hybrid-perovskite thin films via solvent-solvent extraction for high-performance solar cells. J Mater Chem A 3(15):8178–8184. doi:10.1039/c5ta00477b
86. Liu M, Johnston MB, Snaith HJ (2013) Efficient planar heterojunction perovskite solar cells by vapour deposition. Nature 501:395–398
87. Burschka J, Pellet N, Moon SJ, Humphry-Baker R, Gao P, Nazeeruddin MK, Grätzel M (2013) Sequential deposition as a route to high-performance perovskite-sensitized solar cells. Nature 499(7458):316–319. doi:10.1038/nature12340
88. Yantara N, Sabba D, Yanan F, Kadro JM, Moehl T, Boix PP, Mhaisalkar S, Grätzel M, Grätzel C (2015) Loading of mesoporous titania films by $CH_3NH_3PbI_3$ perovskite, single step vs. sequential deposition. Chem Commun 51(22):4603–4606. doi:10.1039/c4cc09556a
89. Yi C, Li X, Luo J, Zakeeruddin SM, Grätzel M (2016) Perovskite photovoltaics with outstanding performance produced by chemical conversion of bilayer mesostructured lead halide/TiO_2 films. Adv Mater 28(15):2964–2970. doi:10.1002/adma.201506049
90. Fakharuddin A, Palma AL, Giacomo FD, Casaluci S, Matteocci F, Wali Q, Rauf M, Carlo AD, Brown TM, Jose R (2015) Solid state perovskite solar modules by vacuum-vapor assisted sequential deposition on Nd:YVO4 laser patterned rutile nanorods. Nanotechnology 26(49):494002
91. Kojima A, Teshima K, Shirai Y, Miyasaka T (2009) Organometal halide perovskites as visible-light sensitizers for photovoltaic cells. J Am Chem Soc 131(17):6050–6051. doi:10.1021/ja809598r
92. Yamada Y, Nakamura T, Endo M, Wakamiya A, Kanemitsu Y (2014) Photocarrier recombination dynamics in perovskite $CH_3NH_3PbI_3$ for solar cell applications. J Am Chem Soc 136:11610–11613. doi:10.1021/ja506624n
93. Wojciechowski K, Saliba M, Leijtens T, Abate A, Snaith HJ (2014) Sub-150 °C processed meso-superstructured perovskite solar cells with enhanced efficiency. Energy Environ Sci 7(3):1142–1147. doi:10.1039/c3ee43707h
94. Leijtens T, Eperon GE, Pathak S, Abate A, Lee MM, Snaith HJ (2013) Overcoming ultraviolet light instability of sensitized TiO_2 with meso-superstructured organometal tri-halide perovskite solar cells. Nat Commun 4. doi:10.1038/ncomms3885
95. Correa Baena JP, Steier L, Tress W, Saliba M, Neutzner S, Matsui T, Giordano F, Jacobsson TJ, Srimath Kandada AR, Zakeeruddin SM, Petrozza A, Abate A, Nazeeruddin MK, Gratzel M,

Hagfeldt A (2015) Highly efficient planar perovskite solar cells through band alignment engineering. Energy Environ Sci 8(10):2928–2934. doi:10.1039/C5EE02608C
96. Bi C, Wang Q, Shao Y, Yuan Y, Xiao Z, Huang J (2015) Non-wetting surface-driven high-aspect-ratio crystalline grain growth for efficient hybrid perovskite solar cells. Nat Commun 6. doi:10.1038/ncomms8747
97. Hu Q, Wu J, Jiang C, Liu T, Que X, Zhu R, Gong Q (2014) Engineering of electron-selective contact for perovskite solar cells with efficiency exceeding 15%. ACS Nano 8(10):10161–10167. doi:10.1021/nn5029828
98. Wei H, Xiao J, Yang Y, Lv S, Shi J, Xu X, Dong J, Luo Y, Li D, Meng Q (2015) Free-standing flexible carbon electrode for highly efficient hole-conductor-free perovskite solar cells. Carbon 93:861–868. doi:10.1016/j.carbon.2015.05.042
99. Wei Z, Chen H, Yan K, Zheng X, Yang S (2015) Hysteresis-free multi-walled carbon nanotube-based perovskite solar cells with a high fill factor. J Mater Chem A 3(48): 24226–24231. doi:10.1039/c5ta07714a
100. Zhang Y, Liu M, Eperon GE, Leijtens T, McMeekin DP, Saliba M, Zhang W, De Bastiani M, petrozza a, Herz L, Johnston MB, Lin H, Snaith H (2015) Charge selective contacts, mobile ions and anomalous hysteresis in organic-inorganic perovskite solar cells. Mater Horiz 2:315–322. doi:10.1039/C4MH00238E
101. Song J, Zheng E, Bian J, Wang X-F, Tian W, Sanehira Y, Miyasaka T (2015) Low-temperature SnO_2-based electron selective contact for efficient and stable perovskite solar cells. J Mater Chem A 3(20):10837–10844. doi:10.1039/C5TA01207D
102. Ke W, Fang G, Liu Q, Xiong L, Qin P, Tao H, Wang J, Lei H, Li B, Wan J, Yang G, Yan Y (2015) Low-temperature solution-processed tin oxide as an alternative electron transporting layer for efficient perovskite solar cells. J Am Chem Soc 137(21):6730–6733. doi:10.1021/jacs.5b01994
103. Park M, Kim J-Y, Son HJ, Lee C-H, Jang SS, Ko MJ (2016) Low-temperature solution-processed Li-doped SnO_2 as an effective electron transporting layer for high-performance flexible and wearable perovskite solar cells. Nano Energy 26:208–215. doi:10.1016/j.nanoen.2016.04.060
104. Docampo P, Ball JM, Darwich M, Eperon GE, Snaith HJ (2013) Efficient organometal trihalide perovskite planar-heterojunction solar cells on flexible polymer substrates. Nat Commun 4:2761. doi:10.1038/ncomms3761
105. Giorgi G, Fujisawa JI, Segawa H, Yamashita K (2013) Small photocarrier effective masses featuring ambipolar transport in methylammonium lead iodide perovskite: A density functional analysis. J Phys Chem Lett 4(24):4213–4216. doi:10.1021/jz4023865
106. Mei Y, Jurchescu OD, Zhang C, Vardeny ZV (2015) Electrostatic gating of hybrid halide perovskite field-effect transistors: balanced ambipolar transport at room-temperature. MRS Commun. doi:10.1557/mrc.2015.21
107. Mei A, Li X, Liu L, Ku Z, Liu T, Rong Y, Xu M, Hu M, Chen J, Yang Y, Gratzel M, Han H (2014) A hole-conductor-free, fully printable mesoscopic perovskite solar cell with high stability. Science 345:295–298. doi:10.1126/science.1254763
108. Li X, Tschumi M, Han H, Babkair SS, Alzubaydi RA, Ansari AA, Habib SS, Nazeeruddin MK, Zakeeruddin SM, Grätzel M (2015) Outdoor performance and stability under elevated temperatures and long-term light soaking of triple-layer mesoporous perovskite photovoltaics. Energy Technol 3:551–555. doi:10.1002/ente.201500045
109. Ku Z, Xia X, Shen H, Tiep NH, Fan HJ (2015) Mesoporous nickel counter electrode for printable and reusable perovskite solar cells. Nanoscale. doi:10.1039/C5NR03610K
110. Tress W (2016) Maximum efficiency and open-circuit voltage of perovskite solar cells. In: Nam-Gyu Park MG, Tsutomu Miyasaka (ed) Organic-inorganic halide perovskite photovoltaics. Springer, pp 53–77
111. Snaith HJ, Abate A, Ball JM, Eperon GE, Leijtens T, Kimberly N, Stranks SD, Wang JT-W, Wojciechowski K, Zhang W, Noel NK (2014) Anomalous hysteresis in perovskite solar cells. J Phys Chem Lett 5:1511–1515

112. Unger EL, Hoke ET, Bailie CD, Nguyen WH, Bowring AR, Heumüller T, Christoforod MG, McGehee MD (2014) Hysteresis and transient behavior in current–voltage measurements of hybrid-perovskite absorber solar cells. Energy Environ Sci 7:3690–3698
113. Jeon NJ, Noh JH, Kim YC, Yang WS, Ryu S, Seok SI (2014) Solvent engineering for high-performance inorganic–organic hybrid perovskite solar cells. Nat Mater 13:897–903
114. Sanchez RS, Gonzalez-Pedro V, Lee J-W, Park N-G, Kang YS, Mora-Sero I, Bisquert J (2014) Slow dynamic processes in lead halide perovskite solar cells. Characteristic times and hysteresis. J Phys Chem Lett 5:2357–2363
115. Frost JM, Butler KT, Walsh A (2014) Molecular ferroelectric contributions to anomalous hysteresis in hybrid perovskite solar cells. APL Mater 2:081506
116. Wei J, Zhao Y, Li H, Li G, Pan J, Xu D, Zhao Q, Yu D (2014) Hysteresis analysis based on the ferroelectric effect in hybrid perovskite solar cells. J Phys Chem Lett 5:3937–3945
117. Chen H-W, Sakai N, Ikegami M, Miyasaka T (2015) Emergence of hysteresis and transient ferroelectric response in organo-lead halide perovskite solar cells. J Phys Chem Lett 6: 164–169
118. Dualeh A, Moehl T, Tétreault N, Teuscher J, Gao P, Nazeeruddin MK, Grätzel M (2014) Impedance spectroscopic analysis of lead iodide perovskite-sensitized solid-state solar cells. ACS Nano 8:362–373
119. Yang Y, Xiao J, Wei H, Zhu L, Li D, Luo Y, Wu H, Meng Q (2014) An all-carbon counter electrode for highly efficient hole-conductor-free organo-metal perovskite solar cells. RSC Adv 4(95):52825–52830. doi:10.1039/c4ra09519g
120. Almora O, Zarazua I, Mas-Marza E, Mora-Sero I, Bisquert J, Garcia-Belmonte G (2015) Capacitive dark currents, hysteresis, and electrode polarization in lead halide perovskite solar cells. J Phys Chem Lett 6:1645–1652
121. Chen B, Yang M, Zheng X, Wu C, Li W, Yan Y, Bisquert J, Garcia-Belmonte G, Zhu K, Priya S (2015) Impact of capacitive effect and ion migration on the hysteretic behavior of perovskite solar cells. J Phys Chem Lett 6:4693–4700
122. Chen B, Yang M, Priya S, Zhu K (2016) Origin of J-V hysteresis in perovskite solar cells. J Phys Chem Lett 7(5):905–917. doi:10.1021/acs.jpclett.6b00215
123. Wojciechowski K, Stranks SD, Abate A, Sadoughi G, Sadhanala A, Kopidakis N, Rumbles G, Li C-Z, Friend RH, Jen AK-Y, Snaith HJ (2014) Heterojunction modification for highly efficient organic-inorganic perovskite Solar cells. ACS Nano 8:12701–12709
124. Seo JW, Park S, Kim YC, Jeon NJ, Noh JH, Yoon SC, Seok SI (2014) Benefits of very thin PCBM and LiF layer for solution-processed P-I-N perovskite solar cells. Energy Environ Sci 7:2642–2646
125. Snaith HJ, Abate A, Ball JM, Eperon GE, Leijtens T, Noel NK, Stranks SD, Wang JTW, Wojciechowski K, Zhang W (2014) Anomalous hysteresis in perovskite solar cells. J Phys Chem Lett 5(9):1511–1515. doi:10.1021/jz500113x
126. Christians JA, Manser JS, Kamat PV (2015) Best practices in perovskite solar cell efficiency measurements. Avoiding the error of making bad cells look good. J Phys Chem Lett 6 (5):852–857. doi:10.1021/acs.jpclett.5b00289
127. Zimmermann E, Ehrenreich P, Pfadler T, Dorman JA, Weickert J, Schmidt-Mende L (2014) Erroneous efficiency reports harm organic solar cell research. Nat Photonics 8(9):669–672
128. Zimmermann E, Wong KK, Müller M, Hu H, Ehrenreich P, Kohlstädt M, Würfel U, Mastroianni S, Mathiazhagan G, Hinsch A, Gujar TP, Thelakkat M, Pfadler T, Schmidt-Mende L (2016) Characterization of perovskite solar cells: towards a reliable measurement protocol. APL Mater 4(9):091901. doi:10.1063/1.4960759
129. Heo JH, Lee MH, Han HJ, Patil BR, Yu JS, Im SH (2016) Highly efficient low temperature solution processable planar type $CH_3NH_3PbI_3$ perovskite flexible solar cells. J Mater Chem A 4(5):1572–1578. doi:10.1039/c5ta09520d
130. Yang J, Siempelkamp BD, Mosconi E, De Angelis F, Kelly TL (2015) Origin of the thermal instability in $CH_3NH_3PbI_3$ thin films deposited on ZnO. Chem Mater 27:150529083734008. doi:10.1021/acs.chemmater.5b01598

131. Yang D, Yang R, Zhang J, Yang Z, Liu S, Li C (2015) High efficiency flexible perovskite solar cells using superior low temperature TiO_2. Energy Environ Sci 8(11):3208–3214. doi:10.1039/c5ee02155c
132. Shin SS, Yang WS, Noh JH, Suk JH, Jeon NJ, Park JH, Kim JS, Seong WM, Seok SI (2015) High-performance flexible perovskite solar cells exploiting Zn_2SnO_4 prepared in solution below 100 °C. Nat Commun 6:7410. doi:10.1038/ncomms8410
133. Xiao Y, Han G, Zhou H, Wu J (2016) An efficient titanium foil based perovskite solar cell: using a titanium dioxide nanowire array anode and transparent poly(3,4-ethylenedioxythiophene) electrode. RSC Adv 6(4):2778–2784. doi:10.1039/C5RA23430A
134. Habisreutinger SN, McMeekin DP, Snaith HJ, Nicholas RJ (2016) Research update: strategies for improving the stability of perovskite solar cells. APL Mater 4(9):091503. doi:10.1063/1.4961210
135. Guo X, Niu G, Wang L (2015) Chemical stability issue and its research process of perovskite solar cells with high efficiency. Acta Chim Sinica 73(3):211–218. doi:10.6023/A14100687
136. Rong Y, Liu L, Mei A, Li X, Han H (2015) Beyond efficiency: the challenge of stability in mesoscopic perovskite solar cells. Adv Energy Mater 5(20). doi:10.1002/aenm.201501066
137. Berhe TA, Su WN, Chen CH, Pan CJ, Cheng JH, Chen HM, Tsai MC, Chen LY, Dubale AA, Hwang BJ (2016) Organometal halide perovskite solar cells: degradation and stability. Energy Environ Sci 9(2):323–356. doi:10.1039/c5ee02733k
138. Shahbazi M, Wang H (2016) Progress in research on the stability of organometal perovskite solar cells. Sol Energy 123:74–87. doi:10.1016/j.solener.2015.11.008
139. Wang D, Wright M, Elumalai NK, Uddin A (2016) Stability of perovskite solar cells. Sol Energy Mater Sol Cells 147:255–275. doi:10.1016/j.solmat.2015.12.025
140. Fakharuddin A, Di Giacomo F, Palma AL, Matteocci F, Ahmed I, Razza S, D'Epifanio A, Licoccia S, Ismail J, Di Carlo A, Brown TM, Jose R (2015) Vertical TiO_2 nanorods as a medium for stable and high-efficiency perovskite solar modules. ACS Nano 9(8):8420–8429. doi:10.1021/acsnano.5b03265
141. Hwang I, Baek M, Yong K (2015) Core/shell structured TiO_2/CdS electrode to enhance the light stability of perovskite solar cells. ACS Appl Mater Interfaces 7(50):27863–27870. doi:10.1021/acsami.5b09442
142. Carrillo J, Guerrero A, Rahimnejad S, Almora O, Zarazua I, Mas-Marza E, Bisquert J, Garcia-Belmonte G (2016) Ionic reactivity at contacts and aging of methylammonium lead triiodide perovskite solar cells. Adv Energy Mater 6(9):n/a–n/a. doi:10.1002/aenm.201502246
143. Guerrero A, You J, Aranda C, Kang YS, Garcia-Belmonte G, Zhou H, Bisquert J, Yang Y (2016) Interfacial degradation of planar lead halide perovskite solar cells. ACS Nano 10(1):218–224. doi:10.1021/acsnano.5b03687
144. Lee YH, Luo J, Humphry-Baker R, Gao P, Grätzel M, Nazeeruddin MK (2015) Unraveling the reasons for efficiency loss in perovskite solar cells. Adv Func Mater 25(25):3925–3933. doi:10.1002/adfm.201501024
145. Leijtens T, Eperon GE, Noel NK, Habisreutinger SN, Petrozza A, Snaith HJ (2015) Stability of metal halide perovskite solar cells. Adv Energy Mater 5(20). doi:10.1002/aenm.201500963
146. Unger EL, Hoke ET, Bailie CD, Nguyen WH, Bowring AR, Heumüller T, Christoforo MG, McGehee MD (2014) Hysteresis and transient behavior in current-voltage measurements of hybrid-perovskite absorber solar cells. Energy Environ Sci 7(11):3690–3698. doi:10.1039/c4ee02465f
147. Tress W, Marinova N, Moehl T, Zakeeruddin SM, Nazeeruddin MK, Grätzel M (2015) Understanding the rate-dependent J-V hysteresis, slow time component, and aging in $CH_3NH_3PbI_3$ perovskite solar cells: the role of a compensated electric field. Energy Environ Sci 8(3):995–1004. doi:10.1039/c4ee03664f
148. Zhao Y, Wei J, Li H, Yan Y, Zhou W, Yu D, Zhao Q (2016) A polymer scaffold for self-healing perovskite solar cells. Nat Commun 7. doi:10.1038/ncomms10228

149. Manshor NA, Wali Q, Wong KK, Muzakir SK, Fakharuddin A, Schmidt-Mende L, Jose R (2016) Humidity versus photo-stability of metal halide perovskite films in a polymer matrix. Phys Chem Chem Phys. doi:10.1039/C6CP03600G
150. Leo K (2015) Perovskite photovoltaics: signs of stability. Nat Nanotechnol 10:574–575. doi:10.1038/nnano.2015.139
151. Xu J, Voznyy O, Comin R, Gong X, Walters G, Liu M, Kanjanaboos P, Lan X, Sargent EH (2016) Crosslinked remote-doped hole-extracting contacts enhance stability under accelerated lifetime testing in perovskite solar cells. Adv Mater 28(14):2807–2815. doi:10.1002/adma.201505630
152. Oosterhout SD, Wienk MM, van Bavel SS, Thiedmann R, Jan Anton Koster L, Gilot J, Loos J, Schmidt V, Janssen RAJ (2009) The effect of three-dimensional morphology on the efficiency of hybrid polymer solar cells. Nat Mater 8(10):818–824. doi:10.1038/nmat2533
153. Huynh WU, Dittmer JJ, Alivisatos AP (2002) Hybrid nanorod-polymer solar cells. Science 295(5564):2425–2427. doi:10.1126/science.1069156
154. Ip AH, Thon SM, Hoogland S, Voznyy O, Zhitomirsky D, Debnath R, Levina L, Rollny LR, Carey GH, Fischer A, Kemp KW, Kramer IJ, Ning Z, Labelle AJ, Chou KW, Amassian A, Sargent EH (2012) Hybrid passivated colloidal quantum dot solids. Nat Nanotechnol 7(9):577–582. doi:10.1038/nnano.2012.127
155. Asil D, Walker BJ, Ehrler B, Vaynzof Y, Sepe A, Bayliss S, Sadhanala A, Chow PCY, Hopkinson PE, Steiner U, Greenham NC, Friend RH (2015) Role of PbSe structural stabilization in photovoltaic cells. Adv Func Mater 25(6):928–935. doi:10.1002/adfm.201401816

Chapter 6
Light-Driven Water Splitting in the Dye-Sensitized Photoelectrosynthesis Cell

Leila Alibabaei, M. Kyle Brennaman and Thomas J. Meyer

Abstract Artificial photosynthesis integrates solar energy conversion and storage in processes that produce solar fuels. The targets are water splitting into H_2 and O_2 or solar-driven reduction of CO_2 by water to carbon-based fuels. Light-driven water-splitting devices, also known as dye-sensitized photoelectrosynthesis cells (DSPECs), show promise and are based on molecular light absorption and catalysis which occur at the surfaces of nanocrystalline oxide semiconductors. Absorption of sunlight by surface-attached molecules leads to electron injection into the semiconductor conduction band followed by catalyst activation. Light-driven water splitting occurs by repetition of this cycle four times at a photoanode with solar fuels generated at the cathode. The underlying design of the DSPEC is based on this photoelectrochemical approach. Light-driven water splitting is made possible by the recent development of molecular water oxidation catalysts. With the components finally available to explore the DSPEC in detail, design principle guidelines are rapidly emerging which will lay the foundation for these devices to harness and utilize solar energy, night or day.

Keywords Light-driven · Water splitting · DSPEC · Photoanode · Photoelectrochemical · Solar fuels · Core/shell · Artificial photosynthesis · Dye-sensitized photoelectrochemical cell · Molecular catalyst · Let the molecules do the work

Abbreviations

FTO	Fluorine-doped tin oxide
ITO	Tin-doped indium oxide
*nano*ITO	Nanocrystalline tin-doped indium oxide
TCO	Transparent conducting oxide
NHE	Normal hydrogen electrode
DSPEC	Dye-sensitized photoelectrosynthesis cell

L. Alibabaei · M.K. Brennaman (✉) · T.J. Meyer
Department of Chemistry, University of North Carolina, Chapel Hill, NC 27599, USA
e-mail: kyleb@email.unc.edu

H. Tian et al. (eds.), *Molecular Devices for Solar Energy Conversion and Storage*, Green Chemistry and Sustainable Technology,
https://doi.org/10.1007/978-981-10-5924-7_6

DSSC	Dye-sensitized solar cell
MLCT	Metal-to-ligand charge transfer
BET	Back electron transfer
TA	Transient absorption
CV	Cyclic voltammetry
TEM	Transmission electron microscopy
UV	Ultraviolet
Vis	Visible
IR	Infrared
ALD	Atomic layer deposition
e	Electron
h+	Hole
hν	Irradiation

6.1 Introduction to Light-Driven Water Splitting

Interest in light-driven, water-splitting devices has grown considerably in recent years from both a fundamental and an applied perspective. These devices are based on the concept of artificial photosynthesis which begins with water oxidation powered by sunlight to release electrons, protons, and molecular oxygen. The water oxidation reaction highlighting the stoichiometry of the products is given by

$$2H_2O \rightarrow 4e^- + 4H^+ + O_2.$$

The electrons and protons available from water oxidation are used for reduction of protons to molecular hydrogen or of CO_2 to reduced forms of carbon to store a portion of the incident solar energy in the chemical bonds of a fuel, i.e., a solar fuel. A light-driven, water-splitting device is traditionally defined as a device that achieves total water splitting to produce H_2 rather than CO_2 reduction products. Such devices will be the focus of this chapter.

An initial step toward using the energy of the sun to drive chemical reactions to generate solar fuels, taken by Honda and Fujishima in 1972 [1], was the demonstration of water splitting by band gap excitation of a TiO_2 semiconductor oxide electrode with UV light. Shortly thereafter, the foundation of an alternate, molecular-based approach was reported though the reactions occurred in solution, not at an electrode surface. This pioneering example was based on $[Ru(bpy)_3]^{2+}$ (bpy = 2,2′-bipyridine) where light absorption by Ru(II) in water yields a metal-to-ligand charge-transfer excited state, $[Ru(bpy)_3]^{2+*}$, lasting on the order of

Scheme 6.1 Oxidative quenching of $[Ru(bpy)_3]^{2+*}$ by MV^{2+}

$$Ru(bpy)_3^{2+} + h\upsilon \rightarrow Ru(bpy)_3^{2+*}$$
$$Ru(bpy)_3^{2+*} + MV^{2+} \rightarrow Ru(bpy)_3^{3+} + MV^{+\bullet}$$
$$Ru(bpy)_3^{3+} + MV^{+\bullet} \rightarrow Ru(bpy)_3^{2+} + MV^{2+}$$

~ 1 μs at room temperature. Diffusional, electron transfer quenching of the excited state by an oxidative quencher, methyl viologen (MV^{2+}), was observed by flash photolysis measurements, Scheme 6.1.

The oxidized chromophore is thermodynamically capable of oxidizing water with $E^{o'}([Ru(bpy)_3]^{3+/2+}) = 1.26$ V versus NHE. The reduced form of methyl viologen, $MV^{+\bullet}$, can perform proton reduction to H_2 in acidic solutions with $E^{o'}(MV^{2+/+}) \sim -0.40$ V versus NHE [2, 3].

In a related reaction, the first report of a light-driven, molecular assembly-based photoelectrosynthesis cell was reported by Meyer and coworkers, for the dehydrogenation of isopropanol [4]. This first example of a dye-sensitized photoelectrosynthesis cell (DSPEC) established an entirely new approach to splitting water with light to produce solar fuels. The design for DSPEC devices is conceptually drawn from the natural photosynthetic apparatus, photosystem II, where molecular-level, light-driven, water oxidation occurs [5]. In a DSPEC, oxidation and reduction reactions are carried out at separate electrodes just as in Honda/Fujishima's example and in the more recently developed dye-sensitized solar cell (DSSC). For both DSSCs and DSPECs, oxidation reactions occur at a mesoporous, nanostructured, semiconductor oxide-based (e.g., TiO_2) photoanode with either surface-bound chromophores (for DSSCs) or chromophore–catalyst assemblies (for DSPECs). Reduction reactions occur at a separate cathode, traditionally platinum. The concept is general and significant advances are being made in the development of integrated devices with separate photoelectrodes for either water or CO_2 reduction [6–9] with the focus here on single electrode water splitting.

A schematic illustrating the operation of a water-splitting DSPEC is shown in Fig. 6.1. Light absorption by the chromophore generates an excited state capable of electron transfer into the semiconductor conduction band. The injected electron diffuses through the nanocrystalline semiconductor film to a transparent conducting oxide (TCO) collector electrode, typically fluorine-doped tin oxide (FTO), and, finally, to the cathode. Meanwhile, the oxidized light absorber transfers its oxidative equivalent to a nearby water oxidation catalyst. The cycle is repeated four times to split water, producing oxygen at the photoanode and hydrogen at the cathode.

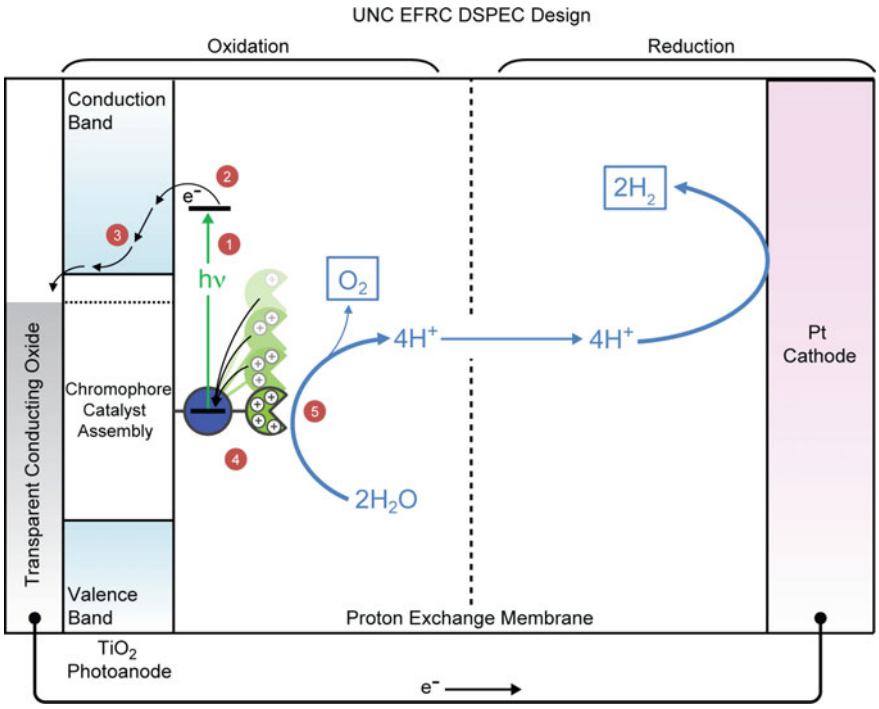

Fig. 6.1 Schematic diagram for a dye-sensitized photoelectrosynthesis cell (DSPEC) for light-driven, water oxidation and proton reduction illustrating: (1) light excitation; (2) electron injection; (3) electron diffusion through the nanoparticle film; (4) electron transfer activation of the water oxidation catalyst; (5) proton transfer to the cathode; and (6) proton reduction at the Pt cathode. Adapted with permission from Ref. [60]. Copyright 2016 American Chemical Society

6.2 The Components of a DSPEC Photoanode

The essential components of a DSPEC photoanode are illustrated in Fig. 6.2 and include (1) a nanostructured, mesoporous, n-type, semiconductor oxide electrode that is transparent to visible light; (2) a light-harvesting chromophore; and (3) a water oxidation catalyst. These three physical components must be stable in aqueous conditions—electrochemically, in the dark, and under visible light illumination. The semiconductor must not undergo corrosion and the molecular components must remain surface-bound and avoid degradation/decomposition. The physical components must be designed to work together, both kinetically and thermodynamically, to carry out electron transfer and catalysis as depicted in Fig. 6.1. Each of these key elements will be considered in this summary.

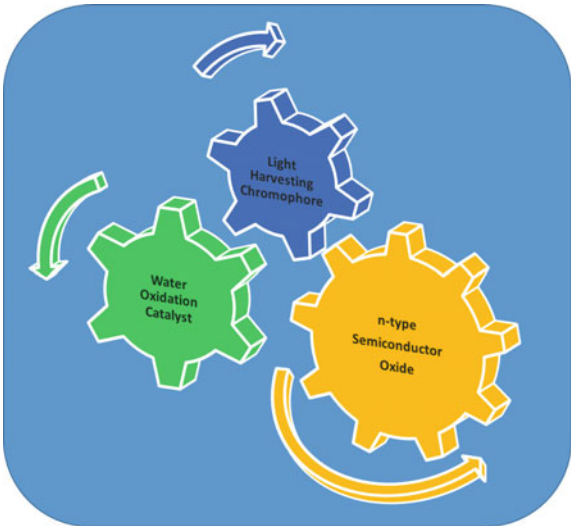

Fig. 6.2 Conceptual design of the key elements of a photoanode in a light-driven, water-splitting photoanode

6.2.1 Semiconductor Electrodes

i. Metal oxides

The earliest observations in this area by Honda and Fujishima were deceptively simple. They were based on water splitting at a single material for light absorption and water oxidation catalysis, namely the wide-band gap, metal oxide, UV-absorber, and crystalline TiO_2 [1]. In order to function efficiently, n-type TiO_2 alone cannot supply the photovoltage required to facilitate net water splitting under standard conditions [10]. Wider band gap metal oxides such as strontium titanates were also found to facilitate unassisted, solar-driven, water splitting [11].

TiO_2 is a mesoporous, n-type semiconductor oxide most commonly used in photoanode applications. It has a pH- and cation-dependent conduction band potential in an appropriate range, 200 mV versus NHE at pH 1. There are well-developed methods for synthesis of TiO_2 nanoparticle films which are stable in water over a broad pH range. Semiconductor/liquid junctions are at the heart of a DSPEC [12], and with water as the solvent, semiconductor photoelectrodes must be stable under aqueous conditions. The need for aqueous stability limits the range of useful semiconductors with Cu_2O, InP, and ZnO, for example, unstable at the highly oxidative potentials required for water oxidation [13–17].

In an initial, preliminary DSPEC study, the photoelectrochemical response of the chromophore $[Ru(bpy)_2(4,4'\text{-}(PO_3H_2)_2bpy)]^{2+}$ (RuP^{2+}) (see Fig. 6.3) on TiO_2 was investigated with triethanolamine or deprotonated EDTA ($EDTA^{4-}$) added as an irreversible reductive scavenger in the external solution. Following light absorption by the chromophore and electron injection from the excited state into the conduction band of TiO_2, $FTO|TiO_2|\text{–}RuP^{2+} + h\upsilon \rightarrow FTO|TiO_2(e^-)|\text{–}RuP^{3+}$, reduction

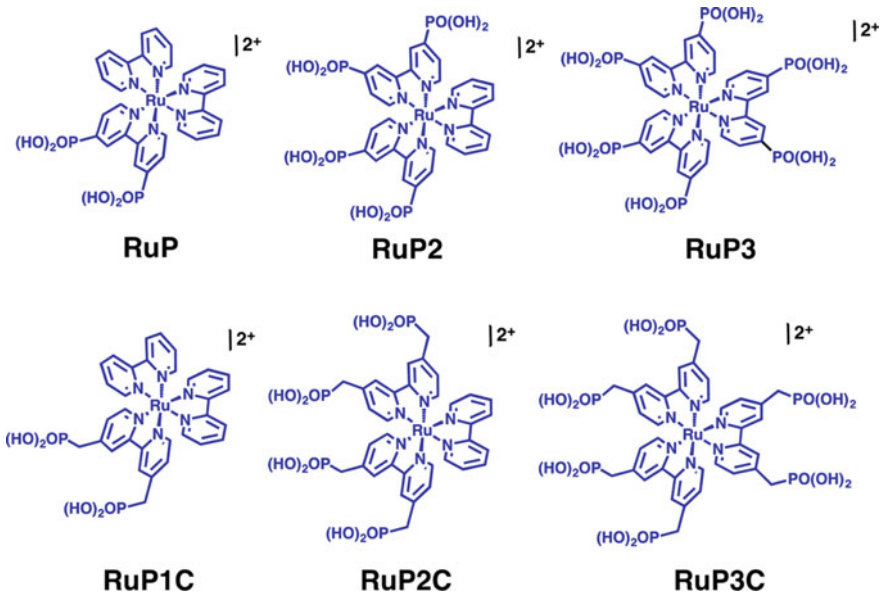

Fig. 6.3 Phosphonate-derivatized Ru(II)–polypyridyl chromophores

of $-RuP^{3+}$ by the added reductive scavengers allowed for the injected electron to transfer to a cathode for H^+ reduction to H_2. For these devices, photocurrents and H_2 production at the cathode were observed with efficiencies approaching 14.7% under steady-state irradiation [18, 19]. In these cells, as for direct excitation of TiO_2, an applied potential of $\sim$0.2 V was required to maximize current efficiencies. Initial experiments were extended to Nb_2O_5 nanocrystalline films functionalized with RuP^{2+} with comparable results obtained [20]. T-phase, orthorhombic, Nb_2O_5 nanocrystalline films are dominated by shallow, band-tail trap states with a conduction flat-band potential slightly positive (<0.1 eV) compared to anatase TiO_2 with a wide distribution of trap states comprising both deep and band-tail trap states. The trap state distributions, conduction band energies, and interfacial barriers for Nb_2O_5 compared to anatase TiO_2 all appear to inhibit back electron transfer and decrease injection yields on the nanosecond time scale, resulting in a lower open-circuit voltage (V_{oc}) for Nb_2O_5. In an operating DSPEC with $EDTA^{4-}$ added as a reductive scavenger, H_2 quantum yield and photostability measurements show that Nb_2O_5 is comparable, but not superior, to TiO_2 as a photoanode material [20].

ii. Core/shell electrodes

A DSPEC photoanode relies on the electron transport properties of mesoporous films, typically 5–15 μm thick, of nanocrystalline semiconductors, e.g., TiO_2 or SnO_2 [19, 21, 22], or of nanocrystalline, transparent conducting oxides,

e.g., *nano*ITO [23, 24], on planar, transparent conductive oxide substrates. A major advance in the development of the DSPEC photoanode is the development of core/shell structures—mesoporous, oxide films conformally coated with ultrathin semiconducting shells—to control interfacial dynamics [12, 23, 25]. Fabrication of core/shell nanostructured photoanodes, also used in DSSCs [26], has been made possible by atomic layer deposition (ALD), a conformal, layer-by-layer gas phase technique.

At the photoanode, electron migration to the underlying FTO is in competition with back electron transfer to the assembly. Back electron transfer is deleterious resulting in loss of the transiently stored oxidative equivalent. Core/shell oxide structures have been found to be advantageous for controlling interfacial electron transfer dynamics [26, 27]. Initial results were reported on DSSCs incorporating core/shell photoanodes (TCO cores/TiO_2 shells) derivatized with the classic Ru-based dye (N719). Short-circuit current densities, open-circuit voltages, and back electron transfer lifetimes were all found to depend on TiO_2 shell thickness. These quantities were optimized with shell thicknesses in the range of 1.8–2.4 nm. Performance diminished as the shell thickness was increased beyond 2.4 nm, presumably due to the appearance of low-energy trap states within the thicker shells which serve to facilitate back electron transfer to Ru(III), a pathway competitive with transport to the core [23]. As described later in this chapter, ALD has also been used successfully for stabilizing phosphonate surface binding of chromophores [22, 28], catalysts [12], and assemblies by depositing overlayers of Al_2O_3 or TiO_2 [25].

6.2.2 Light Absorbers (i.e., Chromophores)

i. Ru-based dyes
ii. Porphyrin-based dyes
iii. Other organic dyes

A variety of light-absorbing molecules suitable for DSPEC applications has been investigated including perylenes, D-π-A organic dyes [29], porphyrins, and Ru(II)-polypyridyl chromophores. Spectroelectrochemical and ultrafast spectroscopic techniques have been utilized to study the interfacial dynamics of photoinjection and charge recombination that occur at the molecule–semiconductor interface in the presence of water. For the most ubiquitous family of Ru(II)-polypyridyl chromophores (Fig. 6.3), a recent systematic study outlined a detailed picture of the factors that govern excited-state injection by this series bound to nanocrystalline TiO_2 [30].

Porphyrins are an appealing class of chromophore partially due to their importance and function in the photosynthetic solar energy antenna. Porphyrins have been studied for DSSC application though less extensively in DSPECs. Porphyrins absorb visible light strongly, especially in the range of 400–450 nm (Soret band),

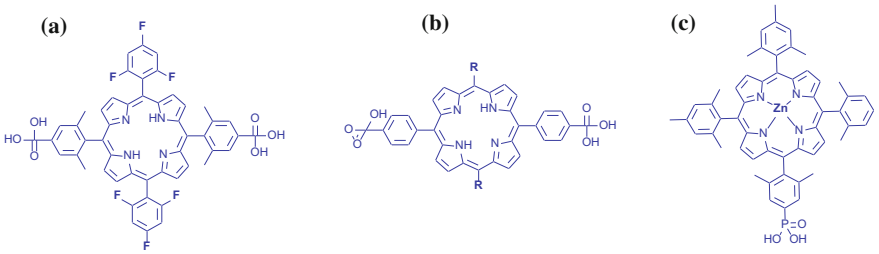

Fig. 6.4 Chemical structures of porphyrins used as dyes in DSPEC devices [25–27]

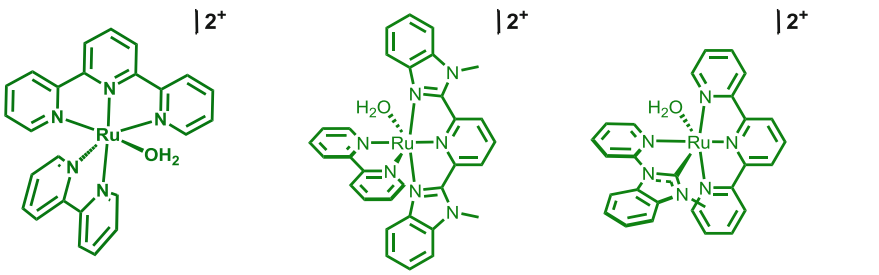

Fig. 6.5 Chemical structures of early examples of Ru-based, single-site water oxidation catalysts. tpy = 2,2′,2″-terpyridine; bpy = 2,2′-bipyridine; Mebimpy = 2,6-bis(1-methylbenzimidazol-2-yl) pyridine; Mebimpy = 3-methyl-1-pyridylbenzimidazol-2-ylidene

and more moderately in the 500–700 nm region arising from two to four Q-band transitions. Porphyrin structures [31–33] that have been used for PEC applications are shown in Fig. 6.4.

6.2.3 Molecular Water Oxidation Catalysis

The first designed molecular water oxidation catalyst was the μ-oxo bridged dimer, often referred to as the "blue dimer", *cis,cis*-$[(bpy)_2(H_2ORu^{III}ORu^{III}(OH_2)(bpy)_2]^{4+}$. Building on the use of polypyridyl complexes, a series of oxygen-evolving complexes has been prepared and characterized within the past decade. This set includes polypyridyl derivatives of the general forms $[Ru(LLL)(LL)(OH_2)]^{2+}$ and $[Ru(LL)(LL)(L)(OH_2)]^{2+}$, e.g., *cis*-$[Ru(bpy)_2(py)(OH_2)]^{2+}$ and $[Ru(tpy)(bpy)(OH_2)]^{2+}$ (tpy = 2,2′,2″-terpyridine) Fig. 6.5 [34]. The first step of the water oxidation mechanism involves oxidation to generate $Ru^{III}–OH_2^{2+}$. This then undergoes proton-coupled electron transfer (PCET) to form $Ru^{IV} = O^{2+}$, a potent oxidant catalyzing transformation of a variety of organic and inorganic functional

groups [35–41]. Water oxidation typically requires further oxidation and electron loss to $Ru^{V}(O)^{3+}$ followed by reaction with water and proton loss to give the peroxide, $Ru^{III}(OOH)^{2+}$, which is rate limiting. The peroxide is subsequently oxidized with O_2 release to give $Ru^{II}(OH_2)^{2+}$ and O_2 [42]. An important feature in this chemistry has been the identification of reaction pathways for O–O bond formation which are first order in added proton acceptor bases (B = acetate, HPO_4^{2-},…) arising from coupled proton loss, $Ru^{V}(O)^{3+} + H_2O + B \rightarrow Ru^{III}(OOH)^{3+} + BH^{+}$ [42–45].

A new generation of single-site, Ru-based, water oxidation catalysts of the type Ru(bda)$(L)_2$ (bda = 2,2′-bipyridine-6,6′-dicarboxylate, L: pyridine or other neutral donor ligands, Fig. 6.6, [46–48] has been developed by Sun and coworkers. Water oxidation is catalyzed at remarkably fast rates though a full mechanistic understanding is still emerging. Studies of these catalysts driven by Ce(IV) in acidic aqueous solutions have identified a route involving a seven-coordinate Ru(V)-oxo and bimolecular O–O coupling [48]. As for the original single-site catalysts, they can be synthetically modified to include functional groups suitable for surface anchoring, e.g., phosphonic acids, vinyl groups, etc.

6.2.4 *Surface Binding and Stabilization*

As for any solar energy conversion device, both the components and the physical attachments between components must remain stable for extended time periods, even up to years. For a DSPEC, there are linkages, or electronic pathways for communication, between chromophore and catalyst as well as between molecular assemblies and semiconductor surfaces. An array of functional groups has been explored for surface attachment, including carboxylates and siloxanes; unfortunately, carboxylates are readily hydrolyzed and siloxanes have proven to be synthetically challenging [49]. Phosphonates have proven to be the most effective

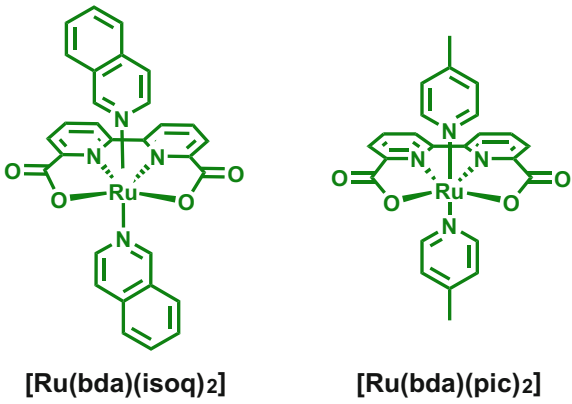

Fig. 6.6 Chemical structures of Ru-based, single-site water oxidation catalysts with the anionic ligand H_2bda where. H_2bda = 2,2′-bipyridine-6,6′-dicarboxylic acid; isoq = isoquinoline; pic = 4-picoline

linkages for anchoring molecules to oxide surfaces in the presence of water. The stability of the phosphonate attachment to oxide surfaces is pH-dependent, favored in acidic solution, but is only robust in the dark without an applied bias [50]. With water oxidation more thermodynamically favorable with increasing pH, and with base-assisted pathways available for facilitating rate-limiting O–O bond formation, operating a DSPEC under basic solution conditions can be advantageous. However, even the phosphonate-oxide surface link is unstable toward hydrolysis as the pH is increased above 5, especially in the presence of added buffer bases [51, 52]. Stabilizing interfacial surface structures is clearly an important element in the overall operation of a successful DSPEC.

A range of stabilization strategies has therefore been established which has significantly improved the robustness of surface binding. The strategies developed so far include the following:

(1) Using atomic layer deposition (ALD) to add stabilizing overlayers of Al_2O_3 or TiO_2 [12, 22, 28].
(2) Adding a hydrophobic polymer film overlayer by a simple dipping procedure [53].
(3) Tethering chromophores and catalysts together at the interface by electropolymerization, and
(4) Adding Nafion to the interface as an additional support [54, 55].

Atomic Layer Deposition. ALD is a layer-by-layer, conformal technique where oxide surfaces with acidic hydroxyl groups are exposed to a reactive precursor in the gas phase—$Al(CH_3)_3$ for Al_2O_3, $TiCl_4$ and other precursors for TiO_2—followed by exposure to water which releases CH_4 or HCl for $TiCl_4$. Because of these self-limiting surface reactions, a single sequence (usually called a cycle) of precursor/water exposure can be used to deposit a monolayer or sub-monolayer of the oxide onto the surface. Multiple gas phase-surface hydrolysis cycles are used to build up multiple oxide layers. This surface reaction method has been used to stabilize molecule-oxide surface binding. By using ALD, inert overlayers of Al_2O_3 or TiO_2 have been deposited on top of chromophores, catalysts, and assemblies already bound by phosphonate linkers to semiconductor surfaces [56].

The addition of Al_2O_3 or TiO_2 overlayers serves to prevent hydrolysis from the surface. A schematic diagram illustrating the surface-bound water oxidation catalyst $[Ru(Mebimpy)(4,4'\text{-}(PO_3H_2CH_2)_2bpy)(OH_2)]^{2+}$ stabilized by TiO_2 is shown in Fig. 6.7. The same figure also compares current time traces for water oxidation by ALD-stabilized and un-stabilized catalyst at pH 11 in a phosphate buffer. Under these conditions, the rate of water oxidation is $\sim 10^4\ s^{-1}$.

Polymer Overlayers. The molecule-oxide linkage has also been stabilized by addition of a polymer overlayer. Figure 6.8 illustrates polymer stabilization of surface-bound chromophores on TiO_2 or *nano*ITO by poly-methylmethacrylate (PMMA) oligomers [53]. In this approach, the surface-bound molecule or assembly is exposed to dichloromethane solutions containing the hydrophobic PMMA

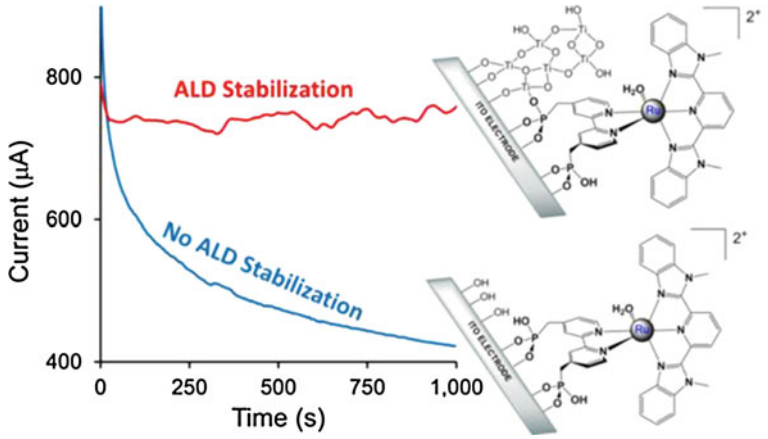

Fig. 6.7 Controlled potential current time traces for $[Ru(Mebimpy)(4,4'\text{-}((HO)_2OPCH_2)_2bpy)(OH_2)]^{2+}$ bound to *nano*ITO with (*red* trace) and without (*blue* trace) ALD TiO_2 overlayer stabilization. Electrolyses were performed at pH 11 in phosphate buffers at 1.6 V versus NHE. Adapted with permission from Ref. [60]. Copyright 2016 American Chemical Society

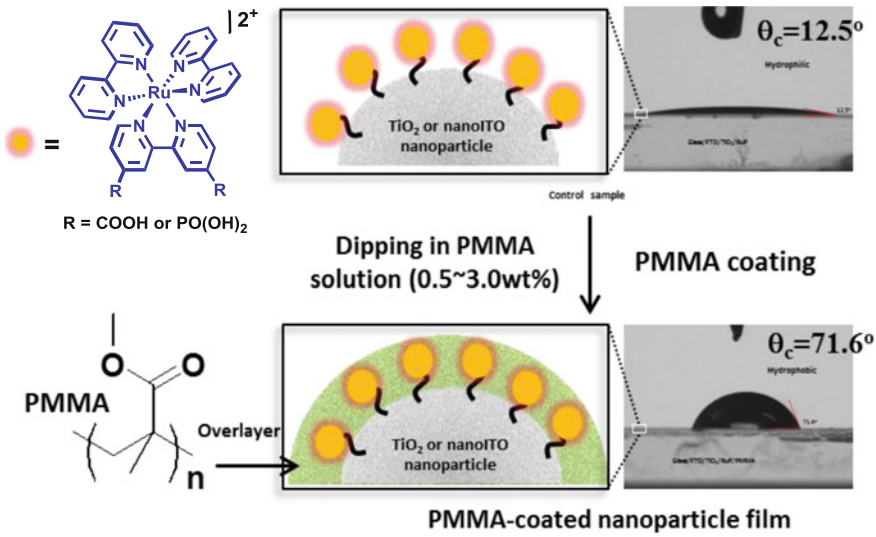

Fig. 6.8 Cartoons and contact angle measurements illustrating PMMA stabilization of a surface-bound $[Ru(bpy)_2(4,4'\text{-}R_2\text{-}bpy)]^{2+}$ (R = $-CO_2H$ or $-PO(OH)_2$ on TiO_2. Adapted with permission from Ref. [53]. Copyright 2016 American Chemical Society

polymer. Overlayer film thicknesses can be varied reproducibly by varying the concentration of polymer in the loading solution with uniform overlayer thicknesses formed as shown by Transmission Electron Microscopy (TEM) imaging.

Electro-assembly. It is well established that electroactive films can be formed at electrode surfaces by reductive electropolymerization of vinyl-derivatized pyridyl ligands in polypyridyl transition metal complexes. Ligand-based reduction of these complexes at the electrode-solution interface induces vinyl-based, C–C coupling leading to interconnected molecular components at the electrode surface. This "electro-assembly" approach has been used to synthesize molecular assemblies within mesoporous, nanoparticle oxide films [57]. In one recent example, phosphonated chromophores, also functionalized with vinyl groups, are first bound to an oxide surface. In the presence of a vinyl-derivatized Fe(II)-bis(terpyridine) complex $[Fe(vtpy)_2]^{2+}$ (vtpy = 4′-vinyl-2,2′:6′,2″-terpyridine) in the external solution, application of negative potentials drives formation of C-C bonds between Ru(II) and Fe(II) chromophores (Fig. 6.9). The photostability of these surface-bound Ru(II) and Fe(II) chromophores exposed to aqueous conditions is enhanced up to

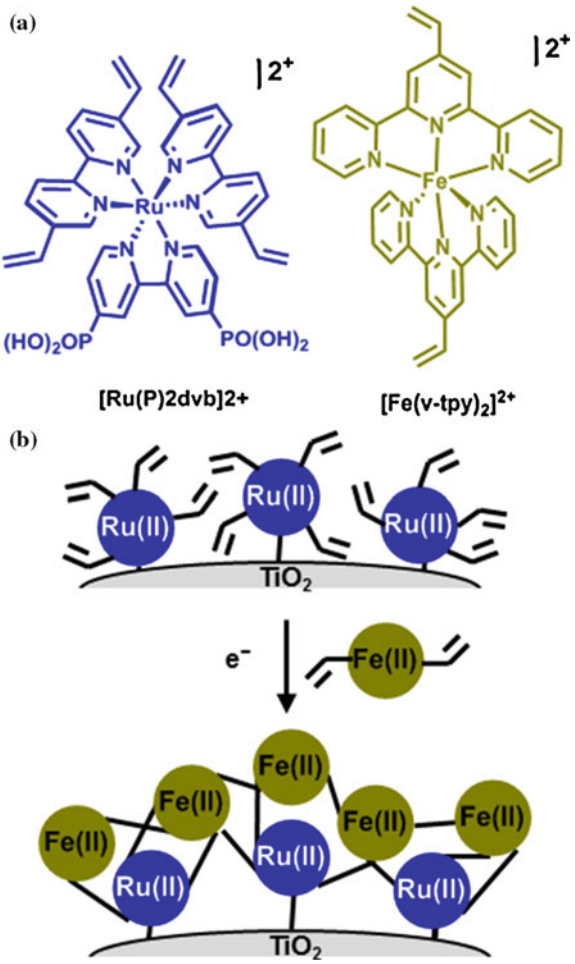

Fig. 6.9 **a** Structures of $[Ru(P)_2dvb]^{2+}$ and $[Fe(vtpy)_2]^{2+}$; dvb = 5,5′-divinyl-2,2′-bipyridine; vtpy = 4′-vinyl-2,2′:6′,2″-terpyridine. **b** Schematic diagram of the surface structure following reductive polymerization of $[Fe(vtpy)_2]^{2+}$ on TiO_2-$[Ru(P)_2dvb]^{2+}$. Adapted with permission from Ref. [60]. Copyright 2016 American Chemical Society

30-fold compared to the Ru(II) complex without an electropolymerized overlayer. Stability in this case comes from the additional stabilization of the surface-formed oligomers.

6.2.5 Chromophore–Catalyst Assembly Synthesis Strategies

At a DSPEC photoanode, chromophores and catalysts must be electronically linked at the electrode surface. Conceptually, this can be accomplished by prior surface bonding, through a modular approach, with pre-linked molecular components bound to the surface of the semiconductor oxide, or by arranging the chromophore and catalyst appropriately following surface attachment.

In the design of chromophore–catalyst assemblies for DSPEC applications, key elements include the absorptivity and excited-state redox potential of the electrode, to maximize light absorption and injection, and the redox potential(s) and reactivity of the catalyst. In order to maximize efficiencies and spectral coverage, reach excited-state potentials that are sufficient, achieve efficient electron injection, and manipulate the semiconductor surface to inhibit back electron transfer, all must be addressed in a working electrode.

A variety of modular, chromophore–catalyst assembly strategies have been developed including co-loading [58], molecular overlayer [59], ALD-based "mummy" [60, 61], layer-by-layer [62–65], electro-assembly [66, 67], and Nafion-based schemes. The simplest approach is co-loading. In this approach, chromophores and catalysts are assembled by allowing each to bind, either sequentially or simultaneously, to the oxide surface through simple soaking procedures with the electrode in solutions containing chromophores, catalysts, or both. This method enables control over both the chromophore:catalyst ratio and extent of surface loading by controlling solution composition and soaking time [58, 68, 69]. For this strategy to be effective, total surface loading should be relatively high to ensure close packing between the molecular components to enable rapid cross-surface intermolecular electron and hole transfer.

The "molecular overlayer" approach, shown in Fig. 6.10b, is a type of co-loading. First, a layer of chromophores is linked to the oxide surface. A catalyst overlayer, where each catalyst is positioned above a chromophore, is formed by catalysts linking to the surface by long chain –(CH_2)– phosphonate linkers [59].

The "layer-by-layer" strategy in Fig. 6.11 is based on initial results from Mallouk and Haga and their coworkers which they applied to planar substrates [70–73]. Chromophores with multiple phosphonate functional groups are adsorbed as the first layer. For $[Ru(bpy)(4,4'\text{-}(PO_3H_2)_2bpy)_2]^{2+}$, oxide surface binding leaves uncoordinated phosphonate groups oriented toward the external solution. Some of the available phosphonates are then coordinated to Zr(IV) which acts as a bridge [33, 64]. The second layer is formed by soaking in a solution with phosphonate-derivatized water oxidation catalyst thereby completing the synthesis of the assembly.

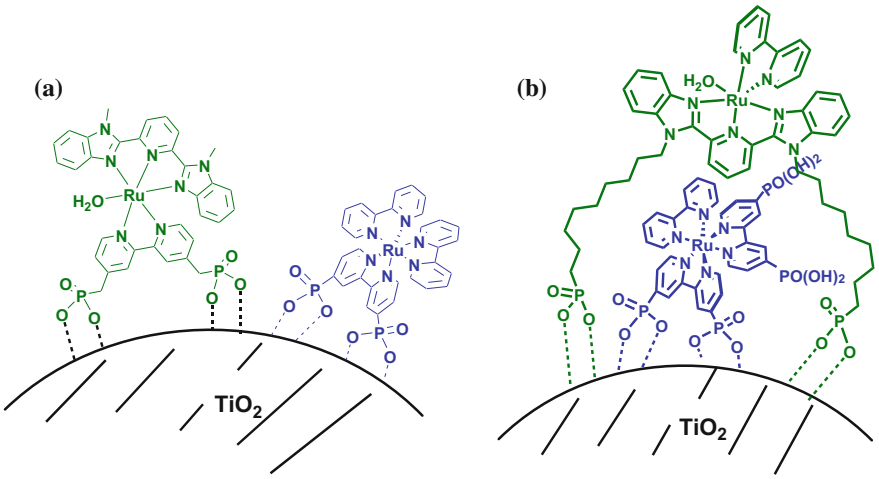

Fig. 6.10 Examples of **a** co-loading and **b** molecular overlayer strategies. Figure is adapted with permission from Ref. [108], an article licensed under ACS AuthorChoice and future permission requests should be directed to the American Chemical Society. Copyright 2015 American Chemical Society

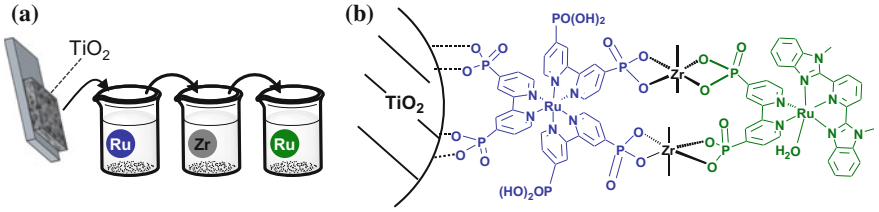

Fig. 6.11 Layer-by-layer strategy. **a** General stepwise procedure, **b** example of a layer-by-layer assembly (Figure is adapted with permission from Ref. [70]. Copyright 2012 Wiley-VCH Verlag)

The "electro-assembly" strategy was described above as applied to improving surface binding stability. This same method can also be extended to building chromophore–catalyst assemblies as shown in Fig. 6.12. Briefly, a phosphonate-derivatized chromophore, which also contains a vinyl-2,2′-bpy ligand or ligands, is surface-bound to the oxide [66, 67]. With this as the working electrode, reductive electrochemical scans in the presence of a vinyl-bpy-derivatized water oxidation catalyst in the external solution lead to assembly formation through C–C bonding between molecular components [74, 75]. The chromophore:catalyst ratio is controlled by the number of reductive scans.

Figure 6.13 depicts the so-called ALD-based "mummy" strategy. Surface adsorption of chromophores is followed by ALD of metal oxide which serves to

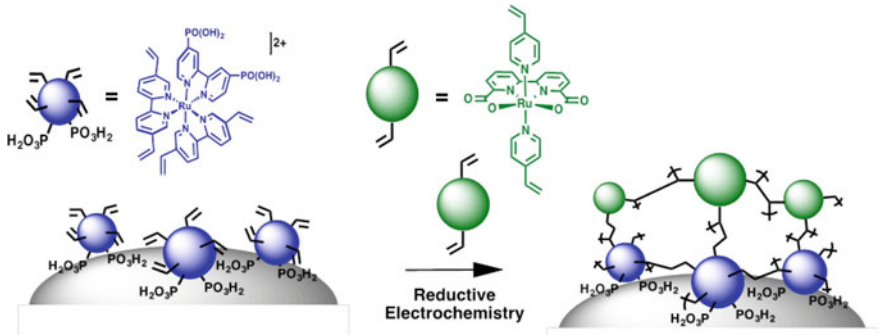

Fig. 6.12 Schematic diagram illustrating surface structure following reductive electropolymerization of: $[Ru(dvb)_2((PO_3H_2)_2bpy)]^{2+}$ ($RuPdvb^{2+}$; dvb = 5,5′-divinyl-2,2′-bipyridine) (*blue*) and vinyl-functionalized molecular water oxidation catalyst (*green*) $(PO_3H_2)_2bpy$ = [2,2′-bipyridine]-4,4′-diylbis(phosphonic acid). Adapted with permission from Ref. [60]. Copyright 2016 American Chemical Society

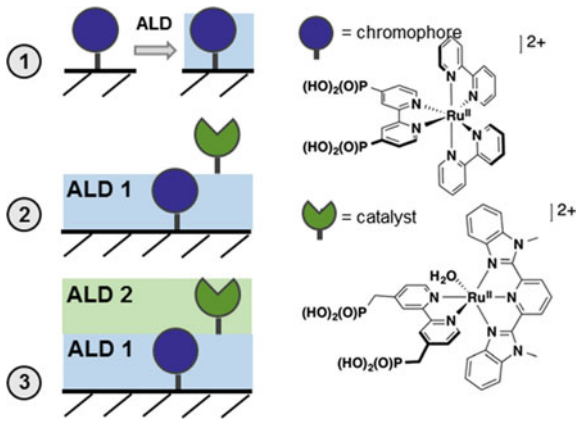

Fig. 6.13 Structure of a "mummy" chromophore–catalyst assembly by: (1) ALD overlayer deposition (labeled ALD 1) following surface binding of $–RuP^{2+}$, (2) addition of $[Ru(Mebimpy)(4,4'-(PO_3H_2CH_2)_2bpy)(OH_2)]^{2+}$, and (3) ALD stabilization (labeled ALD 2). Figure is adapted with permission from Ref. [60]. Copyright 2016 American Chemical Society

stabilize the surface binding and provide a scaffold for adsorption of a layer of catalysts. Finally, a second ALD layer is formed to complete the assembly.

Stepwise assembly of molecular components has also been approached by adding the perfluorinated polymer Nafion after the surface is derivatized. Much like the ALD mummy strategy, a monolayer of chromophores is bound to the surface as a first step. Next, Nafion is applied to produce an overlayer which acts as a surface matrix or scaffold to support catalysts noncovalently. As depicted in Fig. 6.14, using this strategy toward light-driven water splitting, Brimblecombe et al. prepared TiO_2 [54, 55] with a 4.5:1 chromophore:catalyst ratio with the chromophore $[Ru(4,4'-COOH)bpy)(bpy)_2]^{2+}$ surface-bound and the tetra-nuclear Mn-oxo cluster as the catalyst, with L = $(MeOPh)_2PO_2$, supported by Nafion. With this as the photoanode, sustained photocurrents were observed under white light illumination over a 2 h period with no external bias. In a related report [76], Sun and coworkers

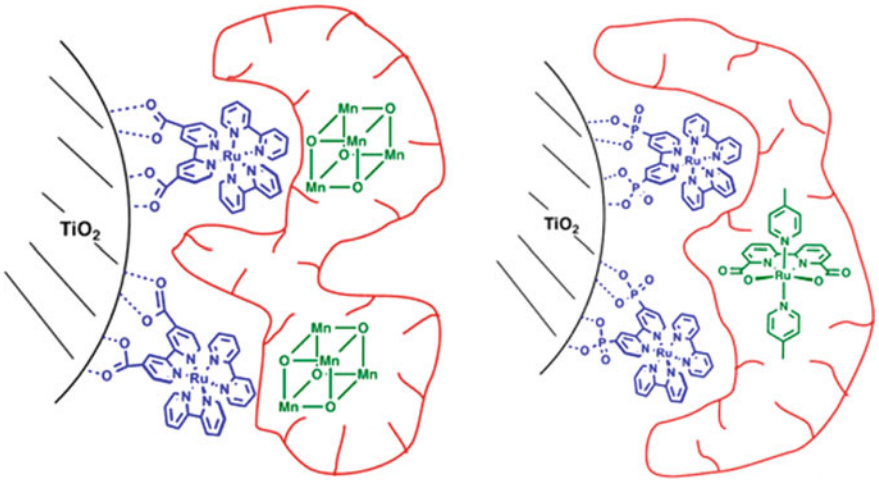

Fig. 6.14 Structure of a PEC photoanode consisting of the chromophore–nafion–catalyst on TiO_2. Figure is adapted with permission from Ref. [108], an article licensed under ACS AuthorChoice and future permission requests should be directed to the American Chemical Society. Copyright 2015 American Chemical Society

used the Nafion approach to prepare a photoanode with $–RuP^{2+}$ and an added bda-derivatized catalyst. Using pH 7 phosphate buffer and a modest external bias of −0.13 V, the combined electrode exhibited 16 turnovers during a 1 h illumination from a 500 W Xe lamp (400 nm long-pass filter). No water splitting was observed at pH 1 because of the pH dependence of the catalyst redox couples.

The other conceptual approach to DSPEC chromophore–catalyst assemblies utilizes preformed assemblies which include those formed by polymer scaffolds [77, 78], peptide scaffolds [79, 80], and covalently linked molecular assemblies [81–87]. Preformed assemblies are appealing because the ratio and separation distance between components are well defined. Unfortunately, preformed assemblies are typically obtained by tedious, multi-step, exceptionally low-yielding syntheses often requiring complex chromatographic separations.

The peptide scaffold strategy is an example of application of a more complex structure to control the relative positions of chromophores and catalysts. It takes advantage of the well-known, auto-arranging behavior of peptide sequences and the well-developed solid-state peptide syntheses pioneered by Merrifield [88]. With this approach, it is possible to control the content and relative spatial arrangement of attached components which ultimately controls intra-assembly electron and energy transfer rates [89].

As an example of the structure [90], Fig. 6.15 shows an oligoproline-supported chromophore–catalyst assembly which demonstrated electrocatalytic water oxidation catalysis which was enhanced by a factor of ten compared to the catalyst alone.

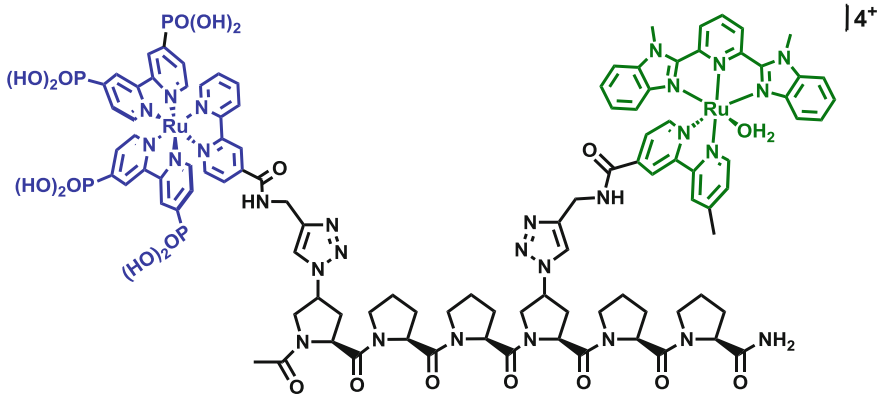

Fig. 6.15 Structure of a chromophore–catalyst assembly based on a peptide scaffold. Adapted with permission from Ref. [60]. Copyright 2016 American Chemical Society

Figure 6.16 illustrates examples of covalently linked chromophore–water oxidation catalyst assemblies investigated by the UNC EFRC. Assembly **3**, $[(4,4'\text{-}(CH_2PO_3H_2)_2bpy)_2Ru^{II}(bpm)Ru^{II}(Mebimpy)(OH_2)]^{4+}$, is notable as a first example of a surface-bound assembly for electrocatalytic water oxidation with sustained water oxidation catalysis demonstrated in acidic solutions for at least 28,000 turnovers without decomposition at a rate of 0.6 s^{-1} [81].

The assemblies of Fig. 6.16 as well as the others presented above are based on Ru(II) chromophores. The use of organic chromophores rather than inorganic ones is advantageous because of relative cost and, with appropriate exploitation, enhanced and wavelength-extended light absorption. Despite their potential advantages, the redox properties of the oxidized or reduced forms of the organic chromophores are characteristically unstable in aqueous environments which can inhibit their exploitation. Important examples of organic chromophore–water oxidation catalyst assemblies are shown in Fig. 6.17 and are based on porphyrin, e.g., **7** [91], and fluorescein, e.g., **8** [92], as well as perylene-3, 4:9, 10-bis(dicarboximide), e.g., **9** and **10,** originally developed by Wasielewski and coworkers [93].

At the photoanode, electron migration to the underlying FTO is in competition with back electron transfer to the assembly. Back electron transfer is deleterious resulting in loss of the transiently stored oxidative equivalent. Core/shell oxide structures have been found to be advantageous for controlling interfacial electron transfer dynamics, note below [26, 27].

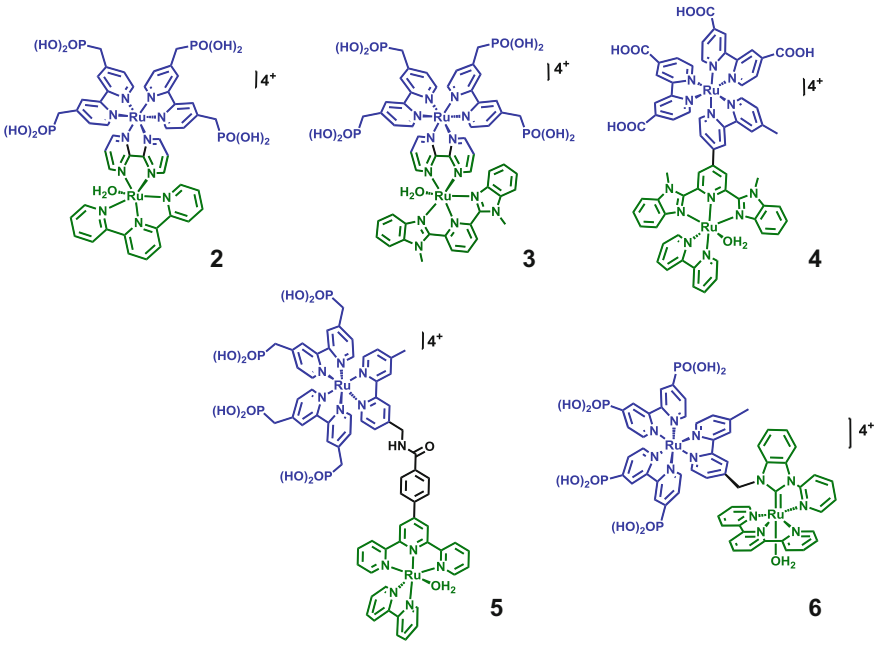

Fig. 6.16 Structures of covalently linked assemblies 2–6. Figure is adapted with permission from Ref. [108], an article licensed under ACS AuthorChoice and future permission requests should be directed to the American Chemical Society. Copyright 2015 American Chemical Society

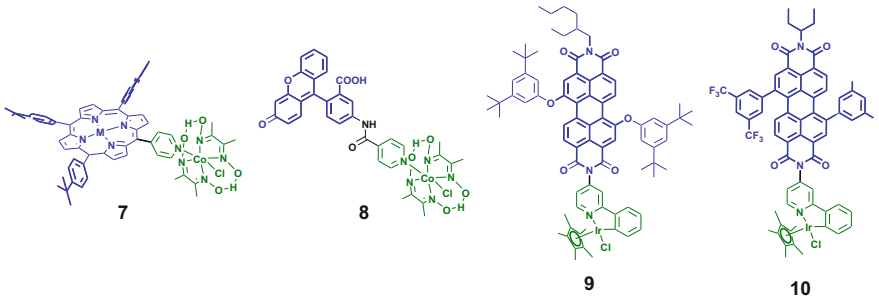

Fig. 6.17 Structures of porphyrin 7 and organic dye-based chromophore–catalyst assemblies 7–10. Figure is adapted with permission from Ref. [70], an article licensed under ACS AuthorChoice and future permission requests should be directed to the American Chemical Society. Copyright 2015 American Chemical Society

6.3 What Have We Accomplished? Examples of State-of-the-Art, Light-Driven, Water-Splitting Devices

6.3.1 Water Oxidation Catalyst–RuP Assembly by Co-loading for Alcohol Oxidation

Partial inhibition of back electron transfer has been achieved by the introduction of core/shell nanostructures. The first core/shell, DSPEC photoanodes incorporated nanoparticle Sn(IV)-doped In_2O_3 (*nano*ITO) or Sb(V)-doped SnO_2 (nanoATO) and a thin (3–5 nm), conformal shell of TiO_2. An initial study compared the performance of nanocrystalline TiO_2 to *nano*ITO/TiO_2 core/shell electrodes for light-driven dehydrogenation of benzyl alcohol (BnOH) to benzaldehyde and hydrogen. Electrodes were co-loaded with a chromophore, RuP^{2+}, and catalyst, $[Ru(Mebimpy)((4,4'\text{-}(OH)_2P(O)CH_2)_2bpy)(OH_2)]^{2+}$ (Mebimpy = 2,6-bis(1-methylbenzimidazol-2-yl) pyridine). For this system, light absorption by the chromophore is rapidly followed by electron injection and cross-surface electron transfer activation of the catalyst. A second photon initiates a second cycle of injection and cross-surface electron transfer which prepares the catalyst as –Ru(IV) = O^{2+}—a powerful enough oxidant to oxidize benzyl alcohol to benzaldehyde. A maximum, sustained, absorbed-photon-to-current efficiency for BnOH dehydrogenation of 3.7% was observed, a tenfold increase compared to TiO_2 (non-core/shell) electrodes.

6.3.2 Covalently Linked Water Oxidation Catalyst–Ru Chromophore Assembly on NanoTCO Core/TiO_2 Shell Electrodes for Water Splitting

A water-splitting DSPEC photoanode was demonstrated by using a core/shell nanostructure derivatized with molecular assembly **6** in Fig. 6.16, $[(4,4'\text{-}PO_3H_2)_2bpy)_2Ru(4\text{-}Mebpy\text{-}4'\text{-}bimpy)Ru(tpy)(OH_2)]^{4+}$ ($[Ru^{II}_a\text{–}Ru^{II}_b\text{–}OH_2]^{4+}$: (4,4′-$PO_3H_2)_2$bpy is 4,4′-bisphosphonic acid-2,2′-bipyridine; 4-Mebpy-4′-bimpy is 4-(methylbipyridin-4′-yl)–N–(benzimid)–N′-pyridine), bound to the TiO_2 shell. Photoexcitation of the chromophoric unit of this assembly led to electron injection into the shell and rapid electron migration through the shell to the conducting core followed by intra-assembly electron transfer to deliver an oxidative equivalent to the catalyst. Using the optimal TiO_2 shell thickness of 3.6 nm, water splitting was observed for FTO|*nano*ITO|TiO_2|–$[Ru^{II}_a\text{–}Ru^{II}_b\text{–}OH_2]^{4+}$ by applying a bias of 0.2 V in the presence of pH 4.6 acetate buffer with a Pt cathode though with a maximum per-photon-absorbed efficiency of only 4.4% upon monochromatic (445 nm) irradiation. The efficiency was low but this was a significant beginning as no water splitting was observed for this assembly on non-core/shell photoanodes. This underscores the importance of the role of the core/shell nanostructure in affecting

the kinetics of deleterious back electron transfer, a process which prevents buildup of oxidative equivalents at the catalyst.

6.3.3 *Covalently Linked Water Oxidation Catalyst–Ru Chromophore Assembly on SnO_2 Core/TiO_2 Shell Electrodes for Water Splitting*

Building on the initial success of water splitting by a DSPEC core/shell photoanode with a conducting core, a ~five-fold increase in efficiency was achieved by exchanging the conducting core material for a semiconducting material, namely SnO_2. The dramatic increase was attributed to the conduction band alignment of the core (SnO_2) and shell (TiO_2) oxides. The conduction band potential of SnO_2 lies +0.4 V positive that of TiO_2. Taking advantage of this thermodynamic offset, photoexcitation of molecular assembly **6**, Figs. 6.16 and 6.18c, resulted in electron

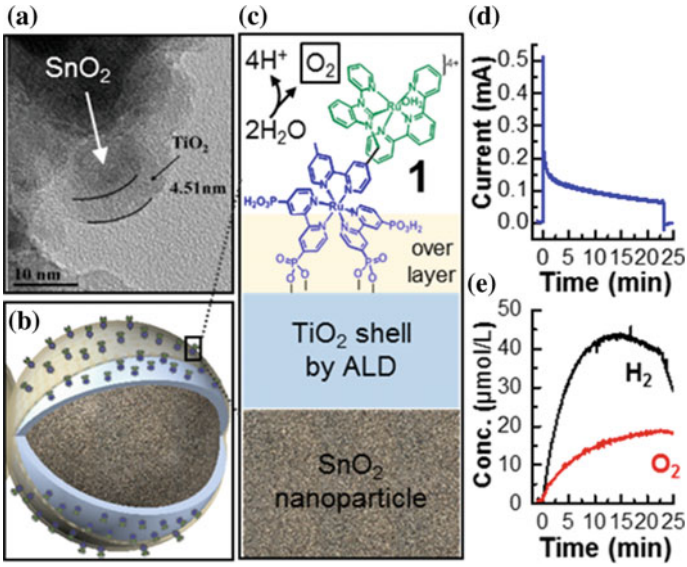

Fig. 6.18 **a** Transmission electron micrograph of SnO_2/TiO_2 core/shell nanostructure. **b** Depiction of core/shell nanoparticle along with a surface-stabilizing overlayer of TiO_2 or Al_2O_3 added by ALD. The drawing is based on a 20-nm-diameter nanoparticle as the "core" (*black/brown speckled pattern*), a 5 nm shell (*light blue*), and a 1.5 nm overlayer (semi-transparent tan). A subset of molecular assemblies bound directly to the shell are also depicted with *blue circles* as chromophores and *green, notched circles* as catalysts. **c** Zoomed-in view highlighting the structure of assembly 6 on the core/shell surface stabilized by an ALD oxide overlayer. DSPEC photoanodes for solar-driven water oxidation were produced by atomic layer deposition of a TiO_2 shell, 3–5 nm thick, on the exposed surfaces of a mesoporous, SnO_2 nanocrystalline film, 5–15 μm thick, on FTO to give FTO|SnO_2/TiO_2–$[Ru^{II}_a–Ru^{II}_b–OH_2]^{4+}$, Adapted with permission from Ref. [60]. Copyright 2016 American Chemical Society

injection into the shell and ultimately the core. With the electron in the core oxide, intra-assembly electron transfer activation of the catalyst occurred. The same thermodynamic offset which provided driving force for electron migration to the core served as a thermodynamic barrier which inhibited back electron transfer from the core through the shell to the oxidized assembly.

With a core/shell structure, an assembly **6** (Figs. 6.16 and 6.18c) derivatized SnO_2/TiO_2 core/shell photoanode-based DSPEC under pH 7 conditions achieved a per-photon-efficiency of ~20% and a maximum photocurrent of 1.97 mA/cm^2 with a 0.6 V applied bias upon monochromatic (445 nm) illumination. Evolution of O_2 at the photoanode and H_2 at the Pt cathode in the expected H_2:O_2 ratio was confirmed by in situ microelectrode analysis, Fig. 6.18d. With this direct evidence for enhanced water splitting compared to the conducting core photoanode, a key DSPEC design principle was established.

6.4 Where Are We Going? Future Challenges for Light-Driven, Water-Splitting Devices

The DSPEC approach to artificial photosynthesis for solar fuels is poised for future game-changing improvements. Only recently have the key elements and design principles of these light-driven, water-splitting devices been uncovered. These strides have been made possible by the use of single-site water oxidation catalysts as well as improvements in oxide electrodes, e.g., the core–shell nano-architecture. At this stage, future progress for DSPEC photoanodes is required in a number of areas notably in overcoming slow chromophore decomposition by the evolution of more complex internal structures and optimization of individual components—absorbers, catalysts, and electrode materials.

Photoanodes. The results of an extended research effort are now available that offer further promise to overcome existing research hurdles. Light absorbers need to be developed which absorb more low-energy visible light yet still have sufficient excited-state redox potentials for photoinjection and catalyst activation. Stable catalysts for both water oxidation and proton reduction are required that achieve catalytic rates that exceed the rate of solar insolation by factors >10. Stability is an ongoing issue with working performances that should exceed 10^7 cycles/year while maintaining initial catalytic activity. Strategies for avoiding decomposition and/or desorption of the molecular components must be further developed to enable long-term stability under DSPEC operating conditions. As progress is made, modifications to semiconductor nano-architectures and molecular assembly structures will undoubtedly lead to improved interfacial electron transfer dynamics to accomplish the conversion of solar photons into redox equivalents at the catalyst with >90% efficiency, even for the higher oxidation states of the catalyst. As noted above, progress is also being made with modified, multi-cell configurations for enhanced light absorption without a need for applied bias.

Photocathodes. Although less well- developed, closely related research continues to evolve on the development of photocathodes for H_2O reduction to H_2 and for CO_2 reduction to CO and other reduced forms of carbon. Research in this area has been dominated by NiO. With the potential of the NiO valence band at $E_{vb} \sim 0.5$ V versus NHE in pH 1, it is an ideal electrode for hole transfer to the excited states of bound chromophores. For example, for the $[Ru(bpy)_3]^{+/2+*}$ couple, with $E^\circ = 0.8$ V versus NHE, the driving force for hole injection from $[Ru(bpy)_3]^{2+*}$ to NiO is ~ 0.3 V.

Nonetheless, advances in this area have been limited by the chemical and physical properties of NiO electrodes. Most of the photocathode work to date has been based on NiO electrodes derivatized with molecular chromophores and/or catalysts for H_2 production or CO_2 reduction [94–100]. The performance of NiO-based photocathodes has been far less impressive than typical oxide photoanodes. For these NiO electrodes, the local electrode dynamics for bound chromophores results in low overall injection efficiencies and there are significant complications in the preparation of reproducible materials [101]. Alternatives to NiO have begun to appear, e.g., Cu_2O [102], although they utilize bandgap excitation. Progress has also been made recently in developing multiple approaches to cell design including integration of DSSC and DSPEC designs which utilize the input from a DSSC to provide the required potential in the water-splitting cells [103–106]. Other, integrated approaches are also being explored including use of an integrated Si solar cell to extend the light absorption characteristics of a single electrode cell [107].

Much has been learned about the DSPEC approach, with clearer appreciation of what the challenges are and ways to deal with them. With success will come a new set of challenges arising from cell design, engineering, and scale-up issues associated with full utilization in a modern energy economy.

Acknowledgements Funding by the UNC EFRC Center for Solar Fuels, an Energy Frontier Research Center funded by the U.S. Department of Energy, Office of Science, Office of Basic Energy Sciences, under award number DE-SC0001011, is gratefully acknowledged.

References

1. Fujishima A, Honda K (1972) Electrochemical photolysis of water at a semiconductor electrode. Nature 238(5358):37–38. doi:10.1038/238037a0
2. Bock CR, Meyer TJ, Whitten DG (1974) Electron transfer quenching of the luminescent excited state of tris(2,2′-bipyridine)ruthenium(ii). flash photolysis relaxation technique for measuring the rates of very rapid electron transfer reactions. J Am Chem Soc 96(14):4710–4712. doi:10.1021/ja00821a078
3. Young RC, Meyer TJ, Whitten DG (1976) Electron transfer quenching of excited states of metal complexes. J Am Chem Soc 98(1):286–287. doi:10.1021/ja00417a073
4. Materna KL, Brennan BJ, Brudvig GW (2015) Silatranes for binding inorganic complexes to metal oxide surfaces. Dalton Trans 44(47):20312–20315. doi:10.1039/C5DT03463A

5. Renger G, Renger T (2008) Photosystem II: the machinery of photosynthetic water splitting. Photosynth Res 98(1):53–80. doi:10.1007/s11120-008-9345-7
6. Grätzel M (2001) Photoelectrochemical cells. Nature 414(6861):338–344. doi:10.1038/35104607
7. Swierk JR, Mallouk TE (2013) Design and development of photoanodes for water-splitting dye-sensitized photoelectrochemical cells. Chem Soc Rev 42(6):2357–2387. doi:10.1039/c2cs35246j
8. Green ANM, Palomares E, Haque SA, Kroon JM, Durrant JR (2005) Charge transport versus recombination in dye-sensitized solar cells employing nanocrystalline TiO_2 and SnO_2 films. J Phys Chem B 109(25):12525–12533. doi:10.1021/jp050145y
9. Ashford DL, Glasson CRK, Norris MR, Hanson K, Concepcion JJ, Keinan S, Brennaman MK, Templeton JL, Meyer TJ (2014) Controlling ground and excited state properties through ligand changes in ruthenium polypyridyl complexes. Inorg Chem 53 (11):5637–5646. doi:10.1021/ic500408j
10. Wrighton MS, Ginley DS, Wolczanski PT, Ellis AB, Morse DL, Linz A (1975) Photoassisted electrolysis of water by irradiation of a titanium dioxide electrode. Proc Natl Acad Sci USA 72(4):1518–1522
11. Bolts JM, Wrighton MS (1976) Correlation of photocurrent-voltage curves with flat-band potential for stable photoelectrodes for the photoelectrolysis of water. J Phys Chem 80 (24):2641–2645. doi:10.1021/j100565a004
12. Vannucci AK, Alibabaei L, Losego MD, Concepcion JJ, Kalanyan B, Parsons GN, Meyer TJ (2013) Crossing the divide between homogeneous and heterogeneous catalysis in water oxidation. Proc Natl Acad Sci USA 110(52):20918–20922. doi:10.1073/pnas.1319832110
13. Paracchino A, Laporte V, Sivula K, Grätzel M, Thimsen E (2011) Highly active oxide photocathode for photoelectrochemical water reduction. Nature Mat 10:456–461. doi:10.1038/nmat3017
14. Poodt P, Lankhorst A, Roozeboom F, Spee K, Maas D, Vermeer A (2010) A high-speed spatial atomic-layer deposition of aluminum oxide layers for solar cell passivation. Adv Mat 22:3564–3568. doi:10.1002/adma.201000766
15. Chen YW, Prange JD, Dühnen S, Park Y, Gunji M, Chidsey CED, McIntyre PC (2011) Atomic layer deposited tunnel oxide stabilizes silicon photoanodes for water oxidation. Nature Mat 10:539–544. doi:10.1038/nmat3047
16. Hu S, Shaner MR, Beardslee JA, Lichterman M, Brunschwig BS, Lewis NS (2014) Amorphous TiO_2 coatings stabilize Si, GaAs, and GaP photoanodes for efficient water oxidation. Science 344(6187):1005–1009. doi:10.1126/science.1251428
17. Lee MH, Takei K, Zhang J, Kapadia R, Zheng M, Chen Y-Z, Nah J, Matthews TS, Chueh Y-L, Ager JW, Javey A (2012) p-type InP nanopillar photocathodes for efficient solar-driven hydrogen production. Angew Chem Int Ed 51(43):10760–10764. doi:10.1002/anie.201203174
18. Song W, Brennaman MK, Concepcion JJ, Jurss JW, Hoertz PG, Luo H, Chen C, Hanson K, Meyer TJ (2011) Interfacial electron transfer dynamics for $[Ru(bpy)_2((4,4'\text{-}PO_3H_2)_2bpy)]^{2+}$ sensitized TiO_2 in a dye-sensitized photoelectrosynthesis cell: factors influencing efficiency and dynamics. J Phys Chem C 115(14):7081–7091. doi:10.1021/jp200124k
19. Song W, Chen Z, Brennaman MK, Concepcion J, Meyer TJ (2011) Making solar fuels by artificial photosynthesis. Pure Appl Chem 83(4):749–768. doi:10.1351/pac-con-10-11-09
20. Luo HL, Song WJ, Hoertz PG, Hanson K, Ghosh R, Rangan S, Brennaman MK, Concepcion JJ, Binstead RA, Bartynski RA, Lopez R, Meyer TJ (2013) A sensitized Nb_2O_5 photoanode for hydrogen production in a dye-sensitized photoelectrosynthesis cell. Chem Mater 25(2):122–131. doi:10.1021/Cm3027972
21. Brennaman MK, Patrocinio AOT, Song WJ, Jurss JW, Concepcion JJ, Hoertz PG, Traub MC, Iha NYM, Meyer TJ (2011) interfacial electron transfer dynamics following laser flash photolysis of $[Ru(bpy)_2((4,4\text{ '-}PO_3H_2)_2bpy)]^{2+}$ in TiO_2 nanoparticle films in aqueous environments. Chemsuschem 4(2):216–227. doi:10.1002/cssc.201000356

22. Hanson K, Losego MD, Kalanyan B, Parsons GN, Meyer TJ (2013) Stabilizing small molecules on metal oxide surfaces using atomic layer deposition. Nano Lett 13(10):4802–4809. doi:10.1021/nl402416s
23. Alibabaei L, Farnum BH, Kalanyan B, Brennaman K, Losego MD, Parsons GN, Meyer TJ (2014) Atomic layer deposition of TiO_2 on mesoporous *nano*ITO: conductive core-shell photoanodes for dye-sensitized solar cells. Nano Lett 14(6):3255–3261. doi:10.1021/nl5006433
24. Song W, Vannucci AK, Farnum BH, Lapides AM, Brennaman MK, Kalanyan B, Alibabaei L, Concepcion JJ, Losego MD, Parsons GN, Meyer TJ (2014) Visible light driven benzyl alcohol dehydrogenation in a dye-sensitized photoelectrosynthesis cell. J Am Chem Soc 136(27):9773–9779. doi:10.1021/ja505022f
25. Alibabaei L, Sherman BD, Norris MR, Brennaman MK, Meyer TJ (2015) Visible photoelectrochemical water splitting into H_2 and O_2 in a dye sensitized photoelectrosynthesis cell. Proc Natl Acad Sci USA 112(19):5899–5902. doi:10.1073/pnas.1506111112
26. Kim DH, Losego MD, Hanson K, Alibabaei L, Lee K, Meyer TJ, Parsons GN (2014) Stabilizing chromophore binding on TiO2 for long-term stability of dye-sensitized solar cells using multicomponent atomic layer deposition. Phys Chem Chem Phys 16:8615–8622. doi:10.1039/C4CP01130A
27. Alibabaei L, Farnum BH, Kalanyan B, Brennaman MK, Losego MD, Parsons GN, Meyer TJ (2014) atomic layer deposition of TiO_2 on mesoporous nanoITO: conductive core-shell photoanodes for dye-sensitized solar cells. Nano Lett 14(6):3255–3261. doi:10.1021/nl5006433
28. Hanson K, Losego MD, Kalanyan B, Ashford DL, Parsons GN, Meyer TJ (2013) Stabilization of $[Ru(bpy)_2(4,4'\text{-}(PO_3H_2)bpy)]^{2+}$ on mesoporous TiO_2 with atomic layer deposition of Al_2O_3. Chem Mater 25(1):3–5. doi:10.1021/cm303172w
29. Wee K-R, Sherman BD, Brennaman MK, Sheridan MV, Nayak A, Alibabaei L, Meyer TJ (2016) An aqueous, organic dye derivatized SnO_2/TiO_2 core/shell photoanode. J Mater Chem A 4(8):2969–2975. doi:10.1039/C5TA06678F
30. Zigler DF, Morseth ZA, Wang L, Ashford DL, Brennaman MK, Grumstrup EM, Brigham EC, Gish MK, Dillon RJ, Alibabaei L, Meyer GJ, Meyer TJ, Papanikolas JM (2016) Disentangling the physical processes responsible for the kinetic complexity in interfacial electron transfer of excited Ru(II) polypyridyl dyes on TiO_2. J Am Chem Soc 138(13):4426–4438. doi:10.1021/jacs.5b12996
31. Call RW, Alibabaei L, Dillon RJ, Knauf RR, Nayak A, Dempsey JL, Papanikolas JM, Lopez R (2016) Growth and post-deposition treatments of $SrTiO_3$ films for dye-sensitized photoelectrosynthesis cell applications. ACS Appl Mater Inter 8(19):12282–12290. doi:10.1021/acsami.6b01289
32. Nayak A, Roy S, Sherman BD, Alibabaei L, Lapides AM, Brennaman MK, Wee K-R, Meyer TJ (2016) Phosphonate-derivatized porphyrins for photoelectrochemical applications. ACS Appl Mater Interfaces 8(6):3853–3860. doi:10.1021/acsami.5b10587
33. Nayak A, Knauf RR, Hanson K, Alibabaei L, Concepcion JJ, Ashford DL, Dempsey JL, Meyer TJ (2014) Synthesis and photophysical characterization of porphyrin and porphyrin-Ru(II) polypyridyl chromophore-catalyst assemblies on mesoporous metal oxides. Chem Sci 5(8):3115–3119. doi:10.1039/C4SC00875H
34. Sheehan SW, Thomsen JM, Hintermair U, Crabtree RH, Brudvig GW, Schmuttenmaer CA (2015) A molecular catalyst for water oxidation that binds to metal oxide surfaces. Nat Commun 6:6469. doi:10.1038/ncomms7469
35. Xiao W, Zhou C-Y, Che C-M (2012) Ruthenium(IV) porphyrin catalyzed phosphoramidation of aldehydes with phosphoryl azides as a nitrene source. Chem Commun 48(47):5871–5873. doi:10.1039/C2CC31686B
36. Zaitsev AB, Gruber S, Pregosin PS (2007) Fast, efficient Ru(IV)-catalysed regioselective allylation of indoles using allyl alcohol (without additives) under mild conditions. Chem Commun 44:4692–4693. doi:10.1039/B710763C

37. Paul A, Hull JF, Norris MR, Chen Z, Ess DH, Concepcion JJ, Meyer TJ (2011) Multiple pathways for benzyl alcohol oxidation by $Ru^{V} = O^{3+}$ and $Ru^{IV} = O^{2+}$. Inorg Chem 50 (4):1167–1169. doi:10.1021/ic1024923
38. Brownell KR, McCrory CCL, Chidsey CED, Perry RH, Zare RN, Waymouth RM (2013) Electrooxidation of alcohols catalyzed by amino alcohol ligated ruthenium complexes. J Am Chem Soc 135(38):14299–14305. doi:10.1021/ja4055564
39. Bryant JR, Matsuo T, Mayer JM (2004) Cumene oxidation by *cis*-$[Ru^{IV}(bpy)_2(py)(O)]^{2+}$. Inorg Chem 43(4):1587–1592. doi:10.1021/ic035298j
40. Seok WK, Meyer TJ (2005) Mechanism of oxidation of benzaldehyde by polypyridyl oxo complexes of Ru(IV). Inorg Chem 44(11):3931–3941. doi:10.1021/ic040119z
41. Shiota Y, Herrera JM, Juhász G, Abe T, Ohzu S, Ishizuka T, Kojima T, Yoshizawa K (2011) Theoretical study of oxidation of cyclohexane diol to adipic anhydride by $[Ru^{IV}(O)(tpa)(H_2O)]^{2+}$ complex (tpa = Tris(2-pyridylmethyl)amine). Inorg Chem 50(13):6200–6209. doi:10.1021/ic200481n
42. Blakemore JD, Crabtree RH, Brudvig GW (2015) molecular catalysts for water oxidation. Chem Rev 115(23):12974–13005. doi:10.1021/acs.chemrev.5b00122
43. Tamaki Y, Vannucci AK, Dares CJ, Binstead RA, Meyer TJ (2014) One-electron activation of water oxidation catalysis. J Am Chem Soc 136(19):6854–6857. doi:10.1021/ja502637s
44. Song N, Concepcion JJ, Binstead RA, Rudd JA, Vannucci AK, Dares CJ, Coggins MK, Meyer TJ (2015) Base-enhanced catalytic water oxidation by a carboxylate-bipyridine Ru(II) complex. Proc Natl Acad Sci USA 112(16):4935–4940. doi:10.1073/pnas.1500245112
45. Kimoto A, Yamauchi K, Yoshida M, Masaoka S, Sakai K (2012) Kinetics and DFT studies on water oxidation by Ce^{4+} catalyzed by $[Ru(terpy)(bpy)(OH_2)]^{2+}$. Chem Commun 48 (2):239–241. doi:10.1039/C1CC15109F
46. Duan L, Araujo CM, Ahlquist MSG, Sun L (2012) Highly efficient and robust molecular ruthenium catalysts for water oxidation. Proc Natl Acad Sci USA 109(39):15584–15588. doi:10.1073/pnas.1118347109
47. Duan L, Bozoglian F, Mandal S, Stewart B, Privalov T, Llobet A, Sun L (2012) A molecular ruthenium catalyst with water-oxidation activity comparable to that of photosystem II. Nat Chem 4(5):418–423. doi:10.1038/nchem.1301
48. Duan L, Wang L, Inge AK, Fischer A, Zou X, Sun L (2013) Insights into Ru-based molecular water oxidation catalysts: electronic and noncovalent-interaction effects on their catalytic activities. Inorg Chem 52(14):7844–7852. doi:10.1021/ic302687d
49. Treadway JA, Moss JA, Meyer TJ (1999) Visible region photooxidation on TiO_2 with a chromophore-catalyst molecular assembly. Inorg Chem 38(20):4386–4387. doi:10.1021/ic990466m
50. Song W, Chen Z, Brennaman MK, Concepcion JJ, Patrocinio AOT, Iha NYM, Meyer TJ (2011) Making solar fuels by artificial photosynthesis. Pure Appl Chem 83(4):749–768. doi:10.1351/pac-con-10-11-09
51. Chen Z, Concepcion JJ, Jurss JW, Meyer TJ (2009) Single-site, catalytic water oxidation on oxide surfaces. J Am Chem Soc 131(43):15580–15581. doi:10.1021/ja906391w
52. Chen Z, Concepcion JJ, Hull JF, Hoertz PG, Meyer TJ (2010) Catalytic water oxidation on derivatized *nano*ITO. Dalton Trans 39(30):6950–6952. doi:10.1039/c0dt00362j
53. Wee K-R, Brennaman MK, Alibabaei L, Farnum BH, Sherman B, Lapides AM, Meyer TJ (2014) Stabilization of ruthenium(II) polypyridyl chromophores on nanoparticle metal-oxide electrodes in water by hydrophobic PMMA overlayers. J Am Chem Soc 136:13514–13517. doi:10.1021/ja506987a
54. Ardo S, Sun Y, Castellano FN, Meyer GJ (2010) Excited-state electron transfer from ruthenium-polypyridyl compounds to anatase TiO_2 nanocrystallites: evidence for a stark effect. J Phys Chem B 114(45):14596–14604. doi:10.1021/jp102349m
55. Brimblecombe R, Koo A, Dismukes GC, Swiegers GF, Spiccia L (2010) Solar driven water oxidation by a bioinspired manganese molecular catalyst. J Am Chem Soc 132(9):2892–2894. doi:10.1021/ja910055a

56. Hanson K, Losego MD, Kalanyan B, Ashford DL, Parsons GN, Meyer TJ (2013) Stabilization of $[Ru(bpy)_2(4,4'\text{-}(PO_3H_2)bpy)]^{2+}$ on mesoporous TiO_2 with atomic layer deposition of Al_2O_3. Chem Mater 25(1):3–5. doi:10.1021/cm303172w
57. Ashford DL, Sherman BD, Binstead RA, Templeton JL, Meyer TJ (2015) Electro-assembly of a chromophore-catalyst bilayer for water oxidation and photocatalytic water splitting. Angew Chem Int Ed 54(16):4778–4781. doi:10.1002/anie.201410944
58. Song W, Ito A, Binstead RA, Hanson K, Luo H, Brennaman MK, Concepcion JJ, Meyer TJ (2013) Accumulation of multiple oxidative equivalents at a single site by cross-surface electron transfer on TiO_2. J Am Chem Soc 135(31):11587–11594. doi:10.1021/ja4032538
59. Glasson CRK, Song W, Ashford DL, Vannucci A, Chen Z, Concepcion JJ, Holland PL, Meyer TJ (2012) Self-assembled bilayers on indium-tin oxide (SAB-ITO) electrodes: a design for chromophore-catalyst photoanodes. Inorg Chem 51(16):8637–8639. doi:10.1021/ic300636w
60. Brennaman MK, Dillon RJ, Alibabaei L, Gish MK, Dares CJ, Ashford DL, House RL, Meyer GJ, Papanikolas JM, Meyer TJ (2016) Finding the way to solar fuels with dye-sensitized photoelectrosynthesis cells. J Am Chem Soc 138(40):13085–13102. doi:10.1021/jacs.6b06466
61. Lapides AM, Sherman BD, Brennaman MK, Dares CJ, Skinner KR, Templeton JL, Meyer TJ (2015) Synthesis, characterization, and water oxidation by a molecular chromophore-catalyst assembly prepared by atomic layer deposition. The "mummy" strategy. Chem Sci 6(11):6398–6406. doi:10.1039/C5SC01752A
62. Hanson K, Torelli DA, Vannucci AK, Brennaman MK, Luo H, Alibabaei L, Song W, Ashford DL, Norris MR, Glasson CR, Concepcion JJ, Meyer TJ (2012) Self-assembled bilayer films of ruthenium(II)/polypyridyl complexes through layer-by-layer deposition on nanostructured metal oxides. Angew Chem Int Ed 51(51):12782–12785. doi:10.1002/anie.201206882
63. Nayak A, Knauf RR, Hanson K, Alibabaei L, Concepcion JJ, Ashford D, Dempsey JL, Meyer TJ (2014) Synthesis and photophysical characterization of porphyrin and porphyrin–Ru(II) polypyridyl chromophore-catalyst assemblies on mesoporous metal oxides. Chem Sci 5:3115–3119. doi:10.1039/C4SC00875H
64. Bettis SE, Hanson K, Wang L, Gish MK, Concepcion JJ, Fang Z, Meyer TJ, Papanikolas JM (2014) Photophysical characterization of a chromophore/water oxidation catalyst containing a layer-by-layer assembly on nanocrystalline TiO_2 using ultrafast spectroscopy. J Phys Chem A 118(45):10301–10308. doi:10.1021/jp411139j
65. Leem G, Sherman BD, Burnett AJ, Morseth ZA, Wee K-R, Alibabaei L, Papanikolas JM, Meyer TJ, Schanze KS (2016) Light-driven water oxidation using polyelectrolyte layer-by-layer chromophore–catalyst assemblies. ACS Energy Lett 1(6):1118–1118. doi:10.1021/acsenergylett.6b00553
66. Lapides AM, Ashford DL, Hanson K, Torelli DA, Templeton JL, Meyer TJ (2013) Stabilization of a ruthenium(II) polypyridyl dye on nanocrystalline TiO_2 by an electropolymerized overlayer. J Am Chem Soc 135(41):15450–15458. doi:10.1021/ja4055977
67. Ashford DL, Lapides AM, Vannucci AK, Hanson K, Torelli DA, Harrison DP, Templeton JL, Meyer TJ (2014) Water oxidation by an electropolymerized catalyst on derivatized mesoporous metal oxide electrodes. J Am Chem Soc 136(18):6578–6581. doi:10.1021/ja502464s
68. Gao Y, Ding X, Liu J, Wang L, Lu Z, Li L, Sun L (2013) Visible light driven water splitting in a molecular device with unprecedentedly high photocurrent density. J Am Chem Soc 135(11):4219–4222. doi:10.1021/ja400402d
69. Zhao Y, Swierk JR, Megiatto JD, Jr., Sherman B, Youngblood WJ, Qin D, Lentz DM, Moore AL, Moore TA, Gust D, Mallouk TE (2012) Improving the efficiency of water splitting in dye-sensitized solar cells by using a biomimetic electron transfer Mediator. Proc Natl Acad Sci USA 109(39):15612–15616, S15612/15611-S15612/15618. doi:10.1073/pnas.1118339109

70. Hanson K, Torelli DA, Vannucci AK, Brennaman MK, Luo H, Alibabaei L, Song W, Ashford DL, Norris MR, Glasson CRK, Concepcion JJ, Meyer TJ (2012) Self-assembled bilayer films of ruthenium(ii)/polypyridyl complexes through layer-by-layer deposition on nanostructured metal oxides. Angew Chem Int Ed 51:12782–12785. doi:10.1002/anie.201206882
71. Lee H, Kepley LJ, Hong HG, Akhter S, Mallouk TE (1988) Adsorption of ordered zirconium phosphonate multilayer films on silicon and gold surfaces. J Phys Chem 92 (9):2597–2601. doi:10.1021/j100320a040
72. Lee H, Kepley LJ, Hong HG, Mallouk TE (1988) Inorganic analogs of langmuir-blodgett films: adsorption of ordered zirconium 1, 10-decanebisphosphonate multilayers on silicon surfaces. J Am Chem Soc 110(2):618–620. doi:10.1021/ja00210a062
73. Ishida T, K-i Terada, Hasegawa K, Kuwahata H, Kusama K, Sato R, Nakano M, Naitoh Y, M-a Haga (2009) Self-assembled monolayer and multilayer formation using redox-active Ru complex with phosphonic acids on silicon oxide surface. Appl Surf Sci 255(21):8824–8830. doi:10.1016/j.apsusc.2009.06.064
74. Abruña HD, Denisevich P, Umana M, Meyer TJ, Murray RW (1981) Rectifying interfaces using 2-layer films of electrochemically polymerized vinylpyridine and vinylbipyridine complexes of ruthenium and iron on electrodes. J Am Chem Soc 103(1):1–5
75. Abruña HD (1988) Coordination chemistry in two dimensions: chemically modified electrodes. Coord Chem Rev 86:135–189. doi:10.1016/0010-8545(88)85013-6
76. Li L, Duan L, Xu Y, Gorlov M, Hagfeldt A, Sun L (2010) A photoelectrochemical device for visible light driven water splitting by a molecular ruthenium catalyst assembled on dye-sensitized nanostructured TiO_2. Chem Commun 46(39):7307–7309. doi:10.1039/c0cc01828g
77. Puodziukynaite E, Wang L, Schanze KS, Papanikolas JM, Reynolds JR (2014) Poly (fluorene-co-thiophene)-based ionic transition-metal complex polymers for solar energy harvesting and storage applications. Polym Chem 5(7):2363–2369. doi:10.1039/C3PY01582C
78. Wang L, Puodziukynaite E, Vary RP, Grumstrup EM, Walczak RM, Zolotarskaya OY, Schanze KS, Reynolds JR, Papanikolas JM (2012) Competition between ultrafast energy flow and electron transfer in a Ru(II)-loaded polyfluorene light-harvesting polymer. J Phys Chem Lett 3(17):2453–2457. doi:10.1021/jz300979j
79. Ma D, Bettis SE, Hanson K, Minakova M, Alibabaei L, Fondrie W, Ryan DM, Papoian GA, Meyer TJ, Waters ML, Papanikolas JM (2013) Interfacial energy conversion in RuII polypyridyl-derivatized oligoproline assemblies on TiO_2. J Am Chem Soc 135(14):5250–5253. doi:10.1021/ja312143h
80. Wilger DJ, Bettis SE, Materese CK, Minakova M, Papoian GA, Papanikolas JM, Waters ML (2012) Tunable energy transfer rates via control of primary, secondary, and tertiary structure of a coiled coil peptide scaffold. Inorg Chem 51(21):11324–11338. doi:10.1021/ic300669t
81. Concepcion JJ, Jurss JW, Hoertz PG, Meyer TJ (2009) Catalytic and surface-electrocatalytic water oxidation by redox mediator-catalyst assemblies. Angew Chem Int Ed 48(50):9473–9476. doi:10.1002/anie.200901279
82. Ashford DL, Stewart DJ, Glasson CR, Binstead RA, Harrison DP, Norris MR, Concepcion JJ, Fang Z, Templeton JL, Meyer TJ (2012) An amide-linked chromophore-catalyst assembly for water oxidation. Inorg Chem 51(12):6428–6430. doi:10.1021/ic300061u
83. Ashford DL, Song W, Concepcion JJ, Glasson CRK, Brennaman MK, Norris MR, Fang Z, Templeton JL, Meyer TJ (2012) Photoinduced electron transfer in a chromophore-catalyst assembly anchored to TiO2. J Am Chem Soc 134(46):19189–19198. doi:10.1021/ja3084362
84. Norris MR, Concepcion JJ, Harrison DP, Binstead RA, Ashford DL, Fang Z, Templeton JL, Meyer TJ (2013) Redox mediator effect on water oxidation in a ruthenium-based chromophore-catalyst assembly. J Am Chem Soc 135(6):2080–2083. doi:10.1021/ja311645d

85. Wang L, Ashford DL, Thompson DW, Meyer TJ, Papanikolas JM (2013) Watching photoactivation in a Ru(II) chromophore-catalyst assembly on TiO2 by ultrafast spectroscopy. J Phys Chem C 117(46):24250–24258. doi:10.1021/jp410571x
86. Norris MR, Concepcion JJ, Fang Z, Templeton JL, Meyer TJ (2013) Low-overpotential water oxidation by a surface-bound ruthenium-chromophore–ruthenium-catalyst assembly. Angew Chem Int Ed 52(51):13580–13583. doi:10.1002/anie.201305951
87. Song WJ, Brennaman MK, Concepcion JJ, Jurss JW, Hoertz PC, Luo HL, Chen CC, Hanson K, Meyer TJ (2011) Interfacial electron transfer dynamics for $[Ru(bpy)_2((4,4'\text{-}PO_3H_2)_2bpy)]^{2+}$ sensitized TiO_2 in a dye-sensitized photoelectrosynthesis cell: factors influencing efficiency and dynamics. J Phys Chem C 115(14):7081–7091. doi:10.1021/jp200124k
88. Merrifield B (1986) Solid-phase synthesis. Science 232(4748):341–347. doi:10.1126/science.3961484
89. Bettis SE, Ryan DM, Gish MK, Alibabaei L, Meyer TJ, Waters ML, Papanikolas JM (2014) Photophysical characterization of a helical peptide chromophore-water oxidation catalyst assembly on a semiconductor surface using ultrafast spectroscopy. J Phys Chem C 118 (12):6029–6037. doi:10.1021/jp410646u
90. Ryan DM, Coggins MK, Concepcion JJ, Ashford DL, Fang Z, Alibabaei L, Ma D, Meyer TJ, Waters ML (2014) Synthesis and electrocatalytic water oxidation by electrode-bound helical peptide chromophore-catalyst assemblies. Inorg Chem 53 (15):8120–8128. doi:10.1021/ic5011488
91. Zhang P, Wang M, Li X, Cui H, Dong J, Sun L (2012) Photochemical hydrogen production with molecular devices comprising a zinc porphyrin and a cobaloxime catalyst. Sci China Chem 55(7):1274–1282. doi:10.1007/s11426-012-4514-0
92. McCormick TM, Han Z, Weinberg DJ, Brennessel WW, Holland PL, Eisenberg R (2011) Impact of ligand exchange in hydrogen production from cobaloxime-containing photocatalytic systems. Inorg Chem 50(21):10660–10666. doi:10.1021/ic2010166
93. Vagnini MT, Smeigh AL, Blakemore JD, Eaton SW, Schley ND, D'Souza F, Crabtree RH, Brudvig GW, Co DT, Wasielewski MR (2012) Ultrafast photodriven intramolecular electron transfer from an iridium-based water-oxidation catalyst to perylene diimide derivatives. Proc Natl Acad Sci USA 109(39):15651–15656. doi:10.1073/pnas.1202075109
94. Bachmeier A, Hall S, Ragsdale SW, Armstrong FA (2014) Selective visible-light-driven CO_2 reduction on a p-type dye-sensitized NiO photocathode. J Am Chem Soc 136 (39):13518–13521. doi:10.1021/ja506998b
95. Queyriaux N, Kaeffer N, Morozan A, Chavarot-Kerlidou M, Artero V (2015) Molecular cathode and photocathode materials for hydrogen evolution in photoelectrochemical devices. J Photochem Photobio C: Photochem Rev 25:90–105. doi:10.1016/j.jphotochemrev.2015.08.001
96. Yu Z, Li F, Sun L (2015) Recent advances in dye-sensitized photoelectrochemical cells for solar hydrogen production based on molecular components. Energy Environ Sci 8(3):760–775. doi:10.1039/C4EE03565H
97. Click KA, Beauchamp DR, Huang Z, Chen W, Wu Y (2016) Membrane-inspired acidically stable dye-sensitized photocathode for solar fuel production. J Am Chem Soc 138(4):1174–1179. doi:10.1021/jacs.5b07723
98. Gross MA, Creissen CE, Orchard KL, Reisner E (2016) Photoelectrochemical hydrogen production in water using a layer-by-layer assembly of a Ru dye and Ni catalyst on NiO. Chem Sci 7(8):5537–5546. doi:10.1039/C6SC00715E
99. van den Bosch B, Rombouts JA, Orru RVA, Reek JNH, Detz RJ (2016) Nickel-based dye-sensitized photocathode: towards proton reduction using a molecular nickel catalyst and an organic dye. ChemCatChem 8(7):1392–1398. doi:10.1002/cctc.201600025
100. Wood CJ, Summers GH, Clark CA, Kaeffer N, Braeutigam M, Carbone LR, D'Amario L, Fan K, Farré Y, Narbey S, Oswald F, Stevens LA, Parmenter CDJ, Fay MW, La Torre A, Snape CE, Dietzek B, Dini D, Hammarström L, Pellegrin Y, Odobel F, Sun L, Artero V, Gibson EA (2016) A comprehensive comparison of dye-sensitized NiO photocathodes for

solar energy conversion. Phys Chem Chem Phys 18(16):10727–10738. doi:10.1039/C5CP05326A
101. Dini D, Halpin Y, Vos JG, Gibson EA (2015) The Influence of the preparation method of NiO_x photocathodes on the efficiency of p-type dye-sensitized solar cells. Coord Chem Rev 304–305:179–201. doi:10.1016/j.ccr.2015.03.020
102. Schreier M, Luo J, Gao P, Moehl T, Mayer MT, Grätzel M (2016) Covalent immobilization of a molecular catalyst on Cu_2O photocathodes for CO_2 reduction. J Am Chem Soc 138 (6):1938–1946. doi:10.1021/jacs.5b12157
103. Shin K, Yoo J-B, Park JH (2013) Photoelectrochemical cell/dye-sensitized solar cell tandem water splitting systems with transparent and vertically aligned quantum dot sensitized TiO_2 nanorod arrays. J Power Sources 225:263–268. doi:10.1016/j.jpowsour.2012.10.036
104. Kim JK, Shin K, Cho SM, Lee T-W, Park JH (2011) Synthesis of transparent mesoporous tungsten trioxide films with enhanced photoelectrochemical response: application to unassisted solar water splitting. Energy Environ Sci 4(4):1465–1470. doi:10.1039/C0EE00469C
105. Shi X, Zhang K, Shin K, Ma M, Kwon J, Choi IT, Kim JK, Kim HK, Wang DH, Park JH (2015) Unassisted photoelectrochemical water splitting beyond 5.7% solar-to-hydrogen conversion efficiency by a wireless monolithic photoanode/dye-sensitised solar cell tandem device. Nano Energy 13:182–191. doi:10.1016/j.nanoen.2015.02.018
106. Prévot MS, Sivula K (2013) Photoelectrochemical tandem cells for solar water splitting. J Phys Chem C 117(35):17879–17893. doi:10.1021/jp405291g
107. Sheridan MV, Hill DJ, Sherman BD, Wang D, Marquard SL, Wee K-R, Cahoon JF, Meyer TJ (2017) All-in-one derivatized tandem p + n-silicon-SnO_2/TiO_2 water splitting photoelectrochemical cell. Nano Lett. doi:10.1021/acs.nanolett.7b00105
108. Ashford DL, Gish MK, Vannucci AK, Brennaman MK, Templeton JL, Papanikolas JM, Meyer TJ (2015) Molecular chromophore-catalyst assemblies for solar fuel applications. Chem Rev 115(23):13006–13049. doi:10.1021/acs.chemrev.5b00229

Chapter 7
Light-Driven Carbon Dioxide Reduction Devices

Takeshi Morikawa, Shunsuke Sato and Takeo Arai

Abstract To address issues related to global warming and a fossil fuel shortage, CO_2 fixation by reduction reaction using water and sunlight energy similar to photosynthesis in plants—is an ideal approach. Mimicking the artificial photosynthetic process in a simplified system is one of the key technologies to construct a carbon-neutral society that will meet the growing global environmental and energy requirements. Therefore, the number of research reports in this field has been increasing in the 2010s, and breakthroughs for a system that utilizes water as an electron donor and proton source have been achieved in recent years. In this chapter, we explain the methodology for the light-driven CO_2 reduction reaction, which stores solar energy in the chemical bonds of organic compounds. The functional combination of molecular catalysts with semiconductors in a system that is unassisted and non-biased, neither electrically nor chemically, provides solar-to-chemical energy conversion that exceeds 4% and realizes CO_2 fixation with a higher efficiency than that of real plants.

Keywords Carbon dioxide · Water · Photocatalysis · Semiconductor · Molecule · Metal complex · Solar energy · Hybrid system · Formic acid

7.1 Introduction

Artificial photosynthesis, which recycles CO_2 by reduction to useful organic chemicals at normal pressure and temperature using water as both an electron donor and a proton source, is considered to be a promising approach to lower total CO_2 emissions and generate renewable energy on an industrial scale. The species produced from CO_2 reduction can be used as a valuable feedstock for other chemical processes. Considering future energy sources, solar hydrogen generation by water splitting is one of the most important approaches. One of the main concerns

T. Morikawa (✉) · S. Sato · T. Arai
Toyota Central Research and Development Labs., Inc., Nagakute, Aichi, Japan
e-mail: morikawa@mosk.tytlabs.co.jp

H. Tian et al. (eds.), *Molecular Devices for Solar Energy Conversion and Storage*, Green Chemistry and Sustainable Technology,
https://doi.org/10.1007/978-981-10-5924-7_7

presently associated with hydrogen is that it is difficult to store. Therefore, solar fuel generation from CO_2 and H_2O—as with photosynthesis in plants—is a very attractive approach. However, it is considerably more difficult to photoreduce CO_2 than to photoreduce water to generate hydrogen.

A list of potentials for CO_2 reduction to various products is provided in Table 7.1. Single-electron reduction of CO_2 to a CO_2 radical anion ($CO_2^{\bullet -}$) is unfavorable because it requires a highly negative potential of –1.9 V versus NHE (normal hydrogen electrode) due to the large reorganization energy from the linear CO_2 molecule to the bent CO_2 radical anion [1]. Therefore, it is difficult to reduce CO_2 molecules using only electrical energy. A more favorable pathway is the reduction of CO_2 molecules through a proton-assisted multiple-electron reaction, as shown in Table 7.1.

Electrocatalytic approaches to facilitate the proton-coupled multi-electron reactions of CO_2 that occur at lower potentials than that for the single-electron reaction is a feasible strategy. The potentials for the reduction of CO_2 to various organic substances decrease with an increase in the numbers of electrons and protons involved in the reactions. However, many electrocatalysts necessitate higher electrical energy (overpotential) than the theoretical values shown in Table 7.1; therefore, the development of electrocatalysts that can reduce CO_2 at lower overpotentials is required. In contrast, a photocatalytic approach is attractive because more simplified systems than electrocatalytic systems can be constructed. However, the photocatalytic approach for the CO_2 reduction reaction is much more difficult because it is dependent on the transient photoexcitation processes of the catalysts. Transition metals and transition-metal compounds are at the forefront of catalyst research. Metal-complex catalysts are also feasible because their reduction potentials can be controlled through ligand modification to match the potential required for CO_2 reduction and provide selectivity toward specific target products from CO_2 molecules. Recently, the technology cross-over of homogeneous and heterogeneous systems has significantly expanded the possibility of an artificial photosynthetic system. In this chapter, an approach towards CO_2 fixation by photoinduced CO_2 reduction using H_2O as an electron donor and proton source—similar to the artificial photosynthesis of natural plants—is explained.

Table 7.1 CO_2 reduction potentials (reported at pH 7)

	E^0/V versus *NHE*
$CO_2 + e^- \rightarrow CO_2 \cdot^-$	>−1.9
$CO_2 + 2H^+ + 2e^- \rightarrow HCOOH$	−0.61
$CO_2 + 2H^+ + 2e^- \rightarrow CO + H_2O$	−0.53
$CO_2 + 4H^+ + 4e^- \rightarrow HCHO + H_2O$	−0.48
$CO_2 + 6H^+ + 6e^- \rightarrow CH_3OH + H_2O$	−0.38
$CO_2 + 8H^+ + 8e^- \rightarrow CH_4 + 2H_2O$	−0.24

7.2 Molecular Photocatalysts for CO_2 Reduction

Hawecker et al. first reported photochemical CO_2 reduction using metal-complex catalysts in 1983. Under light irradiation, $[Re(L)(CO)_3X]$, where X is Cl^- or Br^- and L is 4,4′-R_2-2,2′-bipyridine (R is H or CH_3) or 1,10-phenanthroline is promoted to a metal-to-ligand-charge-transfer (MLCT) excited state, in which the metal center Re(I) is excited to an Re(II) state while an electron is located at the L ligand [2]. In the presence of sacrificial electron donors, the triplet MLCT excited state is reductively quenched to yield a one-electron-reduced species $[Re(L•)(CO)_3X]^-$, (where L• is an anion radical). It has been proposed that the solvent (S) replaces the halide ligand to yield the catalytically active state, $[Re(L•)(CO)_3S]$ [3]. Reactions of $[Re(L•)(CO)_3S]$ with a proton are believed to result in the formation of a rhenium–hydride bond. The CO_2 reduction products are formate or carbon monoxide, which is dependent on the complex structure and solvent. The mechanism for the production of formate is reasonably understood, and formate production is considered to occur by CO_2 insertion into the Re–hydride bond. In contrast, $[Re(L)(CO)_3X]$ photocatalysts exhibit selective CO_2 reduction capacity for CO production. The dissociation of an X^- ligand from the one-electron-reduced species $[Re(L•)(CO)_3X]^-$ was recently reported [4] to be a key step in the photocatalytic CO_2 reduction. The resulting 17-electron species, for which the proposed structure is $[Re(L•)(CO)_3]^-$, reacts with CO_2 to give the CO_2 adduct(s). A further key role of another species of $[Re(L•)(CO)_3X]^-$ is expected to be electron donation to the CO_2 adduct, which gives rise to CO, $[Re(L)(CO)_3]^+$ and $[Re(L)(CO)_3X]$. However, the details of the reaction mechanism have not yet been clarified, because intermediate species such as CO_2 adduct complexes have not been detected. Therefore, mechanistic studies on CO formation are still in progress [5].

The advantages of the $[Re(L)(CO)_3X]$ complex photocatalysts are high selectivity for CO_2 reduction and high quantum efficiency. $[Re(bpy)(CO)_3(P(OEt)_3)]^+$ (bpy: bipyridine) as a mononuclear complex catalyst exhibited the highest quantum efficiency of 0.38 under irradiation at 365 nm in triethanolamine (TEOA)-dimethylformamide (DMF) solution [6].

However, the turnover numbers (TNs) over the Re-complex photocatalysts are generally low due to degradation of the complex. The photoresponse of $[Re(L)(CO)_3X]$ is limited to the UV range and only light at wavelengths shorter than 400 nm is absorbed. The Re system catalyzes the CO_2 reduction reaction in organic solvents containing sacrificial electron donors. Here the TN is defined as the amount of targeted reaction product formed divided by the number of catalytic sites. Metallomacrocyclic compounds and metalloporphyrins are known to be active for electrocatalytic CO_2 reduction. However, the quantum yields under illuminated conditions are very low due to the short lifetimes of the photoexcited states, which are of picosecond order. For example, a very low quantum yield of 6×10^{-4} for CO formation was reported over illuminated $Ni(cyclam)^{2+}$ [6].

Sato and coworkers developed a mononuclear Ir(III) complex photocatalyst, $([Ir(tpy)(R\text{-}ppy)Cl]^+$ (tpy: terpyridine, ppy: 2-phenyl pyridine), which exhibited

efficient and selective CO_2 conversion to CO, driven by visible light at a wavelength of 480 nm in a homogeneous solution, and even in solution containing H_2O [7]. The most efficient photocatalyst, $[Ir(tpy)(Me\text{-}ppy)Cl]^+$, in which electron-donating methyl groups were introduced to the ppy ligands, had a TN of 50 and a quantum yield for CO generation of 0.21 at a wavelength of 480 nm, which is the best reported for homogeneous mononuclear photocatalytic systems under low-energy visible light. As shown in Fig. 7.1, $[Ir(tpy)(ppy)H]^+$ was speculated to be a key intermediate in the photochemical reduction of CO_2 to CO. Notably different ground- and excited-state interactions with CO_2 were identified between two geometric isomers of $[Ir(tpy)(ppy)H]^+$. Only one isomer, C-trans-$[Ir(tpy)(ppy)H]^+$, reacts with CO_2 to generate the formato complex in the ground state at room temperature. Under photocatalytic conditions in CH_3CN/TEOA, this hydride acts as a photoacid to produce a penta-coordinate Ir(I) complex, $[Ir(tpy)(ppy)]^0$, which is involved in the photocatalytic reduction of CO_2 to CO with the same catalytic efficiency, irrespective of the starting isomer or monodentate ligand such as hydride or Cl. In contrast, the other hydride isomer, N-trans-$[Ir(tpy)(ppy)H]^+$, does not react with CO_2 at room temperature or even at higher temperatures to generate the formato complex [8]. However, because the active $[Ir(tpy)(ppy)]^0$ catalyst is produced from the one-electron reduced species of N-trans-$[Ir(tpy)(ppy)H]^+$, it can act as a selective CO_2 reduction photocatalyst.

The total number of mononuclear complex photocatalysts is limited, which has led to the development of systems comprised of a photosensitizer and molecular

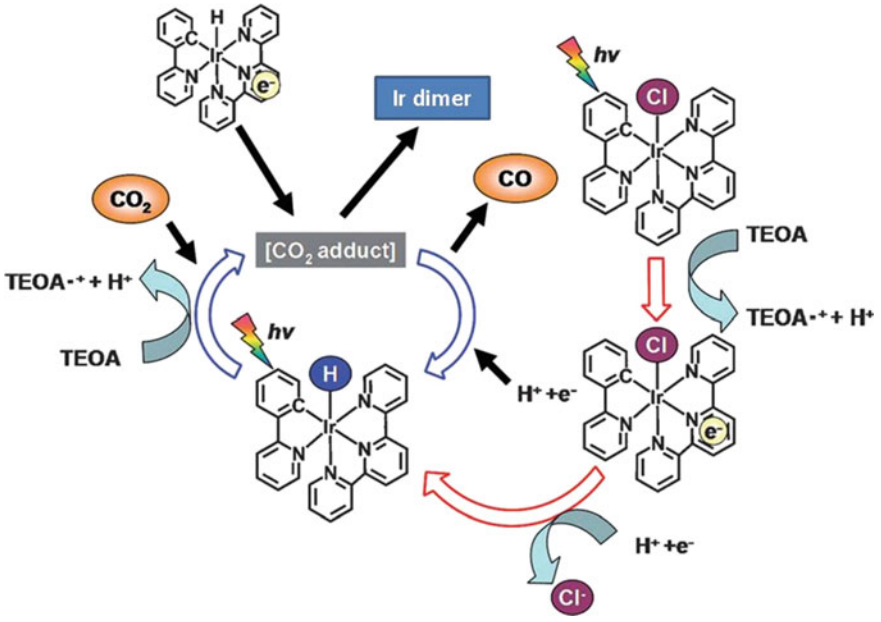

Fig. 7.1 Proposed mechanism for photocatalytic CO_2 reduction with [Ir(tpy)(ppy)Cl]+ in acetonitrile/TEOA mixed solution

catalyst. A molecular light absorber such as ruthenium(II) trisbipyridine, $[Ru(bpy)_3]^{2+}$ in a photoexcited state can be reductively quenched by a sacrificial electron donor, typically triethylamine (TEA) or TEOA, to yield a reduced sensitizer. An electron is transferred from the reduced sensitizer to the molecular catalyst, which generates the reduced active state of the catalyst followed by CO_2 reduction. Tinnemans et al. first investigated $[Ru(bpy)_3]^{2+}$-sensitized CO_2 reduction over transition-metal tetraazamacrocyclic compounds, $[M^{II}L]$ [9]. The CO_2 reduction products were identified as carbon monoxide and formate.

An approach where a supramolecular structure is constructed by attachment of a photosensitizer to a metal complex capable of CO_2 reduction is an effective method that increases the stability and the TN. The linkage of photochemically inactive Ni-cyclam catalysts and Re-complex photocatalysts with a photosensitizer has been demonstrated to sensitize them to the visible light region. Kimura et al. synthesized the [Ru(bpy)2(bpy-6′-cyclam)Ni]$^{4+}$ supramolecular complex shown in Fig. 7.2a [10]. The photochemical stability was increased and higher TNs were achieved [9]. Ishitani and colleagues synthesized supramolecular structures based on $[Ru(bpy)_3]^{2+}$ and $[Re(4,4'\text{-}R_2\text{-}2,2'\text{-}bpy)(CO)_3(X)]^{n+}$, where R = H, CH_3, and CF_3, and X = Cl- (n = 0) or X = $P(OEt)_3$ and pyridine (n = 1) (Fig. 7.2b) [11, 12]. The Ru-polypyridyl sensitizer increased the light-harvesting efficiency over $[Re(4,4'\text{-}R_2\text{-}2,2'\text{-}bpy)(CO)_3(X)]$ alone, thereby addressing a significant drawback to the near-UV-absorbing Re-based catalysts. A supramolecular photocatalyst such as $[Ru(4,4'\text{-}CH_3\text{-}2,2'\text{-}bpy)_2bpyC3bpyRe(CO)_3P(OEt)_3]^{3+}$ exhibited a high quantum efficiency of 0.21 and a TN of 232 [11, 12]. Recently, the TN and quantum efficiency of some supramolecular photocatalysts have been significantly improved. For example, a quantum yield of 0.82 was achieved for the conversion of CO_2 to CO using $[Re(bpy)(CO)_3MeCN]^+$ with a rhenium ring oligomer as a photosensitizer [13], and a TN of over 3000 was achieved for CO production using a Ru–Re supramolecular photocatalyst [14].

Thus, molecular photocatalysts have been recently improved with respect to their photoresponsivity to visible light. Some mononuclear and supramolecular

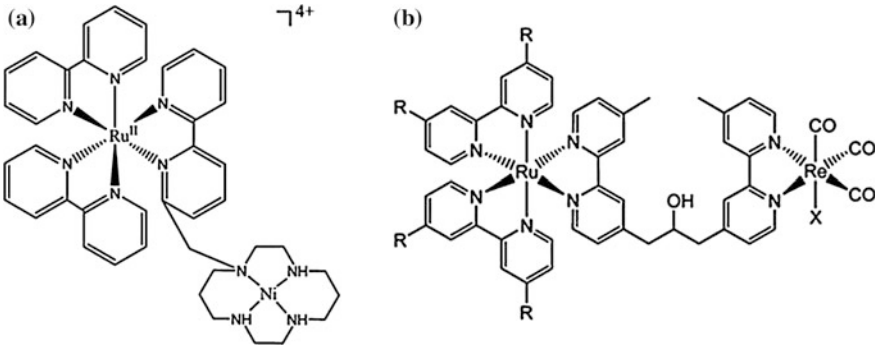

Fig. 7.2 Chemical structure of supramolecular complexes for CO_2 photoreduction: **a** [RuII(bpy)2(bpy-cyclam)NiII]$^{4+}$ and **b** $[Ru(bpy)3]^{2+}$-$[Re(4,4'\text{-}R2\text{-}2,2'\text{-}bpy)(CO)_3(X)]^{n+}$

photocatalysts are responsive to visible light. However, from a molecular approach to solar energy conversion and storage, the photocatalytic functions of these catalysts should be extended for use in aqueous solutions so that water molecules can be utilized as electron donors, because many of the reported metal-complex catalysts used for photocatalytic CO_2 reduction require an organic solvent and a sacrificial electron donor such as TEOA. The utilization of water as an electron donor and proton source is necessary for future industrialization.

7.3 Semiconductor Photocatalysts for CO_2 Reduction

Photocatalytic CO_2 reduction reactions are extremely slow on given semiconductor surfaces, which leads to a significant overpotential for CO_2 reduction. Apart from the high overpotential, these systems have advantages that include sustainability (i.e., nothing is consumed apart from light energy), direct standalone conversion of solar energy to chemical energy, utilization of renewable energy resources such as water for an energy intensive process, and stability (i.e., semiconductors are generally more stable than molecular catalysts under irradiation).

Figure 7.3 shows band-edge positions for selected semiconductors together with redox potentials for CO_2 and protons. Some of the proton-coupled multi-electron CO_2 reduction reactions are located between the conduction band minimum (E_{CBM}) and the valence band maximum (E_{VBM}) of the semiconductors. When E_{CBM} is more negative than the CO_2 reduction potential, electron transfer from the conduction band to the CO_2 molecule is thermodynamically favorable. Therefore, the photoelectrochemical reduction of CO_2 on p-type semiconductors is considered to be feasible. Figure 7.4 shows examples of possible semiconductor configurations for photoelectrochemical CO_2 reduction. In Fig. 7.4a and b, where a single semiconductor is used, a metal electrode is installed as a catalyst for the other half reaction. The configuration in Fig. 7.4a has a p-type semiconductor as a photocathode for

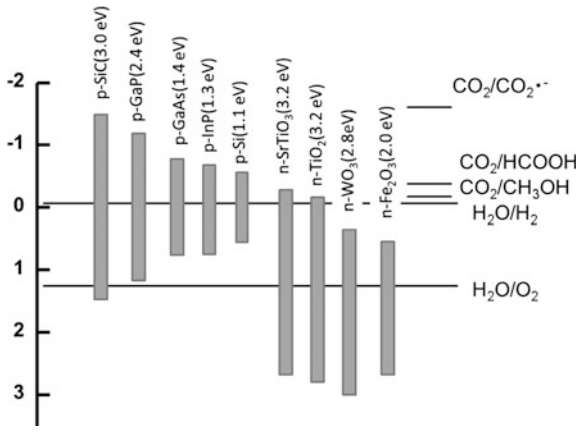

Fig. 7.3 Band-edge positions for various semiconductors at pH 1 and important redox potentials. Note that the uncertainty in the band-edge positions can amount to a few tenths of an electron volt for most semiconductors

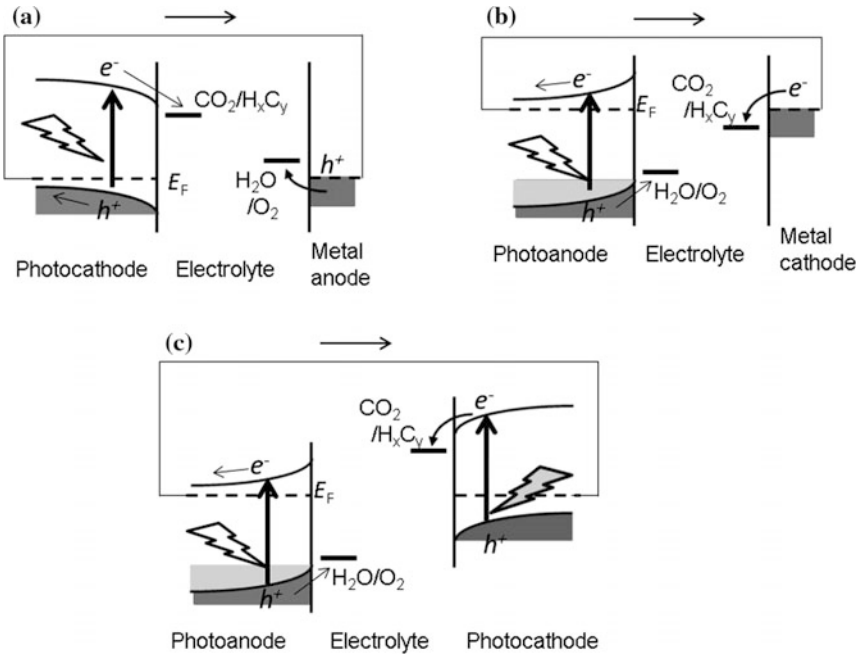

Fig. 7.4 Examples of configurations for photoelectrochemical CO_2 reduction using H_2O as an electron donor. **a** Semiconductor photocathode for CO_2 reduction and a metal catalyst for water oxidation. **b** Semiconductor photoanode for water oxidation and a metal catalyst cathode for CO_2 reduction. **c** Semiconductor photoanode for water oxidation and a photocathode for CO_2 reduction

CO_2 reduction, while a metal electrode is adopted as a water oxidation anode. The configuration in Fig. 7.4b has an n-type semiconductor as a photoanode for water oxidation, while a metal electrode is adopted as the cathode for CO_2 reduction. For the configuration shown in Fig. 7.4c, the energy of the electrons in the two semiconductors is increased in two steps, where E_{CBM} of the photocathode and E_{VBM} of the photoanode should straddle the CO_2 reduction potential and the water oxidation potential, respectively. Semiconductor p-n junctions that efficiently separate the photogenerated electrons and holes in the semiconductor are also applicable as photocathodes and photoanodes for configurations (a)–(c). In photoelectrochemical systems, an external electrical bias voltage can be applied between the two electrodes to assist the chemical reaction. An external chemical bias is also applicable by producing a pH difference between two compartments separated by ion exchange membrane in a reactor with the two electrodes immersed in each compartment. The details of semiconductor photocatalysis have been described previously in the literature [15].

There have been many reports on semiconductor electrodes for CO_2 photoreduction. As a system for the configuration shown in Fig. 7.4a, Halmann first reported the photochemical reduction of aqueous CO_2 using a semiconductor as a photocathode in 1978 [16]. Inoue et al. reported the photocatalytic reduction of CO_2

in aqueous suspensions of semiconductor powders including TiO_2, ZnO, CdS, SiC, and WO_3 under irradiation by a Xe lamp [17]. Small amounts of compounds such as formic acid, formaldehyde, and methanol were reportedly produced. Here, to reduce CO_2 molecules efficiently using photoexcited conduction band electrons, E_{CBM} must be more negative than the CO_2 reduction potentials to facilitate proton-coupled electron transfer to the CO_2 molecules. Because p-type GaP and p-type SiC electrodes possess relatively negative E_{CBM} positions, these electrodes facilitate the transfer of the conduction band electrons to CO_2 molecules for reaction at the semiconductor surface. There have been many such reports recently, for example, a $CuFeO_2$(delafossite)/CuO(monoclinic) mixed composite photocathode was reported to exhibit CO_2 conversion to formate with over 90% selectivity under simulated solar light in a CO_2-purged bicarbonate solution [18].

The concept of semiconductor photocatalysis has been applied to many semiconductors; however, the reaction rates are generally low because of the poor surface properties of the CO_2 reduction catalysts. In cases where the activity at a semiconductor surface is poor for a specific reaction, the corresponding photoelectrochemical reaction rate is very slow, irrespective of the applied potential or the light intensity. Therefore, control of the semiconductor surface chemistry appropriate for each specific reaction is crucial to achieve photoelectrochemical reactions with high efficiency. Loading of cocatalysts on the surfaces of photoelectrodes has also been conducted to enhance the catalytic activity of these systems. Metallic species such as Ag, Au, Zn, Pd, Cd, In, Sn, and Cu are potential candidate cocatalysts based on previous investigations on CO_2 reduction activity at various metal surfaces at relatively high bias voltages such as –1.0 V versus RHE (reversible hydrogen electrode) [19, 20]. Ag, Au, Zn, and Pd mainly produced CO, while Cd, In, and Sn mainly yielded formic acid. Cu is a unique catalyst that produced molecules such as CH_4 and C_2H_4 electrochemically, which is presumably due to the strong adsorption of the intermediate species in the CO_2 reduction reaction. The thickness of such cocatalysts is usually on the nanometer scale.

The semiconductor powder system is a simplified system in which both reductive and oxidative reactions are performed at the semiconductor surface (Fig. 7.5). Under irradiation from a Hg lamp, p-type $CaFe_2O_4$ powder suspended in

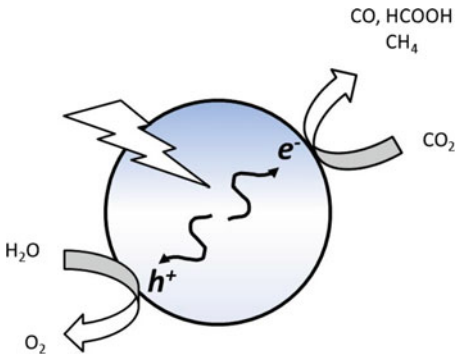

Fig. 7.5 Schematic illustration of semiconductor photocatalysis for CO_2 reduction

a CO_2-saturated NaOH solution yielded methanol and formaldehyde as the main products [21]. The loading of metal cocatalysts in powder systems can also enhance the photocatalytic activity. Cu is known to be an effective cocatalyst for enhancing the CO_2 reduction rate in aqueous solution. As examples of catalyst powders, a mixture of p-SiC and Cu particles was reported to reduce CO_2 to CH_4, C_2H_4, and C_2H_6 in pH-controlled aqueous solution, and 1% Cu-loaded ZrO_2 was reported to reduce CO_2 to CO in $NaHCO_3$ solution under UV irradiation [22, 23] Ag is used as a cocatalyst for CO_2 reduction to CO with high yield. Ag-loaded $ALa_4Ti_4O_{15}$ (A = Ca, Sr, and Ba) photocatalysts with band gaps of 3.79–3.85 eV and layered perovskite structures exhibited activity for CO_2 reduction to form CO and HCOOH by bubbling CO_2 gas into the aqueous suspension under irradiation by a high-pressure Hg lamp [24].

7.4 Photocatalysis by Combination of a Semiconductor and Molecular Catalyst

Some molecular catalysts such as $[Ru(bpy)_2(CO)]^{2+}$ have poor activity for CO_2 reduction under illuminated conditions due to the short lifetime of the photoexcited state. However, they exhibit excellent selectivity toward CO_2 molecules in electrochemical systems. Hence, transition metal complexes are potential catalysts that can have multiple and accessible redox states that promote multi-electron transfer reactivity. Furthermore, the formal reduction potentials can be systematically tuned through ligand modification to match the potential required for CO_2 reduction. In contrast, the advantages of semiconductors are their robustness, tunable band gap by a variety of material compositions and doping technology, and strong oxidative power to extract electrons from molecules such as H_2O and organic chemicals (dependent on E_{VBM}). In this regard, inorganic–organic hybrid photocatalysis systems with advantages of both the photoactivity of the semiconductor and the very high selectivity toward CO_2 reduction at the metal complex have been proposed in the 2010s. To take advantage of both semiconductor and metal-complex catalysts with strong oxidative power and high CO_2 selectivity, respectively, it is essential that photoexcited electrons are transferred from the conduction band of the photoexcited semiconductor to the metal complex in the ground state to facilitate selective CO_2 reduction on the complex catalysts. When E_{CBM} is located at a more negative position than the CO_2 reduction potential (or lowest unoccupied molecular orbital (LUMO)) of the metal-complex catalyst, sufficient electron transfer to promote the reaction can be facilitated (Fig. 7.6). In 2010, Morikawa and coworkers demonstrated a breakthrough concept in the combination of metal-complex electrocatalysts and semiconductor photosensitizers to realize high product selectivity. A mixture of Ru(II)-complex electrocatalyst $[Ru(bpy)_2(CO)_2]^{2+}$ and a p-type semiconductor (N-doped Ta_2O_5, N-Ta_2O_5) exhibited selective CO_2 reduction to produce formate. Furthermore, a $[Ru(dcbpy)_2(CO)_2]^{2+}$ (dcbpy = 2,2′-

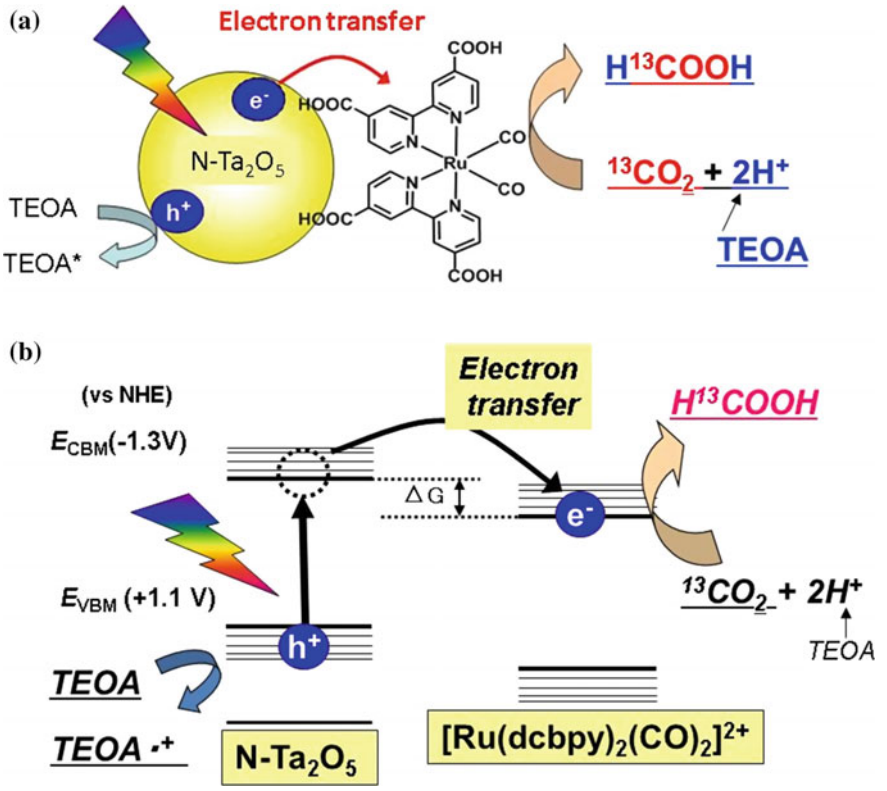

Fig. 7.6 Schematic illustration of a photocatalytic system composed of semiconductor and metal-complex catalyst for CO_2 reduction. **a** A N-Ta_2O_5/$[Ru(dcbpy)_2(CO)_2]^{2+}$ system. **b** Energy diagram for the hybrid photocatalysis

bipyridine-4,4′-dicarboxylic acid) linked with the N-Ta_2O_5 exhibited highly selective CO_2 reduction to produce formate (>70% selectivity) under visible light irradiation in a mixed solution of acetonitrile and TEOA containing CO_2 molecules (Fig. 7.7) [25]. No reaction occurred for either the Ru(II)-complex alone or N-Ta_2O_5 alone. Photoreaction with the hybrid catalysts was active up to a wavelength of 500 nm, which corresponds to the photoresponse of N-Ta_2O_5. The linkage through the dicarboxylic acid anchor is beneficial to achieve effective electron transfer from N-doped Ta_2O_5 to $[Ru(dcbpy)_2(CO)_2]^{2+}$, which results in the highest TN of 89 for formate generation under >400 nm irradiation. Isotope tracer analysis confirmed that CO_2 was the carbon source for the formate and that TEOA was an electron donor and proton source for formate production. The energy difference between E_{CBM} of N-Ta_2O_5 and the LUMO of $[Ru(dcbpy)_2(CO)_2]^{2+}$ is 0.5 V, which is the driving force for the electron transfer of conduction band electrons. A detailed analysis of time-resolved emission measurements after excitation at 400 nm (N 2*p* to Ta 5*d* transition) revealed a fast trapping process from

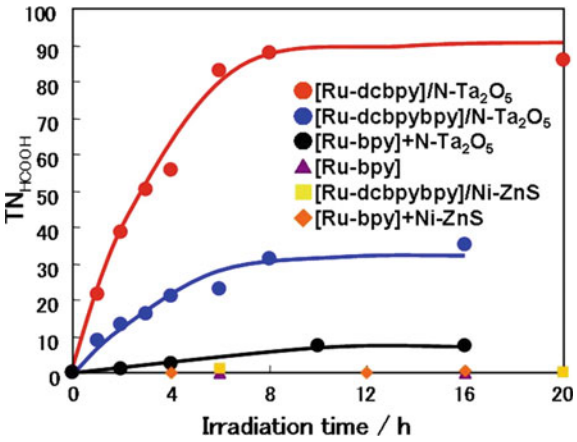

Fig. 7.7 Turnover number (TN) for HCOOH formation from CO_2 as a function of irradiation time. Solutions were irradiated from a Xe lamp with filters producing light in the range of $410 \leq \lambda \leq 750$ nm. The concentration and amount of the photocatalysts were respectively 0.05 mM and 5 mg for Ru complexes and semiconductors in a CO_2-saturated MeCN/TEOA (5:1) solution. The catalysts used were [Ru-bpy] alone, N-Ta_2O_5 alone, Ni-ZnS alone, a mixture of [Ru-bpy] and N-Ta_2O_5, a mixture of [Ru-bpy] and Ni-ZnS, linked [Ru-dcbpybpy]/N-Ta_2O_5, linked [Ru-dcbpy]/N-Ta_2O_5, and linked [Ru-dcbpybpy]/Ni-ZnS. Estimated errors for TN_{HCOOH} are within the range of ±20% (Reprinted with permission from Ref. [25]. Copyright 2010, Wiley–VCH Verlag GmbH)

shallow defect sites to deep defect sites with an ultrafast time constant of 24 ps in N-Ta_2O_5. While in the $[Ru(dcbpy)_2(CO)_2]^{2+}$/N-Ta_2O_5, ultrafast electron transfer from the shallow defect sites of N-Ta_2O_5 to the adsorbed Ru complex occurred with a faster time constant of 12 ps (Fig. 7.8) [26].

A system linked by a phosphonate anchor, N-Ta_2O_5/$[Ru(dpbpy)(bpy)(CO)_2]^{2+}$ (dpbpy: 4,4′-diphosphonate-2,2′-bipyridine), gave a TN 5 times higher for formate generation than that with N-Ta_2O_5/$[Ru(dcbpy)(bpy)(CO)_2]^{2+}$ (dcbpy: 4,4′-dicarboxy-2,2′-bipyridine) [27].

CO_2 reduction potentials over metal complexes are largely more negative than that for hydrogen evolution in aqueous solution; therefore, a sufficiently negative E_{CBM} is required for the semiconductor to facilitate the photoinduced CO_2 reduction reaction. N-Ta_2O_5 is reported to have an extensively negative E_{CBM} of –1.3 V versus NHE [28], which is essential for the CO_2 reduction reaction over the Ru complex [25, 27]. Density functional theory calculations suggested that N-doping of Ta_2O_5 induces the formation of oxygen defects such as oxygen atoms and surface hydroxyl groups, which induce charge redistribution to generate excess negative charges near the doped N atoms and excess positive charges near the defect sites. When the concentration of doped N atoms at the surface is not sufficiently high to compensate the positive charges induced at the surface defects, the remaining positive charges are compensated by N atoms in the inner layers of the Ta_2O_5 lattice. Dipole moments normal to the surface generated in this situation

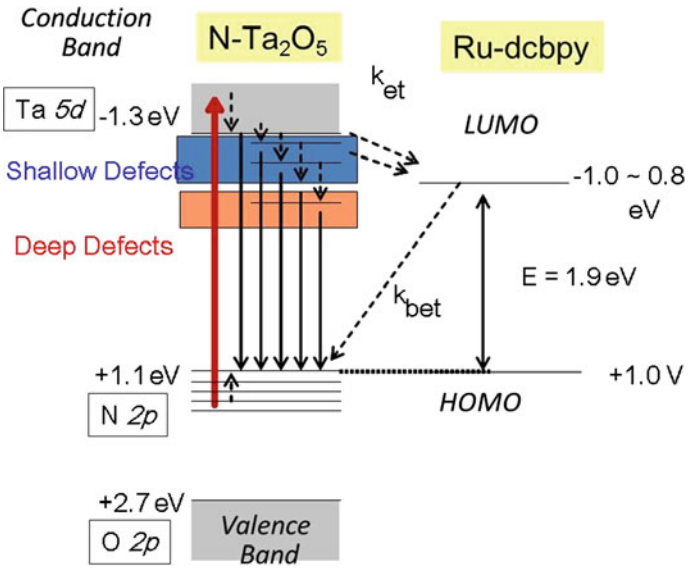

Fig. 7.8 Energy diagram for N-Ta_2O_5 and $[Ru(dcbpy)_2(CO)_2]^+$. All energy levels were normalized with respect to NHE

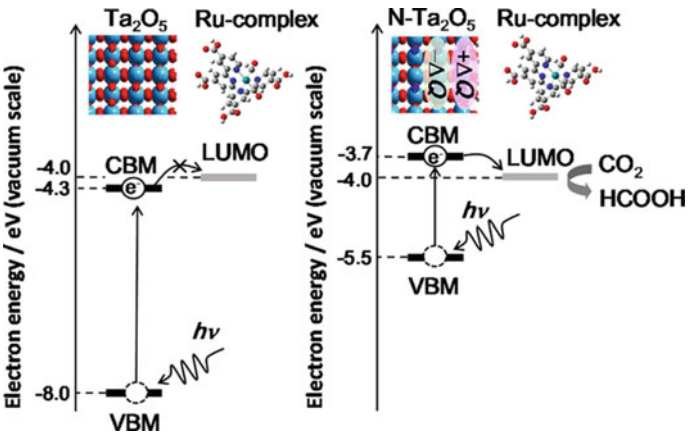

Fig. 7.9 Alignments of conduction band minimum (E_{CBM}) and valence band maximum (E_{VBM}) for Ta_2O_5, N-doped Ta_2O_5 (N-Ta_2O_5), and redox levels (LUMO levels) of a Ru complexes $[Ru(dcbpy)_2(CO)_2]^{2+}$. *Small white spheres* are H atoms, *medium gray spheres* are C atoms, *medium blue spheres* are N atoms, *medium red spheres* are O atoms, and *large green spheres* are Ru atoms (Reproduced with permission from Ref. [29]. Copyright 2015, American Chemical Society)

increase the E_{CBM} and E_{VBM} of Ta_2O_5, which allows photogenerated electrons to transfer from N-doped Ta_2O_5 to the catalytically active sites for CO_2 reduction (Fig. 7.9) [29]. Nonadiabatic molecular dynamics simulations indicated that the

electron transfer is faster in complexes with COOH anchors (7.5 ps) than in complexes with PO_3H_2 groups (56.7 ps), due to greater nonadiabatic coupling [30]. The discrepancy between the CO_2 reaction rates and TN [25, 27], and the theoretical electron transfer [30] results suggests that other factors are likely to play an important role in the total CO_2 reduction reaction.

The concept of a hybrid photocatalyst consisting of a semiconductor and molecular catalyst is highly applicable to lots of materials for photocatalytic reactions. As an alternative semiconductor material, Maeda et al. focused on a carbon nitride polymer that is an earth-abundant polymer semiconductor photocatalyst. Mesoporous graphitic carbon nitride (g-C_3N_4) polymers linked with a ruthenium complex, cis, trans-[Ru{4,4′-($CH_2PO_3H_2$)$_2$-2, 2′-bipyridine}$(CO)_2Cl_2$] also exhibited activity for CO_2 reduction in a MeCN-TEOA mixture (4:1 v/v) under >400 nm irradiation [31]. Although this reaction proceeds in an organic solution containing an organic sacrificial ligand, it is noteworthy that most of the elements in this system are carbon and nitrogen.

7.5 Photocathodes for CO_2 Reduction Over Molecular Catalysts Immobilized at Semiconductor Surfaces

The concept of the molecular/semiconductor organic/inorganic hybrid catalyst is applicable to a photoelectrochemical system. The advantage of the photoelectrochemical CO_2 reaction over dark electrochemical reactions is operation at lower overpotentials. Semiconductor photocathodes are advantageous because the energy of electrons is increased to the level of E_{CBM} with the assistance of photon energy, compared with that for electrocatalysts. In 1998, Chardon-Noblat et al. reported a Ru complex, RuII(L-L)$(CO)_2Cl_2$, which can be polymerized on vitreous carbon (VC) or platinum (Fig. 7.10a) [32]. It was demonstrated that the Ru metal-complex polymer could have metal–metal bonds, and the polymer showed selective

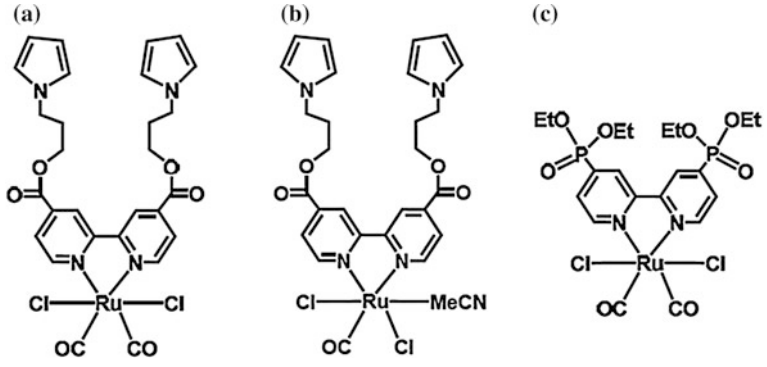

Fig. 7.10 Structure of ruthenium complex electrocatalysts

electrocatalytic activity for CO_2 reduction to formic acid. In 2010, Arai and coworkers modified the Ru complex to RuII(L-L)$(CO)_2$ClMeCN (Fig. 7.10b) and polymerized it on a (100) surface of zinc-doped sphalerite phase indium phosphide (p-InP:Zn), where Zn was doped as an acceptor in InP to induce p-type semiconductivity [33].

An example of a general three-electrode setup for photoelectrochemical CO_2 reduction under visible light irradiation is schematically illustrated in Fig. 7.11a. Figure 7.12 shows typical current–voltage characteristics for CO_2 reduction in aqueous solution (purified water saturated with CO_2) measured under dark conditions and under visible light irradiation with Ag/AgCl and glassy carbon used as reference and counter electrodes, respectively. A Pyrex glass cell was used as the reactor and a xenon light source equipped with an optical filter ($\lambda > 400$ nm) and a cold mirror was used to irradiate visible light [33]. A cathodic reaction current was observed in darkness at potentials more negative than –0.8 V versus Ag/AgCl for the metal cathode in the aqueous solution containing CO_2, while a cathodic photocurrent was observed at potentials more negative than 0.0 V versus Ag/AgCl. The threshold voltage of 0.0 V almost corresponds to the position of E_{VBM} for the semiconductor photocathode. The positive shift of the applied external electrical bias, which lowers the dissipation of electrical energy, is the technical advantage of this photoelectrochemical system. The extent of external bias decrease and the applicable solar energy spectral region are determined by the energy potentials E_{CBM} and E_{VBM}, and by the band gap energy (E_g) for the semiconductor, respectively. Under visible light irradiation with a suitable bias potential (–0.6 V vs. Ag/AgCl) and a standard three-electrode configuration, this InP/RuCP system produces formic acid from CO_2 in water using H_2O as an electron donor and proton source. Isotope tracer analyses were performed with $^{13}CO_2$ and D_2O, which verified that the carbon and proton

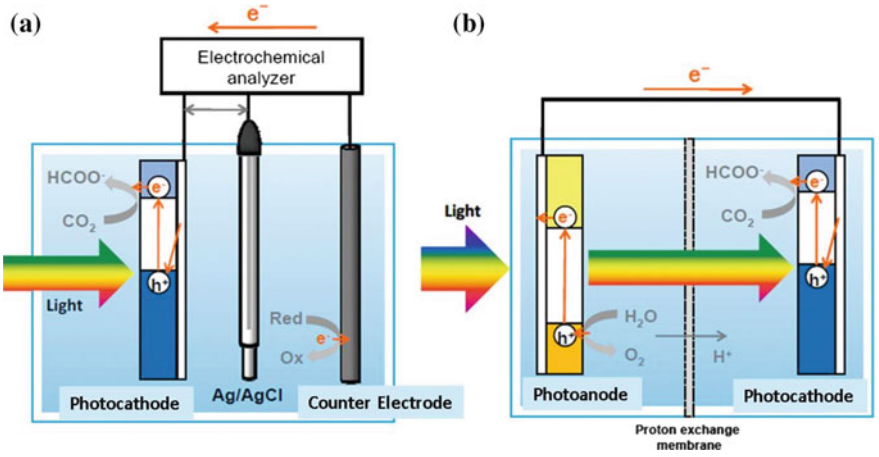

Fig. 7.11 Schematic illustration of the photoelectrochemical reduction of CO_2 **a** with a three-electrode configuration using an InP/Ru-polymer photocathode, and **b** with a two-electrode configuration in the Z-scheme system with no electrical bias using a photoanode for water oxidation and an InP/Ru-polymer photocathode for CO_2 reduction

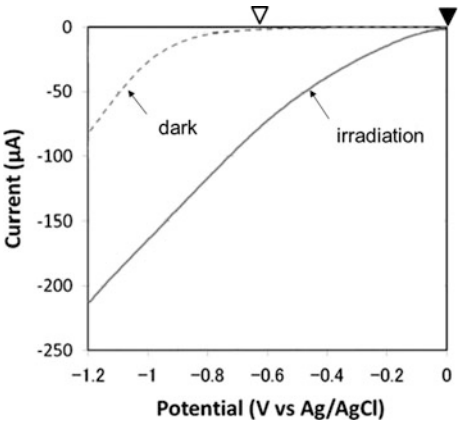

Fig. 7.12 Technological advantage of photoelectrochemical CO_2 reduction over electrochemical CO_2 reduction. External electrical bias voltage (▽) can be reduced to a potential near the valence band maximum E_{VBM} (▼) by photoirradiation

sources for the formate were CO_2 and H_2O, respectively. The Faradaic efficiency formate generation was 62.3%, and this work was the first example of a photocathode with p-InP:Zn as a light absorber modified by the ruthenium complex polymer (RuCP) as a CO_2 reduction catalyst to perform photochemical CO_2 reduction into formic acid under conditions. The important point to note is that the system required a lower applied potential than that for electrocatalytic systems. Other semiconductors such as gallium phosphide (GaP) and nitrogen-doped tantalum pentoxide (N-Ta_2O_5) have also been modified with the polymerized Ru complex, and have also exhibited activity for CO_2 reduction [34]. Immobilization of a molecular catalyst for CO_2 reduction has not been limited to phosphide semiconductors, but was also successful for sulfide semiconductors in aqueous solution [35], and for silicon [36] and oxide [37] semiconductors in organic solvents.

Another system that employs photoelectrochemical CO_2 reduction to synthesize methanol consists of a combination of a semiconductor electrode and a molecular catalyst that does not contain a metallic species. In 2008, Bocarsly and colleagues developed a CO_2 reduction system that consisted of a GaP photocathode and pyridinium ions dissolved in aqueous solution [38]. It is speculated that a redox shuttle processes with protons from pyridinium ions and conduction band electrons from visible light-excited GaP occur to realize the successive six-electron reduction of CO_2 to methanol in an acetate buffer under certain electrical bias. The selectivity for the reduction product was reported to be in the range of 90–51% under low electric bias from –0.3 to –0.7 V (vs. SCE). Photoelectrochemical CO_2 reduction was achieved at wavelengths less than 480 nm, which almost corresponds to the band gap of GaP.

7.6 Z-Scheme Photoreaction Coupling CO_2 Reduction and Water Oxidation

The systems for photoelectrochemical CO_2 reduction by semiconductors on which molecular catalysts are immobilized are designed for half-reactions. When a photocathode capable of CO_2 reduction is functionally coupled with a photoanode

capable of H_2O oxidation under solar irradiation, then artificial photosynthesis, solar-driven CO_2 reduction that uses H_2O as both an electron donor and a proton source, by the Z-scheme mechanism (or two-step photoexcitation) can proceed. A photocathode composed of InP coated with a Ru-polymer comprised of a mixture of Ru complexes (Fig. 7.10b and c) for CO_2 reduction is connected to TiO_2 via a potentiostat, and immersed in a two-compartment reactor separated by a proton exchange membrane filled with an aqueous solution containing CO_2 and an electrolyte as shown in Fig. 7.11b. A Ru-complex with phosphonate anchors at bipyridine (Fig. 7.10c) is incorporated into the polymer catalyst to enhance electron transfer from the InP surface to the catalysts [34]. A solar simulator equipped with an air mass 1.5 (AM 1.5) filter adjusted to a power of one sun (100 mW/cm^2) is used to irradiate the system from the TiO_2 side, while the InP/Ru-polymer photocathode is irradiated with light transmitted through the TiO_2 photoanode and proton exchange membrane. Photoreaction current flows between the photoanode and the photocathode, which originates from electrons extracted from water molecules that react mainly with CO_2 molecules. To facilitate the charge transport from the photoanode to the photocathode without an external electrical bias, the E_{VBM} of the photocatalyst for water oxidation must be more positive, at least thermodynamically, than the potential for water oxidation (theoretically 1.23 V vs. NHE), and the E_{CBM} of the photoanode must be more negative than the E_{VBM} of the photocathode.

To evaluate the CO_2 reduction reaction using H_2O as a proton source, isotope tracer analyses were conducted using $^{13}CO_2$ and D_2O. Furthermore, to verify that the electron source for CO_2 reduction is H_2O, isotope tracer analyses (gas chromatography–mass spectrometry; GC-MS) were conducted using $H_2^{18}O$. Both $^{18}O_2$ and $^{16}O^{18}O$ were observed in the water oxidation reaction at the overall reaction, which verified that CO_2 was reduced to formate via electrons extracted from H_2O during the oxidation process to O_2, and that protons also originated from H_2O, as shown in Eqs. 7.1 and 7.2

$$H_2O + h\nu \rightarrow \frac{1}{2}O_2 + 2H^+ + 2e^- \tag{7.1}$$

$$CO_2 + 2H^+ + 2e^- + h\nu \rightarrow HCOOH \tag{7.2}$$

Therefore, this is a complete photoelectrochemical device that operates CO_2 photoreduction without application of an external electrical bias voltage.

The band alignment of semiconductors is important for improvement of the reaction current. In the case of a WO_3 photoanode, no photocurrent was observed, because E_{CBM} of the WO_3 photoanode does not match E_{VBM} of InP, while for the TiO_2 photoanode, photocurrent flows between TiO_2 and InP. These results correspond to the energy difference (ΔE_{SS}) between E_{CBM} of the photoanode and E_{VBM} of the InP photocathode [39]. This concept is highly applicable to lots of semiconductors; therefore, the conversion efficiency can be enhanced by appropriate replacement of the photoanode. Replacement of the TiO_2 photoanode with a

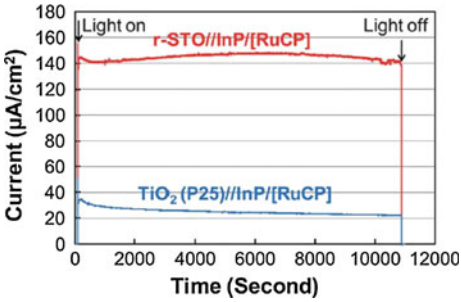

Fig. 7.13 Time courses of the photocurrent observed for the Z-scheme system through combination of an InP/[RuCP] photocathode with $SrTiO_{3-x}$ (*red line*) and TiO_2 (P25) photoanodes (*blue line*) (Reproduced with permission from Ref. [39]. Copyright 2013, The Royal Society of Chemistry)

reduced $SrTiO_3$ ($SrTiO_{3-x}$) photoanode significantly increased the performance of the device. Figure 7.13 shows the photocurrent observed for the Z-scheme reaction, where electrons extracted from water molecules flow from the photoanode to the InP/RuCP photocathode and react with CO_2 molecules, so that the photocurrent is increased from 25 to 140 μA/cm^2 by replacement of the TiO_2 photoanode with $SrTiO_{3-x}$. Formate was generated from CO_2 and H_2O with a solar-to chemical conversion efficiency (E_{SCE} in Eq. 7.3) of 0.14%. $SrTiO_{3-x}$ has a more negative E_{CBM} potential than TiO_2, which increases the energy difference (ΔE_{SS}) with respect to the E_{VBM} of InP, so that the $SrTiO_{3-x}$ system facilitates electron transfer from the photoanode to the photocathode.

$$E_{SCE} = \frac{Gibbs\,free\,energy\,change(from\,CO_2\,to\,formicacid)}{Total\,solar\,energy\,irradiated\left(100\,\mathrm{mWcm^{-2}}, AM1.5\right)} \tag{7.3}$$

7.7 Monolithic System for Solar CO_2 Reduction in Aqueous Solution

Electrochemical reduction of CO_2 using a CO_2 electrolyzer equipped with metal electrodes and photovoltaic cells is a well-known approach. However, an applied voltage of 4–5 V is necessary to operate the CO_2 electrolyzer due to the substantial negative potential for CO_2 reduction over metal electrodes. The CO_2 electrolyzer and photovoltaic cells undergo a potential drop due to various resistances (resistances in the solar cell, between the solar cell and the electrode, and permeance at the proton exchange membrane), so that a complicated potential transformer is also required for impedance matching. Therefore, a simplified system is advantageous. In contrast, metal-complex/carbon cathodes have substantially lower overpotentials than those of metal electrodes for the CO_2 reduction reaction. The molecular

catalyst–semiconductor hybrid system can thus be further integrated to realize a simpler electrode. A monolithic device is feasible for solar-driven CO_2 reduction using water molecules due to its simplicity and lower impedance losses from electrical wiring. A monolithic tablet-shaped device (artificial leaf) for CO_2 photoreduction to liquid organics has been demonstrated in a single-compartment cell, which is composed of a silicon–germanium triple junction (SiGe-jn) as a light absorber, Ru-polymer (RuCP) coated on carbon cloth as a CO_2 reduction catalyst, and IrO_x as a catalyst for H_2O oxidation (Fig. 7.14a) [40]. The SiGe-jn has an open circuit voltage (V_{oc}) of 2.1 eV. The E_{CBM} of the SiGe-jn was estimated to be –0.52 V versus RHE, which is more negative than RuCP (–0.34 V vs. RHE). The E_{VBM} was determined to be 1.58 V (vs. RHE), which is also more positive than the water oxidation potential over IrO_x, 1.5 V versus NHE. Therefore, electron transfer processes from both sides of the SiGe-jn are thermodynamically feasible. The CO_2 photoreduction reaction was demonstrated in CO_2-saturated phosphate buffer

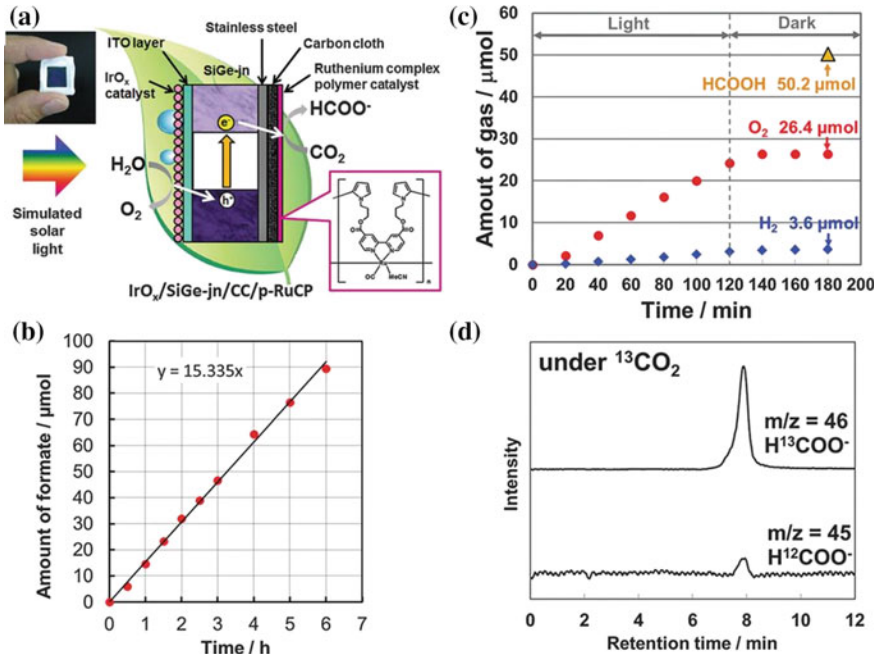

Fig. 7.14 **a** Schematic illustration of the IrOx/SiGe-jn/CC/p-RuCP monolithic tablet-shaped device for CO_2 photoreduction. **b** Time course for the generation of formate during CO_2 photoreduction using IrOx/SiGe-jn/CC/p-RuCP under simulated solar light irradiation (1 sun, AM1.5, 0.25 cm^2). The IrOx/SiGe-jn/CC/p-RuCP monolith was immersed in a single-compartment quartz reactor filled with CO^2-saturated phosphate buffer solution (pH 6.4). **c** Experimental verification of formate production from CO_2 and water molecules; time course for oxygen and hydrogen generation during CO_2 photoreduction using a tablet-shaped wireless configuration. The amount of formate was determined at the end of the photoreaction. **d** IC-TOFMS spectra from a tracer experiment utilizing $^{13}CO_2$ (Reproduced with permission from Ref. [40]. Copyright 2015, The Royal Society of Chemistry)

solution (pH 6.4) under irradiation with simulated solar light (one sun, AM1.5) by immersion of the monolithic tablet-shaped device in a single-compartment reactor. Formate was produced at a linear rate with respect to the irradiation time (Fig. 7.14b), and the solar-to-chemical energy conversion efficiency for formate generation based on the Gibbs free energy change reached 4.6% in the buffer solution without external electrical or chemical bias, or a membrane for separation of the products. The total amount of oxygen generated after 2 h irradiation was 26.4 mmol (Fig. 7.14c), which corresponds to 105.6 mmol of photoexcited holes, while 50.2 mmol of formate in the liquid phase and 3.6 mmol of hydrogen in the gas phase were simultaneously generated after 2 h irradiation, which accounts for 107.6 mmol of photoexcited electrons. The amount of electrons was approximately equal to that of photoexcited holes, which strongly suggests that stoichiometric CO_2 reduction is achieved using electrons extracted from water molecules. The formation of $H^{13}COO^-$ from $^{13}CO_2$ was clarified by ion chromatography interfaced with time-of-flight mass spectrometry (IC-TOFMS) (Fig. 7.14d). The concept can be extended to a powered catalyst system for solar-based synthesis of organic compounds from CO_2 and H_2O in a simplified reactor.

7.8 Conclusions and Future Prospects

A simplified system for an artificial photosynthetic process that synthesizes organic chemicals such as formic acid from CO_2 and H_2O under sunlight irradiation at ambient temperature and pressure is the ultimate goal of solar fuel generation toward the storage of solar photon energy with increasing the size of CO_2 molecules. Exploiting the advantages of molecular catalysts can realize high selectivity for the CO_2 reduction reaction through functional combination with semiconductor photosensitizers in a simplified system as a new approach to realize solar-driven direct hydrocarbon generation using water as both an electron donor and proton source, similar to photosynthesis in plants. A very high solar conversion efficiency exceeding 4% was demonstrated for formic acid production even with a simple tablet-shaped device (artificial leaf), which clarified confirmed the feasibility of solar CO_2 reduction using artificial organic–inorganic hybrid materials.

The technological impact of recycling CO_2 molecules into liquid organic compounds is very high; therefore, rapid progress is desirable in this field. Thus, efficient catalytic reaction, selectivity toward CO_2 conversion, efficient solar absorption, and efficient charge transfer are necessary to further improve this system. In particular, design of the catalyst to realize the synthesis of larger and more useful molecules is desirable. From a practical perspective, there are some differences with CO_2 reduction systems, such as the methods employed for product separation and CO_2 capture. Therefore, the feasibility of practical systems for solar fuel generation through technology cross-over should be discussed further.

References

1. Schwarz HA, Dodson RW (1989) Reduction potentials of CO_2^- and the alcohol radicals. J Phys Chem 93:409–414
2. Hawecker J, Lehn JM, Ziessel R (1983) Efficient photochemical reduction of CO_2 to co by visible-light irradiation of systems containing $Re(bipy)(CO)_3^X$ or $Ru(bipy)_3^{2+}$-CO_2^+combinations as homogeneous catalysts. J Chem Soc Chem Commun 536–538
3. Hayashi Y, Kita S, Brunschwig BS et al (2003) Involvement of a binuclear species with the Re-C(O)O-Re moiety in CO_2 reduction catalyzed by tricarbonyl rhenium(I) complexes with diimine ligands: Strikingly slow formation of the Re-Re and Re-C(O)O-Re species from $Re(dmb)(CO)_3^S$ (dmb = 4, 4′-dimethyl-2, 2′-bipyridine, S = solvent). J Am Chem Soc 125:11976–11987
4. Takeda H, Koike K, Inoue H et al (2008) Development of an efficient photocatalytic system for CO_2 reduction using rhenium(l) complexes based on mechanistic studies. J Am Chem Soc 130:2023–2031
5. Kou Y, Nabetani Y, Masui D et al (2014) Direct detection of key reaction intermediates in photochemical CO_2 reduction sensitized by a rhenium bipyridine complex. J Am Chem Soc 136:6021–6030
6. Craig CA, Spreer LO, Otvos JW et al (1990) Photochemical reduction of carbon-dioxide using nickel tetraazamacrocyclES. J Phys Chem 94:7957–7960
7. Sato S, Morikawa T, Kajino T et al (2013) A highly efficient mononuclear iridium complex photocatalyst for CO_2 reduction under visible light. Angew Chem Int Ed 52:988–992
8. Garg K, Matsubara Y, Ertem MZ et al (2015) Striking differences in properties of geometric isomers of Ir(tpy)-(ppy)H (+): experimental and computational studies of their hydricities, interaction with CO2, and photochemistry. Angew Chem Int Ed 54:14128–14132
9. Tinnemans AHA, Koster TPM, Thewissen D et al (1984) Tetraaza-macrocyclic cobalt(ii) and nickel(ii) complexes as electron-transfer agents in the photo(electro)chemical and electrochemical reduction of carbon-dioxide. Recueil Des Travaux Chimiques Des Pays-Bas-J R Neth Chem Soc 103:288–295
10. Kimura E, Wada S, Shionoya M et al. (1990) A novel 1, 4, 8, 11-tetra-azacyclotetradecane nickel(II) complex appended with a tris-(2, 2′-bipyridine)ruthenium(II) complex. J Chem Soc Chem Commun 397–398
11. Gholamkhass B, Mametsuka H, Koike K et al (2005) Architecture of supramolecular metal complexes for photocatalytic CO_2 reduction: Ruthenium-rhenium bi- and tetranuclear complexes. Inorg Chem 44:2326–2336
12. Sato S, Koike K, Inoue H et al (2007) Highly efficient supramolecular photocatalysts for CO_2 reduction using visible light. Photochem Photobiol Sci 6:454–461
13. Morimoto T, Nishiura C, Tanaka M et al (2013) Ring-shaped Re(I) multinuclear complexes with unique photofunctional properties. J Am Chem Soc 135:13266–13269
14. Tamaki Y, Koike K, Morimoto T et al (2013) Substantial improvement in the efficiency and durability of a photocatalyst for carbon dioxide reduction using a benzoimidazole derivative as an electron donor. J Catal 304:22–28
15. Morikawa T (2016) CO_2 reduction by photoelectrochemistry. In: Solar to chemical energy conversion. Springer, pp 281–296
16. Halmann M (1978) Photoelectrochemical reduction of aqueous carbon dioxide on p-type gallium phosphide in liquid junction solar cells. Nature 275:115–116
17. Inoue T, Fujishima A, Konishi S, Honda K (1979) Photoelectrocatalytic reduction of carbon dioxide in aqueous suspensions of semiconductor powders. Nature 238:637–638
18. Kang U, Choi SK, Ham DJ et al (2015) Photosynthesis of formate from CO_2 and water at 1% energy efficiency via copper iron oxide catalysis. Energy Environ Sci 8:2638–2643

19. Hori Y, Kikuchi K, Murata A et al (1986) Production of methane and ethylene in electrochemical reduction of carbon dioxide at copper electrode in aqueous hydrogencarbonate solution. Chem Lett 6:897–898
20. Hori Y, Murata A, Takahashi R et al (1987) Electroreduction of CO to CH_4 and ethylene at a copper electrode in aqueous solutions at ambient temperature and pressure. J Am Chem Soc 109:5022–5023
21. Matsumoto Y, Obata M, Hombo J (1994) Photocatalytic reduction of carbon-dioxide on p-type $CaFe_2O_4$ powder. J Phys Chem 98:2950–2951
22. Cook RL, Macduff RC, Sammells AF (1988) Photoelectrochemical carbon-dioxide reduction to hydrocarbons at ambient-temperature and pressure. J Electrochem Soc 135:3069–3070
23. Sayama K, Arakawa H (1993) Photocatalytic decomposition of water and photocatalytic reduction of carbon-dioxide over ZrO_2 catalyst. J Phys Chem 97:531–533
24. Iizuka K, Wato T, Miseki Y et al (2011) Photocatalytic reduction of carbon dioxide over ag cocatalyst-loaded $ALa_4Ti_4O_{15}$ (A = Ca, Sr, and Ba) using water as a reducing reagent. J Am Chem Soc 133:20863–20868
25. Sato S, Morikawa T, Saeki S et al (2010) Visible-light-induced selective CO_2 reduction utilizing a ruthenium complex electrocatalyst linked to a p-type nitrogen-doped Ta_2O_5 semiconductor. Angew Chem Int Ed 49:5101–5105
26. Yamanaka K, Sato S, Iwaki M et al (2011) Photoinduced electron transfer from nitrogen-doped tantalum oxide to adsorbed ruthenium complex. J Phys Chem C 115:18348–18353
27. Suzuki TM, Tanaka H, Morikawa T et al (2011) Direct assembly synthesis of metal complex-semiconductor hybrid photocatalysts anchored by phosphonate for highly efficient CO_2 reduction. Chem Commun 47:8673–8675
28. Morikawa T, Saeki S, Suzuki T et al. (2010) Dual functional modification by N doping of Ta_2O_5: p-type conduction in visible-light-activated N-doped Ta_2O_5. Appl Phys Lett 96:142111–142113
29. Jinnouchi R, Akimov AV, Shirai S et al (2015) Upward shift in conduction band of Ta_2O_5 due to surface dipoles induced by n-doping. J Phys Chem C 119:26925–26936
30. Akimov AV, Asahi R, Jinnouchi R et al (2015) What makes the photocatalytic CO_2 reduction on n-doped Ta_2O_5 efficient: insights from nonadiabatic molecular dynamics. J Am Chem Soc 137:11517–11525
31. Maeda K, Sekizawa K, Ishitani O (2013) A polymeric-semiconductor-metal-complex hybrid photocatalyst for visible-light CO_2 reduction. Chem Commun 49:10127–10129
32. Chardon-Noblat S, Deronzier A, Ziessel R et al (1998) Electroreduction of CO, catalyzed by polymeric Ru(bpy)$(CO)_2$ (n) films in aqueous media: parameters influencing the reaction selectivity. J Electroanal Chem 444:253–260
33. Arai T, Sato S, Uemura K et al (2010) Photoelectrochemical reduction of CO_2 in water under visible-light irradiation by a p-type InP photocathode modified with an electropolymerized ruthenium complex. Chem Commun 46:6944–6946
34. Sato S, Arai T, Morikawa T et al (2011) Selective CO_2 conversion to formate conjugated with H_2O oxidation utilizing semiconductor/complex hybrid photocatalysts. J Am Chem Soc 133:15240–15243
35. Arai T, Tajima S, Sato S et al (2011) Selective CO_2 conversion to formate in water using a CZTS photocathode modified with a ruthenium complex polymer. Chem Commun 47:12664–12666
36. Kumar B, Smieja JM, Kubiak CP (2010) Photoreduction of CO_2 on p-type silicon using Re(bipy-Bu′)(CO)(3)Cl: photovoltages exceeding 600 mV for the selective reduction of CO_2 to CO. J Phys Chem C 114:14220–14223
37. Sahara G, Abe R, Higashi M et al (2015) Photoelectrochemical CO_2 reduction using a Ru(II)-Re(I) multinuclear metal complex on a p-type semiconducting NiO electrode. Chem Commun 51:10722–10725

38. Barton EE, Rampulla DM, Bocarsly AB (2008) Selective solar-driven reduction of CO_2 to methanol using a catalyzed p-GaP based photoelectrochemical cell. J Am Chem Soc 130:6342−6344
39. Arai T, Sato S, Kajino T et al (2013) Solar CO_2 reduction using H_2O by a semiconductor/metal-complex hybrid photocatalyst: enhanced efficiency and demonstration of a wireless system using $SrTiO_3$ photoanodes. Energy Environ Sci 6:1274–1282
40. Arai T, Sato S, Morikawa T (2015) A monolithic device for CO_2 photoreduction to generate liquid organic substances in a single-compartment reactor. Energy Environ Sci 8:1998–2002

Chapter 8
Photobatteries and Photocapacitors

Nick Vlachopoulos and Anders Hagfeldt

Abstract This chapter is dedicated to the interfacing of dye-sensitized solar cells (DSSCs) and electrochemical energy storage cells. After a brief introduction to the basic principles of useful and deleterious reactions at the photoelectrode, as related to the analysis of the present chapter, and to the necessary terminology, photobatteries are discussed, of which two main types can be distinguished: these based solely on redox reactions in solution, usually with the necessity for external storage of the solutions, due to the low energy density of the electrolyte solutions, and these incorporating solid energy storage materials with high energy density, e.g., metals, metal oxides or electronically conducting polymers, in one of the electrodes. In addition to the most common three-electrode model, alternative two-electrode and four-electrode (two separate cells in series) systems are presented. Subsequently, photocapacitors are introduced. After a presentation of the basic concepts of electrochemical supercapacitor concepts and operation, the two basic types of photocapacitor, that of two and three-electrode, are presented, with a discussion of the disadvantages of the first type, despite the construction simplicity, as compared to the second one. In the latter, light is harvested by a DSSC, based either on a liquid electrolyte containing a redox mediator or a solid hole conductor, juxtaposed to a capacitor based on carbon, metal oxide or conducting polymer electrodes. For both photobatteries and photocapacitors several systems are discussed, with the various processes at and between the electrodes presented in detail. Moreover, the various formulas for the calculation of energy storage efficiency are explained.

Some symbols used in the text in one place only and which are cleary explained in the texts have not been included in the abbreviation list.

N. Vlachopoulos (✉) · A. Hagfeldt
Laboratory of Photomolecular Science, Institute of Chemical Sciences and Engineering, Swiss Federal Institute of Technology in Lausanne (EPFL), EPFL-FSB-ISIC-LSPM, Chemin des Alambics, Station 6, Lausanne 1015, Switzerland
e-mail: nikolaos.vlachopoulos@epfl.ch

A. Hagfeldt
e-mail: anders.hagfeldt@epfl.ch

H. Tian et al. (eds.), *Molecular Devices for Solar Energy Conversion and Storage*, Green Chemistry and Sustainable Technology,
https://doi.org/10.1007/978-981-10-5924-7_8

Keywords Dye-sensitized solar cell · Photobattery · Photocapacitor · Redox flow battery · Electrochemical supercapacitor · Electrochromic device · Electrochemical double-layer capacitor · Pseudocapacitor · Mesoporous semiconductor oxide electrode · Electronically conducting polymer

Abbreviations

AE	Auxiliary electrode, in a photobattery
CE	Counter electrode
CAP	Capacitor
TCO	Transparent conductive oxide
DSSC	Dye-sensitized solar cell
AC	Activated carbon
EC	Electrochemical supercapacitor
EDLC	Electrochemical double-layer capacitor
EL	Electrolyte
FTO	F-doped tin oxide
$h\nu$	Incident light to photoelectrode
IE	Intermediate electrode, in a photocapacitor
HTM	Hole-transport medium
PBAT	Photobattery
PCAP	Photocapacitor
RF-PBAT	Redox-flow photobattery
PE	Photoelectrode
PSC	Perovskite solar cell
SHE	Standard hydrogen electrode

Roman Characters

CE	Coulombic efficiency
CAP	Capacitor electrode material
D^0	D Initial form of dye
D^{0*}	Excited state of dye
D^+	Oxidized form of dye
e_0	Magnitude of the electron charge
e^-	Electron
E	Electrode potential (vs. a reference electrode)
E^0	Standard electrode potential
E_F	Fermi level
E_F^0	Standard Fermi level
F	Faraday constant
k_B	Boltzmann constant
I	Current

M	Redox species
M^0	Reduced form of mediator M
M^+	Oxidized form of mediator M
Ox	Species participating in redox reaction
P_{in}	Incident light intensity
R	Universal gas constant
R_{ext}	External resistance
Red	Species participating in redox reaction
T	Absolute temperature
t	Time
t_{ch}	Charging time of photocapacitor
t_{dch}	Discharging time of photocapacitor
t_{irr}	Irradiation time
U_{bat}	Battery potential
U_{bias}	External bias potential imposed on a photobattery
U_{cap}	Capacitor potential
U_{dch}	Capacitor discharge potential

Greek Characters

$\eta_{h\nu-ch}$	Conversion of incident solar energy to stored chemical energy
η_{ch-el}	Conversion of stored chemical-to-electrical energy
$\eta_{h\nu-ch}$	Conversion of incident solar energy to electrical energy
ν	Frequency of light
ν_i	Stoichiometric number of species *i* in redox reaction

8.1 Introduction

The storage of solar electrical energy is an important issue due to the intermittent character of its generation, and the need of related research efforts is expected to become more acute with the worldwide increase generation of solar electricity. One obvious solution is the connection of the photovoltaic cell, such as a dye-sensitized solar cell (DSSC), to an external electrochemical device such as a secondary battery, with the products stored inside the device, for example a stationary lithium ion battery or a nickel–hydride battery, a redox flow battery, such as a vanadium battery, or an electrolysis cell, for example one in which water is decomposed to hydrogen and oxygen; in the latter two cases the products of the electrochemical reaction are externally stored. The present section is devoted to the alternative option of hybrid systems, photobatteries and photocapacitors, with both solar energy capture and electrochemical energy storage in the same device. At a first stage such systems can be envisaged for small-scale applications. As related

research and development is under progress, the experience thus obtained can be useful for further scale-up. In this chapter systems composed of separate dye solar cells and batteries or capacitors, often called energy packs, will not be discussed. Similarly, only systems based on dye and perovskite photoelectrodes will be considered. Taking into account the early stage of development of the described research, the emphasis will be on a discussion of the underlying physicochemical principles rather than of the detailed performance of the various systems.

8.2 Dye Solar Cell Overview

The DSSC consists of a dye/mesoscopic semiconductor oxide photoelectrode (PE), a dark (in the sense of not needing light for its operation) counter electrode (CE), and a charge-transport medium in the between, such as a liquid electrolyte containing a redox mediator or a solid-state hole conductor. The DSSC processes can be divided to two categories: that of useful processes, leading to conversion of the energy of photons to that of electrons flowing to the external circuit, and that of deleterious processes, limiting the efficiency of the solar cell [1–4]. The charge-transport medium should not undergo any modification in its overall chemical composition during cell operation; in other terms, the DSSC should operate as a regenerative device. The most common cell configuration from the sunlight-to-electricity power conversion efficiency point of view is based on a dye-coated mesoporous n-type semiconductor oxide PE, e.g., TiO_2, ZnO, SnO_2, Nb_2O_5 Zn_2SnO_4, most commonly TiO_2. The latter oxide will be the support for the systems under discussion in the following analysis.

8.2.1 Useful Processes

- Dye (D) photoexcitation, with the initial form being denoted as D^0 and the excited form as D^{0*}:

$$D^0 \xrightarrow{hv} D^{0*} \tag{8.1}$$

- Electron injection into the semiconductor oxide (SC); the oxidative quenching mechanism, resulting to the conversion will be assumed

$$D^{0*} \rightarrow D^+ + e^-(SC) \tag{8.2}$$

The superscript $^{+}$ denotes the charge in the oxidized form with respect to the reduced form (superscript ^{0}) and not necessarily that the species itself carries a net positive charge.

- Electron collection: electron transfer from SC into the SC support substrate. Usually, with light directed onto the DSSC from the PE side, this is should be transparent. The usual choice is a transparent conducting oxide (TCO), like fluorine-doped tin oxide (FTO) or indium-doped tin oxide (ITO). In some cases, with light directed from a transparent CE, the SC substrate can be an opaque layer with metallic conductivity. Electrons of the SC substrate are designated as $e^{-}(\mathrm{PE})$.

$$e^{-}(\mathrm{SC}) \rightarrow e^{-}(\mathrm{PE}) \tag{8.3}$$

- Dye regeneration: Electron injection from the reduced form M^{0} of a redox mediator M, at the proximity of the PE, to D^{+} in order to regenerate D^{0}:

$$\mathrm{D}^{+} + \mathrm{M}^{0}(\mathrm{PE}) \rightarrow \mathrm{D}^{0} + \mathrm{M}^{+}(\mathrm{PE}) \tag{8.4}$$

with the superscripts ^{0} and $^{+}$ denoting the relative charge and not the actual charge of the respective species.

The overall reaction at the PE is

$$\mathrm{M}^{0}(\mathrm{PE}) \xrightarrow{h\nu} \mathrm{M}^{+}(\mathrm{PE}) + e^{-}(\mathrm{PE}) \tag{8.5}$$

The term $h\nu$ above the arrow indicates the contribution of light to the overall reaction and not photon absorption by species M^{0} (8.4).

In general several electrons and/or several species in each side of the mediator redox half-reaction

$$\mathrm{M}^{0} \rightarrow \mathrm{M}^{+}(\mathrm{PE}) + \mathrm{e}^{-} \tag{8.6}$$

can be involved.

$$\sum \nu_i Red_i \rightarrow \sum \nu_j Ox_j + ne^{-} \tag{8.7}$$

in which case

$$\begin{aligned} \mathrm{M}^{0} &= \frac{\sum \nu_i Red_i}{n} \\ \mathrm{M}^{+} &= \frac{\sum \nu_j Ox_j}{n} \end{aligned} . \tag{8.8}$$

A common case of interest in DSSCs is the 1:3 two-electron iodide-triiodide (I^-/I_3^-) redox, couple

$$3I^- \rightarrow I_3^- + 2e^-. \tag{8.9}$$

or

$$\frac{3}{2} I^- \rightarrow \frac{1}{2} I_3^- + e^-. \tag{8.10}$$

where

$$M^0 = \frac{3}{2} I^- \quad Red_1 = I^-, \quad \nu_1 = 3 \tag{8.11}$$

$$M^+ = \frac{1}{2} I_3^- \quad Ox_1 \quad = I_3^-, \quad \nu_1 = 1 \tag{8.12}$$

$$n = 2 \tag{8.13}$$

- Transport of M^+ from the proximity of PE to that of CE

$$M^+(\text{PE}) \rightarrow M^+(\text{CE}) \tag{8.14}$$

- Electron flow from the TCO substrate to CE. This is the process in which electrical energy $(I \cdot R_{ext})$ is generated, where I is the current and R_{ext} is the external resistance between PE and CE.

$$e^-(\text{PE}) \xrightarrow{I \cdot R_{ext}} e^-(\text{CE}) \tag{8.15}$$

- Heterogeneous (electrochemical) electron transfer from CE, consisting of a conducting substrate, often coated by an electrocatalyst, to the oxidized form of a redox mediator $M^+(\text{CE})$ in solution

$$e^-(\text{CE}) + M^+(\text{CE}) \rightarrow M^0(\text{CE}) \tag{8.16}$$

- Transport of the reduced form of the mediator (M^0) from the CE to the PE

$$M^0(\text{CE}) \rightarrow M^0(\text{PE}) \tag{8.17}$$

By adding together the PE and CE reactions, the transport processes in the electrolyte, and the electron flow at the external circuit, it can be seen that there is a net conversion of sunlight to electricity, without net chemical change in any of the parts of the cell.

8.2.2 Deleterious Processes

- Deactivation of D with evolution of light (luminescence) or heat

$$D^* \xrightarrow{h\nu \text{ or heat}} D^0 \tag{8.18}$$

- Recombination of semiconductor electrons either with the oxidized dye or with the oxidized redox mediator

$$e^-(SC) + D^+ \rightarrow D^0 \tag{8.19}$$

$$e^-(SC) + M^+(PE) \rightarrow M^0(PE) \tag{8.20}$$

  These reactions are related to the regeneration reaction. The first of the two reactions above competes for the oxidized dye with the regeneration reaction. If the latter is sufficient fast, electron recombination with the oxidized redox mediator prevails over that with the oxidized dye. In order to retard the recombination reactions, the D^0 molecule is often specially designed so as to contain long-chain pendant groups at the periphery.
- Recombination of TCO contact electrons $e^-(PE)$ either with the oxidized dye or with the oxidized redox mediator

$$e^-(PE) + D^+ \rightarrow D^0 \tag{8.21}$$

$$e^-(PE) + M^+(PE) \rightarrow M^0(PE) \tag{8.22}$$

The above reactions are important due to the fact that the charge-transport medium can penetrate the porous structure and come into direct contact with the conductive support, TCO in most cases. In particular, the last of the above reactions is important if a mediator exhibits fast electrochemical kinetics with respect to TCO. This is the fact for several one-electron redox mediators such as metal coordination complexes, e.g., these based on cobalt(II/III), or metal-free organic redox mediators such as TEMPO/TEMPO$^+$. Similarly, solid-state hole conductors, either low molecular weight compounds like spiro-OMeTAD, or conducting polymers, like P3HT and PEDOT, exhibit fast recombination with TCO-originating electrons. In these cases it is imperative to interpose a thin, compact blocking semiconducting oxide layer, or underlayer, with thickness of the order of 10–100 nm between TCO and mesoporous dye-coated oxide. Such a layer should hinder recombination reactions but not electron collection; ideally it should be free of fissures, pinholes or other defects permitting electrolyte-TCO glass contact. In the case of a redox mediator with slow electrode kinetics with respect to the TCO substrate, like the multi-electrode redox system I_3^-/I^-, the traditional redox mediator for liquid electrolyte-based DSSCs, the presence of an underlayer is not strictly

necessary from the recombination reaction point of view. However, an underlayer could still be beneficial, not only for increasing the DSSC voltage at the maximum power point but also for improving the adhesion of the mesoporous colloidal TiO_2 layer onto the TCO substrate.

With respect to a photobattery or photocapacitor some of the steps described in this session will be valid; other reactions should be modified or replaced according to the requirements of the system under consideration.

In the following sections the various types of photobatteries and photocapacitors will be described in detail; the order of presentation will be based on the type of device configuration rather than on the time of appearance in the literature. Photobatteries in which the PE operation is based either on direct semiconductor photoexcitation or on dye-sensitization have been reviewed by Yu et al. [5]; photocapacitors have been reviewed by Ng et al. [6].

8.3 Photobatteries with Soluble Species in Both Electrodes

In the usual configuration of the regenerative system discussed up to this point the same redox system, in opposite directions, should interact with PE and CE. If, instead, the storage of chemical energy is the desirable goal, then different redox reactions should be considered in the DSSC for PE and dark CE (Fig. 8.1). Moreover, the PE and the CE should be externally short-circuited, since chemical energy storage should be the goal. The operation of a photobattery (PBAT) consists of two steps: photocharge and dark discharge. The simplest case is that of the two

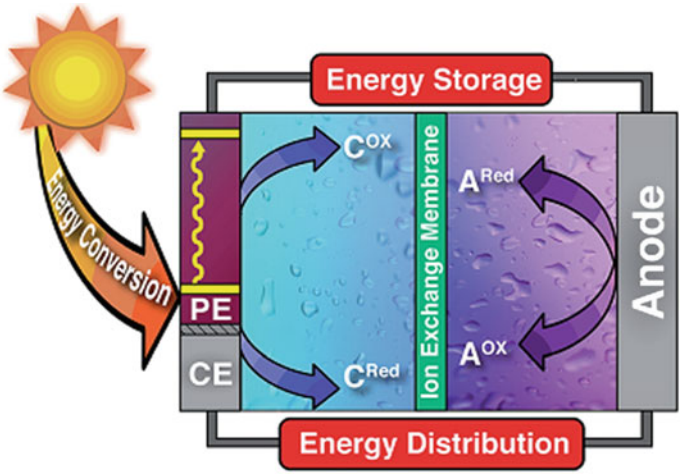

Fig. 8.1 Redox photobattery with both photocharge and dark discharge taking place in the same electrochemical cell. Adopted with permission from Ref. [5]. Copyright (2016) Royal Society of Chemistry

redox couples in solution, $M_{(1)}(PE)$ and $M_{(2)}(CE)$, interacting with the PE and CE, respectively. The electrolytes in contact with the PE and the CE are separated by a diaphragm (non-selective separator, e.g. porous glass or filter paper) or membrane (e.g. cation-permeable membrane, like Nafion® or lithium-conducting glass).

The respective overall PE and CE reactions are

$$e^-(PE) + M^+(PE) \rightarrow M^0(PE) \tag{8.23}$$

$$M^+_{(2)}(CE) + e^-(CE) \rightarrow M^0_{(1)}(CE) \tag{8.24}$$

In this case the redox potential E of $M_{(2)}$ should be more negative than of $M_{(1)}$

$$E(M^0_{(2)}/M^+_{(2)}) < E(M^0_{(1)}/M^+_{(1)}) \tag{8.25}$$

or, equivalently, for the Fermi levels of the respective redox systems,

$$E_F(M^0_{(2)}/M^+_{(2)}) > E_F(M^0_{(1)}/M^+_{(1)}) \tag{8.26}$$

Figure 8.2 gives the energy diagram of a photobattery in the photocharging mode and Fig. 8.3 in the discharging mode.

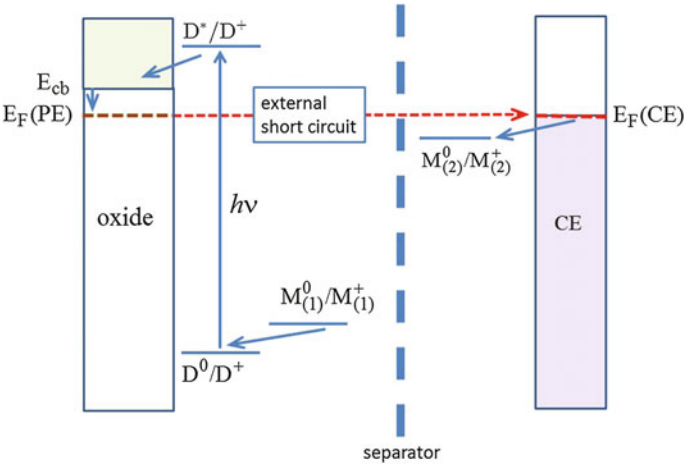

Fig. 8.2 Electron flow diagram for a photobattery in the charging mode. The amount of stored energy corresponds to the Fermi level difference for the two redox mediators. The counter electrode is separated from the photoelectrode by a diaphragm (non-selective, e.g. porous glass) or membrane (selective) barrier

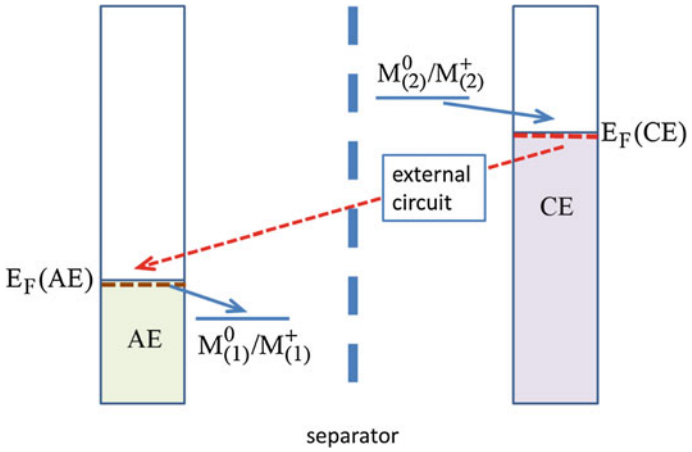

Fig. 8.3 Electron flow diagram for a photobattery in the discharging mode. The amount of recovered energy corresponds to the difference of the Fermi levels between auxiliary and counter electrode, as contrasted to the amount of stored energy, corresponding to the Fermi level difference between the two redox mediators

E and E_F are related as

$$E_F = -e_0 E + E_F(\text{ref}), \tag{8.27}$$

where e_0 is the elementary positive charge (1.609×10^{-19}C) and E_F(ref) is the Fermi level of the reference redox system, versus vacuum, with respect to which E is measured. If the aqueous standard hydrogen reference electrode (SHE) system is chosen, it is [7]

$$E_F(\text{SHE}) = -4.44\,\text{eV} \tag{8.28}$$

with the reference point located in vacuum and just above the electrolyte of the SHE, the latter containing hydrogen ions at unit molal activity (effective concentration of hydrogen ion equal to 1 mol per kg of water) and being saturated with hydrogen at 1 bar pressure. 1 bar is approximately equal to one atmosphere. Until recently, the standard pressure for reporting redox potentials was 1 atm; the error of conversion from 1 bar to 1 arm is negligible for most studies, below 1 mV.

Unless otherwise specified E_F will denote the redox Fermi level in the vacuum scale. The Fermi level in a particular reference electrode scale will be denoted as $E_{F/\text{ref}}$, which is related to the particular electrode potential at the same reference scale by

$$E_{F/\text{ref}} = -e_0 E \tag{8.29}$$

so that, in agreement with (8.27)

$$\mathrm{E_F} = \mathrm{E_{F/ref}} + \mathrm{E_F(ref)} \tag{8.30}$$

In this chapter for redox couples both E and $\mathrm{E_F}$ will be used, depending on the context. For $\mathrm{E_F}$, the Nernst equation in terms of activities α or, approximately, concentrations c for a redox mediator $\mathrm{M/M^+}$, can be expressed as

$$\mathrm{E_F} = \mathrm{E_F^0} + k_\mathrm{B}T \ln \frac{\alpha_{\mathrm{M^0}}}{\alpha_{\mathrm{M^+}}} \approx \mathrm{E_F^0} + k_\mathrm{B}T \ln \frac{c_{\mathrm{M^0}}}{c_{\mathrm{M^+}}}, \tag{8.31}$$

where k_B is the Bolzmann constant and T is the absolute temperature, as compared to the usual form

$$E = E^0 + \frac{RT}{F} \ln \frac{\alpha_{\mathrm{M^+}}}{\alpha_{\mathrm{M^0}}} \approx E^0 + \frac{RT}{F} \ln \frac{c_{\mathrm{M^+}}}{c_{\mathrm{M^0}}} \tag{8.32}$$

where R and F are the universal gas constant and the Faraday constant respectively.

The standard Fermi level $\mathrm{E_F^0}$ is related to the standard electrode potential as

$$\mathrm{E_F^0} = -e_0 E^0 + \mathrm{E_F(ref)}. \tag{8.33}$$

In the PBAT the reactions at the PE and the CE are coupled by the electron flow equation from PE to CE. In this case, since conversion of sunlight-to-chemical energy and not to electricity is desired at the photocharging step, PE and CE are connected through an external short circuit

$$e^-(\mathrm{PE}) \overset{R_\mathrm{ext}=0}{\longrightarrow} e^-(\mathrm{CE}). \tag{8.34}$$

Therefore the overall DSSC process should be written, by combining (8.23), (8.24) and (8.34), as

$$\mathrm{M^0_{(1)}(PE)} + \mathrm{M^+_{(2)}(CE)} \overset{h\nu, R_\mathrm{ext}=0}{\longrightarrow} \mathrm{M^+_{(1)}(PE)} + \mathrm{M^+_{(2)}(CE)}. \tag{8.35}$$

The choice of redox mediators in important with respect both of the Fermi level of the ground state of D, $\mathrm{E_F(D^+/D)}$, and the semiconductor conduction band edge, $\mathrm{E_{cb}}$. For dye regeneration it is essential that

$$\mathrm{E_F(M^0_{(1)}/M^+_{(1)}) > E_F(D/D^+)} \tag{8.36}$$

With respect to the CE interacting with $M_{(2)}$, the Fermi level of the CE lies above that of the redox mediator

$$E_F(CE) > E_F(M^0_{(2)}/M^+_{(2)}) \tag{8.37}$$

In fact, for a CE with good electrocatalytic properties, the difference $E_F(CE) - E_F(M_2/M_2^+)$, corresponding to the electrochemical overpotential of the CE reaction, should be as low as possible.

Moreover, since the DSSC is short-circuited

$$E_F(CE) = E_F(PE) \tag{8.38}$$

Additionally, E_{cb} lies above the Fermi level of the semiconductor $E_F(PE)$, with the gap $E_{cb} - E_F(PE)$ decreasing with increasing light intensity

$$E_{cb} > E_F(PE) \tag{8.39}$$

By combining the last two equations it results that the Fermi level of the redox mediator interacting with the CE should lie below the semiconductor conduction band edge.

$$E_F(M^0_{(2)}/M^+_{(2)}) < E_{cb} \tag{8.40}$$

Therefore, the lower and upper boundaries for the two mediators are E_{cb} and $E_F(D^0/D^+)$

$$E_F(D^0/D^+) < E_F(M^0_{(1)}/M^+_{(1)}) < E_F(M(^0_{(2)}/M^+_{(2)}) < E_{cb} \tag{8.41}$$

Furthermore, the difference $E_F(M^0_{(2)}/M^+_{(2)}) - E_F(M^0_{(1)}/M^+_{(1)})$ should approach $E_{cb} - E_F(D^0/D^+)$, which implies that $E_F(M^0_{(1)}/M^+_{(1)})$ should be as close to $E_F(D^0/D^+)$ as possible. This is not the case if $M_{(1)}$ is I^-/I_3^-, the commonly used mediator in DSSC research and development as well in several photobattery examples mentioned in the following paragraphs. In fact, the difference $E_F(I^-/I_3^-) - E_F(D^0/D^+)$ can be as high as 0.5 eV due to the fact that the overall two-electron reaction may involve both chemical and electron-transfer steps and that the E_F of the species involved in the actual electron transfer reaction with the dye may lie closer to $E_F(D^0/D^+)$ than does $E_F(I^-/I_3^-)$.

In the simplest case of photobattery both light harvesting and recovery of the stored energy occur at the same device, as depicted in Figs. 8.4 and 8.5. The PE compartment contains an auxiliary dark electrode (AE) as well, with electrocatalytic activity toward M_1. This electrode is disconnected from the circuit during the light-harvesting step so that it does not have an influence on the photocharging stage. In the discharging stage the PE is disconnected and the AE is connected to the external circuit. The CE stays connected, but the direction of reaction taking place on it is reversed. $M^0_{(2)}$ is oxidized at the CE and $M^+_{(1)}$ is reduced at the AE.

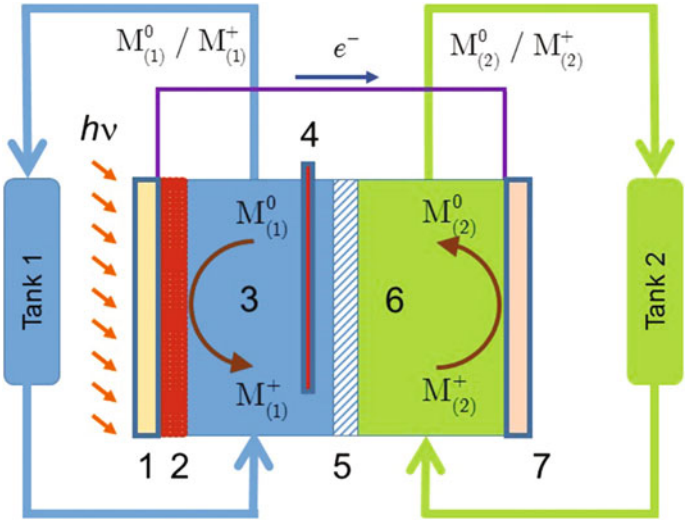

Fig. 8.4 Redox flow photobattery with light harvesting and conversion of the stored energy to electricity in the same cell. Photocharging mode. 1 Transparent conducting oxide substrate; 2 photoelectrode; 3 electrolyte containing redox couple interacting with photoelectrode and auxiliary electrode; 4 auxiliary electrode; 5 separator; 6 electrolyte containing redox couple interacting with counter electrode; 7 counter electrode

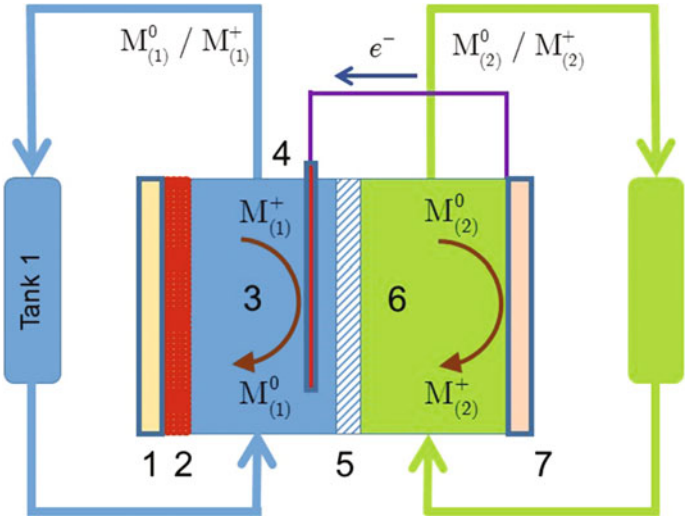

Fig. 8.5 Redox flow photobattery with light harvesting and conversion of the stored energy to electricity in the same cell. Dark discharging mode. 1–7 are the same as in Fig. 8.4

Therefore, upon discharge, with R_{ext} the external resistance connected between AE and CE,

$$M^{+}_{(1)}(AE) + e^{-}(AE) \rightarrow M^{0}_{(1)}(AE) \tag{8.42}$$

$$M^{0}_{(2)}(CE) \rightarrow M^{+}_{(2)}(CE) + e^{-}(CE) \tag{8.43}$$

$$e^{-}(CE) \xrightarrow{IR_{ext}} e^{-}(AE) \tag{8.44}$$

Overall discharging:

$$M^{+}_{(1)}(AE) + M^{0}_{(2)}(CE) \xrightarrow{I \cdot R_{ext}} M^{0}_{(1)}(AE) + M^{+}_{(2)}(CE) + IR_{ext} \tag{8.45}$$

For preliminary, basic research or demonstration-oriented, experiments in the laboratory the redox mediators are confined into the aforementioned electrochemical cell during charge and discharge. However, the amount of charge that can be stored in a liquid electrolyte per unit of volume is significantly lower than that in a solid electrode battery material. Therefore, external storage of the redox mediator solutions is necessary. This redox flow photobattery RF-PBAT depicted in Figs. 8.4 and 8.5 is the photoelectrochemical analog of the traditional redox flow battery, of considerable interest for research and development in recent years for large-scale energy storage [8, 9]. The inclusion of storage tanks, one for each of the redox mediator solutions, as well as pumps directing the solution into and out of each cell compartment, introduces structural and operational complexity into the RF-PB compared to a stationary photobattery. However, the added advantage is that in a redox flow photobattery a much higher amount of charge can be stored, externally, that in a stationary battery, even if the latter includes solid electroactive materials.

A four-electrode RF-BAT modification depicted in Fig. 8.6 involves a cell for recovery of the solar energy (BAT) separate from the DSSC, with pumps and storage tanks in the between. The advantage is that light harvesting and delivery of electricity can take place independently of one another.

At first, solutions containing mostly the $M^{0}_{(1)}$ and $M^{+}_{(2)}$ forms are fed from their respective tanks into and out of the PE and CE compartments of the DSSC, respectively. They are continuously circulating between the tanks and the DSSC until virtually complete conversion to M_1^{+} and M_2^{0} is achieved. When recovery of the stored chemical energy is desired, $M_{(1)}/M^{+}_{(1)}$ solution is fed, from its tank to the cathode compartment (BAT/C) of the separate RB cell, and, similarly, $M_{(2)}/M^{+}_{(2)}$ to the anode compartment (BAT/A) of BAT. In this chapter, the terms anode and cathode are used in the physical electrochemistry sense, as the sites of oxidation and reduction, respectively, independent of electrode polarity.

Circulation between tanks and BAT continues until virtually complete conversion to $M^{0}_{(1)}$ and $M^{+}_{(2)}$ is achieved. These solutions are kept in storage until the next photocharging cycle is initiated.

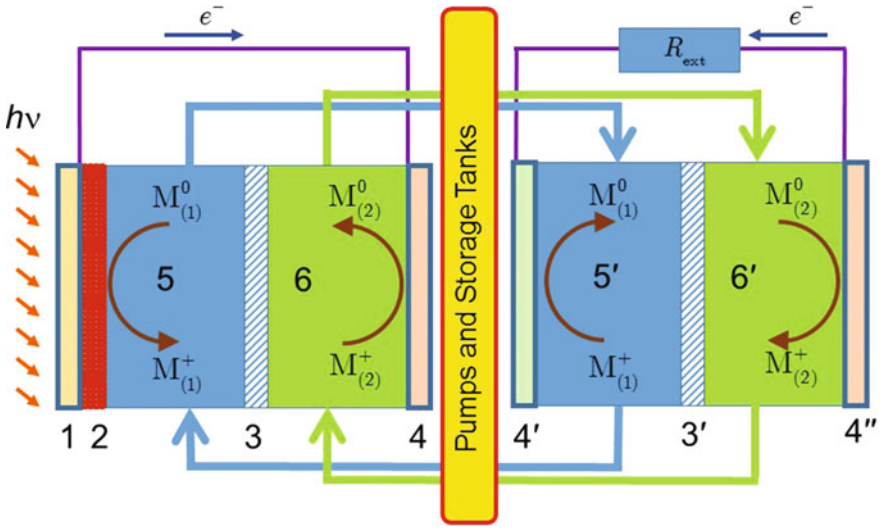

Fig. 8.6 Redox photobattery with light-harvesting DSSC and conversion of the stored energy to electricity in different cells. *1* Transparent conducting oxide substrate; *2* photoelectrode; *3*,*3′* separators; *4* counter electrode of DSSC; *4′*,*4″* metal or other conductive electrodes; *5*,*5′* electrolytes containing redox couple interacting with the photolelectrode of the light-harvesting cell; *6*,*6′* electrolytes containing redox couple interacting with the counter electrode of the light-harvesting cell

The discharge stage at the cathode and anode of the RB cell is

$$\mathrm{M}^{+}_{(1)}(\mathrm{BAT/C}) + e^{-}(\mathrm{BAT/C}) \rightarrow \mathrm{M}^{0}_{(1)}(\mathrm{BAT\text{-}C}) \tag{8.46}$$

$$\mathrm{M}^{0}_{(2)}(\mathrm{BAT/A}) \rightarrow \mathrm{M}^{+}_{(2)}(\mathrm{BAT/A}) + e^{-}(\mathrm{BAT/A}) \tag{8.47}$$

$$e^{-}(\mathrm{BAT/A}) \xrightarrow{I \cdot R_{\mathrm{ext}}} e^{-}(\mathrm{BAT/C}). \tag{8.48}$$

Overall discharging

$$\begin{aligned} &\mathrm{M}^{+}_{(1)}(\mathrm{BAT/C}) + \mathrm{M}^{0}_{(2)}(\mathrm{BAT/A}) \\ &\xrightarrow{I \cdot R_{\mathrm{ext}}} \mathrm{M}^{0}_{(1)}(\mathrm{BAT/C}) + \mathrm{M}^{+}_{(2)}(\mathrm{BAT/A}). \end{aligned} \tag{8.49}$$

AE and CE in the three-electrode RF-PBAT act analogously to BAT/C and BAT-A in the four-electrode RF-PBAT respectively.

The total energy conversion efficiency $\eta_{hv-\mathrm{el}}$ is given as the product of solar to stored chemical energy conversion efficiency ($\eta_{hv-\mathrm{ch}}$) and the efficiency of converting stored energy to electrical energy obtained at the external circuit ($\eta_{\mathrm{ch-el}}$).

$$\eta_{hv-\mathrm{el}} = \eta_{hv-\mathrm{ch}} \cdot \eta_{\mathrm{ch-el}}. \tag{8.50}$$

The radiant-to-chemical stored energy conversion efficiency is expressed either in terms of redox potentials E_1 and E_2 or, alternatively, in terms of Fermi levels $\mathrm{E_{F,1}}$ and $\mathrm{E_{F,2}}$ of the two redox systems $\mathrm{M^0_{(1)}/M^+_{(1)}}$ and $\mathrm{M^0_{(2)}/M^+_{(2)}}$ at the end of the irradiation period, as

$$\begin{aligned} \eta_{hv-\mathrm{ch}} &= 100 \cdot \frac{(E_1 - E_2) \int_o^{t_{irr}} I_{\mathrm{irr}}(t)dt}{P_{\mathrm{in}}\, t_{\mathrm{irr}}} \\ &= 100 \cdot \frac{(\mathrm{E_{F,2}} - \mathrm{E_{F,1}}) \int_o^{t_{irr}} I_{\mathrm{irr}}(t)dt}{e_0 P_{\mathrm{in}}\, t_{\mathrm{irr}}}., \end{aligned} \tag{8.51}$$

where

P_{in} incident light intensity
t_{irr} time of irradiation
$I_{\mathrm{irr}}(t)$ current at time t from the beginning of irradiation

Consider the case of an 1:1 one-electron reaction where initially 1% of the total amount of mediator 1 is oxidized and 1% of the mediator 2 is reduced at $T = 298\,\mathrm{K}$. At the beginning of the irradiation period

$$\mathrm{E_{F,1}}(t=0) = \mathrm{E^0_{F,1}} + 0.025\ \ln\left(\frac{c_{\mathrm{M^0_{(1)}}}}{c_{\mathrm{M^+_{(1)}}}}\right)_{t=t_{\mathrm{irr}}} = \mathrm{E^0_{F,1}} + 0.118\ \mathrm{eV}. \tag{8.52}$$

$$\mathrm{E_{F,2}}(t=0) = \mathrm{E^0_{F,2}} + 0.025\ \ln\left(\frac{c_{\mathrm{M^0_{(2)}}}}{c_{\mathrm{M^+_{(2)}}}}\right)_{t=t_{\mathrm{irr}}} = \mathrm{E^0_{F,2}} - 0.118\ \mathrm{eV}. \tag{8.53}$$

$$(\mathrm{E_{F,2}} - \mathrm{E_{F,1}})_{t=0} = (\mathrm{E^0_{F,2}} - \mathrm{E^0_{F,1}}) - 0.236\ \mathrm{eV} \tag{8.54}$$

At the end of irradiation period

$$\mathrm{E_{F,1}}(t=t_{\mathrm{irr}}) = \mathrm{E^0_{F,1}} + 0.025\ \ln\left(\frac{c_{\mathrm{M^0_{(1)}}}}{c_{\mathrm{M^+_{(1)}}}}\right)_{t=t_{\mathrm{irr}}} = \mathrm{E^0_{F,1}} - 0.118\ \mathrm{eV}. \tag{8.55}$$

$$\mathrm{E_{F,2}}(t=t_{\mathrm{irr}}) = \mathrm{E^0_{F,2}} + 0.025\ \ln\left(\frac{c_{\mathrm{M^0_{(2)}}}}{c_{\mathrm{M^+_{(2)}}}}\right)_{t=t_{\mathrm{irr}}} = \mathrm{E^0_{F,2}} + 0.118\ \mathrm{eV}. \tag{8.56}$$

$$(\mathrm{E_{F,2}} - \mathrm{E_{F,1}})_{t=t_{\mathrm{irr}}} = (\mathrm{E^0_{F,2}} - \mathrm{E^0_{F,1}}) + 0.236\,\mathrm{eV}. \tag{8.57}$$

Therefore, by comparing the last two equations it can be seen that during photocharging $\mathrm{E_{F,2}}$ and $\mathrm{E_{F,1}}$ move far away from one another by 0.47 eV.

$$(\mathrm{E_{F,2}} - \mathrm{E_{F,1}})_{t=t_{\mathrm{irr}}} - (\mathrm{E_{F,2}} - \mathrm{E_{F,1}})_{t=0} = 0.47\,\mathrm{eV}. \tag{8.58}$$

The stored chemical-to-electrical energy conversion efficiency is expressed as

$$\eta_{\mathrm{ch-el}} = \frac{\int_0^{t_{dsch}} U_{\mathrm{dch}}(t) I_{\mathrm{dch}}(t)dt}{(E_1 - E_2)\int_o^{t_{irr}} I_{\mathrm{irr}}(t)dt} = \frac{e_0 \int_0^{t_{dsch}} U_{\mathrm{dch}}(t) I_{\mathrm{dch}}(t)dt}{(E_{\mathrm{F,2}} - E_{\mathrm{F,1}})\int_o^{t_{irr}} I_{\mathrm{irr}}(t)dt}. \tag{8.59}$$

where

$U_{\mathrm{dsch}}(t)$, $I_{\mathrm{dsch}}(t)$ redox battery voltage and current upon discharge.
t_{dsch} time of redox battery discharge.

The radiant-to-electrical energy conversion, after storage, is calculated as

$$\eta_{hv-\mathrm{el}} = \eta_{hv-\mathrm{ch}} \cdot \eta_{\mathrm{ch-el}} = \frac{\int_0^{t_{dsch}} U_{\mathrm{dsch}}(t) I_{\mathrm{dsch}}(t)dt}{P_{\mathrm{in}} t_{\mathrm{irr}}}. \tag{8.60}$$

Quite often the discharge step is conducted under constant current, especially in laboratory tests, in which case discharge continues until the cell potential is virtually zero. In that case

$$\eta_{hv-\mathrm{el}} = \frac{I_{\mathrm{dsch}} \int_0^{t_{disch}} U_{\mathrm{dsch}}(t)dt}{P_{\mathrm{in}}\, t_{\mathrm{irr}}}. \tag{8.61}$$

In the literature there have been three examples of RF-PBAT. The system of Yan et al. [10] consists of a single PBAT cell, where the heterocyclic species quinoxaline ($C_8H_6N_2$) in water is in contact with the CE; both electrolytes contain Li^+. The separator is a Li^+-conducting glass membrane.

The system reported by Liu et al. [11] consists of separate DSSC and BAT cells, $M^0_{(1)}/M^+_{(1)}$ (at PE and BAT/C) is I^-/I_3^- and $M^0_{(2)}/M^+_{(2)}$ (at CE and BAT/A) is the organometallic redox system dimethylferrocene-dimethylferrocenium (DMFC/$DMFC^+$). I^-/I_3^- and $DMFC^+$/DMFC are dissolved in the low-volatility organic polar solvents 3-methoxyproprionitrile and propylene carbonate, respectively. The electrocatalyst in both anode and cathode of the BAT cell was platinum. The solutions in the storage tanks were fed in turn into the DSSC and the BAT for the photocharging and the dark discharging step respectively.

The photocharging and dark discharging processes are formulated as following:

(a) Photocharging

$$\frac{3}{2}\mathrm{I^-(PE)} \xrightarrow{hv} \frac{1}{2}\mathrm{I_3^-(PE)} + e^-(\mathrm{PE}). \tag{8.62}$$

$$\begin{aligned} &\mathrm{DMFC}^{+} + e^{-}(\mathrm{PE}) \rightarrow \mathrm{DMFC} \\ &\text{or} \quad \mathrm{C_8H_6N_2} + e^{-}(\mathrm{CE}) \rightarrow \mathrm{C_8H_6N_2^{-}}. \end{aligned} \tag{8.63}$$

$$e^{-}(\mathrm{PE}) \xrightarrow{R_{\mathrm{ext}}=0} e^{-}(\mathrm{CE}). \tag{8.64}$$

Overall photocharging

$$\frac{3}{2}\mathrm{I^{-}(PE)} + \mathrm{DMFC}^{+} \xrightarrow{h\nu} \frac{1}{2}\mathrm{I_3^{-}(PE)} + \mathrm{DMFC}. \tag{8.65}$$

or

$$\frac{3}{2}\mathrm{I^{-}(PE)} + \mathrm{C_8H_6N_2} \xrightarrow{h\nu} \frac{1}{2}\mathrm{I_3^{-}(PE)} + \mathrm{C_8H_6N_2^{-}}. \tag{8.66}$$

(b) Discharging

$$\frac{1}{2}\mathrm{I_3^{-}(AE)} + e^{-}(\mathrm{AE}) \rightarrow \frac{3}{2}\mathrm{I^{-}(AE)} \tag{8.67}$$

$$\mathrm{DMFC} \rightarrow \mathrm{DMFC}^{+} + e^{-}(\mathrm{PE}) \ \text{ or } \ \mathrm{C_8H_6N_2^{-}} \rightarrow \mathrm{C_8H_6N_2} + e^{-}(\mathrm{CE}) \tag{8.68}$$

$$e^{-}(\mathrm{CE}) \xrightarrow{I \cdot R_{\mathrm{ext}}} e^{-}(\mathrm{AE}). \tag{8.69}$$

Overall discharging

$$\frac{1}{2}\mathrm{I_3^{-}(AE)} + \mathrm{DMFC} \xrightarrow{I \cdot R_{\mathrm{ext}}} \frac{3}{2}\mathrm{I^{-}(AE)} + \mathrm{DMFC}^{+} \tag{8.70}$$

or

$$\frac{1}{2}\mathrm{I_3^{-}(AE)} + \mathrm{C_8H_6N_2^{-}} \xrightarrow{I \cdot R_{\mathrm{ext}}} \frac{3}{2}\mathrm{I^{-}(AE)} + \mathrm{C_8H_6N_2}. \tag{8.71}$$

The system of Yan et al. [12] consists of a single PBAT cell with $\mathrm{I_3^{-}/I^{-}}$ in the PE/AE compartment and $\mathrm{Li_2WO_4/Li_{2+x}WO_4}$ in the CE compartment. The separator is a $\mathrm{Li^{+}}$-conducting glass membrane.

The photocharging and dark discharging processes are formulated as following:

(a) Photocharging

$$\frac{3}{2}\mathrm{I}^{-}(\mathrm{PE}) \xrightarrow{h\nu} \frac{1}{2}\mathrm{I}_3^{-}(\mathrm{PE}) + e^{-}(\mathrm{PE}) \tag{8.72}$$

$$e^{-}(\mathrm{PE}) \xrightarrow{R_{\mathrm{ext}}=0} e^{-}(\mathrm{CE}) \tag{8.73}$$

$$\frac{1}{x}\mathrm{WO}_4^{2-} + e^{-}(\mathrm{CE}) \rightarrow \frac{1}{x}\mathrm{WO}_4^{(2+x)-}. \tag{8.74}$$

Overall photocharging

$$\frac{3}{2}\mathrm{I}^{-} + \frac{1}{x}\mathrm{WO}_4^{2-} \xrightarrow{h\nu} \frac{1}{2}\mathrm{I}_3^{-}(\mathrm{PE}) + \frac{1}{x}\mathrm{WO}_4^{(2+x)-} \tag{8.75}$$

(b) Discharging

$$\frac{1}{2}\mathrm{I}_3^{-}(\mathrm{AE}) + e^{-}(\mathrm{AE}) \rightarrow \frac{3}{2}\mathrm{I}^{-}(\mathrm{AE}) \tag{8.76}$$

$$\frac{1}{x}\mathrm{WO}_4^{(2+x)-} \rightarrow \frac{1}{x}\mathrm{WO}_4^{2-} + e^{-}(\mathrm{CE}) \tag{8.77}$$

$$e^{-}(\mathrm{CE}) \longrightarrow I \cdot R_{\mathrm{ext}}\ e^{-}(\mathrm{AE}) \tag{8.78}$$

Overall discharging

$$\frac{1}{2}\mathrm{I}_3^{-}(\mathrm{AE}) + \frac{1}{x}\{\mathrm{WO}_4^{(2+x)-} \xrightarrow{I \cdot R_{\mathrm{ext}}} \frac{3}{2}\mathrm{I}^{-}(\mathrm{AE}) + \frac{1}{x}\mathrm{WO}_4^{2-} \tag{8.79}$$

For the three systems described above the average U_{dsch} upon constant-current discharge was relatively low, in the range of 0.3–0.7 V, in agreement with the relatively low $\mathrm{E}^0_{\mathrm{F},2} - \mathrm{E}^0_{\mathrm{F},1}$ of the chosen mediators. The $\eta_{h\nu-\mathrm{el}}$ was, when reported, below 2%. Despite of the low performance, these proof-of concept studies demonstrate the feasibility of a DSSC-based RF-PB with liquid redox systems. For performance improvement both the cell configuration and the flow rates have to be optimized.

8.4 Photobatteries Involving Solid Charge-Storage Materials

The choice of the redox mediator for a DSSC is always a challenging task, the more so if two mediators are needed for the aforementioned redox photobattery. Therefore it is an easier task if one of them, at first the liquid redox species

interacting with the CE of the DSSC component, is replaced by a solid electrode material. The previously invoked scheme for photocharge at WE and CE and discharge at AE and CE, in a three-electrode cell, applies to the system of the present section. Two such systems have been proposed by Segawa and coworkers, based on the photoexcitation of a TiO_2 electrode coated by a coordination ruthenium dye; $M_{(1)}$ is I^-/I_3^- and M_2 is either an electronically conducting polymer, polypyrrole (ppy) [13, 14], or an oxide, WO_3 [15, 16]. In both cases at the photoelectrode I^- is oxidized to I_3^-.

At first the case of the ppy film redox reaction at the CE will be discussed. The redox reaction of the ppy film is written in the oxidation direction as

$$\mathrm{ppy} \rightarrow \mathrm{ppy}^{x+} + xe^- \tag{8.80}$$

If the polymer chain is composed of n monomeric units *py*

$$\mathrm{ppy} \equiv (\mathrm{py})_n \tag{8.81}$$

upon reversible oxidation (doping) of the polymer one out every 3–4 *py* units is oxidized so that the fraction *y* of oxidized units will be in the range 0.2–0.4

$$\left.\begin{array}{r} \mathrm{ppy} \rightarrow \mathrm{ppy}^{x+} + xe^- \\ x = yn, \;\; 0.25 \le y \le 0.33 \end{array}\right\} \Rightarrow \mathrm{ppy} \rightarrow \mathrm{ppy}^{x+} + yn\, e^- \tag{8.82}$$

However, the neutrality of the film requires the incorporation, or intercalation, of labile anions A^- from the electrolyte, for example ClO_4^-. Therefore the overall CE reaction is

$$\mathrm{ppy} + x\mathrm{A}^- \rightarrow \mathrm{ppy}^{x+} : x\mathrm{A}^- + xe^- \tag{8.83}$$

or, in terms of a one-electron reaction

$$\frac{1}{x}\mathrm{ppy} + \mathrm{A}^- \rightarrow \frac{1}{x}\{\mathrm{ppy}^{x+} : x\mathrm{A}^-\} + e^- \tag{8.84}$$

The photocharging and dark discharging processes are formulated as following:
Photocharging

$$\frac{3}{2}\mathrm{I}^-(\mathrm{PE}) \xrightarrow{h\nu} \frac{1}{2}\mathrm{I}_3^-(\mathrm{PE}) + e^-(\mathrm{PE}) \tag{8.85}$$

$$\frac{1}{x}\{\mathrm{ppy}^{x+} : x\mathrm{A}^-\}(\mathrm{CE}) + e^-(\mathrm{CE}) \rightarrow \frac{1}{x}\mathrm{ppy}(\mathrm{CE}) + \mathrm{A}^-(\mathrm{CE}) \tag{8.86}$$

$$e^-(\mathrm{PE}) \xrightarrow{R_{\mathrm{ext}}=0} e^-(\mathrm{CE}) \tag{8.87}$$

Overall photocharging

$$\begin{aligned}&\frac{3}{2}\mathrm{I}^{-}(\mathrm{PE})+\frac{1}{x}\{\mathrm{ppy}^{x+}:x\mathrm{A}^{-}\}(\mathrm{CE})\\&\xrightarrow{h\nu}\frac{1}{2}\mathrm{I}_3^{-}(\mathrm{PE})+\frac{1}{x}\mathrm{ppy}(\mathrm{CE})+\mathrm{A}^{-}(\mathrm{CE})\end{aligned}\tag{8.88}$$

Discharging

$$\frac{1}{2}\mathrm{I}_3^{-}(\mathrm{AE})+e^{-}(\mathrm{AE})\rightarrow\frac{3}{2}\mathrm{I}^{-}(\mathrm{AE})\tag{8.89}$$

$$\frac{1}{x}\mathrm{ppy}(\mathrm{CE})+\mathrm{A}^{-}(\mathrm{CE})\rightarrow\frac{1}{x}\{\mathrm{ppy}^{x+}:x\mathrm{A}^{-}\}(\mathrm{CE})+e^{-}(\mathrm{CE})\tag{8.90}$$

$$e^{-}(\mathrm{CE})\xrightarrow{I\cdot R_{\mathrm{ext}}}e^{-}(\mathrm{AE})\tag{8.91}$$

Overall discharging

$$\begin{aligned}&\frac{1}{2}\mathrm{I}_3^{-}(\mathrm{AE})+\frac{1}{x}\mathrm{ppy}(\mathrm{CE})+\mathrm{A}^{-}(\mathrm{CE})\\&\xrightarrow{I\cdot R_{\mathrm{ext}}}\frac{3}{2}\mathrm{I}^{-}(\mathrm{PE})+\frac{1}{x}\{\mathrm{ppy}^{x+}:x\mathrm{A}^{-}\}(\mathrm{CE})\end{aligned}\tag{8.92}$$

where it is reminded that AE is dipped in the same electrolyte as PE and that, upon discharge, PE is disconnected but AE connected.

In the case of tungsten oxide $(\mathrm{WO_3})$ as CE the redox reaction in the reduction direction is

$$\mathrm{WO_3}+xe^{-}\rightarrow\mathrm{WO_3^{x-}}.\tag{8.93}$$

where $x=1$ corresponds to the maximum degree of reduction. $\mathrm{WO_3}$ is a semiconductor; however, under the conditions of the photobattery operation, $\mathrm{E_F}$ lies sufficiently above $\mathrm{E_{cb}}$, within the conduction band so that the electrical conductivity is substantially enhanced. As in the case of the polymeric CE, electroneutrality of the solid material requires the incorporation of a labile cation from the solution. In the case of nonaqueous electrolytes this cation is often Li^{+}, so that the overall reaction is

$$\mathrm{WO_3}+xe^{-}+x\mathrm{Li}^{+}\rightarrow\{\mathrm{WO_3^{x-}}:x\mathrm{Li}^{+}\}\tag{8.94}$$

or, in terms of the one-electron formulation,

$$\frac{1}{x}\mathrm{WO_3}+e^{-}+\mathrm{Li}^{+}\rightarrow\frac{1}{x}\{\mathrm{WO_3^{x-}}:x\mathrm{Li}^{+}\}\tag{8.95}$$

where $x = 1$ corresponds to the maximum degree of reduction.

The photocharging and dark discharging processes are expressed as following

(a) Photocharging:

$$\frac{3}{2}\mathrm{I}^-(\mathrm{PE}) \xrightarrow{h\nu} \frac{1}{2}\mathrm{I}_3^-(\mathrm{PE}) + e^-(\mathrm{PE}) \tag{8.96}$$

$$\frac{1}{x}\mathrm{WO}_3 + \mathrm{Li}^+ + e^-(\mathrm{CE}) \rightarrow \frac{1}{x}\{\mathrm{WO}_3^{x-} : x\mathrm{Li}^+\} \tag{8.97}$$

$$e^-(\mathrm{PE}) \xrightarrow{R_{\mathrm{ext}}=0} e^-(\mathrm{CE}). \tag{8.98}$$

Overall photocharging

$$\begin{aligned} &\frac{3}{2}\mathrm{I}^-(\mathrm{PE}) + \frac{1}{x}\mathrm{WO}_3 + \mathrm{Li}^+ + e^-(\mathrm{CE}) \\ &\xrightarrow{h\nu} \frac{1}{2}\mathrm{I}_3^-(\mathrm{PE}) + \frac{1}{x}\{\mathrm{WO}_3^{x-} : x\mathrm{Li}^+\} \end{aligned} \tag{8.99}$$

(b) Discharging

$$\frac{1}{2}\mathrm{I}_3^-(\mathrm{AE}) + e^-(\mathrm{AE}) \rightarrow \frac{3}{2}\mathrm{I}^-(\mathrm{AE}) \tag{8.100}$$

$$\frac{1}{x}\{\mathrm{WO}_3^{x-} : x\mathrm{Li}^+\}(\mathrm{CE}) \rightarrow \frac{1}{x}\mathrm{WO}_3(\mathrm{CE}) + \mathrm{Li}^+(\mathrm{CE}) + e^-(\mathrm{CE}) \tag{8.101}$$

$$e^-(\mathrm{CE}) \xrightarrow{I \cdot R_{\mathrm{ext}}} e^-(\mathrm{AE}) \tag{8.102}$$

Overall discharging

$$\begin{aligned} &\frac{1}{2}\mathrm{I}_3^-(\mathrm{AE}) + \frac{1}{x}\{\mathrm{WO}_3^{x-} : x\mathrm{Li}^+\}(\mathrm{CE}) \\ &\xrightarrow{I \cdot R_{\mathrm{ext}}} \frac{3}{2}\mathrm{I}^-(\mathrm{AE}) + \frac{1}{x}\mathrm{WO}_3(\mathrm{CE}) + \mathrm{Li}^+(\mathrm{CE}). \end{aligned} \tag{8.103}$$

A system similar to the photobattery, based on the $\mathrm{I}^-/\mathrm{I}_3^-$ system at the PE and WO_3 at the CE, is the photoelectrochromic system, first discussed by Gregg and coworkers [17, 18]. In that case the CE is a transparent in the oxidized state, sufficiently thin WO_3 electrode. Similarly, the dye/oxide layer is of sufficiently low thickness to allow a substantial portion of the incident light to go through. Upon photocharging the WO_3-coated electrode becomes opaque. For the discharge

half-cycle there are two essential differences; at first no separate auxiliary electrode is needed, the TiO_2/dye PE operates as dark cathode when the dye is switched off. Additionally, the two electrodes are short-circuited; the intention in this case is not the electricity storage but the electrochromic operation. For the reduction of I_3^- at the PE a substantial overpotential is required; both the TCO glass and the TiO_2 substrate have poor electrocatalytic activity toward I^-/I_3^-. However, the cell voltage reached at the end of the illumination step is sufficient to cover the overpotential requirement upon discharge.

For some solid battery materials, such as ppy and WO_3, unlike the case of soluble redox species, the redox process takes place over an extended range of electrode potentials. The redox behaviour of such materials cannot always be expressed by a simple form of the Nernst equation.

A particular photobattery design investigated by Hauch et al. [19] involves a PE interacting with two electroactive species, I^-/I_3^- in solution and WO_3, inserted between the dye/TiO_2 layer and the TCO substrate, with the PE configuration illustrated in Fig. 8.7. This composite PE is separated from a CE, catalytic toward

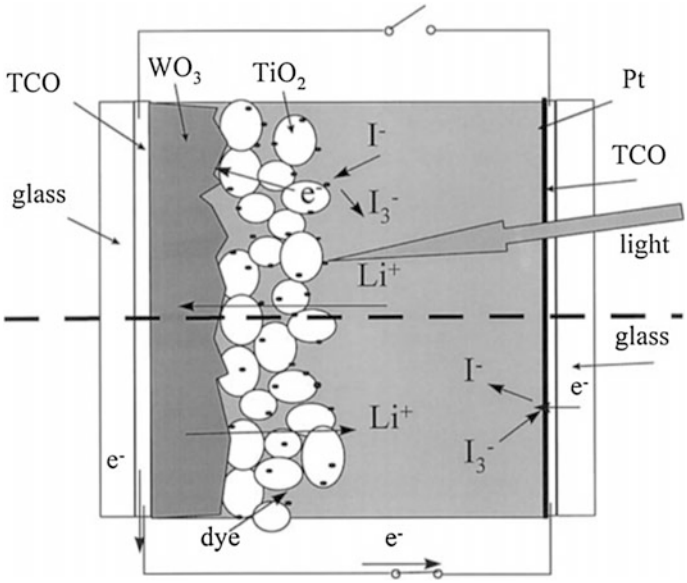

Fig. 8.7 Photobattery with both a liquid electrolyte-dissolved redox mediator and a solid reversible redox material interacting with the dye/TiO_2 photoelectrode. Photocharging is performed under open circuit. Upon discharging the switcher is turned on and the stored energy is delivered to the attached external load. Adopted by permission from Ref. [19]. Copyright (2001) Elsevier

I^-/I_3^-, by the electrolyte (EL) layer containing I^-/I_3^-. Therefore the overall device configuration is

$$TCO/WO_3/TiO_2\,,\text{dye}/EL,I^-/I_3^-/CE \tag{8.104}$$

with no separator needed in between.

The photocharging occurs at open circuit so that only the dye-coated electrode is involved

$$\frac{3}{2}I^-(EL)\xrightarrow{h\nu}\frac{1}{2}I_3^-(EL)+e^-(TiO_2) \tag{8.105}$$

$$e^-(TiO_2)\rightarrow e^-(WO_3) \tag{8.106}$$

$$\frac{1}{x}WO_3+Li^+(EL)+e^-(WO_3)\rightarrow\frac{1}{x}\left\{WO_3^{x-}:xLi^+\right\} \tag{8.107}$$

Overall photocharging (Fig. 8.8)

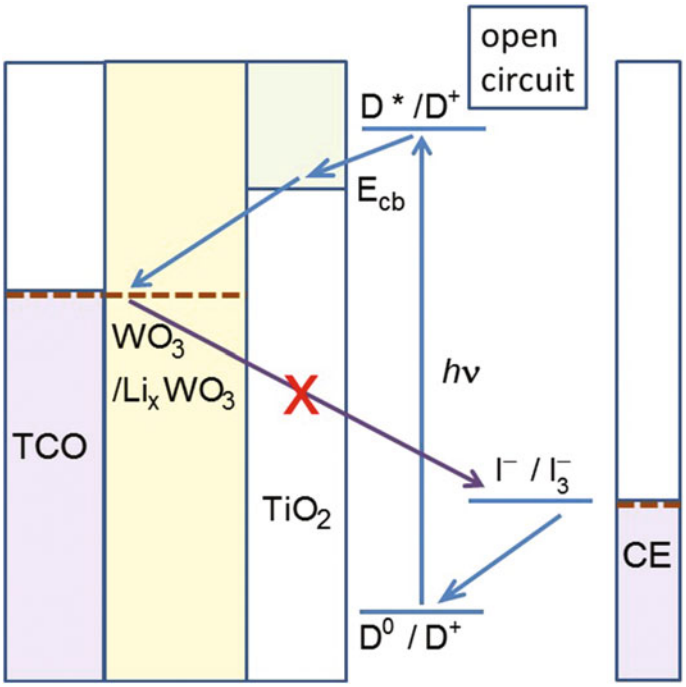

Fig. 8.8 Energy diagram for a photobattery with both a liquid electrolyte-dissolved redox mediator and a solid reversible redox material interacting with the dye/TiO_2 photoelectrode, as described by Hauch and Georg [19]. Charging mode

$$\begin{aligned}&\frac{3}{2}\mathrm{I}^{-}(\mathrm{EL})+\frac{1}{x}\mathrm{WO}_3+\mathrm{Li}^{+}(\mathrm{EL})\\&\xrightarrow{h\nu}\frac{1}{2}\mathrm{I}_3^{-}(\mathrm{EL})+\frac{1}{x}\{\mathrm{WO}_3^{x-}:x\mathrm{Li}^{+}\}\end{aligned}\tag{8.108}$$

In fact the reverse reaction between reduced WO_3 at the PE and $I_3^-(EL)$ in solution

$$\frac{1}{2}\mathrm{I}_3^{-}(\mathrm{EL})+\frac{1}{x}\{\mathrm{WO}_3^{x-}:x\mathrm{Li}^{+}\}\rightarrow\frac{3}{2}\mathrm{I}^{-}(\mathrm{EL})+\frac{1}{x}\mathrm{WO}_3+\mathrm{Li}^{+}\tag{8.109}$$

is thermodynamically spontaneous but kinetically sluggish. Therefore, after the light being switched off, WO_3 remains at the reduced state. The dark discharge process of the above photobattery is

$$\frac{1}{2}\mathrm{I}_3^{-}(\mathrm{EL})+e^{-}(\mathrm{CE})\rightarrow 3\mathrm{I}^{-}(\mathrm{EL})\tag{8.110}$$

$$\frac{1}{x}\{\mathrm{WO}_3^{x-}:x\mathrm{Li}^{+}\}\rightarrow\frac{1}{x}\mathrm{WO}_3+\mathrm{Li}^{+}(\mathrm{EL})+e^{-}(\mathrm{WO}_3)\tag{8.111}$$

$$e^{-}(\mathrm{WO}_3)\rightarrow e^{-}(\mathrm{PE})\tag{8.113}$$

Overall discharging (Fig. 8.9)

$$\frac{1}{x}\{\mathrm{WO}_3^{x-}:x\mathrm{Li}^{+}\}+\frac{1}{2}\mathrm{I}_3^{-}(\mathrm{EL})\xrightarrow{I\cdot R_{\mathrm{ext}}}\frac{1}{x}\mathrm{WO}_3+\mathrm{Li}^{+}\tag{8.113}$$

with $e^-(PE)$ designating electrons at the conductive support of the dye/TiO_2/WO_3 composite electrode undergoing irradiation during photocharging but kept in the dark during discharging. No auxiliary electrode is needed for the discharge reaction.

This electrochemical cell can also work as electrochromic device, in which case, the cell is short-circuited upon discharge, as described by Hauch et al. [20, 21] and recently by Bella et al. [22] with a sufficiently thin, transparent WO_3 substrate.

The systems described up to the present involve light input as the sole source of energy in the photocharging process. As a result, the cell potential available upon discharge is rather low, below 1 V. However it is possible to use light simultaneously with an applied electrical potential bias U_{bias} in order to partially cover the energy required in the charging process. Such a system coupling a dye-sensitized PE in contact with I^-/I_3^- to a lithium metal electrode is described by Wu et al. [23] as depicted in Fig. 8.10; both electrodes are immersed in aqueous solutions. The initial charging potential required for this Li-I battery is 3.6 V with two dark electrodes as compared to 2.9 V with a Li electrode coupled to a dye-sensitized photoelectrode.

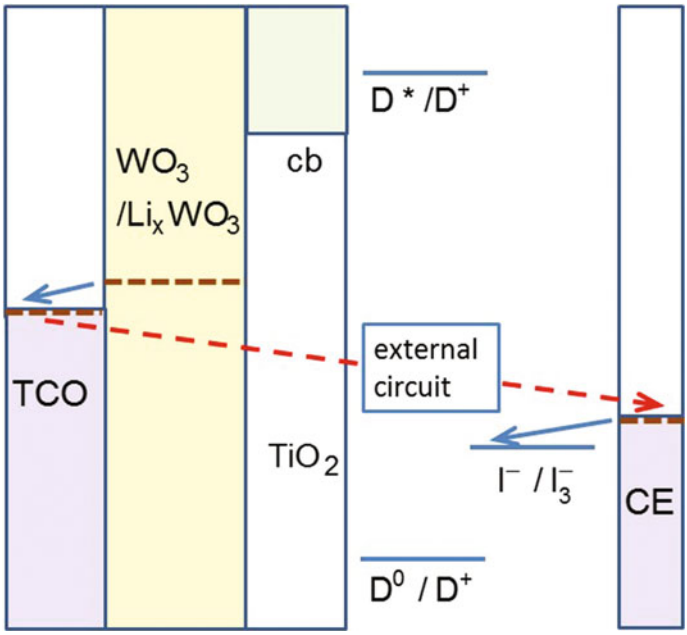

Fig. 8.9 Energy diagram for a photobattery with both a liquid electrolyte-dissolved redox mediator and a solid reversible redox material interacting with the dye/TiO_2 photoelectrode, as described by Hauch and Georg [19]. Discharging mode

The photocharging and dark discharging processes are formulated as following:

(a) Photocharging

$$\frac{3}{2}\mathrm{I}^-(\mathrm{PE}) \xrightarrow{h\nu} \frac{1}{2}\mathrm{I}_3^-(\mathrm{PE}) + e^-(\mathrm{PE}) \tag{8.114}$$

$$\mathrm{Li}^+ + e^-(\mathrm{CE}) \rightarrow \mathrm{Li} \tag{8.115}$$

$$e^-(\mathrm{PE}) \xrightarrow{U_{\mathrm{bias}}} e^-(\mathrm{CE}) \tag{8.116}$$

Overall photocharging

$$\frac{3}{2}\mathrm{I}^-(\mathrm{PE}) + \mathrm{Li}^+ \xrightarrow{h\nu, U_{\mathrm{bias}}} \frac{1}{2}\mathrm{I}_3^-(\mathrm{PE}) + \mathrm{Li} \tag{8.117}$$

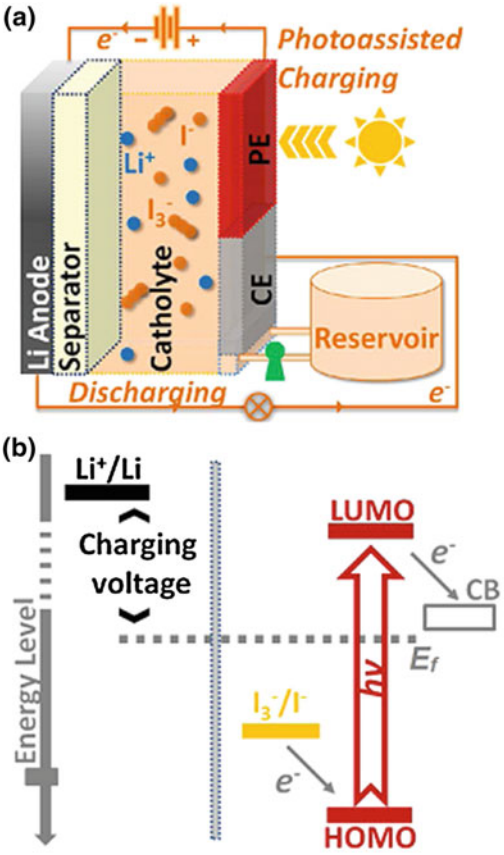

Fig. 8.10 Photobattery with Li cathode charged under auxiliary bias. Adopted by permission from Ref. [23]. Copyright (2015) American Chemical Society

(c)

Photoelectrode - Catholyte:

$$Dye + h\nu \rightarrow Dye^{*} \quad (1)$$

$$TiO_2 + Dye^{*} \rightarrow TiO_2\text{-}e^{-} + Dye^{+} \quad (2)$$

$$3I^{-} + 2Dye^{+} \rightarrow I_3^{-} + 2Dye \quad (3)$$

Anode:

$$Li^{+} + e^{-} \rightarrow Li \quad (4)$$

(b) Dark discharging

$$\frac{1}{2}\mathrm{I}_3^-(\mathrm{AE}) + e^-(\mathrm{AE}) \rightarrow \frac{3}{2}\mathrm{I}^-(\mathrm{AE}) \tag{8.118}$$

$$\mathrm{Li} \rightarrow \mathrm{Li}^+ + \mathrm{e}^-(\mathrm{CE}) \tag{8.119}$$

$$e^-(\mathrm{CE}) \xrightarrow{I \cdot R_{ext}} e^-(\mathrm{AE})$$

$$\mathrm{Li} \rightarrow \mathrm{Li}^+ + \mathrm{e}^-(\mathrm{CE}) \tag{8.120}$$

Overall discharging

$$\frac{1}{2}\mathrm{I}_3^-(\mathrm{AE}) + \mathrm{Li} \xrightarrow{I \cdot R_{ext}} \frac{3}{2}\mathrm{I}^-(\mathrm{AE}) + \mathrm{Li}^+ \tag{8.121}$$

8.5 Photocapacitors

An alternative possibility of storing the DSSC energy output is by means of electrochemical supercapacitors (ECs). A brief introduction of important EC concepts will be presented here. For a detailed treatment, specialized reviews, e.g. these by Winter and Brodd [24], Trasatti and Kurzweil [25], Zhang et al. [26, 27], Simon and Gogotsi [28], Daffos et al. [29], Frackowiak and Beguin [30], and Chen et al. [31] and specialized monographs, e.g., these by Conway [32] and Beguin and Frackowiak [33] can be consulted. A concise introduction to the properties of the electrochemical double layer is provided in the textbook by Bard and Faulkner [34]. The fact that ECs can operate under variable potential is an advantage for them over batteries for solar energy storage; ECs are better adapter to fluctuating irradiation. An additional advantage of ECs for solar applications is that fact that several ECs, for example ECs with carbon electrodes, are more stable upon repeated charge–discharge cycling than batteries, by several orders of magnitude; one million cycles of stable behaviour have been achieved for some capacitor types versus one thousand cycles for the best of batteries.

The differential capacitance across a device consisting of plates 1 and 2 is defined as

$$C = \frac{dQ_1}{dU_{12}}, \tag{8.122}$$

where U_{12} is the voltage applied between 1 and 2, defined in terms of the electrical potential φ as

$$U_{12} = \varphi_1 - \varphi_2 \tag{8.123}$$

and dQ_1 is the incremental charge applied to plate 1. Quite often, but not necessarily, Q denotes the charge as the positive plate of the capacitor. Consider the case of a voltage-independent capacitance. In this case if Q_1 is the charge corresponding to voltage U_{12}, then

$$C = \frac{Q_1}{U_{12}} \tag{8.124}$$

The capacitance is expressed in Farads (F), in terms of the electricity units for charge, coulomb (C), and voltage, volt (V)

$$1\text{F} = \frac{1\text{C}}{1\text{V}} \tag{8.125}$$

In electrochemistry the capacitance per unit area, or specific capacitance per area (C_S), in terms of Fm^{-2} or of related units such as mFcm^{-2} or $\mu\,\text{Fcm}^{-2}$ is often used.

For a planar capacitor the capacitance per unit are is expressed according to the electrostatic theory as

$$C_S = \frac{C}{S} = \frac{\kappa\,\varepsilon_0}{d}, \tag{8.126}$$

where S is the surface area of the capacitor plates, d is the distance between the plates, ε_0 is the vacuum electric permittivity $(8.85 \times 10^{-12}\,\text{Fm}^{-1})$, and κ is the relative electric permittivity or dielectric constant, equal to 1 in vacuum, and approximately in air, and 78 in water at 25 °C. The above equation can be used for approximately estimating C_S if the capacitance is due to double-layer charging effects only and not to redox reactions (see below). However, two facts should be considered. At first, in a real electrochemical interface based on the capacitance of the electrochemical compact double layer (Helmholtz layer) the two-surface planar capacitor is a rough approximation so that d should be seen as an average distance between the charges located in the electronic conductor and these in the electrolyte. Moreover, unlike the traditional capacitor case, d should, in several cases, change with the capacitor voltage, i.e., with the voltage across the double layer. Second, in the double layer the solvent is to some extent immobilized (electrostriction effect), so that κ can be lower than that in the bulk of the electrolyte; for water a value of below 10 should be inserted in the expressions defining the capacitance of the interface.

In electrochemical capacitors the total device capacitance (C_{cell}) is composed of the capacitances of each electrode–electrolyte interface $(C_{\text{el(A)}}, C_{\text{el(B)}})$ in series connection.

$$\frac{1}{C_{\text{cell}}} = \frac{1}{C_{\text{el(A)}}} + \frac{1}{C_{\text{el(B)}}} \tag{8.127}$$

The thickness of such an interface in the presence of concentrated electrolyte solutions can below 1 nm, which is substantial below the thickness of the usual dielectric capacitors (in the μm-range or higher). This explains the interest of supercapacitors for energy storage. A further enhancement of capacitance is expected due to the roughness of the electrode area, with the ratio of real (S_r)-to-geometric (S) surface area, termed roughness factor r, exceeding 1000 in several cases. r is expressed as

$$r = \frac{S_r}{S} \tag{8.128}$$

so that the specific capacitance per area is expressed as

$$\left.\begin{array}{l} \dfrac{C}{S_r} = \dfrac{\kappa\,\varepsilon_0}{d} \\ S_r = rS \end{array}\right\} \Rightarrow C_s = \frac{C}{S} = r\frac{\kappa\,\varepsilon_0}{d} \tag{8.129}$$

For symmetric capacitors, i.e., consisting of the same material at both electrodes (A) and (B), the total capacitance of the cell C_{cell} is expressed in terms of electrode capacitances $C_{\text{el(A)}} = C_{\text{el(B)}} = C_{\text{el}}$

$$C_{\text{cell}} = \frac{C_{\text{el}}}{2} \tag{8.130}$$

There are two basic categories of capacitors; electrochemical double-layer capacitors (EDLCs) and pseudocapacitors. The capacitive charging of the double-layer capacitors is based solely on electrostatic charging of the electronic conductor–electrolyte interface, where the electronic conductor can be a metal or a nonmetallic material of metallic, or approaching metallic, conductivity, such as carbon. No electrochemical reactions take place in this case; such an electrode is termed polarizable electrode. The second category involves redox capacitors or pseudocapacitors, the latter meaning false capacitors, from the Greek word ψεύδος (psévdos), lie. The electrical characteristics (i.e., current potential curves, impedance…) of these capacitors closely resemble these of double-layer capacitors; however the capacitive effect is due to surface-confined electrochemical reactions. The previously mentioned electrode materials tungsten oxide (WO_3) and polypyrrole belong to this category. Other examples of interest to pseudocapacitors are ruthenium oxide (RuO_2), iridium oxide, (IrO_2), and nickel oxide (NiO). Some conducting polymers of interest for capacitors are, in addition to polypyrrole, polyaniline, polythiophene, poly(3, 4-ethylenedioxythiophene) (PEDOT) and poly (3, 4-propylenedioxythiophene) (PProDOT).

However, several pseudocapacitive materials exhibit significant double-layer capacitance, and vice versa. For example, carbons are generally considered as typical double-layer capacitive materials; however, several electroactive groups are present on their surface, e.g., phenolic, carboxylic or o-hydroquinoid groups. In particular, such groups are electroactive in aqueous electrolytes since their redox reactions often involve as reactants or products H_2O, H^+ or OH^-. For a comparison of capacitor materials an important concept is that of specific capacitance per mass $C_{sp,m}$, usually expressed in units of F/g. It is defined for a single electrode–electrolyte interface. Usually materials involving pseudocapacitance have higher $C_{sp,m}$ than these based on double-layer capacitance. For RuO_2-based ECs $C_{sp,m}$ values in the range of 1000–2000 F/g have been measured. For carbon-based, (mostly) EDLC capacitors $C_{sp,m}$ lies in the range 100–300 F/g. Moreover, hybrid materials based on mixing carbon and redox materials, for example, RuO_2, MnO_2, polypyrrole and polyaniline, have been extensively investigated for EC appications.

The specific capacitance $C_{sp,m}$ is related to the specific volume of the material $V_{sp,m}$ per mass unit, defined as the real volume per mass unit. For porous materials, including mesoporous (nanostructured) materials, $V_{sp,m}$ values exceeding $10^7\ cm^2/g$ have been achieved. The importance of $V_{sp,m}$ to ECs is comparable to that in DSSCs, where the introduction of high-surface area oxides as dye supports has revolutionized the photoelectrochemical field. The roughness factor is related to $C_{sp,m}$, $V_{sp,m}$ and the mass m of material deposited on the electrode as following:

$$\left.\begin{aligned} r &= \frac{S_r}{S} \\ S_r &= mV_{sp} \end{aligned}\right\} \Rightarrow r = \frac{m}{S}V_{sp} \tag{8.131}$$

with m/S usually in the order of 1–10 $mgcm^{-2}$, determined by the mechanical stability of the material, the electronic conductivity of the solid material, and the ionic conductivity of the electrolyte penetrating the pores.

However, it should be noted that the V_{sp} should include only the area of the pores which are accessible to the electrolyte, to the exclusion of too narrow micropores (usually below 2 nm—the threshold depending on the electrolyte composition).

Electrochemical capacitors present the disadvantage of a lower energy density, on a mass or volume basis, compared to batteries. However they exhibit higher power densities that have to be preferred for applications in which the supply of a relatively small amount of energy in a short time is desired, as, for example, in the case of starting a motor vehicle.

If Q is the charge on the plates, the energy stored is equal to

$$\text{Energy}_{cap} = \frac{1}{2}QU_{cap} = \frac{1}{2}CU_{cap}^2 = \frac{1}{2}\frac{Q^2}{C} \tag{8.132}$$

In comparison, the case of connecting of a battery to a solar cell will be briefly considered. Assume an idealized situation in which the battery operates reversibly, without ohmic and electrochemical overpotential losses, and that its electromotive

force U_{bat} is equal to the dye solar cell voltage at the maximum power point $U_{DSSC(mpp)}$. In this case, upon connection of a solar cell to an initially discharged battery, 100% of the solar cell output is be stored. In case of difference between U_{bat} and $U_{DSSC(mpp)}$, a number of batteries n_{bat} can be serially connected to a number of solar cells n_{s-cell} so that

$$n_{bat}U_{bat} \approx n_{s-cell}U_{DSSC(mpp)} \tag{8.133}$$

If charge Q has been introduced into the battery, the theoretical amount of stored energy is

$$\text{Energy}_{bat} = Q \cdot U_{bat} \tag{8.134}$$

The first systematic work on hybrid DSSC-EC systems, or photocapacitors (PCAPs) was published by Miyasaka and coworkers in a series of publications [35–37], to which the critical comment by Acevedo [38] and the response by Miyasaka and Murakami [39] should be included.

The first- and simpler system of interest was that of the two-electrode photocapacitor [35, 40] depicted in Fig. 8.11a. In the work of Miyasaka et al. [35] the PCAP configuration included a solid hole-transport material (HTM), LiI_3/LiI, with both redox forms initially present. Onto the HTM layer an additional layer of EC material $(CAP_{(1)})$, activated carbon (AC), was superposed. This composite

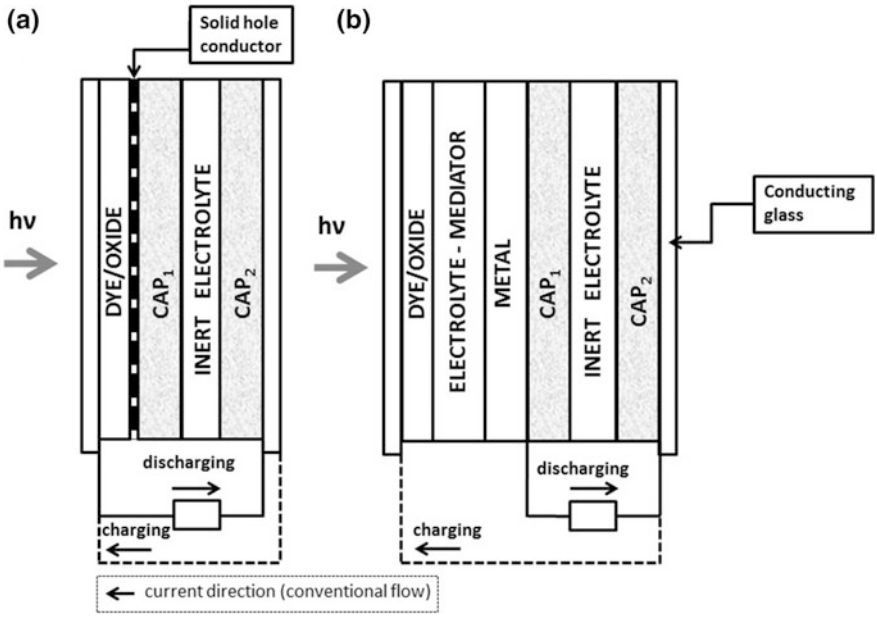

Fig. 8.11 Two (**a**) and three (**b**)-electrode photocapacitors

$CAP_{(1)}/HTM/dye/TiO_2$ PE was separated from an AC layer ($CAP_{(2)}$), designated as CE, by an inert electrolyte; the two layers $CAP_{(1)}$ and $CAP_{(2)}$ constitute a symmetric EC within the PCAP. A similar system was investigated by Skunik et al. [40] in which the EC material was a PEDOT-carbon nanotube composite. Upon photocharging, PE and CE were short-circuited. Holes were injected from the photoexcited dye into HT and then into $CAP^0_{(1)}$, imparting to it positive charge ($CAP^+_{(1)}$). Photoinjected electrons were ultimately driven through the external circuit to $CAP^0_{(2)}$ at the CE, imparting to it negative charge ($CAP^-_{(2)}$). Upon dark discharging, an external load was connected between PE and CE. Electrons were transferred from $CAP^-_{(2)}$ at the CE through the external circuit, the TCO support plate and the TiO_2 layer to $CAP^+_{(1)}$ so that the initial forms of the EC materials were recovered.

In the following part of this section M^0/M^+ denote the oxidized and reduced forms of either a solid HTM or of a redox mediator in a liquid electrolyte, so that the equations of this and the previous section can be compared. Therefore the photocharging and discharging cycles are as following:

(a) Photocharging

$$M^0 \xrightarrow{hv} M^+(PE) + e^-(PE) \tag{8.135}$$

$$M^+(PE) + CAP_{(1)}(PE) \rightarrow CAP^+_{(1)}(PE) + M(PE) \tag{8.136}$$

Overall half-reaction at the PE

$$CAP^0_{(1)}(PE) \xrightarrow{hv} CAP^+_{(1)}(PE) + e^-(PE) \tag{8.137}$$

External circuit upon photocharging

$$e^-(PE) \xrightarrow{R_{ext}=0} e^-(CE) \tag{8.138}$$

Counter electrode upon photocharging

$$e^-(CE) + CAP^0_{(2)}(CE) \rightarrow CAP^-_{(2)}(CE) \tag{8.139}$$

Overall cell reaction upon photocharging

$$CAP^0_{(1)}(PE) + CAP^0_{(2)}(CE) \xrightarrow{hv} CAP^+_{(1)}(PE) + CAP^-_{(2)}(CE) \tag{8.140}$$

(b) Dark discharging at the dye-coated electrode

$$\mathrm{CAP}^{+}_{(1)}(\mathrm{PE}) + \mathrm{M}^{0}(\mathrm{PE}) \rightarrow \mathrm{CAP}^{0}_{(1)}(\mathrm{PE}) + \mathrm{M}^{+}(\mathrm{PE}) \tag{8.141}$$

$$\mathrm{M}^{+}(\mathrm{PE}) + e^{-}(\mathrm{PE}) \rightarrow \mathrm{M}^{0}(\mathrm{PE}) \tag{8.142}$$

Total reaction at the dye-coated semiconductor electrode in the dark

$$\mathrm{CAP}^{+}_{(1)}(\mathrm{PE}) + e^{-}(\mathrm{PE}) \rightarrow \mathrm{CAP}^{0}_{(1)}(\mathrm{PE}) \tag{8.143}$$

Counter electrode reaction upon discharging

$$\mathrm{CAP}^{-}_{(2)}(\mathrm{CE}) \rightarrow \mathrm{CAP}^{0}_{(2)}(\mathrm{CE}) + e^{-}(\mathrm{CE}) \tag{8.144}$$

External circuit upon discharging

$$e^{-}(\mathrm{CE}) \xrightarrow{I \cdot R_{\mathrm{ext}}} e^{-}(\mathrm{PE}) \tag{8.145}$$

Overall discharging reaction

$$\mathrm{CAP}^{+}_{(1)}(\mathrm{PE}) + \mathrm{CAP}^{-}_{(2)}(\mathrm{CE}) \xrightarrow{I \cdot R_{\mathrm{ext}}} \mathrm{CAP}^{0}_{(1)}(\mathrm{PE}) + \mathrm{CAP}^{0}_{(2)}(\mathrm{CE}) \tag{8.146}$$

There are two disadvantages of the present system. One concerns the substantial overpotential for the reduction of M^{+} at the PE upon discharge. For $\mathrm{I}_3^{-}/\mathrm{I}^{-}$ as $\mathrm{M}^{+}/\mathrm{M}^{0}$ the electrochemical reduction is sluggish, at both the TCO sites exposed to M^{+} and the TiO_2/HTM interface.

In the case of other, kinetically faster M^{+} species, the reaction is sluggish due to the precautions taken in order to decrease the M^{+} reduction at the illumination step, including the insertion of an underlayer between TCO and TiO_2 and the attachment of recombination-blocking groups at the dye, as previously explained. Therefore, precautionary measures which are beneficial to recombination suppression upon irradiation are detrimental to the dark discharge operation and, as a result, the amount of power ultimately recovered is seriously diminished.

Moreover, there is a possibility that the inert electrolyte between $\mathrm{CAP}_{(1)}$ and $\mathrm{CAP}_{(2)}$ leaks through the $\mathrm{CAP}_{(1)}$ layer into the HTM layer and cause its partial dissolution so that, upon photocharging, charge leaks between $\mathrm{CAP}_{(1)}$ and $\mathrm{CAP}_{(2)}$. Consequently, the PCAP operation is impeded [40]. Upon photocharging, the PCAP will in fact operate as a short-circuited DSSC.

Therefore, the three-electrode PCAP (Fig. 8.11b), with an intermediate electrode (IE) between PE and CE, as in the case of the auxiliary electrode in several photobattery designs, is more promising and has been further exploited by several groups. [36–39, 41–46]. This design is somewhat analogous to that of a photobattery design with an auxiliary electrode, as in Figs. 8.4 and 8.5. The IE side

facing the PE (IE-PE) acts as counter electrode for the DSSC part of the PCAP, being separated from the PE by the M^0/M^+-containing layer. The other side the IE faces the CE of the PCAP (IE-CE) and is covered by a charge-storage $CAP_{(1)}$ layer. The CE is coated by a charge-storage layer, $CAP_{(2)}$, and is separated from the $CAP_{(1)}$ by an inert electrolyte layer.

Therefore, the PCAP device configuration is as

$$\mathrm{TCO}\,/\,\mathrm{TiO_2(dye)}\,/\,(\mathrm{M^0},\mathrm{M^+})/\,\mathrm{IE}\,/\,\mathrm{CAP_{(1)}}/\,\mathrm{EL}\,/\,\mathrm{CAP_{(2)}} \tag{8.147}$$

with EL denoting the inert capacitor electrolyte, or, by considering the separate DSSC and EC parts,

$$\underbrace{\mathrm{TCO}\,/\,\mathrm{TiO_2(dye)}\,/\,(\mathrm{M^0},\mathrm{M^+})\,/\,(\text{IE-PE})}_{\text{DSSC}}-\underbrace{(\text{IE-CE})/\,\mathrm{CAP_{(1)}}\,/\,\mathrm{EL}\,/\,\mathrm{CAP_{(2)}}}_{\text{EC}} \tag{8.148}$$

As regards the separate photocharging and dark discharging stages the connections to the external circuit are as following.

$$\underbrace{\mathrm{TCO}\,/\,\mathrm{TiO_2}\text{ - dye}\,/\,(\mathrm{M^0},\mathrm{M^+})\,/\,(\text{IE-PE})}_{\text{light on}}\;-\;\overbrace{(\text{IE-CE})/\,\mathrm{CAP_{(1)}}\,/\,\mathrm{EL}\,/\,\mathrm{CAP_{(2)}}}^{\text{light off}}. \tag{8.149}$$

Upon charging, M^0 is oxidized to M^+ which, as in the normal DSSC operation, is reduced back to M^0 at the IE-PE. However, the difference with the normal DSSC situation lies in the fact that, instead of the electrons to the arriving from the PE, through an external circuit containing a load, to the CE, they are transferred through a short circuit from the PE to the $CAP_{(1)}$ layer at the opposite side of the IE.

Therefore, if e^-(IE-PE) and e^-(IE-PE) denote electrons at the IE just opposite the PE and the CE, the IE operation upon photocharging can be expressed as

$$\mathrm{CAP^0_{(1)}} \rightarrow \mathrm{CAP^+_{(1)}} + e^-(\text{IE-CE}). \tag{8.150}$$

$$e^-(\text{IE-CE}) \rightarrow e^-(\text{IE-PE}). \tag{8.151}$$

$$\mathrm{M^+} + e^-(\text{IE-PE}) \rightarrow \mathrm{M^0}. \tag{8.152}$$

Overall reaction at IE upon photocharging

$$\mathrm{CAP^0_{(1)}} + \mathrm{M^+} \rightarrow \mathrm{CAP^+_{(1)}} + \mathrm{M^0}. \tag{8.153}$$

Upon discharge, the PE is disconnected from the external circuit; IE and CE are connected by an external load so that the capacitor constituted of IE-CE and CE is discharged.

Therefore, the photocharging and dark discharging half-cycles are as following:

(a) Photocharging

$$M^0 \xrightarrow{h\nu} M^+ + e^-(\text{PE}) \tag{8.154}$$

$$\text{CAP}_1^0 + M^+ \rightarrow \text{CAP}_1^+ + M^0 \tag{8.155}$$

$$e^-(\text{CE}) + \text{CAP}_2^0 \rightarrow \text{CAP}_2^- \tag{8.156}$$

$$e^-(\text{PE}) \xrightarrow{R_{\text{ext}}=0} e^-(\text{CE}) \tag{8.157}$$

Overall photocharging

$$\text{CAP}_1^0(\text{IE}) + \text{CAP}_2^0(\text{PE}) \xrightarrow{h\nu} \text{CAP}_1^+(\text{PE}) + \text{CAP}_2^-(\text{CE}) \tag{8.158}$$

(b) Discharging

$$\text{CAP}_1^+ + e^-(\text{IE-CE}) \rightarrow \text{CAP}_1^0 \tag{8.159}$$

$$\text{CAP}_2^- \rightarrow \text{CAP}_2^0 + e^-(\text{CE}) \tag{8.160}$$

$$e^-(\text{CE}) \xrightarrow{I \cdot R_{\text{ext}}} e^-(\text{IE-CE}) \tag{8.161}$$

Overall operation upon discharging

$$\text{CAP}_1^+(\text{IE}) + \text{CAP}_2^-(\text{CE}) \xrightarrow{I \cdot R_{\text{ext}}} \text{CAP}_1^0(\text{IE}) + \text{CAP}_2^-(\text{CE}) \tag{8.162}$$

The radiant-to-electrical energy conversion efficiency is expressed as

$$\begin{aligned} \eta_{h\nu-el} &= -\left(\int_{q_{\text{dch}}}^{0} U(t)\, dq \right) / P_{\text{in}}\, t_{\text{irr}} = -\left(\int_{0}^{t_{\text{dch}}} U(t) I(t) dt \right) / P_{\text{in}}\, t_{\text{irr}} \\ &= -\left(\int_{U_{\text{dch}}}^{0} C U(t) dU(t) \right) / P_{\text{in}}\, t_{\text{irr}}, \end{aligned} \tag{8.163}$$

where the discharge continues for time t_{dch} until $U = 0$. U_{dsch} is the initial capacitor voltage just before discharge, q_{dch} is the initial charge at the positive capacitor electrode, $U(t)$ is the capacitor voltage upon discharging, and $I(t)$ is the discharging current from the initially positive plate $(I(t) < 0)$.

For the simpler case of constant capacitance

$$\eta_{hv-el} = \frac{\left(\frac{1}{2} C^2 \cdot U_{\mathrm{dch}}\right)}{P_{\mathrm{in}} \cdot t_{\mathrm{irr}}} \tag{8.164}$$

Quite often discharging measurements are performed at constant current I from the positive to the negative EC electrode (in the present case IE-CE and CE, respectively) t, $(I = -|I|)$, in which case, for constant C, the voltage versus time is expressed as

$$U(t) = U_{\mathrm{dch}} - \frac{|I|}{C} t \tag{8.165}$$

so that C can be determined from the slope of U versus t.

If the capacitor is self-discharging, due to Faradaic side-reactions or ion rearrangement at the electrode interfaces, then the voltage at the end of the photocharging step U_{ch} is higher than U_{dsch}, the difference depending on the resting time between photocharging and discharging. Similarly, the magnitude of the photocharge (q_{ch}) is higher than the charge delivered upon discharging (q_{dch}). In this case the concept of coulombic efficiency (CE) is of interest, defined as

$$CE = 100 \cdot \frac{q_{\mathrm{dch}}}{q_{\mathrm{ch}}} \tag{8.166}$$

The initial three-electrode PCAP work by Miyasaka and coworkers [36–39] involved a liquid electrolyte-based DSC, with on a ruthenium coordination complex-type sensitizer and I_3^-/I^- as M^+/M^0 in an organic solvent. The IE-CE symmetric capacitor system was based on AC layers, with a liquid inert organic electrolyte, the same as in their two-electrode PCAP. U_{dsch} was 0.8 V, favorably compared with that obtained for their two-electrode capacitor, below 0.4 V. On the basis of their published data η_{hv-el} for the three-electrode PCAP was below 0.4%.

Ho and coworkers in two publications describe a photocapacitor system composed of a DSSC with a Ru dye and an organic I_3^-/I^--based electrolyte coupled to a symmetric capacitor based on a conducting polymer, PEDOT [41] or PproDOT [42], with a liquid inert electrolyte. For 100% sunlight they obtained U_{dch} in the range 0.7–0.9 V and $\eta_{hv-\mathrm{el}}$ below 0.5%. Furthermore, CE was below 50%.

A photocapacitor based on both a solid-state DSSC and a solid-state capacitor was investigated by Kulesza, Hagfeldt, and coworkers [43, 44]. In the DSSC the sensitizer was an organic-metal-free, charge-transfer dye, and the HTM was the conducting polymer poly-(3-hexylthiophene) (P3HT). A symmetric high-performance RuO_2/carbon pseudocapacitor was superposed on top of the CE

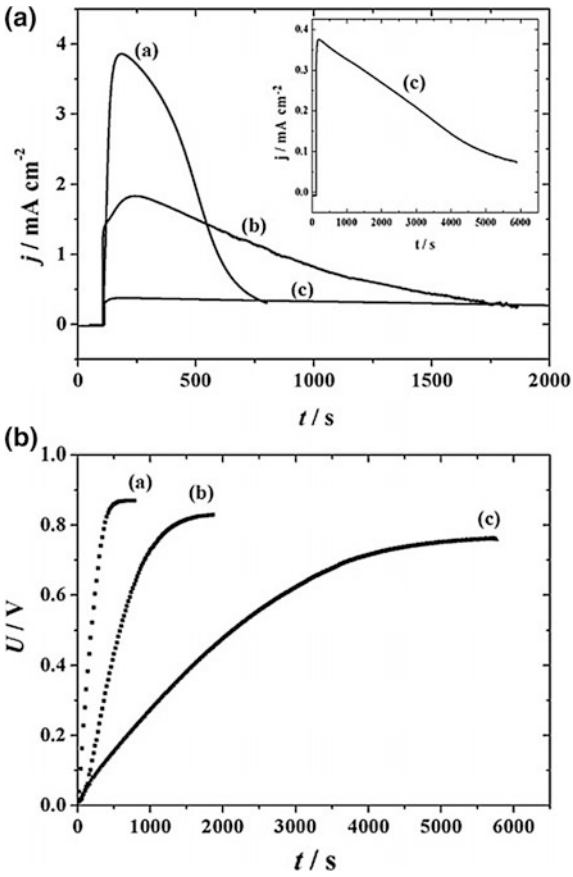

Fig. 8.12 Current (**a**) and voltage (**b**) of photocapacitor upon photocharging with (*a*) 100% (*b*) 50% and (*c*) 10% simulated sunlight. Photocapacitor with organic dye/P3HT/Ag DSSC coupled to a RuO_2-based capacitor. Illumination with (*a*) 100% (*b*) 50% and (*c*) 10% simulated sunlight. *Inset* of (**a**) charging time 6000 s. Adopted with permission from [43]. Copyright (2013) Elsevier

of the DSSC. The electrolyte was Nafion®, a proton-conducting polymer electrolyte membrane. Upon 100% sunlight irradiation the U_{dsch} exceeded 0.8 V, with the *CE* approaching 90% and the $\eta_{h\nu-el}$ was 0.8%. For this system the variation of photocharging current and potential for three light intensity values is shown in Fig. 8.12. Figure 8.13 depicts constant-current discharge curves corresponding either to different currents after 100% sunlight charging or to a fixed discharge current following photocharging with three different light intensities.

An alternative system consisting of a liquid electrolyte DSSC coupled to an asymmetric capacitor, with cobalt-doped nickel oxide (Ni(Co)O) at the positive electrode and activated carbon (AC) at the negative electrode, as depicted in Fig. 8.14, was studied by Bagheri et al. [45]. The DSSC, of a recently developed conception, was based on a metal-free organic charge-transfer dye coupled to a Co (II/III) polypyridyl redox mediator in a liquid organic solvent. The CE of the DSSC/IE of the PCAP was a PEDOT layer, with electrocatalytic properties toward the cobalt redox mediator, deposited onto a nickel foil, the opposite side of which as covered by the capacitive Ni(Co)O layer. The opposite AC capacitive layer was

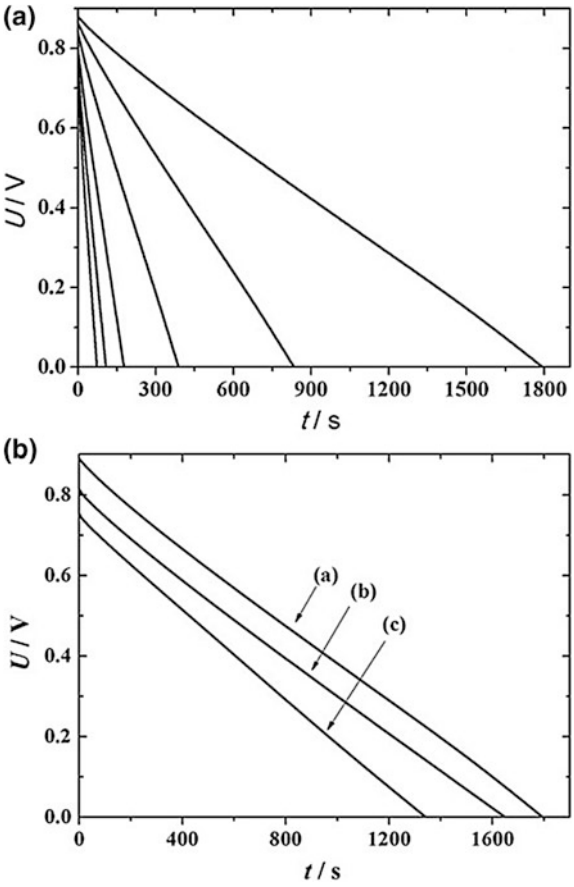

Fig. 8.13 Discharging of photocapacitor with DSSC composed of organic dye/P3HT/Ag DSSC coupled to a RuO_2-based capacitor, at constant current. **a** The capacitor was previously photocharged under 100% simulated sunlight. Current density, from left to right, 0.8, 1.6, 3.2, 6.4, 9.6 and 12.8 $mAcm^{-2}$. **b** Discharge under 0.8 $mAcm^{-2}$ of a capacitor previously photocharged under (*a*) 100% (*b*) 50% and (*c*) 10% simulated sunlight. Adapted by permission from [43]. Copyright (2013 Elsevier

separated from Ni(CO)O by an aqueous KOH electrolyte. Upon 100% sunlight the values of $U_{\text{dsch}} = 0.8\,\text{V}$, $CE = 54\%$ and $\eta_{hv-el} = 0.6\%$ were attained.

A PCAP system of a different configuration based on anodic titanium oxide (ATO) nanotube layers as both dye support in the DSSC part and charge-storage material of the EC was developed by Xu et al. [46]. The DSSC was based to the classical design with a Ru coordination dye and an organic I_3^-/I^- electrolyte. The ATO material used for the capacitor was hydrogenated (H-ATO) in order to enhance the specific capacitance. The PCAP configuration was somewhat different that that described before. The terminal electrodes were a Pt-coated TCO glass plate $(TCO_{(1,Pt)})$, acting as CE for the DSSC component, and a TCO plate covered by ATO-H $(TCO_{(2)})$ and acting as the positive plate of the EC component. The IE consists of a Ti plate coated on the one side by the dye/ATO PE and on the other side by ATO-H, the latter acting as the negative plate of the EC component. Light impinges on the $TCO_{(1,Pt)}$ electrode and traverses the mediator-containing electrolyte before reaching the dye/ATO layer. The PCAP is configured as

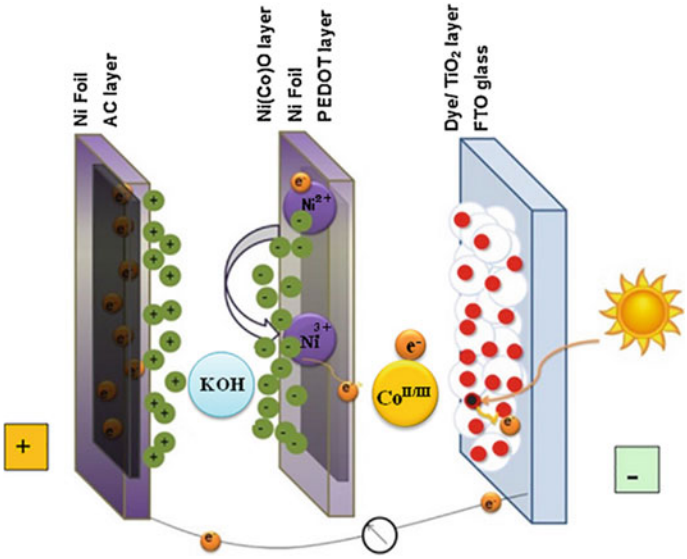

Fig. 8.14 Photocapacitor based on the superposition of a DSSC, the electrolyte of which contains a cobalt coordination complex as redox mediator, and an asymmetric nickel oxide-activated carbon supercapacitor. Adopted by permission from [45]. Copyright (2014) Elsevier

$$\mathrm{TCO_{(1,Pt)}\,/\,(M^0,M^+)/\overbrace{dye/ATO/Ti/H\text{-}ATO_{(1)}}^{IE}\,/\,EL\,/H\text{-}ATO_{(2)}/TCO_{(2)}} \tag{8.167}$$

where M^0/M^+ is I^-/I_3^- in a liquid electrolyte, $CAP_{(1)}$ and $CAP_{(2)}$ are both identical ATO-H capacitor electrodes, and EL the inert electrolyte between the capacitive electrodes. By considering the separate DSSC and EC parts the above cell configuration is written as

$$\underbrace{\mathrm{TCO_{(1,Pt)}/(M^0,M^+)/dye/ATO/}}_{\text{DSSC}}\,\mathrm{Ti/}\underbrace{\mathrm{H\text{-}ATO_{(1)}/EL/H\text{-}ATO_{(2)}/TCO_{(2)}}}_{\text{EC}} \tag{8.168}$$

With respect to the separate photocharging and dark discharging stages, the cell connection is

$$\underbrace{\mathrm{TCO_{(1,Pt)}\,/\,(M^0,M^+)/dye/ATO/}\overbrace{\mathrm{Ti/H\text{-}ATO_{(1)}/EL/H\text{-}ATO_{(2)}/TCO_{(2)}}}^{\text{light off}}}_{\text{light on},R_{ext}=0} \tag{8.169}$$

As in the previously considered scheme, upon irradiation the terminal electrodes are short-circuited. Upon discharge, $TCO_{(1)}$(Pt) is disconnected; IE and $TCO_{(2)}$ are attached to the external load.

The separate photocharging and dark discharging stages are as following:

(a) Photocharging

Intermediate electrode

$$M^0 \xrightarrow{h\nu} M^+ + e^-(\text{ATO}) \tag{8.171}$$

$$e^-(\text{ATO}) \rightarrow e^-(\text{Ti}) \tag{8.171}$$

$$e^-(\text{Ti}) + \text{H-ATO}^0_{(1)} \rightarrow \text{H-ATO}^-_{(1)} \tag{8.172}$$

Overall intermediate electrode reaction upon photocharging

$$M^0 + \text{H-ATO}^0_{(1)} \xrightarrow{h\nu} M^+ + \text{H-ATO}^-_{(1)} \tag{8.173}$$

Reaction at platinized TCO electrode (left)

$$M^+ + e^-(\text{TCO}_{(1,\text{Pt})}) \rightarrow M \tag{8.174}$$

Reaction at H-ATO/TCO electrode (right)

$$\text{H-ATO}^0_{(2)} \rightarrow \text{H-ATO}^+_{(2)} + e^-(\text{TCO}_{(2)}) \tag{8.175}$$

External circuit

$$e^-(\text{TCO}_{(2)}) \xrightarrow{R_{\text{ext}}=0} e^-(\text{TCO}_{(1,\text{Pt})}) \tag{8.176}$$

Overall cell reaction upon photocharging

$$(\text{H-ATO})^0_{(1)} + (\text{H-ATO})^0_{(2)} \xrightarrow{h\nu} (\text{H-ATO})^+_{(1)} + (\text{H-ATO})^-_{(2)} \tag{8.177}$$

(b) Discharging

Intermediate electrode

$$\text{H-ATO}^-_{(1)} \rightarrow \text{H-ATO}^0_{(1)} + e^-(\text{ATO}) \tag{8.178}$$

$$e^-(\text{ATO}) \rightarrow e^-(\text{Ti}) \tag{8.179}$$

Overall reaction at intermediate electrode upon discharging

$$\text{H-ATO}^{-}_{(1)} \rightarrow \text{H-ATO}^{0}_{(1)} + e^{-}(\text{Ti}) \tag{8.180}$$

TCO electrode (right)

$$\text{H-ATO}^{+}_{(2)} + e^{-}(\text{TCO}_{(2)}) \rightarrow \text{H-ATO}_{(2)} \tag{8.181}$$

External circuit

$$e^{-}(\text{Ti}) \xrightarrow{IR_{\text{ext}}} e^{-}(\text{TCO}_{(2)}) \tag{8.182}$$

Overall cell reaction upon discharging

$$\text{H-ATO}^{+}_{(1)} + \text{H-ATO}^{-}_{(2)} \rightarrow \text{H-ATO}^{0}_{(1)} + \text{H-ATO}^{0}_{(2)} \tag{8.183}$$

For this system $U_{\text{dsch}} = 0.8\,\text{V}$ and $\eta_{hv-el} = 0.6\%$.

Finally, PCAP systems based on organohalide lead perovskite PEs (PSCs) are of actual interest, taking profit of the rapid development of perovskite solar cells in the last 5 years, with solar energy efficiencies higher than 20% being attained by several research groups. Since the open-circuit voltage of PSCs, routinely exceeding 1 V, is in general higher than that of most DSSCs, higher U_{dsch} values are expected for PSC-based PCAPs as well in comparison to DSSC-based PCAPs.

Such a system was recently developed by Zhou et al. [47] incorporating a PSC with spiro-OMeTAD as HTM coupled to either a symmetric WO_3/EL/WO_3 or an asymmetric WO_3/EL/MoO_3 capacitor, with EL being an aqueous gel-like electrolyte based on polyvinyl alcohol (PVA) and H_2SO_4. The operation principles are the same than for the DSSC-based photocapacitors and will not be reported here in detail. These PCAPs were used as electrochromic devices, termed by the authors as "perovskite photovoltachromic supercapacitors". Both configurations with the PE positioned either as terminal electrode, or at the intermediate electrode, were considered. A U_{dsch} of around 1.0 V was attained.

8.6 Concluding Remarks

The storage of solar energy is a challenging task. In addition to the evident choice of connecting a solar cell to an electrochemical energy storage cell, such as a battery, an electrochemical capacitor (EC) or an electrolysis cell, the option of an integrated device incorporating both a solar cell and a battery or capacitor is of interest. In this review emphasis was given to the dye-sensitized solar cell (DSSC) as light-harvesting unit. In the case of photobatteries, the challenge is to energetically match the Fermi levels of two redox systems to the energy levels of the

dye/oxide support. For a stand-alone DSSC identifying a charge-transport medium which, in addition to the energy level requirement, fits several other criteria, has been proven an uphill undertaking. Introducing two charge-transport media in a DSSC-based photobattery is even more challenging. In addition, a provision should be taken to store a substantial amount of chemical energy, so that cell designs different from the usual DSSC thin-layer cell should be devised, including, in particular, the flow photobattery approach. For photocapacitors, energy level matching is less of a challenge; however, issues related to charge leakage across the capacitor between the charge and discharge steps should be addressed. Moreover, devising suitable configurations for the intermediated electrode separating the DSSC and the electrochemical capacitor subunits of the photocapacitor is an additional requirement. The research results obtained up to the present time for DSSC output storage should be considered as preliminary; however, they pave the way for further development of the science and technology of interfacing electrochemical storage systems not only to DSSCs but also to the newly developed perovskite solar cells, the structure and operation, of which resembles in several aspects that of DSSCs.

References

1. Grätzel M (2001) Photoelectrochemical cells. Nature 414:338–344
2. Hagfeldt A, Boschloo G, Sun L et al (2010) Dye-sensitized solar cells. Chem Rev 110:6595–6663
3. Kalyanasundaram K (2010) Dye-sensitized solar cells. EPFL Press, Lausanne
4. Vlachopoulos N, Zhang J, Hagfeldt A (2015) Dye-sensitized solar cells : new approaches with organic solid-state hole conductors 69:41–51
5. Yu M, McCulloch WD, Huang Z, et al. (2016) Solar-powered electrochemical energy storage: an alternative to solar fuels. J Mater Chem A 0:1–17
6. Ng CH, Lim HN, Hayase S et al (2015) Potential active materials for photo-supercapacitor: a review. J Power Sources 296:169–185
7. Trasatti ST (1986) The absolute electrode potential: an explanatory note (recommendations 1986). Pure Appl Chem 58:955–966
8. Soloveichik GL (2011) Battery technologies for large-scale stationary energy storage. Annu Rev Chem Biomol Eng 2:503–527
9. Soloveichik GL (2015) Flow batteries: current status and trends. Chem Rev 115:11533–11558
10. Yan NF, Li GR, Gao XP (2014) Electroactive organic compounds as anode-active materials for solar rechargeable redox flow battery in dual-phase electrolytes. J Electrochem Soc 161: A736–A741
11. Liu P, Cao YL, Li GR et al (2013) A solar rechargeable flow battery based on photoregeneration of two soluble redox couples. Chemsuschem 6:802–806
12. Yan NF, Li GR, Gao XP (2013) Solar rechargeable redox flow battery based on Li2WO4/LiI couples in dual-phase electrolytes. J Mater Chem A 1:7012–7015
13. Nagai H, Segawa H (2004) Energy-storable dye-sensitized solar cell with a polypyrrole electrode. Chem Commun 10:974–975
14. Saito Y, Ogawa A, Uchida S et al (2010) Energy-storable dye-sensitized solar cells with interdigitated nafion/polypyrrole–Pt comb-like electrodes. Chem Lett 39:488–489

15. Saito Y, Uchida S, Kubo T, Segawa H (2009) Energy-storable dye-sensitized solar cells with tungsten oxide charge-storage electrode. ECS Trans. 27–34
16. Saito Y, Uchida S, Kubo T, Segawa H (2010) Surface-oxidized tungsten for energy-storable dye-sensitized solar cells. Thin Solid Films 518:3033–3036
17. Bechinger C, Ferrere S, Zaban A et al (1996) Photoelectrochromic windows and displays. Nature 383:608–610
18. Pichot F, Gao W, Gregg BA et al (1999) Self-powered electrochromic coatings. Proc SPIE 3788:59–68
19. Hauch A, Georg A, Krašovec UO, Orel B (2002) Photovoltaically self-charging battery. J Electrochem Soc 149:A1208–A1211
20. Hauch A, Georg A, Krašovec UO, Orel B (2002) Comparison of photoelectrochromic devices with different layer configurations. J Electrochem Soc 149:H159–H163
21. Hauch A, Georg A, Baumgärtner S et al (2001) New photoelectrochromic device. Electrochim Acta 46:2131–2136
22. Bella F, Leftheriotis G, Griffini G et al (2016) A new design paradigm for smart windows: photocurable polymers for quasi-solid photoelectrochromic devices with excellent long-term stability under real outdoor operating conditions. Adv Funct Mater 26:1127–1137
23. Yu M, McCulloch WD, Beauchamp DR et al (2015) Aqueous lithium-iodine solar flow battery for the simultaneous conversion and storage of solar energy. J Am Chem Soc 137:8332–8335
24. Winter M, Brodd RJ (2004) What are batteries, fuel cells, and supercapacitors? Chem Rev 104:4245–4270
25. Trasatti S, Kurzweil P (1994) Electrochemical supercapacitors as versatile energy stores. Platin Met Rev 38:46–56
26. Zhang Y, Feng H, Wu X et al (2009) Progress of electrochemical capacitor electrode materials: a review. Int J Hydrogen Energy 34:4889–4899
27. Zhang LL, Zhao XS (2009) Carbon-based materials as supercapacitor electrodes. Chem Soc Rev 38:2520–2531
28. Simon P, Gogotsi Y (2008) Materials for electrochemical capacitors. Nat Mater 7:845–854
29. Daffos B, Taberna P-L, Gogotsi Y, Simon P (2010) Recent advances in understanding the capacitive storage in microporous carbons. Fuel Cells 10:819–824
30. Frackowiak E, Béguin F (2001) Carbon materials for the electrochemical storage of energy in capacitors. Carbon N Y 39:937–950
31. Chen S, Ramachandran R, Mani V, Saraswathi R (2014) Recent advancements in electrode materials for the high- performance electrochemical supercapacitors: a review. Int J Electrochem Sci 9:4072–4085
32. Conway BE (1999) Electrochemical Supercapacitors: Scientific Fundamentals and Technological Applications. Kluwer Academic/Plenum Publishers, New York
33. Béguin F, Frackowiak E (2013) Supercapacitors: Materials, Systems, and Applications. Wiley, Weinheim
34. Bard AL, Faulkner LR (2001) Electrochemical Methods, Fundamentals and Applications, 2nd edn. Wiley, New York
35. Miyasaka T, Murakami TN (2004) The photocapacitor: An efficient self-charging capacitor for direct storage of solar energy. Appl Phys Lett 85:3932–3934
36. Murakami TN, Kawashima N, Miyasaka T (2005) A high-voltage dye-sensitized photocapacitor of a three-electrode system. Chem Commun (Camb) 3346–3348
37. Miyasaka T, Ikeda N, Murakami TN, Teshima K (2007) Light energy conversion and storage with soft carbonaceous materials that solidify mesoscopic electrochemical interfaces. Chem Lett 36:480–487
38. Morales-Acevedo A (2005) The photocapacitor: an efficient self-charging capacitor for direct storage of solar energy. Appl Phys Lett 86:196101–1–196101-2
39. Miyasaka T, Murakami TN (2005) Response to “comment on ‘the photocapacitor: an efficient self-charging capacitor for direct storage of solar energy”. Appl Phys Lett 86:196102-1–196102-2

40. Skunik M, Kulesza PJ, Vlachopoulos N, et al. (2011) Development of hybrid organic-inorganic materials for efficient charging/discharging in electrochemical and photo-electrochemical capacitors. ECS Trans 25:93–102
41. Chen H-W, Hsu C-Y, Chen J-G et al (2010) Plastic dye-sensitized photo-supercapacitor using electrophoretic deposition and compression methods. J Power Sources 195:6225–6231
42. Hsu C-Y, Chen H-W, Lee K-M et al (2010) A dye-sensitized photo-supercapacitor based on PProDOT-Et2 thick films. J Power Sources 195:6232–6238
43. Skunik-Nuckowska M, Grzejszczyk K, Kulesza PJ et al (2013) Integration of solid-state dye-sensitized solar cell with metal oxide charge storage material into photoelectrochemical capacitor. J Power Sources 234:91–99
44. Kulesza PJ, Skunik-Nuckowska M, Grzejszczyk K et al (2013) Development of solid-state photo-supercapacitor by coupling dye-sensitized solar cell utilizing conducting polymer charge relay with proton-conducting membrane based electrochemical capacitor. ECS Trans 50:235–244
45. Bagheri N, Aghaei A, Ghotbi MY et al (2014) Combination of asymmetric supercapacitor utilizing activated carbon and nickel oxide with cobalt polypyridyl-based dye-sensitized solar cell. Electrochim Acta 143:390–397
46. Xu J, Wu H, Lu L, et al. (2014) Integrated photo-supercapacitor based on Bi-polar TiO_2 nanotube arrays with selective one-side plasma-assisted hydrogenation. 24:1840–1846
47. Zhou F, Ren Z, Zhao Y et al (2016) Perovskite photovoltachromic supercapacitor with all-transparent electrodes. ACS Nano 10:5900–5908

Chapter 9
Molecular Solar-Thermal Energy Storage: Molecular Design and Functional Devices

Anders Lennartson and Kasper Moth-Poulsen

Abstract Solar energy is abundant all over the world, but to be useful, the energy received must either be transformed to electricity, heat or latent chemical energy. The latter two options have the advantages that the energy can be stored. In molecular solar-thermal energy storage (MOST), solar energy is stored in chemical bonds; this is achieved using compounds undergoing photoinduced isomerisation to metastable isomers. Using a catalyst, the isomer can be recycled to its original form and the stored energy released as heat. This chapter describes the principles of the MOST concept and goes into details about the most studied MOST systems. The last part of the chapter deals with the integration of MOST systems into operational devices.

Keywords Solar energy storage · Energy storage materials · Molecular solar-thermal · Thermal energy storage · Solar-thermal fuels

9.1 Introduction

There are many approaches to the storage of solar energy, the simplest is probably hot water or molten salt techniques, which albeit scientifically simple, suffer from the fact that the storage medium must be kept well insulated to avoid thermal losses. A further development of this technique is solar driven thermally activated reactions, such as cracking of dicyclopentadiene [1], a topic not discussed in this chapter. In molecular solar-thermal energy storage (Fig. 9.1), a chemical compound undergoes a light-induced chemical reaction to form a metastable product. In contrast to a solar fuel, the storage medium is recycled by passage over a catalyst to regenerate the solar harvesting medium with the evolution of heat. While some very simple inorganic processes, such as the photolysis of nitrosyl chloride [2], have

A. Lennartson · K. Moth-Poulsen (✉)
Department of Chemistry and Chemical Engineering, Chalmers University of Technology, Gothenburg, Sweden
e-mail: kasper.moth-poulsen@chalmers.se

H. Tian et al. (eds.), *Molecular Devices for Solar Energy Conversion and Storage*, Green Chemistry and Sustainable Technology,
https://doi.org/10.1007/978-981-10-5924-7_9

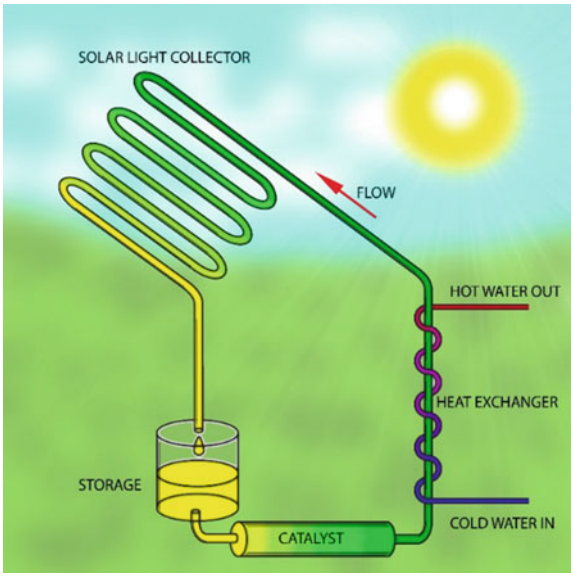

Fig. 9.1 Schematic illustration of the MOST concept

been proposed, the main focus has been on organic compounds that undergo photoinduced isomerisation. This will be the topic of this chapter.

9.2 Background

The first study of the influence of light on a pure chemical compound was the study of silver chloride by the Swedish pharmacist Scheele in *c*. 1768–1770, the results being published in 1777 [3]. Scheele noticed that light could reduce silver chloride to silver, and after splitting a sunbeam with a prism, he found that the reducing ability of light depend on its colour. Violet rays had a greater reducing power than red rays. Scheele's explanation for this observation was that since violet light is slowed down more by passing through a prism than red light, it would have more time to decompose silver chloride than a beam of red light. Scheele extended his photochemical studies to the decomposition of nitric acid [4], a study curtailed by his premature death.

It was Grotthuß who first stated that the light of a certain colour would cause a photochemical reaction (in his case photobleaching) only if that colour corresponded to the absorption of the substance [5]. Further progress in the understanding of photochemical reactions were slow, since it was not until second half of the nineteenth century that the nature of light was more clearly understood. Nevertheless, more examples of photochemical reactions were discovered; for example, the first photochemical study of a pure organic compound was the study of the natural product santonin **1** by Trommsdorff in 1834. Santonin crystals were

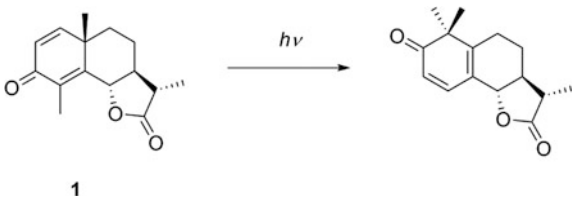

Fig. 9.2 Irreversible photoisomerisation of santonin

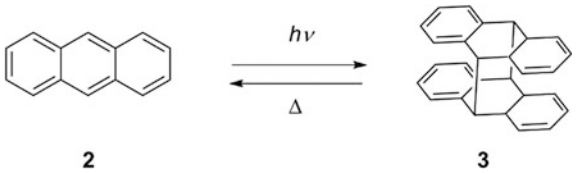

Fig. 9.3 Photoinduced, reversible dimerisation of anthracene

found to turn yellow and burst when exposed to solar light [6], but the underlying process (Fig. 9.2) was not understood until much later [7, 8].

In 1867, Fritzsche reported that irradiation of anthracene solutions with solar light give rise to crystals. These crystals had a higher melting point than anthracene, **2**, but were converted back to anthracene on melting [9]. The explanation was later found to be a light induced, reversible dimerisation of anthracene to obtain dianthracene, **3** (Fig. 9.3). This reaction was studied in detail by Luther and Weigert in the early 1900s [10–12]. Weigert was, for the first time, able to determine the fraction of solar light that could be stored as chemical energy. He irradiated anthracene to dianthracene, and measured the heat released by heating the product in a calorimeter. The conclusion was that 5% of the supplied solar energy could be recovered as heat [13]. He used these results to discuss the efficiency of photosynthesis in green plants, but he also concluded that "[…] at least 5% of the light energy can be artificially converted to useful mechanical work without the use of living green plants. We are still far from achieving this value practically. Here lies a main problem in a future light technology" [14]. This publication, which appeared in a "year book of photography" edited by Edler, can be regarded as the first introduction of the concept of storing solar energy in strained, synthetic molecular compounds.

9.3 The MOST Concept

The term Molecular Solar-Thermal (MOST) energy storage has been introduced for systems like anthracene, where solar energy is stored by reversible molecular rearrangements [15]. The reactant, sometimes referred to as the parent compound, must absorb solar light to form a metastable photoisomer, and this process must be reversible. For an efficient system, a number of criteria have to be met [16, 17]:

(1) The reactant must absorb (or be sensitised to) ultraviolet and visible light.
(2) The photoisomer must not compete with the reactant for the photons, i.e. the reaction must be photochromic. The photoisomer may not quench any sensitiser.
(3) The quantum yield for the process must be high, preferably close to unity even in the presence of oxygen.
(4) The isomerisation must have a high ground state enthalpy.
(5) The molecular weight must be low to achieve a high energy density. As a consequence, for device realisations where the material is to be used as a fluid, both the reactant and photoisomer must be liquid or have high solubilities in common solvents.
(6) The back-reaction must be controlled by heterogenous catalysis with high turnover number and high turnover frequency. This reaction must occur quantitatively.
(7) The barrier for the uncatalysed back-reaction must be high to achieve long storage times.
(8) The materials must be cheap, non-toxic, chemically stable and easy to handle.

The anthracene system appears to have been the only suggestion for storage of solar energy in organic isomers until 1958 when Calvin (shortly after his pioneering study of photosynthesis) noted that irradiation of nitrones **4** formed oxaziridines **5** (Fig. 9.4), and that "this reaction constitutes a conversion and storage of electromagnetic energy as chemical energy" [18]. While some of the studied nitrones absorbed visible light, the corresponding oxaziridines only absorb in the UV region [19]. A drawback of the system is that the compounds are reactive, and some of the oxaziridines decompose rapidly on storage.

Molecular solar-thermal energy storage started to receive more interest in the 1970s, presumably as a consequence of the 1973 oil crisis. As a result, a few new systems were proposed (Fig. 9.4): 3,3-diaryl-isoxanolines **6** [20], *endo*-tricyclo [5.2.1.$0^{2,6}$]deca-4,8-diene-3-one **8** [21] and 1-Ethoxycarbonyl-l*H*-azepine **10** [22], to mention three examples.

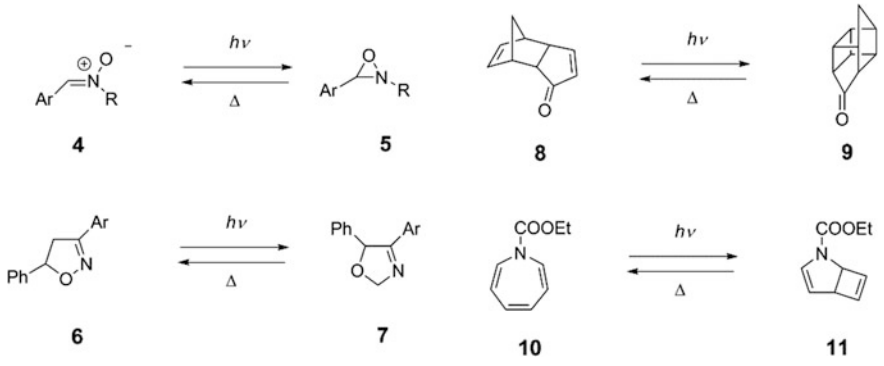

Fig. 9.4 Early proposed systems for storage of solar energy

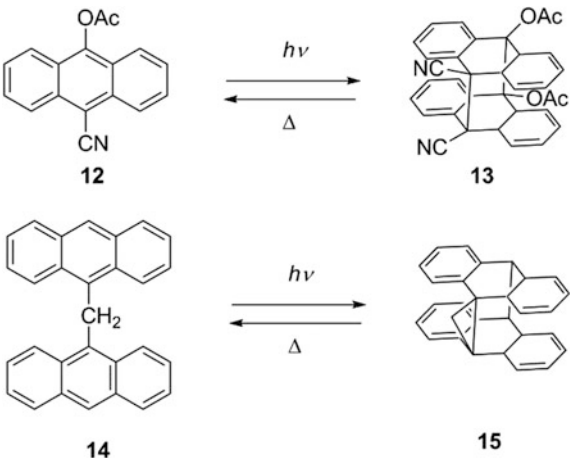

Fig. 9.5 Anthracene derivatives from the study by Jones and co-workers

Another important study was also carried out by Jones et al. to improve the properties of the original anthracene system by chemical means (Fig. 9.5). By functionalising anthracene with electron donating and accepting groups, e.g. **12**, the storage enthalpy could be increased from 64 to 84 kJ mol^{-1} [23]. By linking anthracene units together, they also attempted to solve the concentration dependence of the quantum yield. The quantum yield is approaching 0.3 at high anthracene concentrations, but a slightly higher value, 0.36, was observed for some linked derivatives, e.g. **14** [23]. More recently, the dimerisation of anthracene has been used to construct dynamic polymers [24].

9.4 *Cis-trans* Isomerisation

Light can induce isomerisation of *trans*-alkenes to more strained *cis*-alkenes. This process is similar to what occurs naturally in the rod cells of the eye, where a light sensitive receptor protein, rhodopsin, is responsible for the perception of light. The co-factor of rhodopsin, retinal, is a conjugated alkene that relaxes from its strained *cis*-isomer to the all-*trans* isomer upon irradiation. The conditions for isomerisation of the simples alkenes, such as 1,2-dideuteroethylene are harsh [25], but a few examples of MOST systems based on isomerisation of alkenes have been proposed.

While irradiation of *trans*-stilbene, **16**, in the presence of oxygen was reported to give benzoic acid and resinous products [26], Stroemer could also isolate *cis*-stilbene, **17**, after irradiating a benzene solution of *trans*-stilbene for eight days (Fig. 9.6) [27].

While having a low molecular weight, stilbene itself suffer from both negligible absorption of visible light, and a low storage enthalpy. Mancini and co-workers investigated a series of 9-styrylacridines (**18–20**; Fig. 9.7), with more redshifted

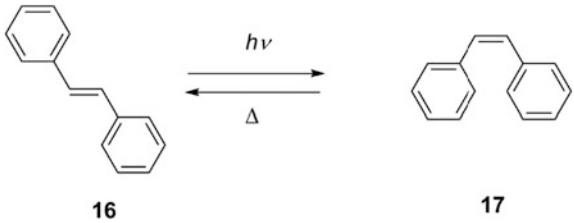

Fig. 9.6 Reversible isomerisation of stilbene

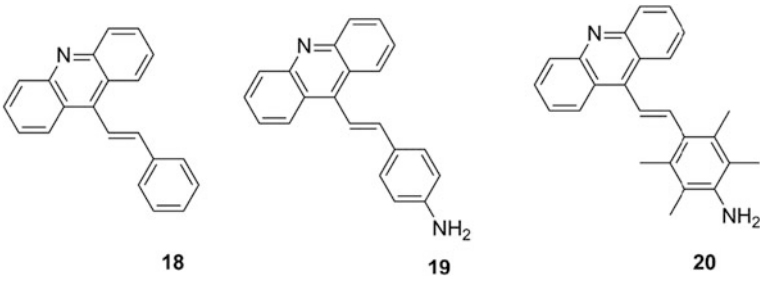

Fig. 9.7 9-styrylacridine derivatives **18–20**

spectra compared to stilbene. The storage enthalpy of 9-styrylacridine **18** is, like for stilbene, 5 kJ mol^{-1} [28, 29]. An electron withdrawing amino substituent increased the storage enthalpy to 18 kJ mol^{-1} in **19** [29], and a similar effect was observed by replacing the phenyl group with a 1-naphtyl-group [29]. Introduction of sterically demanding methyl groups increased the storage enthalpy even more, the highest value obtained being 104 kJ mol^{-1} for compound **20** [29].

The *trans-cis* isomerisation of azobenzene, **21** (Fig. 9.8), was serendipitously discovered by Hartley, who obtained irreproducible results while determining the solubility of *trans*-azobenzene by photometry [30, 31]. The photoisomerisation was studied in more detail by Adamson and co-workers [32]. The storage enthalpy was determined to 49 kJ mol^{-1} and the quantum yield to 0.49. The half live of *cis*-azobenzene was reported to be 4.2 days. A more detailed study of different derivatives was performed by Olmsted and co-workers [33]. The conclusion was that the more redshifted derivatives (such as the azo dye methyl orange) have half-lives in the orders of seconds, and that azobenzene derivatives were unsuitable for energy storage.

More recently, Grossman and Kolpak reported DFT calculations (Quantum Espresso, wB97XD and M06) on azobenzene functionalised carbon nanotubes (Fig. 9.9) [34, 35]. These calculations suggested that steric interaction would stabilise the *trans*-isomer over the *cis*, and thus increase the storage enthalpy by 30%. By introducing hydroxyl-substituents on the azobenzene moieties, favourable hydrogen bonding would increase the half-life of the *cis* form to over one year.

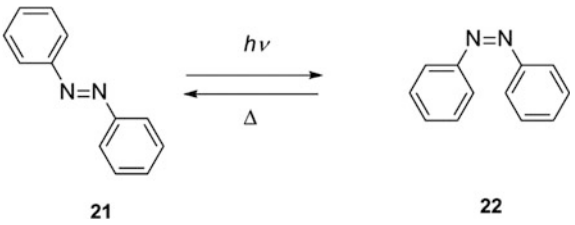

Fig. 9.8 Photoisomerisation of azobenzene

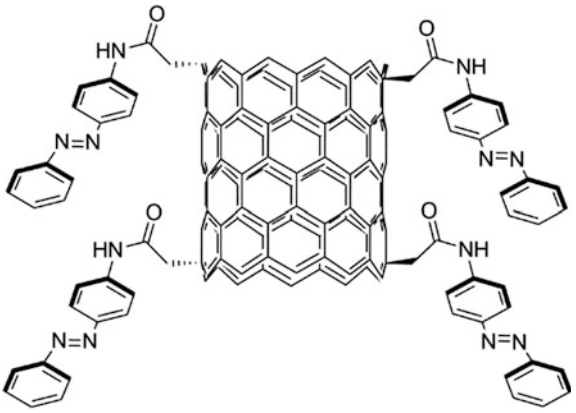

Fig. 9.9 Azobenzene functionalised carbon nanotubes

Energy densities per volume comparable to state of the art lithium ion batteries are reported to be feasible [35]. Unsubstituted azobenzene/carbon nanotube material was finally synthesised, but unfortunately the challenging synthesis meant that the high azobenzene densities used in the calculations could not be fully realised, and the material showed no improvements compared to free azobenzene [36]. Bundling in the solid state was, on the other hand, found to increase the storage density by a factor two [36]. Preceding the work of Grossman by a few months, Feng and co-workers functionalised graphene with azobenzene units showing similar nano-templating effects [37]. An even more recent contribution from the Grossman group is a thin film material with azobenzene units bound to a polymer backbone. This material undergoes photoisomerisation, and the irradiated film release excess energy as heat when placed on a hot plate [38]. Computational work has also suggested that azobenzene units forming macrocycles may have storage densities up to 600 kJ kg^{-1} [39]. Wachtveitl and co-workers have studied the photoisomerisation of *o*-, *m*-, and *p*-bisdiazobenzenes (**23–25**; Fig. 9.10). The highest degree of conjugation was observed in the *p*-isomer, but this led to reduced excited state life time and comparably low isomerisation quantum yield [40].

In 2014, Kimizuka and co-workers demonstrated that it is possible to add solubilising side chains to the azobenzene motif and by that form a high energy density liquid that is completely solvent free [41]. It has also been reported that azobenzene derivatives could undergo ionic to liquid crystal transformation upon photoisomerisation [42].

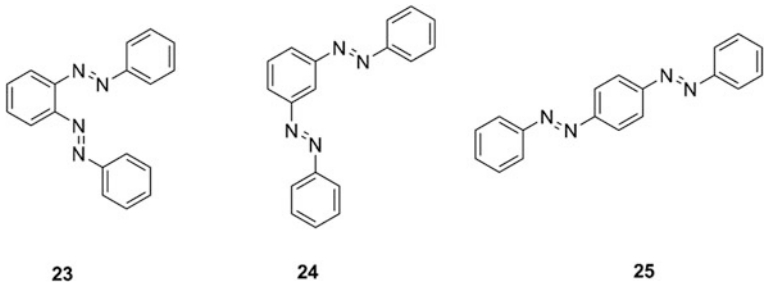

Fig. 9.10 Bisdiazobenzene derivatives **23–25**

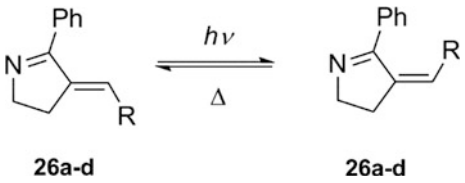

Fig. 9.11 *Trans-cis* isomerisation of compounds **26a–d**

Other examples of light induced geometric isomerisation around carbon–carbon double bonds include indigo derivatives [43], but these systems have received little interest compared to stilbene and azobenzene, mainly due to low quantum yields [44] and short half-lives of the photoisomers [45]. A more recent system based on *cis*/*trans* isomerisation was proposed by Sampedro and co-workers [46]: compounds **26a–d** (Fig. 9.11) undergo a *trans-cis* isomerisation when irradiated at approximately 300 nm. The reaction is reversible, and the back-reaction occurs spontaneously at ambient temperature [46, 47]. By modifying the R-group (R = Ph (**26a**), *p*-MeOPh (**26b**), *p*-NO_2Ph (**26c**), 2-naphthyl (**26d**)) the absorption properties could be modified, and protonation of the imine nitrogen atom increased the barrier of the back-reaction (these derivatives were stable for at least 6 days at room temperature) [46].

9.5 Intramolecular Cycloaddition Reactions: The Norbornadiene System

While deriving its name from its structural similarity with natural product borneol, norbornadiene is not a natural product, but is purely synthetic. Norbornadiene-2,3-dicarboxylic acid **27** and its dimethyl ester were prepared by Diels and Alder through the cycloaddition reaction of cyclopentadiene and acetylene dicarboxylic acid or acetylene dicarboxylic acid dimethylester, respectively, in 1931 (Fig. 9.12) [48]. Unsubstituted norbornadiene, **28**, was first obtained through a Diels-Alder reaction between cyclopentadiene and acetylene and reported in a patent from 1951 [49].

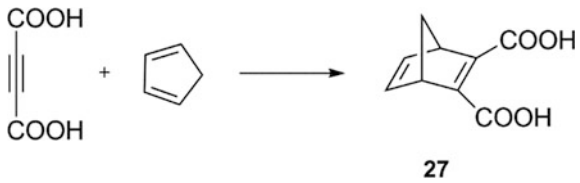

Fig. 9.12 Synthesis of norbornadiene-2,3-carboxylic acid

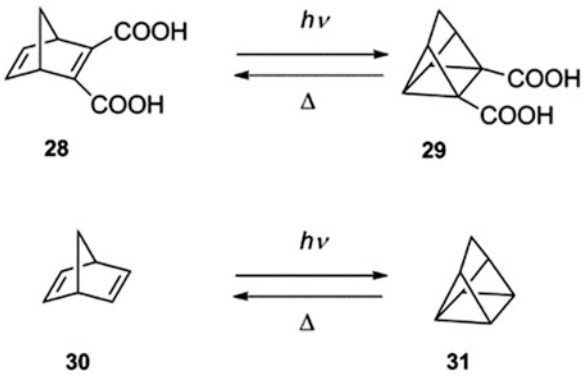

Fig. 9.13 Photoisomerisation of norbornadiene derivatives to quadricyclanes

Other chemists had become interested in the quadricyclane ring system, and several unsuccessful attempts to prepare quadricyclane derivatives were conducted before Cristol and Snell irradiated **27** with UV-light [50]; this produced the corresponding quadricyclane dicarboxylic acid, **29** through an intramolecular [2 + 2] cycloaddition (Fig. 9.13). Unsubstituted quadricyclane, **30**, was first obtained by direct irradiation of norbornadiene, **28** [51] and, independently, in the presence of triplet photosensitisers [52]. When irradiation was performed in the vapour phase, **28** was found to isomerise to toluene, or to decompose to cyclopentadiene and acetylene [53]. Upon heating, quadricyclane is quantitatively converted back to norbornadiene through a Woodward-Hoffmann forbidden pathway. One of the two bonds is cleaved entirely before the transition state [54].

Norbornadiene has several attractive properties. It can store a significant amount of energy (ΔH = 89 kJ/mol) [55], it is commercially available and has a low molecular weight. It is a mobile liquid which can easily be pumped through a device without the need to dilute it with solvent, and several effective catalysts have also been developed for the backward reaction [56]. On the other hand, **28** is prone to polymerisation, and may form explosive peroxides in the presence of air and light. It is volatile (boiling point 89 °C) and flammable. Most important, however, **28** only absorb UV-light, and is hardly isomerised by sunlight. While there are several strategies to red shift the absorption, see below, a common problem is that norbornadiene derivatives with more redshifted spectra typically correspond to quadricyclanes with short half-lives. Introducing methyl substituents on the bridge

head, and trifluoromethyl groups on one of the double bonds has been shown to improve the life time of the quadricyclane [57].

Since the 1980s, considerable efforts have been put into designing norbornadiene derivatives with better performance. Consequently, the norbornadiene system is the most thoroughly studied MOST system to date, and the literature up to 2002 has been reviewed previously [56, 58]. For example, attempts have been made to increase the isomerisation quantum yield by coordination of metal ions to the π-system of norbornadiene. Formation of charge-transfer bands also help to red shift the absorption. Only Cu^+ has given promising results [59–61]. A second class of photosensitisers does not form complexes with norbornadiene in the ground state, but their exited states can transfer energy to norbornadiene and cause photoisomerisation. Most frequently used are aromatic ketones [62]. For synthetic purposes, norbornadiene is best converted to quadricyclane using acetophenone as a sensitiser [63].

The most widely employed strategy is to introduce electron withdrawing, or a combination of an electron withdrawing and an electron donating group at the vinylic positions. Introducing aromatic substituents at the vinylic positions give rise to an extended conjugated system that is broken on photoisomerisation (Fig. 9.14). This helps to blue shift the spectrum of the quadricyclane compared to the norbornadiene, and thus helps to fulfil requirement 2 in Sect. 9.3. Apart from red-shifting the absorption, introduction of substituents at the C=C double bond frequently leads to an increased isomerisation quantum yield [58]. Simple substituents, such as COOH, COOMe or CN do not shift the absorption onset to more than ca 365 nm [56]. Norbornadienes having two aryl [64] or one aryl- and one aroyl substituent, was shown to display absorption onsets of up to 450 nm [65]. More complicated substitution patterns were found to give even stronger red shifts, but at the expense of much higher molecular weights. Since substituted norbornadiene/quadricyclanes appears to have very similar molar storage energies, the most rational design parameter is to search for ways to improve absorption without compromising energy density by increase in molecular weight [66].

Another series of norbornadienes, including compound **33**, displaying large cationic heterocyclic substituents had excellent spectroscopic properties, with absorption onsets up to 580 nm [67], causing compound **33** to isomerise readily to **34** in diffuse light. This is indeed very close to the calculated optimal absorption for a MOST system of *ca.* 600 nm [68]. Unfortunately, irradiation lead to the formation

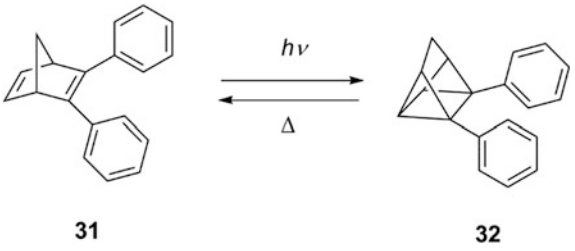

Fig. 9.14 By introducing aromatic substituents in 2- and 3-position of norbornadiene, an extended conjugated system is created. The conjugation is broken upon photoisomerisation causing a hypsochromic shift

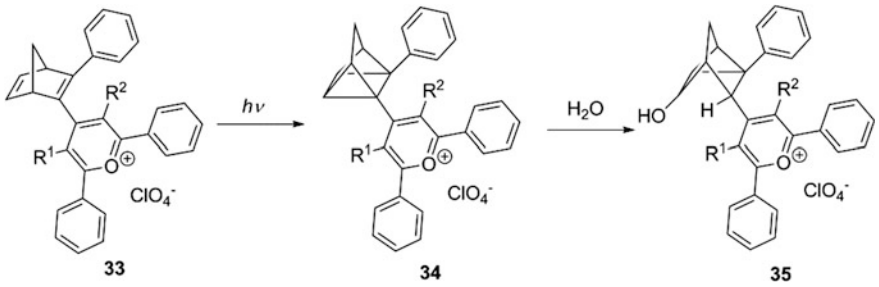

Fig. 9.15 Photoisomerisation and decomposition of 33 in the presence of moisture

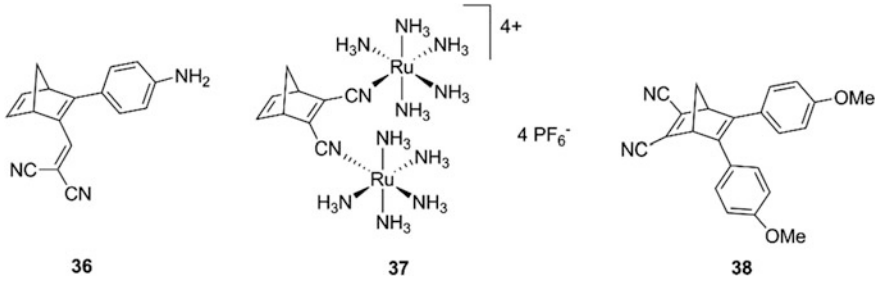

Fig. 9.16 Norbornadiene derivatives with red shifted absorption spectra

of a photostationary equilibrium mixture, and in addition the photoisomer was found to be chemically unstable. Traces of moister resulted in hydration and carbon–carbon bond breakage in the quadricyclane, thus compromising the cyclability of the system (Fig. 9.15).

While compound **33** absorb in the green part of the spectrum, compound **36** (Fig. 9.16) with an absorption onset of 620 nm, absorb orange light [69]. The quantum yield for that particular compound was 0.1, far from ideal in a practical system. Although compound **37** has an absorption onset of 700 nm, the quantum yield of only $8.3 \cdot 10^{-4}$ at 500 nm is disappointing [70]. Nevertheless, these compounds still holds the records in red shift for norbornadiene derivatives. Rather than introducing substituents around a single C=C bond in norbornadiene, attempts have also been made to substitute at all vinylic positions in the molecule. One of the more efficient compounds, **38**, has an absorption onset of 557 nm [17]. High quantum yields have been retained when norbornadienes were included in thin poly-methyl methacrylate films [71].

There are some reports of photoswitching polymers containing norbornadiene moieties (Fig. 9.17). The most convenient way of forming these polymers is to start from substituted norbornadiene-2,3-dicarboxylic acid or norbornadiene-2-carboxylic acid, and prepare polyesters (e.g. **39** [72]) or polyamides (e.g. **40** [73]). There is only one example of a heteroatom free polymer, **41**,

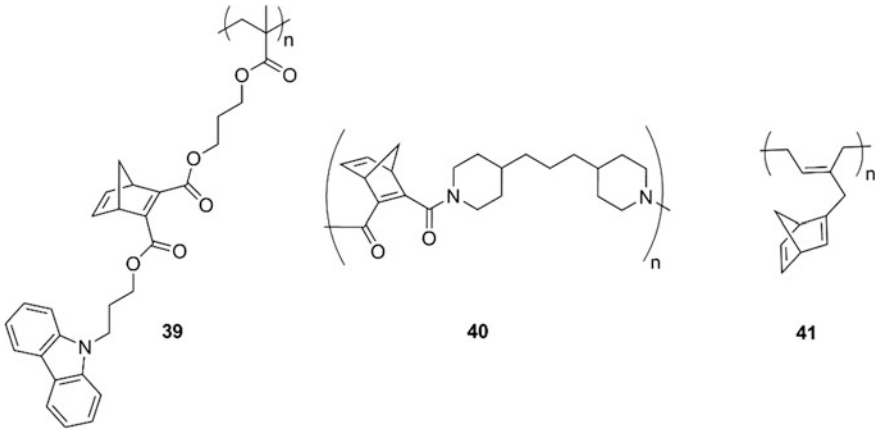

Fig. 9.17 Norbornadiene based polymers

Fig. 9.18 Pentafulvalene and dihydropentafulvalene

where norbornadiene is connected to a polyisoprene backbone [74]. Polymers containing photosensitising substituents such as carbazole [72] or benzophenones [75] have also been described in the literature.

9.6 Intramolecular Rearrangements in Organometallic Compounds: The Fulvalene Diruthenium System

Several attempts had been made during the years to synthesise the hydrocarbon pentafulvalene, **42** (Fig. 9.18). One of the more well-known failures resulted in the discovery of ferrocene by Kealy and Pouson in 1951 [76]. A few years later, a synthesis of **42** appeared in a Ph.D. thesis, and spectroscopic evidence was put forward in 1959 [77]. The first peer-reviewed paper describing isolation of **42** solutions appeared in 1986 [78]. Thought **42** itself is thermally highly unstable, several organometallic complexes displaying the fulvalene dianion as a ligand have been reported. These were typically prepared by coupling of cyclopentadienyl metal complexes, thus avoiding the handling of reactive uncoordinated fulvalene species.

In 1983, however, Vollhardt and co-workers reported that the more stable dihydrofulvalene, **43**, reacts with triruthenium dodecacarbonyl in refluxing 1,2-dimethoxyethane or xylenes to give tetracarbonyl fulvalene diruthenium, **44** [79, 80]. Compound **44** is a yellow solid, sparingly soluble in moderately polar

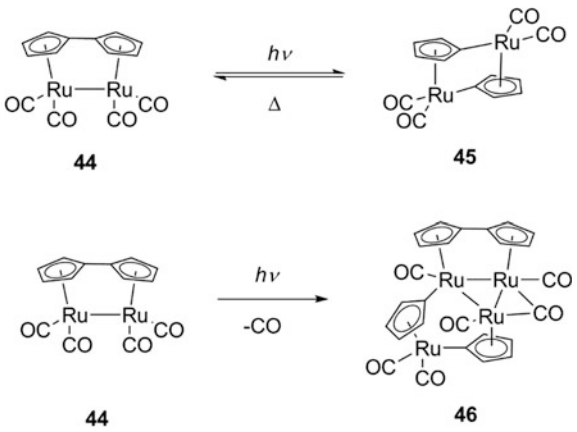

Fig. 9.19 *Top* photoisomerisation of tetracarbonyl fulvalene diruthenium. *Bottom* degradation of **44** by UV-light

organic solvents such as tetrahydrofuran or toluene, but insoluble in water or aliphatic hydrocarbons. The compound can be handled in air for shorter times, but on longer storage it gradually decomposes. Compound **44** has an absorption onset of 470 nm, and when its solutions are irradiated with visible light, **44** was found to undergo reversible photoisomerisation to **45** [79]. The photoisomer does not absorb in the visible region, and yellow solutions of **44** turn colourless upon irradiation, although a brown colour is often seen as a result of degradation. For instance, UV-light may cause irreversible loss of carbonyl ligands and formation of **46** (Fig. 9.19) [81]. The mechanism of photoisomerisation of **44** has been studied in some detail. First, a concerted reaction mechanism was proposed [81], but continued investigation by X-ray transient absorption spectroscopy, picosecond IR spectroscopy and computational methods showed that the isomerisation occurs via two short-lived intermediates (**47** and **48**; Fig. 9.20) [82, 83].

One of the important problems with the fulvalene diruthenium system is the solubility, which is further complicated by the fact that **19** is even less soluble (by an order of magnitude) than **44** [84]. Higher solubility was observed for the *tert*-butyl substituted compound **49** (Fig. 9.21) [85]. Unfortunately, however, the synthesis of compound **49** is rather complicated, five steps are required to prepare the 2,3-di-*tert*-butyl-cyclopenta-1,3-diene precursor. A more accessible alternative to **23** was found in compounds **50** and **51** [15], where the corresponding dihydrofulvalene solution is prepared in a one-pot reaction from commercial starting materials. Two isomers of the product are obtained and are not easily separated, but were found to have identical photochemical properties. Perfluorinated analogues of compounds **50** and **51** have also been synthesised [86], but while aliphatic groups increase the solubility compared to **44**, perfluorinated alkane chains had the opposite effect and reduces the solubility significantly.

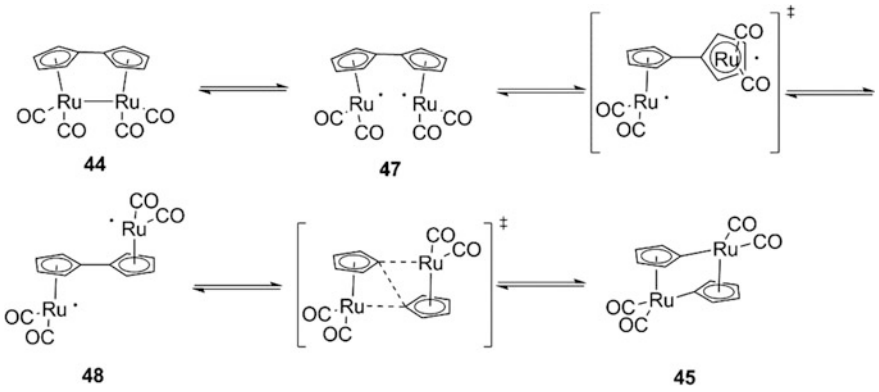

Fig. 9.20 Proposed mechanism for the isomerisation of **44**

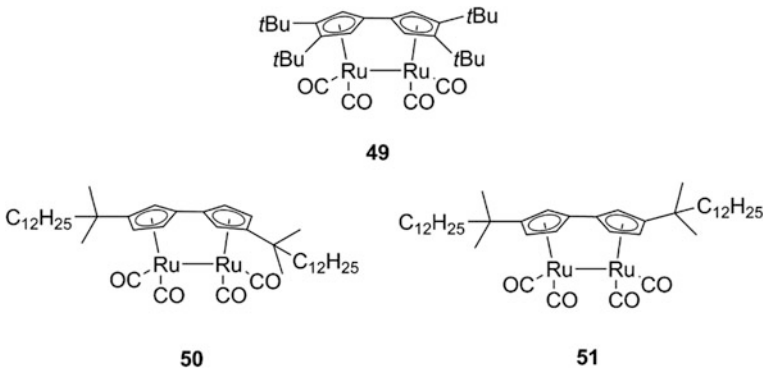

Fig. 9.21 Fulvalene diruthenium derivatives with increased solubility

Ruthenium appears to be essential for this system. Attempts have been made to replace the expensive ruthenium with inexpensive iron, the lightest member of group eight in the periodic table, but the iron analogue does not form any isolatable photoisomer [85]. The explanation is that irradiation of the diiron analogue of **44** gives a singlet *syn*-diradical (corresponding to **47**), which is too short-lived to undergo intersystem crossing to the triplet surface, where isomerisation occurs for ruthenium [87]. An osmium analogue of **44** has also been synthesised and this compound do photoisomerise, but the isomerisation is irreversible. In 2016, it was shown that steric strain caused by introduction of methyl substituents on the fulvalene rings resulted in increased quantum yields for compounds **52** and **53** (Fig. 9.22) [88].

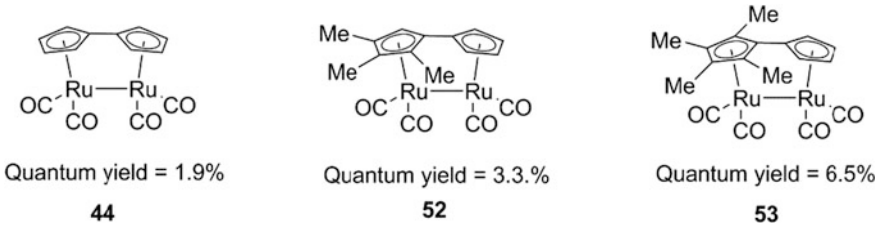

Fig. 9.22 Tuning the quantum yields of fulvalene-ruthenium compounds by sterically demanding groups

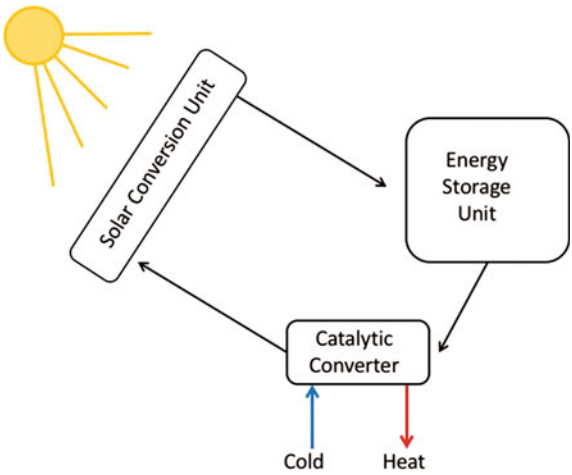

Fig. 9.23 Schematic of a MOST device consisting of a solar collector part, a storage reservoir and a catalytic energy release reactor

9.7 Integration into Devices

For practical use of the MOST concept in future applications, two different types of devices have been envisioned, notably (i) liquid-based systems where the MOST material is used as a fluid that can be pumped from a solar collector to a storage reservoir and recycled upon energy release by catalytic reactions or (ii) solid state systems, where the energy storage is co-located with the need for energy extraction. MOST energy systems based on norbornadiene derivatives dissolved in an organic solvent (toluene or octanes) have been demonstrated in the laboratory already in the 1980s by Yoshida and co-workers [17, 89] as well as by Marangozis and co-workers [90, 91]. A typical system consists of a solar collector part, a storage reservoir and a catalytic reactor (Fig. 9.23).

The catalytic conversion of quadricyclane to norbornadiene was first reported by Mango and Schachtschneider using transition metal complexes of rhodium, palladium and platinum [92]. Several catalytic systems have been identified, notably metal containing compounds employing iron [93], cobalt [93–96], nickel [93, 97–100], molybdenum [99–101], rhenium [21, 93, 97, 100–111], palladium [97, 109–117],

silver [65, 110, 118–121], tin [116, 122], tungsten [100], platinum [109], mercury [123] and others [124, 125]. Of these, porphyrin and phtalocyanine as well as more flexible Schiff base ligands containing cobalt or copper seems to be among the more promising [89, 126]. For practical applications, the catalyst should be immobilised on a solid support. This has been done by covalent attachment of porphyrins to polymer support such as polystyrene [126, 127] or by impregnating alumina or activated carbon with molecular catalyst species [126, 128]. Important parameters for a catalytic system are the rate of conversion as well as the turn over number. In this regard Maruyama et al. demonstrated a catalytic system based on a copper phtalocyanine catalyst on activated carbon support. The turnover frequency of the catalyst dropped over time, but the catalyst could be regenerated by washing in pure solvent (Fig. 9.24).

The catalytic conversion of quadricyclane to norbornadiene using tin or copper salts have been explored in detail by Lin and co-workers, demonstrating that the conversion is occurring through a one-site coordination [129–131]. Recently, the transition metal catalysed reaction has been analysed by Dronskowski and co-workers [132].

Perhaps the most important parameter in a MOST system is the catalysed heat-release part of the reaction. Only a handful of reports demonstrate catalysed heat release with a measured temperature gradient either obtained using quadricyclane derivatives in batch type reactors [133] or in flow type reactors [89] and for a fulvalene diruthenium compound **49** [15]. By transforming a 1 M solution of 1,2,3-trimethyl-5,6-dicyano quadricyclane, **54**, in octanes over a heterogeneous catalyst made from Co(II)(Salphen-CO_2H) on aminosulphone impregnated alumina substrate, Yoshida and co-workers was able to demonstrate a temperature gradient

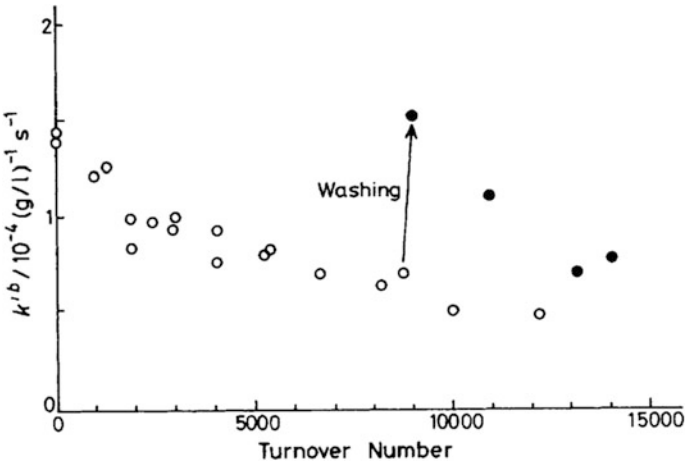

Fig. 9.24 Catalytic reaction rate of conversion of quadricyclane to norbornadiene using a copper phtalocyanine catalyst on activated carbon. Reprinted with the permission from Ref. [126]. Copyright 1986 American Chemical Society

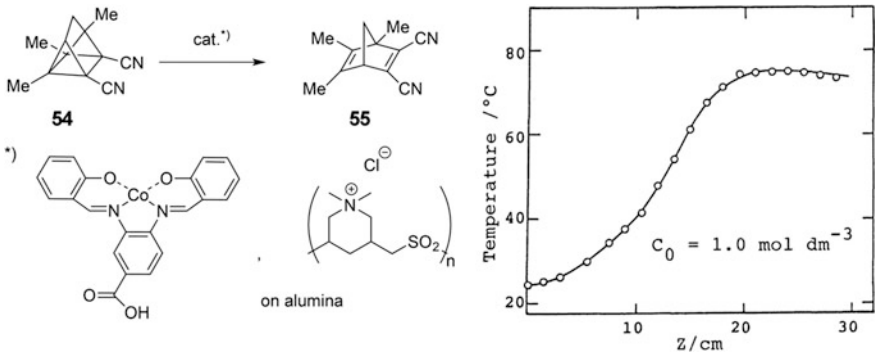

Fig. 9.25 Temperature profile from heat-release experiment reported by Yoshida and co-workers, the temperature is recorded along the centre of a 58 cm long and 4 cm diameter flow reactor [89]. Reproduced from Ref. [89] by permission of The Chemical Society of Japan

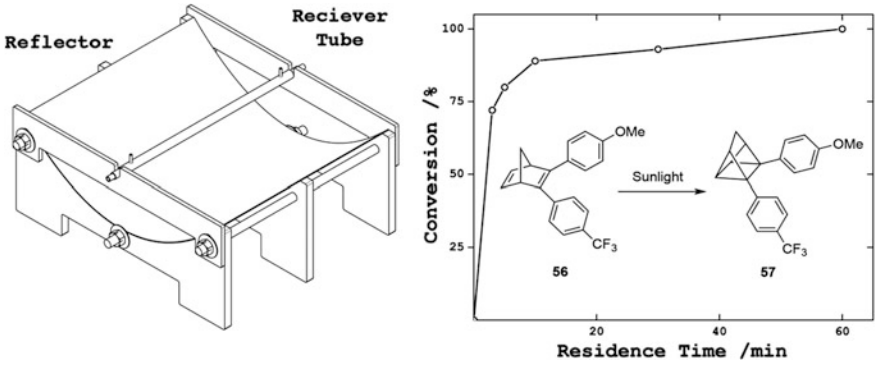

Fig. 9.26 (*Left*) Illustration of a parabolic mirror that is used to focus light onto a receiver tube converting 2-(4-methoxyphenyl)-3-(4-trifluoromethylphenyl)norbornadiene **56** into the corresponding quadricyclane **57** [64]

of *c*. 60 °C (Fig. 9.25), greatly exceeding temperature gradients typically attainable by, e.g. phase change materials.

Since the majority of the studied systems mentioned above only absorbs light in the UV-range, the majority of researchers has used high intensity UV lamps for the photoconversion of norbornadiene to quadricyclane. In 2014, Gray et al. published a device where light from a solar simulator was focused onto a glass tube using a through-based solar collector geometry at a residence time of 60 min, and a concentration of 0.1% w/v the compound was fully converted [64]. The device is very simple in the sense that only reflective coatings and glass tubes are needed (Fig. 9.26), also the size of the device (30 by 30 cm) demonstrates the simple scalability of MOST systems based on fluid material.

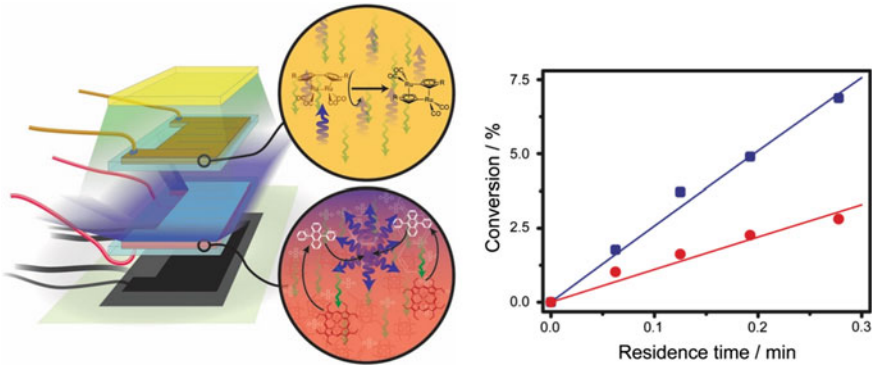

Fig. 9.27 *Left* schematic of device that combines photon upconversion with molecular solar-thermal system. *Right* graph displaying the conversion as a function of residence time in the photoreactor with (*blue*), and without (*red*) photon upconversion. Reproduced from Ref. [134] by permission of The Royal Society of Chemistry (RSC)

To mitigate challenges with solar spectrum match, Börjesson et al. designed a device that combine a fulvalene diruthenium molecular solar-thermal system with photon upconversion materials, that is materials capable of converting two low energy photons into one high energy photon (Fig. 9.27) [134]. The process for upconversion employed here is known as triplet annihilation (TTA-UC). In this device, a transparent microfluidic chip containing a mixture of the fulvalene-ruthenium compounds (**50–51**) is placed on top of a microfluidic chip containing the upconversion material. The mixture of compounds **50–51** is capable of absorbing light in the blue end of the spectrum, while low energy green photons are transmitted through the top layer of the device towards to the lower layer. In the lower layer, the green photons are absorbed by the TTA-UC material (a toluene solution containing palladium octaethyl porphyrin (sensitiser) and diphenyl anthracene (emitter) and transformed into blue photons that are re-emitted and sent back to the MOST layer for full utilisation. By incorporating the upconversion material, the energy conversion efficiency of the system was increased by 130%.

9.8 Energy Conversion Devices in the Solid State

While the majority of MOST systems have been designed to work in fluid reactors, also solid state variants have been explored. Notably the systems embedded in polymers [71], modified carbon nanotubes [35] or modified graphene-based systems [37]. Recently Zhitomirsky, Cho and Grossman designed an energy release polymer based on the azobenzene system [38]. The system can create a local temperature gradient of 10 °C upon heating (Fig. 9.28). One future potential application of such systems is de-icing of car windshields [135].

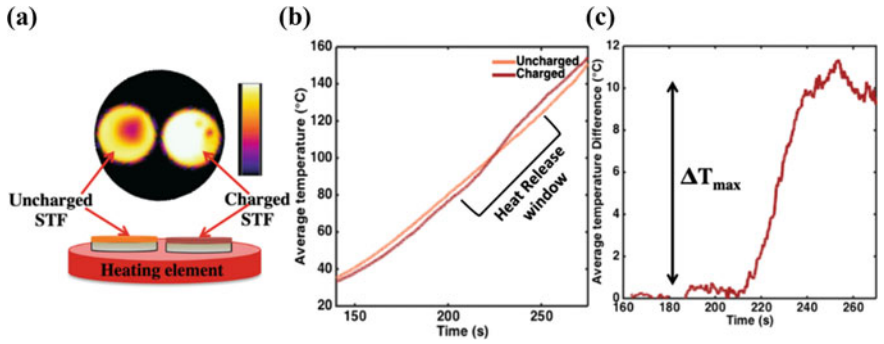

Fig. 9.28 *Left* thermal image of parent (uncharged) and photoisomerised (charged) polymer. *Centre* temperature of the two polymer samples when exposed to heating on a hot plate, *right* temperature gradient (ΔT) between the two polymers. Reproduced from Ref. [38] by permission of John Wiley & Sons Ltd.

This demonstration is interesting as it shows that future devices implementing photorecharged—heat release molecules might not necessarily be found in large scale applications, but perhaps in niche applications where energy supplied in the form of heat is needed on the local scale.

9.9 Summary and Outlook

The research field of molecular solar-thermal systems saw much attention in the 1970s and 1980s. During that period, in particular the norbornadiene system saw a rapid development towards good solar spectrum match, catalytic heat release and robust, multicycle systems [47, 56, 58]. Recently, other systems are being explored and combined with, e.g. nanomaterial templates [35, 37] leading to systems with much improved storage densities. Also, the norbornadiene system is being re-explored using modern computational methods [54, 66, 136, 137] leading to new opportunities for future molecular design. Entirely new systems are also being explored [138–140] as well as new device types and geometries [38, 64, 134]. All together, we are enthusiastic about the future development of molecular solar-thermal systems towards real applications.

References

1. Dinda M, Chakraborty S, Kanti Si M, Samanta S, Ganguly B, Maiti S, Ghosh PK (2014) Solar driven uphill conversion of dicyclopentadiene to cyclopentadiene: an important synthon for energy systems and fine chemicals. RSC Adv 4(97):54558–54564

2. Marcus RJ, Wohlers HC (1961) Photochemical systems for solar energy conversion: nitrosyl chloride. Sol Energy 5:44–57
3. Scheele CW (1777) In: Chemische Abhandlung von der Luft und dem Feuer. Magn. Swederus, Uppsala and Leipzig, pp 61–80
4. Scheele CW (1786) Von Hrn. Scheele in Köping. Chemische Annalen für die Freunde der Naturlehre. (1):part 1, 332
5. Grotthuss T (1819) Auszug aus vier Abhandlungen Physikalisch-chemischen Inhalts. Ann Phys 61:50–74
6. Trommsdorff H (1834) Ueber Santonin. Ann Chem Pharm 11(2):190–207
7. Matsuura T, Sata Y, Ogura K, Mori M (1968) Photoinduced reactions. XXIII. A novel photorearrangement of santonin in the solid state. Tetrahedron Lett 44:4627–4630
8. Natarajan A, Tsai CK, Khan SI, McCarren P, Houk KN, Garcia-Garibay MA (2007) The photoarrangement of α-santonin is a single-crystal-to-single-crystal reaction: a long kept secret in solid-state organic chemistry revealed. J Am Chem Soc 129(32):9846–9847
9. Fritzsche (1867) Ueber die festen Kohlenwasserstoffe des Steinkohlentheers. J Prakt Chem 101:333–343
10. Luther R, Weigert F (1905) Reversible photochemical reactions in a homogeneous system, I. Z Phys Chem Stoechiom Verwandtschaftsl 51:297
11. Luther R, Weigert F (1905) Reversible photochemical reactions in homogeneous systems. Anthracene and dianthracene. II. Zeit physikal Chem 53:385–427
12. Weigert F (1908) The thermodynamic treatment of photochemical processes. Z physik Chem 63:458–466
13. Weigert F (1909) Chemical action of light (IV). Further contributions to the thermodynamic theory of photochemical processes. Ber Dtsch Chem Ges 42:850–862
14. Weigert F (1909) Ueber die Verwandelbarkeit von Licht in chemische Energie. Jahrbuch für Photographie, Kinematographie und Reproduktionsverfahren:109
15. Moth-Poulsen K, Coso D, Börjesson K, Vinokurov N, Meier SK, Majumdar A, Vollhardt KPC, Segalman RA (2012) Molecular solar thermal (MOST) energy storage and release system. Energy Environ Sci 5(9):8534–8537
16. Jones G II, Chiang S-H, Phan Thanh X (1979) Energy storage in organic photoisomers. J Photochem 10(1):1–18
17. Yoshida Z (1985) New molecular energy storage systems. J Photochem 29(1–2):27–40
18. Splitter JS, Calvin M (1958) Preparation of oxaziranes by irradiation of nitrones. J Org Chem 23:651
19. Splitter JS, Calvin M (1965) Oxaziridines. I. The irradiation products of several nitrones. J Org Chem 30(10):3427–3436
20. Giezendanner H, Rosenkranz HJ, Hansen HJ, Schmid H (1973) Photoreactions. 30. Photochemistry of 3,5-diaryl-2-isoxazolines. Helv Chim Acta 56(7):2588–2611
21. Jones G II, Ramachandran BR (1976) Catalytic activity in the reversion of an energy storing valence photoisomerization. J Org Chem 41(5):798–801
22. Jones G II, Turbini LJ (1976) Valence photoisomerization of 1-ethoxycarbonyl-1H-azepine and its thermal reversion. Quantitative aspects including energy surface relations. J Org Chem 41(14):2362–2367
23. Jones G II, Reinhard TE, Bergmark WR (1978) Photon energy storage in organic materials. The case of linked anthracenes. Sol Energy 20(3):241–248
24. Xu J-F, Chen Y-Z, Wu L-Z, Tung C-H, Yang Q-Z (2013) Dynamic covalent bond based on reversible [4 + 4| photocycloaddition of anthracene for construction of double-dynamic polymers. Org Lett 15(24):6148–6151
25. Douglas JE, Rabinovitch BS, Looney FS (1955) Kinetics of the thermal cis-trans isomerization of dideuterioethylene. J Chem Phys 23:315–323
26. Ciamician GL, Silber P (1903) Chemische Lichtwirkungen. (VII. Mittheilung.). Ber. 36:4266–4272
27. Stoermer R (1910) Über die Umlagerung stabiler stereo-isomerer Äthylenkörper in labile durch ultraviolettes Licht (I). Ber. 42:4865–4871

28. Caia V, Cum G, Gallo R, Mancini V, Pitoni E (1983) A high enthalpy value in thermal isomerization of photosynthesized cis-9-styrylacridines. Tetrahedron Lett 24(36):3903–3904
29. Bastianelli C, Caia V, Cum G, Gallo R, Mancini V (1991) Thermal isomerization of photochemically synthesized (Z)-9-styrylacridines. An unusually high enthalpy of Z → E conversion for stilbene-like compounds. J Chem Soc Perkin Trans 2(5):679–683
30. Hartley GS (1937) Cis form of azobenzene. Nature 140:281
31. Hartley GS (1938) Cis form of azobenzene and the velocity of the thermal cis ⇆ trans conversion of azobenzene and some derivatives. J Chem Soc 633–642
32. Adamson AW, Vogler A, Kunkely H, Wachter R (1978) Photocalorimetry. Enthalpies of photolysis of trans-azobenzene, ferrioxalate and cobaltioxalate ions, chromium hexacarbonyl, and dirhenium decarbonyl. J Am Chem Soc 100(4):1298–1300
33. Olmsted J III, Lawrence J, Yee GG (1983) Photochemical storage potential of azobenzenes. Sol Energy 30(3):271–274
34. Kolpak AM, Grossman JC (2013) Hybrid chromophore/template nanostructures: a customizable platform material for solar energy storage and conversion. J Chem Phys 138(3):034303/1–034303/6
35. Kolpak AM, Grossman JC (2011) Azobenzene-functionalized carbon nanotubes as high-energy density solar thermal fuels. Nano Lett 11(8):3156–3162
36. Kucharski TJ, Ferralis N, Kolpak AM, Zheng JO, Nocera DG, Grossman JC (2014) Templated assembly of photoswitches significantly increases the energy-storage capacity of solar thermal fuels. Nat Chem 6(5):441–447
37. Feng Y, Liu H, Luo W, Liu E, Zhao N, Yoshino K, Feng W (2013) Covalent functionalization of graphene by azobenzene with molecular hydrogen bonds for long-term solar thermal storage. Sci Rep 3:3260
38. Zhitomirsky D, Cho E, Grossman JC (2016) Solid-state solar thermal fuels for heat release applications. Adv Energy Mater 6:1502006
39. Durgun E, Grossman JC (2013) Photoswitchable molecular rings for solar-thermal energy storage. J Phys Chem Lett 4(6):854–860
40. Slavov C, Yang C, Schweighauser L, Boumrifak C, Dreuw A, Wegner HA, Wachtveitl J (2016) Connectivity matters—ultrafast isomerization dynamics of bisazobenzene photoswitches. Phys Chem Chem Phys
41. Masutani K, M-a Morikawa, Kimizuka N (2014) A liquid azobenzene derivative as a solvent-free solar thermal fuel. Chem Commun 50(99):15803–15806
42. Ishiba K, Morikawa M-a, Chikara C, Yamada T, Iwase K, Kawakita M, Kimizuka N (2015) Photoliquefiable ionic crystals: a phase crossover approach for photon energy storage materials with functional multiplicity. Angew Chem Int Ed 54(5):1532–1536
43. Giuliano CR, Hess LD, Margerum JD (1968) Cis-trans isomerization and pulsed laser studies of substituted indigo dyes. J Am Chem Soc 90(9):587–594
44. Ikegami M, Arai T (2003) Photoisomerization and fluorescence properties of hemiindigo compounds having intramolecular hydrogen bonding. Bull Chem Soc Jpn 76(9):1783–1792
45. Pouliquen J, Wintgens V, Toscano V, Jaafar BB, Tripathi S, Kossanyi J, Valat P (1984) Photoisomerization of N, N′-disubstituted indigos. A search for energy storage. Can J Chem 62(11):2478–2486
46. Blanco-Lomas M, Martinez-Lopez D, Campos PJ, Sampedro D (2014) Tuning of the properties of rhodopsin-based molecular switches. Tetrahedron Lett 55(22):3361–3364
47. Kucharski TJ, Tian Y, Akbulatov S, Boulatov R (2011) Chemical solutions for the closed-cycle storage of solar energy. Energy Environ Sci 4(11):4449–4472
48. Diels O, Alder K (1931) Synthesis in the hydroaromatic series. XI. Diene syntheses of cyclopentadiene, cyclohexadiene and butadiene with acetylenedicarboxylic acid and its esters. Justus Liebigs Ann Chem 490:236–242
49. Hyman I (1951) Bicycloheptadienes. Application: BE Patent BE 498176
50. Cristol SJ, Snell RL (1958) Bridged polycyclic compounds. VI. The photoisomerization of bicyclo[2.2.1]hepta-2,5-diene-2,3-dicarboxylic acid to quadricyclo [2.2.1,02,6,03,5] heptane-2,3-dicarboxylic acid. J Am Chem Soc 80:1950–1952

51. Dauben WG, Cargill RL (1961) Photochemical transformations. VIII. Isomerization of bicyclo[2.2.1]hepta-2,5-diene to quadricyclo[2.2.1.02.6.03,5]-heptane (quadricyclene). Tetrahedron 15:197–201
52. Hammond GS, Turro NJ, Fischer A (1961) Photosensitized cycloaddition reactions. J Am Chem Soc 83:4674–4675
53. Roquitte BC (1963) Photolysis of bicyclo[2.2.1]hepta-2,5-diene in the vapor phase. J Am Chem Soc 85(22):3700
54. Qin C, Zhao Z, Davis SR (2005) Ab initio study of the thermal isomerization of quadricyclane to norbornadiene. J Mol Struct Theochem 728(1–3):67–70
55. X-w An, Y-d Xie (1993) Enthalpy of isomerization of quadricyclane to norbornadiene. Thermochim Acta 220(1–2):17–25
56. Bren VA, Dubonosov AD, Minkin VI, Chernoivanov VA (1991) Norbornadiene-quadricyclane: an effective molecular system for solar energy storage. Russ Chem Rev 60 (5):451–469
57. Nagai T, Fujii K, Takahashi I, Shimada M (2001) Trifluoromethyl-substituted donor-acceptor norbornadiene, useful solar energy material. Bull Chem Soc Jpn 74(9):1673–1678
58. Dubonosov AD, Bren VA, Chernoivanov VA (2002) Norbornadiene-quadricyclane as an abiotic system for the storage of solar energy. Russ Chem Rev 71(11):917–927
59. Schwendiman DP, Kutal C (1977) Transition metal photoassisted valence isomerization of norbornadiene. An attractive energy-storage reaction. Inorg Chem 16(3):719–721
60. Kutal C, Schwendiman DP, Grutsch P (1977) Use of transition metal compounds to sensitize a photochemical energy storage reaction. Sol Energy 19(6):651–655
61. Schwendiman DP, Kutal C (1977) Catalytic role of copper(I) in the photoassisted valence isomerization of norbornadiene. J Am Chem Soc 99(17):5677–5682
62. Arai T, Oguchi T, Wakabayashi T, Tsuchiya M, Nishimura Y, Oishi S, Sakuragi H, Tokumaru K (1987) Mechanistic approach to the sensitization process of aromatic ketones in the isomerization between norbornadiene and quadricyclane. Bull Chem Soc Jpn 60 (8):2937–2943
63. Smith CD (1971) Quadricyclane. Org Syn 51:133–136
64. Gray V, Lennartson A, Ratanalert P, Boerjesson K, Moth-Poulsen K (2014) Diaryl-substituted norbornadienes with red-shifted absorption for molecular solar thermal energy storage. Chem Commun 50(40):5330–5332
65. Toda T, Hasegawa E, Mukai T, Tsuruta H, Hagiwara T, Yoshida T (1982) Organic photochemistry. 61. Photochemical reaction of 2-aroyl-3-arylnorbornadienes. Chem Lett 10:1551–1554
66. Kuisma MJ, Lundin AM, Moth-Poulsen K, Hyldgaard P, Erhart P (2016) Comparative ab-initio study of substituted norbornadiene-quadricyclane compounds for solar thermal storage. J Phys Chem C 120(7):3635–3645
67. Koblik AV, Murad'yan LA, Dubonosov AD, Zolotovskova GP (1990) Ethynyl carbocations. 3. Diels-Alder reaction of 4-(phenylethynyl)pyrylium salts. Khim Geterotsikl Soedin 3:307–311
68. Börjesson K, Lennartson A, Moth-Poulsen K (2013) Efficiency limit of molecular solar thermal energy collecting devices. ACS Sustain Chem Eng 1(6):585–590
69. Dubonosov AD, Galichev SV, Chernoivanov VA, Bren VA, Minkin VI (2001) Synthesis and photoinitiated isomerizations of 3-(4-nitrophenyl)- and 3-(4-aminophenyl)bicyclo[2.2.1] hepta-2,5-diene-2-carbaldehyde and -2-carboxylic acid derivatives. Russ J Org Chem 37 (1):67–71
70. Laine P, Marvaud V, Gourdon A, Launay J-P, Argazzi R, Bignozzi C-A (1996) Electron transfer through norbornadiene and quadricyclane moieties as a model for molecular switching. Inorg Chem 35(3):711–714
71. Miki S, Asako Y, Yoshida Z (1987) Photochromic solid films prepared by doping with donor-acceptor norbornadienes. Chem Lett 1:195–198

72. Wang XS, Zhang BW, Cao Y (1996) Valence isomerization of norbornadiene in polymer systems for solar energy storage. J Photochem Photobiol A 96(1–3):193–198
73. Nishikubo T, Kameyama A, Kishi K, Nakajima T (1994) Synthesis of new photoresponsive polyamides containing norbornadiene residues in the main chain. Macromolecules 27(5): 1087–1092
74. Wright ME, Allred GD, Wardle RB, Cannizzo LF (1993) Polymers containing ring-strain energy. 1. New monomers and polymers based on cyclopropane, norbornadiene, and quadricyclane. J Org Chem 58(15):4122–4126
75. Nishimura I, Kameyama A, Nishikubo T (1998) Synthesis of self-photosensitizing polyesters carrying pendant norbornadiene (NBD) moieties and benzophenone groups and their photochemical reactions. Macromolecules 31(9):2789–2796
76. Kealy TJ, Pauson PL (1951) A new type of organo-iron compound. Nature 168:1039–1040
77. DeMore WB, Pritchard HO, Davidson N (1959) Photochemical experiments in rigid media at low temperatures. II. The reactions of methylene, cyclopentadienylene, and diphenylmethylene. J Am Chem Soc 81:5874–5879
78. Escher A, Rutsch W, Neuenschwander M (1986) Fulvenes, fulvalenes. Part 50. Synthesis of pentafulvalene by oxidative coupling of cyclopentadienide with copper(II) chloride. Helv Chim Acta 69(7):1644–1654
79. Vollhardt KPC, Weidman TW (1983) Synthesis, structure, and photochemistry of tetracarbonyl(fulvalene)diruthenium. Thermally reversible photoisomerization involving carbon-carbon bond activation at a dimetal center. J Am Chem Soc 105(6):1676–1677
80. Vollhardt KPC, Weidman TW (1984) Efficient syntheses of new fulvalene-bridged carbonyl complexes of cobalt, ruthenium, chromium, molybdenum, and tungsten. Organometallics 3(1):82–86
81. Boese R, Cammack JK, Matzger AJ, Pflug K, Tolman WB, Vollhardt KPC, Weidman TW (1997) Photochemistry of (fulvalene)tetracarbonyldiruthenium and its derivatives: efficient light energy storage devices. J Am Chem Soc 119(29):6757–6773
82. Kanai Y, Srinivasan V, Meier SK, Vollhardt KPC, Grossman JC (2010) Mechanism of thermal reversal of the (fulvalene)tetracarbonyldiruthenium photoisomerization: toward molecular solar-thermal energy storage. Angew Chem Int Ed 49(47):8926–8929
83. Harpham MR, Nguyen SC, Hou Z, Grossman JC, Harris CB, Mara MW, Stickrath AB, Kanai Y, Kolpak AM, Lee D, Liu D-J, Lomont JP, Moth-Poulsen K, Vinokurov N, Chen LX, Vollhardt KPC (2012) X-ray transient absorption and picosecond IR spectroscopy of fulvalene(tetracarbonyl)diruthenium on photoexcitation. Angew Chem Int Ed 51(31): 7692–7696
84. Börjesson K, Coso D, Gray V, Grossman Jeffrey C, Guan J, Harris Charles B, Hertkorn N, Hou Z, Kanai Y, Lee D, Lomont Justin P, Majumdar A, Meier Steven K, Moth-Poulsen K, Myrabo Randy L, Nguyen Son C, Segalman Rachel A, Srinivasan V, Tolman Willam B, Vinokurov N, Vollhardt KPC, Weidman Timothy W (2014) Exploring the potential of fulvalene dimetals as platforms for molecular solar thermal energy storage: computations, syntheses, structures, kinetics, and catalysis. Chem Eur J 20:15587–15604
85. Zhu B, Miljanic OS, Vollhardt KPC, West MJ (2005) Synthesis of 2,2′,3,3′-tetramethyl- and 2,2′,3,3′-tetra-tert-butylfulvalene: Attractive platforms for dinuclear transition metal fragments, as exemplified by (η5:η5-2,2′,3,3′-t-Bu4C10H4)M2(CO)n (M = Fe, Ru, Os, Mo) and first X-ray crystal structures of fulvalene diiron and diosmium complexes. Synthesis 19:3373–3379
86. Börjesson K, Lennartson A, Moth-Poulsen K (2014) Fluorinated fulvalene ruthenium compound for molecular solar thermal applications. J Fluorine Chem 161:24–28
87. Hou Z, Nguyen SC, Lomont JP, Harris CB, Vinokurov N, Vollhardt KPC (2013) Switching from Ru to Fe: picosecond IR spectroscopic investigation of the potential of the (fulvalene) tetracarbonyldiiron frame for molecular solar-thermal storage. Phys Chem Chem Phys 15 (20):7466–7469
88. Lennartson A, Lundin A, Börjesson K, Gray V, Moth-Poulsen K (2016) Tuning the photochemical properties of the fulvalene-tetracarbonyl-diruthenium system. Dalton Trans

89. Miki S, Maruyama T, Ohno T, Tohma T, Toyama S, Yoshida Z (1988) Alumina-anchored cobalt(II) Schiff base catalyst for the isomerization of trimethyldicyanoquadricyclane to the norbornadiene. Chem Lett 5:861–864
90. Philippopoulos C, Economou D, Economou C, Marangozis J (1983) Norbornadiene-quadricyclane system in the photochemical conversion and storage of solar energy. Ind Eng Chem Prod Res Dev 22(4):627–633
91. Philippopoulos C, Marangozis J (1984) Kinetics and efficiency of solar energy storage in the photochemical isomerization of norbornadiene to quadricyclane. Ind Eng Chem Prod Res Dev 23(3):458–466
92. Mango FD, Schachtschneider JH (1967) Molecular orbital symmetry conservation in transition metal catalyzed transformations. J Am Chem Soc 89(10):2484–2486
93. Hautala RR, King RB, C. K (1979) Solar energy; chemical conversion and stoarage. The Humana Press, Clifton
94. Maruyama K, Tamiaki H, Yanai T (1985) Valence isomerization between water-soluble norbornadiene and quadricyclane derivative. Bull Chem Soc Jpn 58(2):781–782
95. Manassen J (1970) Catalysis of a symmetry-restricted reactions by transition metal complexes. Importance of the ligand. J Catal 18(1):38–45
96. Wilson HD, Rinker RG (1976) Kinetics of quadricyclene-norbornadiene isomerization reaction for use in modeling supported liquid-phase catalysis. J Catal 42(2):268–274
97. Maruyama K, Terada K, Yamamoto Y (1981) Exploitation of solar energy storage systems. Valence isomerization between norbornadiene and quadricyclane derivatives. J Org Chem 46(26):5294–5300
98. Noyori R, Umeda I, Kawauchi H, Takaya H (1975) Nickel-catalyzed reactions involving strained bond. XII. Nickel(0)-catalyzed reaction of quadricyclane with electron-deficient olefins. J Am Chem Soc 97(4):812–820
99. King RB, Ikai S (1979) (Triphenylcyclopropenyl)nickel derivatives as catalysts for the isomerization of quadricyclane to norbornadiene. Inorg Chem 18(4):949–954
100. Hoffmann RW, Barth W, Carlsen L, Egsgaard H (1983) Carbene reactions. Part 16. Thermolyses of 7-norbornadienespiro-2-(1,3-dithiolane) S-oxides. J Chem Soc Perkin Trans 2(11):1687–1692
101. Minkin VI, Bren VA, Chernoivanov VA, Dubonosov AD, Galichev SV (1994) Photochromic behavior of 2,3-substituted norbornadienes. Mol Cryst Liq Cryst Sci Technol Sect A 246:151–154
102. Volger HC, Hogeveen H (1967) N.M.R. kinetic investigation of the system norbornadiene-μ-dichloro dirhodium dinorbornadiene. Recl Trav Chim Pays-Bas 86 (11):1066–1076
103. Cassar L, Halpern J (1970) Oxidative addition of quadricyclene to di-μ-chlorotetracarbonyldirhodium(I) and the mechanism of rhodium(I)-catalyzed isomerization of quadricyclene to norbornadiene. J Chem Soc D 17:1082–1083
104. Bruggink A, Hogeveen H (1972) Transition metal promoted isomerizations of 7-oxanorbornadienes and 3-oxaquadricyclanes. Tetrahedron Lett 49:4961–4964
105. Hogeveen H, Nusse BJ (1973) Rhodium(I) catalyzed valence isomerization of quadricyclanes. Tetrahedron Lett 38:3667–3670
106. Maruyama K, Terada K, Yamamoto Y (1981) Highly efficient valence isomerization between norbornadiene and quadricyclane derivatives under sunlight. Chem Lett 7:839–842
107. Taylor RB, Jennings PW (1981) Solvent effects on the valence isomerization catalyst (norbornadiene)rhodium chloride dimer. Inorg Chem 20(11):3997–3999
108. Chen MJ, Feder HM (1979) Valence isomerization of quadricyclane catalyzed by bis (μ-acetato)-bis(norbornadiene)dirhodium: evidence for a rhodocyclobutane intermediate. Inorg Chem 18(7):1864–1869
109. Hogeveen H, Volger HC (1967) Valence isomerization of quadricyclene to norbornadiene catalyzed by transition metal complexes. J Am Chem Soc 89(10):2486–2487
110. Hogeveen H, Nusse BJ (1974) Mechanistic differences between the rhodium(I)-, palladium (II)-, and silver(I)-catalyzed isomerization of quadricyclanes. Tetrahedron Lett 2:159–162

111. Behr A, Keim W, Thelen G, Scharf HD, Ressler I (1982) Solar energy storage with quadricyclane systems. J Chem Technol Biotechnol 32(6):627–630
112. Gassman PG, Patton DS (1968) Acid-catalyzed rearrangement of quadricyclanone and quadricyclanone dimethyl ketal. Product dependency on carbon protonation versus oxygen protonation. J Am Chem Soc 90(26):7276–7282
113. Babsch H, Fritz H, Prinzbach H (1975) Rearrangement of tetracyclo[3.2.0.02,7.04,6]heptane to tricyclo[4.1.0.02,7]heptene. Tetrahedron Lett 52:4677–4680
114. Bleasdale C, Jones DW (1983) A convenient synthesis of 7-substituted norbornadienes. J Chem Soc Chem Commun 5:214–216
115. Bleasdale C, Jones DW (1984) Donor-acceptor accelerated norbornadiene rearrangements. J Chem Soc Chem Commun 18:1200–1202
116. Patrick TB, Bechtold DS (1984) Kinetics of the isomerization of quadricyclane to norbornadiene promoted by tin(II) chloride and palladium(II) chloride. J Org Chem 49 (11):1935–1937
117. Miki S, Ohno T, Iwasaki H, Maeda Y, Yoshida ZI (1988) Catalysis of cyclopropenylidenepalladium(II) complexes for the isomerization of quadricyclane to norbornadiene. Tetrahedron 44(1):55–60
118. Menon BC, Pincock RE (1969) Study of potential cyclopropyl-silver ion complex formation. Can J Chem 47(18):3327–3331
119. Nelsen SF, Gillespie JP, Hintz PJ (1971) Electrophilic reactions of 2,3-dicarbomethoxy-7-isopropylidenequadricyclane. Tetrahedron Lett 25:2361–2364
120. Koser GF, Pappas PR, Yu S-M (1973) Ag(I)-promoted reaction of tetracyclo[3.2.0.0.2,7,4,6] heptane (guadricyclene), methyl tetracyclo[3.2.0.0.2,704,6]heptane-1-carboxylate (2-(methoxycarbonyl)quadricyclene), and dimethyl tetracyclo[3.2.0.0.2,704,6]heptane-1,2-dicarboxylate (2,3-bis(methoxycarbonyl)quadricyclene). Tetrahedron Lett 49:4943–4946
121. Koser GF, Faircloth JN (1976) Silver(I)-promoted reactions of strained hydrocarbons. Oxidation vs. rearrangement. J Org Chem 41(3):583–585
122. Landis ME, Gremaud D, Patrick TB (1982) Cycloreversion of quadricyclane to norbornadiene catalyzed by tin(II) complexes. Tetrahedron Lett 23(4):375–378
123. Rood IDC, Klumpp GW (1984) Catalysis of the thermal quadricyclane → norbornadiene isomerization by mercury(II) halides. Recl J R Neth Chem Soc 103(11):303–304
124. Hirao K, Yamashita A, Yonemitsu O (1988) Cycloreversion of acylquadricyclane to acylnorbornadiene promoted by metal oxides. Tetrahedron Lett 29(33):4109–4112
125. Yamashita A, Hasebe K, Hirao K (1992) Cycloreversion of electron-rich quadricyclane initiated by metal oxides. Chem Lett 8:1481–1482
126. Maruyama K, Tamiaki H, Kawabata S (1986) Exothermic isomerization of water-soluble quadricyclanes to norbornadienes by soluble and insoluble catalysts. J Chem Soc Perkin Trans 2(4):543–549
127. King RB, Sweet EM (1979) Polymer-anchored cobalt tetraarylporphyrin catalysts for the conversion of quadricyclane to norbornadiene. J Org Chem 44(3):385–391
128. Kuroda R, Saito Y (2000) Circular dichroism of inorganic complexes: interpretation and applications. Circular dichroism, 2nd edn
129. Chuang EC-C, Lin K-C (2002) Fourier transform near-infrared absorption spectroscopic study of catalytic isomerization of quadricyclane to norbornadiene by copper(II) and tin(II) salts. J Phys Chem B 106(1):132–136
130. Fan H-F, Chin T-L, Lin K-C (2004) Kinetics of catalytic isomerization of quadricyclane to norbornadiene using near infrared absorption spectroscopy: conversion rate and diffusion motion in heterogeneous reaction. J Phys Chem B 108(26):9364–9370
131. Fan H-F, Chang C-Y, Chin T-L, Ho T-I, Lin K-C (2006) Catalytic isomerization of quadricyclane using fourier transform near-infrared absorption spectroscopy: diffusion, conversion, and temperature effect. J Phys Chem B 110(11):5563–5569
132. Tchougreeff AL, Tokmachev AM, Dronskowski R (2013) Resonance theory of catalytic action of transition-metal complexes: Isomerization of quadricyclane to norbornadiene catalyzed by metal porphyrins. Int J Quantum Chem 113(14):1833–1846

133. Maruyama T, Yoshida Z, Miki S (1985) Laboratory liquid-solid reactor in heterogeneous catalysis. J Chem Eng Jpn 18(6):515–519
134. Börjesson K, Dzebo D, Albinsson B, Moth-Poulsen K (2013) Photon upconversion facilitated molecular solar energy storage. J Mater Chem A 1(30):8521–8524
135. Shames SWL, Zhang CM, Ferralis N, Grossman Jeffrey C (2013) Rapid windshield de-icing using solar thermal fuels. Int J Energy Effic Veh Des 15:1114–1119
136. Antol I (2013) Photodeactivation paths in norbornadiene. J Comput Chem 34(17): 1439–1445
137. Vessally E (2009) Maximizing the solar energy storage of the norbornadiene-quadricyclane system: mono-heteroatom effect by DFT calculations. Phosphorus Sulfur Silicon Relat Elem 184(9):2307–2313
138. Lindbaek Broman S, Brondsted Nielsen M (2014) Dihydroazulene: from controlling photochromism to molecular electronics devices. Phys Chem Chem Phys 16(39):21172–21182
139. Cacciarini M, Skov AB, Jevric M, Hansen AS, Elm J, Kjaergaard HG, Mikkelsen KV, Brondsted Nielsen M (2015) Towards solar energy storage in the photochromic dihydroazulene-vinylheptafulvene system. Chem Eur J 21(20):7454–7461
140. Olsen ST, Elm J, Storm FE, Gejl AN, Hansen AS, Hansen MH, Nikolajsen JR, Nielsen MB, Kjaergaard HG, Mikkelsen KV (2015) Computational methodology study of the optical and thermochemical properties of a molecular photoswitch. J Phys Chem A 119(5):896–904

Chapter 10
Impedance Spectroscopy in Molecular Devices

Francisco Fabregat-Santiago, Eva M. Barea, Sixto Giménez and Juan Bisquert

Abstract In this chapter, we deal with the application of impedance spectroscopy in the characterization of dye solar cells and hematite electrodes for the production of solar hydrogen. We show in detail which type of information IS provides access to and how the technique can be used to understand the behavior and limitations of these devices. The same procedures and models presented here for the impedance analysis may be employed in the study of other types of solar cells and electrodes used for solar fuel production.

Keywords Dye solar cells · Charge recombination · Charge separation · Water splitting · Impedance spectroscopy · Chemical capacitance · Transmission line · Equivalent circuit · Open-circuit voltage · Hematite

Abbreviations

c_{ox}	Concentration of acceptor species in the electrolyte
C	Capacitance
C_{BL}	Capacitance of back layer TCO/electrolyte interface,
C_{bulk}	Bulk capacitance
C_H	Helmholtz capacitance
C_{IrOx}	IrO_x capacitance
C_μ	Chemical capacitance
$C_{M\text{-}S}$	Mott–Schottky capacitance
C_{Pt}	Capacitance of the interface between platinized electrode and electrolyte
Css	Capacitance of surface states
C_{trap}	Trap capacitance
D	Diffusion coefficient
d	Thickness of the material
d_H	Thickness of Helmholtz layer

F. Fabregat-Santiago (✉) · E.M. Barea · S. Giménez · J. Bisquert
Institute of Advanced Materials (INAM), Universitat Jaume I, 12006 Castelló de la Plana, Spain
e-mail: fabresan@uji.es

H. Tian et al. (eds.), *Molecular Devices for Solar Energy Conversion and Storage*, Green Chemistry and Sustainable Technology,
https://doi.org/10.1007/978-981-10-5924-7_10

DOS	Density of states
DSC	Dye solar cell
E_c	Energy of the conduction band (edge)
E_{Fn}	Fermi level of electrons
E_{Fp}	Fermi level of Holes
EIS	Electrochemical Impedance Spectroscopy
E_{redox}	Equilibrium energy of redox species or redox energy level
E_t	Energy of trap state
E_v	Energy of the valence band (edge)
f	Frequency
FF	Fill factor
FTO	Fluorine doped tin oxide
g_{trap}	Trap density of states
HCE	Hole collecting electrode
HOMO	Highest occupied molecular orbital
HTM	Hole transporting material
IMPS	Intensity-modulated photocurrent spectroscopy
IPCE	Incident photon to current conversion efficiency
IS	Impedance Spectroscopy
I	Current
I_{sc}	Short-circuit current
J	Current density
J_0	Dark current
J_{bias}	Current density at certain applied bias voltage
J_{sc}	Short-circuit current density
J–V	Current density–voltage
k_B	Boltzmann constant
k_r	Recombination rate constant
L	Film thickness
L_d	Diffusion length
LUMO	Lowest unoccupied molecular orbital
N719	Di-tetrabutylammonium cis-bis(isothiocyanato)bis(2,2′-bipyridyl-4,4′-dicarboxylato)ruthenium(II)
N_s	Number of electronic states contributing to the recombination
N_t	Number of trap states
PIA	Photo induced absorption spectroscopy
P_{in}	Incident power of light
P_{max}	Maximum power generated by the solar cell
q	Electron charge
R	Resistance
$R_{\|\|}$	Effective recombination resistance
R_0	Recombination resistance at $V_F = 0$
R_{BL}	Charge recombination from TCO at the back layer of TiO_2 to electrolyte
R_{ct}	Charge transfer resistance

$R_{ct,bulk}$	Charge transfer resistance from conduction or valence bands
$R_{ct,IrOx}$	IrO_x charge transfer resistance
$R_{ct,trap}$	Charge transfer resistance from trap surface states
R_d	Diffusion resistance
R_{DC}	DC or low-frequency resistance
R_{IrOx}	IrO_x resistance
R_{Pt}	Charge transfer at platinized electrode
R_{rap}	Trap resistance
R_{rec}	Recombination resistance
R_{series}	Total series resistance
R_{tr}	Transport resistance in TiO_2
T	Absolute temperature
TCO	Transparent conductive oxide
TiO_2	Titanium dioxide
V_0	Voltage loss in short-circuit conditions
V_{bias}	Bias or applied voltage
V_{ecb}	Voltage at the equivalent conduction band
V_F	Voltage corrected from series resistance
V_{fb}	Flat band potential
V_{oc}	Open-circuit voltage
Z	Impedance
Z_d	Diffusion impedance
α	Shape factor of the distribution of states below the conduction band
α-Fe_2O_3	Hematite
β	Transfer factor
ΔE_c	E_c band shift with respect to a reference
ΔE_{redox}	Difference in energy of different redox materials
ΔV_{Jsc}	Change in voltage associated to differences in J_{sc}
ΔV_k	Change in voltage due to differences in recombination kinetics
ΔV_{rec}	Change in voltage due to differences in recombination
ε	Permittivity of a material
ε_0	Vacuum permittivity
ε_r	Relative permittivity of a material
η	Efficiency
λ	Reorganization energy of acceptor species
σ	Energy width of the density of states distribution
τ_c	Characteristic time
ω	Angular frequency: $\omega = 2\pi f$
ω_d	Diffusion frequency

10.1 Introduction

Electrochemical impedance spectroscopy (EIS) or, in a broader context, simply impedance spectroscopy (IS) is a useful technique that allows studying electrical properties such transport, accumulation, transfer, and losses of charge in materials and devices. One of the main advantages of the technique is that these properties may be measured under operational conditions of the samples, for instance at different bias potential or under different illumination or environmental situations. This property facilitates the analysis of electrical processes occurring in the system, enabling the development of models that describe the physicochemical behavior of systems and, eventually, unveil the mechanisms that enhance their performance or produce their degradation.

IS measurements are based on the application of a small AC perturbation ($\tilde{V}$) at a fixed frequency (f) over a sample in equilibrium at stationary bias voltage (V_{bias}). Current crossing the sample (J_{bias}) will be then modified by an AC modulation ($\tilde{J}$), see Fig. 10.1, and the impedance is calculated as [1–3]

$$Z(f) = \frac{\tilde{V}}{\tilde{J}} \tag{10.1}$$

for this specific frequency. To obtain a full impedance spectrum, this procedure is repeated at different frequencies in a range that may vary from MHz to mHz.

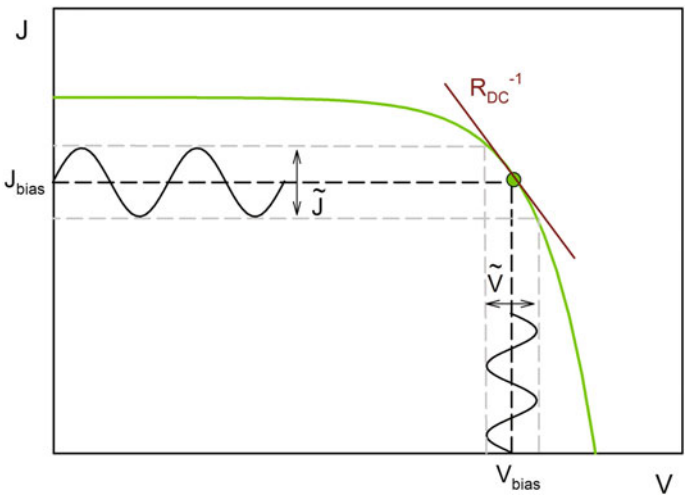

Fig. 10.1 Procedure to obtain impedance spectrum: AC signal is applied at stationary bias and effect of perturbation recorded to calculate impedance according to Eq. (10.1). Measurement is repeated for the frequencies of interest in the material. Bias potential may be swept along the full J–V curve. *Red line* represents the slope of the J–V curve at V_{bias}, that correspond to the inverse of DC resistance at this voltage

To investigate the electrical properties of the system at the different operating conditions, IS measurements may be carried out changing illumination or sweeping the bias voltage (or current) along the complete current density–voltage (J–V) curve of a device. Impedance spectra may be also obtained by applying an AC current at a stationary current and recording the resulting AC voltage. In all the cases, it is needed that AC perturbation becomes small enough so that response of the system is linear and, if stationary response is reached, keeping the system in the measurement conditions time enough for the system to stabilize.

Impedance data are typically represented in complex plane plots as shown in Fig. 10.2. In the complex plane, plot impedance data produces as many arcs as processes occurring at different characteristic times (τ_c) take place in our sample. In a simplified vision, each arc in the complex plot of impedance may be associated to an equivalent electrical circuit given by the parallel combination of a resistor (R) and a capacitor (C), which provides the characteristic time of the associated process through the relationship

$$\tau_c = RC \tag{10.2}$$

In terms of frequency representation, τ is related with the inverse of the characteristic angular frequency

$$\omega_c = 1/\tau_c \tag{10.3}$$

with $\omega_c = 2\pi f_c$. When these τ_c's are different enough, IS produces well-resolved arcs and it is possible to study these processes independently and with great accuracy.

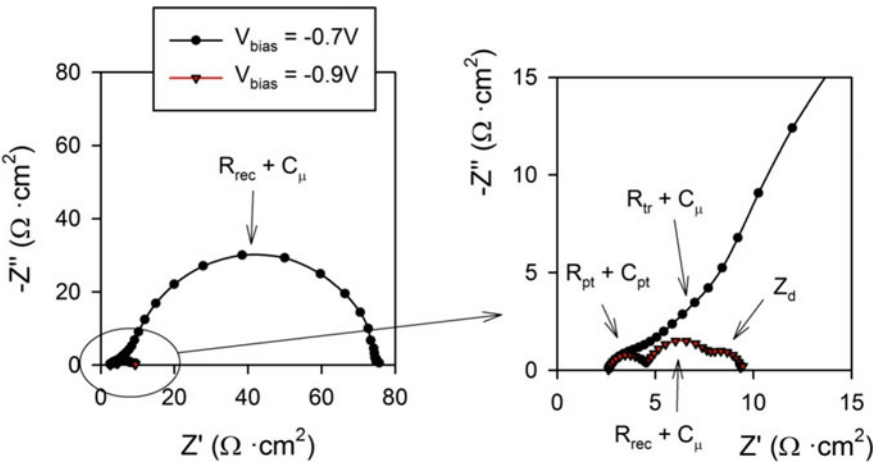

Fig. 10.2 Typical spectra of dye solar cells in the dark at two different voltages represented in impedance Nyquist plot

These resistances and capacitances may be associated to different electrical processes occurring in the materials and interfaces that compose films and devices. Resistances describe effects such charge transport, charge transfer at interfaces (between materials, through/from surface states, between bands, etc.), while capacitances are related to charge polarization and accumulation processes, providing a range of capacitances that include dielectric (material polarization, semiconductor depletion layer, Helmholtz layer, etc.) and chemical ones [4].

In general, impedance response of systems and devices is more complex than simple resistors and capacitors, therefore, a several electrical elements such inductances (L), constant phase elements (CPE), Warburg elements, Gerischer element, transmission lines, etc., are used to describe inductive phenomena, nonideal capacitances and resistances, diffusion processes, and many others. Detailed description of these elements is provided in literature and reference books [2, 3, 5, 6].

The key aspect of IS analysis is the correct identification of the electrical equivalent circuit that describes accurately the physicochemical processes contributing to the electrical response of the system under analysis. The analysis of the evolution of these processes under different bias or illumination conditions allows a deep understanding of fundamentals and performance limitations of these systems, and a validation of physical models.

10.2 Impedance Model for Dye Solar Cells

The mechanisms of charge injection transport and losses that govern dye-sensitized solar cells (DSC), see Fig. 10.3, are well known and described in detail in other chapters of this book. In this section, we will quickly review them to emphasize which of these processes may be analyzed using IS.

The different processes occurring in dye solar cell shown in Fig. 10.3b may be labeled as: (1) light absorption with electron and hole generation. (2) Electron injection from the lowest unoccupied molecular orbital (LUMO) of the dye to the conduction band of TiO_2. (3) Transport of electrons in the TiO_2. (4) Charge transfer from TiO_2 to transparent conductive oxide (TCO). (5) Hole transfer from highest

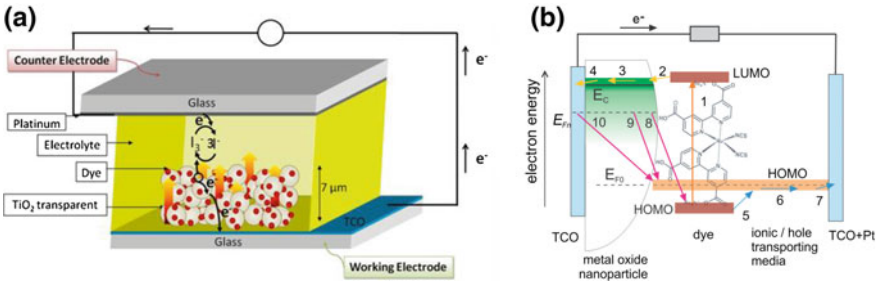

Fig. 10.3 **a** DSC structure, **b** schematic of the processes that take place in the dye solar cell

occupied molecular orbital (HOMO) to hole transporting material (HTM, a redox couple or solid hole conductor), also named dye regeneration. (6) Hole (ion) transport toward the hole-collecting electrode (HCE). (7) Charge transfer from HTM to HCE. (8) Recombination (losses) of electrons in the TiO_2 with holes in the HOMO of unregenerated dye. (9) Recombination of electrons in the TiO_2 with holes in the HTM. (10) Recombination of electrons in the TCO with holes in the HTM.

Impedance spectroscopy may not provide direct information about light absorption (1) and charge injection from the absorber to transporting media (2 and 5). For that purpose, there are available other optoelectronic techniques (UV–vis spectrometry, IPCE, IMPS, PIA, etc.). However, IS is a very powerful tool for the study of all the other processes, which have a significant influence in solar cell response.

As said in previous section, analysis of impedance data needs the use of an equivalent circuit to fit experimental data and relate physicochemical parameters with electrical elements. In particular for the analysis of DSCs with liquid electrolyte, the transmission line equivalent circuit in Fig. 10.4a has been developed to adjust impedance data. The transmission line models have been defined in several publications [5, 7–9]. We distinguish upper case parameter for the whole active film of thickness L, and lower case specifies local parameters. We have the following elements:

R_{tr} (= $r_{tr} \cdot L$) represents transport resistance in TiO_2,
R_{rec} (= r_{rec}/L) the recombination resistance accounting for charge losses in TiO_2 surface (including both recombination to electrolyte and to unregenerated dye),
C_{μ} (= $c_{\mu} \cdot L$) the chemical capacitance,
R_{TCO} the series resistance associated to collecting electrodes, contacts, etc.,
R_{BL} charge recombination from TCO at the back layer of TiO_2 to electrolyte,
C_{BL} capacitance representing charge accumulation at back layer TCO/electrolyte interface,
R_{Pt} charge transfer at platinized electrode acting as HCM,
C_{Pt} charge accumulation at electrolyte/platinized electrode interface and
Z_d the diffusion impedance describing transport in the electrolyte diffusion layer given by

$$Z_d = R_d \frac{\tanh(i\omega/\omega_d)^{1/2}}{(i\omega/\omega_d)^{1/2}} \tag{10.4}$$

where R_d is the diffusion resistance, $i = \sqrt{-1}$, ω is the (angular) frequency of the measurement and $\omega_d = D/L_d^2$ the diffusion frequency, with D the diffusion coefficient and L_d the thickness of the diffusion boundary layer.

The general model in Fig. 10.4a can be simplified in many operational situations. In fact, R_{tr} is only observable in a window of voltages typically narrower than 0.25 V. Thus, when large voltage bias is applied (close to V_{oc}), Fermi level of electrons (and consequently electron concentration) in TiO_2 increases, yielding to a negligible R_{tr} and equivalent circuit shown in Fig. 10.4b. In the opposite case, for

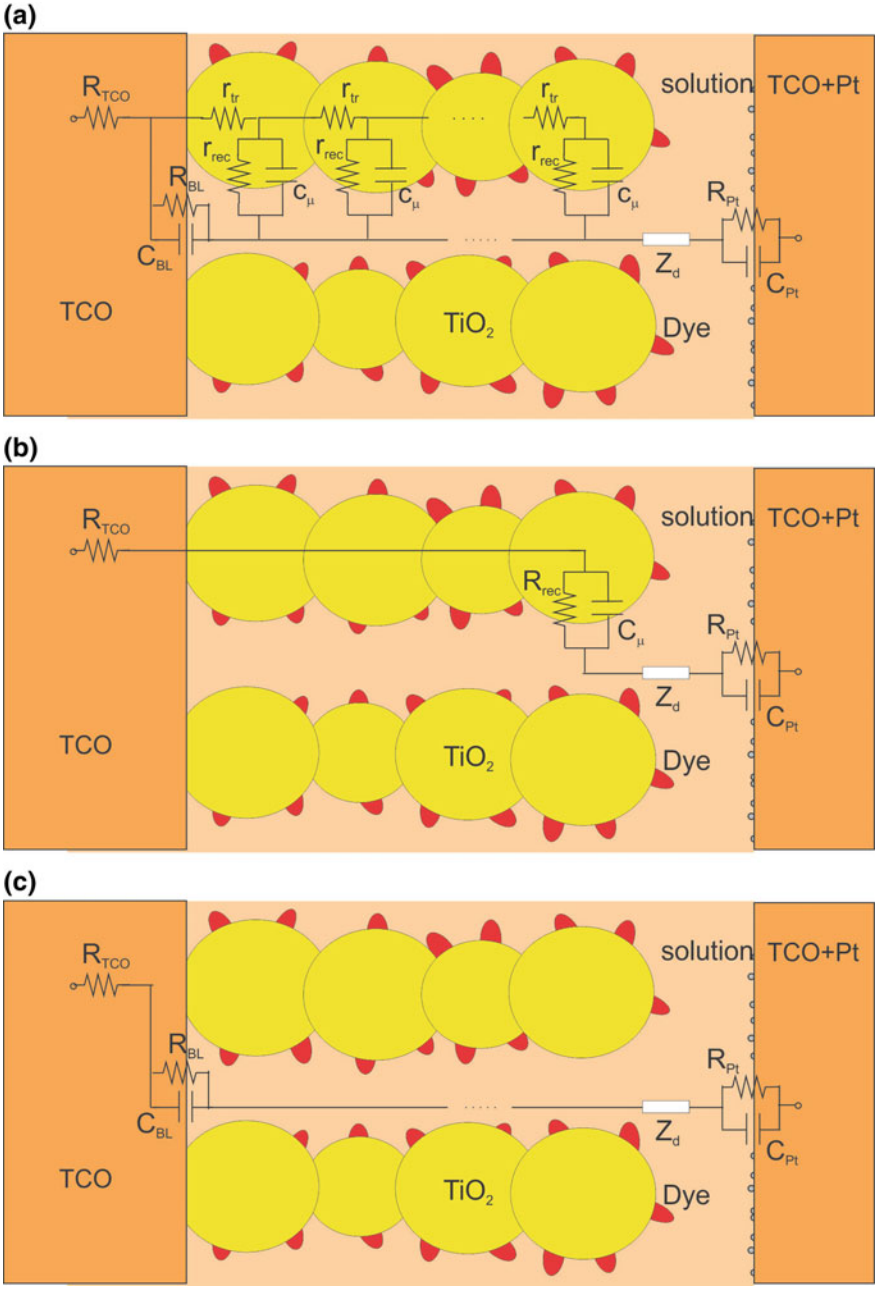

Fig. 10.4 **a** Equivalent circuit model for impedance spectra of dye solar cells. **b** simplification of (**a**) when R_{tr} becomes small at high bias. **c** Simplification of the model when R_{tr} becomes large at low bias

low bias (close to short circuit), R_{tr} becomes very large and the equivalent circuit reduces to the one in Fig. 10.4c.

This type of model may be also used in other systems with similar geometry, i.e., porous structures with active molecules absorbed in the surface for applications like sensing, water splitting, electrochromism, etc.

10.2.1 Application of Impedance Spectroscopy to Solar Devices. Generalities

The main performance parameters in solar cells are efficiency (η), short-circuit current (J_{sc}), open-circuit voltage (V_{oc}), maximum power (P_{max}), and fill factor (FF), see Fig. 10.5. Efficiency provides the ratio at which incident light power (P_{in}) is transformed into electrical power. By convention, the efficiency is calculated at the maximum power the solar cells may provide.

$$\eta = 100 \times \frac{P_{\max}}{P_{in}}. \tag{10.5}$$

P_{in} is given by the product of irradiance and cell area. FF is calculated from:

$$FF = \frac{P_{\max}}{J_{sc} \cdot V_{oc}}. \tag{10.6}$$

The FF informs us about which is the part of the area beneath the J–V curve that can be used to obtain the maximum power. The use of IS provides direct information to identify and evaluate which elements in the device control FF and V_{oc}. In an indirect way, it may also provide data about J_{sc} limitations. To access all this

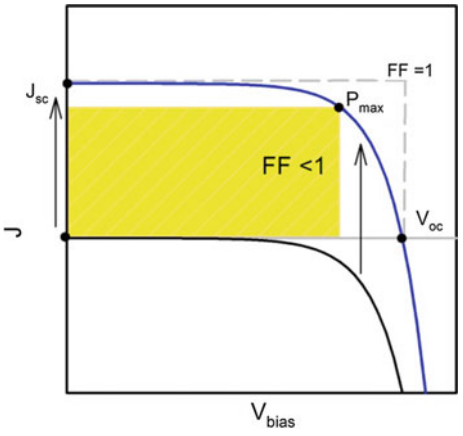

Fig. 10.5 Main electrical parameters of a solar cell

information, IS analysis requires a number of procedures that will be described in the following paragraphs

Once impedance spectra are taken at different points of J–V curve and under the same illumination, the first step is fitting the data to the appropriate equivalent circuit model (in DSC, the one in Fig. 10.4) to obtain the resistances and capacitances that describe the different physicochemical processes occurring in the device.

The resistances obtained from the fit will be used for the analysis of J–V curve. For impedance measurements at low frequencies ($\sim$DC condition), capacitive contributions become infinite and reactive ones vanish thus, transient during the measurement disappear. If the AC perturbations in Eq. (10.1) are small enough to keep linearity of the measurement, they can be approached to their amplitude ($\tilde{V} = dV$ and $\tilde{J} = dJ$). Therefore DC resistance, R_{DC} (which becomes the total resistance of the system), may be written as the inverse of the slope of J–V curve [5, 8]

$$R_{DC} = \left.\frac{dV}{dJ}\right|_{V_{bias}}. \tag{10.7}$$

As plotted in Fig. 10.1, R_{DC} depends on the bias voltage at which it is measured.

Integrating Eq. (10.7), it is possible to reproduce the J–V curve using the short-circuit current and the R_{DC} values obtained at different voltages along the J–V curve taken under constant illumination:

$$J(V_{bias}) = J_{sc} - \int_0^{V_{bias}} \frac{dV}{R_{DC}(V)} \tag{10.8}$$

The right side of this equation determines the shape of the J–V curve while J_{sc} displaces the curve along J axis according to how efficiently light is harvested. For devices in general and for molecular solar cells, in particular, we can classify the resistances into two types: series and parallel resistances, so that the total resistance at DC obtained from impedance may be written as

$$R_{DC} = R_{series} + R_{||} \tag{10.9}$$

R_{series} includes the contribution of the resistances associated to difficulties in transporting the charge: transport resistances in collecting electrodes (wires, connections, transparent conducting electrodes, e.g., R_{TCO}), the diffusion in the electrolyte (R_d), the resistance associated to resistivity of materials (R_{tr}), and the charge transfer resistance at interfaces between materials or at connections (R_{Pt}), etc. In transmission line equivalent circuit of Fig. 10.4a $R_{series} = R_{TCO} + R_{tr}/3 + R_d + R_{Pt}$, which in Fig. 10.4b reduces to $R_{series} = R_{TCO} + R_d + R_{Pt}$.

The most relevant effect of series resistance on the performance of solar cells is the decrease in fill factor, see Fig. 10.6. In extreme cases in which R_{series} becomes too large, short-circuit current may also decrease. As a rule of thumb, all

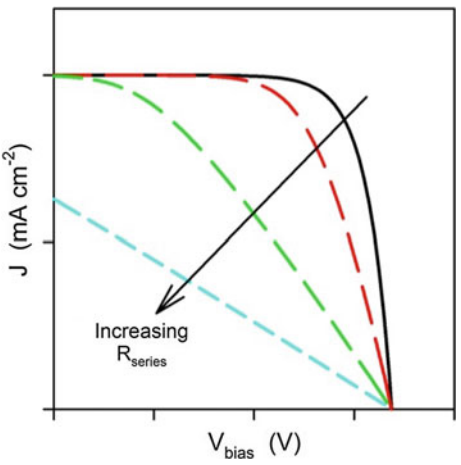

Fig. 10.6 Effect of series resistance on the J–V curve: The larger the resistor, the lower the FF

contributions to series resistance should be minimized. IS may help in identifying which specific element (e.g., the conductivity of TCO or electrolyte, the catalyst in the counter electrode) needs to be improved in the process of device optimization.

$R_{||}$ accounts for all the parallel processes associated to charge losses like recombination at TiO_2/dye/electrolyte interface (R_{rec}) or recombination at the TiO_2 back layer (R_{BL}). Formally, $R_{||}$ corresponds to the parallel combination $R_{rec}| \, |R_{BL}$ however, in good cells and for most of the voltages in J–V curve, $R_{BL} \gg R_{rec}$ therefore $R_{||} \approx R_{rec}$ and commonly, parallel resistance is named recombination resistance.

Recombination between electrons and holes can be processed from band to band, from band to a redox shuttle or from semiconductor band to molecular orbital (CB to HOMO or VB to LUMO), and these processes may take place directly or mediated through distributed or localized states (traps). Knowing the fundamental physicochemical parameters that control how $R_{||}$ (or R_{rec}) evolves with voltage or under illumination is a key aspect needed to understand the limits of device efficiency.

If we focus now on a single recombination mechanism, either the simplest or the most sophisticated models describing the process of charge loses may be described in terms of a R_{rec}, that will contain the kinetic rate of the charge transfer reactions and information about the density and distribution of donor and acceptor states. R_{rec} allows calculating the ideal J–V curve through

$$J = J_{sc} - \int_0^{V_F} \frac{dV}{R_{rec}}, \tag{10.10}$$

where V_F is the voltage free from series resistance effects. The term ideal (or internal) curve relies on the fact that it provides the maximum performance

attainable by the device, with no voltage losses due to the R_{series} that as said above, reduces the performance to provide real response. Therefore, it is R_{rec} the element that ultimately determines the shape of the ideal J–V_F curve.

From Eq. (10.9) and taking the equation for recombination resistance in Eq. (10.15) of Table 10.1, the expression for the J–V_F curve can be obtained:

$$J = J_{sc} - \frac{k_B T}{\beta q R_0} \exp\left[-\beta \frac{q V_F}{k_B T}\right] \tag{10.11}$$

There are several aspects to emphasize in this equation: By one side, defining $J_0 = k_B T/\beta q R_0$ and provided that in general $J_{sc} \gg J_0$, Eq. (10.11) is the same as the one describing the curve of a p-n junction solar cell with diode quality (or ideality) factor m = $1/\beta$ [5, 10]. This fact allows the application of standard models used for the characterization of p-n junction solar cells in the analysis of molecular devices despite the differences in the interpretation of the parameters obtained.

By other side at Eq. (10.8) at open circuit (J = 0) provides the open-circuit voltage

$$V_{oc} = \frac{k_B T}{\beta q} \ln \frac{\beta q R_0 J_{sc}}{k_B T} \tag{10.12}$$

which, using the equivalency with p-n junction solar cell notation, yields

$$V_{oc} = \frac{k_B T}{\beta q} \ln \frac{J_{sc}}{J_0} \tag{10.13}$$

Equation (10.12) points out the dependence of V_{oc} with the transfer factor β, R_0, and the photocurrent. As we will see later, the changes in V_{oc} associated to variations in J_{sc} are small (in the order of few mV), due to its logarithmic dependence. However, the large variations in R_0 among samples and the differences in β values yield to relevant changes in V_{oc}. Therefore, we can say that R_{rec} is the dominant factor determining photovoltage.

Equation (10.11) may be also written as

$$J = J_{sc} - \frac{k_B T}{\beta q} \frac{1}{R_{rec}} \tag{10.14}$$

Table 10.1 Characteristic resistances and capacitances found in molecular devices

Element	Short	Equations	
Recombination resistance [7]	R_{rec}	$R_0 \exp\left[-\beta \frac{E_{Fn}-E_{Fp}}{k_B T}\right]$	(10.15)
Transport resistance for electrons and holes [12]	R_{tr}	$R_{tr,0} \exp\left[\frac{E_c-E_{Fn}}{k_B T}\right]; R_{tr,0} \exp\left[\frac{E_{Fp}-E_V}{k_B T}\right]$	(10.16)
Dielectric capacitance	C_D	$\frac{\varepsilon}{d}$	(10.17)
Helmholtz capacitance [1]	C_H	$\frac{\varepsilon_{sol}}{d_H}$	(10.18)
Mott-Schottky capacitance [11, 13]	$C_{M\text{-}S}$	$\left[\frac{2}{q\varepsilon N_d}\left(V_F - V_{fb} - \frac{k_B T}{q}\right)\right]$	(10.19)
Chemical capacitance of electrons and holes [4]	C_μ	$q^2 \frac{dn}{dE_{Fn}}; q^2 \frac{dp}{dE_{Fp}}$	(10.20)
Chemical capacitance of traps in a tail distribution below E_c [4]	C_{trap}	$(1-p)\frac{\alpha q^2 N_L}{k_B T} \exp\left[\alpha \frac{E_{Fn}-E_c}{k_B T}\right]$	(10.21)
Chemical capacitance of traps in an energy confined state [4]	C_{trap}	$(1-p)\frac{q^2 N_t}{k_B T\sqrt{2\pi\sigma}} \exp\left[\frac{(E_F-E_t)^2}{2\sigma^2}\right]$	(10.22)

Parameter meanings: The transfer factor β ($1 > \beta > 0$) is a constant related to the way the charge recombines; q is the electron charge, k_B is the Boltzmann constant; T is the temperature; E_{Fn} and E_{Fp} are the Fermi level of electrons and holes (in the case of DSCs $E_{Fp} = E_{redox}$ the energy of the redox shuttle); R_0, a parameter that determines the onset of recombination and depends on charge concentration and distribution of donor and acceptor states energy level distribution and recombination rate; E_c and E_v are the conduction and valence band energy edge position; $R_{tr,0}$, a parameter related to resistivity of electrons or holes; ε ($= \varepsilon_r \cdot \varepsilon_0$) is the dielectric constant of the material; d is the thickness of the material; ε_{sol} is the dielectric constant of solution; d_H is the thickness of Helmholtz layer; $V_F = -(E_{Fn} - E_{Fp})/q$ is the applied or bias voltage in the ideal case $R_{series} = 0$; V_{fb} is the flat band potential of the semiconductor; N_d is the dopant density; α ($1 > \alpha > 0$) is a constant related the shape of the distribution of states in the tail below the conduction band; p is film porosity; N_L is the total number of traps in this tail of localized states; N_t is the total number of traps in a density of states distributed around a given energy E_t; σ is the energy width of this density of states distribution. Resistances are given in $\Omega\ cm^2$ while capacitances in $F\ cm^{-2}$. Note that chemical and trap capacitances scale with the film thickness

Therefore, when R_{rec} follows Eq. (10.15), there is a linear dependence of J with the inverse of R_{rec}. This fact allows the validation of this particular recombination model without taking into account the effects of series resistances.

From the capacitance analysis, fundamental parameters such dielectric constant, density of states, or energy level distribution may be estimated. Any of the capacitances found in the device will be then classified according to the kind of information we can extract from them. In dye solar cells, the main contributions to capacitance are: (i) the interface between TCO and electrolyte, both at the platinized and the porous film electrode, which follow a Mott-Schottky behavior as it is dominated by TCO capacitance [11]. (ii) The chemical capacitance associated to the distribution of states below the conduction band of TiO_2. Eventually, the contribution of energy confined trap states could also produce some contribution to the chemical capacitance.

Last step in the IS analysis is the interpretation and evaluation of resistances and capacitances in order to understand their effect on device performance and extract

physicochemical characteristics that govern their behavior. Table 10.1 shows the expression and voltage dependence of some of the resistances and capacitances appearing in molecular devices and the fundamental parameters that control this response.

In general, recombination processes as the one given in Eq. (10.15) provide a R_0 which is inversely proportional to a constant rate associated to the kinetics of the recombination, the concentration of donor and acceptor states and the difference in energy between these states. In the particular case of dye solar cells, one of the proposed mechanisms for charge losses is the recombination from electron trap states in TiO_2 to acceptor states in a redox couple, that yields to [8]

$$R_0 = \frac{\sqrt{\pi \lambda k_B T}}{q^2 L \alpha k_r c_{ox} N_s} \exp\left[\alpha \frac{E_c - E_{redox}}{k_B T} + \frac{\lambda}{4 k_B T}\right] \tag{10.23}$$

with c_{ox}, the concentration of acceptor species in the electrolyte, λ the reorganization energy of acceptor species, N_s the total number of electronic states contributing to the recombination, and k_r a constant accounting for recombination rate.

During optimization process of solar devices, the change of molecular absorbers, redox species, additives concentration, electrolyte, preparation process, etc., may yield to changes in V_{oc} that will be related to the modification of all the parameters that determine R_0, β and consequently R_{rec}. Knowing these variations with respect to a well-known reference sample is of great help to determine if the optimization routes used to improve the device flow in the correct direction. In detail, the changes in V_{oc} between samples may be associated to differences in photogenerated current, energy of the conduction band, energy of the redox, (valence band or HOMO) and recombination kinetics:

$$\Delta V_{oc} = \Delta V_{Jsc} + \Delta E_c/q - \Delta E_{redox}/q + \Delta V_k \tag{10.24}$$

From these, the changes in V_{oc} associated to R_{rec} are given by

$$\Delta V_{rec} = \Delta E_c/q - \Delta E_{redox}/q + \Delta V_k \tag{10.25}$$

In the next section, we will show a practical example of the IS analysis procedure followed in the analysis of a collection of DSC samples to characterize them and evaluate the contributions to *FF* and V_{oc} of the different modifications we introduced during the preparation of these samples [14]. The DSCs were made of 10 μm thick TiO_2 mesoporous layer (7 μm transparent + 3 μm scatter) sensitized with N719 dye in which different electrolytes have been used to modify bands position and recombination. Characteristics of these electrolytes are summarized in Table 10.2.

Table 10.2 Composition of electrolytes employed in the fabrication of DSCs

DSC name	BMII	I_2	GuSCN	LiI	tBP	Solvent
A	0.6 M	0.03 M	0.1 M	–	0.5 M	A/V (85:15)
B	–	0.05 M	–	0.5 M	0.5 M	MPN
C	–	0.05 M	–	0.5 M	–	MPN
D	0.6 M	0.03 M	0.1 M		0.5 M	MPN

Abbreviations of the additives: *BMII* stands for 1-butyl-3-methylimidazolium iodide, *GuSCN* for guanidinium thiocyanate, *LiI* for Lithium Iodide, *tBP* for 4-*tert*-butylpyridine. The solvents denominations are *MPN* for methoxypropionitrile, and *A/V* for a mixture of acetonitrile and valeronitrile 85:15 in volume

10.2.2 The Analysis Procedure

An accurate analysis of voltage dependent resistances and capacitances requires, first, the correction of applied bias from drops in series resistance to estimate the real position of the Fermi level voltage. There are two ways of calculating V_F depending if the focus is given to R_{series} or to $R_{||}$. In the first case,

$$V_F = V_{bias} + \int_{J_{sc}}^{J_{bias}} R_{series} dJ + V_0 \tag{10.26}$$

In the second case,

$$V_F = \int_{J_{sc}}^{J_{bias}} R_{||} dJ + V_0, \tag{10.27}$$

where V_0 is the potential difference between the photoactive film and the contacts at short circuit or in other words, the voltage drop in R_{series} at J_{sc}. It may be estimated through

$$V_0 = -\int_{J_{sc}}^{0} R_{series} dJ = V_{oc} - \int_{J_{sc}}^{0} R_{||} dJ \tag{10.28}$$

Note that in general, R_{series} is a variable that depends on the bias voltage (current), therefore the integral in Eqs. (10.24) and (10.26) are needed to obtain the voltage drop in the series resistance (V_{series}). When estimating voltage of the Fermi level in TiO_2, R_{series} does not include transport resistance in the material (R_{tr}), as only external voltage drop has to be considered, therefore in this case, $R_{series} = R_{Pt} + R_{TCO} + R_d$.

As can be seen in Figs. 10.7 and 10.8, V_{series} correction, introduce important modifications in the representation of data versus voltage. The J–V_F curves provide the maximum possible *FF,* power, and efficiency attainable by the cell in the ideal condition $R_{series} = 0$. In the present case, the potential increase in *FF* associated to

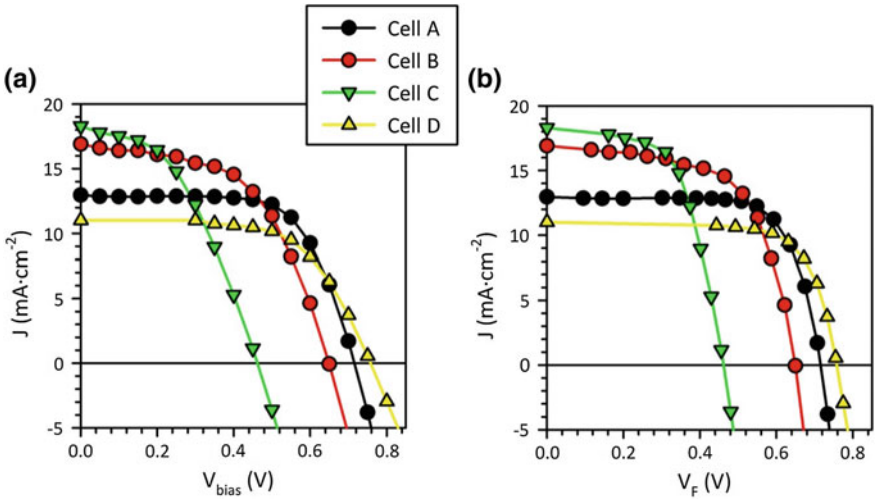

Fig. 10.7 J–V curves **a** before and **b** after R_{series} correction

eliminating series resistance ranges from 8 to 37% see Table 10.3. This result highlights the importance of optimizing series resistance in solar cells, for which both device design and materials employed are key.

The R_{series} free *FF* (*internal FF*) is governed by β (= 1/m) and V_{oc} according to the expression [5]

$$internal\ \ FF = \frac{V_r - \ln(V_r + 0.72)}{V_r + 1} \tag{10.29}$$

with $V_r = \beta q V_{oc}/k_B T$. The closer β to 1 and the higher the V_{oc} the larger *FF*.

In Fig. 10.8, it is shown how data of resistances and capacitances become linear (in the logarithmic scale) after representation versus V_F. This allows calculating the parameters β, α, R_0, etc. governing R_{rec} and C_μ with accuracy enough to understand the origin of solar cell performance differences among samples.

From the fitting of R_{rec} a straight line in the semi logarithmic scale of Fig. 10.8c the values of R_0 (from the R_{rec}-axis intersection) and β (from the slope) may be obtained. The spacing between the R_{rec} of the different samples indicates which is the change in V_{oc} due to the charge recombination (ΔV_{rec}). From Eq. (10.12), ΔV_{rec} may be estimated through

$$\Delta V_{rec} = \frac{k_B T}{q} \ln \frac{(\beta R_0)^{\beta}}{\left(\beta_{ref} R_{0,ref}\right)^{\beta_{ref}}}, \tag{10.30}$$

where the subindex *ref* stands for data from sample taken as reference to compare (black dots in Figs. 10.7 and 10.8). In the graph, this is represented by the distance between R_{rec} and $R_{rec,ref}$ at the V_{oc}. If β is constant, Eq. (10.26) simplifies to

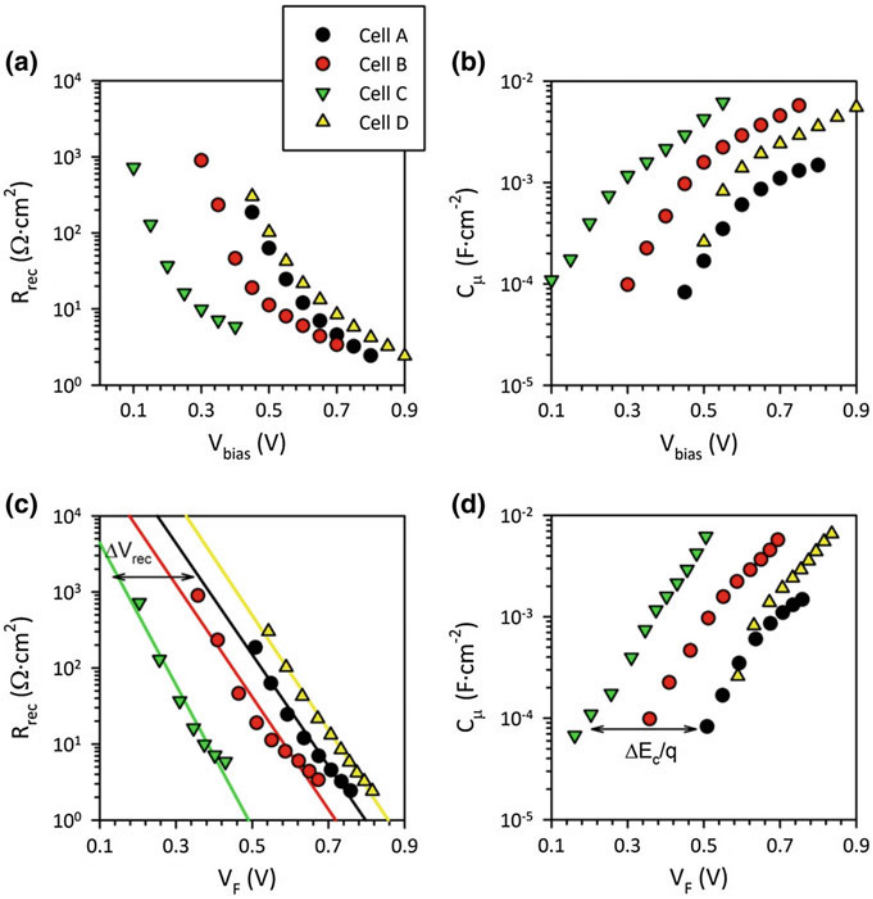

Fig. 10.8 Recombination resistance and chemical capacitance before (**a**), (**b**) and after (**c**), (**d**) R_{series} correction

$$\Delta V_{rec} = \frac{k_B T}{\beta q} \ln \frac{R_0}{R_{0,ref}} \tag{10.31}$$

As can be seen in Table 10.3, the V_{oc} differences among the samples are mainly due to $\Delta V_{rec,}$ leaving photocurrent contribution to the change in V_{oc} (ΔV_{Jsc}) a residual value despite the relevant variations in J_{sc}. ΔV_{rec} has two components, one associated to the kinetics of recombination the other to the energy of conduction band and redox level.

Data from R_{tr} and traps C_μ allow estimating band edge displacements in conduction band as Eqs. (10.16) and (10.21) indicate. In fact, when comparing two samples with different conduction band edge both C_μ and R_{tr} are displaced in the X-axis the amount $\Delta E_c/q$. Note that in this case, samples were measured under illumination and R_{tr} could be only fitted accurately at two bias voltages. For this

Table 10.3 Photovoltaic parameters obtained from IS analysis

Parameters	Cell A	Cell B	Cell C	Cell D
J_{sc} (mA cm^{-2})	12.9	16.9	18.3	11.0
V_{oc} (V)	0.716	0.650	0.462	0.758
Calculated V_{oc} (V)	0.712	0.651	0.454	0.768
η	6.19	5.95	3.70	5.22
FF	0.67	0.53	0.44	0.63
Internal η	6.72	6.92	5.09	5.95
Internal FF	0.73	0.62	0.61	0.72
Average R_{series} (Ω cm^2)	3.78	4.42	5.58	6.83
R_0 (Ω cm^2)	6.82×10^5	2.05×10^5	1.13×10^4	2.87×10^6
β	0.439	0.443	0.477	0.452
α	0.282	0.308	0.349	0.259
$E_c - E_{redox}$ (eV)	0.976	0.801	0.618	0.936
ΔV_{Jsc} (mV)	Ref.	0	−2	−2
ΔV_{rec} (mV)	Ref.	−66	−252	+44
$\Delta E_c/q$ (mV)	Ref.	−180	−330	−50
ΔV_k (mV)	Ref.	+114	+78	+96
k_r (s^{-1} cm^3)	2.4×10^{-14}	2.3×10^{-15}	3.7×10^{-15}	3.1×10^{-15}
$k_r \cdot c_{ox}$ (s^{-1})	4.3×10^5	6.8×10^4	1.1×10^5	5.6×10^4

R_{series} is the series resistance of the cell; R_0 is the recombination prefactor parameter from Eq. (10.3); β is the charge transfer coefficient for recombination of electrons; α is the exponential electron trap distribution parameter; calculated V_{oc} is the open-circuit voltage obtained from Eq. (10.11) at T = 305 K; $E_c - E_{redox}$ the value estimated from Eq. (10.20), taking $N_t = 2.5 \times 10^{19}$ cm^{-3}; ΔE_c is the energy shift needed to compare all the cells at the same conduction band level obtained after displacing the capacitances in Fig. 10.3b; ΔV_k is the voltage difference in R_{rec} due to the differences in recombination rates; ΔV_{Rrec} is the change in V_{oc} associated to R_{rec} which is the sum of $\Delta E_c/q$ and ΔV_k; All these incremental values are taken with respect to sample A that is taken as reference. k_r is the estimated value for recombination kinetics rate obtained from Eq. (10.22) using $\lambda = 0.5$ V and $N_s = N_t$; The product $k_r \cdot c_{ox}$ yields to the inverse of time constant typically used for recombination rate

reason to estimate ΔE_c with a better accuracy only C_μ data in Fig. 10.8d was used. Another way to estimate E_c from is the fitting of data in Fig. 10.8d to Eq. (10.21): From the slope, α may be calculated and from the C-axis intercept, assuming $N_t = 2.5 \times 10^{19}$ cm^{-3}, E_c may be obtained, see Table 10.3. Note that a good agreement is found between ΔE_c changes obtained from the estimations of E_c and with the V_F-axis shift of capacitance despite the changes in α.

In the case of changes in the energy level of the redox shuttle, those changes can be measured by other techniques such cyclic or differential scanning voltammetry and then its contribution (ΔE_{redox}) to the V_{oc} has to be also considered.

Variation in E_c and E_{redox} between samples may be corrected in the voltage to highlight the changes in R_{rec} associated to recombination kinetics. We define the voltage at the equivalent conduction band (and redox energy) position as [15]

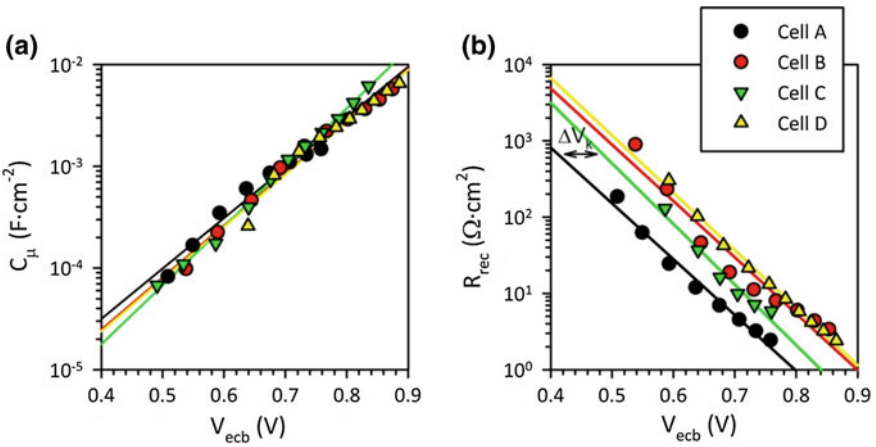

Fig. 10.9 Chemical capacitance (**a**) and recombination resistance (**b**) at equivalent conduction band voltage

$$V_{ecb} = V_F - \Delta E_c/q + \Delta E_{redox}/q \tag{10.32}$$

At V_{ecb} all capacitances overlap as shown in Fig. 10.9a. If we assume no changes in c_{ox}, the differences in X-axis interception of R_{rec} data represented versus V_{ecb}, see Fig. 10.9b provide the change in V_{oc} associated to the differences in the kinetics of charge transfer (ΔV_k). With the appropriate model for R_0, kinetic constant rate may be estimated as given in Table 10.3.

Table 10.3 summarizes the parameters obtained from J–V curve, R_{rec}, C_μ and the different voltage contribution from each parameter.

10.3 Analysis of Solar Cells with Different Dyes

During last decades, many efforts have been focused on the development of organic dyes, trying to increase the absorption and solar spectra overlapping to improve performance and also to reduce the cost of the dye with the idea of minimizing the cost of the final product. Nevertheless, the use of organic dyes as sensitizers for DSC is related with new or different problems, specially the increase in the recombination processes [16], which is directly connected with the decrease in the value of the open-circuit voltage (V_{oc}) [17–19] and sometimes aggregation problems.

The different classes of chromophores that have been developed for their use in dye solar cell may be classified into two main families: (i) Organometallic dyes, which include Ru-based complexes and Zn-porphyrin complexes, and (ii) metal-free dyes, with indoline, perylene, and coumarin as some of the most common.

They result in different behavior on electron transfer at titania/dye/electrolyte interface, where the dye molecule plays a pivotal role, as a consequence of dye structural and electronic properties: the substituent's nature, the size, and nature of

the π-bridge, the type of absorption onto titania surface, the structure of donor electron moiety or the anchoring group.

During long time, in this context, special care has been taken to construct photosensitizers featuring desirable electronic and steric properties. A general problem that has been found in this technology is the need of a detailed understanding of the titania/dye/electrolyte interface, because there are some controversial ideas about how the dye structure can interact with the rest of the components of the cell under illumination, like co-adsorbents [20], redox shuttle [21–23] and electrolyte components, and how these interactions affect the cell performance. At that point, impedance spectroscopy can clarify many aspects of the mechanics that take place during the function of the DSC and also can help to improve the development of new dyes.

It is well known that within a typical D-π-A chromospheres for DSCs, the electronic and steric traits of the electron donor not only play a pivotal role in determining the molecular energy levels, which intimately correlate with the light-harvesting capacity of a photosensitizer and some dynamic processes such as exciton dissociation and dye regeneration. But also affects the physicochemical interactions of multiple components at the titania/dye/electrolyte interface, which also have deep effects on the ultimate power output of a DSC. This recognition in the last decade had translated into massive efforts in designing push-pull organic dyes featuring various electron donors, including triarylamines [24–27], carbazoles [28, 29], coumarins [30], indolines [31, 32] and heteroanthracenes (e.g., phenothiazine) [33, 34], etc. See also Chap. 3 for more details.

Among various strategies to improve the capacity of dye-sensitized solar cells to convert sunlight to electrical power, successful molecular engineering of some photosensitizers has remarkably contributed to the performance progress of this photovoltaic technology and impedance spectroscopy played an important role. Generally, an elaborately engineered photosensitizer is supposed to meet two requirements: (i) enhancing the overlap between the spectral coverage of dye molecules and the standard AM1.5G solar emission spectrum through energy level engineering and (ii) concomitantly achieving high open-circuit photovoltage with reduced energy losses. In this context, special care has to be taken to construct photosensitizers featuring desirable electronic and steric properties. The use of Impedance Spectroscopy allows a deep analysis of recombination process through R_{rec}, what helps to unveil the mechanisms of charge losses and provides practical information about which dye configurations behave according to expectations and which depart from previsions.

For dyes based on Ru, the only recombination mechanism that needs to be taken into account is charge transfer from TiO_2 to the electrolyte. The electron charge transfer to the oxidized dye may be considered negligible because in the case of Ruthenium dyes, like N719 dye based DSCs benefit from good spatial separation between injected electrons and the dye cation, thereby reducing recombination to oxidized dye [35]. This is achieved by the electron donating thiocyanate ligands which shift the distribution of the highest occupied molecular orbital (HOMO) on the dye cation away from the reacting TiO_2 surface and reducing the recombination rate to electrolyte accordingly [36].

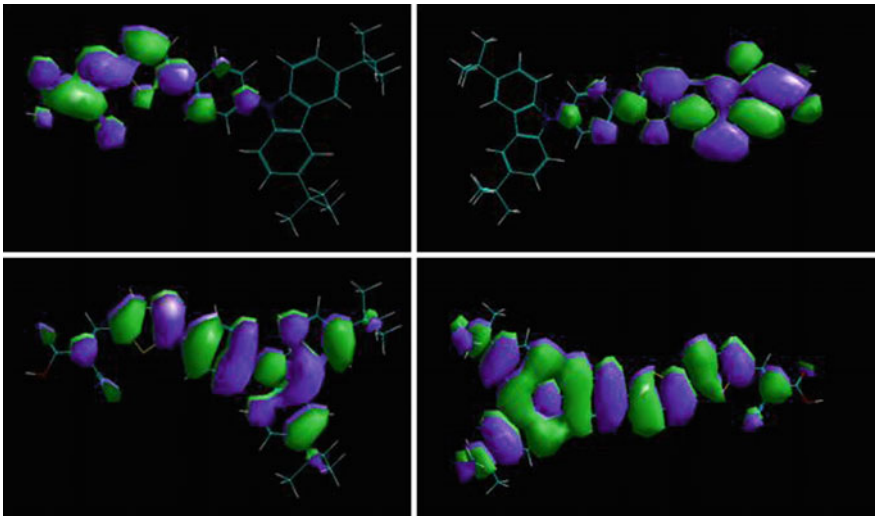

Fig. 10.10 Optimized chemical structures and frontier molecular orbitals of BG-1 (*left*) and BG-2 (*right*) at HOMO (*lower*) and LUMO (*upper*)

However, when intensive research on organic dyes started due to their bigger advantages as the best overlap with the solar spectra, high extinction coefficient, lower sensibilization time, cheaper fabrication processes, and materials, etc. [16, 37], it was observed that the overall recombination was higher than for Ru-based dyes. Initially, this result was mainly attributed to the fact that the HOMO on the organic dye is delocalized along the structural backbone between the binding moiety and the remainder of the dye [38] as shown in Fig. 10.10. This spatial distribution of the HOMO level was found common for diverse organic dyes [39, 40]. Further research revealed that during regeneration process, organic dyes generate intermediate state involving the formation of a bond between dye cation and iodide species [40–43]. This intermediate state creates a new path for the electron recombination which could also contribute to the large decrease in the charge recombination resistance in the case of organic dyes versus ruthenium dyes. These new charge losses processes appearing with the use of organic dyes create significant limitations compared to organometallic dyes that need to be solved to be able of taking advantage beneficial characteristics of organic dyes [44–46].

The charge recombination between the electrons injected in the TiO_2 and the I_3^- ion in electrolyte can be effectively reduced by inhibiting the approaching of I_3^- ions to the TiO_2 surface. The introduction of hydrophobic long alkyl and alkoxy chains on donor moiety or on π-bridges unit effectively block approaching of hydrophilic I_3^- ions to the TiO_2 surface and thus suppress the charge recombination, resulting in increasing the efficiency close to the commercial Ru-dyes.

Here, impedance spectroscopy will be used to illustrate the importance of recombination in DSCs sensitized with organic dyes we present some results using

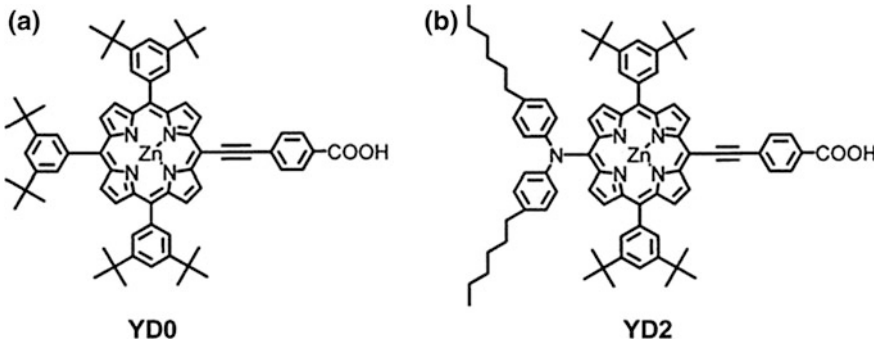

Fig. 10.11 Dye structure for **a** YD0 and **b** YD2 porphyrin dye

Table 10.4 Values of V_{oc}, FF, J_{sc}, efficiency, internal FF and internal efficiency, β, R_0, J_0 α, $\Delta E_c/q$, ΔV_k and average R_{series} obtained at steady state measurement under 100 mW cm^{-2} light intensity and AM 1.5 global radiation for DSC sensitized with YD0, YD2 and N719 dyes

Sample name	YD2	YD0	N719
J_{sc} (mA/cm^{-2})	15.4	6.92	12.6
V_{oc} (V)	0.66	0.65	0.74
FF	0.62	0.73	0.70
η (%)	6.36	3.29	6.54
Internal FF	0.73	0.81	0.81
Internal η (%)	7.41	3.58	7.54
R_0 (Ω cm^2)	3.23×10^5	3.92×10^7	2.03×10^8
α	0.24	0.28	0.30
β	0.47	0.63	0.62
J_0 (mA/cm^{-2})	1.75×10^{-7}	1.03×10^{-9}	2.04×10^{-10}
Area (cm^2)	0.29	0.30	0.24
ΔE_c/q (mV)	−123	−32	Ref.
ΔV_k (mV)	+5	−75	Ref.
Average R_{series} (Ω cm^2)	5.66	5.82	4.18

porphyrin dyes, YD0 and YD2 with structure shown in Fig. 10.11. YD2 dye consists of diarylamino group with two hexyl chains attached to the porphyrin ring acting as an electron donor, π-conjugated phenylethynyl group as a bridge, and the carboxylic acid moiety as an acceptor. The porphyrin chromophore itself constitutes the π bridge as a light-harvesting center in this particular D-π-A structure. YD0 dye does not have the diarylamino substituent, serving as a reference dye to test the effect of the electron donor and also to check its effect as a surface blocking to I_3^- (Table 10.4). Results will be compared with a Ru-based dye N719 to highlight the resemblances and differences in the observed behavior.

As in previous section, from IS data we obtained the values of R_{series}, that were used to obtain V_F and represent R_{rec} and C_μ. in Fig. 10.12. From C_μ data shown in Fig. 10.12a, we can identify a downward shift of the conduction band edge of TiO_2

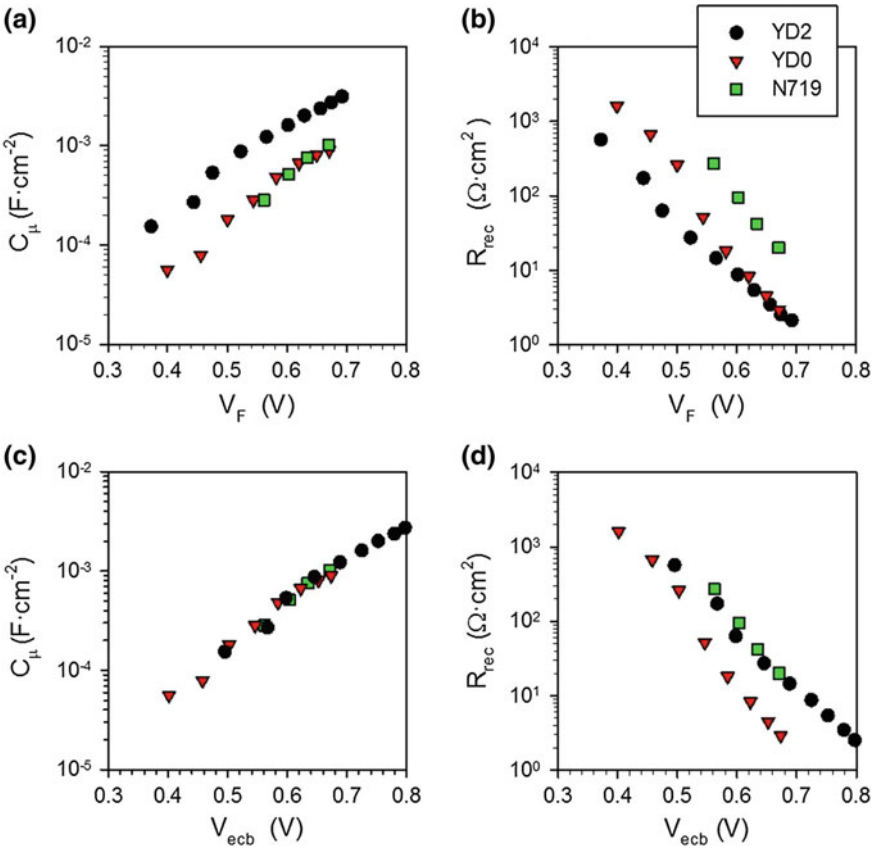

Fig. 10.12 **a** Capacitance and **b** Recombination resistance, with respect to Fermi level voltage after removing the effect of series resistance. **c** Capacitance and **d** Recombination resistance plotted with respect to equivalent common conduction band voltage

in the case of DSC sensitized with YD2 dye with respect to the cell sensitized with N719. This shift is much smaller for sample sensitized with YD0, see Table 10.4. As is well known [8], the lower position of the conduction band facilitates the electron injection from the dye to TiO_2 and may explain the difference in photocurrent despite the similarities in the absorption spectrum, see Fig. 10.13.

The drawback of a E_c downward shift is that, if recombination rate does not change, the energy difference between electrons Fermi level in TiO_2 and the I^-/I_3^- redox potential of the electrolyte also decreases, resulting in a lower value of $V_{oc} = -(E_{Fn} - E_{redox})/q$. However, we find that V_{oc} is very similar both for YD0 and YD2 samples suggesting a change in recombination kinetics. When representing C_μ and R_{rec} data as a function of equivalent common conduction band voltage (using N719 as reference) as in Fig. 10.12c, d, it is clearly observed that the R_{rec} values of YD0 are smaller than those of YD2 and N719 which are almost

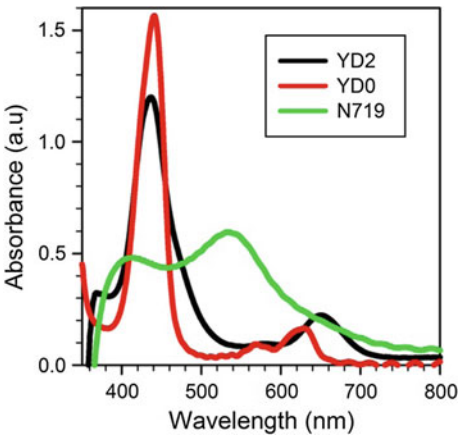

Fig. 10.13 Absorbance spectra of YD0, YD2 and N719 dyes

equal. This result indicates charge recombination rate is much faster in YD0 than in YD2 and N719. From these results, we may conclude that the drop in E_c found for YD2 is compensated by a decrease in the recombination kinetics with respect to YD0, yielding to the similarity found in V_{oc} [16]. The improvement in photocurrent associated to the better injection in YD2 is the origin of improved efficiency.

This result confirms that the diarylamino group is effective at least in one of the actions it is designed for: repeling the triiodide ions from the titania surface and diminish recombination to oxidized dye [42]. This result confirms that a good synthesis design is crucial to avoid the recombination process to the electrolyte [43].

10.4 Impedance Spectroscopy in Water Splitting

Many research has been dedicated to explore the possibility of using photocatalysis as a mean to store energy from the sun into chemical bonds. The most studied reactions is the photolysis of water for the production of hydrogen. Many materials and composites have or are being investigated to produce efficient devices that may carry this reaction at competitive prices. Among these materials, we find TiO_2, WO_3, $\alpha-Fe_2O_3$, IrO_x, $BiVO_4$, Pt, RuO_2, MoS_2, NiFe, NiMo, $Ni(OH)_2$, NiOOH, $LaMoO_3$, $LaNiO_3$, Co_3O_4, $NiCo_2O_4$, and multiple metal oxide combinations [47–52].

Here, we will use the case of hematite ($\alpha-Fe_2O_3$) and hematite functionalized with iridium oxide (IrO_x) as two examples of the use of impedance spectroscopy in the analysis of devices that use photocatalysis for solar fuel production [53–55].

The impedance spectroscopy of a 60 nm thick hematite electrode in aqueous solution is shown in Fig. 10.14. Large differences are observed when measuring in the dark and under illumination. In the first case, a single arc appears with a very large resistor up to bias potentials of 1.2 V versus Ag/AgCl. Under illumination, impedance spectra transform into two arcs and associated resistances decrease ~four orders of magnitude with respect to dark conditions.

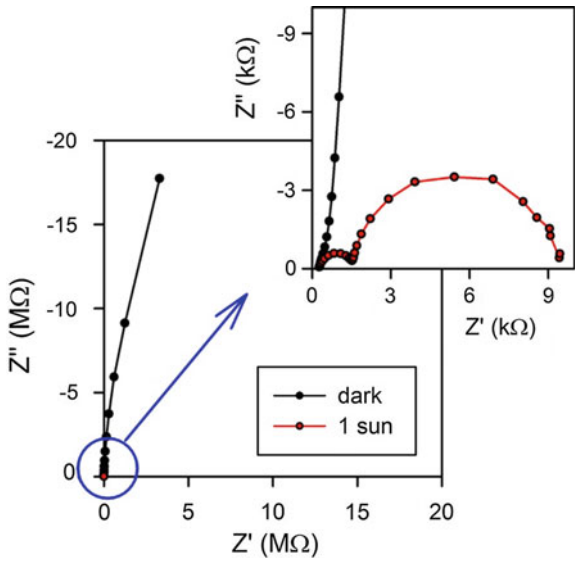

Fig. 10.14 Impedance of a hematite electrode at 0.65 V versus Ag/AgCl in the dark and under illumination

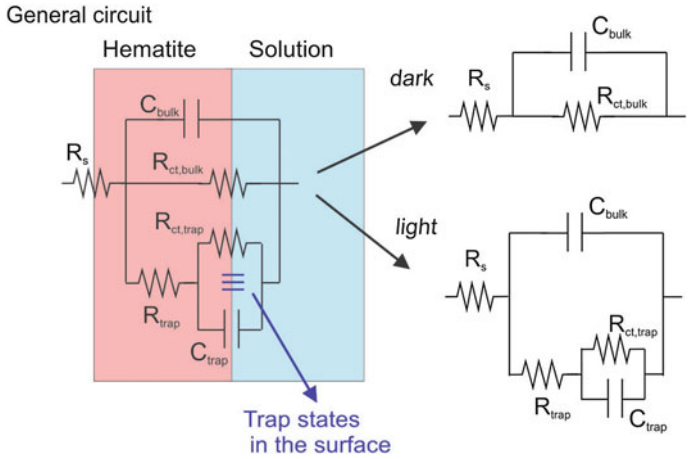

Fig. 10.15 Generalized equivalent circuit to describe impedance of α-Fe_2O_3 electrodes and simplifications used for the analysis of dark and illuminated measurements

The general equivalent circuit model used to fit these spectra is plotted in Fig. 10.15. The model includes the effect of surface trap states with localized energy, which are associated to the presence of intermediate species in the reaction of oxygen generation attached to the hematite surface [53]. These surface states act as recombination centers, trapping holes form the valence band and electrons from the conduction band [54]. Thus in the general circuit of Fig. 10.15, $R_{ct,bulk}$ describes the process of hole trapping associated to the photooxidation of chemical species in hematite surface and $R_{ct,trap}$ describes the mechanism of electron–hole recombination at the intermediate states, which is associated to the reduction of these

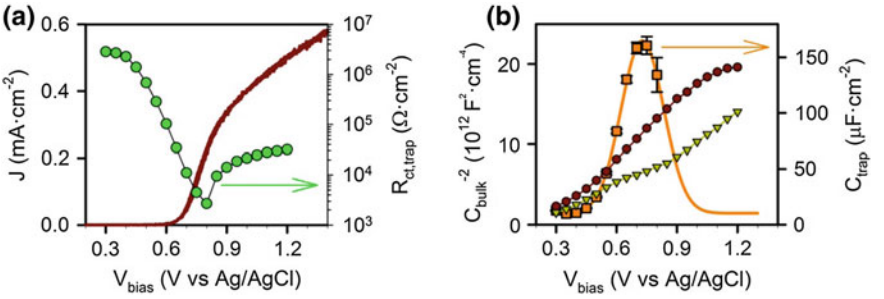

Fig. 10.16 **a** J-V curve (*line*, left axis) and charge transfer resistance (*green dots*, right axis) for α-Fe_2O_3 electrodes in water solution under illumination. **b** Left axis, Mott–Schottky plot of hematite bulk capacitance in the dark (*dark red circle*) and under illumination (*dark yellow triangle*). Right axis, surface states trap capacitance (*orange squares*)

oxidized surface species. The general equivalent circuit includes another pathway of direct charge transfer loss from semiconductor band which is described by $R_{ct,bulk}$. The model is completed with C_{trap}, that provides the density of states (DOS, g_{trap}) or energetic distribution density of the surface intermediate species,

$$C_{trap}(V) = q\, g_{trap}(E_{Fn} - E_t), \tag{10.33}$$

C_{bulk} the capacitance associated to electron distribution inside the hematite semiconductor and R_s, a series resistance that includes contributions from transport resistance in hematite, contacts, wires resistances, etc. [53, 54].

In the dark holes are injected in the hematite only at very high positive voltages, therefore traps do not appear until these high values are reached. For the other voltages (the ones measured in this work), the elements associated to the surface traps do not contribute to the impedance of the hematite, yielding to the simplified circuit given by R_s, C_{bulk} and $R_{ct,bulk}$ shown in Fig. 10.15, that due to the large values obtained for $R_{ct,bulk}$ produces the single unclosed arc given in Fig. 10.14.

Under illumination, the situation is different: hole generation induces hole transfer to solution and the development of surface intermediates (i.e., surface traps). Due to the fact that $R_{trap} + R_{ct,trap} \ll R_{ct,bulk}$, circuit simplifies as indicated in Fig. 10.15.

As shown in Fig. 10.16a, $R_{ct,trap}$ decreases when current in hematite starts to flow. This fact is related to the onset of photocurrent that simultaneously generates the trap states, which at pH 6.9 distribute around 0.75 V following Eq. 10.22, see Fig. 10.16b. Note that to obtain J–V curve in Fig. 10.16a, Eq. 10.8 also applies, here using

$$R_{DC} = R_S + R_{trap} + R_{ct,trap} \tag{10.34}$$

The close relationship between the DOS and the oxygen reduction may be observed in Fig. 10.17. For the two pH measured, 6.9 and 13.3, DOS (C_{trap}) peaks

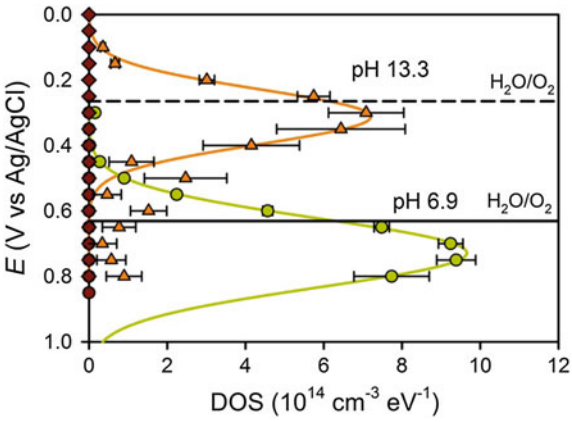

Fig. 10.17 DOS for pH 6.9 (*green dots*) and pH 13.3 (*orange dots*). *Lines* represent fitting to a Gaussian distribution as in Eq. 10.22. *Dark red dots* are the values obtained in the dark

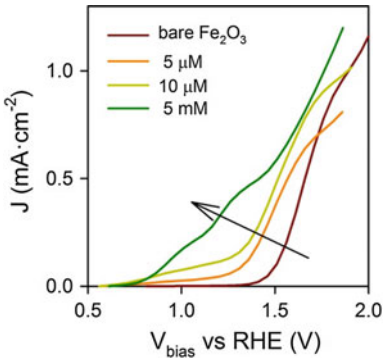

Fig. 10.18 J–V curves for hematite electrodes with different concentration of IrO_x absorbed in the surface

at voltages very close to the formal potential for the oxygen reduction reaction. This result, together with the fact that the surface state only appears under illumination (or at very high positive applied potentials) fact together with theoretical calculations [56], and current transient measurements, helped to relate the trap states with the absorbed species related to the first oxidation oxidative step in the water oxidation reaction where the origin of the trap states is [53]. Charge transfer through surface states has been also found to explain results in other semiconductors used for water splitting such $CuWO_4$, TiO_2 nanotubes and FeS_2 [57–59].

To complete characterization of Hematite Mott-Schottky analysis of C_{bulk} was done. As shown in Fig. 10.16b, C_{bulk} in the dark follows an ideal behavior from which flat band potential (V_{fb} = 0.25 V vs. Ag/AgCl) and donor density in the hematite (4.9×10^{19} cm^{-3}) could be obtained. Under illumination, Mott–Schottky plot is flattened at the potentials where the peak of C_{trap} is found. This behavior is observed when the number of trapping states in the hematite is large enough to produce to Fermi level pining.

Improved electrodes with higher performance may be obtained when incorporating catalysts such IrO_x or Co-Pi to the surface of the hematite [55, 60]. In the particular case of iridium oxide, in Fig. 10.18 it may be observed that for increasing

amounts of the catalyst electrodeposited on hematite, the onset voltage is reduced up to 0.7 V and at the same time, the shape of J–V curve improved. The quantity of IrO_x was controlled by changing the concentration of the organometallic molecular complex $(Cp^*Ir(H_2O)_3)(SO_4)$ used as a precursor in the electrodeposition solution from 5 μM to 5 mM.

With the incorporation of the catalyst, the impedance model needs to be adapted to a new situation in which the hematite electrode may be partially or totally coated by the catalyst. Figure 10.19 shows the general equivalent circuit proposed to describe this case. This circuit includes a new branch that takes into account the charge transfer resistance from hematite to IrO_x (R_{IrOx}), the charge transfer from the catalyst to the solution ($R_{ct,IrOx}$) and its capacitive contribution (C_{IrOx}).

Experimental data produces two arcs in the impedance spectrum for most of the potentials [55]. These impedance data may be fit using the simplified circuit shown in Fig. 10.19 which takes into account the parallel coupling of resistances and capacitors present in the general circuit. Therefore, $R_{bulk} = R_{IrOx} | R_{trap}$, $R_{ct} = R_{ct,IrOx} | R_{ct,trap}$ and $C_{ss} = C_{IrOx} | C_{trap}$. Eventually, at high voltages R_{ct} becomes negligible and simplified circuit reduces to R_s in series with the parallel combination of C_{bulk} and R_{bulk}.

Figure 10.20 compares the values obtained for C_{ss} and R_{ct} for bare hematite with those for increasing amounts IrO_x. At the low concentrations of IrO_x, for most of the voltages, C_{ss} is very similar to the one from the bare hematite. Only at the lowest voltages, where the current dominated by hematite capacitance at most potentials. Only at the lowest voltages, C_{ss} shows a clear contribution from Iridium

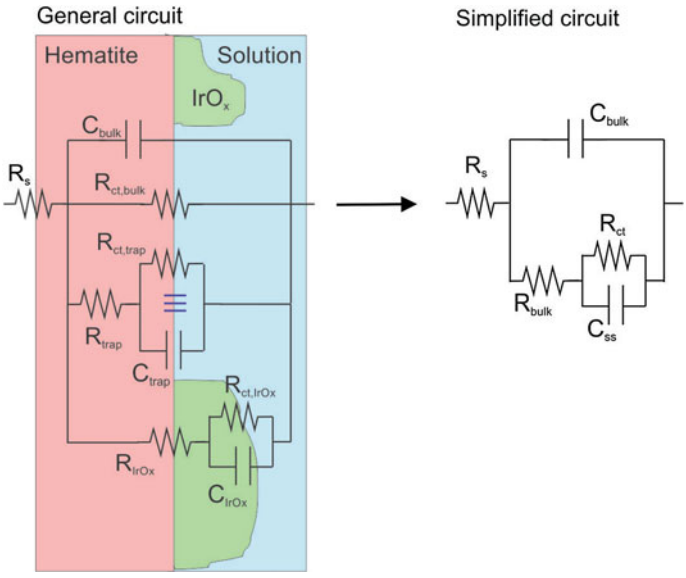

Fig. 10.19 General impedance model for hematite covered with IrO_x and simplified equivalent circuit

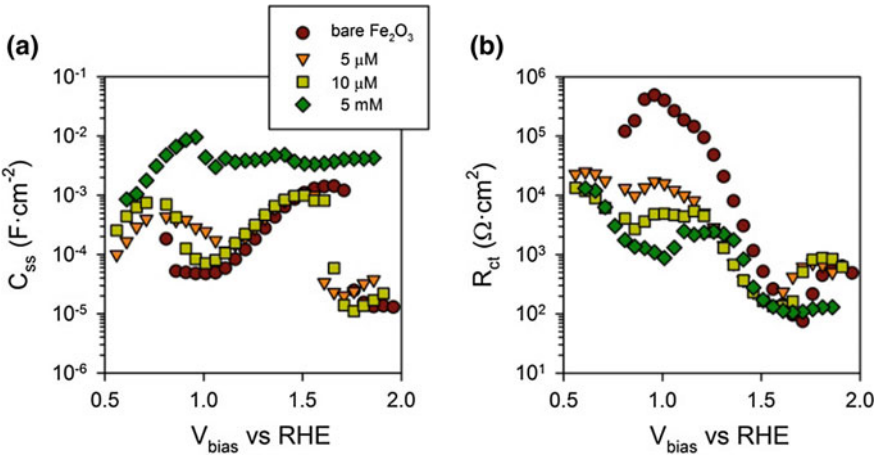

Fig. 10.20 comparison of capacitance (**a**) and charge transfer resistance (**b**) for hematite with different concentrations of deposited IrO_x

oxide, which was related to redox capacitance of IrO_x [55]. For high iridium contents, C_{ss} becomes dominated at all voltages by the one from IrO_x. This result suggests a superior charge separation ability for the catalytic film.

In Fig. 10.20b, R_{ct} shows clear differences between the bare hematite and iridium containing electrodes: The higher IrO_x deposited on the hematite, the lower R_{ct}, indicating that with the increased generation, the probability of charge recombination with the larger concentration of intermediate acceptor species also increases. Only at the highest voltages, all R_{ct} values tend to converge. This result matches very well with the results observed in J–V curves in Fig. 10.18 showing increased water oxidation efficiencies for electrodes with higher contents of IrO_x.

These combined results allow a more clear understanding of the origin of performance improvements and limitations of the catalyst coupled with semiconductor electrode for water-splitting applications.

10.5 Conclusions

IS is a unique technique able of distinguishing the different resistive and capacitive contributions of the devices, what enables the detailed analysis of the fundamental parameters that determine their performance. In solar cells, the IS procedure described in this chapter allows separating the different contributions to *FF* and V_{oc} provided by the series resistances, the transfer factor, the photocurrent, the conduction band or the redox level energies, and the kinetics of recombination, whose results of great help to optimize the performance of solar cells. Similarly, models used to describe impedance of electrodes for water splitting help to understand the mechanisms that govern their performance.

References

1. Bard AJ, Faulkner LR (2001) Electrochemical methods, fundamentals and applications, 2nd edn. Wiley, Weinheim
2. Orazem ME, Tribollet B (2008) Electrochemical impedance spectroscopy. Wiley, Pennington, NJ. doi:10.1002/9780470381588
3. Macdonald JR (1987) Impedance spectroscopy. Wiley, New York
4. Bisquert J (2003) Chemical capacitance of nanostructured semiconductors: its origin and significance for heterogeneous solar cells. Phys Chem Chem Phys 5:5360
5. Fabregat-Santiago F, Garcia-Belmonte G, Mora-Sero I, Bisquert J (2011) Characterization of nanostructured hybrid and organic solar cells by impedance spectroscopy. Phys Chem Chem Phys 13(20):9083–9118. doi:10.1039/c0cp02249g
6. Bisquert J (2015) Nanostructured energy devices: equilibrium concepts and kinetics. CRC Press, Boca Raton, FL
7. Fabregat-Santiago F, Bisquert J, Garcia-Belmonte G, Boschloo G, Hagfeldt A (2005) Influence of electrolyte in transport and recombination in dye-sensitized solar cells studied by impedance spectroscopy. Sol Energy Mater Sol Cells 87(1–4):117–131. doi:10.1016/j.solmat.2004.07.017
8. Wang Q, Ito S, Graetzel M, Fabregat-Santiago F, Mora-Sero I, Bisquert J, Bessho T, Imai H (2006) Characteristics of high efficiency dye-sensitized solar cells. J Phys Chem B 110 (50):25210–25221. doi:10.1021/jp064256o
9. Kalyanasundaram K (2010) Dye-sensitized Solar Cells. In: Kalyanasundaram K (ed) Dye-sensitized solar cells. CRC Press, Boca Raton
10. Sze SM (1981) Physics of semiconductor devices, 2nd edn. Wiley, New York
11. Fabregat-Santiago F, Garcia-Belmonte G, Bisquert J, Bogdanoff P, Zaban A (2003) Mott-Schottky analysis of nanoporous semiconductor electrodes in dielectric state deposited on SnO_2(F) conducting substrates. J Electrochem Soc 150(6):E293–E298. doi:10.1149/1.1568741
12. Bisquert J, Garcia-Belmonte G, Fabregat-Santiago F, Ferriols NS, Bogdanoff P, Pereira EC (2000) Doubling exponent models for the analysis of porous film electrodes by impedance. Relaxation of TiO_2 nanoporous in aqueous solution. J Phys Chem B 104(10):2287–2298. doi:10.1021/jp993148h
13. de Gryse R, Gomes WP, Cardon F, Vennik J (1975) On the interpretation of Mott-Schottky plots determined at semiconductor/electrolyte systems. J Electrochem Soc 711–712
14. Raga SR, Barea EM, Fabregat-Santiago F (2012) Analysis of the origin of open circuit voltage in dye solar cells. J Phys Chem Lett 3(12):1629–1634. doi:10.1021/jz3005464
15. Zhang J, Long H, Miralles SG, Bisquert J, Fabregat-Santiago F, Zhang M (2012) The combination of a polymer-carbon composite electrode with a high-absorptivity ruthenium dye achieves an efficient dye-sensitized solar cell based on a thiolate-disulfide redox couple. Phys Chem Chem Phys 14(19):7131–7136. doi:10.1039/c2cp40809k
16. Barea EM, Caballero R, Fabregat-Santiago F, De La Cruz P, Langa F, Bisquert J (2010) ChemPhysChem 11:245–250
17. Miquel P, Pellej L, Clifford JN, Pastore M, De Angelis F, Lopez N, Marderc SR, Palomares E (2011) Energy Environ Sci 4:1820–1829
18. Cai N, Zhang J, Zhou D, Yi Z, Guo J, Wang P (2009) J Phys Chem C 113:4215–4221
19. Mingfei X, Difei Z, Ning C, Jingyuan L, Renzhi L, Peng W (2011) Energy Environ Sci 44735–4742
20. Hara K, Dan-oh Y, Kasada C, Ohga Y, Shinpo A, Suga S, Sayama K, Arakawa H (2004) Effect of additives on the photovoltaic performance of coumarin-dye-sensitized nanocrystalline TiO_2 solar cells. Langmuir
21. Feldt SM, Gibson EA, Gabrielsson E, Sun L, Boschloo G, Hagfeldt A (2010) Design of organic dyes and cobalt polypyridine redox mediators for high-efficiency dye-sensitized solar cells. J Am Chem Soc 132(46):16714–16724

22. Mosconi E, Yum J-H, Kessler F, Gómez García CJ, Zuccaccia C, Cinti A, Nazeeruddin MK, Grätzel M, De Angelis F (2012) Cobalt electrolyte/dye interactions in dye-sensitized solar cells: a combined computational and experimental study. J Am Chem Soc 134(47):19438–19453
23. Richards CE, Anderson AY, Martiniani S, Law C, O'Regan BC (2012) The mechanism of iodine reduction by TiO_2 electrons and the kinetics of recombination in dye-sensitized solar cells. J Phys Chem Lett 3(15):1980–1984
24. Kitamura T, Ikeda M, Shigaki K, Inoue T, Anderson NA, Ai X, Lian T, Yanagida S (2004) Chem Mater 16:1806
25. Kim S, Lee JK, Kang SO, Ko J, Yum JH, Fantacci S, De Angelis F, Di Censo D, Nazeeruddin MK, Graatzel M (2006) J Am Chem Soc 128:16701
26. Hagberg DP, Yum J-H, Lee H, De Angelis F, Marinado T, Karlsson KM, Humphry-Baker R, Sun L, Hagfeldt A, Gratzel M, Nazeeruddin MK (2008) J Am Chem Soc 130:6259
27. Li R, Liu J, Cai N, Zhang M, Wang P (2010) J Phys Chem B 114(4461)
28. Ooyama Y, Shimada Y, Ishii A, Ito G, Kagawa Y, Imae I, Komaguchi K, Harima Y (2009) J Photochem Photobiol A 203:177
29. Wang Z-S, Koumura N, Cui Y, Takahashi M, Sekiguchi H, Mori A, Kubo T, Furube A, Hara K (2008) Chem Mater 20:3993
30. Horiuchi T, Miura H, Sumioka K, Uchida S (2004) J Am Chem Soc 126:12218
31. Kuang D, Uchida S, Humphry-Baker R, Zakeeruddin SM, Gratzel M (2008) Angew Chem Int Ed 47:1923
32. Kim D, Song K, Kang M-S, Lee J-W, Kang SO, Ko J (2009) J Photochem Photobiol A 201:102
33. Tian H, Yang X, Chen R, Pan Y, Li L, Hagfeldt A, Sun L (2007) Chem Commun 3741
34. Zhou G, Pschirer N, Schoneboom JC, Eickemeyer F, Baumgarten M, Mullen K (2008) Chem Mater 20:1808
35. Robertson N (2006) Angew Chem. Int Ed 45:2338
36. Clifford JN, Palomares E, Nazeeruddin MK, Gratzel M, Nelson J, Li X, Long NJ, Durrant JR (2004) J Am Chem Soc 126:5225
37. Do K, Kim D, Cho N, Paek G, Song K, Ko J (2012) Org Lett 1:222–225
38. Hara K, Wang ZS, Sato T, Furube A, Katoh R, Sugihara H, Dan-Oh Y, Kasada C, Shinpo A, Suga S (2005) J Phys Chem B 109:15476
39. Koops SE, Barnes PRF, O'Regan BC, Durrant RJ (2010) J Phys Chem C 114:8054–8061
40. Barea EM, Zafer C, Gultekin B, Aydin B, Koyuncu S, Icli S, Fabregat Santiago F, Bisquert J (2010) J Phys Chem C 114:19840–19848
41. Clifford JN, Palomares E, Nazeeruddin MK, Gratzel M, Durrant JR (2007) J Phys Chem C 111:6561
42. Barea EM, Gónzalez-Pedro V, Ripollés-Sanchis T, Wu HP, Li L, Yeh C-Y, Diau EW-G, Bisquert J (2011) J Phys Chem C 115(21):10898–10902. doi:10.1021/jp2018378
43. O'Regan BC, Walley K, Juozapavicius M, Anderson A, Matar F, Ghaddar T, Zakeeruddin SM, Klein C, Durrant JR (2009) J Am Chem Soc 131:3541–3548
44. Koops SE, O'Regan BC, Barnes PRF, Durrant JR (2009) J Am Chem Soc 131:10
45. Morandeira A, Lopez-Duarte I, O'Regan BC, Martinez-Diaz MV, Forneli A, Palomares E, Torres T, Durrant JR (2009) J Mater Chem 19:5016
46. O'Regan BC, Lopez-Duarte I, Martinez-Diaz MV, Forneli A, Albero J, Morandeira A, Palomares E, Torres T, Durrant JR (2008) J Am Chem Soc 130:2906
47. Giménez S, Bisquert J (2016) Photoelectrochemical Solar Fuel Production From basic principles to advanced devices, vol 1. Springer. doi:110.1007/978-3-319-29641-8
48. Luo J, Im J-H, Mayer MT, Schreier M, Nazeeruddin MK, Park N-G, Tilley SD, Fan HJ, Grätzel M (2014) Water photolysis at 12.3% efficiency via perovskite photovoltaics and Earth-abundant catalysts. Science 345 (6204):1593–1596. doi:10.1126/science.1258307
49. Hamdani M, Singh RN, Chartier P (2010) Co_3O_4 and Co-based spinel oxides bifunctional oxygen electrodes. Int J Electrochem Sci 5(4):556–577

50. Lin F, Boettcher SW (2014) Adaptive semiconductor/electrocatalyst junctions in water-splitting photoanodes. Nat Mater 13(1):81–86. doi:10.1038/nmat3811. http://www.nature.com/nmat/journal/v13/n1/abs/nmat3811.html#supplementary-information
51. Horkans J, Shafer MW (1977) An investigation of the electrochemistry of a series of metal dioxides with rutile-type structure: MoO_2, WO_2, ReO_2, RuO_2, OsO_2, and IrO_2. J Electrochem Soc 124(8):1202–1207. doi:10.1149/1.2133528
52. Smith RDL, Prévot MS, Fagan RD, Zhang Z, Sedach PA, Siu MKJ, Trudel S, Berlinguette CP (2013) Photochemical route for accessing amorphous metal oxide materials for water oxidation catalysis. Science 340(6128):60–63. doi:10.1126/science.1233638
53. Klahr B, Gimenez S, Fabregat-Santiago F, Bisquert J, Hamann TW (2012) Electrochemical and photoelectrochemical investigation of water oxidation with hematite electrodes. Energy Environ Sci 5(6):7626–7636. doi:10.1039/c2ee21414h
54. Klahr B, Gimenez S, Fabregat-Santiago F, Hamann T, Bisquert J (2012) Water oxidation at hematite photoelectrodes: the role of surface states. J Am Chem Soc 134(9):4294–4302. doi:10.1021/ja210755h
55. Badia-Bou L, Mas-Marza E, Rodenas P, Barea EM, Fabregat-Santiago F, Gimenez S, Peris E, Bisquert J (2013) Water oxidation at hematite photoelectrodes with an iridium-based catalyst. J Phys Chem C 117(8):3826–3833. doi:10.1021/jp311983n
56. Hellman A, Pala RGS (2011) First-principles study of photoinduced water-splitting on Fe_2O_3. J Phys Chem C 115(26):12901–12907. doi:10.1021/jp200751j
57. Pyper KJ, Yourey JE, Bartlett BM (2013) Reactivity of $CuWO_4$ in photoelectrochemical water oxidation is dictated by a midgap electronic state. J Phys Chem C 117(47):24726–24732. doi:10.1021/jp408434v
58. Cachet H, Sutter EMM (2015) Kinetics of water oxidation at TiO_2 nanotube arrays at different pH domains investigated by electrochemical and light-modulated impedance spectroscopy. J Phys Chem C 119(45):25548–25558. doi:10.1021/acs.jpcc.5b06103
59. Cabán-Acevedo M, Kaiser NS, English CR, Liang D, Thompson BJ, Chen H-E, Czech KJ, Wright JC, Hamers RJ, Jin S (2014) Ionization of high-density deep donor defect states explains the low photovoltage of iron pyrite single crystals. J Am Chem Soc 136(49):17163–17179. doi:10.1021/ja509142w
60. Klahr B, Gimenez S, Fabregat-Santiago F, Bisquert J, Hamann TW (2012) Photoelectrochemical and impedance spectroscopic investigation of water oxidation with "Co-Pi"-coated hematite electrodes. J Am Chem Soc 134(40):16693–16700. doi:10.1021/ja306427f

Chapter 11
Time-Resolved Laser Spectroscopy in Molecular Devices for Solar Energy Conversion

Leif Hammarström, Reiner Lomoth, Carlito S. Ponseca Jr., Pavel Chábera, Jens Uhlig and Villy Sundström

Abstract A complete characterization of solar energy conversion devices and the processes underlying their function is a challenge, and require a multitude of different experimental methods. This chapter discusses investigations of molecular solar cells and solar fuels devices by time-resolved laser spectroscopic methods. These methods have established important concepts we now use for understanding the function of devices for solar energy conversion into primary products. We give examples of scientific insight provided by ultrafast methods using detection in the regions from X-ray to THz radiation, and particularly highlight the case where the use of different methods has provided complementary information. Charge collection and solar fuel catalysis on the other hand occur on longer time scales, which opens for the use of time-resolved magnetic resonance and microwave conductivity methods. We also point out that, with suitable precautions, time-resolved laser spectroscopy is able to give information relevant for *in operando* device conditions.

Keywords Solar cells · Solar fuels · Time-resolved · Ultrafast · Laser spectroscopy · Charge separation · Catalyst · Perovskite · Dye-sensitized

Abbreviations

List of abbreviations used for spectroscopic techniques in this chapter:

CIDNP	Chemically induced dynamic nuclear polarization
EPR	Electron paramagnetic resonance
FTIR	Fourier-transform infrared
NMR	Nuclear magnetic resonance
SFG	Sum-frequency generation

L. Hammarström (✉) · R. Lomoth
Department of Chemistry – Ångström Laboratory, Uppsala University,
Box 523, 751 20 Uppsala, Sweden
e-mail: leif.hammarstrom@kemi.uu.se

C.S. Ponseca Jr. · P. Chábera · J. Uhlig · V. Sundström (✉)
Division of Chemical Physics, Lund University, Box 124, 221 00 Lund, Sweden
e-mail: villy.sundstrom@chemphys.lu.se

H. Tian et al. (eds.), *Molecular Devices for Solar Energy Conversion and Storage*, Green Chemistry and Sustainable Technology,
https://doi.org/10.1007/978-981-10-5924-7_11

TRIR	Time-resolved infrared
TRLS	Time-resolved laser spectroscopy (general for all laser-based time-resolved spectroscopies)
TRMC	Time-resolved microwave conductivity
TRTS	Time-resolved THz spectroscopy
XAS	X-ray absorption spectroscopy (XAFS and XANES are subdivisions of XAS)
XAFS	X-ray absorption fine structure
XANES	X-ray absorption near-edge structure
XDS	X-ray diffuse scattering
XES	X-ray emission spectroscopy
XPS	X-ray photoelectron spectroscopy

11.1 Introduction

The systems discussed in this book involve processes on a wide range of time scales, from the initial events of light-harvesting, exciton migration, and charge separation that typically occur on a femto- to picosecond time scale, to charge collection or catalysis that typically occur on the time scale of milliseconds to seconds, or even slower. A complete characterization of solar energy conversion devices and the processes underlying their function is a challenge, and require a multitude of different experimental methods.

Time-resolved laser spectroscopy (TRLS) is the only class of experimental methods that has sufficient time resolution to follow the early events after light absorption. These methods have established important concepts we now use for understanding the function of devices for solar energy conversion into primary products. The solar energy systems have often been important case studies for chemical reaction dynamics of general and fundamental interest. In natural photosynthesis, for example, they have demonstrated the intricate light-harvesting mechanisms of antennas, extending our conceptual framework from incoherent Förster-type hopping to excitonic coupling and coherent energy transfer [1, 2]. Studies of reaction centers have demonstrated the ultrafast time scale of initial charge separation, and helped in clarifying the intricate structural and electronic features that control the directionality and high efficiency of electron transfer from one side of the membrane to the other [3–5]. Natural photosynthesis has also served as a blueprint for synthetic molecular systems that mimic photosynthesis [6–8], and with the use of TRLS such systems have helped to firmly establish theoretical models for excitation energy and electron transfer.

In this chapter, we will discuss molecular solar cells, for which TRLS has provided unique information on the still controversial mechanisms for charge separation. We will also discuss molecular solar fuel devices, and how TRLS yields

information on the coupling of charge separation to catalysis. Our focus is on ultrafast methods, predominantly pump-probe methods, where a short laser pulse initiates a reaction and a second pulse probes the sample response at different time delays after the pump. This second pulse can be in very different regions of the electromagnetic spectrum, and in practice all regions from hard X-rays to the terahertz (THz) radiation is being used for ultrafast experiments. On slower time scales also micro- and radiowave frequencies are used in laser flash-induced time-resolved microwave conductivity, electron paramagnetic resonance (EPR), and nuclear magnetic resonance (NMR) experiments.

A combination of spectroscopic methods is often an important advantage, as it allows for probing of more species and states involved in the reactions, and therefore for safer assignments. For example, if experiments are restricted to the UV-VIS region only, different states can give very similar transient spectra, and different species often overlap, which complicates assignment. Also, catalysts and semiconductor charge carriers often do not give distinct absorption bands in the visible region, while the required information can be obtained by instead probing in the X-ray, mid-IR, or THz regions.

Performance of a device is typically a complex function of all components, which interact with each other and may alter both energetics and dynamics of individual reactions. Therefore, it is important to make measurements that are relevant for *in-operando* conditions of a device. Care must be taken when designing a model system or component for study, and in interpreting the resulting data. For measurements on a complete device this must be sufficiently transparent in the spectral range employed, and in the case of X-ray photoelectron spectroscopy (XPS), it must allow escape of at least some photoelectrons to reach the detector (see Chap. 12). Furthermore, the laser pump intensity must be sufficiently low that the results are relevant for solar irradiation conditions. However, this does not mean that the flux during a short laser pulse has to match the solar flux, as discussed in next chapter. Thus, with suitable precautions, TRLS is able to give information relevant for in-operando device conditions.

The subject of this book chapter is rapidly developing and we present a personal selection of work that illustrate important topics and have provided new insights from a combination of TRLS experiments.

11.2 Experimental Methods

11.2.1 General Considerations

Time-resolved spectroscopy as we know it today developed in the 1950s and early 60s as flash photolysis and relaxation methods, a development that culminated with the Nobel Prize in chemistry 1967 to Porter, Norrish, and Eigen. This work gave us the millisecond and microsecond timescales. With the advent of lasers and

Q-switching and mode-locking techniques a giant leap into the nano- and picosecond domain occurred. Finally, mode-locking of dye lasers and Kerr lens mode-locking of the titanium-sapphire laser gave us the femtosecond time scale. A parallel development of pulse amplification and compression techniques and implementation of various nonlinear optics techniques broadened the wavelength range of ultrashort pulses to cover the spectral region from the infrared to the UV. Today, with the availability of free-electron lasers, femtosecond pulses can be generated from THz frequencies to hard X-rays.

When we perform time-resolved experiments to monitor time evolution of chemical reactions, we rely on the principles already introduced through flash photolysis—an excitation pulse that initiates the reaction and a delayed probe pulse to monitor the progress of the reaction. With the help of a variable time delay kinetics is measured, and by using a broadband probe pulse a time-resolved (transient) spectrum can be measured. With the broad range of ultrashort pulse wavelengths available, virtually any molecule can be excited and process initiated, and most molecular and material absorptive or emissive responses monitored. These types of experiments are generally termed pump-probe measurements and are very versatile due to the flexibility in choice of pump and probe pulses. Other responses like Raman or coherences can be probed in multi-pulse pump-probe measurements.

Early time-resolved laser spectroscopy measurements were often performed with low repetition rate and high energy (many photons) pulses, which often lead to nonlinear effects and dynamics that did not reflect the process under investigation. An example is exciton-exciton annihilation occurring at high excitation densities in coupled molecular systems like molecular aggregates or photosynthetic antennas. At sufficiently high intensities the process is manifested as a fast decay of excited-state population, which would distort energy transfer dynamics in the system. Today it is possible to obtain high-quality pump-probe data with rather low pump pulse energies, thanks to more stable lasers, higher laser repetition frequencies and more sensitive detectors. This allows for TRLS of devices under conditions relevant for solar operation. A common misconception in this regard is to compare the fluxes of sunlight and a single laser pulse and consider this as the relevant excitation density. A full sun delivers on the order of 100 mW cm^{-2}, which is on the order of 10^{-6} mol photons cm^{-2} s^{-1}. With the same flux, a 100 fs laser pulse, typically focused on ca. 10^{-3} cm^2, would contain only about 100 photons. In reality, optical pump-probe experiments typically use on the order of 10^9–10^{11} photons per pulse, or 10^{12}–10^{14} photons cm^{-2}. This simple comparison is misleading, however, as the laser only fires at typically 1 kHz repetition frequency, so the number of photons cm^{-2} s^{-1} can be similar to solar irradiation conditions. Thus, the steady-state concentrations of intermediates are similar. For the transiently higher concentrations after each laser pulse, it is sufficient to lie at pulse energies below the limit of nonlinear dependence of the different processes in the system under study. Typically, experiments can be easily conducted far below the limit for two-photon absorption, and also below that for exciton annihilation. Charge carrier recombination depends on their concentrations and care must be taken not to

accelerate charge recombination beyond solar conditions [9–12]. Where this point lies depends on the particular system under study, and good practice is to vary the pump intensity to verify intensity-independent dynamics.

Pump-probe measurements are repetitive and the repetition rate must be low enough that the system relaxes to the starting state or desired steady state. Ideally, the experiment should be performed with the same background concentration of intermediates, trap filling, etc., as under solar conditions. Systems for solar fuels generation present a particular challenge, as catalysis is a multi-electron/-proton reaction, and requires several photon absorption and charge separation processes to complete a cycle [13]. This means that multiple catalyst states are present under continuous irradiation. It is an outstanding challenge to develop experimental protocols to follow all steps of a catalytic cycle that is rapidly turning over. Pump-probe experiments usually excite only a fraction of the chromophores in a sample, and it is therefore hard to synchronize the redox states of the sample.

It is beyond the scope of this chapter to provide an exhaustive account of time-resolved methods. Below we discuss a few techniques that have been used in our work discussed here.

11.2.2 Laser Pump-Probe Spectroscopy

In general, a UV/VIS pump is used to start the photochemical reaction, and a probe pulse measures the absorbance of the sample. By comparing with the absorbance before the pump pulse, the transient (change in) absorbance induced by the pulse can be determined. Thus, the measurement is based on Lambert–Beer's law as in a typical steady-state spectrometer. The pump and probe pulses are generated from the same laser pulse, by different nonlinear optics techniques, which allows for precise timing of the two pulses. The experiment is repeated, typically at a frequency of at least 1 kHz, and the signals from many pump-probe pulse pairs are averaged. As light travels about 0.3 μm in 1 fs, a set of movable mirrors are used to delay one of the pulses and thus vary the timing between pump and probe to build up the time evolution of the signal. In this way time-resolved spectra in the UV to mid-IR ranges are routinely taken.

Time-resolved X-ray experiments instead mainly use a separate probe pulse from a synchrotron or free-electron laser, which presents particular challenges regarding timing, as described below. Also, THz probing of transient photoconductivity data contains more information than just population density and is therefore described in some more detail.

11.2.3 Time-Resolved X-Ray Spectroscopy and Scattering

During absorption of an X-ray photon an electron is selectively excited from a highly localized core orbital into either a vacant or bound electronic state, or the continuum. The energy and intensity distribution measured during X-ray absorption fine structure spectroscopy (XAFS) allow conclusions to be drawn on oxidation state, coordination and local structure around the absorber, and was one of the first X-ray based techniques reaching sub-picosecond resolution [14–17]. Recent developments in pulse brilliance [18–20], high repetition rate systems [21, 22] and detector technology [23] have advanced the use of pulsed x-radiation in the study of electron dynamics. Photon hungry techniques like X-ray emission spectroscopy (XES) can now use weaker but more sensitive transitions (e.g., the Kβ emission line or valence to core transitions) [24–26] and time-resolved scattering experiments of non-crystalline media (X-ray diffuse scattering—XDS) [27–29], are now available for the study of large structural changes of a solute, or solvent cage.

The localized nature and high energy of the core-hole allows in situ, near background-free spectroscopic transient probing of electron energies around a single atomic sensor in a very complex molecular structure. Changes in oxidation state and electron spin lead to recognizable features that compared to measured reference spectra [30–32], or simulations, allow characterization of the dynamics around the absorbing/emitting atomic sensor. Experiments then combine optical excitation with one or more of the complementary X-ray based techniques. The combination of X-ray absorption spectroscopy (XAS) and XES for example can overcome the limitation of energy resolution due to the lifetime of the excited states [33–35]. XES and XDS (as shown in Fig. 11.1) can be performed simultaneously with the same, fixed excitation energy at sources with limited excitation bandwidth (like X-ray free-electron lasers) to obtain electronic and structural information from

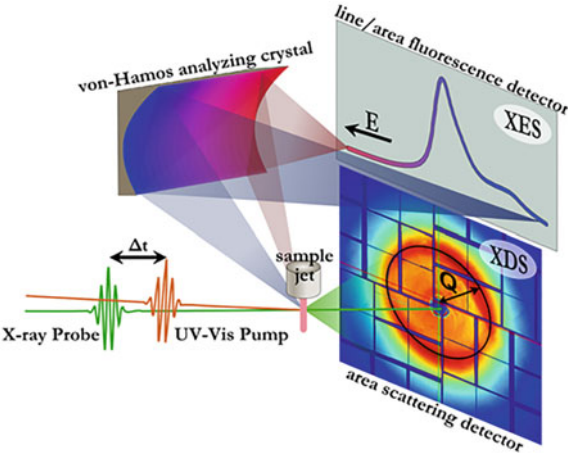

Fig. 11.1 Scheme of simultaneous XES and XDS pump-probe spectroscopy. The cylindrical bend crystal in the von-Hamos geometry focuses the full spectrum of each X-ray pulse onto an area detector. A second segmented area detector behind the fast flowing liquid sample jet collects the diffuse scattering simultaneously

the same system, elucidating the influence of solvent dynamic and energy transfer [22, 28]. Examples later in this book emphasize the strength of combining spectroscopies in multiple wavelength regions to fully understand the dynamics of complex systems.

The mismatch between optical absorption and X-ray interaction length poses a challenge for the experimenter. The required compromises often include the need for fast flowing thin jets (sample damage and mismatch between speed of light), high excitation yields (typically the X-ray flux is limited to 10^{12} ph/s), and high sample concentrations, which in turn lead to the need for a significant amount sample material to perform these experiments.

11.2.4 Transient Photoconductivity Measurements

Upon light excitation, charged species, either loosely bound excitons or highly mobile charges, can be generated in a solar cell material. The photoinduced charged species give rise to a transient change of conductivity ($\Delta\sigma$), which will be detected by the THz or GHz probe radiation. The transient photoconductivity, $\Delta\sigma$, can be calculated using the equation below.

$$\frac{\Delta\boldsymbol{\sigma}}{\boldsymbol{n_{exc}e_0}} = \boldsymbol{\xi} \times (\mu_e + \mu_h) = -\frac{\boldsymbol{\Delta E_{exc}(\omega)}}{\boldsymbol{E_{gs}(\omega)}} \cdot \frac{\boldsymbol{\varepsilon_0 c}}{\boldsymbol{Fe_0}} \cdot \frac{1}{1 - \boldsymbol{e^{-\alpha L}}} \tag{11.1}$$

where n_{exc} is the charge density, ξ is quantum yield of charged species, μ_e and μ_h are the electron and hole mobility, respectively, ΔE_{exc} is the change in the THz electric field transmitted through the sample with excitation, E_{gs} is the ground state THz electric field without excitation, ε_0 is permittivity of vacuum, c is velocity of light, F is the fluence in ph/cm^2, e_0 is the elementary charge, α is the absorption coefficient, and L the thickness of the sample. The quantity from this expression has a unit of mobility in cm^2/Vs. As shown, $\Delta\sigma$ is a product of $\Delta\sigma$ quantum yield (photon to charge ratio) and mobility. This means that to obtain, the photogenerated species should be (1) charged and (2) mobile. A tightly bound exciton will not be detected since it has no overall charge (neutral). In the same manner, if the pump pulses create ions, whose mobility is very low, this may also not be detected. The temporal evolution of the charge population and mobility defines the shape of the THz transient photoconductivity kinetics. On one hand, a rise in the photoconductivity kinetics reflects generation of charged species and/or increase in mobility of the charges. On the other hand, a decay represents decrease of the mobility (maybe due to relaxation) and/or disappearance of charge carriers, either by recombination, or injection to a low mobility acceptor material. The pulsed THz radiation is generated by pumping a ZnTe crystal with 800 nm, 120 fs, 100 uJ/pulse via optical rectification process. Another ZnTe crystal was used for detection by spatially and temporally overlapping the pulsed THz radiation with an 800 nm probe beam in a process known as electro-optical sampling. The transient THz

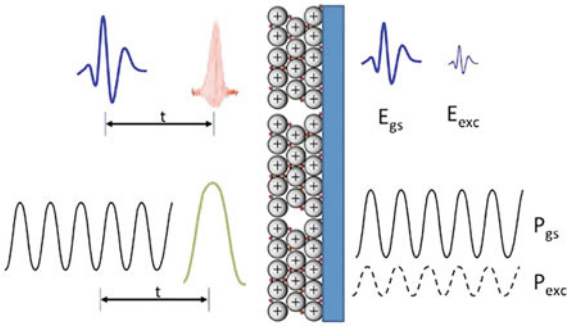

Fig. 11.2 Schematic diagram of the transient photoconductivity setup used in probing charge carrier dynamics in PSC solar cell. *Upper part* Visible pump pulse (*red*) is about 80 fs while THz pulse probe is about 1 ps. Transmitted THz electric fields, E_{gs} and E_{exc} are collected and Eq. 11.1 is used to obtain transient photoconductivity at desired pump-probe delay (t). *Lower part* Visible ns pump pulse (*green*) is about 2 ns while continuous GHz is used as probe. An electronic delay circuit is used to determine time zero between pump and probe (t). *Note* In the laboratory, TRMC is done in reflection mode

photoconductivity kinetics is collected by fixing the gating delay at the peak of the THz electric field and scanning the pump-probe delay within a desired time interval, typically up to 1 ns. This is schematically shown in the upper part of Fig. 11.2. We note that at the earliest timescale, ξ is often assumed to be 1, while at longer times this represents the change in charge population at a particular time. ξ near unity means that all absorbed photons are converted to mobile charges. Since accurate measurement of ξ is often difficult, this assumption means that mobilities reported here are lower limits, and can be much higher, if for instance $\xi = 10\%$ only, an order of magnitude higher.

For longer time scale, i.e., from tens of ns to tens of μs, the transient photoconductivity can be monitored using GHz (microwave) frequencies. As such, the difference between the time-resolved microwave conductivity (TRMC) technique and time-resolved THz spectroscopy (TRTS) lies in the pulse duration of the excitation and the detection window. In the lower part of Fig. 11.2, a ns pulse (green trace) is used as pump light, while continuous microwave radiation (8–9 GHz) is used as probe. The power of the reflected microwave signals with (ΔP_{exc}) and without (P_{gs}) excitation are measured and used to estimate mobility. By simply substituting ΔP_{exc} for ΔE_{exc} and P_{gs} for E_{gs} in Eq. 11.1, the mobility at longer time scale can be calculated.

11.3 Solar Cell Technologies

11.3.1 Dye-Sensitized Solar Cells

11.3.1.1 Harvesting the Photons–Electron Injection from Sensitizer to Semiconductor

Initial work on excited state and electron dynamics in dye-sensitized solar cell materials focused on the dye to semiconductor electron injection process. A large body of work identified this process as decisive for efficient light-harvesting [36–45] and conversion of the light energy to energy-rich electrons. For efficient utilization of absorbed photons and excited-state energy of the sensitizer, electron injection into the semiconductor has to be significantly faster than the sum of all other excited-state deactivation processes. For many of the sensitizers used, nanosecond and longer excited-state lifetimes are not unusual, implying that injection times on the few-ps time scale is sufficient for close to 100% quantum efficiency injection. Our early work on RuN_3 sensitized nanostructured TiO_2 electrodes illustrates this point [37–39, 46]. The strong visible absorption of metal-polypyridyl molecules is due to singlet and triplet excited states. For the Ru-based molecules discussed here, the lowest excited state is a triplet metal-to-ligand charge transfer state (^{3}MLCT) and there is a ^{1}MLCT state at higher energy responsible for the main absorption band. Light absorption into this band therefore generates the excited ^{1}MLCT state, but within a very short time ($\sim$100 fs) the molecule has relaxed into the lowest ^{3}MLCT state [47, 48]. For efficient electron injection and energy conversion in the sensitized semiconductor system, the energy of the lowest ^{3}MLCT state has to be above the conduction band edge of the semiconductor. The resulting scenario is illustrated by Fig. 11.1, showing the valence and conduction bands of the semiconductor, as well as the ground and excited states of the RuN_3 sensitizer. By carefully identifying the different transient absorption characteristics of the dye excited and oxidized states, one can distinguish the ultrafast injection process. Our work [37, 38, 42, 43, 49] showed that following light absorption to the ^{1}MLCT state, $\sim$60% of the molecules inject electrons directly from this state into the semiconductor conduction band with a characteristic time constant of $\sim$50 fs. Upon excitation to higher lying vibrational states of the ^{1}MLCT state, even faster injection occurs ($\sim$20 fs), in competition with vibrational energy relaxation and redistribution. The residual $\sim$40% of the excited sensitizers relax to the triplet state, from which they inject electrons much more slowly on the 1–100 ps time scale [46, 50], see Fig. 11.3. Many other Ru-sensitizers [36, 51–53], but also porphyrins [52, 54], phtalocyanines and organic dyes [55–57] have demonstrated fast and efficient injection. Time-resolved infrared (TRIR) experiments monitor electrons injected into the conduction band and are consistent with this picture [58, 59]. Also, hole injection in the photocathode material NiO from several different organic dyes have been shown to occur predominantly on the 100–400 fs time scale [60, 61]. Thus, to achieve efficient

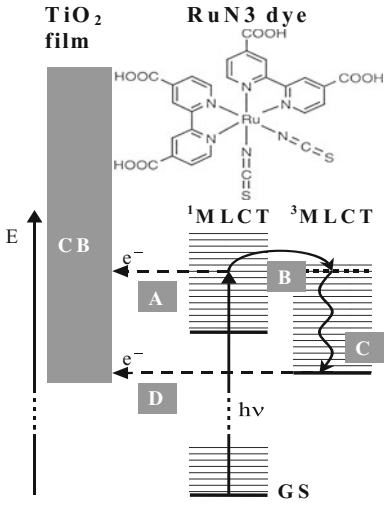

Fig. 11.3 Schematic model of two-state electron injection and structure of RuN_3. Following MLCT excitation (at 530 nm) of the RuN_3-sensitized TiO_2 film, an electron is promoted from a mixed ruthenium NCS state to an excited p* state of the dcbpy-ligand and injected into the conduction band (CB) of the semiconductor. *GS* ground state of RuN_3. *Channel A* electron injection from the non-thermalized, singlet ^{1}MLCT excited state. *Channel B and C* Intersystem crossing (ISC) followed by internal vibrational relaxation in the triplet ^{3}MLCT excited state. *Channel D* electron injection from the thermalized, triplet ^{3}MLCT excited state

electron or hole injection from a sensitizer dye to a metal oxide nanostructured film appears to be a relatively manageable task.

Experiments on the Ru-dye-based champion cells, with the RuN_3 and N719 dyes and an electrolyte composition as for a working cell, suggested a somewhat different picture of the relative importance of fs- and ps-injection in TiO_2. From a combination of probing in the visible/NIR (dye cation), mid-IR $\left(e^-_{CB}\right)$ and fluorescence $\left(\text{dye}^3\text{MLCT state}\right)$ it was concluded that injection on a 1–1000 ps time scale dominates [62, 63]. These results can be understood as a consequence of a shift to higher energy of the conduction band, which slows down the triplet injection. Singlet injection, which in a sensitized electrode in contact with solvent occurs with a yield of 50–60% and on the sub-50 fs time scale [37, 39, 63], appeared to have a lower yield (10–20%) in a solar cell (containing electrolyte and redox couple) when the injection was probed by electron absorption in the infrared [63]. The reason for this apparent lower yield of injected electrons from the singlet state in a solar cell could be formation of an electron–cation complex that dissociates on a slower ps time scale [64–66].

11.3.1.2 Electron–Cation Recombination

Electron injection from dye to semiconductor is just the first step in a series of processes that eventually lead to a photocurrent and voltage in an external circuit. For the electrons to be extracted in high yield, recombination with the holes on the oxidized dye has to be much slower than the re-reduction of the oxidized sensitizer by the redox couple of the hole transport material (HTM). The rate of this process depends on the nature of HTM and if it is a liquid or solid state material. Electron-hole recombination times on the hundreds of ns and slower time scale are generally sufficient for efficient utilization of the light generated charges. The realization that electron-hole recombination is a process directly related to solar cell efficiency—every recombined electron is a lost electron and lost photocurrent, and recombination also reduces the open circuit voltage—has motivated work to understand the factors controlling the process. We have performed a systematic study of how sensitizer binding to the semiconductor surface controls the electron transfer processes in general and electron–cation recombination in particular.

For Ru-polypyridyl dyes (e.g., RuN_3, the black dye) resulting in very efficient solar cells, electron–cation recombination has been shown to be very slow (microsecond timescale) [67–69] and slower than regeneration of the oxidized sensitizer by the redox mediators [70], and therefore not a limiting factor for the efficiency of a solar cell based on these dyes. This fact, established for some Ru-polypyridyl sensitizers often seems to have been extrapolated to suggest that this is also the case for other dyes [54], leading to a picture where variations in solar cell efficiency have been directly correlated to the efficiency and rate of electron injection [54]. Our recent work has shown that electron–cation recombination can be a more important process for controlling solar cell efficiency [52]. This leads to a correlation of electron injection and recombination rates with the binding geometry of the sensitizer, and hence the steps towards the goal of designing nanostructured dye-sensitizer materials with predictable electron transfer properties. We will use some of our recent results for Zn- porphyrin/TiO_2 electrodes to illustrate this. A combination of ultrafast spectroscopy, surface sensitive vibrational sum-frequency generation (SFG) and measurements of solar cell power conversion efficiency leads to a picture where we can correlate binding geometry to electron transfer dynamics, which in its turn controls the conversion efficiency of the solar cell.

By using a series of Zn-porphyrins (Zn-P) (Fig. 11.4), we could vary several molecular properties of importance for dye-semiconductor binding [36, 52]. The electron transfer dynamics were monitored by transient absorption (TA) spectra and kinetics [52, 53]. The time evolution of the TA spectrum of a Zn-porphyrin/TiO_2 electrode can be described as a non-exponential process involving only two species, the singlet excited state and the Zn-porphyrin radical cation formed as a result of electron injection from the Zn-P to TiO_2. The excited state of the sensitizer is formed within the time resolution (<100 fs) of the experiment and then transforms with multi-exponential kinetics to the oxidized sensitizer, which then decays back to the ground state by charge recombination with conduction band electrons. This

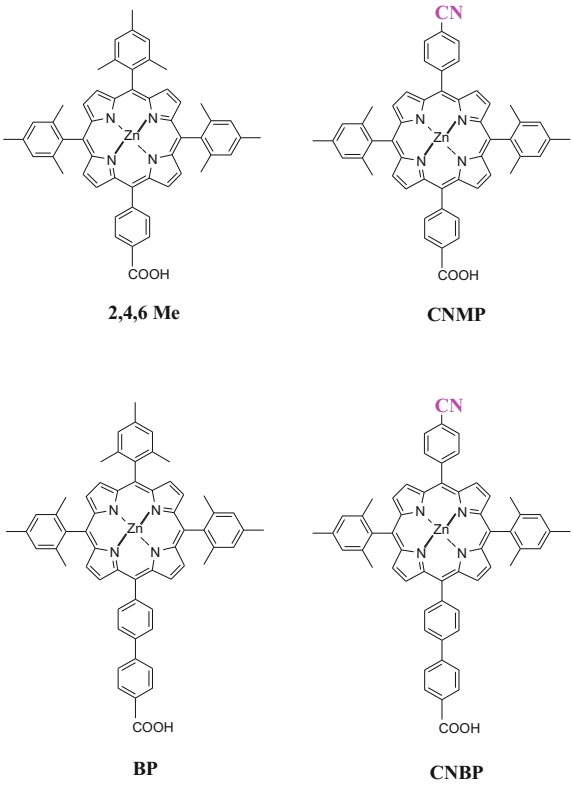

Fig. 11.4 Molecular structure of zinc porphyrins studied by [52, 53]

recombination can be described for most dyes by two lifetimes, one on the tens to hundreds of picoseconds time scale and another much slower, >50 ns.

From Marcus theory of electron transfer [71–73] and its modifications for interfacial electron transfer [74, 75] it is expected that the electron transfer rate should have a strong (exponential) distance dependence. If electron transfer between the porphyrin core and the semiconductor occurs via the connecting spacer, as often envisaged, making this spacer longer should slow down the transfer. With the help of the sensitizers 2,4,6-Me and BP (see Fig. 11.4) we could test this expectation; introduction of the extra phenyl moiety in the biphenyl spacer of TiO_2/BP relative to TiO_2/2,4,6-Me would result in approximately 1.5 times longer through-bond distance between the porphyrin core and the TiO_2 surface and therefore result in considerably smaller electronic coupling and much slower electron injection and recombination. Transient absorption kinetics of the two molecules attached to the TiO_2 film showed that the charge recombination process does not meet this expectation—the BP sensitizer with the longer connecting spacer has a much faster recombination rate than 2,4,6-Me [54]. Also the electron injection is faster for BP/TiO_2. This shows that both electron injection and recombination are overall faster for the sensitizer with the longer connecting spacer. For an analog to 2,4,6-Me, lacking the methyl groups on the phenyl substituents on the porphyrin

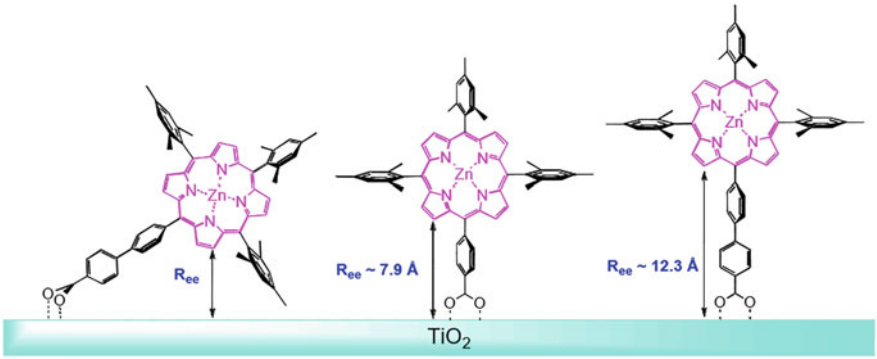

Fig. 11.5 Binding model for Zn-porphyrins to TiO_2. The edge-to-edge distance (R_{ee}) is decreased upon tilting dye molecule

core, the effect is even more pronounced with very fast injection and complete recombination within 500 ps. Obviously, electron transfer does not occur as could be anticipated via the spacer connecting the porphyrin core to the TiO_2 surface. Instead, we suggested a picture where the single carboxyl anchoring group allows a flexible binding geometry; for some of the porphyrins, depending on structural factors such as length of the spacer group and bulkiness of the porphyrin core, a fraction of the molecules are bound at an angle to the semiconductor surface and electron transfer occurs through space rather than through the linker group connecting the porphyrin core to the anchoring COOH group [52]. This binding model is illustrated in Fig. 11.5.

When the tilt angle is changed as a result of a change of porphyrin molecule size or shape, the distance between the porphyrin core and semiconductor surface changes, which will lead to a change in the through-space electron transfer rate. Owing to the expected exponential distance dependence of electron transfer, only a modest change of distance (and thus angle) will have a dramatic impact on the transfer rate.

Electron transfer rates are, of course, not an unambiguous measure of binding geometry; for that an experimental method providing more direct structural information is required. To this end we have used vibrational sum-frequency generation spectroscopy (SFG) on the Zn-porphyrins of Fig. 11.4 labeled with a CN infrared active chromophore [53]. The IR transition dipole moment of the CN-group is along the symmetry axis of the Zn-porphyrin molecules; sum-frequency generation (SFG) spectroscopy will therefore give the orientation of the porphyrin relative to the semiconductor surface (the tilt angle). These measurements showed that there is a direct correlation between tilt angle of the Zn-P molecule and amplitude of long-lived (>50 ns) conduction band electrons that can contribute to photocurrent—smaller tilt angle leads to higher amplitude of long-lived electrons. By comparing tilt angles obtained from the SFG measurements with solar cell power conversion this correlation can be taken one step further—a smaller tilt angle leads to higher cell efficiency, meaning that solar cell power conversion efficiency is directly

related to the extent of slow electron–cation recombination, i.e., the concentration of long-lived electrons in the conduction band. The results suggest a method to characterize the structure of the sensitizer/semiconductor interface and thus pave the way toward providing DSC materials with predictable electron transfer properties.

11.3.1.3 Earth Abundant Sensitizers for Dye-Sensitized Solar Cells

Even if organic dyes have received more attention in recent years [76, 77], most studies of dye-sensitized solar cells have been performed on ruthenium(II)-complexes, which have favorable excited-state properties for solar cells, e.g., long excited-state lifetimes, efficient electron injection to metal oxide semiconductors and generally slow electron-hole recombination [36, 78, 79]. Using iron instead of ruthenium in such complexes would be an important step to promote light-harvesting applications on a large scale, as iron is earth abundant, inexpensive, and environmentally benign [80–82]. However, its intense metal-to-ligand charge transfer (MLCT) absorption has been considered unexploitable in energy conversion applications, due to the low-lying metal-centered (MC) quintet (Q) high-spin state that typically deactivates the ^{1,3}MLCT manifolds on a sub-picosecond timescale [83]. Studies of the prototype $[Fe(bpy)_3]^{2+}$ (bpy = 2,2-bipyridine) complex have revealed an excited-state decay mechanism that involves ultrafast intersystem crossing (ISC) from the first populated ^{1}MLCT state to the ^{3}MLCT state, followed by an ultrafast (sub-picosecond) cascade of ISCs to the ^{3}MC, and then to the ^{5}MC state [84, 85], or possibly a direct process to the lowest ^{5}MC state. Thus destabilizing these MC states should result in a longer lived MLCT state. To this end we recently synthesized a Fe-NHC complex, $[Fe(CNC)_2](PF_6)_2$ (CNC = 2,6-bis (3-methylimidazole-1-ylidine)pyridine), and ultrafast transient absorption measurements showed a 100-fold extended excited-state life time of 9 ps as compared to previously known Fe^{II}-polypyridyl complexes ($\sim$100 fs; [80, 86]). The observed spectral evolution was tentatively assigned as <100 fs relaxation from a spectrally very broad (500–700 nm) ^{1}MLCT state to the ^{3}MLCT state characterized by a transient absorption band at $\sim$530 nm decaying with a $\sim$9 ps time constant. No spectral signatures of a ^{5}MC state, and therefore no significant population of such a state was observed. This suggested a <2 ps lifetime of metal-centered excited states, dramatically different from much longer, several hundred picoseconds, lifetimes known for Fe^{II}-polypyridyl complexes [36, 78, 87].

The measured excited-state dynamics was rationalized with the help of DFT and TD-DFT calculations, showing that the exceptionally long (9 ps) ^{3}MLCT lifetime for this type of Fe-complex is achieved through a significant destabilization of both triplet and quintet metal-centered states compared to other Fe^{II}-complexes [88]. In addition, a shallow ^{3}MLCT potential energy surface with a low-energy transition path from the ^{3}MLCT to ^{3}MC, and facile crossing from the ^{3}MC state to the ground state, were identified as key features for the excited-state deactivation. The pathway of excited-state relaxation is indicated by the arrows in the potential energy curve diagram of Fig. 11.6. These potential energy curves nicely explain both the

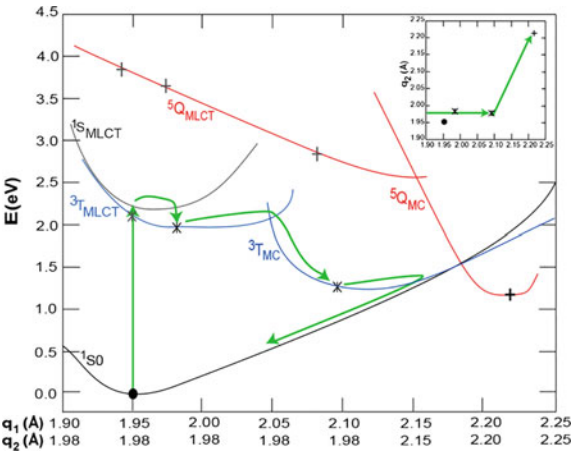

Fig. 11.6 Schematic excitation and deactivation pathways based on DFT and TD-DFT calculated potential energy curves. Reprinted with permission from [89]. Copyright the American Chemistry Society, 2014

several-picoseconds lifetime of the ^{3}MLCT state, as well as the unusually short lifetime of the ^{3}MC state through its near crossing with the ground state. The ^{5}MC state is not populated at all because of its high energy.

Photosensitization of TiO_2 nano-films provides an important ground for testing the viability of the Fe-NHC light-harvesting complexes in driving photoinduced electron transfer and associated charge transfer processes. In the late 1990s, Ferrere and Gregg first demonstrated the sensitization of TiO_2 with $Fe(dcbpy)_2(CN)_2$ (dcbpy = 2,2′-bipyridine-4,4′-dicarboxylic acid) and its derivatives [82]. These sensitizers suffered from band-selective sensitization behavior so that only UV light could be utilized. This was rationalized by Jakubikova and colleagues as a result of competition between injection processes and ultrafast sensitizer deactivation on a ~100 fs timescale [90, 91].

In order to examine the photosensitization capability of the Fe-NHC complexes, a Fe^{II}-NHC photosensitizer with carboxyl anchoring groups at the electron-accommodating pyridine moieties (Fig. 11.7a), was thus synthesized [87]. This functionalization also significantly stabilized the MLCT states, accounting for a red-shift of the MLCT absorption maximum by 70 nm compared to the non-functionalized molecule. More importantly, a doubled ^{3}MLCT lifetime of 18 ps was achieved in MeCN solution, which further increased to 37 ps upon immobilization on Al_2O_3 nano-films, the longest ^{3}MLCT lifetime reported to date of a Fe^{II} complex [87].

A combination of electron paramagnetic resonance, optical transient absorption and time-resolved tetrahertz spectroscopy [92], demonstrated interfacial electron injection on the few-ps timescale with a yield of 92% (Fig. 11.7b and c). Such highly efficient electron injection from the lowest energy MLCT band is in great contrast to the earlier Fe sensitizers. A detailed QC study on both the excited-state molecular properties and interfacial interactions of relevant Fe^{II}-based light harvesters corroborated the fundamentally favorable injection capabilities to nano-TiO_2 in terms of driving force and interfacial electronic coupling [93].

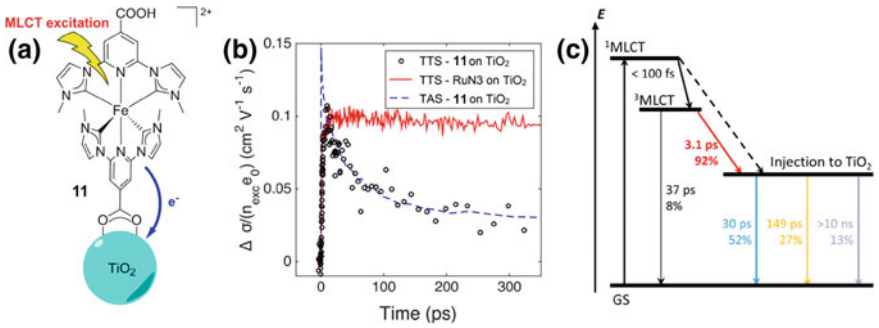

Fig. 11.7 **a** Chemical structure of **11**–TiO_2 assembly, **b** its TAS and TTS kinetics excited at 485 nm in comparison to RuN_3, and **c** Jablonski diagram of the electronic states involved in photoinduced electron transfer between **11** and TiO_2. Reprinted from [92]. Copyright Nature Publishing Group 2015

The Fe-NHC/TiO_2 assembly of Fig. 11.7a still suffers from relatively fast charge recombination, leaving approximately only 15% of the charge-separated state at time scales longer than nanoseconds. This may explain the still poor photovoltaic performance of this sensitizer in a working DSC device, highlighting the importance of further research to develop systems with improved interfacial control and excited-state properties.

11.3.2 Perovskite Solar Cells

First used in 2009 as a light harvester in a Grätzel-type solar cell with a meager 3.8% overall power conversion efficiency (PCE) [94], metal ammonium lead triiodide ($MAPbI_3$), now generally known as organometal halide perovskite solar cell (PSC), has rose to fame due to its unprecedented improvement in PCE, currently at 22.1% (National Renewable Energy Labs efficiency chart, 2016: http://www.nrel.gov/ncpv/). This has changed the landscape in solar cell science and technology prompting many groups to shift from the traditional photovoltaic materials, e.g., organic and dye sensitized, to PSC-based solar cells. These efforts have snowballed to other fields where it has been shown to perform well as light emitting diode [95], as laser material [96], and for water photolysis [97]. Despite this, little is known on its transient photo physical properties on the ultrafast time scale. In this section we will discuss the nature of photo generated species, charge dissociation, mobility, and recombination dynamics of this new class of materials. In addition, we will also discuss the mechanisms and time scale of charge transfer from perovskite to metal oxide (TiO_2 and Al_2O_3) and organic (PCBM and Spiro-OMeTAD) electrodes.

Shown in Fig. 11.8a is the early time THz transient photoconductivity of neat $MAPbI_3$, $MAPbI_3/Al_2O_3$, and $MAPbI_3/TiO_2$. Notice that the rise time of neat $MAPbI_3$ and $MAPbI_3/Al_2O_3$ is composed of an instrument-limited rise, which is

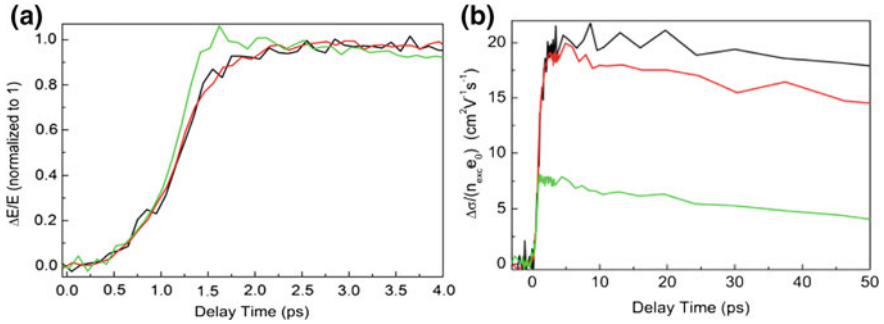

Fig. 11.8 **a** Early time THz transient photoconductivity neat $MAPbI_3$ (*black*), $MAPbI_3/Al_2O_3$ (*red*), and $MAPbI_3/TiO_2$ (*green*) normalized to 1. **b** THz transient photoconductivity for the first 50 ps of similar samples but normalized with $n_{exc}e$. λ_{pump} = 400 nm, $I_{exc} = 1.7 \times 10^{13}$ ph/cm^2 per pulse. Reprint with permission from [98], Copyright 2014, American Chemical Society

about 70% of the total amplitude of the signal, followed by a 2–3 ps additional rise of about 30% of the total signal. The two-step rise can be interpreted in two ways. Either those two events are happening successively, or simultaneously. On the former scenario, charged species are first generated on the ultrafast time scale, but are Coulombically bound, and in 2–3 ps, these charges dissociate, allowing them to gain mobility manifested as additional rise in the THz transient photoconductivity. We have measured the exciton binding energy of this particular sample (about 35 meV), which is very similar to room temperature thermal energy kT [99]. This could suggest that initially generated excitons dissociate on the timescale of 2–3 ps. The alternative explanation is that the two events are concurrently unfolding and that the ultrafast rise (70%) means that highly mobile charges are created together with Coulombically bound excitons (30%) which then dissociates in a few ps. However, this will require that there is a distribution of exciton binding energies within the material. Recent work report exciton binding energies in the interval from 4 to 50 meV [100–104], suggesting that indeed, both highly mobile charges and excitons may be photogenerated simultaneously.

In contrast, to the two-step rise in the transient photoconductivity of neat $MAPbI_3$ and $MAPbI_3/Al_2O_3$, the rise time of $MAPbI_3/TiO_2$ is just one component and is instrument-limited. This suggests that there is only a single mechanism of charge generation. For dye-sensitized nanostructured TiO_2 we previously reported very similar, if not identical, rise of the THz photoconductivity. On this basis, we assigned the single step ultrafast rise as electron injection from perovskite to TiO_2. To support this conjecture, we normalized the THz transient photoconductivity to the excitation density, which yields the photoconductivity per photon absorbed, or mobility in cm^2/Vs. As shown in Fig. 11.8b, the calculated mobility for neat $MAPbI_3$ and $MAPbI_3/Al_2O_3$ is 20 cm^2/Vs; for both cases, electrons and holes stay in the perovskite material, because for neat $MAPbI_3$ there is nowhere else to go, while for $MAPbI_3/Al_2O_3$ electron injection into Al_2O_3 is not possible due to unfavorable band alignment. For $MAPbI_3/TiO_2$, the obtained mobility is lower,

7.5 cm^2/Vs, which can be understood as disappearance of either the electrons or holes. There is at least 0.2 eV difference in the energy levels of conduction bands of perovskite and TiO_2 [105], and since TiO_2 is a well-known electron transport material, we conclude that ultrafast electron injection, in combination with low electron mobility in TiO_2 (0.1 cm^2/Vs [106]), are the reasons for the lower mobility measured. The very low mobility of electrons in TiO_2 also means that the measured mobility of $MAPbI_3/TiO_2$, 7.5 cm^2/Vs, is that of holes in $MAPbI_3$. Knowing the mobility of holes, this implies that from the mobility of 20 cm^2/Vs obtained for neat $MAPbI_3$, 12.5 cm^2/Vs comes from electrons. Electron and hole mobilities of this material is at least 2 orders of magnitude higher than some organic solar cell materials (μ_e = 0.005 cm^2/Vs, μ_h = 0.02 cm^2/Vs) [107]. Moreover, since the mobilities of electrons and holes in $MAPbI_3$ do not differ more than a factor of two they could arrive in the electrodes almost at the same time, lowering the possibility of creating space charge-limited photocurrent that lowers the photoconversion efficiency (PCE) [108].

Using time-resolved microwave conductivity (TRMC) measurements we investigated the charge dynamics of $MAPbI_3$ on a much longer time scale, up to microseconds (μs). Shown in Fig. 11.9 is the plot of photoconductivity, normalized to the number of absorbed photons, up to 1 μs. For neat $MAPbI_3$ and $MAPbI_3/Al_2O_3$, the mobility obtained is 3.0 cm^2/Vs, within signal to noise almost time independent. This shows that both the charge population and mobility of the carriers remain the same on this timescale. A similar kinetic behavior can be seen for the trace of $MAPbI_3/TiO_2$, but the mobility is lower 1.0 cm^2/Vs. The lower mobility reaffirms our result from the TRTS measurements that electrons are injected from the perovskite into TiO_2, and that this mobility represents the mobility of holes left in perovskite. From this we conclude that the mobility at microwave frequencies of electron in neat $MAPbI_3$ and $MAPbI_3/Al_2O_3$ is at least 2.0 cm^2/Vs, consistent with our TRTS results that the electron and hole mobilities do not differ by more than a factor of two. We also obtained the TRMC kinetics at even longer time scale, up 100 μs [98], showing that the onset of decay occurs on tens of μs,

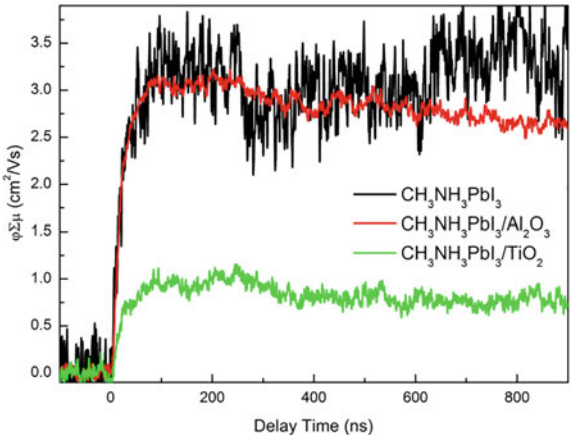

Fig. 11.9 Time-resolved microwave conductivity kinetics measured at an excitation density of 5.9 × 10^9 ph/cm^2 per pulse. Reprint with permission from [98], Copyright 2014, American Chemical Society

and is complete at approximately 100 μs. This result strongly suggesting that most, if not all, of the photo generated charge carriers can reached the electrodes and get extracted, rationalizing the very high PCE obtained for these devices.

Charge transport layers are often used to transport electrons and holes from the light absorbing (perovskite) layer to electrodes. Metal oxides are frequently used for this purpose, but organic materials are useful alternatives. Two of the most preferred organic choices are PCBM as electron transport layer (ETL), and Spiro-OMeTAD as hole transport layer (HTL). Shown in Fig. 11.10 is the THz transient photoconductivity of neat $MAPbI_3$, $MAPbI_3$/PCBM and $MAPbI_3$/Spiro-OMeTAD normalized to the excitation density used. The mobility for the neat $MAPbI_3$ material used in this study was 15 cm^2/Vs, which within the signal to noise, stayed constant up to 1 ns. Comparing this to the neat $MAPbI_3$ presented earlier (Fig. 11.8, 20 cm^2/Vs), this particular sample had somewhat lower mobility. A slight difference in the preparation procedure is the likely reason for this difference. Recently, it was shown that preparation conditions such as the length of thermal annealing time has major influence on the type and concentration of defects that a perovskite material will have [109]. Moreover, depending on the morphology of the prepared film, one could observe saturation in the absorption spectra [110] that complicates the accurate normalization of the photoconductivity data. In any case, all of our past measurements yielded a mobility from 15 to 25 cm^2/Vs for neat $MAPbI_3$ thin films, a variation sufficiently small not to affect the interpretations of photo physical properties. The transient photoconductivity kinetic trace of neat $MAPbI_3$ in Fig. 11.11 can then be straightforwardly interpreted as follows: highly mobile charges, both electrons and holes, are generated in the perovskite materials on the ultrafast timescale, where population and mobility remained constant for at least 1 ns. For $MAPbI_3$/Spiro-OMeTAD the time evolution of the transient photoconductivity is very similar to that of neat $MAPbI_3$, but with a mobility three times less, 5 cm^2/Vs. Spiro-OMeTAD has been demonstrated as a very good hole transporting material, i.e., most of the highest PCE obtained from operating

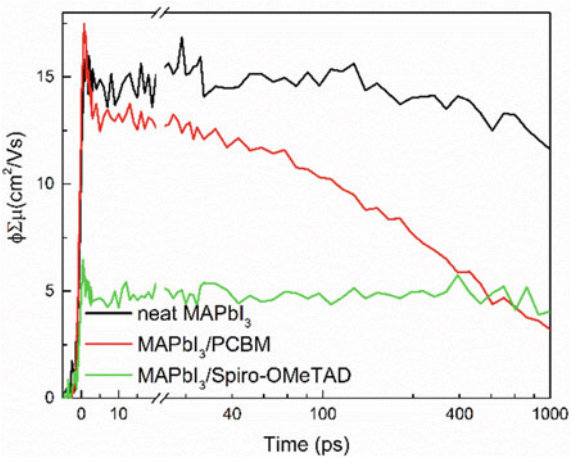

Fig. 11.10 Transient photoconductivity of (**a**) neat $MAPbI_3$, $MAPbI_3$/PCBM and $MAPbI_3$/Spiro-OMeTAD (λ_{pump} = 590 nm, 2.1 × 10^{12} ph/cm^2 per pulse) up to 1 ns. Reprint with permission from [98], Copyright 2014, American Chemical Society

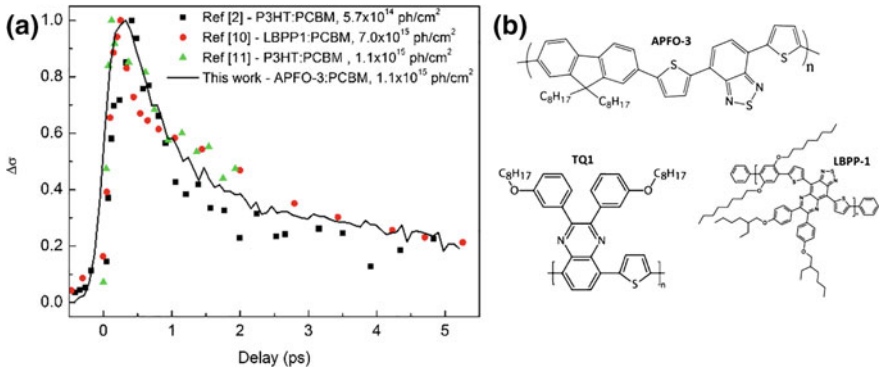

Fig. 11.11 **a** Early time transient photoconductivity kinetics of several other polymer:PCBM blends (*black* trace) [119]. Data points were adapted from [103, 104]. Reprinted with permission from [119], Copyright the American Chemical Society 2012. Re (**b**) Molecular structure of different electron donating polymers

perovskite solar cells have used this as HTL, despite its very low conductivity, 10^{-8} S/cm [111]. However, its valence band has a 0.57 eV difference with respect to the valence band of perovskite [112], highly favorable for charge transfer, and explaining the good performance in solar cells. The reduction in the mobility of $MAPbI_3$/Spiro-OMeTAD can now be understood as ultrafast hole injection from perovskite to Spiro-OMeTAD, where the holes become "invisible" to the THz spectroscopy due to the low mobility. This also means that since the conductivity of Spiro-OMeTAD is very low, the measured mobility (5 cm^2/Vs) should be coming from the electrons left in the perovskite material. From this and from the mobility of the neat $MAPbI_3$ used in these experiments (15 cm^2/Vs), one can conclude that the hole mobility is 10 cm^2/Vs. Again, this is consistent to the findings above that the difference in the mobilities of the charge carriers in these materials do not differ more than a factor of two. Here, the hole mobility is higher while in a previous sample the electron mobility was higher. From this, we can conclude that the neat $MAPbI_3$ sample in Fig. 11.8 is n-type doped while the neat $MAPbI_3$ sample in Fig. 11.10 is p-type, similar to what we concluded in [113]. Small differences in preparation conditions, as fully discussed in the work of Wang et al., can lead to either n-type, intrinsic or p-type semiconductor perovskite material [109].

Unlike the transient photoconductivity kinetics of neat $MAPbI_3$ and $MAPbI_3$/Spiro-OMeTAD, there is a substantial decay in the trace of $MAPbI_3$/PCBM. Initially, its mobility is similar to neat $MAPbI_3$, showing that both electrons and holes are in the perovskite. In the span of 1 ns, the mobility slowly diminishes to about 30% of its initial value. It should be noted that the difference in the conduction band levels of perovskite and PCBM is merely 0.2 eV [109]. This could have a considerable influence on the time scale of electron injection from perovskite to PCBM. But since it has been demonstrated that an operating solar cell device can be made with PCBM as ETL, we conclude that the sub-ns decay in the kinetics is due to electron injection. Another channel by which the transient photoconductivity

may decay on the sub-ns timescale, is as a consequence of intensity dependent second order non-geminate recombination. However, as seen in Fig. 11.11, the trace of neat $MAPbI_3$ and $MAPbI_3$/Spiro-OMeTAD do not have any decay on the nanosecond time scale. This means that the excitation intensity used in this experiment is sufficiently low to avoid non-geminate recombination. We further note that the mobility of electrons in PCBM is also very low as we previously measured, $\mu_e = 0.005$ cm^2/Vs [107]. This implies that as the electrons are slowly being injected from the perovskite into PCBM, they are pinned near the interface of the two materials due to low mobility in PCBM, while holes that are left in perovskite is highly mobile (10 cm^2/Vs). The high mobility of holes in the perovskite leads to a high probability for holes to find and recombine with electrons at the interface, which would manifest as decay in the transient conductivity kinetics. We therefore conclude that the sub-ns decay of photoconductivity in $MAPbI_3$/PCBM is a convolution of two effects—electron injection from perovskite to PCBM and recombination between the injected electrons in PCBM and holes left in perovskite.

11.3.3 Organic Solar Cells

Unlike silicon-based solar cells that require highly industrialized settings for fabrication, organic-based solar cells only rely on "kitchen chemistry," wherein solutions of both light-harvesting molecules and acceptor molecules are mixed together in order to prepare the active material. This inexpensive and easy route to manufacture solar cell devices is the main motivation why it has attracted extensive research for the past 20 years. The most studied organic bulk heterojunction material is the polymer/fullerene system, where the polymer absorbs light and excitons (bound electron-hole pairs) are formed. The fullerene, whose conduction band is lower than that of the polymer, then accepts the photoexcited electron and transports it to the electrode. The generally accepted picture is that electrons are transferred to the fullerene balls on the ultrafast time scale, leaving free holes on the polymer chains, which are eventually extracted at the counter electrode.

There are several reports on the transient photoconductivity of these bulk heterojunction materials [114–116]. Our early work using TRTS included results on two polymer types, APFO-3 and LBPP-1 (Fig. 11.11b) mixed with PCBM (Phenyl-C61-butyric acid methyl ester). For both samples the transient photoconductivity was very similar to the previous works on P3HT:PCBM. However, the assigned origin of the fast decay was rather different. The few-ps decay in LBPP-1:PCBM was interpreted as a transition from a hot regime to a quasi-equilibrium state which was surmised to be not longer than 2 ps [117]. During this transition, hot holes on the polymer are able to pass potential barriers, but as they cool down, the barrier restricts their motion thereby lowering the mobility, manifested as a fast decay in the transient photoconductivity kinetics. Two different excitation fluencies were used for investigation of APFO-3:PCBM and it was shown that the initial decay is speeding up at higher pump intensity. It was suggested that the dependence

is related to the lifetime of the coupled polaron pair, which was reported to be the charge species generated [118].

The mobility of charge carriers in polymers and PCBM are typically on the order of 10^{-3} cm^2/Vs. Therefore, in order to obtain decent signal to noise, one should increase the concentration of charge carriers. To do this, very high excitation densities are generally required. The disadvantage of this approach is that the charge dynamics may be altered by nonlinear effects as shown in previous transient absorption studies of polymer:PCBM blends [11]. Shown in Fig. 11.4 is the early time transient photoconductivity kinetics of several polymer:PCBM films discussed above. Notice that the excitation fluency used is typically on the order of 10^{15} ph/cm^2 per pulse and the few-ps decay is consistently dominant in all of the samples.

Our previous transient absorption results show that at low excitation density ($\sim 10^{13}$ ph/cm^2 per pulse), the onset of charge recombination occurs on the several nanosecond or slower time scale. However, at high excitation densities ($\sim 10^{15}$ ph/cm^2 per pulse) a few-ps decay of charge population due to polaron pair annihilation was observed [10, 11]. This was explained as follows: At high excitation fluence, the average distance between photo generated charge pairs is small (~ 4 nm), implying that only very limited diffusion of charge carriers would lead to recombination, i.e., non-equilibrated charge pairs recombine or "annihilate" more or less immediately after their formation. Such a process is highly intensity dependent and occurs on the few-ps time scale [9]. To examine whether the similar mechanism is at operation in the THz measurements and manifested as the ultrafast decay of the photoconductivity response, we systematically lowered the excitation intensity in several steps down to a fluence of 9.1×10^{12} photons/cm^2/pulse. The resulting photoconductivity kinetics is shown in Fig. 11.12. At the highest pump fluence (1.8×10^{15} ph/cm^2 per pulse), the kinetics is very similar to that presented in Fig. 11.11; ultrafast rise, few-ps decay and a small long-lived signal extending up to 100 ps. As the excitation is lowered the decay is becoming slower such that at the lowest intensity (9.1×10^{12} ph/cm^2 per pulse) the photoconductivity kinetics

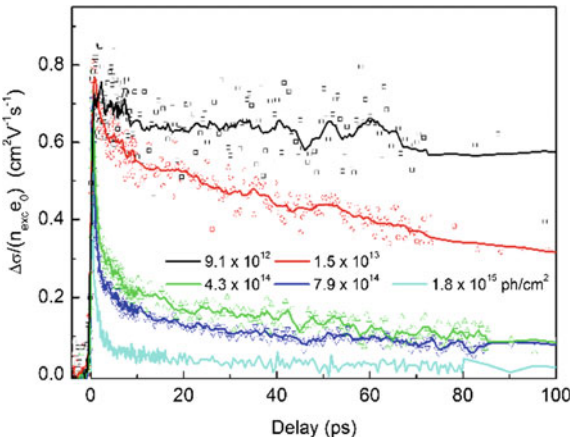

Fig. 11.12 Transient photoconductivity kinetics of TQ1:PCBM at varying excitation densities. Solid lines in the kinetics are smoothed data for clarity of the plot except for highest excitation fluence. Reprinted with permission from [119], Copyright the American Chemical Society 2012

does not exhibit any decay (within signal to noise). Based on the similar time scale and intensity dependence of the THz photoconductivity decay and the charge pairs recombination discussed above [10, 11], it was concluded that the same mechanism causes the ultrafast decay of the THz response [119].

Further information about the electron-hole separation process in polymer:-fullerene bulk heterojunctions was obtained from ultrafast time-resolved-electric field-induced-second-harmonic (TREFISH) measurements [120]. The charge drift was directly measured in a P3HT:PCBM blend and it was show that initially, immediately after photoexcitation, only closely separated (<1 nm) charge pairs are created and that they separate by several nanometers during the first several picoseconds. Charge pairs overcome Coulomb attraction and form free carriers on a subnanosecond time scale. Numerical simulations complemented these experimental results and showed that fast three-dimensional charge diffusion within an energetically disordered medium, augmented by the correlated entropy change, is sufficient to drive the charge separation process. These results and work pointing to the importance of delocalized hot charge states for efficient charge separation [121, 122] can be combined in the following picture of charge separation: Charge delocalization reduces the electron-hole electrostatic interaction to a level where fast diffusion can separate charges to distances where recombination is inefficient, in only a few picoseconds, and free carriers are formed on the sub-ns time scale.

11.3.4 Solar Fuels—From Model Systems to Functional Devices

Solar fuels denote renewable fuels that are produced with solar energy as the only energy input. Typically, this refers to light-driven water splitting to H_2 and O_2, or reduction of CO_2 to carbon-based fuels. Many of the principles underlying these processes are the same as for natural oxygenic photosynthesis, and a large number of molecular systems have been built to mimic photosynthesis and investigate light-induced excitation energy and electron transfer in model systems [6–8, 123]. Molecular catalysts are promising for solar fuels production, as they offer far greater tunability, product selectivity and turnover frequency per metal center, and smaller footprint, than heterogeneous ones. Thus, the number of molecular catalysts performing water oxidation and reduction of protons or carbon dioxide has increased dramatically during the last few years. Complete devices for water splitting and CO_2 reduction, which are based on molecular catalysts and dyes, have also begun to emerge (see Chaps. 6 and 7 of this book). For TRLS, investigation of these devices present additional challenges to those typically met in studies of solar cells. First, one photon typically separates a single electron–hole pair only, while catalysis involves multiple electrons and protons. Therefore, the catalysts evolve through many states upon absorption of several photons. Typically, only the light-triggered steps leading up to the first oxidation or reduction are followed by TRLS.

Alternatively, if TRLS is performed under continuous background irradiation, several states are present at the same time, and their respective evolution upon laser excitation is difficult to deconvolute.

11.3.4.1 Charge Separation in Sensitizer-Catalyst Model Systems

Understanding and designing the dynamics of photoinduced electron transfer is essential for building artificial photocatalytic systems. In nature as well as in artificial systems, as illustrated in Fig. 11.13, the full cycle from the absorption of light, over the generation of a charge-separated state, the transport to the reaction center, the catalyzed reaction and the regeneration of the catalytic site often involves multiple sites and occurs over a wide range of time scales, making the study of the full system very challenging. Therefore, it is often useful and meaningful to investigate the "early" processes in the overall catalytic reaction in model systems. In the design of such systems one can choose which part of the overall reaction one wants to examine in detail. These processes are generally rapid and spectroscopic methods with high time resolution are required to resolve the various reaction steps.

Key to studying photoinduced electron transfer is the selective excitation of a light absorber (sensitizer) and the consequent tracing of the excitation and charge transfer through the system. In recent years the availability of novel ultrafast techniques like element selective X-ray spectroscopies or single and multidimensional spectroscopy with light in the visible, infrared and terahertz wavelength range have provided us with powerful tools to study light-induced processes. Improvement in predictive and time dependent calculations has enabled new approaches to study electron transfer. Not only can we now directly probe the movement of electrons through a complex molecular system, but the new level of

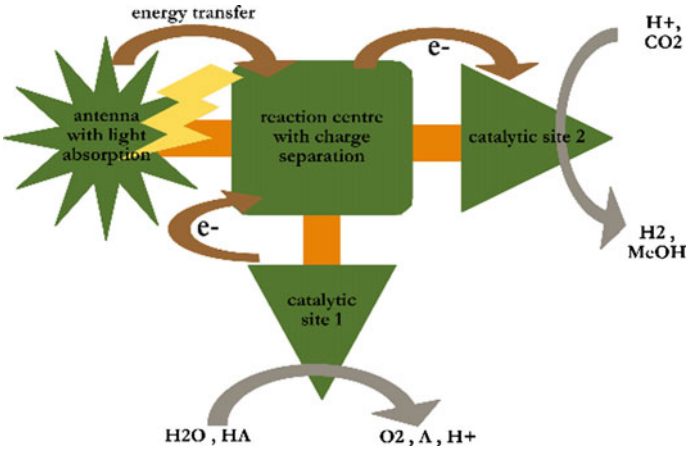

Fig. 11.13 Sketch of charge transfer pathways in light-harvesting systems for solar fuel production

predictive calculation can start to guide the synthesis of novel complexes. In this section we shall review selected model systems, focusing on studies of excitation/charge transfer from a sensitizer over bridging structures to the catalytic site that used a combination of experimental techniques to get detailed insight into the reactions. The molecular systems we are examining consist of transition metal complexes as building blocks connected by organic bridges. The actual catalytic processes are discussed in the following section.

For catalytic molecular assemblies based on transition metal complexes as modules, studies of single-metal-center complexes is motivated by the need to understand energy and electron localization and dynamics of these molecules in their function as sensitizers or catalysts in solar energy converting systems. Classical model systems studied in this category are polypyridyl-based complexes of ruthenium. Tris-2,2′-bipyridine ruthenium(II) ($[Ru(bpy)_3]^{2+}$) is one of the most studied representative of these metal organic complexes. Many of these d^6 systems have D_3 symmetry and a low-energy single-electron excitation dominating the visible absorption that promotes a metal-based π electron into a ligand-based π^* orbital, giving rise to an allowed metal-to-ligand charge transfer band. These complexes have been studied over a very long time and the dynamics following a single-electron excitation are well understood [20, 124, 125]. $[Ru(bpy)_3]^{2+}$ and other single-center complexes with, e.g., Co, Cu, Fe and Os have also been important targets for the development of the new time-resolved X-ray techniques [20, 126–130].

Biomimetic models for the electron donor side of Photosystem II were developed with a $Ru(bpy)_3$-based sensitizer covalently linked to mono- and dinuclear manganese(II) complexes [8, 131]. Flash photolysis studies followed the reaction of the excited R_u^{II} and photo-oxidized R_u^{III} states by fluorescence/phosphorescence and visible transient absorption on a ns timescale. This revealed the kinetics of intramolecular electron transfer from Mn^{II} to photogenerated Ru^{III} in the first artificial sensitizer-manganese systems, which were made before the structure of the oxygen evolving complex in Photosystem II was known. This also demonstrated the competing energy transfer quenching of excited Ru^{II} by the appended Mn^{II} complex that competed with oxidative quenching by the external viologen electron acceptor. These studies provided insight into the distance dependence of the competing processes and demonstrated the effect of ligand modifications that result in localization of the Ru^{II} MLCT state on the non-bridging ligands of the sensitizer. This allows for maximizing the yield of the desired electron transfer reaction by optimal linker length and attachment.

Continuation of the above work led ultimately to a first synthetically linked electron donor–sensitizer–acceptor triad with a manganese complex as electron donor (Fig. 11.14) [132]. Photoexcitation of the R_u^{II}-polypyridine unit of the triad led to the reduced naphthalenediimide ($NDI^{\bullet-}$) and oxidized manganese dimer complex $\left(Mn_2^{II,III}\right)$, the fully charge-separated state persisting for about 600 μs at room temperature. The charge recombination showed a strong temperature dependence, resulting in a remarkable lifetime of 1–10 s at 140 K. This was

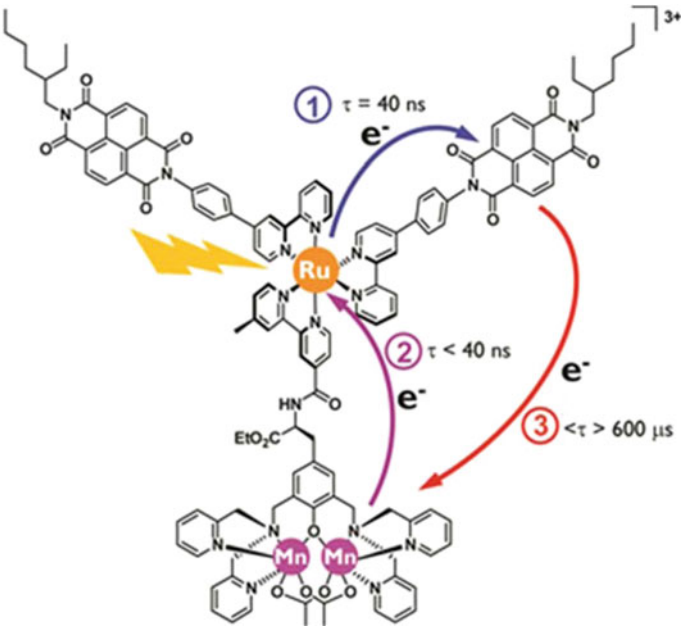

Fig. 11.14 A $Mn_2^{II,II}$-Ru^{II}-NDI_2 triad showing long-lived charge separation at room temperature, studied by ns-transient absorption and EPR spectroscopy [132]. Figure reprinted from [133], with permission. Copyright the American Chemical Society 2010

attributed to an unusually large inner reorganization energy for the $\left(Mn_2^{II,II}\right)$-to-$Mn_2^{II,III}$ conversion, as supported by comparison of published crystal structures of the Mn_2 unit in the two oxidation states. The initial oxidative quenching of the sensitizer by the NDI acceptor and the subsequent oxidation of the Mn_2 donor were studied by time-resolved optical spectroscopy and electron paramagnetic resonance (EPR) spectroscopy. While optical spectroscopy readily monitors the kinetic evolution of the intermediate states of the Ru-complex and the $NDI^{\bullet-}$ radical, EPR detection was used to directly demonstrate light-induced formation of the oxidized manganese dimer complex ($Mn_2^{II,III}$) that is associated to relatively minor optical absorption changes.

The Ru=Co complex $([(bpy)_2Ru^{II}(tpphz)^1Co^{III}(bpy)_2](PF_6)_5)$ (tpphz = tetrapyrido (3,2-*a*:2′3′-*c*:3″,2″-*h*::2‴,3‴-*j*) phenazine) in Fig. 11.15 was designed to study the primary light-induced processes in a bimetallic complex having a Ru-sensitizer moiety coupled to a model Co-catalytic center via a tetrapyrido phenazine (tpphz) aromatic bridge. The molecule was chosen as a system anticipated to contain many of the features and light-triggered processes of a fully active photocatalytic system—light-induced electron transfer, an optically dark Co^{3+}-center (like many other catalytic transition metal complexes), spin changes on the metal centers, metal-ligand structural changes, dissipation of excess excitation energy. Our own as well as earlier time-resolved optical studies of this and similar

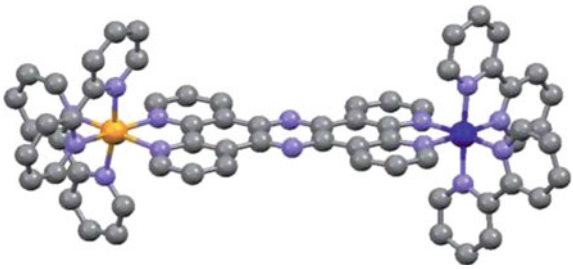

Fig. 11.15 Ru=Co model system for time-resolved studies of primary light-induced processes

bimetallic complexes [134] showed that light absorption by the Ru^{2+}-center results in electron transfer to the aromatic bridge, but due to the lack of clear spectroscopic signatures in the optical part of the spectrum, direct evidence for the $Co^{3+} \rightarrow Co^{2+}$ reduction was not achieved. Similarly, optical studies are blind to spin changes, structural changes and energy dissipation. By implementing ultrafast X-ray spectroscopy and scattering, in combination with more traditional ultrafast optical measurements, we hoped to resolve all these processes, characterizing the first few steps of any photocatalytic reaction.

Optical transient absorption showed that photoexcitation of the Ru-center leads to electron transfer to the tpphz bridge within the time resolution of the experiment (<50 fs) and the electron leaves the bridge with a time constant of approx. 0.5 ps. Time-resolved XAS measurements with ~100 ps synchrotron pulses, probing the Co K-edge showed that Co^{III} is reduced to Co^{II} much faster than the ~100 ps instrument response function of the measurements. Figure 11.16a displays the XAS spectrum without laser illumination (black) and 3 ns after excitation at 527 nm (red). The transient difference signal is shown in Fig. 11.16b. Comparison of this spectrum with a reference trace (Fig. 11.16b), which is constructed as the difference between the steady-state XAS of the mononuclear complexes $[^4Co^{II}(bpy)_3]^{2+}$ $(\pi t_{2g})5(\sigma e_g)^2$ (high spin, HS) and $\left[^1Co^{III}(bpy)_3\right]^{2+}(\sigma e_g)^2$ (low spin, LS) shows that electron transfer to the Co center has occurred and is accompanied by a spin flip in the relaxed photoproduct. The transient fingerprints reflect the change in electronic configuration from $(\pi t_{2g})^6$ to $(\pi t_{2g})^5(\sigma e_g)^2$ and the driven atomic rearrangements. They can be explained within a simple molecular orbital description of the X-ray induced transitions which shows that population of the antibonding, e.g., orbital in the Co^{II} moiety causes the Co–N bond length to increase by 0.2 Å (Fig. 11.16b). X-ray kinetics (Fig. 11.17) of the RuCo complex shows that the Co is reduced within the time resolution of the experiment (~80 ps), determined by the duration of the synchrotron X-ray pulses. The decay of the X-ray response on the tens of ns time scale reflects the $Co^{II} \rightarrow Ru^{III}$ back electron transfer.

In an attempt to time resolve the ruthenium → cobalt electron transfer process and at the same time achieve spin selective detection, XES measurements with sub-picosecond pulses were performed. Figure 11.18 shows the transient Co $K\alpha_1$ difference XES spectrum acquired at time delays Δt fixed to 2.5, 20 and 150 ps after the selective excitation of the ^{1}MLCT state in the Ru^{II} moiety at 400 nm.

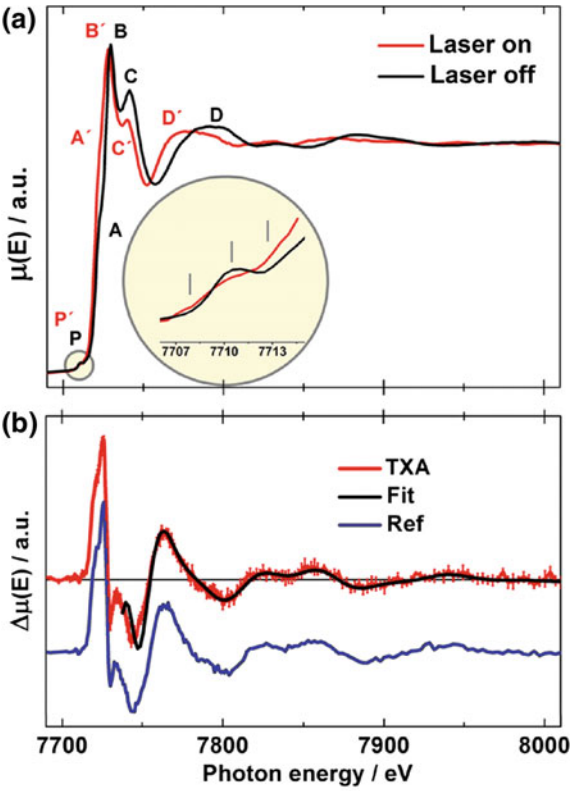

Fig. 11.16 **a** Transient X-ray absorption spectra acquired for RuCo in acetonitrile at the Co K-edge, laser off (*black*), and laser on (*red*) with a delay of 3 ns. Insert shows the pre-edge region. **b** Difference spectrum (laser on)–(laser off) (*red line*), reference spectrum (*blue line*) and FEFF 9.0 simulations based on crystal structures (*black line*). Reprinted with permission from [135]. Copyright 2013 American Chemical Society

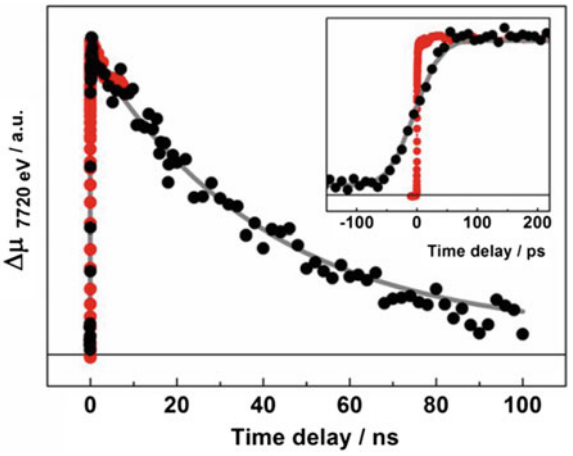

Fig. 11.17 X-ray kinetics of RuCo taken at 7720 eV (*black*) and single-exponential fit (*grey*). The onset of the ground state bleach recovery from transient optical kinetics measured at 490 nm is inverted and scaled for comparison (*red*). Reprinted with permission from [135]. Copyright 2013 American Chemical Society

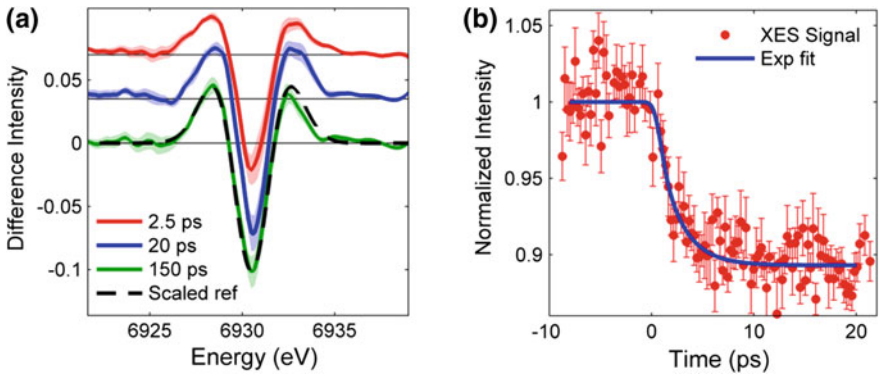

Fig. 11.18 Co Kα difference XES spectrum at 2.5 (*red*), 20 (*blue*) and 150 (*green*) ps pump-probe delay. The *black dashed curve* is the simulated reference spectrum for a CoIII (LS) to CoII(HS) conversion scaled to the 150 ps measured spectrum. **b** Kinetics at 6.93 keV (*red dots*) and single-exponential fit with a 1.9 ps time constant broadened by a 520 ± 410 fs XFEL instrument response function (*blue* trace). Reprinted with permission from [138]. Copyright Nature Publishing group 2015

Steady-state [35, 136] and time-resolved [21, 22, 137] experiments have established that for spin state transitions (SST) in 3d transition metal ions, the full width at half maximum (FWHM) of this 2p → 1 s transition subsequent to 1s core ionization is directly proportional to the number of unpaired electrons. In order to assign the transient XES signal, it is compared to a reference spectrum constructed by subtracting the normalized line shape obtained for a $(\pi t_{2g})^6$ [$^1Co^{III}$] center in the low-spin (LS) state from the one simulated for a $(\pi t_{2g})^5$ $(\sigma e_g)^2$ [$^4Co^{II}$] center in the high-spin (HS) state. The excellent agreement with the transient spectrum at $\Delta t =$ 150 ps demonstrates that ET from Ru^{II*} to $^1Co^{III}$ (LS) and a SST at the Co^{II} center have both taken place during this time interval. This finding agrees with the synchrotron-based XAS experiments discussed above (Figs. 11.16 and 11.17). The kinetics of the Co^{II} HS state formation was monitored at the peak of the transient XES spectrum (6.93 keV) showing that it is formed with a time constant of 1.9 ps. Contrasting this time of appearance of the Co^{II} HS state with the ∼0.5 ps decay of the reduced bridge state, suggest that there is an intermediate between these states. Two possibilities can be considered—a reduced bpy ligand of the Co metal center, or the Co^{II} LS excited state. Since no transient spectral features characteristic of bpy^- in the 300–400 nm range was detected, it was concluded that the intermediate is the LS Co^{II} state. Further information about the global structural changes and the interaction of the complex with its surroundings was obtained from an X-ray diffuse scattering experiment performed in parallel with the time-resolved XES experiment [28, 138]. The results confirmed the ∼0.2 Å Co–N bond extension following electron transfer, previously observed in synchrotron XAS measurements. In addition, the XDS measurements showed that dissipation to the solvent environment of excess electronic energy occurs more than ten times slower, ∼10 ps, than that the Ru to Co electron transfer and thus out of thermal equilibrium. This implies

that the optical excitation energy is used to effectively drive the charge transfer from Ru to Co, before it is lost as heat to the environment. The total reaction event and associated rates of the various steps of the Ru=Co molecule following optical excitation of the Ru-moiety are summarized in Fig. 11.19.

In order to explore the role of the organic bridge connecting the Ru and Co centers in the RuCo molecule discussed above, the aromatic bridge was replaced by a saturated aliphatic bridge. Using a combination of time-resolved optical and X-ray spectroscopy it was found that the nature of the bridge plays a decisive role in the electron transfer. In the molecule with the saturated bridge the forward electron transfer is almost thousand times slower, ~300 ps, and the electron recombination is considerably faster [127]. Quantum chemistry calculations rationalized the differences in electron transfer rates as a result of the different electronic structure of the bridge for the forward process and differing molecular structure for the charge recombination.

A complementary combination of ultrafast optical and X-ray absorption spectroscopy was also employed to study the light-induced formation of the Ir^{IV} intermediate in the catalytic cycle of a functional water-oxidation catalyst (Fig. 11.20) [139]. The highly reactive Ir^{IV} state of the Ir^{III}-based water-oxidation catalyst Cp*Ir(ppy)Cl (ppy = 2-phenylpyridine) was photogenerated in a covalent electron acceptor-chromophore-Cp*Ir(ppy)Cl triad, with a NDI acceptor and a perylene-3,4-dicarboximide (PMI) chromophore. A combination of reductive quenching of the PMI excited S_1 state by the Ir catalyst and oxidative quenching by the NDI acceptor occur in less than 5 ps. The subsequent charge shift reactions result in the fully charge-separated state $NDI^{\bullet-}$–PMI–Ir^{IV} that recombines on the nanosecond time scale. While the electron transfer reactions of the chromophore and electron donor moieties are readily detected by the pronounced optical absorption changes, direct evidence for the change in the Ir oxidation state from Ir^{III} to Ir^{IV} was obtained from X-ray absorption measurements that show a new absorption feature at the L-III-edge of Ir and a blue-shifted white-line peak at

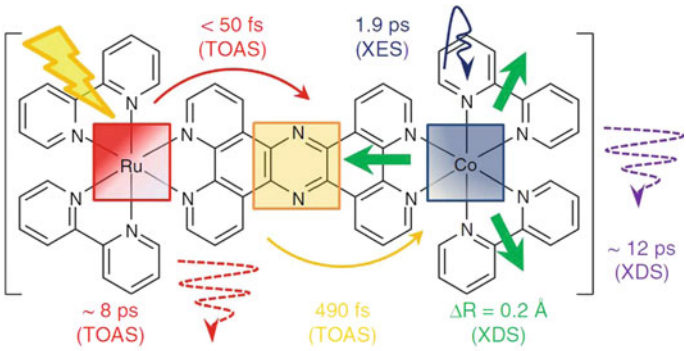

Fig. 11.19 Summary of light-induced Ru to Co electron transfer and associated spin flips, structural change and heat dissipation. Reprinted with permission from [138]. Copyright Nature Publishing group 2015

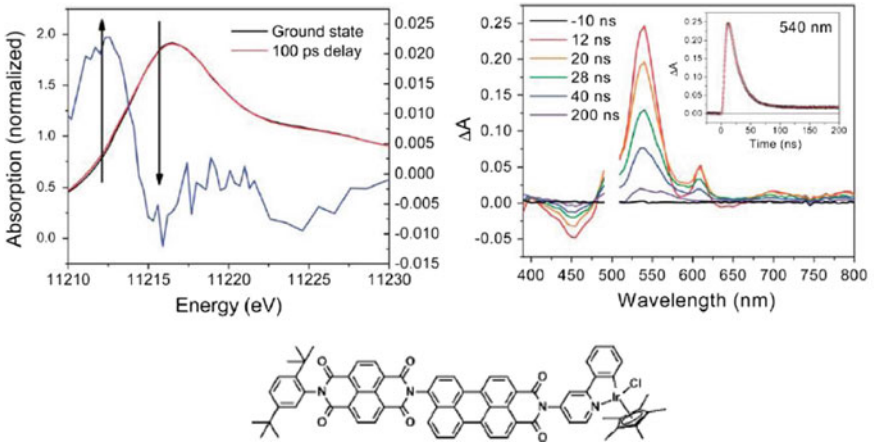

Fig. 11.20 A covalent electron acceptor-chromophore-Cp*Ir(ppy)Cl triad, where a water-oxidation catalyst complex Cp*Ir(ppy)Cl (ppy = 2-phenylpyridine) was photo-oxidized by the appended PMI chromophore-NDI acceptor units (NDI = naphthalene-1,8:4,5-bis(dicarboximide), PMI = perylene-3,4-dicarboximide); (*left panel*) XANES spectra of the ground state (*black*) and at 100 ps after excitation at 527 nm (*red*) and the light-dark difference spectrum (*blue*) showing the expected Ir^{IV}–Ir^{III} differences; (*right panel*) optical transient absorption spectra showing the decay of the charge-separated state NDI^{-}–PMI–Ir^{IV} (signals from a combination of NDI^{-} absorption and a Stark shift of the PMI ground state absorption. Reprinted from [139] with permission. Copyright The Royal Society of Chemistry, 2013

100 ps after PMI photoexcitation. This example underlines the effectiveness of ultrafast X-ray absorption spectroscopy for the characterization of reactive intermediates of solar fuels catalysts generated in covalent electron donor–acceptor assemblies.

Time-resolved infrared (TRIR) spectroscopy offers advantages over optical spectroscopy in UV-VIS range in form of narrower, less overlapping bands, as well as stronger and more direct correlations between spectra and molecular structure that aids structural elucidation of unknown transients. Many classes of molecular solar fuel catalyst contain functional groups such as carboxylate or carbonyl ligands with particularly strong IR absorption that are at the same time very sensitive to electronic and structural changes. TRIR is therefore a powerful probe for redox processes or change in protonation state, as well as other structural rearrangements like substrate binding and changes in coordination mode. TRIR measurements can follow either absorptions of reporter groups such as CO ligands in, e.g., H_2 formation catalysts or substrate itself as in CO_2 reduction catalysts.

In early studies of H_2 formation catalysts modeled after the active site of [FeFe]-hydrogenases, one-electron reduced intermediates were observed by optical spectroscopy following light-induced electron transfer either as bimolecular reactions with flash-quench generated reductants [140, 141] or as intramolecular electron transfer in a donor–acceptor dyad where a porphyrin dye (5,10,15-tri-*n*-pentyl-20-phenylporphyrin) was linked to a $(NMI)S_2Fe_2(CO)_6$ complex [142].

While the optical absorption changes could monitor the kinetics of the electron transfer processes, information on structural changes of the catalyst, induced by the electron transfer step, only became available from studies with complementary TRIR detection of the catalytic intermediates. Thus, for the proton reduction catalyst $[Fe_2(bdt)(CO)_6]$ (bdt = benzenedithiolate), the structure and reactivity of reactive intermediates in the photocatalytic cycle were inferred from TRIR measurements on the ns to ms time scale, following ns-laser flash-induced reduction (Fig. 11.21) [143]. For the one-electron reduced catalyst, $[Fe_2(bdt)(CO)_6]^-$ the transient IR spectra in the CO region revealed an asymmetrically distorted geometry around the Fe–Fe core with one broken Fe-S bond and six terminal CO ligands instead of the μ-CO motif characteristic of the stable, two-electron reduced catalyst $[Fe_2(bdt)(CO)_6]^{2-}$. The TRIR spectra further revealed that protonation of $[Fe_2(bdt)(CO)_6]^-$ yields a hydride-bridged species $[Fe_2(bdt)(CO)_6]H$ that resemble structurally and electronically the parent complex $[Fe_2(bdt)(CO)_6]$. For this catalyst TRIR hence led to the characterization of two reactive intermediates in the photoinduced proton reduction cycle that are too short-lived to be accessible with conventional (electro)chemical methods. It also established the mechanistic difference from electrochemical hydrogen formation with the same catalyst, which had been shown to proceed via the two-electron reduced catalyst $[Fe_2(bdt)(CO)_6]^{2-}$ that subsequently is protonated (Fig. 11.21).

Pump-probe TRIR on the ps time scale has been applied to evaluate the effects of different bridging motifs and axial ligands on charge separation and recombination

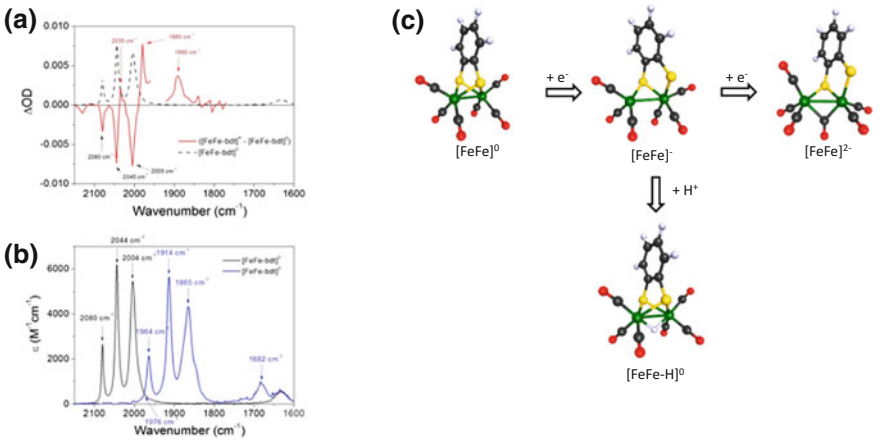

Fig. 11.21 **a** TRIR difference spectra after single-electron reduction of the $[Fe_2(bdt)(CO)_6]^0$ complex by laser flash-quench (*red*), the *dashed line* shows the FTIR spectrum of the initial $[Fe_2(bdt)(CO)_6]^0$ complex; **b** FTIR spectra of the $[Fe_2(bdt)(CO)_6]^0$ and $[Fe_2(bdt)(CO)_6]^{2-}$ complexes; **c** structures of the $[Fe_2(bdt)(CO)_6]$ complex in different reduced and protonated states detected by FTIR and TRIR spectroscopy, which are intermediates in the catalytic cycle for H_2 generation. The photochemical mechanism occurs protonation of the reduced catalyst to form $[Fe_2(bdt)(CO)_6H]^0$, while the electrochemical mechanism is believed to involve two reduction steps before the first protonation. Reprinted by permission from [143]. Copyright the American Chemical Society 2014

kinetics in a series of dyads consisting of CO_2 reduction catalysts [Re^I(2,2′-bipyridine)$(CO)_3L]^{+/0}$ (L = Br or 3-picoline) covalently linked to zinc porphyrin chromophores via amide linkers ($C_6H_4NHC(O)$, $C_6H_4NHC(O)C_6H_3(OMe)NHC(O)$ or $C_6H_4NHC(O)CH_2$) [144].

Laser pump—NMR probe spectroscopy can be anticipated to develop into a powerful tool for the characterization of reactive intermediates given the detailed structural information available from NMR spectra and the time resolution that can be attained with laser flash triggered reactions. Applications in time-resolved pump–probe measurements rely, however, on major enhancement of the sensitivity of the NMR experiment given by the very small Boltzmann population differences between nuclear spin states. Signal enhancements on the order of 10^2 due to spin polarization in spin-correlated radical pairs can be exploited by the photochemically induced dynamic nuclear polarization (photo-CIDNP) method that has been able to detect short-lived radicals on millisecond to second time scales. The time resolution limits might be significantly improved by *para*-hydrogen (*para*-H_2) hyperpolarization of NMR as recently demonstrated for the laser-induced reactions of *para*-H_2 with transition metal hydride complexes [145]. With this method delays as short as 10 μs between a nanosecond laser pump pulse and a radio frequency (rf) probe pulse were applied to produce a high-resolution, single-scan ^{1}HNMR spectrum that can be followed in time as the pump-probe delay is increased. The frequencies of amplitude oscillations arising from magnetic coherence effects were shown to match the chemical shift difference between chemically inequivalent hydrides in *cis*-Ru$(dppe)_2(H)_2$ or the difference between couplings of the hydrides to the equatorial ^{31}P nuclei in Ru-$(PPh_3)_3(CO)(H)_2$. Given the detailed structural information and comparatively excellent time resolution of this NMR technique, this might be exploited in the characterization of metal hydride species with pertinence to catalytic H_2 formation.

11.3.4.2 Accumulative Charge Separation

Coupling photoinduced one-electron transfer steps to multi-electron catalytic processes is a key requirement for any solar fuel device. However, photodriven accumulation of several oxidation or reduction equivalents without sacrificial agents has been demonstrated only in very few molecular systems, particularly designed for the purpose, as shown by the representative examples below. As was discussed before [13, 146], accumulative charge separation leads to formation of new intermediate states that open up competing processes that usually are not a problem for charge separation on a single-electron level. First, because an excited dye is in general both a good donor and acceptor, the units that accumulate electrons or holes are thermodynamically quite able to send these back to the dye after the next excitation (reverse electron transfer). Second, the one-electron intermediates are usually radicals or metal complexes that may quench the dye by paramagnetic interaction or unproductive energy transfer. Even if these states do not show strong optical absorption, they may have low-lying excited states that quench by

Dexter (exchange) energy transfer, as shown, e.g., by the colorless Mn^{II} complexes discussed above that quenched the excited $Ru(bpy)_3$ complexes [131]. In Photosystem II, accumulation of holes on the Oxygen Evolving Complex and electrons on $quinone_B$ works with high efficiency because these units are placed far away from the central chlorophylls to avoid the competing reactions. Instead, charge separation is initiated by very rapid electron transfer ($\sim$10 ps) from the chlorophylls to the pheophytin.

Inspired by this strategy, we designed a system for accumulative charge separation, in which a R_u^{II}-polypyridine dye was covalently bound to a oligotriarylamine (OTA) donor and attached at the other end to a mesoporous TiO_2 film (Fig. 11.22) [146]. Ultrafast electron injection (<1 ps) and subsequent hole shift (biphasic, with $\tau_1 = 30$ ps and $\tau_2 = 1$ ns) to the OTA unit upon single pulse laser excitation of the Ru^{II} unit was verified by optical transient absorption. Charge recombination was relatively slow, on the time scales of 10 μs–10 ms. The OTA^+ and OTA^{2+} states show quite different optical absorption spectra. Thus, two strong laser pulses, separated by 1 μs, were applied to the sample, each exciting about 30% of the dyes. The time delay allowed the Ru^{II} dye to be regenerated, while no significant charge recombination between OTA^+ and the TiO_2 electrons had occurred. In these experiments, the transient optical spectra showed strong contribution from the OTA^{2+}, corresponding to about 10% of the molecules. This showed that $\sim$100% of the dyes that absorbed two consecutive photons produced a doubly charge-separated state, with two holes on OTA^{2+} and two electrons in the TiO_2 particle. Also this state decayed slowly, on a 10 μs–10 ms time scale, which approaches the time scale of catalytic turnover in, e.g., hydrogenase enzymes and other rapid molecular catalysts. This was the first proof-of-principle demonstration of accumulative charge separation in a molecular system. Chemical energy was transiently stored in the charge-separated state, which is different from catalytic half-reactions with sacrificial counterparts that consume, e.g., an energy-rich electron donor to produce H_2. The study intended to bridge between single-electron charge separation and multi-electron catalysis. To proceed toward solar fuels production such a system must obviously be coupled to catalytic units.

This was done in a system where a Ru^{II}-polypyridine dye $\left(Ru^{II}_{dye}\right)$ and a water oxidizing Ru^{II}-catalyst $\left(Ru^{II}_{cat}\right)$ were co-adsorbed into mesoporous TiO_2 [147]. ns-TRSL in the visible region demonstrated that within the 20 ns experimental time-resolution, the catalyst had been photo-oxidized to Ru^{III}_{cat}, presubmably via excitation and electron injection from excited Ru^{II}_{dye} followed by rapid surface electron transfer from Ru^{II}_{cat} to the oxidized Ru^{III}_{dye}. When the catalyst had been electrochemically pre-oxidized to Ru^{III}_{cat}, no further oxidation to Ru^{IV}_{cat} was observed in the laser experiments. Instead, the injected electrons reduced the Ru^{II}_{cat} to the Ru^{II}_{cat} state, followed by a slower (μs–ms) hole migration on the surface from the Ru^{III}_{dye} to Ru^{II}_{cat}, regenerating the species present prior to laser excitation. By continuous irradiation instead, and application of a potential bias to extract the injected electrons, the authors could eventually demonstrate a slow build up of Ru^{IV}_{cat} [147].

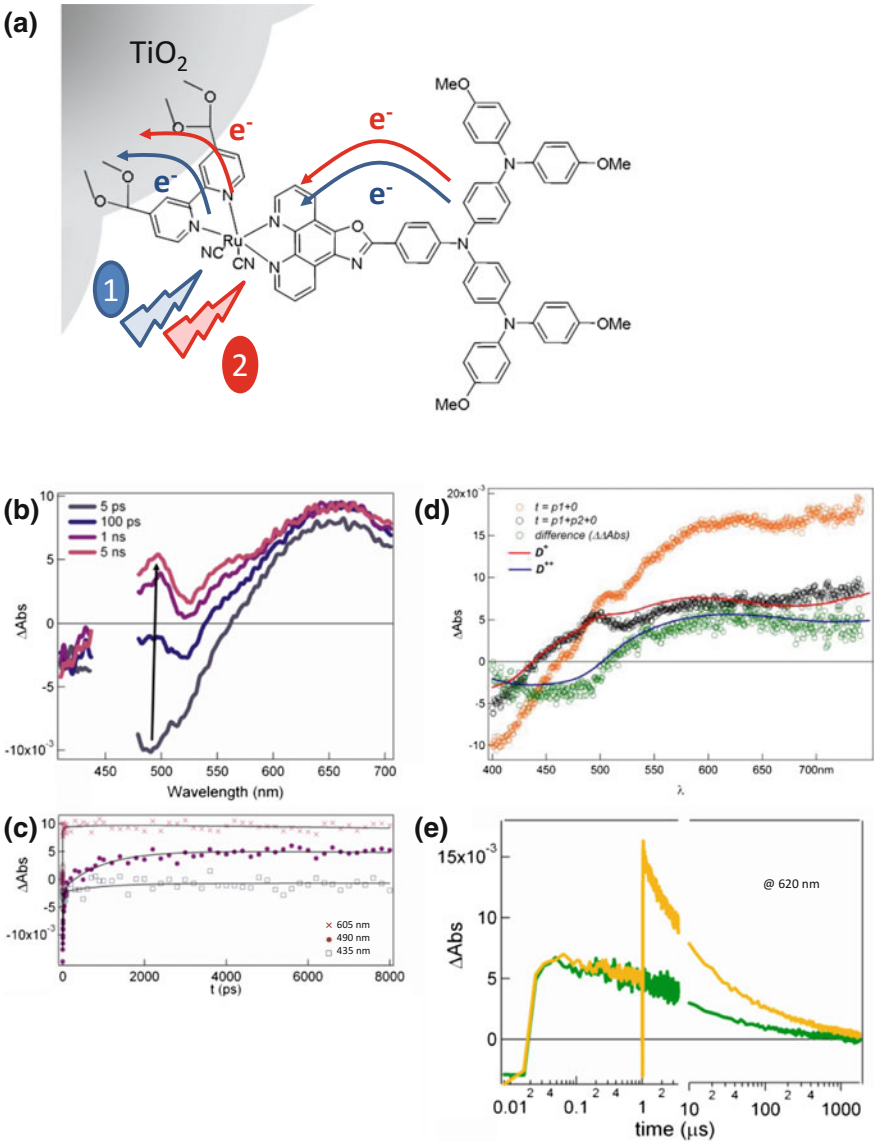
(a)
TiO2
e-
e-
e-
e-
1
2
MeO
OMe
OMe
MeO
(b)
5 ps
100 ps
1 ns
5 ns
ΔAbs
Wavelength (nm)
(c)
ΔAbs
605 nm
490 nm
435 nm
t (ps)
(d)
t = p1+0
t = p1+p2+0
difference (ΔΔAbs)
D+
D++
ΔAbs
λ
(e)
@ 620 nm
ΔAbs
time (μs)

◂**Fig. 11.22** **a** Schematic illustration of reaction sequence in the Ru^{II}-polypyridine-oligotriarylamine (Ru^{II}-OTA) dyad bound to a mesoporous TiO_2 film Successive absorption of two photons, separated in time by 1 μs, by the Ru^{II} dye leads to successive charge accumulation with two hole on the OTA unit and two electrons in the TiO_2 conduction band; **b** transient absorption spectra after single photon excitation, showing how the dye is regenerated and OTA^+ is formed; **c** kinetic traces of the same data as in (**b**); **d** (*black circles*) transient absorption spectrum at ~100 ns after excitation with a single, 10 ns-laser pulse, which agrees with the reference spectrum for OTA^+ (*red line*); (*orange circles*) transient absorption spectrum after two excitation pulses, separated in time by 1 μs; (*green*) the spectrum following double excitation after subtraction of the signal from singly excited molecules (*orange*—1.4 × *black*), this is in excellent agreement with that for the reference spectrum of the double oxidized OTA^{2+} (*blue line*). The derivative features around 490 nm in panels (**b**) and (**d**) are due to Stark shift of the ground state absorption; **e** transient absorption traces at 620 nm after one (*green*) and two (*yellow*) laser pulses, showing that the charge-separated state remains up to the millisecond time scale. Reprinted with permission from [146]. Copyright the American Chemistry Society 2010

11.3.4.3 Devices

Photocathodes and -anodes made from various semiconductor materials modified with molecular sensitizers and molecular or nanoparticle catalysts, as well as complete dye-sensitized solar fuel devices (DSSFDs) [148, 149], have been studied. For most of the devices photoelectrochemical properties and product analysis have been reported, with little mechanistic information about the photoinduced reaction steps involved and the limiting reactions. Here we bring to attention some studies where TRLS has contributed important information regarding the mechanisms of these emerging devices.

The charge transfer processes underlying photoreduction of aqueous protonson dye-sensitized semiconductors modified with molecular cobalt catalysts were investigated by transient absorption spectroscopy and time-correlated single photon counting techniques [150]. Photoexcitation of the $Ru^{II}(bpy)_3$-type sensitizer attached to TiO_2 nano particles via phosphonate anchoring groups led to essentially quantitative electron injection into the semiconductor in approximately 180 ps. Subsequent electron transfer from the TiO_2 conduction band to the phosphonate anchored cobaloxime-type catalyst occurred on a 10 μs timescale and is essentially quantitative, owing to the much slower recombination of conduction band electrons with the oxidized dye. This was based on TRLS experiments where the decay of the photogenerated conduction band electrons was followed by their absorption at 900 nm, while reduction of the catalyst resulted in too small optical changes to be useful. Nevertheless, in a later publication the authors suggested that the second reduction of the cobaloxime catalyst was at least 10^4 times slower than the first [151]. By capturing the holes with a sacrificial donor they shut down recombination with the oxidized dye and could follow the conduction band electrons on a longer time scale. When they increased the laser intensity they injected more electrons per catalyst. Thus, while the initial decay kinetics at 900 nm was the same as at lower laser intensities, the later part of the decay was much slower, by at least four orders of magnitude. This then becomes slower than the average electron-hole

recombination lifetime in the system, which suggests that the bottleneck of photocatalysis is at the later reduction steps. Recombination is therefore more severe than the initial experiments suggested, and explains the poor quantum yield of H_2 production of the complete photocatalytic system.

Ultrafast electron transfer between dye and catalyst co-adsorbed on a NiO surface could be investigated by transient optical spectroscopy owing to the clear UV-VIS spectroscopic signature of the reduced catalyst (Fig. 11.23) [152]. The transient absorption measurements were able to monitor the ultrafast interfacial electron transfer ($\tau \approx 200$ fs) from the NiO valence band to the excited coumarin

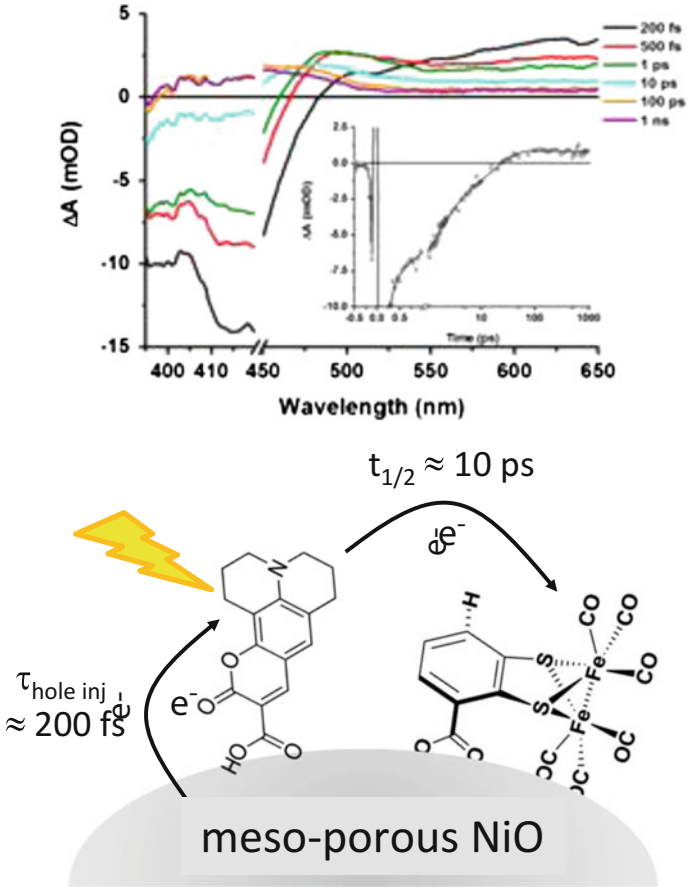

Fig. 11.23 (*top*) Schematic illustration of the co-sensitized mesoporous NiO photocathode with surface-bound coumarin C343 dyes and $[Fe_2(cbdt)(CO)_6]$ proton reduction catalysts; (*bottom*) transient absorption spectra on a 200 fs–1 ns time scale after excitation with a 120 fs pulse at 430 nm; (inset): kinetic trace at 410 nm; the data show the recovery of the C343 ground state bleach and growth of the reduced catalyst absorption, with $t_{1/2} \approx 10$ ps, indicating very rapid intramolecular electron transfer on the NiO surface. Reprinted with permission from [152]. Copyright the American Chemical Society, 2016

C343 dye, the subsequent rapid ($t_{1/2} \approx 10$ ps) and efficient surface electron transfer from $C343^-$ to the co-adsorbed proton reduction catalyst [FeFe](cbdt)$(CO)_6$ (cbdt = 3-carboxy-benzyldithiolate) and the subsequent charge recombination with NiO holes on the microsecond time scale. This combination of rapid reduction of the catalyst by electron transfer on the NiO surface, and slow charge recombination, are promising features with regard to the development of photocathodes for DSSFDs.

Studies of interfacial electron transfer in photoanodes based on phosphorus(V) porphyrin sensitizers co-adsorbed on SnO_2 with the $Ir^{III}Cp^*$ water-oxidation pre-catalyst employed time-resolved THz spectroscopy (TRTS) to determine electron injection efficiency and dynamics, via interaction of the injected charge carriers with the THz field [153]. The ability of the oxidized sensitizer drive oxidation of $Ir^{III}Cp^*$ to $Ir^{IV}Cp^*$ makes these assemblies promising photoanode components for direct solar water-oxidation devices. TRTS provided insight on the effect of the dye anchoring group on forward and reverse interfacial electron transfer between the porphyrin and the conduction band of SnO_2, with faster and more efficient electron transfer from directly bound porphyrins than from those bound via and anchor group.

The electron transfer reactions in a complete photoelectrochemical cell for photoassisted overall water splitting were studied by optical transient absorption spectroscopy [154]. The cell consisted of a dye-sensitized nanocrystalline anatase anode and a Pt cathode. A heteroleptic ruthenium tris(bipyridyl) dye was attached to the porous TiO_2 electrode through phosphonate groups and to IrO_2 nanoparticles through a malonate group, IrO_2 acting as a water-oxidation catalyst. Under visible illumination and with a bias positive of −325 mV versus Ag/AgCl the cell generated oxygen at anode and hydrogen at the cathode from pH 5.75 aqueous buffer, but the internal quantum yield for photocurrent generation was only ca. 0.9%. The transient absorbance experiments revealed that the bottleneck for overall water splitting in this system can be attributed to slow electron transfer ($\sim$2.2 ms) from IrO_2 to the oxidized dye that cannot compete effectively with the back electron transfer reaction ($\tau_{av} \sim 0.37$ ms) from TiO_2 to the oxidized dye. The quantum yield could be more than doubled in a related system that employed an electron transfer mediator to oxidize the IrO_2 catalyst, modeled after the tyrosine$_Z$-histidine pair electron transfer mediator in Photosystem II [155].

To conclude this chapter, TRLS has contributed greatly to our fundamental understanding of artificial photosynthesis, and these methods will be important for the investigation and development of molecular devices for solar fuel generation, which are still in a very early stage of development. An important challenge is to develop methods and experimental protocols to study also the later steps of a photocatalytic process and to follow the reactions of complex samples under *in-operando* conditions where several molecular states are present and undergo parallel reactions.

Acknowledgements The authors want to thank all our coworkers and long-term collaboration partners. We also gratefully acknowledge financial support from The Swedish Research Council, The Knut and Alice Wallenberg Foundation and The Swedish Energy Agency.

References

1. Pullerits T, Sundstrom V (1996) Photosynthetic light-harvesting pigment-protein complexes: toward understanding how and why. Acc Chem Res 29(8):381–389. doi:10.1021/ar950110o
2. Scholes GD, Fleming GR, Olaya-Castro A, van Grondelle R (2011) Lessons from nature about solar light harvesting. Nat Chem 3(10):763–774. doi:10.1038/nchem.1145
3. Holzapfel W, Finkele U, Kaiser W, Oesterhelt D, Scheer H, Stilz HU, Zinth W (1990) Initial electron-transfer in the reaction center from rhodobacter-sphaeroides. Proc Natl Acad Sci USA 87(13):5168–5172. doi:10.1073/pnas.87.13.5168
4. Heller BA, Holten D, Kirmaier C (1995) Control of electron-transfer between the L-side and M-side of photosynthetic reaction centers. Science 269(5226):940–945. doi:10.1126/science.7638616
5. Berera R, van Grondelle R, Kennis JTM (2009) Ultrafast transient absorption spectroscopy: principles and application to photosynthetic systems. Photosynth Res 101(2–3):105–118. doi:10.1007/s11120-009-9454-y
6. Wasielewski MR (1992) Photoinduced electron transfer in supramolecular systems for artificial photosynthesis. Chem Rev (Washington, DC, US) 92(3):435–461. doi:10.1021/cr00011a005
7. Gust D, Moore TA, Moore AL (2001) Mimicking photosynthetic solar energy transduction. Acc Chem Res 34(1):40–48. doi:10.1021/ar9801301
8. Sun LC, Hammarstrom L, Akermark B, Styring S (2001) Towards artificial photosynthesis: ruthenium-manganese chemistry for energy production. Chem Soc Rev 30(1):36–49. doi:10.1039/a801490f
9. Hendry E, Koeberg M, Schins JM, Nienhuys HK, Sundström V, Siebbeles LDA, Bonn M (2005) Interchain effects in the ultrafast photophysics of a semiconducting polymer: THz time-domain spectroscopy of thin films and isolated chains in solution. Phys Rev B 71 (12):125201
10. Pal SK, Kesti T, Maiti M, Zhang F, Inganäs O, Hellström S, Andersson MR, Oswald F, Langa F, Österman T, Pascher T, Yartsev A, Sundström V (2010) Geminate charge recombination in polymer/fullerene bulk heterojunction films and implications for solar cell function. J Am Chem Soc 132(35):12440–12451. doi:10.1021/ja104786x
11. De S, Pascher T, Maiti M, Jespersen KG, Kesti T, Zhang FL, Inganas O, Yartsev A, Sundstrom V (2007) Geminate charge recombination in alternating polyfluorene Copolymer/Fullerene blends. J Am Chem Soc 129(27):8466–8472. doi:10.1021/ja068909q
12. Haque SA, Tachibana Y, Willis RL, Moser JE, Gratzel M, Klug DR, Durrant JR (2000) Parameters influencing charge recombination kinetics in dye-sensitized nanocrystalline titanium dioxide films. J Phys Chem B 104(3):538–547. doi:10.1021/jp991085x
13. Hammarstrom L (2015) Accumulative charge separation for solar fuels production: coupling light-induced single electron transfer to multielectron catalysis. Acc Chem Res 48(3):840–850. doi:10.1021/ar500386x
14. Bressler C, Chergui M (2010) Molecular structural dynamics probed by ultrafast X-ray absorption spectroscopy. Annu Rev Phys Chem 61:263–282
15. van Bokhoven JA, Lamberti C (2016) X-ray absorption and X-ray emission spectroscopy: theory and applications. Wiley, Chichester, West Sussex
16. Calvin S (2013) XAFS for everyone. CRC Press, Boca Raton

17. Lemke HT, Bressler C, Chen LX, Fritz DM, Gaffney KJ, Galler A, Gawelda W, Haldrup K, Hartsock RW, Ihee H, Kim J, Kim KH, Lee JH, Nielsen MM, Stickrath AB, Zhang W, Zhu D, Cammarata M (2013) Femtosecond X-ray absorption spectroscopy at a hard X-ray free electron laser: application to spin crossover dynamics. J Phys Chem A 117(4):735–740
18. Gawelda W, Szlachetko J, Milne CJ (2016) X-ray spectroscopy at free electron lasers. In: X-ray absorption and X-ray emission spectroscopy, vol 1. Wiley-Blackwell, pp 637–669
19. Milne CJ, Penfold TJ, Chergui M (2014) Recent experimental and theoretical developments in time-resolved X-ray spectroscopies. Coord Chem Rev 277–278:44–68
20. Chergui M (2015) Ultrafast photophysics of transition metal complexes. Acc Chem Res 48 (3):801–808
21. Vankó G, Bordage A, Glatzel P, Gallo E, Rovezzi M, Gawelda W, Galler A, Bressler C, Doumy G, March AM, Kanter EP, Young L, Southworth SH, Canton SE, Uhlig J, Smolentsev G, Sundström V, Haldrup K, van Driel TB, Nielsen MM, Kjaer KS, Lemke HT (2013) Spin-state studies with XES and RIXS: from static to ultrafast. J Electron Spectrosc Relat Phenom 188:166–171
22. Haldrup K, Vankö G, Gawelda W, Galler A, Doumy G, March AM, Kanter EP, Bordage A, Dohn A, van Driel TB, Kjaer KS, Lemke HT, Canton SE, Uhlig J, Sundström V, Young L, Southworth SH, Nielsen MM, Bressler C (2012) Guest-host interactions investigated by time-resolved X-ray spectroscopies and scattering at MHz rates: solvation dynamics and photoinduced spin transition in aqueous Fe(bipy)3(2+). J Phys Chem A 116(40):9878–9887
23. Uhlig J, Doriese WB, Fowler JW, Swetz DS, Jaye C, Fischer DAA, Reintsema CD, Bennett DA, Vale LR, Mandal U, O'Neil GC, Miaja-Avila L, Joe YI, El Nahhas A, Fullagar W, Parnefjord Gustafsson F, Sundström V, Kurunthu D, Hilton GC, Schmidt DR, Ullom JN (2015) High-resolution X-ray emission spectroscopy with transition-edge sensors: present performance and future potential. J Synchrotron Radiat 22(3):766–775
24. Ament LJP, van Veenendaal M, Devereaux TP, Hill JP, van den Brink J (2011) Resonant inelastic X-ray scattering studies of elementary excitations. Rev Mod Phys 83(2):705–767
25. Bergmann U, Glatzel P (2009) X-ray emission spectroscopy. Photosynth Res 102(2–3): 255–266
26. Rovezzi M, Glatzel P (2014) Hard X-ray emission spectroscopy: a powerful tool for the characterization of magnetic semiconductors. Semicond Sci Technol 29(2):023002
27. Lee JH, Wulff M, Bratos S, Petersen J, Guerin L, Leicknam J-C, Cammarata M, Kong Kim Q, Møller KB, Ihee H (2013) Filming the birth of molecules and accompanying solvent rearrangement. J Am Chem Soc 135(8):3255–3261
28. Haldrup K, Gawelda W, Abela R, Alonso-Mori R, Bergmann U, Bordage A, Cammarata M, Canton SE, Dohn AO, van Driel TB, Fritz DM, Galler A, Glatzel P, Harlang T, Kjaer KS, Lemke HT, Moeller KB, Németh Z, Pápai M, Sas N, Uhlig J, Zhu D, Vankó G, Sundström V, Nielsen MM, Bressler C (2016) Observing solvation dynamics with simultaneous femtosecond X-ray emission spectroscopy and X-ray scattering. J Phys Chem B 120 (6):1158–1168
29. Alonso-Mori R, Kern J, Sokaras D, Weng TC, Nordlund D, Tran R, Montanez P, Delor J, Yachandra VK, Yano J, Bergmann U (2012) A multi-crystal wavelength dispersive X-ray spectrometer. Rev Sci Instrum 83(7). doi:10.1063/1.4737630
30. Lee N, Petrenko T, Bergmann U, Neese F, DeBeer S (2010) Probing valence orbital composition with iron K beta X-ray emission spectroscopy. J Am Chem Soc 132(28): 9715–9727
31. Zhang W, Alonso-Mori R, Bergmann U, Bressler C, Chollet M, Galler A, Gawelda W, Hadt RG, Hartsock RW, Kroll T, Kjaer KS, Kubicek K, Lemke HT, Liang HW, Meyer DA, Nielsen MM, Purser C, Robinson JS, Solomon EI, Sun Z, Sokaras D, van Driel TB, Vanko G, Weng TC, Zhu D, Gaffney KJ (2014) Tracking excited-state charge and spin dynamics in iron coordination complexes. Nature 509(7500):345–348. doi:10.1038/nature13252

32. Kjaer KS, van Driel TB, Kehres J, Haldrup K, Khakhulin D, Bechgaard K, Cammarata M, Wulff M, Soerensen TJ, Nielsen MM (2013) Introducing a standard method for experimental determination of the solvent response in laser pump, X-ray probe time-resolved wide-angle X-ray scattering experiments on systems in solution. Phys Chem Chem Phys 15(36):15003–15016
33. Bauer M (2014) HERFD-XAS and valence-to-core-XES: new tools to push the limits in research with hard X-rays? Phys Chem Chem Phys 16(27):13827–13837
34. Glatzel P, Weng T-C, Kvashnina K, Swarbrick J, Sikora M, Gallo E, Smolentsev N, Mori RA (2013) Reflections on hard X-ray photon-in/photon-out spectroscopy for electronic structure studies. J Electron Spectrosc Relat Phenom 188:17–25
35. Glatzel P, Bergmann U (2005) High resolution 1s core hole X-ray spectroscopy in 3d transition metal complexes electronic and structural information. Coord Chem Rev 249(1–2):65–95
36. Ardo S, Meyer GJ (2009) Photodriven heterogeneous charge transfer with transition-metal compounds anchored to TiO_2 semiconductor surfaces. Chem Soc Rev 38(1):115–164. doi:10.1039/b804321n
37. Benko G, Kallioinen J, Korppi-Tommola JE, Yartsev AP, Sundstrom V (2002) Photoinduced ultrafast dye-to-semiconductor electron injection from nonthermalized and thermalized donor states. J Am Chem Soc 124(3):489–493
38. Benko G, Kallioinen J, Myllyperkio P, Trif F, Korppi-Tommola JEI, Yartsev AP, Sundstrom V (2004) Interligand electron transfer determines triplet excited state electron injection in RuN_3-sensitized TiO_2 films. J Phys Chem B 108(9):2862–2867. doi:10.1021/jp036778z
39. Benko G, Myllyperkio P, Pan J, Yartsev AP, Sundstrom V (2003) Photoinduced electron injection from Ru(dcbpy)2(NCS)2 to SnO_2 and TiO_2 nanocrystalline films. J Am Chem Soc 125(5):1118–1119. doi:10.1021/ja029025j
40. Furube A, Katoh R, Yoshihara T, Hara K, Murata S, Arakawa H, Tachiya M (2004) Ultrafast direct and indirect electron-injection processes in a photoexcited dye-sensitized nanocrystalline zinc oxide film: the importance of exciplex intermediates at the surface. J Phys Chem B 108(33):12583–12592. doi:10.1021/jp0487713
41. Katoh R, Furube A, Barzykin AV, Arakawa H, Tachiya M (2004) Kinetics and mechanism of electron injection and charge recombination in dye-sensitized nanocrystalline semiconductors. Coord Chem Rev 248(13–14):1195–1213. doi:10.1016/j.ccr.2004.03.017
42. Katoh R, Furube A, Fuke N, Fukui A, Koide N (2012) Ultrafast relaxation as a possible limiting factor of electron injection efficiency in black dye sensitized nanocrystalline TiO_2 films. J Phys Chem C 116(42):22301–22306. doi:10.1021/jp302768q
43. Katoh R, Yaguchi K, Furube A (2011) Effect of dye concentration on electron injection efficiency in nanocrystalline TiO_2 films sensitized with N719 dye. Chem Phys Lett 511(4–6):336–339. doi:10.1016/j.cplett.2011.06.046
44. Wenger B, Gratzel M, Moser JE (2005) Rationale for kinetic heterogeneity of ultrafast light-induced electron transfer from Ru(II) complex sensitizers to nanocrystalline TiO_2. J Am Chem Soc 127(35):12150–12151. doi:10.1021/ja042141x
45. Thorsmolle VK, Wenger B, Teuscher J, Bauer C, Moser JE (2007) Dynamics of photoinduced interfacial electron transfer and charge transport in dye-sensitized mesoscopic semiconductors. Chimia 61(10):631–634. doi:10.2533/chimia.2007.631
46. Kallioinen J, Benko G, Sundstrom V, Korppi-Tommola JEI, Yartsev AP (2002) Electron transfer from the singlet and triplet excited states of Ru(dcbpy)(2)(NCS)(2) into nanocrystalline TiO_2 thin films. J Phys Chem B 106(17):4396–4404. doi:10.1021/jp0143443
47. Damrauer NH, Cerullo G, Yeh A, Boussie TR, Shank CV, McCusker JK (1997) Femtosecond dynamics of excited-state evolution in Ru(bpy)(3) (2+). Science 275 (5296):54–57. doi:10.1126/science.275.5296.54
48. Cannizzo A, van Mourik F, Gawelda W, Zgrablic G, Bressler C, Chergui M (2006) Broadband femtosecond fluorescence spectroscopy of Ru(bpy)(3) (2+). Angew Chem-Int Ed 45(19):3174–3176. doi:10.1002/anie.200600125

49. Kallioinen J, Benko G, Myllyperkio P, Khriachtchev L, Skarman B, Wallenberg R, Tuomikoski M, Korppi-Tommola J, Sundstrom V, Yartsev AP (2004) Photoinduced ultrafast dynamics of Ru(dcbpy)(2)(NCS)(2)-sensitized nanocrystalline TiO_2 films: the influence of sample preparation and experimental conditions. J Phys Chem B 108(20):6365–6373. doi:10.1021/jp037265v
50. Myllyperkio P, Benko G, Korppi-Tommola J, Yartsev AP, Sundstrom V (2008) A study of electron transfer in Ru(dcbpy)2(NCS)2 sensitized nanocrystalline TiO_2 and SnO_2 films induced by red-wing excitation. Phys Chem Chem Phys 10(7):996–1002. doi:10.1039/b713515g
51. Katoh R, Furube A, Kasuya M, Fuke N, Koide N, Han L (2007) Photoinduced electron injection in black dye sensitized nanocrystalline TiO_2 films. J Mater Chem 17(30):3190–3196. doi:10.1039/b702805a
52. Imahori H, Kang S, Hayashi H, Haruta M, Kurata H, Isoda S, Canton SE, Infahsaeng Y, Kathiravan A, Pascher T, Chabera P, Yartsev AP, Sundstrom V (2011) Photoinduced charge carrier dynamics of Zn-porphyrin-TiO_2 electrodes: the key role of charge recombination for solar cell performance. J Phys Chem A 115(16):3679–3690. doi:10.1021/jp103747t
53. Ye S, Kathiravan A, Hayashi H, Tong YJ, Infahsaeng Y, Chabera P, Pascher T, Yartsev AP, Isoda S, Imahori H, Sundstrom V (2013) Role of adsorption structures of Zn-Porphyrin on TiO_2 in dye-sensitized solar cells studied by sum frequency generation vibrational spectroscopy and ultrafast spectroscopy. J Phys Chem C 117(12):6066–6080. doi:10.1021/jp400336r
54. Imahori H, Umeyama T, Ito S (2009) Large pi-aromatic molecules as potential sensitizers for highly efficient dye-sensitized solar cells. Acc Chem Res 42(11):1809–1818. doi:10.1021/ar900034t
55. Zhao JH, Yang XC, Cheng M, Li SF, Sun LC (2013) new organic dyes with a phenanthrenequinone derivative as the pi-conjugated bridge for dye-sensitized solar cells. J Phys Chem C 117(25):12936–12941. doi:10.1021/jp400011w
56. Zhao JH, Yang XC, Cheng M, Li SF, Wang XN, Sun LC (2013) Highly efficient iso-quinoline cationic organic dyes without vinyl groups for dye-sensitized solar cells. J Mater Chem A 1(7):2441–2446. doi:10.1039/c2ta00905f
57. Hao Y, Yang XC, Cong JY, Hagfeldt A, Sun LC (2012) Engineering of highly efficient tetrahydroquinoline sensitizers for dye-sensitized solar cells. Tetrahedron 68(2):552–558. doi:10.1016/j.tet.2011.11.004
58. Asbury JB, Wang YQ, Lian TQ (1999) Multiple-exponential electron injection in Ru(dcbpy)(2)(SCN)(2) sensitized ZnO nanocrystalline thin films. J Phys Chem B 103(32):6643–6647. doi:10.1021/jp991625q
59. Anderson NA, Lian TQ (2005) Ultrafast electron transfer at the molecule-semiconductor nanoparticle interface. Annu Rev Phys Chem 56:491–519. doi:10.1146/annurev.physchem.55.091602.094347
60. Zhang L, Favereau L, Farré Y, Mijangos E, Pellegrin Y, Blart E, Odobel* F, Hammarström L (2016) Ultra-fast and slow charge recombination dynamics of Diketopyrrolopyrrole-NiO dye sensitized solar cells. Phys Chem Chem Phys 18:18515–18527
61. Odobel F, Pellegrin Y, Gibson EA, Hagfeldt A, Smeigh AL, Hammarstrom L (2012) Recent advances and future directions to optimize the performances of p-type dye-sensitized solar cells. Coord Chem Rev 256(21–22):2414–2423. doi:10.1016/j.ccr.2012.04.017
62. Juozapavicius M, Kaucikas M, Dimitrov SD, Barnes PRF, van Thor JJ, O'Regan BC (2013) Evidence for "Slow" electron injection in commercially relevant dye-sensitized solar cells by vis-NIR and IR pump-probe spectroscopy. J Phys Chem C 117(48):25317–25324. doi:10.1021/jp408989q
63. Antila LJ, Myllyperkio P, Mustalahti S, Lehtivuori H, Korppi-Tommola J (2014) Injection and ultrafast regeneration in dye-sensitized solar cells. J Phys Chem C 118(15):7772–7780. doi:10.1021/jp4124277

64. Furube A, Katoh R, Hara K (2014) Electron injection dynamics in dye-sensitized semiconductor nanocrystalline films. Surf Sci Rep 69(4):389–441. doi:10.1016/j.surfrep.2014.09.003
65. Brauer JC, Marchioro A, Paraecattil AA, Oskouei AA, Moser JE (2015) Dynamics of interfacial charge transfer states and carriers separation in dye-sensitized solar cells: a time-resolved terahertz spectroscopy study. J Phys Chem C 119(47):26266–26274. doi:10.1021/acs.jpcc.5b06911
66. Nemec H, Rochford J, Taratula O, Galoppini E, Kuzel P, Polivka T, Yartsev A, Sundstrom V (2010) Influence of the electron-cation interaction on electron mobility in dye-sensitized ZnO and TiO_2 nanocrystals: a study using ultrafast terahertz spectroscopy. Phys Rev Lett 104(19):ARTN 197401. doi:10.1103/PhysRevLett.104.197401
67. Haque SA, Handa S, Peter K, Palomares E, Thelakkat M, Durrant JR (2005) Supermolecular control of charge transfer in dye-sensitized nanocrystalline TiO_2 films: towards a quantitative structure-function relationship. Angew Chem Int Ed Engl 44(35):5740–5744. doi:10.1002/anie.200500363
68. Moser JE, Gratzel M (1993) Observation of temperature independent heterogeneous electron-transfer reactions in the inverted Marcus region. Chem Phys 176(2–3):493–500. doi:10.1016/0301-0104(93)80257-A
69. Oregan B, Moser J, Anderson M, Gratzel M (1990) Vectorial electron injection into transparent semiconductor membranes and electric-field effects on the dynamics of light-induced charge separation. J Phys Chem 94(24):8720–8726. doi:10.1021/j100387a017
70. Fitzmaurice DJ, Frei H (1991) Transient near-infrared spectroscopy of visible-light sensitized oxidation of I- at Colloidal TiO_2. Langmuir 7(6):1129–1137. doi:10.1021/la00054a019
71. Marcus RA (1956) On the theory of oxidation-reduction reactions involving electron transfer. J Chem Phys 24(5):966–978. doi:10.1063/1.1742723
72. Marcus RA (1964) Chemical + Electrochemical electron-transfer theory. Annu Rev Phys Chem 15:155-&. doi:10.1146/annurev.pc.15.100164.001103
73. Marcus RA, Sutin N (1985) Electron transfers in chemistry and biology. Biochim Biophys Acta 811(3):265–322. doi:10.1016/0304-4173(85)90014-X
74. Gerischer H (1969) Charge transfer processes at semiconductor-electrolyte interfaces in connection with problems of catalysis. Surf Sci 18(1):97–+. doi:10.1016/0039-6028(69)90269-6
75. Gerischer H (1972) Electrochemical techniques for study of photosensitization. Photochem Photobiol 16(4):243–+
76. Kakiage K, Aoyama Y, Yano T, Oya K, Fujisawab J, Hanaya M (2015) Highly-efficient dye-sensitized solar cells with collaborative sensitization by silyl-anchor and carboxy-anchor dyes. Chem Commun (Cambridge, UK) 51(88):15894–15897. doi:10.1039/c5cc06759f
77. Mathew S, Yella A, Gao P, Humphry-Baker R, Curchod BFE, Ashari-Astani N, Tavernelli I, Rothlisberger U, Nazeeruddin MK, Gratzel M (2014) Dye-sensitized solar cells with 13% efficiency achieved through the molecular engineering of porphyrin sensitizers. Nat Chem 6(3):242–247. doi:10.1038/nchem.1861
78. Gratzel M (2009) Recent advances in sensitized mesoscopic solar cells. Acc Chem Res 42(11):1788–1798. doi:10.1021/ar900141y
79. Lobello MG, Wu KL, Reddy MA, Marotta G, Gratzel M, Nazeeruddin MK, Chi Y, Chandrasekharam M, Vitillaro G, De Angelis F (2014) Engineering of Ru(II) dyes for interfacial and light-harvesting optimization. Dalton Trans 43(7):2726–2732. doi:10.1039/c3dt53272k
80. Monat JE, McCusker JK (2000) Femtosecond excited-state dynamics of an iron(II) polypyridyl solar cell sensitizer model. J Am Chem Soc 122(17):4092–4097. doi:10.1021/ja992436o
81. Meyer TJ (1986) Photochemistry of metal coordination-complexes—metal to ligand charge-transfer excited-states. Pure Appl Chem 58(9):1193–1206. doi:10.1351/pac198658091193

82. Ferrere S, Gregg BA (1998) Photosensitization of TiO_2 by Fe-II(2,2′-bipyridine-4,4′-dicarboxylic acid)(2)(CN)(2): band selective electron injection from ultra-short-lived excited states. J Am Chem Soc 120(4):843–844. doi:10.1021/ja973504e
83. Cho H, Strader ML, Hong K, Jamula L, Gullikson EM, Kim TK, de Groot FM, McCusker JK, Schoenlein RW, Husea N (2012) Ligand-field symmetry effects in Fe(II) polypyridyl compounds probed by transient X-ray absorption spectroscopy. Faraday Discuss 157:463–474; discussion 475–500
84. Sousa C, de Graaf C, Rudavskyi A, Broer R, Tatchen J, Etinski M, Marian CM (2013) Ultrafast deactivation mechanism of the excited singlet in the light-induced spin crossover of [Fe(2,2′-bipyridine)(3)](2+). Chem-A Eur J 19(51):17541–17551. doi:10.1002/chem.201302992
85. Zhang W, Alonso-Mori R, Bergmann U, Bressler C, Chollet M, Galler A, Gawelda W, Hadt RG, Hartsock RW, Kroll T, Kjae r, Kasper S., Kubicek K, Lemke HT, Liang HW, Meyer DA, Nielsen MM, Purser C, Robinson JS, Solomon EI, Sun Z, Sokaras D, van Driel TB, Vankó G, Weng T-C, Zhu D, Gaffney KJ (2014) Tracking excited-state charge and spin dynamics in iron coordination complexes. Nature 509(7500):345–348
86. Gawelda W, Cannizzo A, Pham VT, van Mourik F, Bressler C, Chergui M (2007) Ultrafast nonadiabatic dynamics of Fe-II(bpy)(3) (2+) in solution. J Am Chem Soc 129(26):8199–8206. doi:10.1021/ja070454x
87. Liu Y, Harlang T, Canton SE, Chabera P, Suarez-Alcantara K, Fleckhaus A, Vithanage DA, Goransson E, Corani A, Lomoth R, Sundstrom V, Warnmark K (2013) Towards longer-lived metal-to-ligand charge transfer states of iron(II) complexes: an N-heterocyclic carbene approach. Chem Commun (Camb) 49(57):6412–6414. doi:10.1039/c3cc43833c
88. Fredin LA, Warnmark K, Sundstrom V, Persson P (2016) Molecular and interfacial calculations of Iron(II) light harvesters. ChemSusChem 9(7):667–675. doi:10.1002/cssc.201600062
89. Fredin LA, Papai M, Rozsalyi E, Vanko G, Warnmark K, Sundstrom V, Persson P (2014) Exceptional excited-state lifetime of an Iron(II)-N-Heterocyclic carbene complex explained. J Phys Chem Lett 5(12):2066–2071. doi:10.1021/jz500829w
90. Bowman DN, Blew JH, Tsuchiya T, Jakubikova E (2013) Elucidating band-selective sensitization in Iron(II) polypyridine-TiO_2 assemblies. Inorg Chem 52(15):8621–8628. doi:10.1021/ic4007839
91. Jakubikova E, Bowman DN (2015) Fe(II)-Polypyridines as chromophores in dye-sensitized solar cells: a computational perspective. Acc Chem Res 48(5):1441–1449. doi:10.1021/ar500428t
92. Harlang TC, Liu Y, Gordivska O, Fredin LA, Ponseca CS Jr, Huang P, Chabera P, Kjaer KS, Mateos H, Uhlig J, Lomoth R, Wallenberg R, Styring S, Persson P, Sundstrom V, Warnmark K (2015) Iron sensitizer converts light to electrons with 92% yield. Nat Chem 7(11):883–889. doi:10.1038/nchem.2365
93. Mukherjee S, Bowman DN, Jakubikova E (2015) Cyclometalated Fe(II) complexes as sensitizers in dye-sensitized solar cells. Inorg Chem 54(2):560–569. doi:10.1021/ic502438g
94. Kojima A, Teshima K, Shirai Y, Miyasaka T (2009) Organometal halide perovskites as visible-light sensitizers for photovoltaic cells. J Am Chem Soc 131(17):6050–6051. doi:10.1021/ja809598r
95. Tan Z-K, Moghaddam RS, Lai ML, Docampo P, Higler R, Deschler F, Price M, Sadhanala A, Pazos LM, Credgington D, Hanusch F, Bein T, Snaith HJ, Friend RH (2014) Bright light-emitting diodes based on organometal halide perovskite. Nat Nano 9(9):687–692. doi:10.1038/nnano.2014.149
96. Zhu H, Fu Y, Meng F, Wu X, Gong Z, Ding Q, Gustafsson MV, Trinh MT, Jin S, Zhu XY (2015) Lead halide perovskite nanowire lasers with low lasing thresholds and high quality factors. Nat Mater 14(6):636–642. doi:10.1038/nmat4271
97. Luo J, Im J-H, Mayer MT, Schreier M, Nazeeruddin MK, Park N-G, Tilley SD, Fan HJ, Grätzel M (2014) Water photolysis at 12.3% efficiency via perovskite photovoltaics and Earth-abundant catalysts. Science 345(6204):1593–1596

98. Ponseca CS, Savenije TJ, Abdellah M, Zheng K, Yartsev A, Pascher T, Harlang T, Chabera P, Pullerits T, Stepanov A, Wolf J-P, Sundström V (2014) Organometal halide perovskite solar cell materials rationalized: ultrafast charge generation, high and microsecond-long balanced mobilities, and slow recombination. J Am Chem Soc 136 (14):5189–5192. doi:10.1021/ja412583t
99. Savenije TJ, Ponseca CS, Kunneman L, Abdellah M, Zheng K, Tian Y, Zhu Q, Canton SE, Scheblykin IG, Pullerits T, Yartsev A, Sundström V (2014) Thermally activated exciton dissociation and recombination control the carrier dynamics in organometal halide perovskite. J Phys Chem Lett 5(13):2189–2194. doi:10.1021/jz500858a
100. Miyata A, Mitioglu A, Plochocka P, Portugall O, Wang JT-W, Stranks SD, Snaith HJ, Nicholas RJ (2015) Direct measurement of the exciton binding energy and effective masses for charge carriers in organic-inorganic tri-halide perovskites. Nat Phys 11(7):582–587. doi:10.1038/nphys3357
101. Lin Q, Armin A, Nagiri RCR, Burn PL, Meredith P (2015) Electro-optics of perovskite solar cells. Nat Photon 9(2):106–112. doi:10.1038/nphoton.2014.284
102. Sum TC, Mathews N (2014) Advancements in perovskite solar cells: photophysics behind the photovoltaics. Energy Environ Sci 7(8):2518–2534. doi:10.1039/C4EE00673A
103. Sheng C, Zhang C, Zhai Y, Mielczarek K, Wang W, Ma W, Zakhidov A, Vardeny ZV (2015) Exciton versus free carrier photogeneration in organometal trihalide perovskites probed by broadband ultrafast polarization memory dynamics. Phys Rev Lett 114 (11):116601
104. Sun S, Salim T, Mathews N, Duchamp M, Boothroyd C, Xing G, Sum TC, Lam YM (2014) The origin of high efficiency in low-temperature solution-processable bilayer organometal halide hybrid solar cells. Energy Environ Sci 7(1):399–407. doi:10.1039/C3EE43161D
105. Etgar L, Gao P, Xue Z, Peng Q, Chandiran AK, Liu B, Nazeeruddin MK, Grätzel M (2012) Mesoscopic $CH_3NH_3PbI_3/TiO_2$ heterojunction solar cells. J Am Chem Soc 134(42):17396–17399. doi:10.1021/ja307789s
106. Hendry E, Koeberg M, O'Regan B, Bonn M (2006) Local field effects on electron transport in nanostructured TiO_2 revealed by terahertz spectroscopy. Nano Lett 6(4):755–759. doi:10.1021/nl0600225
107. Ponseca CS, Němec H, Vukmirović N, Fusco S, Wang E, Andersson MR, Chabera P, Yartsev A, Sundström V (2012) Electron and hole contributions to the terahertz photoconductivity of a conjugated polymer: fullerene blend identified. J Phys Chem Lett 3(17):2442–2446. doi:10.1021/jz301013u
108. Blom PWM, Mihailetchi VD, Koster LJA, Markov DE (2007) Device physics of polymer: fullerene bulk heterojunction solar cells. Adv Mater (Weinheim, Ger) 19(12):1551–1566. doi:10.1002/adma.200601093
109. Wang Q, Shao YC, Xie HP, Lyu L, Liu XL, Gao YL, Huang JS (2014) Qualifying composition dependent p and n self-doping in $CH_3NH_3PbI_3$. Appl Phys Lett 105(16). doi:10.1063/1.4899051
110. Tian Y, Scheblykin IG (2015) Artifacts in absorption measurements of organometal halide perovskite materials: what are the real spectra? J Phys Chem Lett 6(17):3466–3470. doi:10.1021/acs.jpclett.5b01406
111. Nguyen WH, Bailie CD, Unger EL, McGehee MD (2014) Enhancing the hole-conductivity of Spiro-OMeTAD without oxygen or lithium salts by using Spiro(TFSI)2 in perovskite and dye-sensitized solar cells. J Am Chem Soc 136(31):10996–11001. doi:10.1021/ja504539w
112. Abrusci A, Stranks SD, Docampo P, Yip H-L, Jen AKY, Snaith HJ (2013) High-performance perovskite-polymer hybrid solar cells via electronic coupling with fullerene monolayers. Nano Lett 13(7):3124–3128. doi:10.1021/nl401044q
113. Ponseca CS, Hutter EM, Piatkowski P, Cohen B, Pascher T, Douhal A, Yartsev A, Sundström V, Savenije TJ (2015) Mechanism of charge transfer and recombination dynamics in organo metal halide perovskites and organic electrodes, PCBM, and Spiro-OMeTAD: role of dark carriers. J Am Chem Soc 137(51):16043–16048. doi:10.1021/jacs.5b08770

114. Ai X, Beard MC, Knutsen KP, Shaheen SE, Rumbles G, Ellingson RJ (2006) Photoinduced charge carrier generation in a Poly(3-hexylthiophene) and methanofullerene bulk heterojunction investigated by time-resolved terahertz spectroscopy. J Phys Chem B 110 (50):25462–25471. doi:10.1021/jp065212i
115. Cunningham PD, Hayden LM (2008) Carrier dynamics resulting from above and below gap excitation of P3HT and P3HT/PCBM investigated by optical-pump terahertz-probe spectroscopy. J Phys Chem C 112(21):7928–7935. doi:10.1021/jp711827g
116. Esenturk O, Melinger JS, Heilweil EJ (2008) Terahertz mobility measurements on poly-3-hexylthiophene films: device comparison, molecular weight, and film processing effects. J Appl Phys 103(2). doi:10.1063/1.2828028
117. Němec H, Nienhuys H-K, Zhang F, Inganäs O, Yartsev A, Sundström V (2008) Charge carrier dynamics in alternating polyfluorene copolymer: fullerene blends probed by terahertz spectroscopy. J Phys Chem C 112(16):6558–6563. doi:10.1021/jp710184r
118. Němec H, Nienhuys H-K, Perzon E, Zhang F, Inganäs O, Kužel P, Sundström V (2009) Ultrafast conductivity in a low-band-gap polyphenylene and fullerene blend studied by terahertz spectroscopy. Phys Rev B 79(24):245326
119. Ponseca CS, Yartsev A, Wang E, Andersson MR, Vithanage D, Sundström V (2012) Ultrafast terahertz photoconductivity of bulk heterojunction materials reveals high carrier mobility up to nanosecond time scale. J Am Chem Soc 134(29):11836–11839. doi:10.1021/ja301757y
120. Vithanage DA, Devizis A, Abramavicius V, Infahsaeng Y, Abramavicius D, MacKenzie RCI, Keivanidis PE, Yartsev A, Hertel D, Nelson J, Sundstrom V, Gulbinas V (2013) Visualizing charge separation in bulk heterojunction organic solar cells. Nat Commun 4. doi:10.1038/ncomms3334
121. Bakulin AA, Rao A, Pavelyev VG, van Loosdrecht PHM, Pshenichnikov MS, Niedzialek D, Cornil J, Beljonne D, Friend RH (2012) The role of driving energy and delocalized states for charge separation in organic semiconductors. Science 335(6074):1340–1344. doi:10.1126/science.1217745
122. Gelinas S, Rao A, Kumar A, Smith SL, Chin AW, Clark J, van der Poll TS, Bazan GC, Friend RH (2014) Ultrafast long-range charge separation in organic semiconductor photovoltaic diodes. Science 343(6170):512–516. doi:10.1126/science.1246249
123. Closs GL, Miller JR (1988) Intramolecular long-distance electron-transfer in organic molecules. Science 240(4851):440–447. doi:10.1126/science.240.4851.440
124. McCusker JK (2003) Femtosecond absorption spectroscopy of transition metal charge-transfer complexes. Acc Chem Res 36(12):876–887. doi:10.1021/ar030111d
125. Thompson DW, Ito A, Meyer TJ (2013) Ru(bpy)(3)(2+)* and other remarkable metal-to-ligand charge transfer (MLCT) excited states. Pure Appl Chem 85(7):1257–1305. doi:10.1351/pac-con-13-03-04
126. Bressler C, Chergui M (2004) Ultrafast X-ray absorption spectroscopy. Chem Rev (Washington, DC, US) 104(4):1781–1812
127. Canton SE, Zhang X, Liu Y, Zhang J, Papai M, Corani A, Smeigh AL, Smolentsev G, Attenkofer K, Jennings G, Kurtz CA, Li F, Harlang T, Vithanage D, Chabera P, Bordage A, Sun L, Ott S, Wärnmark K, Sundström V (2015) Watching the dynamics of electrons and atoms at work in solar energy conversion. Faraday Discuss 185:51–68
128. Chen LX (2005) Probing transient molecular structures in photochemical processes using laser-initiated time-resolved X-ray absorption spectroscopy. Annu Rev Phys Chem 56:221–254
129. Chen LX, Jäger WJ, Jennings G, Gosztola DJ, Munkholm A, Hessler JP (2001) Capturing a photoexcited molecular structure through time-domain x-ray absorption fine structure. Science (New York, NY) 292(5515):262–264
130. Zhang X, Canton SE, Smolentsev G, Wallentin C-J, Liu Y, Kong Q, Attenkofer K, Stickrath AB, Mara MW, Chen LX, Wärnmark K, Sundström V (2014) Highly accurate excited-state structure of [Os(bpy)2dcbpy]2+ determined by X-ray transient absorption spectroscopy. J Am Chem Soc 136(24):8804–8809

131. Abrahamsson MLA, Baudin HB, Tran A, Philouze C, Berg KE, Raymond-Johansson MK, Sun L, Aakermark B, Styring S, Hammarstroem L (2002) Ruthenium-manganese complexes for artificial photosynthesis: factors controlling intramolecular electron transfer and excited-state quenching reactions. Inorg Chem 41(6):1534–1544
132. Borgstroem M, Shaikh N, Johansson O, Anderlund MF, Styring S, Aakermark B, Magnuson A, Hammarstroem L (2005) Light induced manganese oxidation and long-lived charge separation in a Mn2II, II-RuII(bpy)3-acceptor triad. J Am Chem Soc 127(49):17504–17515
133. Magnuson A, Anderlund M, Johansson O, Lindblad P, Lomoth R, Polivka T, Ott S, Stensjo K, Styring S, Sundstrom V, Hammarstrom L (2009) Biomimetic and microbial approaches to solar fuel generation. Acc Chem Res 42(12):1899–1909. doi:10.1021/ar900127h
134. Tschierlei S, Presselt M, Kuhnt C, Yartsev A, Pascher T, Sundström V, Karnahl M, Schwalbe M, Schäfer B, Rau S, Schmitt M, Dietzek B, Popp J (2009) Photophysics of an intramolecular hydrogen-evolving Ru-Pd photocatalyst. Chemistry (Weinheim an der Bergstrasse, Germany) 15(31):7678–7688
135. Canton SE, Zhang X, Zhang J, van Driel TB, Kjaer KS, Haldrup K, Chabera P, Harlang T, Suarez-Alcantara K, Liu Y, Pérez J, Bordage A, Papai M, Vankó G, Jennings G, Kurtz CA, Rovezzi M, Glatzel P, Smolentsev G, Uhlig J, Dohn AO, Christensen M, Galler A, Gawelda W, Bressler C, Lemke HT, Moeller KB, Nielsen MM, Lomoth R, Wärnmark K, Sundström V (2013) Toward highlighting the ultrafast electron transfer dynamics at the optically dark sites of photocatalysts. J Phys Chem Lett 4(11):1972–1976
136. Vankö G, Neisius T, Molnar G, Renz F, Karpati S, Shukla A, de Groot FMF (2006) Probing the 3d spin momentum with X-ray emission spectroscopy: the case of molecular-spin transitions. J Phys Chem B 110(24):11647–11653
137. Vankö G, Glatzel P, Pham V-T, Abela R, Grolimund D, Borca CN, Johnson SL, Milne CJ, Bressler C (2010) Picosecond time-resolved X-ray emission spectroscopy: ultrafast spin-state determination in an iron complex. Angew Chem Int Ed 49(34):5910–5912
138. Canton SE, Kjaer KS, Vankö G, van Driel TB, S-i Adachi, Bordage A, Bressler C, Chabera P, Christensen M, Dohn AO, Galler A, Gawelda W, Gosztola D, Haldrup K, Harlang T, Liu Y, Moeller KB, Németh Z, Nozawa S, Papai M, Sato T, Sato T, Suarez-Alcantara K, Togashi T, Tono K, Uhlig J, Da Vithanage, Wärnmark K, Yabashi M, Zhang J, Sundström V, Nielsen MM (2015) Visualizing the non-equilibrium dynamics of photoinduced intramolecular electron transfer with femtosecond X-ray pulses. Nat Commun 6:6359
139. Vagnini MT, Mara MW, Harpham MR, Huang J, Shelby ML, Chen LX, Wasielewski MR (2013) Interrogating the photogenerated Ir(IV) state of a water oxidation catalyst using ultrafast optical and X-ray absorption spectroscopy. Chem Sci 4(10):3863–3873. doi:10.1039/c3sc51511g
140. Na Y, Pan J, Wang M, Sun L (2007) Intermolecular electron transfer from photogenerated Ru(bpy)3+ to [2Fe2S] model complexes of the iron-only hydrogenase active site. Inorg Chem 46(10):3813–3815
141. Na Y, Wang M, Pan J, Zhang P, Åkermark B, Sun L (2008) Visible light-driven electron transfer and hydrogen generation catalyzed by bioinspired [2Fe2S] complexes. Inorg Chem 47(7):2805–2810. doi:10.1021/ic702010w
142. Samuel APS, Co DT, Stern CL, Wasielewski MR (2010) Ultrafast photodriven intramolecular electron transfer from a zinc porphyrin to a readily reduced diiron hydrogenase model complex. J Am Chem Soc 132(26):8813–8815. doi:10.1021/ja100016v
143. Mirmohades M, Pullen S, Stein M, Maji S, Ott S, Hammarström L, Lomoth R (2014) Direct observation of key catalytic intermediates in a photoinduced proton reduction cycle with a diiron carbonyl complex. J Am Chem Soc 136(50):17366–17369. doi:10.1021/ja5085817
144. Windle CD, George MW, Perutz RN, Summers PA, Sun XZ, Whitwood AC (2015) Comparison of rhenium-porphyrin dyads for CO_2 photoreduction: photocatalytic studies and charge separation dynamics studied by time-resolved IR spectroscopy. Chem Sci 6(12):6847–6864. doi:10.1039/C5SC02099A

145. Torres O, Procacci B, Halse ME, Adams RW, Blazina D, Duckett SB, Eguillor B, Green RA, Perutz RN, Williamson DC (2014) Photochemical pump and NMR probe: chemically created NMR coherence on a microsecond time scale. J Am Chem Soc 136 (28):10124–10131. doi:10.1021/ja504732u
146. Karlsson S, Boixel J, Pellegrin Y, Blart E, Becker HC, Odobel F, Hammarstrom L (2010) Accumulative charge separation inspired by photosynthesis. J Am Chem Soc 132 (51):17977–17979. doi:10.1021/ja104809x
147. Song WJ, Ito A, Binstead RA, Hanson K, Luo HL, Brennaman MK, Concepcion JJ, Meyer TJ (2013) Accumulation of multiple oxidative equivalents at a single site by cross-surface electron transfer on TiO_2. J Am Chem Soc 135(31):11587–11594. doi:10.1021/ja4032538
148. Ashford DL, Gish MK, Vannucci AK, Brennaman MK, Templeton JL, Papanikolas JM, Meyer TJ (2015) Molecular chromophore-catalyst assemblies for solar fuel applications. Chem Rev (Washington, DC, US) 115(23):13006–13049. doi:10.1021/acs.chemrev.5b00229
149. Tian HN (2015) Molecular catalyst immobilized photocathodes for water/proton and carbon dioxide reduction. Chemsuschem 8(22):3746–3759. doi:10.1002/cssc.201500983
150. Lakadamyali F, Reynal A, Kato M, Durrant JR, Reisner E (2012) Electron transfer in dye-sensitised semiconductors modified with molecular cobalt catalysts: photoreduction of aqueous protons. Chem—A Eur J 18(48):15464–15475. doi:10.1002/chem.201202149
151. Reynal A, Lakadamyali F, Gross MA, Reisner E, Durrant JR (2013) Parameters affecting electron transfer dynamics from semiconductors to molecular catalysts for the photochemical reduction of protons. Energy Environ Sci 6(11):3291–3300. doi:10.1039/c3ee40961a
152. Brown AM, Antila LJ, Mirmohades M, Pullen S, Ott S, Hammarström L (2016) Ultrafast electron transfer between dye and catalyst on a mesoporous NiO surface. J Am Chem Soc. doi:10.1021/jacs.6b03889
153. Poddutoori PK, Thomsen JM, Milot RL, Sheehan SW, Negre CFA, Garapati VKR, Schmuttenmaer CA, Batista VS, Brudvig GW, van der Est A (2015) Interfacial electron transfer in photoanodes based on phosphorus(V) porphyrin sensitizers co-deposited on SnO_2 with the Ir(III)Cp* water oxidation precatalyst. J Mater Chem A 3(7):3868–3879. doi:10.1039/c4ta07018f
154. Youngblood WJ, Lee SHA, Kobayashi Y, Hernandez-Pagan EA, Hoertz PG, Moore TA, Moore AL, Gust D, Mallouk TE (2009) Photoassisted overall water splitting in a visible light-absorbing dye-sensitized photoelectrochemical cell. J Am Chem Soc 131(3):926–+. doi:10.1021/ja809108y
155. Zhao YX, Swierk JR, Megiatto JD, Sherman B, Youngblood WJ, Qin DD, Lentz DM, Moore AL, Moore TA, Gust D, Mallouk TE (2012) Improving the efficiency of water splitting in dye-sensitized solar cells by using a biomimetic electron transfer mediator. Proc Natl Acad Sci USA 109(39):15612–15616. doi:10.1073/pnas.1118339109

Chapter 12
X-Ray Photoelectron Spectroscopy for Understanding Molecular and Hybrid Solar Cells

Ute B. Cappel, Valeria Lanzilotto, Erik M.J. Johansson, Tomas Edvinsson and Håkan Rensmo

Abstract X-ray photoelectron spectroscopy is a powerful tool for the characterization of molecular and hybrid solar cells. This technique allows for atomic-level characterization of their components as well as for the determination of the electronic structure that governs the key conversion processes. In this chapter, we introduce the basic concepts of electronic structure in molecules and semiconducting materials followed by a description of the concepts of photoelectron spectroscopy and how they relate to electronic structure. Finally, we give examples of the application of photoelectron spectroscopy to different types of molecular and hybrid solar cell materials demonstrating the type of information that can be obtained, to gain fundamental understanding and to further develop such devices.

Keywords Photoemission spectroscopy · Hard X-ray photoelectron spectroscopy · Electronic structure · Dye-sensitized solar cells · Organic solar cells · Perovskite solar cells · Interface · Fermi level · Work function · Surface structure

Abbreviations

XUV	Extreme ultraviolet
VB	Valence band
CB	Conduction band
XPS	X-ray photoelectron spectroscopy
PES	Photoelectron spectroscopy
E	Energy
$\Psi(r, t)$	Time-dependent wave function

U.B. Cappel · V. Lanzilotto · H. Rensmo (✉)
Department of Physics and Astronomy, Uppsala University, Uppsala, Sweden
e-mail: hakan.rensmo@physics.uu.se

E.M.J. Johansson
Department of Chemistry—Ångström, Uppsala University, Uppsala, Sweden

T. Edvinsson
Department of Engineering Sciences, Uppsala University, Uppsala, Sweden

H. Tian et al. (eds.), *Molecular Devices for Solar Energy Conversion and Storage*, Green Chemistry and Sustainable Technology,
https://doi.org/10.1007/978-981-10-5924-7_12

$\Psi(r)$	Time-independent wave function
DFT	Density functional theory
AO	Atomic orbital
MO	Molecular orbital
LCAO	Linear combination of atomic orbitals
S	Orbital overlap
HOMO	Highest occupied molecular orbital
LUMO	Lowest unoccupied molecular orbital
MLCT	Metal-to-ligand charge transfer
bpy	Bipyridine
E_F	Fermi level
E_B	Binding energy
E_K	Kinetic energy
KT	Koopmans' theorem
ε	Orbital energy
HF	Hartee–Fock
I	Ionization energy
ϕ_s	Work function of a solid
UPS	Ultraviolet photoelectron spectroscopy
SOXPES	Soft X-ray photoelectron spectroscopy
HAXPES	Hard X-ray photoelectron spectroscopy
TMPc	Transition metal phthalocyanine
ML	Monolayer
IMFP	Inelastic mean free path
ϕ_a	Work function of the analyzer
Δ	Change in sample work function
UHV	Ultrahigh vacuum
OTiPc	Titanyl phthalocyanine
HOPG	Highly oriented pyrolytic graphite
SCL	Space charge layer
HC	Hole-conductor
F_4-TCNQ	Tetra-fluoro-tetracyano-quinodimethane
ITO	Indium tin oxide
P3HT	Poly-3-hexylthiophene
DSC	Dye-sensitized solar cell
HTM	Hole transporting material
TAA	Trialylamine
CA	Cyano
MA	Methylammonium
FA	Formamidinium

12.1 Introduction

The worldwide efforts to develop efficient and sustainable energy systems have now reached a stage, where an understanding of the fundamental processes on the atomic level is critical for further improvements. Guided design of these materials requires answers to a range of fundamental questions related to the photoexcitation process and how the electronic energy is distributed among the atoms—the electronic energy landscape. The electronic energy landscape is controlled by material design in terms of composition. This can also include the scale of the produced materials (1D, 2D or 3D quantum confinement effects) as well as bulk and surface defects. The fundamental limitations for many charge generation and charge transfer processes common for solar cells, solar fuel, fuel cells and electrolysis are critically dependent on the details of how the atoms in the different materials are arranged, the electronic states of the different materials and material interfaces as well as the dynamics controlled by this (see Fig. 12.1 for these concepts relating to dye-sensitized solar cells). In short, electronic structure engineering at the atomic level is mandatory to both obtain a fundamental understanding of the limiting processes in the systems as well as to attain major efficiency breakthroughs in the corresponding molecular devices. Such development inevitably requires studies of the interaction between photons and electrons on the atomic length and time scale

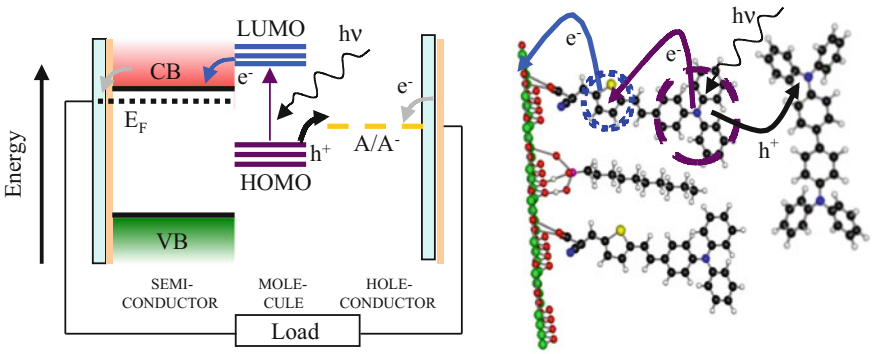

Fig. 12.1 Schematic figures highlighting the electronic structure and key functions in a molecular solar cell. *Left panel* The energy diagram of how the different materials should be matched to support the function of a dye-sensitized solar cell. *Red/green* represent valence band/conduction band (VB/CB) in a semiconductor with a band gap, *purple/blue* represents the frontier electronic structure of a dye molecule that can be excited upon visible light illumination, *yellow* represent the energy levels or redox potentials in a molecular hole-conductor or a liquid redox system. The figure also highlights the energy levels, which for a functional system determine the photovoltage. *Right panel* A molecular structure representation showing the key interface for light to electrical energy conversion. The interface contains molecules that upon light illumination inject electrons to the semiconductor material and holes to the molecular material. X-ray photoelectron spectroscopy is an excellent tool for the interfacial electronic structure of these kinds of energy materials, as it can be used to measure the relative energies and characters of the different states

for surfaces and interfaces under practical ambient conditions. Prime tools for such studies are based on X-ray and extreme ultraviolet (XUV) radiation. In the following chapter, we will briefly introduce the basics of electronic structure and how it can be investigated by X-ray photoelectron spectroscopy including new opportunities with recent developments in the field. This will be done using examples on systems related to both solid and liquid molecular systems, including perovskite solar cells, dye-sensitized solar cells, polymer and small-molecule solar cells. The first sections contain very brief introductions to the basics of electronic structure and to X-ray photoelectron spectroscopy. For those of you already familiar with these concepts one can jump directly to Sect. 12.4.

12.2 Basics of Electronic Structure

Insight into the electronic structure is of importance in the development and understanding of all molecular devices including molecular and hybrid solar cell materials. Some of the basic background of electronic structure in molecules and crystals is outlined below. This introduction will facilitate the discussion of X-ray photoelectron spectroscopy (XPS), also referred to as photoemission spectroscopy or photoelectron spectroscopy (PES), and examples of its application to molecular and hybrid solar cells in the later part of this chapter. For references, we refer to textbooks in physical chemistry, quantum chemistry and condensed matter physics.

12.2.1 From Atoms to Molecules

Theoretically the various atomic, molecular and condensed matter structural and electronic properties are obtained by solving the Schrödinger equation, which in the general and the time-independent form looks as follows:

$$\left(-\frac{\hbar}{2m}\nabla^2 + V(r,t)\right)\Psi(r,t) = i\hbar\frac{\delta\Psi(r,t)}{\delta(t)} \tag{12.1}$$

$$\left(-\frac{\hbar}{2m}\nabla^2 + V(r)\right)\Psi(r) = E\Psi(r) \tag{12.2}$$

where the kinetic energy operator, K, is represented by $-\hbar/2\mathrm{m}$ and the second-order Nabla operator (∇^2), while the potential is represented by V. K + V is often referred to as the Hamiltonian, H. E is the energy of the system and Ψ(r,t) and, Ψ(r) are the time-dependent and time-independent wave functions, respectively, where the latter is generally used in the absence of a time-dependent potential field. Using the Born–Oppenheimer approximation, the total wave function can be factorized into an electronic and a nuclear component, $\Psi_{\mathrm{total}} = \Psi_{\mathrm{electronic}} \times \Psi_{\mathrm{nuclear}}$,

where the nuclei wave function includes the quantum mechanical states of the nuclei (vibrational, rotational, spin, etc.). The time-independent electronic Schrödinger equation can then be constructed for a specific geometry by treating the nuclei intra-potential constant and solutions can generally be approximated with numerical methods such as wave function-based methods or correspondingly with the Kohn–Sham equation in density functional theory (DFT).

Analytical solutions to Eqs. 12.1 and 12.2 also exist in the case of, for example the free particle, the particle in a box and the hydrogen atom. These solutions are often used in idealized models as a solution to the Schrödinger equations and this simplicity can be valuable in the conceptual understanding of energy states and their possible interactions. Numerical solutions of wave function-based and DFT methods supply a more complete description of the material system instead and aid in a more specific understanding and, ultimately, insights into how to control molecular and condensed matter properties. Below we give brief introductions to how an overall electron configuration for a molecule can be constructed from a product of single electron wave functions, so-called orbitals, and as indicated above we specifically focus on the electronic properties.

For single atoms, the symmetry of the wave functions are used for calculating the electronic energy assuming a shielded central potential. This gives rise to a density dependence around the nuclei with orbital energy and symmetry described by the quantum numbers n and l (for example, for 1s n = 1 and l = 0 and for 3d n = 3 and l = 2) similar to the simpler (and analytical solvable) hydrogen atom, where the different energy levels are represented by energy levels called orbitals. A product of orbitals describes the overall electron configuration for a multi-electron atom. As an example, the oxygen atom has an electron configuration of $1s^2 2s^2 2p^4$ indicating a combination of a 1s, 2s and 2p orbitals that has 4 degenerate electrons in the 2p subshell. Spin-orbit interactions split the degeneracy further and are of specific importance for heavier elements.

When solving the Schrödinger equation for atoms bonding together to form molecules, different approximations are used. In the molecular orbital method, one generally uses the states describing the atomic orbitals (AOs) to construct molecular orbitals (MOs) from linear combination of AOs. This procedure is denoted as a linear combination of atomic orbitals (LCAO). For a diatomic molecule, a simple procedure combines one state from each atom (ψ_A and ψ_B with orbital energies α_A and α_B and coefficients c_A and c_B) to give $\Psi_{MO} = C_A\Psi_A + C_B\Psi_B$ (Fig. 12.2a). Based on such a wave function, the Schrödinger equation for a heteronuclear diatomic molecule results in two new solutions Ψ_{MO1} and Ψ_{MO2} with energies $E_+ \approx \alpha_A - (kS)^2/\Delta E$ and $E_- \approx \alpha_B + (kS)^2/\Delta E$. The values of E_+ and E_- can be calculated at different levels of approximation. The expressions shown here emphasize the dependence on the energy difference of the atomic orbitals, $\Delta E = \alpha A - \alpha B$, and on S, which is the orbital overlap, $S = \int \Psi_A \Psi_B$. For a homonuclear diatomic molecule, the equations are sometimes approximated as $E_\pm \approx \alpha \pm kS$ (Fig. 12.2a).

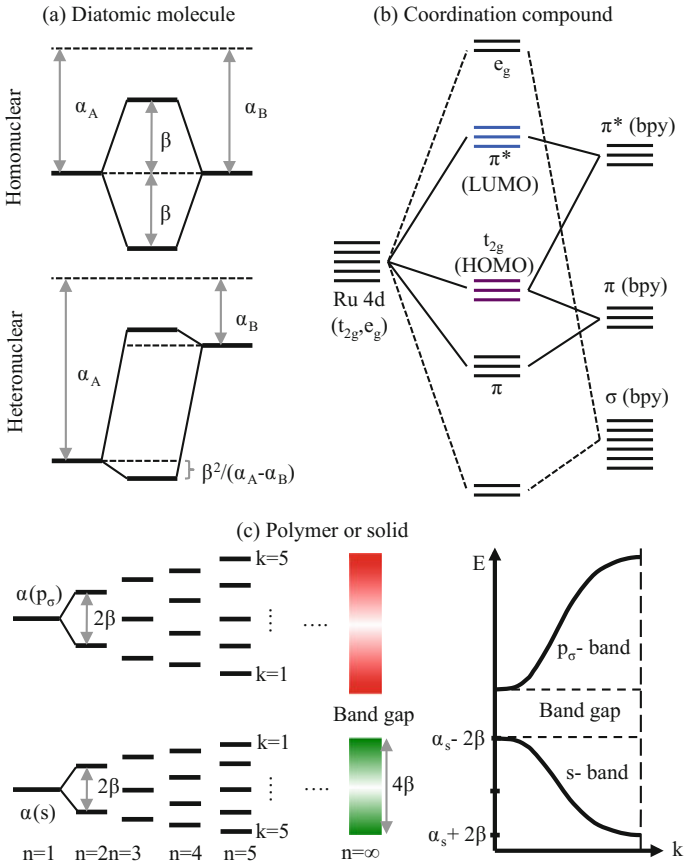

Fig. 12.2 **a** Diatomic molecule—schematic representation of linear combination of molecular orbitals to form MOs from two AOs, which are the same, and from two AOs, which are different in energy. Based on such a wave function, the Schrödinger equation for a heteronuclear diatomic molecule result in two new solution Ψ_{MO1} and Ψ_{MO2} with energies E_+ and E_- depending on the difference in ionization (orbital) energy of ψ_A and ψ_B, $\Delta E = \alpha_A - \alpha_B$, as well as the orbital overlap, $S = \int \psi_A \psi_B$. The latter statement is based on the approximation, $\beta \approx kS$ where $\beta = \int \psi_A H_{\psi B}$. **b** Similar concepts can also be used for larger molecules. The example shows a schematic representation of a $Ru(bpy)_3^{2+}$ based on an octahedral symmetry around the Ru metallic centre. The highest occupied orbitals in Ru (Ru4d) is divided to a t_{2g} and e_g set in the octahedral symmetry. The e_g orbitals interact with the nitrogen lonepair resulting in sigma type orbitals while the t_{2g} set interacts with π and π*. **c** For structures with long-range order (e.g. crystalline solids or polymers) similar concepts can also be used to model the electronic structure. In this case, the levels from the single units form bands with a spread, 4β, in the continuous distribution of energy levels, the dispersion that has a similar origin as the energy splitting for the diatomic molecule. The figure shows the origin of a band gap. The band dispersion of the valence band (VB) in *red* and conduction band (CB) in *green* highlight variations in the density of states as indicated by the colour gradient (see also Fig. 12.1)

For the diatomic molecules the molecular orbitals Ψ_{MO1} and Ψ_{MO2} are often referred to as π-type orbitals when they contain a node on the symmetry axes between the atoms and σ-type when lacking such a node. The method can also distinguish between the valence states (or molecular orbitals) and the core levels to some extent. The latter are deeper energy levels were the localization of the atomic orbitals limit overlap and the orbitals therefore retain a strong atomic character. This concept for diatomic molecules gives insight to, e.g. the origin of the chemical bond and the character of electronic transitions.

12.2.2 From Small Molecules to Large Molecules

The concepts for diatomic molecules may also be used for larger molecules, where orbital interaction via hybridization is an important concept exemplified by the sp, sp^2 and sp^3 hybridization in carbon-based materials. In this case as well as for compounds containing metals or other heavier elements, symmetry reduces the complexity and is often used when describing states as well as possible electronic transitions. Metal-organic molecules have been used as light absorbers in molecular solar cells. For many such molecules, an approach very similar to that for smaller molecules can be utilized while analyzing the sub-symmetry around the metallic centre, and while assigning the dominant orbital character of the quantum mechanical states as well. The metal centre's electronic structure is then described by s, p and d orbitals, while the coordinating organic material's electronic structure may be described by molecular orbital concepts such as π-types and σ-types. An example for the coordination of Ru to bipyridine (bpy) is shown in Fig. 12.3. An ideal $Ru(bpy)_3^{2+}$ has a D_3 symmetry but an octahedral (O_h) symmetry around the Ru centre is often used as an approximation, where the ligand field splitting separates the five d orbitals of the metallic centre into three orbitals referred to as the t_{2g} and two orbitals referred to the as e_g set. A schematic figure of the electronic structure for $Ru(bpy)_3^{2+}$ is shown in Fig. 12.2b Based on this figure one can learn that the light absorption at low energy from the highest occupied molecular orbital (HOMO) to the lowest unoccupied molecular orbital (LUMO) is a metal-to-ligand charge transfer (MLCT) in which the electron density redistributes to the exterior of the ligands. Moreover, the model can be used for understanding how to fine-tune the properties of the metal-organic complex. The exchange of one bpy unit with two NCS units breaks the symmetry of the molecule and the NCS units have an energy that is similar to that of the Ru t_{2g} set and thus efficiently mix with these states (see Figs. 12.2 and 12.3 and Sect. 12.4.3.3). Another example of a class of molecules, which have been widely used as light absorbers in molecular solar cells, are organic donor-π-acceptor dyes. The HOMO and LUMO for one such dye is shown in Fig. 12.3 (bottom). In such a system, exciting an electron from the HOMO to the LUMO results in a charge transfer along the extension of the molecule. Both the MLCT and the donor-π-acceptor molecular designs are beneficial for charge

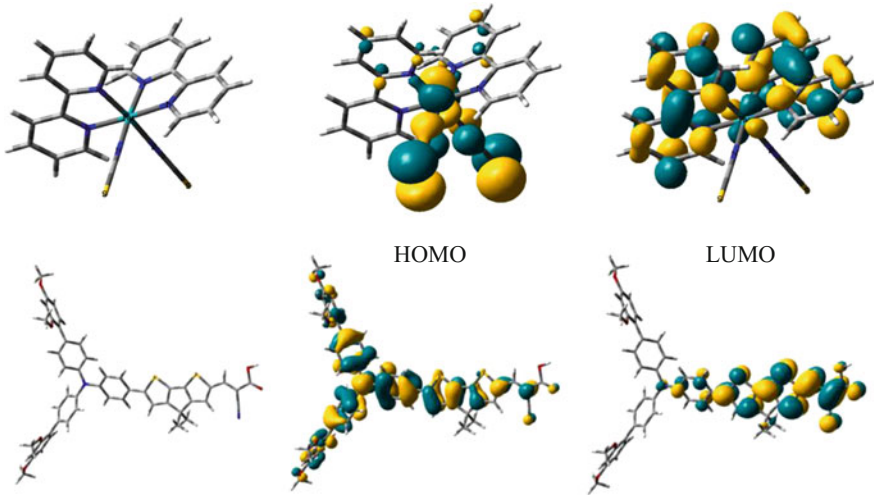

Fig. 12.3 Ground state structure and frontier orbitals of a metal-organic Ru-bis-pyridine-NCS dye calculated with density functional theory using the HSE06 hybrid functional and the Stuttgart–Dresden scalar-relativistic pseudo potentials (*top*) and an LEG4, an organic donor-π-acceptor system (*bottom*) calculated on a B3LYP/6-311G** level

separation in molecular systems for photoconversion and knowledge of electronic structure and electronic transitions provides insight for design of new molecules.

12.2.3 From Bonds to Bands

There are different approaches for calculating the electronic structure of solid-state compounds with different kinds of long-range order. For molecular compounds such as semiconducting polymers versions of the LCAO approach are often instructive. In this approach the orbitals (e.g. s or p) are initially treated separately and the MOs contain linear combinations of orbitals originating from the same level, e.g. a pσ level. The combination of the orbitals results in a series of different combinations of the MOs spread over a particular energy interval. The order of the orbitals essentially depends on the number of bonding and anti-bonding combinations with the completely bonding combination having the lowest energy and the completely anti-bonding combination having the highest energy. A schematic figure for the s and p level is shown in Fig. 12.2c. For an infinite series of atoms (N = ∞), the separation between the orbitals represented by the quantum number k is so small that the resulting level is better described as a continuous band than by discrete levels. The distribution of the level is referred to as its dispersion and can be used to obtain a density of states at each energy. The dispersion can be described by a simple model as $E = \alpha + 2\beta\cos(k\pi/N+1)$, where α is the orbital energy in

the atomic orbital, β is dominated by the orbital overlap ($\beta \approx$ kS) as discussed for the diatomic molecule above and k is a quantum number that accounts for the different states. The bandwidth of the dispersion approaches 4β as the number of orbitals, N, approaches infinity.

For traditional semiconductor solids a similar approach may be used to get some insight into the character of the energy bands and how they relate to orbitals in the atoms building the solid unit cells. Following the LCAO approach for a solid described by repeating the unit cells, orbital overlap will give splitting for each unit cell extension eventually leading to dense bands of orbitals where the ones with lower energies are bonding orbitals and the ones with higher orbital energies are anti-bonding. The bands from bonding orbitals are filled and the highest filled band is referred to as the valence band, while the lowest unfilled band is referred to as the conduction band. If the bands (with the same or different orbital symmetry) overlap so that electrons easily can be thermally excited into non-bonding orbitals and thus free to move in conducting states, the material is classified as a metal. If there is a gap between the anti-bonding and bonding bands, one obtains a two-state system where a substantial amount of energy from temperature or light is needed to populate conducting states, the material is classified as a semiconductor. The Fermi level (E_F) in a material is the electrochemical potential for the electrons. While this is directly linked to the redox potential in an electrolyte solution, it is the energy of the highest occupied state at T = 0 K for a solid material. At temperatures higher than the absolute zero, the Fermi level and can be defined as where the probability of finding an electron is 0.5. For a pure semiconductor at $T \neq 0$ K, E_F is generally found in the middle between the valence and the conduction band, while for n-doped semiconductors the Fermi level is closer to the conduction and for p-doped closer to valence band. When bringing two materials in contact their Fermi energies align, often leading to a charge transfer across the interface and associated band bending representing polarization or electric fields.

Low-dimensional systems in between a molecular system and a large crystal show an increased band gap and are classified as quantum confined systems (e.g. a quantum dot if confined in 3D). The size where this occurs depends on the symmetry of the orbitals involved and on the magnitude of the overlap integral, and thus the magnitude of the orbital splitting.

In a crystalline solid, an alternative approach to construct the electronic wavefunction is to introduce a periodic potential, U(r), which is the same in a symmetric direction in the crystal after some period T, that is U(r) = U(r + T), which motivates the replacement of the ordinary wave function with Bloch functions that are periodic via

$$\psi(\boldsymbol{k}, \boldsymbol{r} + \boldsymbol{T}) = e^{ikT}\psi(\boldsymbol{k}, \boldsymbol{r}) \tag{12.3}$$

where the crystal wavefunction $\psi(\boldsymbol{k}, \boldsymbol{r})$ is defined only in the periodic system. The states described by this relation are for those for which a vector k exists such that a translation by a lattice vector T reproduces the original wave function multiplied by a phase factor, $e^{i\boldsymbol{kT}}$. The eigenvalues of the Hamiltonian operator working on the

crystal wavefunction are the band structure energies, $E_n(k)$, in reciprocal space. Here, crystal orbital energies along special high symmetry directions in lattice form energy dispersion diagrams (similar to Fig. 12.2c) where both the energy gaps and curvatures of the bands give information of possible optical transmissions and the inherent mobilities of the electrons and holes.

The photoanode interface in a molecular solar cell is depicted in Fig. 12.1. The orbitals in medium-sized molecules as well as the bands and Fermi level for an n-type semiconductor are illustrated during an electron transfer reaction upon illumination with colours linked to Fig. 12.2. X-ray photoelectron spectroscopy can be used to measure the valence levels of such a system as well as core levels associated with the different chemical elements at the semiconductor/molecule interface (the basic concepts for this and interpretations are introduced in the next section).

12.3 Basic Concepts of X-Ray Photoelectron Spectroscopy

X-ray photoelectron spectroscopy (XPS), synonymously referred to as photoemission spectroscopy (PES), is one of the main techniques, which can be used for experimental determinations of the electronic structure. Its high relevance for the characterization of molecular and hybrid solar cells stems from the fact that it can be applied to both molecular as well as to crystalline and amorphous materials and to materials combinations. In the following section, we will summarize the basic concepts of photoemission spectroscopy necessary for understanding its application to materials combinations used in devices for energy conversion. More complete descriptions of the technique can for example be found in references [1–5].

12.3.1 Basic Concepts

Upon irradiation of a material with monochromatic radiation $(h\nu)$ in the X-ray or UV regime, the photoemission of electrons can be observed. When considering conservation of energy, the following relation has to be true for each emitted electron with a kinetic energy of E_K:

$$E_{tot}^{i}(N) + h\nu = E_{tot}^{f}(N-1) + E_K \tag{12.4}$$

where $E_{tot}^{i}(N)$ is the initial state energy of the system with N electrons and $E_{tot}^{f}(N-1)$ is the final-state energy of the system with $(N-1)$ electrons. A photoemission experiment in which the photon energy is known and the kinetic energy is measured, therefore gives access to the difference in energy between the system after and before photoemission. This energy difference is then defined as the binding energy of the electron within the material (E_B):

$$E_B = E^f_{tot}(N-1) - E^i_{tot}(N) = h\nu - E_K \tag{12.5}$$

According to Koopmans' theorem (KT), which imposes that the final one-electron orbitals are identical to the initial ones (*frozen-orbital approximation*), the binding energy of a photoelectron can be simply identified with the negative of its orbital energy ε, as calculated using the Hartee–Fock (HF) method:

$$E_B = E^f_{tot}(N-1)^{KT} - E^i_{tot}(N) = -\varepsilon \tag{12.6}$$

For bound-state orbitals ε is negative, so E_B has a positive sign. This approximation neglects the relaxation of the remaining electrons upon removal of an electron and may be directly compared to the schemes in Fig. 12.2. For all excitations, electronic relaxations occur on the same time scale as photoemission and therefore affect $E^f_{tot}(N-1)^{KT}$, usually by lowering it and partially explaining why an E_B lower than $-\varepsilon$ is generally observed (Fig. 12.4). Furthermore, the Hartree–Fock method is an approximation itself, as it neglects some electron correlation, and the energies of both ionized and neutral systems are higher than the real ones. Correlation energies are usually larger for systems with higher number of particles. It follows that correlation effects tend to increase E_B (Fig. 12.4), and so there must be some cancellation of the corrections due to relaxation and correlation effects. In comparison DFT has an advantage of the HF methods for systems where correlation is important. Although relaxation and correlation are important for modelling accurate binding energies, the orbitals with energies as defined by Koopmans' theorem are still a good approximation for the origin and character of the bond-states measured through photoemitted electrons. They are, therefore, often used to discuss both core level- and valence-level photoemission spectra (see below).

The first ionization energy (I) of a sample is the same as the binding energy of the loosest bound electrons and $h\nu$ needs to be higher than this for photoemission to occur $(E_K > 0)$. In this definition, the binding energy is, therefore, referenced to the vacuum level just outside the sample (E^s_{vac}). For gaseous samples, this vacuum

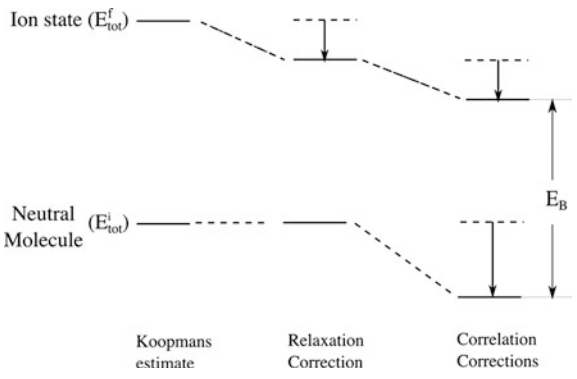

Fig. 12.4 Koopmans Theorem with correction for relaxation and for correlation

level is equal to the vacuum level at infinity (E^{∞}_{vac}) providing a common reference level for measurements of different samples and the binding energy can be calculated from the measured kinetic energy according to Eq. 12.5.

However, for solid materials, there is a difference between E^{∞}_{vac} and E^{s}_{vac}. One contribution to such effects is the surface dipole formed by the tail of the electron cloud that spills out from the surface leaving vacuum and bulk side negatively and positively charged, respectively. E^{s}_{vac} is, therefore, characteristic for a given surface and cannot be used as an invariant reference level. For this reason, it is often convenient to express the binding energies for solid samples relative to the Fermi level (E_F):

$$E_{\mathrm{B}} = h\nu - E_K - \phi_s \tag{12.7}$$

where ϕ_s is the work function of the solid, which is defined as the energy separation between E_F and E^{s}_{vac} just outside the material surface.

Photoemission spectroscopy can be divided in two branches, the one devoted to the study of the inner energy levels, *core level photoemission spectroscopy*, and the one dedicated to the study of the outer energy levels which are involved in chemical bonds, *valence level photoemission spectroscopy* (see Fig. 12.5).

An alternative division of photoemission spectroscopy comes from the photon energies used for measurements. Home-lab sources are usually either based on the use of ultraviolet photons from a Helium discharge lamp with $h\nu$ = 21.22 eV for He (I) and $h\nu$ = 40.8 eV for He(II) or of X-ray photons from an anode source with $h\nu$ = 1486.7 eV for Aluminium K_α or $h\nu$ = 1253.7 eV for Magnesium K_α. In the former case, the technique is often referred to as *ultraviolet photoelectron spectroscopy* (UPS), while in the latter case as *X-ray photoelectron spectroscopy* (XPS). Synchrotron light sources offer many opportunities as tunable photon sources for PES measurements. Generally, two types of beamlines are available which rely on

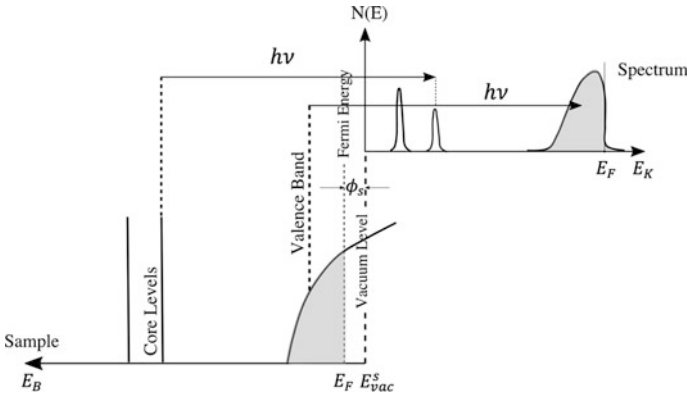

Fig. 12.5 Relation between the electron binding energy (E_B) in a solid sample and the electron kinetic energy distribution observed in the corresponding photoemission spectrum

different types of monochromators for the selection of the photon energy: those providing soft X-rays up to energies of 2000 eV for *soft X-ray photoelectron spectroscopy* (SOXPES) and those providing harder X-rays with energies above 2000 eV for hard X-ray photoelectron spectroscopy (HAXPES). To allow for the detection of photoelectrons emitted from a material without a loss in kinetic energy before reaching the detector, PES measurements have to be carried out under very high or ultra-high vacuum conditions. A detailed description of experimental setups used for PES including the description of detectors can for example be found in reference [5].

12.3.2 Core-Level Spectra

The core levels measured in photoelectron spectroscopy relate to orbitals with high electron binding energies, which strongly maintain their atomic orbital character, as there is little or no overlap with orbitals from neighbouring atoms. Therefore, the binding energies of core electrons from a specific orbital fall within a narrow range and are characteristic for each element. This allows for the determination of the elemental composition of an unknown sample from core electron binding energies. Small shifts, so-called chemical shifts, of core levels can be observed for an atom with different chemical environments. In other words, core level photoemission allows for both elemental and chemical analysis. An example of core level spectra is shown in Fig. 12.6 for vapours of Fe(II)-phthalocyanine (FePc) [6]. Phthalocyanines adsorbed on well-defined surfaces are good model systems that highlight many of the fundamental interactions at a molecular interface. They are also interesting since they are used in energy relevant applications.

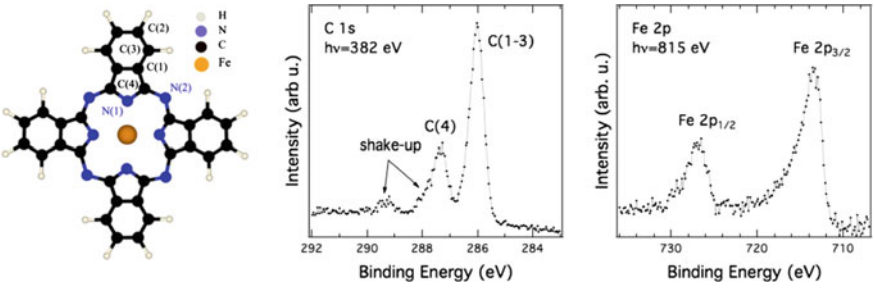

Fig. 12.6 *Left panel* Molecular structure of the iron phthalocyanine (FePc) molecule. Non-equivalent nitrogen and carbon atoms are indicated in the sketch. N(1) and C(4) are pyrrole-like nitrogen and carbon atoms, respectively. N(2) are aza-bridge type nitrogen and C(1), C(2), C(3) are benzene-like carbon atoms. C 1*s* (*middle panel*) and Fe 2*p* (*right panel*) spectra for gaseous Fe(II)-phthalocyanine referenced to the vacuum level. Adapted from Ref. [6] by permission of John Wiley & Sons Ltd

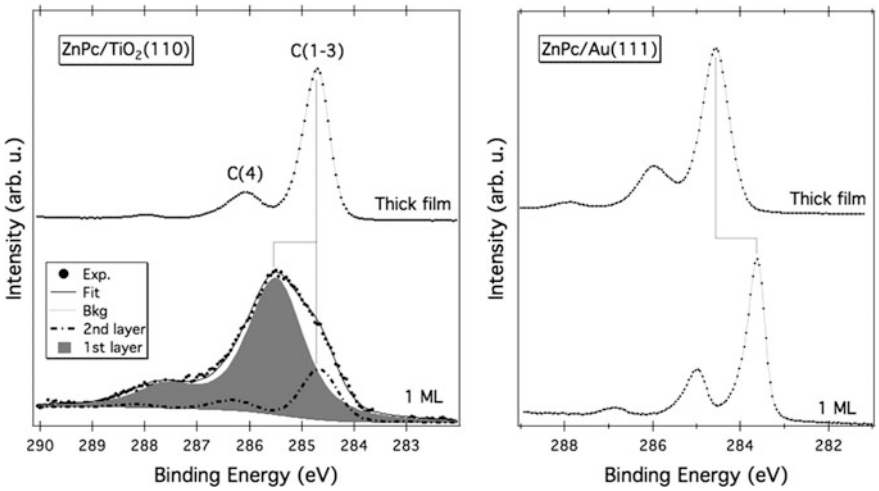

Fig. 12.7 *Left panel* C 1s level for a nominal thickness of 0.9 ML and a thick film of ZnPc on TiO_2 (110) with curve fitting included for the 0.9 ML spectrum; *Right panel* C 1s for a monolayer and a thick film of ZnPc on Au(111). The spectra are referenced to the Fermi level. Adapted from Ref. [7] (*left panel*) and [8] (*right panel*), with the permission of AIP Publishing

Transition metal phthalocyanines are characterized by the presence of four non-equivalent carbon atoms, which can be grouped as benzene-type and pyrrole-type (Fig. 12.6). The corresponding C 1*s* spectrum consists of two main peaks at 285.9 and 287.4 eV, i.e. a chemical shift of 1.5 eV. Usually, the energy resolution of the technique (in this case 320 meV) is larger than the size of the chemical shifts between the benzene-like carbons and therefore these only give rise to one peak at 285.9 eV. On the other hand, the electron withdrawing effect of the N atoms strongly affects the binding energy of the C 1*s* electrons associated with the pyrrole atoms causing a shift of $\sim$1.5 eV to higher binding energies. At $\sim$289.3 eV, we observe an additional feature which is known as a *shake-up satellite* (another one is responsible for the shoulder of the C(4) peak). Such signals arise from those photoelectrons that have lost part of their kinetic energy to promote a valence electron into an unoccupied molecular state (see book references for more details).

Molecule–substrate interactions can also be responsible for a chemical shift of the core levels. Figure 12.7 shows the C 1*s* level for a nominal thickness of 0.9 monolayers (ML) and a thick film of ZnPc, both grown on the TiO_2(110) surface [7]. The thick layer displays the same features already described for the C 1*s* of gaseous FePc. At 0.9 ML, the C 1*s* peak is strongly broadened and characterized, according to the fitting procedure, by the presence of two components: a smaller one (dashed line curve) close in binding energy to the thick film, and another main component (grey-filled curve) shifted to higher binding energies by about 0.8 eV. While the first component can be associated with a few second-layer molecules, the

second one arises from molecules in direct contact with the surface. The strong broadening and the direction of the binding energy shift indicate a strong interaction between the organic ligand and the TiO_2 surface characterized by a charge transfer from the molecule to the substrate, i.e. the organic ligand becomes partly oxidized.

In absence of a particular molecule–substrate interaction, core levels can still shift with varying the molecular coverage. Usually, they shift to higher binding energies (up to $\sim$1.0 eV) with increasing thickness of the organic layer. This kind of shifts should not be interpreted in terms of a traditional initial state-based chemical shift, but as a shift containing large *final-state screening effects*. Such effects can for example occur, when photoemission involves a molecule in direct contact with a metal substrate and the core-hole (the vacancy in the inner shell remaining on the atom after photoemission) will be efficiently screened by the substrate electrons. Compared to the monolayer, core-holes created in the subsequent layers will not be screened as well leading to a binding energy shift to higher values. This is clearly shown for the thick film of ZnPc on Au(111) where the C 1*s* peak shifts to higher binding energies by $\sim$1.0 eV relative to the monolayer (left panel of Fig. 12.7) [8].

The Fe 2*p* core level of the $Fe^{II}Pc$ (Fig. 12.6) is a typical example of how core levels from closed-shells with $l > 0$ (p, d, f) are observed in core-level spectroscopy. In this case, the 2*p* level consists of two components at 713.5 and 726.8 eV. This doublet structure arises from the so-called *spin-orbit coupling*. After photoemission from the p closed-shell, the spin-state left behind interacts with its orbital angular momentum giving states referred to by j-values ($j = l + s$) of 1/2 and 3/2 with the latter being lower in binding energy. The ratio of their respective degeneracies ($2j + 1$) determines the intensities of the components.

An aspect to be considered when measuring core level spectra is the influence of *Auger* electrons, which arise from the radiationless decay of the core-hole. For instance, a 1*s* hole (K) can be filled by an electron from the 2s level (L_1) leading to the emission of a second electron from the 2p level ($L_{2,3}$), which is emitted with a kinetic energy of $E_K\left(KL_1L_{2,3}\right) = E_B(K) - E_B(L_1) - E_B\left(L_{2,3}\right)$.

As the kinetic energy of Auger electrons only depends on the binding energies of the levels involved, and their spectroscopic structure may be distinguished from that of a core level by tuning the photon energy.

12.3.3 Surface Sensitivity and Quantification

When considering a solid sample, photoelectrons can be generated at different depths ranging from the top monolayer to nearly a μm underneath. However, only photoelectrons, which are able to escape from the surface without losing kinetic energy, will contribute to the photoemission peak (*primary electrons*). On the other hand, electrons, which suffer energy loss but still have sufficient energy to escape from the sample will contribute to the background signal (*secondary electrons*). The

probability P of an electron to escape from a given depth (z, normal to the surface) without losing energy is given by the exponential decay:

$$P(z) = exp(-z/\lambda) \tag{12.8}$$

where λ is usually referred as the *inelastic mean free path* (IMFP) and represents the depth from which on average 1/e (37%) of photoelectrons produced there can escape without losing energy. From a different point of view, λ can be regarded as the thickness (down from the surface; $0 < z < \lambda$) from which 63% of primary electrons are originated. Another term, which is often used, is the *sampling depth* (3λ) known as the thickness from which 95% of detected electrons originate. Figure 12.8 shows the inelastic mean free path as a function of the electron kinetic energy calculated for different elemental solids [9]. From the figure it can be observed that photoemission spectroscopy of the primary electrons can be a very surface sensitive technique: the IMFP has a minimum of a few Å at kinetic energies in a range between 20 and 100 eV for most elements. Therefore, only electrons from the surface layers of the samples will be detected for kinetic energies in this region. From this minimum, λ increases for all elements to values of above 10 nm at very high kinetic energies. As a consequence, different sampling depths can be accessed through a variation of the photon energy, and therefore the measured kinetic energy (Eq. 12.7). This allows, for example for the study of molecular orientation on surfaces (see Sect. 12.4.3.2). By using X-rays in the hard X-ray regime (HAXPES at synchrotron beamlines), the sampling depth can even be extended to tens of nanometers. This is interesting for the study of buried interfaces and of the "bulk-like" electronic structure of for example solid molecular or hybrid materials (see Sect. 12.4.4).

By considering different factors, the area A_{ij} of the core-level peak j of a specific element i can be related to its concentration (n_i) in the sample, through the following equation [3]:

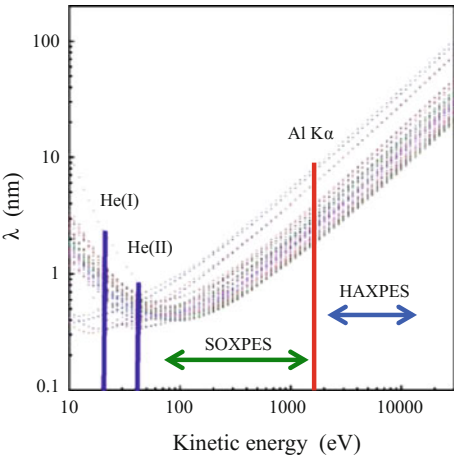

Fig. 12.8 Inelastic mean free path (λ) of electrons as a function of the electrons' kinetic energy calculated for 41 elemental solids. See Ref. [9] for details. The soft and hard X-ray regime are indicated in *green* and *blue*, respectively. Adapted from Ref. [9] by permission of John Wiley & Sons Ltd

$$A_{ij} = KT(E_K)L_{ij}(\gamma)\sigma_{ij}\int n_i(z)e^{-z/\lambda(E_K)cos\theta}dz \tag{12.9}$$

where K is an instrumental constant (i.e. X-ray flux, area of the sample irradiated, solid angle of photoelectrons accepted by the analyzer), $T(E_K)$ is the transmission function of the analyzer, $L_{ij}(\gamma)$ is a factor which accounts for the type of orbital j and the angle γ between the incident X-ray polarization and the emitted photoelectrons, σ_{ij} is the photoionization cross-section of the orbital j from element i, $n_i(z)$ is the concentration of element i at a distance z below the surface and θ is the take off angle of the photoelectrons measured with respect to the surface normal. Typically, only elemental concentration ratios or percentages are calculated, which allows to cancel/neglect most of the quantities in Eq. 12.9.

12.3.4 Valence, Fermi Level and Work Function

In valence-level photoemission spectroscopy, the levels which are related to molecular orbitals in molecules and energy bands in crystalline materials can be studied. As discussed above, PES measurement for solid samples are often referenced to the Fermi level instead of to the vacuum level. The example below is, therefore, intended to highlight the relation between work function, Fermi level and valence levels and is based on UPS measurements using the He(I) line ($h\nu$ = 21.22 eV) from a Helium discharge lamp. However, the procedure is not limited to this photon energy and the principle is also valid at higher ones.

Figure 12.9 shows the valence spectrum of a gold single crystal exposing the 111 crystallographic face. The spectrum was taken at normal electron emission and with He(I). A bias of −10.0 V was applied to the sample (see later), resulting in a shift of +10.0 eV of the kinetic energy range. In the first 2 eV below the Fermi level, E_B^F, it shows the flat 6*s* valence band, followed by the structured 5*d* band between 2 and 7 eV in binding energy. The third feature is a sloping background created by secondary electrons with a sharp cut-off at 16.02 ± 0.05 eV binding energy, $E_B^{cut-off}$. This cut-off represents electrons that leave the sample with a kinetic energy approaching zero just outside the material surface.

To understand the origin of the cut-off and its importance for determining the sample work function as defined in Eq. 12.7, we should refer to Fig. 12.10. In a real measurement, photoelectrons experience not only the work function of the sample, but also the one of the electron analyzer, ϕ_a. This is illustrated in the left panel of Fig. 12.10, which shows the situation for a conducting sample with $\phi_s > \phi_a$. The electrical contact between sample and analyzer ensures that the Fermi levels of both are aligned. When passing from the surface of the sample into the analyzer, the photoelectrons will feel an accelerating potential equal to $\phi_s - \phi_a$. Thus, the initial kinetic energy, E_K, at the surface of the sample becomes $E_K^{'}$ inside the analyser:$E_K^{'} = E_K + (\phi_s - \phi_a)$.

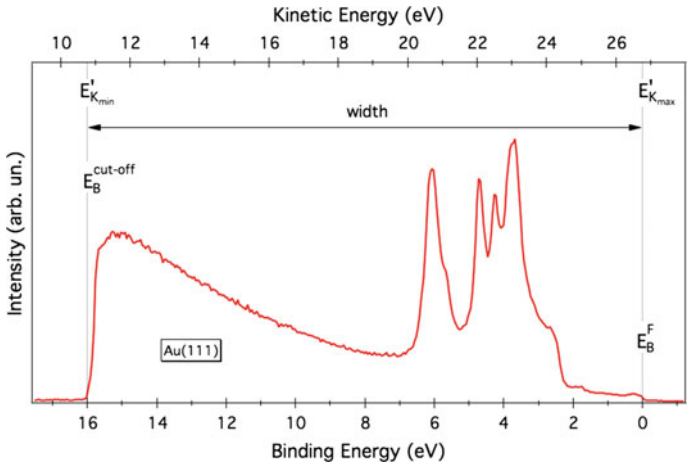

Fig. 12.9 Valence structure of Au(111) taken at normal electron emission with He(I) (hν = 21.22 eV). The work function (ϕ_s) of this surface is given by subtracting the width of the spectrum from the photon energy: $\phi_s = h\nu - \left(E'_{K_{max}} - E'_{K_{min}}\right)$ in kinetic energy and $\phi_s = h\nu - E_B^{cut-off}$ in binding energy if $E_B^F = 0$

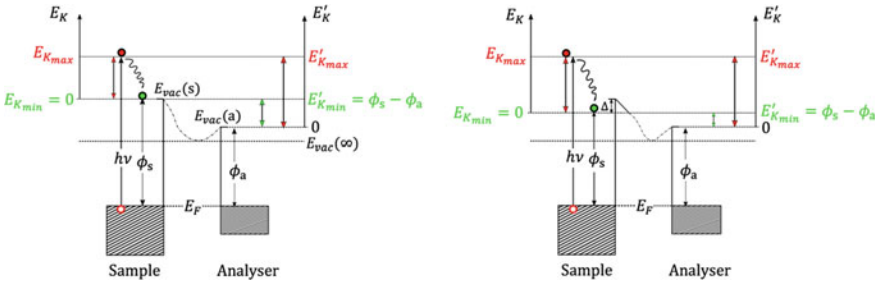

Fig. 12.10 Energy diagram of a metal substrate and electron analyzer in equilibrium before (*left*) and after (*right*) work function change. Adapted from Ref. [57] by permission of John Wiley & Sons Ltd

Substituting E_K accordingly into Eq. 12.7, this leads to the following expression for the kinetic energy inside the analyzer:

$$E'_K = h\nu - (E_B + \phi_a) \tag{12.10}$$

Equation 12.10 shows that E'_K does not depend on the sample work function. This is true for those photoelectrons, which did not suffer inelastic collisions (i.e.

primary electrons). On the other hand, the minimum kinetic energy $E'_{K_{min}}$ of the photoelectron energy distribution strongly depends on ϕ_s. $E'_{K_{min}}$ corresponds to the so-called secondary edge cut-off and represents those photoelectrons that have just enough kinetic energy to overcome the sample work function. They can be either excited from a bound state just hv below the E^s_{vac} or are higher energy photoelectrons that have lost energy via scattering on their way towards the surface (i.e. secondary electrons). At the surface of the sample, these cut-off electrons have zero kinetic energy, while in the electron analyzer they are detected with a kinetic energy $E'_{K_{min}} = \phi_s - \phi_a$. The right panel of Fig. 12.10 clearly shows how a change in the sample work function (Δ), for example as that induced by molecular adsorption (see later), affects $E'_{K_{min}}$ and not the E'_K of the primary electrons. In this case, a decrease of ϕ_s will result in a higher E_K, but also in a smaller acceleration potential with no net changes to the final E'_K for primary electrons. On the contrary, the zero energy cut-off will move to lower E'_K by Δ.

The analyzer work function can be easily obtained by measuring the maximum of the kinetic energy $(\phi_a = hv - E'_{K_{max}})$, which corresponds to electrons coming from the Fermi level. On the other hand, determination of the sample work function requires knowledge of both the maximum and minimum kinetic energy of the photoelectron energy distribution according to $\phi_s = hv - \left(E'_{K_{max}} - E'_{K_{min}}\right)$, which is equivalent to $\phi_s = hv - E_{K_{max}}$ (defined by Eq. 12.7) or to $\phi_s = hv - E_B^{cut-off}$ (Fig. 12.9).

In practice, a negative bias is often applied to the sample in order to create a further accelerating potential (E_{acc}) felt by the emitted electrons (see Fig. 12.9). This potential ensures both that the work function determination can also be carried out when $\phi_s < \phi_a$ and that the cut-off is easily distinguishable from other sources of low energy electrons. In this case a kinetic energy spectrum is measured where:

$$E'_K = hv - (E_B + \phi_a) + E_{acc} \tag{12.11}$$

12.4 Examples from Molecular and Hybrid Devices

After introducing the basic theories of electronic structure in molecules and solids and some of the basics of photoelectron spectroscopy, we will in the following give some examples of the application of photoelectron spectroscopy to studies on systems that relate to molecular and hybrid solar cells. The interfaces include material combinations responsible for the initial charge separation in the conversion processes. However, of major importance are also the metal contacts to the molecular materials and the following will also include such examples.

12.4.1 Electronic Structure of Well-Defined Molecular Interfaces

We will start with the fundamentals of interfacial energetics with examples of importance for molecular solar cells and other molecular devices. Specifically, this section focuses on the fundamentals of well-defined molecular interfaces and mainly gives examples from small molecule interfaces prepared under ultrahigh vacuum (UHV) conditions.

12.4.1.1 Energy-Level Alignment

Figure 12.11 shows how the molecular energy levels align relative to the Fermi level of a metallic electrode before and after formation of the organic/metal interface as obtained by ultra-high vacuum (UHV) deposition of a thin molecular layer on a clean substrate. When the metal and the molecular material are far away from each other, they share the vacuum level at infinity, E_{vac}^{∞} (Fig. 12.11a). When they come into contact, the organic layer is within the potential of the surface dipole layer of the metal, and its energy levels are changed to a new common vacuum level ($E_{vac}^{m} = E_{vac}^{org}$), according to the Schottky–Mott model (Fig. 12.11b). However, molecular adsorption can also induce the formation of an additional surface dipole which rises or lowers the pre-existing surface potential with the establishment of a new common vacuum level characterized by an abrupt shift Δ of the metal vacuum level (see Fig. 12.11c).

The energy separation between the HOMO level and the E_{vac}^{org} represents the first ionization potential I of the molecular species in the condensed phase which is slightly different from that of an isolated molecule, I_{∞}. In the condensed state, the electronic polarization in the medium surrounding the ionized molecule stabilizes the ion leading to a lowering of the ionization energy from that of the gas phase [10].

The sign and the magnitude of Δ will dictate the energy alignment of occupied and unoccupied states in the molecule with respect to the substrate. As a consequence also the energy separation between the HOMO and the metal Fermi level, also known as hole injection barrier ϕ_b^p, will depend on Δ:

$$\phi_b^p = I - (\phi_m + \Delta) \tag{12.12}$$

where ϕ_m is the metal work function (note that the sign of Δ is negative when the metal vacuum level is lowered by molecular deposition). If the HOMO–LUMO gap E_{gap} of the organic layer is known, we can also determine the electron injection barrier ϕ_b^n:

$$\phi_b^n = E_{gap} - \phi_b^p \tag{12.13}$$

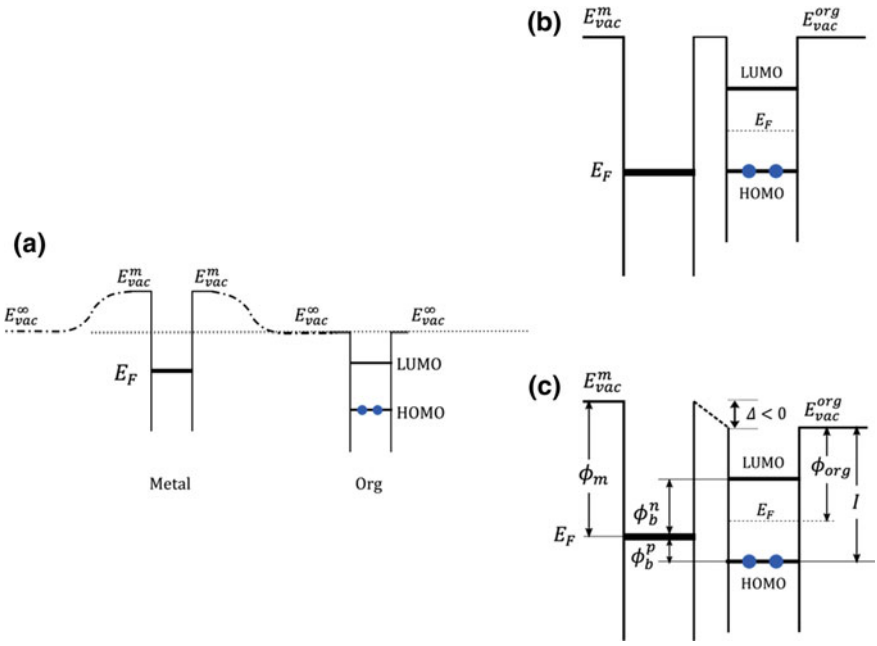

Fig. 12.11 Energy level diagram of metal and molecule: **a** at infinite distance; **b** in contact according to the Schottky–Mott model of a thin film; **c** in contact with formation of an interface dipole which determines an abrupt shift Δ of the vacuum level of the metallic substrate. Adapted from Ref. [10] by permission of John Wiley & Sons Ltd

Note that ϕ_b^p is similar to the HOMO binding energy relative to the metal E_F measured in photoemission spectroscopy, E_B^{HOMO}. However, it is often better defined as the energy difference between the onset of the HOMO peak and the Fermi level reflecting the transition from discrete energy levels to bands with dispersion when forming a condensed molecular film.

Figure 12.12 explains how all the aforementioned physical quantities I, Δ and ϕ_b^p can be determined by photoelectron spectroscopy, which has often been implemented using traditional UPS setups.

The origin for the interface dipole can be very complicated and there are different mechanisms, which are discussed in literature [10, 11]. One effect to consider when a molecule adsorbs on a metal is the so-called "push-back" or "pillow" effect. The tail of the metal electrons that spills into vacuum is pushed back by the Coulomb repulsion arising from the overlap with the electron cloud of the molecule. This suppression reduces the original surface dipole causing a lowering of the work function, i.e. the zero energy cut-off is shifted to higher binding energies $(\Delta < 0)$ (Fig. 12.12). Another phenomenon, which can contribute to the breakdown of the "Schottky–Mott" vacuum level alignment, is a molecule's intrinsic permanent dipole. According to the dipole orientation, a lowering (dipole pointing

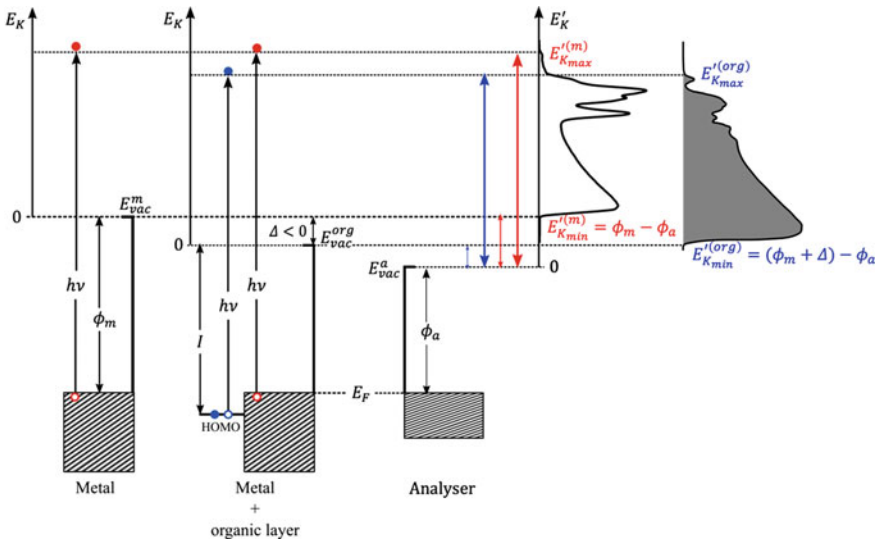

Fig. 12.12 Principle of the UPS study of an organic/metal interface. The right side of the figure shows the UPS spectra arising from the clean substrate (*not filled curve*) and the organic film (*grey-filled curve*). Minimum ($\boldsymbol{E'^{(m)}_{K_{min}}}, \boldsymbol{E'^{(org)}_{K_{min}}}$) and maximum kinetic ($\boldsymbol{E'^{(m)}_{K_{max}}}, \boldsymbol{E'^{(org)}_{K_{max}}}$) energies in both spectra are indicated and their origin clarified by comparison to the electronic structure of the corresponding sample (*left side* of the figure). The ionization potential $\boldsymbol{I}$ for a molecule can be regarded as the equivalent of the work function for a metal solid and derived according to $\boldsymbol{I = h\nu - \left(E'^{(org)}_{K_{max}} - E'^{(org)}_{K_{min}}\right)}$. The work function shift and the hole injection barrier will be equal to $\Delta = \boldsymbol{E'^{(org)}_{K_{min}} - E'^{(m)}_{K_{min}}}$ and $\phi^p_b = \boldsymbol{h\nu - \left(E'^{(org)}_{K_{max}} + \phi_a\right)}$, respectively

away from the surface) or a rising (dipole pointing towards the surface) of the work function can be observed. Another contribution is charge redistribution between the molecule and the substrate. In this case the sign of Δ is not always predictable, in particular when chemical bonds are formed, but usually a rising of the work function is observed when charge flows from substrate to molecule and a lowering is observed when charge flows from molecule to substrate.

Often most of the work function changes occur with the formation of the first molecular layer. Usually, after monolayer coverage is reached the work function changes much less. Shifts past one monolayer can result from structural changes (see OTiPc/graphite example below) and band bending effects (Sect. 12.4.1.2).

An instructive example on the work function changes caused by deposition of a molecule with a permanent dipole is given by the titanyl phthalocyanine (OTiPc)/graphite interface, which has been extensively studied by the group of *N. Ueno* [12–14]. In the case of graphite, the push-back effect is nearly negligible allowing to examine only the effect of the molecule dipole moment. As shown in Fig. 12.13a, OTiPc has an electric dipole moment $P = 1.43D$ perpendicular to the molecular plane and pointing towards the Ti atom.

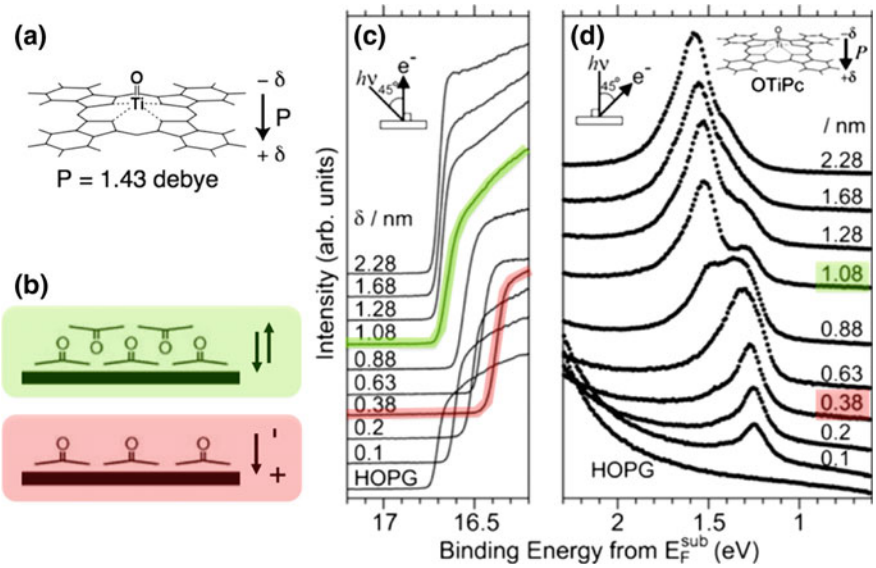

Fig. 12.13 **a** Molecular structure of OTiPc and schematics of the direction of the molecular dipole moment. **b** The schematic film structure and molecular orientation of OTiPc on graphite (HOPG, highly oriented pyrolytic graphite) for coverages of up to one monolayer (*red*) and between 1 and 2 monolayers (*green*). (*Right panel*) UPS spectra as a function of the OTiPc coverage on HOPG in the zero energy cut-off region (**c**) and in the HOMO band region (**d**). The coverage is given as a thickness, δ, where δ = 0.38 nm corresponds to 1 monolayer and δ = 1.08 nm corresponds to a bilayer. **a** Reprinted from [14], with permission from Elsevier. **c** and **d** reprinted figure with permission from Ref. [13]. Copyright 2006 by the American Physical Society

Submonolayer depositions of OTiPc (thickness $\delta < 0.38$ nm for this example) induce an increase of the sample work function as seen by the shift of the zero energy cut-off to lower binding energies (see Fig. 12.13c). The increase in the work function indicates that the dipole moments of the molecules are directed towards the surface suggesting an upward molecular orientation in which the oxygen atoms point outwards to the vacuum (Fig. 12.13b, red sketch). Up to 1 ML ($\delta = 0.38$ nm), the sample work function changes almost linearly with the coverage. Past one monolayer coverage, the work function starts decreasing again. This can be explained by a change in the molecular orientation of the second molecular layer, which has a downward orientation of the oxygen atom (towards the surface, Fig. 12.13b green sketch). The upward and downward configurations cancel each other's dipoles leading to the original work function after the bilayer is completed. After that no major changes are observed when increasing the coverage. It is worth noting that the work function shift between the first and second layer is very similar to the corresponding shift observed in the binding energy of the HOMO peak in full agreement with Eq. 12.12.

In contrast to the example above, most often work function changes result from the sum of counteracting contributions and it is a challenge to identify and

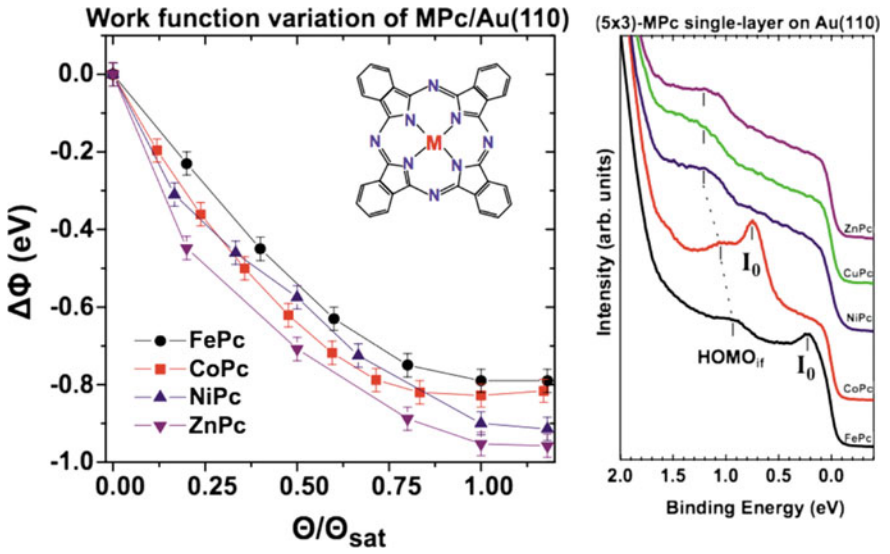

Fig. 12.14 *Left panel* Work function variation as a function of the TMPc coverage (Θ) on Au (110). The saturation coverage Θ_{sat} corresponds to the completion of one monolayer. *Inset* sketch of the TMPc molecule. *Right panel* UPS spectra in the region close to the Fermi level for TMPc monolayers. Reprinted figures with permission from Ref. [15]. Copyright (2010) by the American Physical Society

disentangle them. In that respect the comparison of UPS spectra acquired for a same family of molecules on a specific substrate can help in understanding the origin of Δ. Figure 12.14 shows an example of this for transition metal phthalocyanines (TMPcs) on Au(110) [15]. A drop in the work function is observed upon deposition for all four different TMPcs. However, the magnitude of the drop varies for the different molecules with a work function decrease of 0.79 eV for FePc, of 0.83 eV for CoPc, of 0.90 eV for NiPc, and of 0.95 eV for ZnPc at completion of one monolayer ($\Theta = \Theta_{sat}$). The smaller reduction for FePc and CoPc is consistent with the presence of a charge transfer from the substrate to the molecule (i.e. to an empty 3d-like state on the metal) that counteracts the push-back mechanism. This is confirmed by the occurrence of interface states (I_0) only in the Fermi energy region of FePc/Au(110) and CoPc/Au(110) (right panel of Fig. 12.14).

12.4.1.2 Fermi-Level Alignment and Band Bending

For an interface with an organic layer ≫ monolayer, Fermi-level alignment and effects similar to band bending should also be considered. As shown at the interface of Fig. 12.11, the work functions for the electrode and the organic layer are different and the Fermi levels alignment is not established. If the amount of available mobile carriers in the organic layer is sufficiently large (either in a rather thick

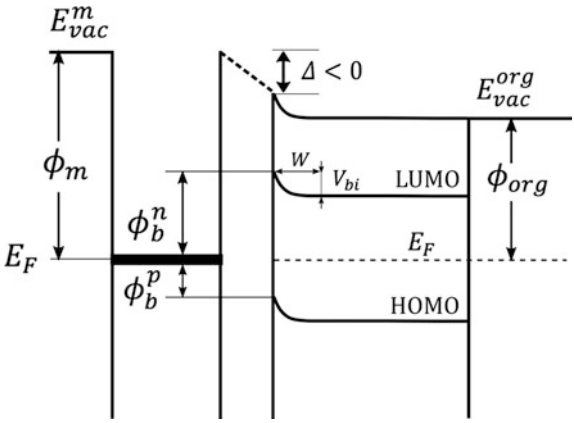

Fig. 12.15 Interfacial energy diagram between a metal and a thick organic layer with band bending of the organic material indicated. Adapted from Ref. [10] by permission of John Wiley & Sons Ltd

organic film or organic layer with good semiconducting character), there will be a substantial flow and redistribution of charge across the interface until the Fermi levels are aligned. In the case of Fig. 12.11c, $\Phi_{org} < \Phi_m$, electrons flow from the organic layer to the metal leaving the organic layer positively charged within a depletion region of width W (space charge layer, SCL) and the metal becomes negatively charged. The *band bending* (or *energy level bending*) is a result of the internal electric field that accompanies an extended charge separation at the interface (see Fig. 12.15). The built-in potential (V_{bi}) in the space charge layer corresponds to the difference of work functions between the electrode (corrected by the amount of Δ) and the organic layer:

$$V_{bi} = (\Phi_m + \Delta) - \Phi_{org} \tag{12.14}$$

Because of the large band gap of organic semiconductors and consequently small amount of available mobile carriers, band bending is expected to occur in a wide space charge layer, which can be investigated by means of UPS thickness-dependent studies (from a few layers to several nm). The main problem regarding the application of the PES technique to the study of band bending, is that final-state screening shifts (see Sect. 12.3.2) and charging effects can complicate the interpretation of the photoemission spectra [16]. In particular, the core-hole screening effect due to the high polarizability of a metal substrate can induce energy level shifts that can be easily mistaken for downward band bending. Such a problem can probably be neglected when both the substrate and the overlayer have similar screening capabilities, as in the case reported by *E. Johansson* et al. [17] where a hole-conductor (HC) molecule (Fig. 12.16a) was deposited on the semiconducting $TiO_2(111)$ surface. In this case the observed HC energy level shifts (which are shown in Fig. 12.16b and summarized in the schematic of Fig. 12.16c) were interpreted in terms of a continuous charge transfer from the molecule to the substrate in order to equilibrate the Fermi level of the two materials. The binding energy of the HC peaks in the $\gg$35 Å film was only $\sim$0.08 eV higher than the

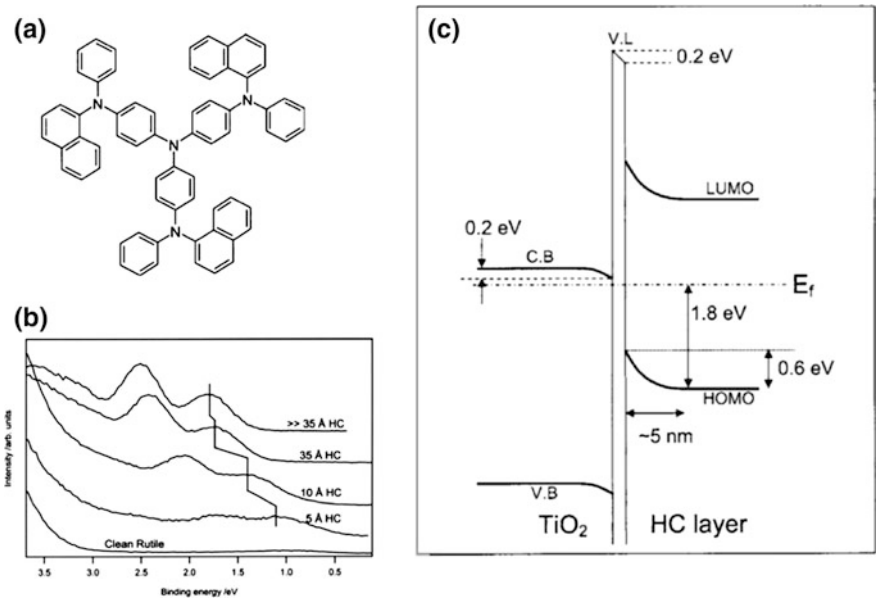

Fig. 12.16 **a** Molecular structure of a triarylamine based hole-conductor (HC) molecule. **b** UPS thickness dependent spectra for HC deposited on rutile TiO_2(110) surface. **c** A schematic energy-level diagram summarizing the shifts of the TiO_2 and HC levels going from the clean substrate to multilayer of HC molecules. Reproduced from [17], with the permission of AIP Publishing

binding energy of the peaks in the 35 Å film, suggesting that the equilibrium process is almost completed after depositing 35 Å of HC.

Surface potential measurements using Kelvin probe methods represent a valid alternative for unambiguously investigating intrinsic band bending leading to Fermi-level alignment. However, basic studies performed on high purity molecular films prepared under ultra-high vacuum (UHV) have shown that Fermi-level alignment does not always happen even in 100 nm thick films [18]. This is probably due to the high purity of the sample (low concentration of impurities/doping), which requires a much wider space charge layer. In order to reduce the SCL thickness and observe band bending behaviour, controlled doping of organic layers has proven to be a successfully strategy. Figure 12.17a show the concept of doping for ZnPc (host) and tetra-fluoro-tetracyano-quinodimethane-F_4-TCNQ (dopant) [19, 20]. The match between the ZnPc ionization energy and the Fe_4-TCNQ electron affinity suggests an energetically favourable electron transfer from the host to the dopant, resulting in efficient p-type doping. Figure 12.17b shows UPS measurements for increasing thickness of ZnPc: 0.3% F_4-TCNQ and ZnPc: 3% F_4-TCNQ deposited on Au and the corresponding interface electronic structure (Fig. 12.17c). As expected, the 3% doping induces a larger molecular level bending (0.18 eV closer to the Fermi level) and a narrower space charge region than the 0.3% doping (30–40 Å vs. 120 Å).

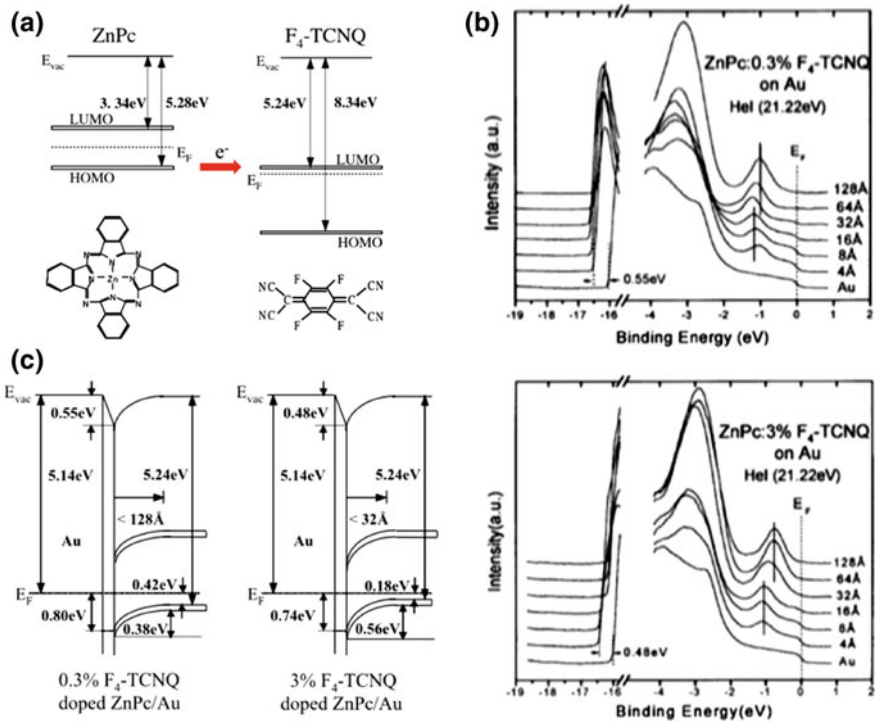

Fig. 12.17 **a** Chemical structure of ZnPc and F_4-TCNQ and concept of the doping process. Doping concentrations of a few mol% were achieved by co-evaporating the host and the dopant with different evaporation rates. **b** UPS spectra acquired for increasing thickness of ZnPc: 0.3% F_4-TCNQ (*top graph*) and ZnPc: 3% F_4-TCNQ (*bottom graph*) on Au. **c** Interfacial energy level diagrams for ZnPc: 0.3% F_4-TCNQ (*left*) and ZnPc: 3% F_4-TCNQ (*right*). Reprinted from Ref. [19] with permission from Elsevier

As a final evidence of Fermi-level alignment, *Ishii* et al. proposed a criterion that the energy separation between the vacuum level of the organic layer and the Fermi level does not depend on the contact material [18]. *Olthof* et al. showed that doped organic layers can satisfy such a requirement by comparing UPS data of a doped hole conductor on substrates with different physical and chemical properties and which are commonly used in device fabrication, i.e. Ag, ITO (Indium Tin Oxide) and PEDOT:PSS [21]. Different magnitudes and directions of band bending were found, but the work functions of thick films were very similar indicating that Fermi-level alignment occurs independent of the contact material.

An alternative and more recent approach for studying the energy alignment between materials involves the use of hard X-ray for the measurement of buried interfaces. These measurements make use of the increased probing depth when using HAXPES. Using this approach, the energy level alignment in a fully assembled three material (TiO_2/molecule/polymer) system was characterized

[22, 23]. The relative shifts of the Ti 2*p* core level of TiO_2 and the S 2*p* core level of the conducting polymer poly-3-hexylthiophene (P3HT) were measured for several molecules with different magnitudes and directions of dipole moment. Such measurements can either give an insight into how the energy alignment between two materials can be controlled [22] or into what effect particular dye molecules have on the energy of the TiO_2 in relation to other components in the solar cell [23]. This method is particular relevant for ex situ prepared samples, as only buried interfaces are of importance and the effect of surface contamination on the measurements becomes negligible.

12.4.2 Energetics in Polymer Solar Cells Including New Opportunities with Time-Resolved Measurements

In polymer-based solar cells, an organic polymer is used as the main light absorbing material to harvest the solar light. Upon light absorption in the polymer, an electron is excited to an unoccupied level in the polymer and an excited state (exciton) is formed. The binding energy of the exciton is usually rather large, and the electron is therefore bound to the positive hole. To achieve separation of the excited electron and the hole, the polymer is combined with electron accepting molecules such as fullerene derivatives. After light absorption the electron can transfer to the fullerene and separation of the electron and the hole is thereby achieved. However, during the transfer of the electron from the polymer to the fullerene potential energy is usually lost, and the maximum possible voltage of the solar cell is decreased. More generally understanding and controlling charge carrier injection and energy matching is of importance for optimizing these devices. Much of the discussions in the Sect. 12.4.1 also applies to polymer solar cells. As for single-molecule thin films, polymer properties depend to a first approximation on the molecular building blocks with charge localization. Therefore, interface energetics can be fine-tuned by a structural modification of these building blocks. In this context, PES has been an excellent tool to follow such fine-tuning [24]. Many of the interfaces with polymers are however even more complex. Some such complexity arises from the fact that polymer interfaces are often prepared ex situ (outside of a vacuum environment) allowing for some contamination of the surfaces. This contamination may shift the material work functions and limit the direct contact between active materials.

The energy matching between the active materials can also be followed. Examples include the potential energy loss related to the energy levels of the polymer and the fullerene. The energy of the lowest unoccupied molecular orbital (LUMO) of the fullerene should have a lower energy compared to the LUMO of the polymer for efficient electron transfer. The difference in energy should be large enough for the electron transfer to be quicker than relaxation of the excited electron back to the ground state.

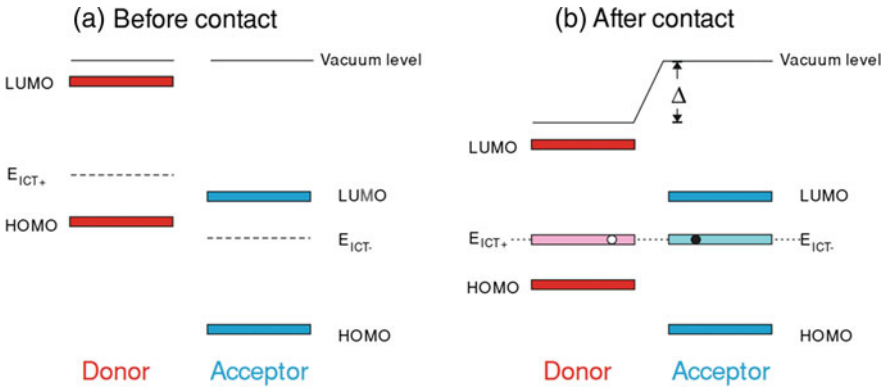

Fig. 12.18 Energy level alignment diagrams for a donor–acceptor solar cell before (**a**) and after contact (**b**) between the donor (polymer) and acceptor (fullerene). After contact the Fermi levels are in equilibrium and new states are formed at the interface between the materials. Figure reprinted from Ref. [19] with permission from Wiley

The relation between the energy levels of the polymer and the fullerene is, therefore, highly important for the function and efficiency of the solar cell. Photoelectron spectroscopy has been used to measure the valence electronic structure of different polymers and fullerenes used in solar cells (see e.g. [25–27]). From the measurements of the electronic structure it was found that the energy levels of the individual polymer and fullerene molecules may be rather different to the energy levels when they are combined in the solar cell (see Fig. 12.18) [27]. The charge transfer states formed when combining the two materials were also found to affect the recombination (loss) of the photogenerated charges in the solar cell.

The energy-level changes found for the combination of the polymer and the fullerene is similar to the changes observed for small molecules on surfaces as discussed in the sections above. The effects of the interactions between materials are, therefore, very important to consider also for the solar cell function and in the design of new molecules for solar cells. Photoelectron spectroscopy can in this case be a useful tool to determine the energy levels for these combinations of molecules, in order to understand and optimize the solar cell function.

The PES technique is constantly under development that will give new opportunities in the future. One such development is the combination of the technique with a (visible) laser pump, which can generate excited states in the material. In this case, the binding energies of electrons related to the excited state of a material can be measured directly. An example of this is shown for the polymer PCPDTBT, which is often used in polymer solar cells, in Fig. 12.19 [28]. Here, the sample was irradiated by both a 800 nm laser pulse and a XUV pulse with a photon energy of 39 eV generated by the same femtosecond laser. The relative arrival times of the pulses were controlled through a delay stage. Arrival of the XUV pulse before the 800 nm pulse leads to the measurement of a normal (ground state) photoemission

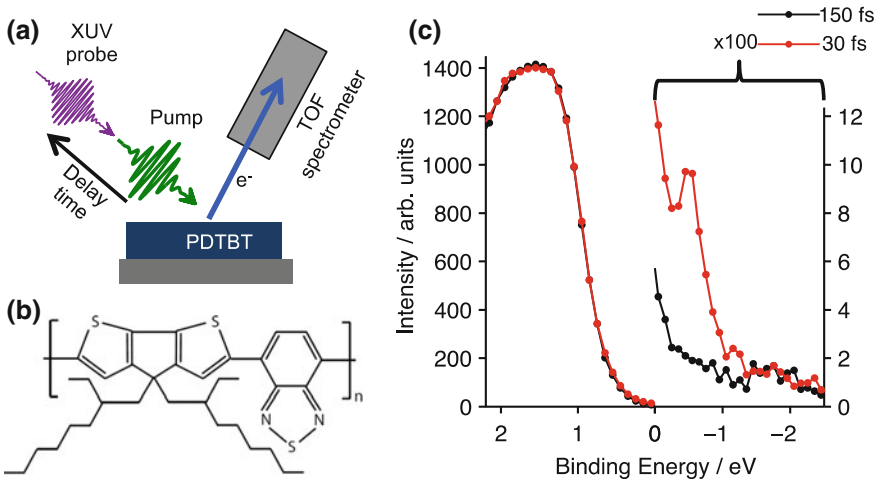

Fig. 12.19 **a** Concept of time-resolved photoelectron spectroscopy with XUV probe and visible pump pulses and a time-of-flight (TOF) spectrometer. **b** Molecular structure of the polymer PCPDTBT. **c** Time-resolved photoelectron spectra of PCPDTBT where the XUV probe arrived at the sample 150 fs before the 800 nm pump pulse (*black line*) and 30 fs after it (*red line*). Reproduced from Ref. [28] with permission from the PCCP Owner Societies

spectrum, while measurements, where the 800 nm pulse arrived at the sample 30 fs before the XUV pulse shows an additional signal above the valence band edge assigned to photoemission of electrons in the excited state of PCPDTBT. By varying the delay time between the two pulses it was possible to follow the evolution of the excited state signal in terms of energy distribution and decay back to the ground state.

12.4.3 Application to Dye-Sensitized Solar Cells—Molecular and Electronic Structure

12.4.3.1 Introduction

In dye-sensitized solar cells (DSCs), dye molecules are attached to a semiconductor electrode in order to absorb visible light (Fig. 12.1). The semiconductor consists of nanoparticles fused together to a mesoporous network, which has a large surface area where dye molecules can attach. Compared to the geometrical area of the semiconductor electrode the "inner" surface can be more than 1000 times larger, and a large number of dye molecules can attach to this surface. Although a single dye molecule only absorbs little light, the dye-sensitized mesoporous electrode can absorb a large fraction of light in the visible region of the solar spectrum. After light absorption excited electrons are injected from the dye molecules into the

semiconductor nanoparticles, which are usually TiO_2. The injected electrons diffuse in the mesoporous electrode until they reach the contact on the substrate. After electron injection the dye is in an oxidized state and can be reduced back to the neutral state (regenerated) by electron transfer from a liquid electrolyte with a redox couple in contact with the dye, or by electron transfer from a hole transporting material (HTM). Another way to describe this process is as hole transfer from the dye to the electrolyte or to the HTM. The hole is then further transported through the electrolyte or the HTM to the other contact. A photovoltage is, hence, built up between the contacts during illumination, and the DSC shows a photovoltaic effect. At the same time several recombination processes occur, in which the photogenerated electrons and holes are lost, which reduce the photovoltage.

The kinetics of the different electron transfer processes occurring during illumination depend on a number of factors. Some of these factors can be assessed through the study of dye-sensitized electrodes by PES, for example, the dye attachment to the nanoparticle surface and the geometry of the dye molecule on the surface and the energy levels of the dye molecule, the semiconductor, and the HTM (or redox couple), and also the distribution of the different electronic orbitals in the dye molecule. In particular, PES allows for the study of these material properties in relation to each, which allows to directly address how the materials function in the solar cell. Below we will describe examples of how photoelectron spectroscopy (PES) can be used to study the materials in the DSC and the interfaces important in the solar-to-electricity conversion process.

12.4.3.2 Binding and Geometry of Dye Molecules on Semiconductor Surfaces

The surface of the semiconductor nanoparticle, the dye attachment to the semiconductor and the geometry of the dye molecule on the surface is very important for the electron processes occurring during illumination in a DSC as mentioned above. Therefore, many experiments have been performed to address these factors and we will here specifically show some examples from photoelectron spectroscopy measurements. Since PES usually is very surface sensitive (when using soft X-rays), these factors can be efficiently studied with PES. PES also give element specific information, and can also be used to analyze the interaction and binding between different atoms, which is an advantage when performing these investigations.

The attachment of the dye molecules to the semiconductor surface have been studied several times using PES [29–37]. The most efficient dye molecules usually have carboxylic acid groups that anchor to the TiO_2 surface, and this anchoring can be specifically studied using a model system with a clean TiO_2 surface in ultra-high vacuum (UHV) and small molecules containing carboxylic acid groups deposited onto this surface [30]. A very clean model system is necessary to study the attachment between TiO_2 and the carboxylic acid, since oxygen and carbon in carboxylic acid is also present in many contaminants that are observed on TiO_2 (and most other surfaces) under ambient (non UHV) conditions. The oxygen and carbon

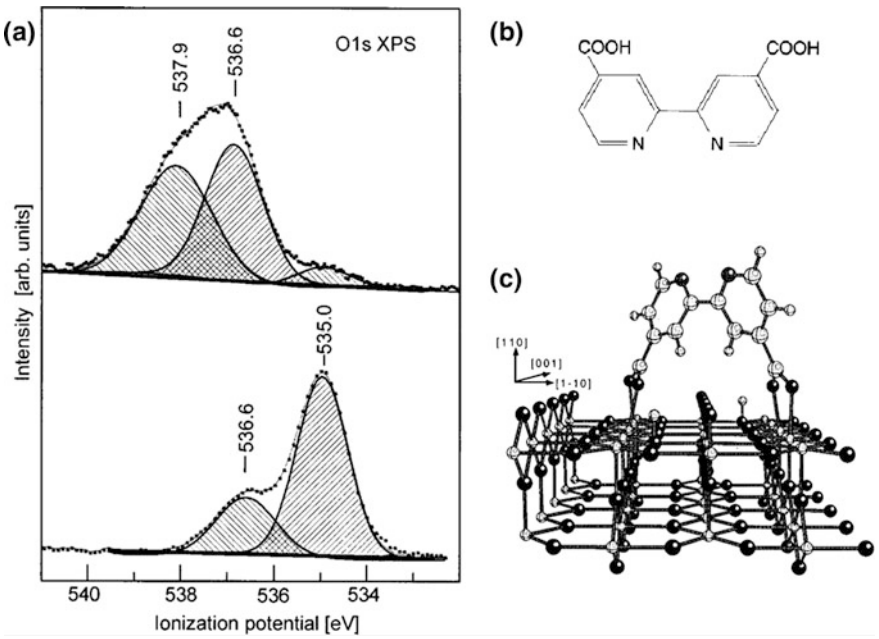

Fig. 12.20 **a** O1s PES spectrum of a multilayer of bi-isonicotinic acid on TiO_2 rutile (110), *top*, and O1s spectrum of a submonolayer of bi-isonicotinic acid on TiO_2 rutile (110), *bottom*. **b** Molecular structure of bi-iosnicotinic acid. **c** Theoretically optimized adsorption geometry of bi-isonicotinic acid on TiO_2 rutile (110) inferred to be the likely absorption geometry from PES measurements. Reprinted from [30], with the permission of AIP Publishing

atoms from the carboxylic acid can in the UHV system then be studied without presence of contaminants, which makes the interpretation easier. An example of O1s PES spectra of bi-isonicotinic acid on TiO_2 rutile (110) is presented in Fig. 12.20 [30]. In the spectra of a multilayer of bi-isonicotinic acid on TiO_2, three different peaks corresponding to the oxygen in TiO_2 and the two different types of oxygen in the carboxylic group can be observed. For a monolayer of bi-isonicotinic acid on TiO_2 only one type of oxygen from the carboxylic group can be observed, which suggests that the oxygen atoms have a similar chemical surrounding and it was therefore concluded that the carboxylic unit binds to the TiO_2 in a 2-bidentate configuration [30].

From experiments of this type, we can obtain a very detailed picture of the binding between the dye molecule and the semiconductor surface at an atomic level, which, for example, is very important for understanding and modelling the electron transfer between the dye and the nanoparticle.

In addition to the attachment of the dye to the surface, the geometry and configuration of the dye molecule at the surface will be very important for the electron transfer processes. Different methods in PES can be used to investigate this, and one example for the organic dye D5 on mesoporous TiO_2 is shown in Fig. 12.21

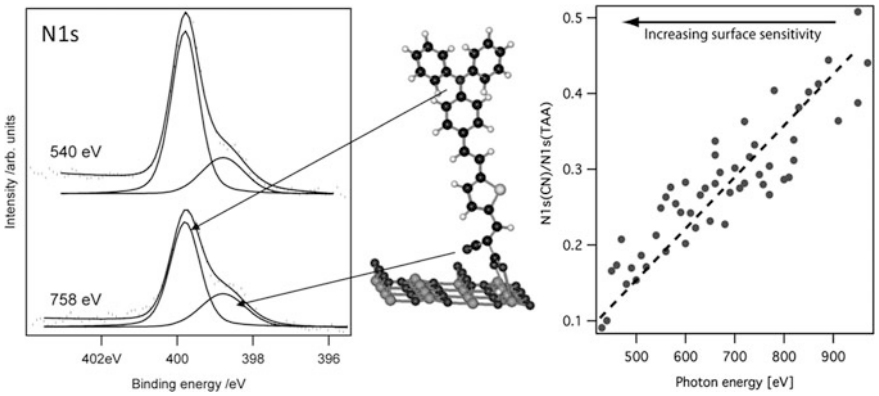

Fig. 12.21 *Left* N1s PES spectra of the organic dye D5 on mesoporous TiO_2 deposited from solution. The spectra were measured using two different X-ray energies (758 and 540 eV). *Right* the ratio of the different signal intensity of the N1s spectral contributions (cyano (CN) and triarylamine (TAA)) from spectra measured using different X-ray energies. Reproduced from Ref. [29] by permission of John Wiley & Sons Ltd

[29, 38]. From the intensity relation between the signals from the triarylamine (TAA) unit and the cyano (CN) unit in the dye, it is possible to analyze the geometry of the dye on the TiO_2 surface. The PES signal is lower for the signal from the CN unit compared to the TAA unit, and this difference increases for more surface sensitive measurements (using lower X-ray photon energy). It was possible to conclude that the dye is standing up on the TiO_2 surface with the TAA unit pointing out [38]. Similar measurements have been performed for a series of organic dyes containing TAA and CN units to investigate the geometry of the dye molecules on the surface, which have important implications for the function in the solar cells [39, 40]. These examples show some of the possibilities for PES to both determine the chemical bond between the dye and the surface, and also the geometry of the dye on the semiconductor surface.

12.4.3.3 Valence Molecular Orbitals

The light absorption process and charge transfer processes from the dye is dependent on the electronic structure of the dye molecule. Using PES, it is possible to obtain information about the atomic composition of the different molecular orbitals in the dye (compare to Fig. 12.2). For example, PES with different X-ray photon energy will result in different sensitivity for different elements due to the difference in cross-section for X-ray absorption and emission of electrons. By comparing measurements at different X-ray energies it is therefore possible to find the atomic composition of the valence orbitals. An example of the valence structure of two ruthenium based metal-organic dye is shown in Fig. 12.22. The measurements were performed using 2800 eV, where the cross-section for Ru 4d is much

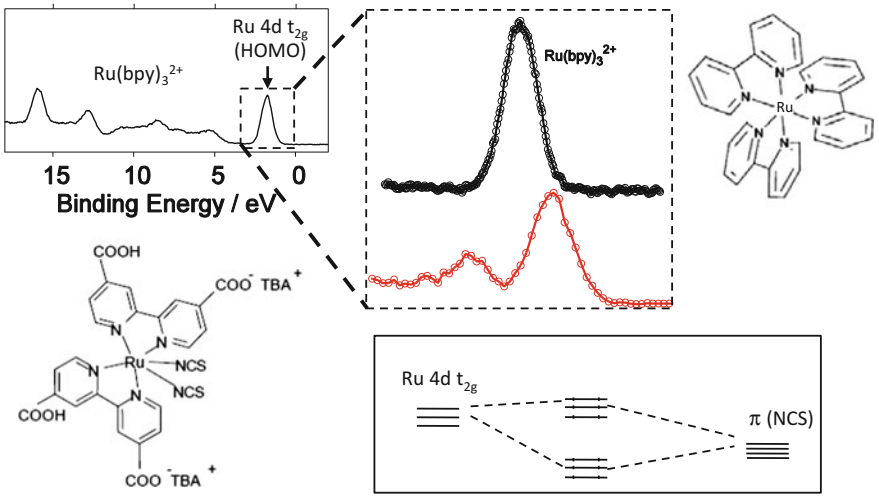

Fig. 12.22 Valence electronic structure of the $Ru(bpy)_3^{2+}$ (see *top left*) measured at 2800 eV. Also shown is a zoom of the Ru4d level of $Ru(bpy)_3^{2+}$ together with the N719 dye in which one bpy unit is exchanged by two NCS units (see *bottom left*). The highest occupied orbitals in the NCS units over lap in energy and symmetry with the Ru4d t_{2g} set and this level is split into two energy levels containing where the outermost level has a higher Ru4d character. A simple mechanism for this interaction is shown in the figure at the bottom right

stronger than the cross-section for the organic parts of the dye molecule [41]. The spectra clearly show the Ru 4d levels observed as a single peak for $Ru(bpy)_3^{2+}$ (t_{2g} manifold). In the N719 dye, two peaks are observed for the Ru 4d levels. This can be rationalized by an overlap in energy and symmetry of the highest occupied orbitals in the NCS units with the Ru4d t2 g set leading to a splitting of this level (Fig. 12.22) [42].

Another method to obtain element specific information about the valence electronic structure is to use resonant PES. In resonant PES, the valence electronic structure is measured using a range of X-ray energies, where some of the X-ray energies are "resonant" in that an electron is excited to an unoccupied orbital from a specific core electronic level. From this measurement, it was for example possible to determine the contribution of different nitrogen atoms in the valence electronic structure of a dye molecule [43].

12.4.3.4 Energy-Level Mapping

For the charge transfer processes in the DSCs, the energy alignment of the dye, the semiconductor and the HTM is very important. For the electron transfer from the dye to the semiconductor to be efficient, the excited electron in the dye should gain (potential) energy by transfer to the semiconductor. Thereafter, the electron in the HTM should gain energy by transfer to the positively charged dye. Therefore, it is

important to measure the energy levels of these materials, in order to understand and optimize these processes. Usually the energy levels of the different materials are measured separately (for example by electrochemistry) and then compared to investigate if the materials should work together. However, it is important to measure the energy levels of the materials, when they are in contact (for example the dye on the TiO_2 surface or the HTM on the dye) since there may be interactions between the materials and also dipoles influencing the energy level alignment in the system.

In Fig. 12.23, the valence electronic structure of different rylene dye molecules attached to a mesoporous TiO_2 surface and the energy alignment derived from these measurements is shown. The XPS results indicated that ID28 and ID1 have more favourable energetics for electron injection into TiO_2 than ID176 and indeed electron injection was much more efficient for ID28 and ID1 than for ID176 in absence of any other components to the system. This result was not predicted by electrochemical measurements, which suggested similar redox potentials for the excited states of both ID1 and ID176 in relation to an external reference electrode [23].

From measurements of the valence electronic structure it is possible to compare the outermost electronic structure of different dyes on a TiO_2 surface. Comparing

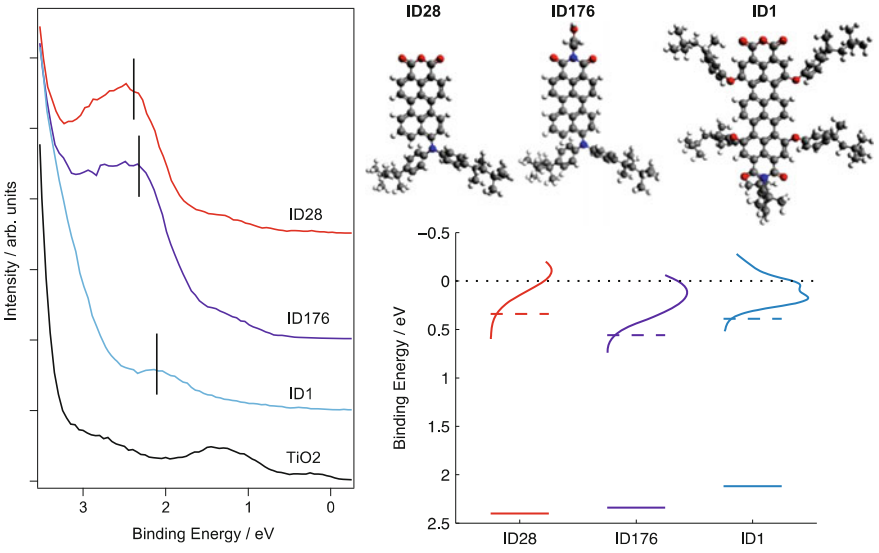

Fig. 12.23 *Left panel* Valence electronic structure of different rylene dye molecules (*top right panel*) attached to a TiO_2 surface. The spectra were energy calibrated in relation to the TiO_2 Fermi edge, which was measured for the bare TiO_2 substrates. *Bottom right panel* The energy alignment of the rylene dyes derived from the HOMO peaks measured with XPS with excited state energies added from the addition of the absorption energies to the HOMO level in relation to the TiO_2 conduction band pinned to the Fermi level. Reproduced from Ref. [23] with permission from the PCCP Owner Societies

TiO_2 without dye molecules and TiO_2 with dye molecules, the highest occupied electronic structure of the dyes is clearly observed. Figure 12.23 shows that energy differences of the highest occupied electronic structure of the dyes can be quantified. Combining this information with the absorption spectra for the dyes an approximate energy-level diagram can be obtained for these systems, which is useful in analyzing the different electron transfer processes in the system.

12.4.3.5 HTMs and Electrolytes

After light absorption by the dye and injection of the excited electron to the semiconductor, the dye is regenerated by the redox couple in the electrolyte or by the HTM as described above. For an efficient regeneration of the dye (efficient electron transfer from the HTM to the dye), the energy levels of the dye and the redox couple/HTM must be appropriate for this electron transfer, and the energy loss in the electron transfer should be minimized in order to have an optimal voltage from the solar cell. For solid HTMs, the energy levels for the complete photovoltaic interface, TiO_2/dye/HTM can be measured using PES, see for example Ref. [38]. The energy levels for the complete system can then be measured and compared to understand more about the driving force for the electron transfer processes. In addition to the energy levels, the molecular structure and the geometry at the interfaces are very important for the electron transfer processes. For example, in Ref. [38] the TiO_2/dye/HTM interface was investigated using PES for different HTMs and it was concluded that the HTM may in some cases penetrate through the dye layer, which results in a direct contact between the TiO_2 and different HTM, see Fig. 12.24. This direct contact is disadvantageous for the solar cell function since the back electron transfer from the TiO_2 to the HTM can increase, which means that the photogenerated charges can recombine rather quickly in such a system.

Using PES it is therefore possible to investigate the complete TiO_2/dye/HTM photovoltaic interface in a solid-state DSC. Also the effect of additives to the HTM, often used in solar cells can be investigated. For example, the effect of additives of

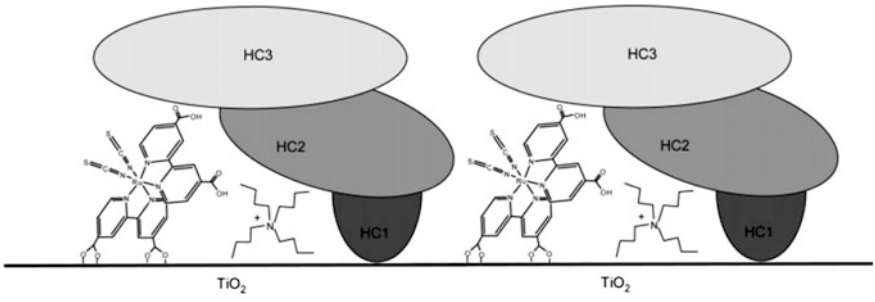

Fig. 12.24 Suggested molecular structure for TiO_2/dye/HTM interfaces for different hole transport materials (HC1, HC2 and HC3) obtained from PES results in Ref. [38]

the HTM spiro-OMeTAD was investigated using PES [44]. It was concluded that the additives can be used to shift the Fermi level of the HTM, which suggests that the HTM is partly oxidized.

PES measurements of DSCs with liquid electrolytes are more difficult, as PES measurements are generally performed in ultra-high vacuum. However, with the development of new instruments for measurements on liquids in vacuum it has been possible to measure the liquid iodide based electrolyte using PES [45]. Other experiments have shown the possibility to perform PES measurements of a dye-sensitized TiO_2 surface under higher pressures than is usually used in PES, and enables the investigation of the influence of the electrolyte solvent and of water on the dyes on the surface of TiO_2 [37]. The development of the PES techniques will therefore further increase the possibilities to measure on the most relevant complete DSC systems and from these measurements obtain essential information about the molecular and atomic-level properties of these systems.

12.4.4 Perovskite Solar Cells—Bulk and Interface Structure

The use of PES for the characterization of hybrid organic–inorganic perovskites has developed in the last few years simultaneously with their application in solar cells and PES has been shown to be an important tool for the understanding of their function in these devices. Core level spectroscopy from soft to hard X-rays has been used to characterize the chemical composition and stoichiometry of the materials from the surface to the bulk. This has included investigations of the stability both towards X-ray illumination and to external factors such as humidity and sample heating. Valence band measurements with ultraviolet photons to hard X-rays have been used to characterize the valence band structure and to determine the Fermi level position and the energy alignment with other components in the solar cell. Below, we will show examples, which highlight the use of photoelectron spectroscopy for the different aspects of perovskite solar cell characterization.

12.4.4.1 Valence-Level Spectroscopy and Energy Alignment

Figure 12.25 shows the valence spectrum and crystal structure of $CH_3NH_3PbI_3$ ($MAPbI_3$, methylammonium lead triiodide, the perovskite used in the earlier perovskite solar cells [46, 47]) measured with a photon energy of 2480 eV [48]. A comparison to theory shows the character of the electronic structure at different energies. The valence band of the perovskite consists mainly of electrons associated with iodide p-states with some smaller contribution from lead p-states. The character linked to the cation $CH_3NH_3^+$ is mostly found at higher binding energies.

For valence band measurements of perovskite materials, HAXPES with photon energies > 2000 eV is of particular interest: At these energies, the orbitals from the heavy elements (Pb and I), which mostly contribute to the perovskite valence band

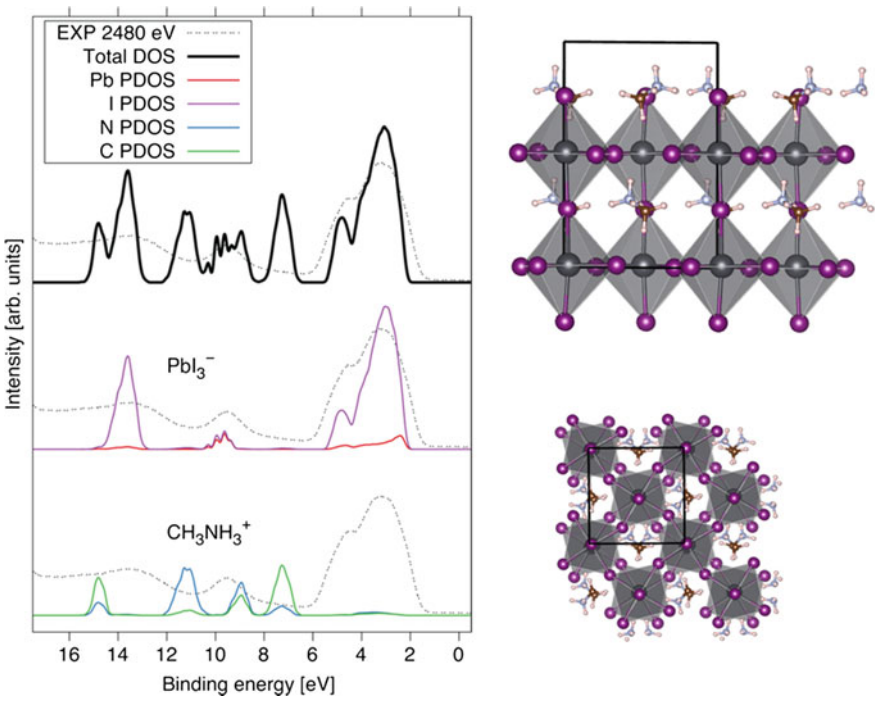

Fig. 12.25 *Left panel* Experimental valence structure of $MAPbI_3$ measured with a photon energy of 2480 eV compared to the calculated total and partial density of states (total DOS and PDOS). *Right panel* The geometry optimized crystal structure of tetragonal $CH_3NH_3PbI_3$ using the PBE functional and 800 eV cut-off using VASP 5.2. *Left panel* Reprinted with permission from [48]. Copyright (2014) American Chemical Society

(Fig. 12.25) have higher absorption cross sections compared to orbitals from carbon, nitrogen and oxygen. Furthermore, the higher probing depth allows for the determination of a valence band structure, which becomes representative of the bulk of the sample with little contribution from surface defects. Both the cross sections and the decrease in surface sensitivity also help to reduce the contribution from contaminants such as oxygen and carbon, which are typically found on the surface of ex situ prepared samples.

While the development of perovskite solar cell started from a surface sensitized-type liquid type solar cell, it has developed to a more traditional thin film solar cell, in which different n- and p-type materials can be used as selective contacts for the perovskite. XPS and UPS studies have been used to determine the energy alignment with different contact materials. This has included the evaporation of hole conducting materials and the study of their band bending at the interface with the perovskite [49–51]. Furthermore, perovskite materials have been studied after deposition onto different substrates [52, 53]. Here, it was found that the distance between the valence band edge and the Fermi level observed for the

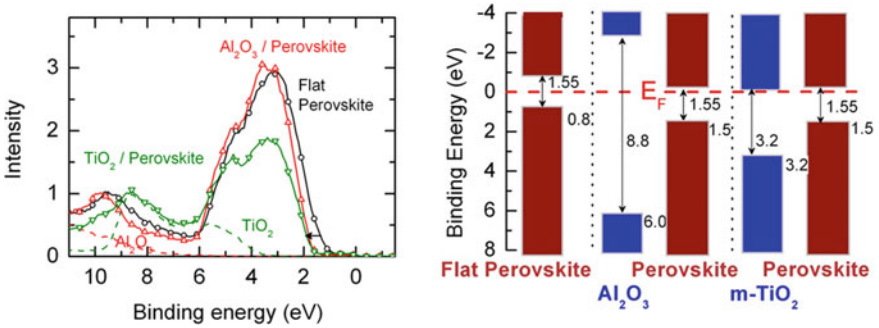

Fig. 12.26 *Left panel* Valence band spectra of perovskite films deposited on mesoporous TiO_2 (*green inverted triangles*) and Al_2O_3 (*red triangles*) and as a thicker film on a conducting glass substrate (*flat perovskite*, *black circles*) compared to spectra of mesoporous TiO_2 (*green dotted line*) and Al_2O_3 (*red dotted line*) measured with a photon energy of 4000 eV. *Right panel* Energy diagrams estimated by addition of the band gap to the valence band maxima determined from the HAXPES spectra. All energies are referenced to the Fermi level at 0 eV binding energy. Reprinted with permission from [53]. Copyright (2014) American Chemical Society

perovskite depends on the substrate. Figure 12.26 shows an example for this of $MAPbI_3$ with $PbCl_2$ added in the synthesis where the valence band was measured for the material on different substrates. From the energy diagrams inferred from a combination of the HAXPES measurements and the known band gap values of the materials shows that the perovskite appears n-type on mesoporous TiO_2 and Al_2O_3 layers, while the Fermi level is in the middle between the valence and conduction bands for a thicker film of perovskite on a conducting glass substrate. These properties are characteristic of intrinsic materials with few defects.

12.4.4.2 Chemical Composition

The development of perovskite solar cells in the past few years has included the development of perovskite structures containing different anions and cations in its structure. Furthermore, different film preparation methods have been developed. Both these developments have led to significant improvements in the power conversion efficiencies of devices. Core-level photoelectron spectroscopy can be an important tool in enabling these developments, as it can be used to confirm the chemical structure and stoichiometry of new materials at the surface and towards the bulk. An example of this is shown in Fig. 12.27, where films were measured after different reaction times of PbI_2 with MAI vapours leading to the eventual formation of $CH_3NH_3PbI_3$ ($MAPbI_3$) films [54]. The I4d and Pb5d core levels allow for an accurate determination of the I/Pb ratios in the film according to the intensity dependence of core levels described in Sect. 12.3.3: they are the same type of orbital and have similar binding energies and therefore the measured electrons originate from a similar probing depth. The spectra shown in Fig. 12.27 and their

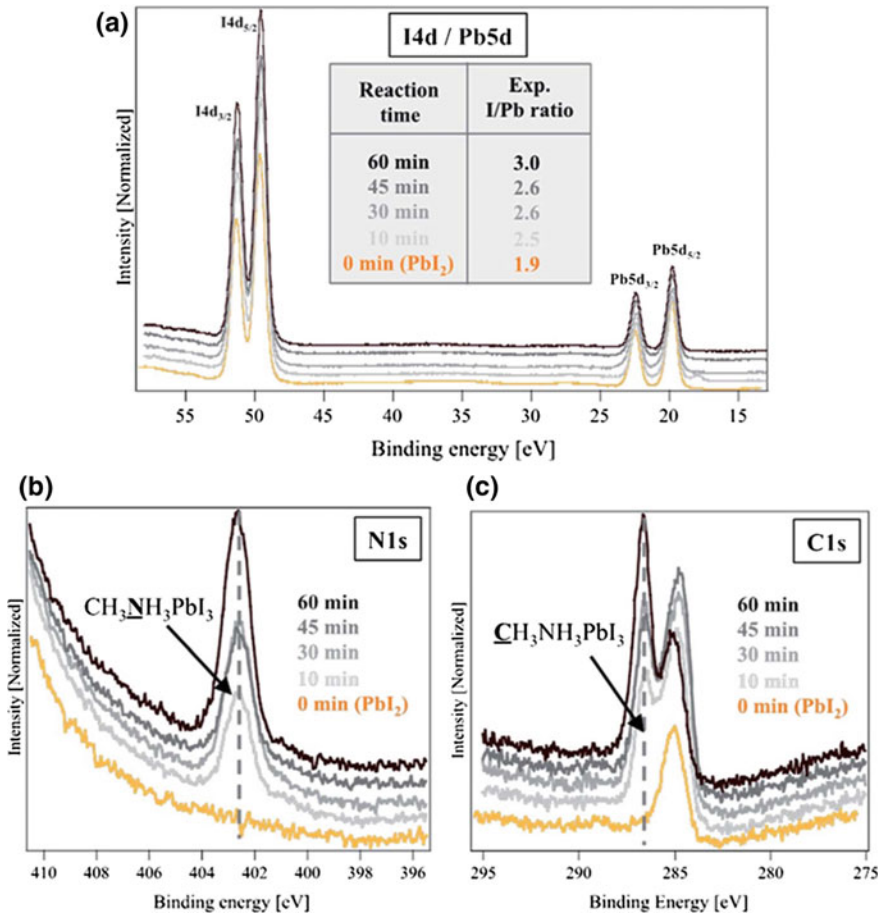

Fig. 12.27 Core level spectra of I4d/Pb5d (**a**), N1s (**b**) and C1s (**c**) of a PbI_2 layer and after different reaction times with MAI vapours showing the formation of $MAPbI_3$ for prolonged reaction times. The *inset* in panel (**a**) shows the I/Pb ratios calculated using the photoionization cross sections of I4d and Pb5d at the photon energy of 1486.7 eV. Reproduced from Ref. [54] with permission from The Royal Society of Chemistry

quantification confirm that an increased reaction time leads from a I/Pb ratio related to PbI_2 to a ratio in agreement with a perovskite structure. The formation of the perovskite could be further confirmed by the emergence of N1s and C1s core-level peaks associated with the perovskite structure.

As discussed in Sect. 12.3.3, studies with different photon energies allow for depth profiling and therefore for a comparison of the bulk and surface composition in the case of perovskite materials. For a mixed ion perovskite of the nominal formula $FA_{0.85}MA_{0.15}PbBr_{0.45}I_{2.55}$ (where FA stands for formamidinium), it was

possible to show using photon energies ranging from several 100 to several 1000 eV that an excess of PbI_2 exists in the bulk of the perovskite, while an excess of FAI was present at the surface [55].

12.4.4.3 Stability and Reproducibility of Perovskite Solar Cell Materials

Studies during the past few years have shown that the results of both solar cells as well as of other measurements on the perovskite materials critically depend on the details of the preparation procedure. For example, the presence of metallic lead was often observed in XPS studies of "first generation" $MAPbI_3$ samples [48]. In general, more variation between samples can be expected, when a measurement is more sensitive to the surface of the sample. It has been shown that valence band edge measurements in relation to the Fermi level were much more reproducible for different $MAPbI_3$ samples when determined by XPS with Al(Kα) at 1486.8 eV instead of by UPS measurements with a He lamp at 21.22 eV [52].

To ensure reproducible XPS results of ex situ prepared perovskite samples, a strict sample handling protocol can be adapted from the sample preparation to the transfer of samples into vacuum. Such a protocol should minimize the exposure of samples to environmental factors such as moisture and illumination. Also, the possible degradation of the material under UV and X-ray irradiation should be considered.

On the other hand, XPS also provides opportunities for studying and understanding the impact of heating, air/moisture exposure and illumination on the stability of the perovskite structure [56]. Exposure to these factors can often be precisely controlled in the analysis chambers for XPS measurements and their impact on the chemical composition and electronic structure of the material can be determined from core- and valence-level spectroscopy. The formation of metallic lead can be clearly observed through its shifted core-level peaks compared to Pb within the perovskite structure. The formation of PbI_2 can be observed from a change in the I/Pb ratio determined as described above as well as from a small shift in the Pb core levels and from a decrease in intensity of the N1s level [56].

References

1. Fadley CS (1978) Basic concepts of X-ray photoelectron spectroscopy. In: Brundle CR, Baker AD (eds) Electron spectroscopy: theory, techniques and applications. Academic Press, London, pp 1–156
2. Orchard AF (1977) Basic principles of photoelectron spectroscopy. In: Briggs D (ed) Handbook of X-ray ultraviolet photoelectron spectroscopy. Heyden, London, pp 1–14
3. Ratner BD, Castner DG (2009) Electron spectroscopy for chemical analysis. In: Vickerman JC, Gilmore IS (eds) Surface analysis—the principal techniques, 2nd edn. Wiley, Chichester, pp 47–112

4. Hüfner S (1995) Photoelectron spectroscopy: principles and applications. Springer, Berlin
5. Heide P Van der (2011) X-ray photoelectron spectroscopy: an introduction to principles and practices, 1st edn. Wiley, pp 1–12. doi:10.1002/9781118162897.ch1
6. Bidermane I, Lüder J, Totani R et al (2015) Characterization of gas phase iron phthalocyanine with X-ray photoelectron and absorption spectroscopies. Phys Status Solidi Basic Res 252:1259–1265. doi:10.1002/pssb.201451147
7. Yu S, Ahmadi S, Sun C et al (2012) Inhomogeneous charge transfer within monolayer zinc phthalocyanine absorbed on TiO_2(110). J Chem Phys 136:154703. doi:10.1063/1.3699072
8. Ahmadi S, Shariati MN, Yu S, Göthelid M (2012) Molecular layers of ZnPc and FePc on Au (111) surface: charge transfer and chemical interaction. J Chem Phys 137:84705. doi:10.1063/1.4746119
9. Tanuma S (2011) Calculations of electron inelastic mean free paths. IX. Data for 41 elemental solids over the 50 eV to 30 keV range. Surf Interface Anal 43:689–713. doi:10.1002/sia.3522
10. Ishii H, Sugiyama K, Ito E, Seki K (1999) Energy level alignment and interfacial electronic structures at organic metal and organic organic interfaces. Adv Mater 11. doi:10.1002/(SICI)1521-4095(199906)11:8<605::AID-ADMA605>3.0.CO;2-Q
11. Goiri E, Borghetti P, El-Sayed A et al (2016) Multi-component organic layers on metal substrates. Adv Mater 28:1340–1368. doi:10.1002/adma.201503570
12. Kera S, Yabuuchi Y, Yamane H et al (2004) Impact of an interface dipole layer on molecular level alignment at an organic-conductor interface studied by ultraviolet photoemission spectroscopy. Phys Rev B 70:85304. doi:10.1103/PhysRevB.70.085304
13. Fukagawa H, Yamane H, Kera S et al (2006) Experimental estimation of the electric dipole moment and polarizability of titanyl phthalocyanine using ultraviolet photoelectron spectroscopy. Phys Rev B 73:41302. doi:10.1103/PhysRevB.73.041302
14. Yamane H, Honda H, Fukagawa H et al (2004) HOMO-band fine structure of OTi- and Pb-phthalocyanine ultrathin films: effects of the electric dipole layer. J Electron Spectro Relat Phenom 137:223–227. doi:10.1016/j.elspec.2004.02.054
15. Gargiani P, Angelucci M, Mariani C, Betti MG (2010) Metal-phthalocyanine chains on the Au(110) surface: interaction states versus d -metal states occupancy. Phys Rev B 81:85412. doi:10.1103/PhysRevB.81.085412
16. Schlaf R, Parkinson BA, Lee PA et al (1999) Absence of final-state screening shifts in photoemission spectroscopy frontier orbital alignment measurements at organic/semiconductor interfaces. Surf Sci. doi:10.1016/S0039-6028(98)00850-4
17. Johansson EMJ, Odelius M, Karlsson PG et al (2008) Interface electronic states and molecular structure of a triarylamine based hole conductor on rutile TiO_2(110). J Chem Phys 128:184709. doi:10.1063/1.2913245
18. Ishii H, Hayashi N, Ito E et al (2004) Kelvin probe study of band bending at organic semiconductor/metal interfaces: examination of Fermi level alignment. Phys status solidi 201:1075–1094. doi:10.1002/pssa.200404346
19. Gao W, Kahn A (2002) Electronic structure and current injection in zinc phthalocyanine doped with tetrafluorotetracyanoquinodimethane: interface versus bulk effects. Org Electron 3:53–63. doi:10.1016/S1566-1199(02)00033-2
20. Gao W, Kahn A, K IH and S, et al (2003) Electrical doping: the impact on interfaces of -conjugated molecular films. J Phys Condens Matter 15:S2757–S2770. doi:10.1088/0953-8984/15/38/014
21. Olthof S, Tress W, Meerheim R et al (2009) Photoelectron spectroscopy study of systematically varied doping concentrations in an organic semiconductor layer using a molecular p-dopant. J Appl Phys 106:103711. doi:10.1063/1.3259436
22. Johansson EMJ, Schölin R, Siegbahn H et al (2011) Energy level alignment in TiO_2/dipole-molecule/P3HT interfaces. Chem Phys Lett 515:146–150. doi:10.1016/j.cplett.2011.09.014
23. Cappel UB, Plogmaker S, Johansson EMJ et al (2011) Energy alignment and surface dipoles of rylene dyes adsorbed to TiO_2 nanoparticles. Phys Chem Chem Phys 13:14767–14774. doi:10.1039/c1cp20911f

24. Hwang J, Wan A, Kahn A (2009) Energetics of metal-organic interfaces: new experiments and assessment of the field. Mater Sci Eng R Rep. doi:10.1016/j.mser.2008.12.001
25. Davis RJ, Lloyd MT, Ferreira SR et al (2011) Determination of energy level alignment at interfaces of hybrid and organic solar cells under ambient environment. J Mater Chem 21:1721–1729. doi:10.1039/C0JM02349C
26. Aarnio H, Sehati P, Braun S et al (2011) Spontaneous charge transfer and dipole formation at the interface between P3HT and PCBM. Adv Energy Mater 1:792–797. doi:10.1002/aenm.201100074
27. Bao Q, Sandberg O, Dagnelund D et al (2014) Trap-assisted recombination via integer charge transfer states in organic bulk heterojunction photovoltaics. Adv Funct Mater 24:6309–6316. doi:10.1002/adfm.201401513
28. Cappel UB, Plogmaker S, Terschlüsen JA et al (2016) Electronic structure dynamics in a low bandgap polymer studied by time-resolved photoelectron spectroscopy. Phys Chem Chem Phys 18:21921–21929. doi:10.1039/C6CP04136A
29. Johansson EMJ, Lindblad R, Siegbahn H et al (2014) Atomic and electronic structures of interfaces in dye-sensitized, nanostructured solar cells. ChemPhysChem 15:1006–1017. doi:10.1002/cphc.201301074
30. Patthey L, Rensmo H, Persson P et al (1999) Adsorption of bi-isonicotinic acid on rutile TiO_2(110). J Chem Phys 110:5913–5918. doi:10.1063/1.478491
31. Johansson EMJ, Hedlund M, Siegbahn H, Rensmo H (2005) Electronic and molecular surface structure of Ru(tcterpy)(NCS)3 and Ru(dcbpy)2(NCS)2 adsorbed from solution onto nanostructured TiO_2: a photoelectron spectroscopy study. J Phys Chem B 109:22256–22263. doi:10.1021/jp0525282
32. Karlsson PG, Bolik S, Richter JH et al (2004) Interfacial properties of the nanostructured dye-sensitized solid heterojunction TiO_2/$RuL_2(NCS)_2$/CuI. J Chem Phys 120:11224–11232. doi:10.1063/1.1739399
33. Hahlin M, Johansson EMJ, Schölin R et al (2011) Influence of water on the electronic and molecular surface structures of ru-dyes at nanostructured TiO_2. J Phys Chem C 115:11996–12004. doi:10.1021/jp1076609
34. Schoölin R, Quintana M, Johansson EMJ et al (2011) Preventing dye aggregation on ZnO by adding water in the dye-sensitization process. J Phys Chem C 115:19274–19279. doi:10.1021/jp206052t
35. Schnadt J, Henningsson A, Andersson MP et al (2004) Adsorption and charge-transfer study of bi-isonicotinic acid on in situ-grown anatase. J Phys Chem B 2:3114–3122. doi:10.1021/jp0344491
36. Mayor LC, Ben Taylor J, Magnano G et al (2008) Photoemission, resonant photoemission, and x-ray absorption of a Ru(II) complex adsorbed on rutile TiO_2(110) prepared by in situ electrospray deposition. J Chem Phys 129:114701. doi: 10.1063/1.2975339
37. Eriksson SK, Hahlin M, Axnanda S et al (2016) In-situ probing of H_2O effects on a ru-complex adsorbed on TiO_2 using ambient pressure photoelectron spectroscopy. Top Catal 59:583–590. doi:10.1007/s11244-015-0533-3
38. Johansson EMJ, Karlsson PG, Hedlund M et al (2007) Photovoltaic and interfacial properties of heterojunctions containing dye-sensitized dense TiO_2 and tri-arylamine derivatives. Chem Mater 19:2071–2078. doi:10.1021/cm062498v
39. Hahlin M, Johansson EMJ, Plogmaker S et al (2010) Electronic and molecular structures of organic dye/TiO_2 interfaces for solar cell applications: a core level photoelectron spectroscopy study. Phys Chem Chem Phys 12:1507. doi:10.1039/B913548K
40. Eriksson SK, Josefsson I, Ellis H et al (2016) Geometrical and energetical structural changes in organic dyes for dye-sensitized solar cells probed using photoelectron spectroscopy and DFT. Phys Chem Chem Phys Phys Chem Chem Phys 252:252–260. doi:10.1039/c5cp04589d
41. Johansson EMJ, Odelius M, Plogmaker S et al (2010) Spin-orbit coupling and metala-ligand interactions in Fe(II), Ru(II), and Os(II) complexes. J Phys Chem C 114:10314–10322. doi:10.1021/jp103884c

42. Johansson EMJ, Odelius M, Gorgoi M et al (2008) Valence electronic structure of ruthenium based complexes probed by photoelectron spectroscopy at high kinetic energy (HIKE) and modeled by DFT calculations. Chem Phys Lett 464:192–197. doi:10.1016/j.cplett.2008.09.016
43. Johansson EMJ, Hedlund M, Odelius M et al (2007) Frontier electronic structures of Ru(tcterpy)$(NCS)_3$ and Ru$(dcbpy)_2$ $(NCS)_2$: a photoelectron spectroscopy study. J Chem Phys 126:244303. doi:10.1063/1.2738066
44. Schölin R, Karlsson MH, Eriksson SK et al (2012) Energy level shifts in spiro-OMeTAD molecular thin films when adding Li-TFSI. J Phys Chem C 116:26300–26305. doi:10.1021/jp306433g
45. Eriksson SK, Josefsson I, Ottosson N et al (2014) Solvent dependence of the electronic structure of I^- and I_3^-. J Phys Chem B 118:3164–3174. doi:10.1021/jp500533n
46. Lee MM, Teuscher J, Miyasaka T, et al (2012) Efficient hybrid solar cells based on meso-superstructured organometal halide perovskites. Science (80-) 338:643–7. doi:10.1126/science.1228604
47. Kim H-S, Lee C-R, Im J-H, et al (2012) Lead iodide perovskite sensitized all-solid-state submicron thin film mesoscopic solar cell with efficiency exceeding 9%. Sci Rep 2:591. doi:10.1038/srep00591
48. Lindblad R, Bi D, Park B-W et al (2014) Electronic structure of TiO2/CH3NH3PbI3 Perovskite solar cell interfaces. J Phys Chem Lett 5:648–653. doi:10.1021/jz402749f
49. Chen S, Goh TW, Sabba D et al (2014) Energy level alignment at the methylammonium lead iodide/copper phthalocyanine interface. APL Mater 2:81512. doi:10.1063/1.4889844
50. Schulz P, Edri E, Kirmayer S et al (2014) Interface energetics in organo-metal halide perovskite-based photovoltaic cells. Energy Environ Sci 7:1377. doi:10.1039/c4ee00168k
51. Liu P, Liu X, Lyu L et al (2015) Interfacial electronic structure at the CH3NH3PbI3/MoOx interface. Appl Phys Lett 106:193903. doi:10.1063/1.4921339
52. Miller EM, Zhao Y, Mercado CC et al (2014) Substrate-controlled band positions in $CH_3NH_3PbI_3$ perovskite films. Phys Chem Chem Phys 16:22122–22130. doi:10.1039/C4CP03533J
53. Leijtens T, Stranks SD, Eperon GE et al (2014) Electronic properties of meso-superstructured and planar organometal halide Perovskite films: charge trapping, photodoping, and carrier mobility. ACS Nano 8:7147–7155. doi:10.1021/nn502115k
54. Jain SM, Philippe B, Johansson EMJ et al (2016) Vapor phase conversion of PbI_2 to CH3NH3PbI3: spectroscopic evidence for formation of an intermediate phase. J Mater Chem A 4:2630–2642. doi:10.1039/C5TA08745G
55. Jacobsson TJ, Correa-Baena J-P, Halvani Anaraki E et al (2016) Unreacted PbI_2 as a double-edged sword for enhancing the performance of perovskite solar cells. J Am Chem Soc 138:10331–10343. doi:10.1021/jacs.6b06320
56. Philippe B, Park BW, Lindblad R et al (2015) Chemical and electronic structure characterization of lead halide perovskites and stability behavior under different exposures-A photoelectron spectroscopy investigation. Chem Mater 27:1720–1731. doi:10.1021/acs.chemmater.5b00348
57. Cahen D, Kahn A (2003) Electron energetics at surfaces and interfaces: concepts and experiments. Adv Mater 15:271–277. doi:10.1002/adma.200390065

Chapter 13
Stability of Molecular Devices: Halide Perovskite Solar Cells

Yegraf Reyna, Amador Pérez-Tomás, Alba Mingorance and Mónica Lira-Cantú

Abstract Novel hybrid organic-inorganic perovskite solar cells (PSCs) have radically transformed the photovoltaic and energy-conversion arena. Their remarkable and unprecedented improvement of power conversion efficiencies, currently at 22%, has occurred within only the past few years, and has benefitted from prior developments in other new photovoltaic technologies, e.g. dye sensitized solar cells (DSSCs) and organic solar cells (OPVs). This technology has all the ingredients needed to rapidly achieve maturity: (a) inexpensive, light-harvesting perovskite-type minerals, (b) the straightforward design and composition of derivatives and homologous substances, and (c) facile solution-based processing methods. Another advantage of PSCs is their ability to be integrated in tandem architectures with silicon-based solar cells. As a result, mechanically flexible and semi-transparent light-harvesting arrays possessing polychromic sensitivity can be attainable. The long-term stability of halide PSCs is an important and urgent challenge to be overcome before their commercial potential can be realized. A greater understanding of their intrinsic and extrinsic degradation mechanisms has led to an increase in PSC stability relative to initially low values. This review documents the most promising and recent of those results, and sets the stage for future improvements in PSC device efficiency, stability and lifetime.

Keywords Halide perovskite solar cells · Mesoscopic perovskite solar cells · Stability · Lifetime · ISOS protocols

Y. Reyna · A. Pérez-Tomás · A. Mingorance · M. Lira-Cantú (✉)
Nanostructured Materials for Photovoltaic Energy Group, Catalan Institute of Nanoscience and Nanotechnology (ICN2), CSIC and Barcelona Institute of Science and Technology (BIST), Campus UAB Edifici ICN2, Bellaterra, Barcelona 08193, Spain
e-mail: monica.lira@cin2.es

H. Tian et al. (eds.), *Molecular Devices for Solar Energy Conversion and Storage*, Green Chemistry and Sustainable Technology,
https://doi.org/10.1007/978-981-10-5924-7_13

13.1 Introduction

The plan to reduce greenhouse emissions by 80% by 2050 will require significant future investments in renewable energy [1]. The most reliable, affordable, independent and inexhaustible renewable energy technologies employ solar, hydro and wind. Currently, for the harvesting of photovoltaic energy on rooftops or in solar farms, silicon photovoltaic technology is predominant [2]. Outside of those application areas, high levels of efficiency, mechanical flexibility, semi-transparency and polychromic sensitivity are still required. To meet this anticipated demand, novel devices such as halide perovskite solar cells (PSCs) are emerging as promising technologies. The power conversion efficiency of PSC cells has skyrocketed from an initial value of 3.8%, obtained by Miyasaka in 2009 [3], to a currently unprecedented efficiency of 22% [4]. Interestingly, halide perovskites are not new compounds for materials scientists, as their synthesis and the study of their properties both date back to 1893 [5]. The initial discovery of their photoconductivity is attributed to Moller in 1957 [6], and was followed by widespread interest in their properties over the 1980s [7]. The perovskite unit cell is based on the ABX_3 stoichiometry, and hence comprises five atoms in a cubic structure. More than half of all the elements in the periodic table can be located in at least one of the three lattice sites [8], and hence a great variety of inorganic perovskites, each having unique properties and characteristics, are possible. Additionally, replacement of oxygen atoms in the A-position of ABX_3 by either halides or organic molecules, results in a sub-class of perovskites, the hybrid organic-inorganic metal halide perovskites [9]. For these, modification of chemical composition permits extensive fine-tuning of, e.g. optical parameters, band gap alignment or ion mobilities. Generally, in PSC, organic or inorganic cations occupy the A-position of ABX_3 and halides are located in the X position. The most widely known hybrid organic-inorganic metal halide perovskite is methyl ammonium (MA) lead iodide, $CH_3NH_3PbI_3$. Substitution of tin(II) for lead(II), or chloride or bromide for iodide, is also possible. Current studies on mixed halide and/or cation perovskites indicate that these too can display optimal conversion efficiencies and stabilities [8].

In spite of a power conversion efficiency (PCE) of 22.1% [4], the operational stability PSCs remain of foremost concern. As will be fully described in Sect. 13.2, PSC degradation issues are placed into three different categories. The most general type involves light, atmosphere, moisture and temperature (LAMT). Complex factors, which can be classified as either *intrinsic* or *extrinsic*, are also important and are depicted in Fig. 13.2.

As an example of a LAMT phenomenon, it is worthwhile to compare methyl ammonium lead halide perovskite, $MAPbX_3$ to formamidinium cation perovskite, $FAPbX_3$, and caesium lead halide perovskite, $CsPbX_3$. Whereas $MAPbX_3$ displays phase instability at low temperature [10] and is relatively sensitive to temperature, moisture [11, 12] and light [13], $FAPbX_3$ is much less so. Hence, phase segregation of the halide component in $MAPbX_3$ but not $FAPbX_3$ occurs [13]. On the other hand, for $CsPbX_3$ a higher annealing temperature than for MAPbX, above 300 °C,

is required$_3$ to induce photoactivity. Fortunately, this also leads to $CsPbX_3$ having greater thermally stability under device operational conditions [14]. *Intrinsic* degradation processes involve, for example, mobile ions within the crystal lattice [15]. Lattice defects can function as deep traps for charge carriers [16], modify the actual perovskite crystal structure [17, 18], or induce iodization of the metal electrodes. This is especially the case for scalable Ag cathodes [19]. Another *intrinsic* degradation process affecting device stability is perovskite stoichiometry. A successful approach to addressing this latter issue, and which has led to state-of-the-art certified photovoltaic devices, uses mixed perovskites [20–24]. Finally, improvement of device stability [25] and resistance to degradation by either solvents or thermal stress [21–24] can result from use of mixed cation/halide perovskites. Some examples of *extrinsic* degradation are dopants within the hole transport materials (HTM), which may lower device lifetime [26, 27], or the device configuration, where the inverted planar PSC configuration have shown good stability [28, 29]. A large number of other studies on methods to improve efficiency and lifetime of PSCs through optimization of materials and devices have also been undertaken.

In this work, we aim to summarize the latest developments on the stability of PSCs through the review of the different degradation processes reported in state-of-the-art devices. We will introduce the reader to basic concepts of PSC configuration and materials utilization, as well as the efforts undertaken by the photovoltaic research community to improve device lifetime [30–36]. The final section of this chapter summarizes studies on PSC degradation processes. This information is summarized in tabular form, and is divided into two general categories: in the absence of light, or upon irradiation. Sub-topics include (a) the functional roles of materials such as halide perovskites, electrodes, interfaces, etc. (b) configurational differences of PSC, (c) interpretation of testing conditions, and (d) stabilities achieved for the technology. It is our intention that, through providing this information in tabular form, we can provide the reader with a lucid overview of degradation issues and the research issues which are yet to be addressed. It is only after those challenges have been met that devices having sufficient stability for practical PSC applications can be realized.

13.1.1 Best Practices for Measuring PSCs Performance

Standardization of procedures for measuring and reporting solar cells performance permits comparison of devices from different laboratories worldwide, avoids the misrepresentation of solar cell performance and boosts the credibility of the specific photovoltaic technology under consideration for commercialization. Over the years, many publications have appeared on the issues and problems leading to unintentional misrepresentation of solar cell performance and the recommendations to avoid its occurrence [37–56]. Fundamental discrepancies can involve experimental device characterization techniques such as spectral mismatch, effects of aperture

size on the results of external quantum efficiency (EQE, also known as incident photon-to-electron conversion efficiency, IPCE) determination, bias voltage, bias illumination intensity, etc. [37, 42, 43]. Issues associated with recommendations for device standardization include source calibration [45] and masking [39, 45]. Another best practice is the comparison of the current density (J_{sc}) response obtained from current–voltage (IV) curves with that obtained from IPCE measurements. These recommendations appear in a variety of well-established technical journals [50, 57, 58]. After minor modifications, all are applicable to the characterization of emerging solar cell technologies including dye sensitized solar cells (DSSCs) [38, 39, 47, 59], organic solar cells (OPVs) [40, 41, 44, 58], hybrid solar cells (HSCs) [46, 60], tandem OPVs [50–52], and, more recently, PSCs [53–55, 61–64]. Certification of solar cell performance from authorized, independent laboratories is also important to obtain. Other helpful practices are the worldwide exchange of research samples between laboratories using different measurement protocols [65, 66], inter-laboratory collaborations [67–70], comparison and prediction of solar cell lifetimes according to ageing tests [48] and contrasting measurements conducted outdoors and indoors [49].

The best practices recommended for the measurement and interpretation of PSC performance are summarized as follows:

Steady-state conditions (SSC). Specifically for PSC, hysteresis and the strong dependence of photocurrent on voltage-scan rate and scan direction are major concerns [71, 72]. Hysteresis-related artefacts can lead to under- or over-estimation of PCE values [53–55]. Use of SSC is recognized as the only valid method to verify PSC performance and several methods have been published to attain SSCs [55, 56, 64]. A simple means of doing so is to monitor the observed current density while holding the device at constant potential. Under those conditions, the J_{sc} obtained using this method should be identical to that obtained from the IV curve. Only in this case the J_{sc} obtained at constant potential is valid [55, 56, 64].

Device architecture. The first feature to take into account is the device configuration. As will be detailed in Sect. 13.1.2, the PSC can have different device configurations depending on the position and nanostructure of each device layer. Two general architectures which depend on nanostructure are the *mesoscopic* and the *planar* configuration PSC. The main difference between them is that the planar configuration is constructed from flat and dense thin-film layers, which avoids relying on mesoscopic films, made of nanoparticles, nanorods, nanowires or similar nanostructures. In 2014, Seok et al. showed the hysteresis effect to be particularly severe for the planar device configuration [73]. Since then, new device designs and architectures have become available. One of these has resulted in mesoscopic and planar configurations for either inverted or conventional configurations (c.f., Tables 13.1 and 13.2). Thus, whereas conventional planar structures based on TiO_2 usually suffer from a large degree of J–V hysteresis, the new inverted planar device structures containing PCBM show negligible J–V hysteresis effects [29, 74]. This result is attributed to stabilization of ion movement in the presence of PCBM. The PCBM penetrates into grain boundaries and interacts with the perovskite, forming a halide radical. In turn, this process reduces internal electrostatic forces,

Table 13.1 Examples of nanostructured perovskite solar cells with conventional and inverted configuration applying organic or inorganic hole transport layers (HTL)

Nanostructured	TE[a]/BL[b]	Perovskite	BL	E[c]	PCE (%)	V_{oc} (V)	J_{sc} (mA/cm^2)	FF	Refs.
Conventional									
Organic HTL[d]	FTO/TiO_2-c/Li-TiO_2-m	$Cs_x(MA_{0.17}FA_{0.83})_{(100-x)}Pb(I_{0.83}Br_{0.17})_3$	spiro-OMeTAD	Au	19.20	1.132	22.69	0.74	[20]
	FTO/TiO_2-NRs	$CH_3NH_3PbI_{3-x}Cl_x$	spiro-OMeTAD	Au	10.5	3.37	22.2	0.56	[111]
Inorganic HTL[d]	FTO/TiO_2-c/TiO_2-m	$CH_3NH_3PBI_3$	Al_2O_3/NiO	C					[114]
	FTO/TiO_2-c/TiO_2-m	$CH_3NH_3PBI_3$	ZrO_2/NiO- ns	C	14.2	0.93	20.4	0.72	[79]
Inverted									
Organic HTL[d]	ITO/PEDOT:GeOx np	$CH_3NH_3PbI_{3-x}Cl_x$	PCBM:BiPhen	Ag	16.77	1.01	21.35	0.78	[96]
	ITO/PEDOT	$CH_3NH_3PbI_{3-x}Cl_x$	PCBM/ZnO-np	Al	8.51	0.83	14.65	0.70	[190]
Inorganic HTL[d]	FTO/NiO_x-c/NiO-m	$MAPbI_3$	PCBM/BCP	Al	13.7	1.01	22.1	0.61	[115]
	ITO/NiO-m	$MAPbI_3$	PCBM	LiF/Al	17.3	1.06	20.2	0.81	[82]

[a]*TE* Transparent Electrode
[b]*BL* Barrier Layer
[c]*E* back Electrode
[d]*HTL* Hole transport Layer
[e]*PCE* Power Conversion Efficiency

Table 13.2 Examples of planar perovskite solar cells with conventional and inverted configuration applying organic or inorganic Hole Transport layers

Planar	TE[a]/BL[b]	Perovskite	BL[b]	E[c]	PCE[e] (%)	V_{oc} (V)	J_{sc} (mA/cm^2)	FF	Refs.
Conventional									
Organic HTL[d]	FTO/SnO_2	$CH_3NH_3PbI_3$	Spiro-MeOTAD	Ag	13				[179]
	FTO/Al-ZnO	$CH_3NH_3PbI_3$	Spiro-MeOTAD	Au	12.6	0.93	20.2	0.67	[152]
Inorganic HTL[d]	FTO/TiO_2	$CH_3NH_3PbI_{3-x}Cl_x$	NiOx	Ni	7.28	0.77	17.88	0.53	[191]
	ITO/TiO_2	$CH_3NH_3PbI_3$	P3HT:MoO_3	Al	14.6	0.95	27.4	0.56	[192]
Inverted									
Organic HTL[d]	ITO/PEDOT	$CH_3NH_3PbI_3$	$PC_{61}BM$:CBL	Ag	15.5				[154]
	ITO/PEDOT	$CH_3NH_3PbI_{3-x}Cl_x$	PCBM	Al	11.5	0.87	18.5	0.72	[193]
	ITO/PEDOT	$CH_3NH_3PbI_{3-x}Cl_x$	ZnO:PCBM	Al	14.2	0.98	19.6	0.74	[172]
Inorganic HTL[d]	FTO/PEDOT:V_2O_5	$MAPbI_{3-x}Br_x$	TiO_x:DEA	Ag	16.09	1.07	18.34	0.82	[19]
	FTO/NiMgLiO	$MAPbI_3$	PCBM/Ti(Nb)O_x	Ag	22.35	1.27	20.42	0.85	[167]
	ITO/NiO_x	$CH_3NH_3PbI_3$	ZnO	Al	16.1	1.01	21.0	0.76	[187]

[a]*TE* Transparent Electrode
[b]*BL* Barrier Layer
[c]*E* back Electrode
[d]*HTL* Hole transport Layer
[e]*PCE* Power Conversion Efficiency

thereby lowering charge accumulation, capacitance and hysteresis [29]. In several novel PSC configurations, it has been possible to eliminate or reduce the amount of PCBM or even entirely eliminate it through the use of transition metal oxides (TMOs), for example NiO [75–83], CuO_x [84–86], MoO_x [87–91], V_2O_5 [19, 92–95], GeO_2 [96] or doped oxides such as Cu-doped NiO and CrO_x [97–100] (see Sect. 13.4.1). The latter also reduce hysteresis. Zimmermann et al. examined six different types of PSCs architectures prepared in different laboratories, applying different fabrication methods and material combinations, and reported noticeable changes in their response and hysteresis behaviour [56]. This demonstrates the importance of taking into account device architecture and verifying performance under SSC.

Sweep rate and direction. As previously described, hysteresis in IV-curves is observed when solar cell measurements are carried out under non-steady-state conditions. For that reason, parameters such as scan rate and sweep direction should be carefully taken into account. This response delay can have intrinsic or extrinsic origins, but regardless of its cause, the sweep rate must still be carefully analysed and selected. Until 2014, sweep rates above 200 mV/s were common among the photovoltaic community. After that time, the most commonly used rate had dropped to <50 mV/s. Cases of rates down to 5 mV/s have also been reported (see Tables 13.3 and 13.5). Still, minimization of the scan rate is not adequate to achieve the best PSC performance. In addition, verification of the steady-state performance characteristics of individual devices is necessary.

As described by Christians et al. a simple method of verifying the steady state is possible by holding the solar cell at constant potential and recording the current density obtained. The resulting J_{sc} should be the same as that obtained from the IV curve. If this criterion is not met, then it becomes necessary to verify the scan rate, since the J_{sc} value at constant potential is the only value having any real-world significance [55]. Furthermore, the IV-curves should be recorded in both forward and reverse directions, since significant exaggerations of PCE values have been found in PSCs when recording in the reverse direction. When the solar cell is at steady state, the photovoltaic responses of both curves should be the same.

Maximum power point tracking (MPPT). MMPT is an older technique used in photovoltaic systems (and turbines) used to maximize the power output independent of testing conditions. According to this method, determination of the PSC device response is made by holding the solar cell at maximum voltage (V_{mp}); this happens at the point where constant current density is achieved [55, 56, 101]. Recently, publications have begun to report values obtained using both methods [20], and these should agree with each other.

IPCE (incident photon-to-electron conversion efficiency). The process by which charges are extracted from the solar cell under short circuit conditions is wavelength-dependent, and the efficiency of this process is termed its incident photon-to-electron conversion efficiency (IPCE), also known as external quantum efficiency (EQE). Knowledge of this parameter allows determination of the solar cell current density. Thus, integration of the IPCE spectrum over the AM1.5G solar spectrum gives the J_{sc} for the device. This value of J_{sc} should be the same as that

obtained from the IV curve. Thus, it is recommended to show the plots of current density from IPCE and the calculation of J_{sc} in the same graph.

Preconditioning of the solar cell. Preliminary solar cell treatment can include light soaking, annealing and electrical manipulation, either in the absence of light or at low temperature, among other protocols. Light soaking is reported to affect PSC performance and depends on the materials and the device configuration. Loi et al. recently reported the elimination of the light soaking effect by the use of fullerene derivatives as electron transport materials [102]. Interestingly, Nie et al. described a self-healing effect for perovskite solar cells in the absence of light. After storage in the absence of light and at low temperature, the initial PSC performance is restored [103]. The mechanism by which this phenomenon occurs appears to be related to charge accumulation on the solar cell interfaces in the absence of light [104–107]. Those results appear to indicate that preconditioning of the solar cell by standing in the absence of light and at low temperature can improve solar cell response and lifetime. A clear description of the preconditioning methods will be of obvious help to future researchers.

Other best practices: masking, active area and statistics. Correct masking of the solar cell is necessary to delineate the solar cell active area and avoid misinterpretation of the solar cell performance [39, 45]. Active areas smaller than 0.1 cm^2 can result in greater values for J_{sc} and FF (full factor) [55, 61]. When determining performance parameters from a large number of solar cells, it is also advisable to provide their statistical deviations, in addition to the maximum performance which was obtained.

Determination of long-term stability. For determination of long-term stability, it is recommended to adhere to established, published protocols. The organic photovoltaic community [108] has published the ISOS protocols which achieve this. The standardized measurement conditions are: in the dark (ISOS-D), outdoors (ISOS-O), testing under laboratory conditions (ISOS-L), thermal cycling in the dark (ISOS-T) and thermal cycling under low-intensity irradiation conditions (ISOS-LT) [108]. These protocols have been recently reviewed and updated [53, 54]. For evaluation of long-term stability, it is also important to include the method used to seal the devices (if any). Some sealants are made of epoxies which may react with the components of the solar cell and promote its early degradation [109].

13.1.2 Classification of Halide Perovskite Solar Cells

The stabilities of state-of-the-art PSCs depends on the material structure and configuration, as well as device interfaces. It is thus necessary to understand the composition and configuration of different types of halide PSC. For simplification, a classification scheme for thin-film solar cells (TFSC) is presented in Fig. 13.1; this is applicable to virtually all types of emerging solar cells. We consider five basic thin-film layers: two current collectors (CCs), two barrier layers (BLs) and the active layer (AL).

- The AL contains the light-harvesting material. Due to its importance, it also determines the overall solar cell classification. For example, if the AL is made of organic donor/acceptor molecules, the device is an Organic Solar Cell (OSC); if these organic materials are organic polymers, it is a Polymer Solar Cell (PSC); if it is composed of TiO_2/dye molecules, it is a dye-sensitized solar cell (DSSC), and if it consists of halide perovskites (i.e. TiO_2/perovskite), it is a halide PSC. The AL is "sandwiched" between the two BLs and, together, these three layers are sandwiched between the two CCs.
- The CCs are of two types: one is a back electrode, which is made of either a conducting metal, such as gold, silver or aluminium (Au, Ag, Al, etc.), or a carbon-based material such as graphene. The other is the front electrode, which should be transparent in order for the light to penetrate into the active layer. These include fluorine-doped tin oxide (FTO), indium tin oxide (ITO) or newer ITO-free electrodes based on materials similar to graphene.
- The BLs work as the hole transport layer (or electron barrier layer), HTL, and the electron transport layer (or hole barrier layer), ETL. The BLs can be organic or inorganic semiconductors, or a mixture of both.

The layers comprising the PSC—especially the photoactive halide perovskite layer—are in the mesoscopic size range (up to 1000 nm). This allows a simple classification of the mesoscopic PSC according to either solar cell *configuration* or *mesostructure*, as shown in Fig. 13.1.

Classification by the type of device configuration. Depending on the relative location of the BLs with respect to the transparent electrode, the PSC is either *conventional* or *inverted*. In a *conventional* configuration (also referred to as normal or regular), the electron transport material (ETM, or *n*-type) is adjacent to the transparent electrode. This configuration is also called the *n-i-p* structure, where the *n-type* material is adjacent to the transparent electrode. In contrast, the *inverted* configuration has the hole transport layer (HTL, or *p*-type) alongside the transparent electrode, as shown in Fig. 13.1. This configuration is also called the *p-i-n* structure, with the *p*-layer located next to the transparent electrode.

The inverted configuration originates from thin-film solar cells, such as the OPV, where a hole transport layer (usually poly(3,4-ethylenedioxythiophene) polystyrene sulfonate, PEDOT:PSS) is applied on top of the transparent electrode made of indium or fluor tin oxide (ITO, FTO). The conventional configuration stems from the DSSC, where a thin-film layer of mesoscopic TiO_2 (the ETL) is coated on top of the transparent electrode (FTO).

Classification by solar cell mesostructure. Depending on the (nano) structure of *any* of the layers, the PSCs are labelled *planar* or *nanostructured*. A *planar* PSC contains dense thin films throughout all of the constituent layers. In a nanostructured (or mesoscopic) PSC, at least one of the layers contains nanostructural components, i.e. structures in the 1–100 nm range. Such materials can be nanoparticles, nanorods, nanoplates, quantum dots, etc. The most well-known and studied PSC is a mesoscopic solar cell having a configuration characterized as being both *conventional* and *mesoscopic* (*nanostructured*). It contains a layer of TiO_2

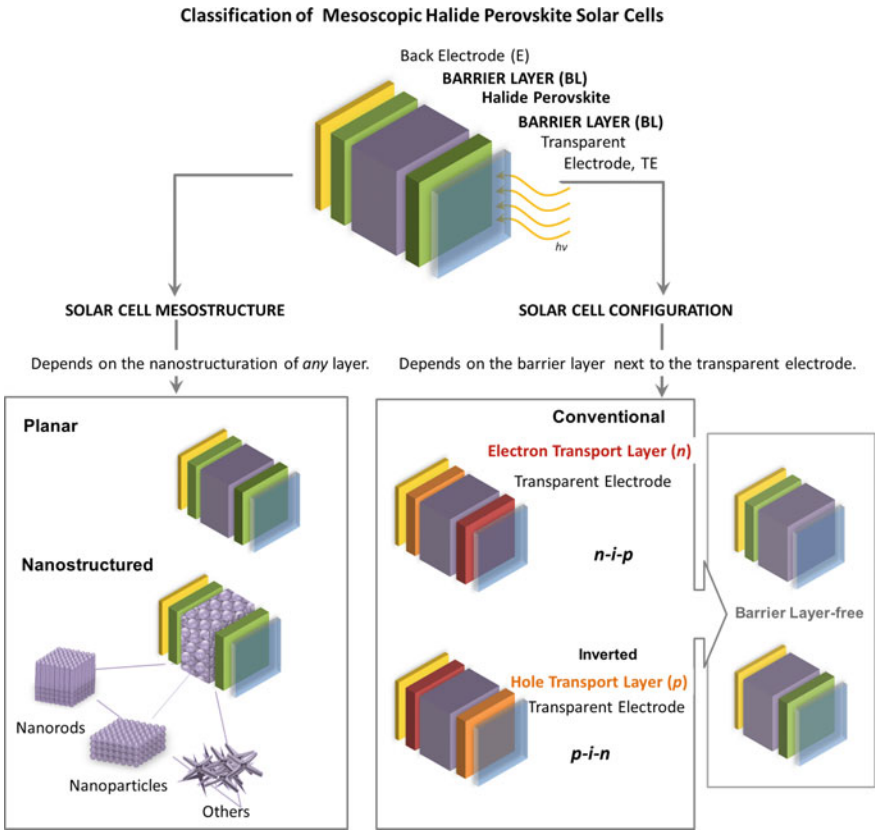

Fig. 13.1 Schematic representation of the basic structure of a Mesoscopic Halide Perovskite Solar Cell (*above*) and the classification depending on mesostructure (*below*, *left*), solar cell configuration (*below*, *centre*) and solar cell configuration without one barrier layer, BL-free (*below*, *right*)

nanoparticles which is deposited on top of the transparent electrode. While TiO_2 is the most common nanoparticulate layer, other nanostructured materials, for example nanorods [110, 111], nanosheets [79], core-shell [112], quantum dots [113], etc. have also been evaluated.

In Table 13.1, summarizes some typical mesoscopic PSCs having different nanostructures throughout any of their layers, in either conventional or inverted configurations. The conventional configuration, containing layers of either TiO_2 nanoparticles [20, 114] or nanorods [111], is the most common. For solar cells containing HTL oxides, an inverted configuration is also possible. For example, nanoparticulate oxides composed of either mesoscopic NiO which is deposited on top of a FTO substrate [115], or GeO_2, which can be applied as a hybrid hole transport layer with PEDOT:PSS [96]. Qiao et al. reported an inverted configuration of

mesostructured PSC, in which $MAPbI_3$ nanorods participate in a device constructed as ITO/PEDOT:PSS/$MAPbI_3$ nanorods/$PC_{60}BM$/rhodamine/Ag. For this system, growth of nanocrystal halide perovskite films under ambient conditions but 40% relative humidity enhanced the crystallization of thin-film nanorods and resulted in devices having PCE values of 16.8% [116]. In a different approach to obtaining a mesoscopic configuration, nanoparticles of various metal oxides, e.g. Al_2O_3 [114, 117, 118], ZrO_2 [119] or SiO_2 [120], were employed as nanostructured scaffolding for the final device. Mesoporous lead dimer (Pb_2) has also been used as a scaffolding platform. In this case, careful control of its nucleation and growth mechanism resulted in solar cell efficiencies of 15.7% [121]. To date, the most successful scaffolding system for PSC is constructed as a fully printable, TiO_2/ZrO_2/carbon system, has a >15% PCE, can be applied over larger areas and has a stability in excess of 1000 h under continuous low-intensity irradiation conditions [122].

By definition, PSCs having entirely planar components consist of densely packed thin films; these can be fabricated in either conventional or inverted configurations. The most important advantage which they have over nanostructured (mesoscopic) PSCs is their compatibility with materials processed at relatively low temperatures or in solution such as PEDOT:PSS, the ([6,6]-Phenyl-C61Buttersäuremethylester) or PCBM, crystalline or amorphous oxides, amongst others. On the other hand, nanostructured (mesoscopic) PSC must undergo sintering of their ETL nanostructured thin films at temperatures above 450 °C. Hence, a planar configuration is amendable towards inexpensive fabrication processes and ease of scaling up production; both of these factors increase the potential for commercialization.

A relatively new type of PSCs configuration is the barrier-layer-free (BL-free) PSC (Table 13.3), which is known for the simple, low-temperature conditions required for its fabrication. The first BL-free planar configuration resulted from studies directed towards removing the need for ETL electrodes such as mesoporous TiO_2, because those require high fabrication temperatures. In terms of scalability and efficiency, the BL-free PSC is one of the most advanced PSCs specially the HTL-free perovskite solar cell known as the "triple junction perovskite solar cell" [123, 124]. Initially, this type of solar cell demonstrated a PCE value of 11%, which suggests that inclusion of an ETL may not be necessary [125]. This device contains a mesoscopic layer of TiO_2 nanoparticles, followed by a porous layer of ZrO_2 scaffolding. Deposition of the ZrO_2 framework is amendable to screen-printing techniques, as are the remaining manufacturing steps for these cells. Importantly, this device configuration eliminates the use of expensive and unstable HTL layers, and avoids the use of precious metal electrodes, e.g. those made of gold. Instead, they use a carbon-based paste, which is applied on top of the ZrO_2 scaffolding layer and acts as a back contact. The final step is to infiltrate a halide perovskite solution into the scaffolding. As will be discussed in the final section of this work (Sect. 13.4.2), this device configuration is highly stable either in the absence of light or upon irradiation—even under ambient atmospheric conditions [122]. Either conventional or inverted configuration barrier layer-free PSCs can be manufactured,

Table 13.3 Examples of Barrier Layer free (BL-free) perovskite solar cells with conventional and inverted configuration

Conventional	TE[a]	ETL[b]	Perovskite	BL[c]	E[d]	PCE[e]	V_{oc}	J_{sc}	FF	Refs.
HTL-free	FTO	TiO_2	$MAPbI_3$		C					[194]
HTL-free	FTO	TiO_2-c	$CsPbIBr_2$		Au	4.7	0.95	8.7	0.56	[195]
HTL-free	FTO	TiO_2:ZrO_2	$(5\text{-}AVA)_x(MA)_{1-x}PbI_3$		C	11.6	0.83	21.1	0.65	[119]
ETL-free	FTO		$CH_3NH_3PbI_{3-x}Cl_x$	spiro-OMeTAD	Au	10.67	0.97	17.10	0.61	[196]
ETL-free	FTO									
Inverted	TE	HTL	Perovskite	BL	E	PCE	V_{oc}	J_{sc}	FF	Refs.
HTL-free	hc-PEDOT		$CH_3NH_3PbI_{3-x}Cl_x$	PCBM:ZnO-np	Al	7.95	0.88	16.88	0.53	[197]
HTL-free	ITO		$CH_3NH_3PbI_3$	PCBM	Al	9.7	0.96	14.8	0.68	[198]
HTL-free	FTO		$CH_3NH_3PbI_3$	PCBM:bis-C_{60}	Ag	11.0	1.0			[199]
HTL-free	ITO		$CH_3NH_3PbI_3$	MoO_3	Ag					[200]

BLs can be hole or electron transport materials (HTM or ETM, respectively.)
[a]*TE* Transparent Electrode
[b]*ETL* Electron Transport Layer
[c]*BL* Barrier Layer
[d]*E* back Electrode
[e]*PCE* Power Conversion Efficiency

although to date no ETL-free cells having inverted configurations have been reported (Table 13.3).

13.2 Stability of Halide Perovskite Solar Cells

As mentioned above, the reasons behind reduced PSC stability fall into three general categories (see Fig. 13.2) [26–28, 30, 31, 33–35, 126–128]: (a) light, atmosphere, moisture and temperature (LAMT); (b) *intrinsic* and (c) *extrinsic* factors. LAMT are very well known and studied, and can be most significant for halide perovskites. *Intrinsic* factors influence the physical and chemical properties of materials in device components such as the halide perovskite active layer, barrier layers or electrodes, as well as their interfaces. Yet other stability issues may affect physical properties related to crystallinity, morphology or intrinsic ionic drift defects, etc. *Extrinsic* factors affect the entire device, e.g. its configuration, fabrication details, additives, solvents or encapsulation. Commercialization of perovskite photovoltaic technology will only become viable after all such degradation issues of materials and complete devices have been thoroughly studied and understood.

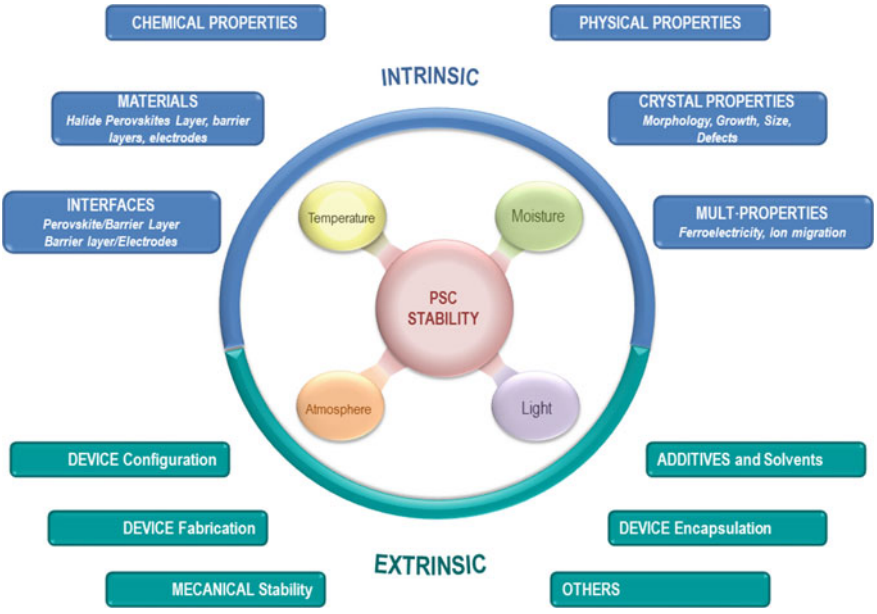

Fig. 13.2 Different degradation issues observed for halide perovskite solar cells: **a** the LAMT issues: light, atmosphere, moisture and temperature; **b** intrinsic and **c** extrinsic issues

13.2.1 Main Degradation Issues: Light, Atmosphere, Moisture and Temperature (LAMT)

Light irradiation can affect PSC over different wavelength ranges, depending on device architecture and materials composition. Likewise, materials in OPV, HSC and DSCs devices are known to be sensitive to UV light [26, 34]. PSCs having normal configurations may contain a nanostructured TiO_2 layer which is in direct contact with the halide perovskite. In this case, the photoactivation of binary semiconductor oxides at $\lambda < 400$ nm may induce degradation at the oxide/perovskite interface. Irradiation under ambient conditions causes oxygen vacancy sites (O_{vac}) in TiO_2 to adsorb molecular oxygen, which results in the formation of charge transfer complexes of the type [O_2–Ti_4^+], followed by the release of adsorbed oxygen and the formation of vacant O_{vac} sites [26, 34]. Simultaneously, a free electron is deposited into the conduction band. In this respect, a mechanism for oxygen release and exchange is known for TiO_2, and similar semiconductor oxides in hybrid solar cells (HSCs). Its mechanism involves direct contact between molecular oxygen and organic semiconductors [129–131]. The formation of O_{vacs}, which are effective deep surface traps and recombination centres, are responsible for degradation of device performance. Thus, the interplay between oxygen, light and atmosphere, can result in oxidative processes which, may induce elimination of the halide ion (I^-) from the halide perovskite. This will damage the perovskite crystal structure, releasing I_2 and HI as by-products [26, 34].

Low-intensity light. Very few reports can be found on the effect of low-intensity irradiation conditions on PSC performance levels. In 2013, Burschka et al. reported a PCE value of 12.9% for a light intensity of 95.6 mW/cm^2. The same device showed a similar PCE of 12.6% at a light intensity of only 9.3 mW/cm^2. Surprisingly, these two values corresponded to $J_{sc} = 17$ and 1.7 mA/cm^2, respectively, i.e. an order of magnitude difference. In either case, values for V_{oc} of $\sim$0.9 V were determined, even under low-intensity irradiation conditions [101]. Similar responses were observed for a mesoscopic PSC studied by Edgar et al. They found values for PCE of 7.2% under low-intensity irradiation conditions (10 mA/cm^2), but 5.5% at 1 sun (100 mA/cm^2). Values of 2.1 and 16.1 mA/cm^2, respectively, for J_{sc} again bespeak of a difference of one order of magnitude. However, in this case V_{oc} was slightly lower for the device measured at low light intensity (0.56 V vs. 0.63 V) [132]. Recently, similar responses were found using PSCs evaluated in realistic outdoors testing conditions. At low light intensity (less than 10 mW/cm^2), V_{oc}, FF and PSC were all, to a significant extent, noted to be constant and at their approximate maximum values. However, the value for J_{sc} was observed to be very low, and directly proportional to light intensity. This behaviour was explained in terms of a "double current ionic-electronic model". This model agreed with the experimental data and predicted that the ionic component of the halide perovskite dominates at low light intensity, whereas the electronic component predominates at high light intensity [133]. Investigations on the relation between light intensity on PSCs and PCE are in their infancy, but are anticipated to

facilitate the understanding of the operational mechanisms in mixed ionic-electronic halide perovskite solar cells. Furthering this knowledge will also bring the use of PSC for indoor lighting closer to reality, in addition to applications based on the IoT (internet of things) or ICT (information and communication technologies) [134].

Investigations, in particular as reported by Haque et al. [135], have indicated that ambient atmosphere, specifically molecular oxygen, can adversely affect device stability [135]. Upon irradiation in a dry O_2 atmosphere, it is believed that the photoexcited electrons in the halide perovskite react with molecular oxygen, forming superoxide (O_2^-) which in turn will readily react with the methyl ammonium cation. The degradation products of this process are lead(II) iodide, molecular iodine and water molecules [135]. Many research papers and reviews [26, 31] have appeared which describe the effects of adventitious water on PSC [26, 31]. Generally, the hydrolysis of the halide perovskite, $MAPbI_3$, occurs in the presence of water, resulting in the formation of lead(II) iodide and MAI, together with the subsequent formation of aminomethane and hydroiodic acid [26, 31]. Some variations on this mechanism include the formation of intermediate compounds, usually hydrates such as $(CH_3NH_3)_4PbI_6 \cdot 2H_2O$. However, independent of the exact degradation mechanism, the halide perovskite decomposes into PbI_2 and CH_3NH_3I. Many attempts to improve the stability towards moisture of halide perovskites have been described. Palazon et al. reported that exposure of caesium halide perovskite films to a low flux of X-rays can enhance their stabilities. This effect was postulated to arise from the formation of C=C bonds between the organic ligands, which are present on the perovskite surfaces. The same authors also reported that this treatment helped to immobilize the halide anions, thereby eliminating or reducing ion exchange reactions [136]. Using density functional theory, other researchers modelled the effects of both methylammonium cation orientation and the infiltration of water molecules into empty surface sites on water sensitivity. They proposed that interfacial engineering by, for example, the control of dipole orientation from poling would reduce sensitivity to water [137]. Liu et al. reported on the synthesis of super-hydrophobic materials having great tolerance to humidity. The authors proposed the use of oxide layers such as Mn_3O_4, ZnO and TiO_2, which would be obtained by a simple and scalable fabrication method, based "on-the-fly" functionalization of nanoparticle [138]. One intriguing application for such oxides involves dual-function derivatives which could be applied as both charge carrier layer and as a hydrophobic agent. For example, within the PSC device: as a charge carrier layer and as a repulsive de-wetting agent. Another recently proposed technique for lowering halide perovskite moisture sensitivity involves the application of oxo-functionalized graphene (oxo-G) to PSC. Here, hydroscopic PEDOT is used as the hole transport layer. Along these lines, the authors have already demonstrated that oxo-G can effectively slow down the ingress of water vapour into the device. The resulting material is stable to continuous illumination for 500 h. Stability analyses of the device resulted in T_{60} after 1000 h of light soaking (where 60 in T_{60} represents the remaining PCE, as a percentage, after a specific duration of stability analysis, at which point the stability test will have been completed) [139]. Leijtens et al. showed that lithium ion dopants of the hole transport layer also induce

moisture uptake and device degradation. They furthermore suggested a new hydrophobic hole transport layer to avoid those issues [140]. While halide perovskites are sensitive towards moisture, at the same time humidity has also been shown to facilitate their formation and growth of their thin films [140–144]. In 2014, Yang et al. reported a method for fabricating PSC in humid environments and evaluated the quality of their thin films, grain size, carrier mobility and device stability [144]. Perovskite thin films which have been fabricated under controlled humidity atmospheres have a less continuous morphology and a significant improvement in photoluminescence. This finding has been attributed to a reduction in trap density within the film, which arises from partial solvation of the MA component and "self-healing" of the perovskite lattice [143]. Zhao et al. reported that water vapour has a beneficial effect on the crystallization of perovskite thin films. The effect is reversible and disappears upon removal of the water molecules. The authors studied the mechanism by which water bonds to the halide perovskite and its effect on solar cell performance. It was found that water molecules may undergo hydrogen bonding to uncoordinated ions located on the thin-film surface. This interaction decreases the density of states, which in turn deactivates non-radiative recombination centres [142]. It was found that the concentration of water for thin-film fabrication must lie below 7%, preferably at 5% [141] (Fig. 13.3).

Processing temperature is relevant to two of the most important factors for PSCs, namely halide perovskite crystal growth and overall solar cell stability. High-quality thin films result from solution-state self-assembly and careful control of the annealing temperature. Ideal temperatures for the fabrication of entire devices using scalable fabrication methods lie between 50 and 150 °C.

The transition of the $MAPbI_3$ crystal lattice from a tetragonal to a cubic phase is known to occur at ~50 to ~60 °C. This is accompanied by a distortion of the PbI_6 octahedral around the c-axes, into which the MA^+ cation cannot fit [10]. Whilst the methyl ammonium halide perovskite has been shown to be stable at temperatures exceeding 300 °C, recent results have proven that the degradation of the organic component may take place at relatively low temperatures (~140 °C for $MAPbI_3$).

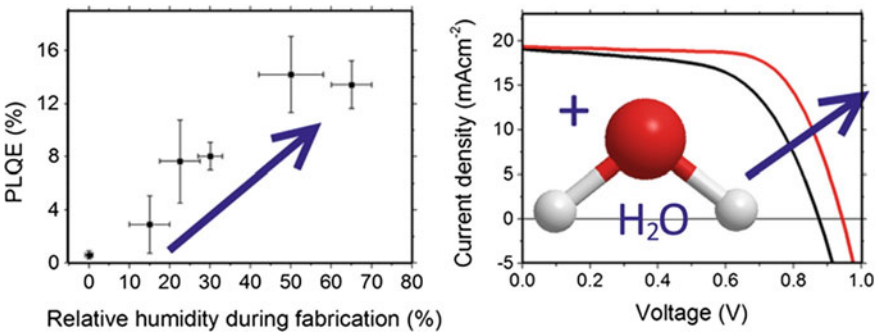

Fig. 13.3 Effect of the relative humidity on the device efficiency during halide perovskite formation. Reprinted with permission from [143]. Copyright 2015 American Chemical Society

The sublimation of the CH_3NH_2 and HI residues results in the decomposition of the halide perovskite and the formation of PbI_2 [145]. The fact that the FA perovskites display thermal stability greater than that of MA is also well documented [146]. For the analogous caesium halide perovskite, the thermal stability is much higher, e.g. 250 °C [147]. However, halide perovskites respond in different ways to elevated temperatures. Factors influencing this outcome include halide composition [148–150], ambient atmosphere [148, 149], fabrication method [34] or thin-film growth substrate [148]. Bryant et al. studied light- and oxygen-induced degradation of $MAPbI_3$ perovskites having a variety of compositions under ambient conditions. The rate of the degradation process was decreased upon exposure to 5% relative humidity in nitrogen gas. The same authors also reported that the use of specific interlayers can reduce the degradation rate [135]. However, in order to validate long-term stability studies according to the ISOS testing and stability procedures [53, 108], temperatures between −40 and 85 °C must be considered. This is relevant because most field studies are undertaken in warmer surroundings (85 °C) [53, 108]. Moreover, temperature is the only variable in many studies on PSC stability. Yet, especially for experiments conducted out of doors, the correlation between other variables becomes important. For example, the composition of the halide perovskite (either single or mixed cations) can influence its thermal stability, in addition to its response to factors like humidity, intensity of irradiation and ambient atmosphere [34]. Furthermore, it has been reported that the internal pressure of encapsulated PSCs will increase together with ambient pressure and temperature [35]. It can therefore be appreciated that much research remains outstanding on the thermal stability of halide perovskites. This is especially true for those new mixed halide perovskites which reach power conversion efficiencies above 21% [20, 23] and are stable over longer periods of time [20].

13.2.2 Intrinsic Factors Affecting Device Stability

Materials: halide perovskites, barrier layers and electrodes. Halide perovskite degradation has been the focus of many research studies and several papers have appeared describing means of reducing the associated processes. In one, the partial substitution of the caesium cation for $HC(NH_2)^{2+}$ in a $FAPbI_3$ perovskite was proposed. Indeed, stability towards light and moisture was improved after this modification; this is attributed to an interaction between $HC(NH_2)^{2+}$ and iodide. The same authors also reported a reduction of trapping sites and an increase in V_{oc}. Also, the PCE improved from 14.9 to 16.5% [146].

A different approach uses TMOs as barrier layers acting as the hole and/or the electron transport layers. Not only TiO_2, but also many other transition metal oxides, can find use as charge transfer electrodes in PSCs, as well as in DSSCs, HSCs and OPVs. TMOS are also replacing certain organic semiconductors, for example spiro-OMeTAD, PEDOT or P3HT (among others). For those latter materials, the costs of synthesis and purification are great and they are produced in

low yield. When used with PSCs, they are also less stable. On the other hand, TMOs have the advantage of being easy to synthesize, inexpensive, having multipurpose conductivity and functionality and being amendable to scalable and low-cost deposition techniques. When used as barrier layers, their moisture resistance has also been shown to enhance the long-term stability of PSCs. However, TMOs are also sensitive to UV light, and any material at their interfaces can readily undergo photodegradation. Indeed, Nishino et al. reported on the formation of PbI_2 from $MAPbI_3$ after irradiation [151]. A general mechanism for this phenomenon proposes the extraction of an electron by TiO_2 from I^- of the $MAPbI_2$, and this leads to $MAPbI_3$ decomposition and I_2 formation. The likelihood of such reactions depends on the optical quality of the oxide surface. Defect states, for example from oxygen vacancies on the oxide surface, may function as reaction sites; thus the crystalline quality of the oxide is of utmost importance. A mechanism is known by which the release of oxygen and its exchange with the ambient atmosphere occurs after irradiation of polymer/oxide solar cells in air. In that case, defects formed upon release of oxygen from the crystalline structure of the oxide may be eliminated through re-exposure of the oxide surface to oxygen. The formation of defect sites can also be either *partially* diminished or suppressed by irradiation through a UV filter. A more detailed section on the application of TMOs in PSCs is presented in Sect. 13.4.1. An alternative solution was proposed by Ito et al. and involves the insertion of a layer of antimony disulfide (Sb_2S_3) into the interface between TiO_2 and $CH_3NH_3PbI_3$ perovskite in a CuSCN-based hole transport layer PSC. The resulting solar cell was stable to light exposure without encapsulation [151]. In the absence of Sb_2S_3, complete device degradation after only 12 h occured and, as a result of the formation of PbI_2 from $CH_3NH_3PbI_3$, the device colour changed to yellow. In yet another approach, the low-temperature solution processablility, high conductivity and excellent electron transfer properties of zinc oxide (ZnO) have led to its application as an ETL in solar cells. Unfortunately, several other reports have found that the halide perovskite degrades at a greater rate in the presence of ZnO than with TiO_2. Finally, Zhao et al. reported that the use of aluminium-doped ZnO as ETL gave a noteworthy enhancement of PSC thermal stability. They ascribed their results to a reaction between the ZnO (a Lewis acid) and the halide perovskite (a Lewis base) [152].

Engineering and functionalization of interfaces. Another means of enhancing solar cell efficiency, stability and lifetime is through interfacial engineering. One strategy started from the functionalization of a layer of poly (3,4-ethylenedioxythiophene)–poly (styrenesulfonate) (PEDOT:PSS) with poly(4-styrenesulfonic acid) (PSSH) to result in planar, inverted PSCs. The interface between the perovskite and PEDOT layers was characterized by electrostatic interactions between sulfonyl functional groups of PEDOT:PSS and the perovskite precursor ions. This modification resulted in printed PSC devices in which PCE values increased from 6 to 10% upon functionalization [153]. The approach of Chan et al. used the solution-processed thiol-functionalized cationic surfactant (11-mercaptoundecyl)

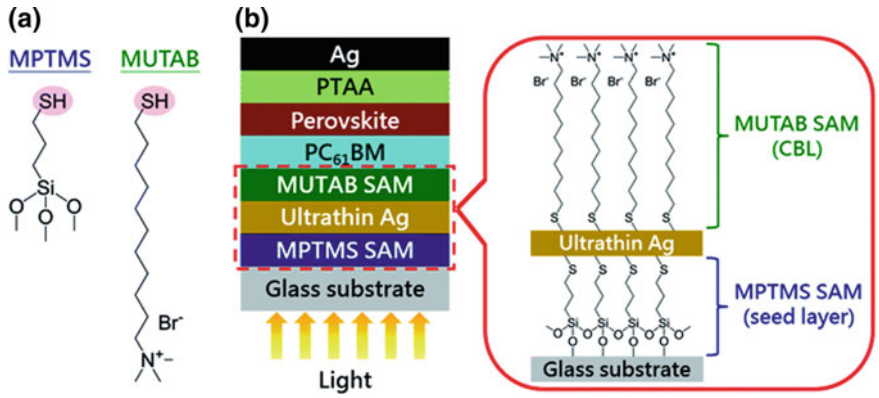

Fig. 13.4 **a** Chemical structures of SAM molecules. **b** Schematic illustration of the device architecture used in this study. Reproduced from [155] with permission from The Royal Society of Chemistry

trimethylammonium bromide (MUTAB) as a cathode buffer layer (CBL) in PSCs. MUTAB interacts with the Ag metal electrode, forming a covalent Ag–S bond. This resulted in reduced contact resistance and highly air-stable solar cells. The same modified Ag electrode was used to fabricate semi-transparent PSCs [154]. Large-area ITO-free PSCs were also produced by layering two thiol-functionalized self-assembled monolayers (SAMs), one containing MUTAB and the other 3-mercapto propyl trimethoxysilane (MPTMS; see Fig. 13.4). According to yet another functionalization method for the silver electrode, ultrathin 8-nm anodes having excellent interfacial properties, low resistance, high transmittance and high stability towards solvents and mechanical deformation were obtained. These authors also reported the presence of interfacial dipoles which can adjust the work function (WF) of the silver electrode from high- to low-WF. These allowed the fabrication of PSCs having 1.2 cm^2 active area and 16% efficiency under ambient pressure and without encapsulation [155].

Several studies have compared solar cell stability before and after interface modification or functionalization. For example, Yao et al. described using polyethylenimine (PEI) cations within the layers of 2D perovskite compounds of the type $(PEI)_2(MA)_{n-1}Pb_nI_{3n+1}$ (n = 3, 5, 7). They observed an improvement in moisture resistance and an increase of charge transport rate. They also found an enhancement of solar cell stability over 500 h in air and in the absence of light (ISOS-D). Afterwards, the cell having a functionalized interface had dropped to T_{80} (a 20% device degradation), while the cells without PEI had experienced complete degradation [156]. A new concept for enhancement of both efficiency and stability of planar PSCs, based on the introduction of an interfacial modification layer which contains the amine-mediated titanium sub-oxide (AM-TiO_x) system, was also demonstrated. Use of this system to protect either aluminium or silver electrodes allowed the extraction and stabilization of ionic defects, which would otherwise

migrate from the perovskite layer into the barrier layer. The PSC which was thereby fabricated possessed vastly improved long-term stability, maintaining T_{90} after 4000 h and T_{80} even after 9000 h (ca. one year) of storage in the absence of light under nitrogen, or 200 h under ambient conditions and without encapsulation [19].

13.2.3 Extrinsic Factors Affecting Device Stability

Device configuration: inverted planar PSCs. In this section, we must initially distinguish between the hysteresis effect and device stability. A solar cell having substantial hysteresis can still be very stable in the absence of light or during experiments using weak illumination. It is true that the hysteresis effect is especially severe for PSCs having a conventional planar configuration (based on TiO_2). However, a new, inverted planar device structure using PCBM as *n*-type conductor showed negligible J–V hysteresis effects [29, 74]. Furthermore, those same investigations indicated that the post-irradiation stability of the PSC cell was different for conventional, mesoscopic and inverted planar configurations (also see Tables 13.4 and 13.5). A PSC with the conventional mesoscopic configuration can show a lifetime greater than 1000 h—when the TiO_2 dense/mesoscopic electrode configuration is used [114, 119, 122, 133, 157]. However, a planar and inverted configuration PSCs of the type FTO/PEDOT:V_2O_5/$MAPbI_{3-x}Br_x$/TiO_x/Ag has obtained one of the greatest device stability known, which is 4000 h at 1 sun illumination and at room temperature [19].

Fabrication issues: additives and solvents. The reason for the use of additives in PSC, is to increase device stability without lowering device performance. To that end, Nazeeruddin et al. explored the use of an aliphatic fluorinated amphiphillic additive, 1,1,1-trifluoro-ethyl ammonium iodide (FEAI). The goal of those studies was to enhance the stability of the PSEs which exhibited a 18% PCE, by modification of the perovskite layer morphology. It was found that this additive increased surface coverage, which reduced solar cell degradation. Those devices showed negligible hysteresis and were resistant to the incursion of moisture. On a molecular level, this phenomenon could be attributed to the hydrophobic nature of the terminal trifluoromethyl groups of FEAI, which were located on the perovskite surface [158].

In another example, the presence of butylphosphonic acid 4-ammonium chloride during the perovskite thin-film fabrication process facilitated the infiltration of the perovskite into the TiO_2 nanoparticles. Consequently, increases in device performance and moisture resistance were both observed. This was attributed to strong hydrogen-bond-mitigated interactions between terminal $–PO(OH)_2$ and $–NH_3^+$ groups of the additive, which induce crosslinking between the perovskite grains and the surface [159]. Yang et al. added acetylacetonate derivatives to PSCs to enhance their electron transport properties. The additives of divalent (II), trivalent (III), and tetravalent (IV) to hexavalent (VI) acetylacetonate were applied and acted as intermediates with the TiO_2 ETM [160]. Solvents and mixture of solvents can also

Table 13.4 Summary of perovskite solar cells stability carried out under shelf conditions (stored in the dark), ISOS-D protocol

Type[a]	Configuration	Area (cm^2)	Eff (%)	Scan rate (mV/s)	Time (h)	T_x	Conditions	Refs.
MC	FTO/TiO_2/$CH_3NH_3PbI_3$/carbon	0.125	6.2		0	T_{100}	Unencap, Air, RT	[201]
MC	FTO/TiO_2-c/TiO_2/$CH_3NH_3PbI_{3-x}Cl_x$/DMC: Spiro-MeOTAD-F4TCNQ/Au	0.16	8.9	200	0	T_{100}	Vacuum	[202]
MC	FTO/TiO_2-c/TiO_2/$CH_3NH_3PbI_{3-x}Cl_x$/Spiro-MeOTAD/Au	0.16	13.5	200	0	T_{100}	Air	[202]
MC	FTO/TiO_2-c/TiO_2/$CH_3NH_3PbI_{3-x}Cl_x$/Spiro-MeOTAD/Au	0.16	11.1	200	0	T_{100}	Vacuum	[202]
MC	FTO/TiO_2-c/TiO_2/$CH_3NH_3PbI_{3-x}Cl_x$/DMC: Spiro-MeOTAD-F4-TCNQ/Au	0.16	4.8	200	0	T_{100}	Air	[202]
MC	FTO/TiO_2-c/TiO_2-m/MeNH3PI3/spiro-OMeTAD/Au	0.045	8.48	125	12	T_{100}	Encap., 1 sun w-LED, Dry N_2	[135]
MC	FTO/TiO_2-c/TiO_2/$FAPbI_3$/Spiro-MeOTAD/Au	0.16	10.4	50	50	T_{10}	Unencap, Ambient	[166]
PI	ITO/PEDOT/$CH_3NH_3PbI_3$/$PC_{61}BM$/CBL/Ag,	0.12	7.03	150	96	T_{10}	Air, 30 °C	[154]
PI	ITO/PEDOT/$CH_3NH_3PbI_3$/$PC_{61}BM$/CBL/Ag,	0.12	15.5	150	96	T_{80}	Air, 30 °C	[154]
MC	FTO/TiO_2-c/Al_2O_3/$CH_3NH_3PbI_3$/SWNT/PC/Ag	0.063	11.2		96	T_{95}		[203]
MC	FTO/TiO_2-c/Al_2O_3/$CH_3NH_3PbI_3$/SWNT/PMMA/Ag	0.063	11.1		96	T_{90}		[203]
PI	FTO/CrO_x/$CH_3NH_3PbI_3$/PCBM/Ag	0.09	9.27	100	140	T_{70}	Air	[100]
PI	FTO/Cu-CrO_x/$CH_3NH_3PbI_3$/PCBM/Ag	0.09	9.27	100	140	T_{10}	Air	[100]
PI	FTO/NiO/$CH_3NH_3PBI_3$/PCBM/Ag	0.07	14.4	20–1000	150	T_{80}	Air, 45–56%RH	[75]
PI	FTO/NiMgLiO/$CH_3NH_3PBI_3$/PCBM/TiO_2/Ca/Ag	>1	18.3	70, 20, 10, 5	168	T_{50}	25 °C, 20%RH	[167]
PI	FTO/NiMgLiO/$CH_3NH_3PBI_3$/PCBM/TiO_2/LiF/Ag	>1		70, 20, 10, 5	168	T_{85}	25 °C, 20%RH	[167]
PI	FTO/NiMgLiO/$CH_3NH_3PBI_3$/PCBM/Ti(Nb)Ox/Ag	>1		70, 20, 10, 5	168	T_{95}	25 °C 20%RH	[167]
MC	FTO/TiO_2-c/TiO_2/$CH_3NH_3PbI_3$/H101/Au	0.2	13.2		168		70 °C	[204]
MC	FTO/TiO_2-c/TiO_2/$CH_3NH_3PbI_3$/Spiro-MeOTAD/Au	0.2	13.7		168		70 °C	[204]
PI	FTO/NiMgLiO/$MAPbI_3$/PCBM/LiF/Ag	0.09/1.02		70, 20, 10, 5	168	T_{85}	Unencap., 20%RH	[167]

(continued)

Table 13.4 (continued)

Type[a]	Configuration	Area (cm^2)	Eff (%)	Scan rate (mV/s)	Time (h)	T_x	Conditions	Refs.
PI	FTO/NiMgLiO/$MAPbI_3$/PCBM/Ca/Ag	0.09/1.02		70, 20, 10, 5	168	T_{55}	Unencap., 20%RH	[167]
PI	FTO/NiMgLiO/$MAPbI_3$/PCBM/Ti(Nb)O_x/Ag	0.09/1.02	18.3	70, 20, 10, 5	168	T_{95}	Unencap., 20%RH	[167]
PI	ITO/PEDOT/$CH_3NH_3PbI_3$/PC_{61}BM/CBL/Ag,	0.12	7.03	150	192	T_{40}	Inert, 65 °C	[154]
PI	ITO/PEDOT/$CH_3NH_3PbI_3$/PC_{61}BM/CBL/Ag,	0.12	15.5	150	192	T_{100}	Inert, 65 °C	[154]
PC	Glass-SAM-Ag-SAM/PCBM/$FAPbI_3$/PTAA: F4TCNQ/Ag	0.122	16.2	150	200	T_{65}	Air	[155]
PI	FTO/PEDOT:V_2O_5/$MAPbI_{3-x}Br_x$/CIL/Ag	0.046	16.09	50–1000	200		Unencap	[19]
MC	FTO/TiO_2-c/TiO_2/$CH_3NH_3PbI_3$/Spiro-MeOTAD/Au	0.1	12.2		240	T_{80}	Unencap	[183]
MC	FTO/TiO_2-c/TiO_2/$CH_3NH_3PbI_3$/TSHBC/Au	0.1	12.8		240	T_{85}	Unencap	[183]
MC	FTO/TiO_2-c/TiO_2/$CH_3NH_3PbI_3$/TSHBC-Graphene/Au	0.1	14		240	T_{90}	Unencap	[183]
MC	FTO/TiO_2-c/TiO_2/$CH_3NH_3PBI_3$/PNBA/Au	3 × 10 mm	11.4		240	T_{92}	Unencap, 25 °C, 30% RH	[205]
MC	FTO/TiO_2-c/TiO_2/$CH_3NH_3PbI_3$/C	0.06	6.9		250	T_{100}	Unencap, 25 °C	[206]
MC	FTO/TiO_2-c/TiO_2/$CH_3NH_3PbI_3$/Au	0.06			250	T_{10}	Unencap, 25 °C	[206]
PI	FTO/MoO_3:PEDOT/PVsk/C60/Bphen/Ag	0.18	3.08	50	250	T_{20}	Unencap, 25 °C, 30% RH	[88]
PI	FTO/MoO_3/$CH_3NH_3PbI_3$/C60/Bphen/Ag	0.18	2.9	50	250	T_{100}	Unencap, 25 °C, 30% RH	[88]
MC	FTO/TiO_2-c/TiO_2/$CH_3NH_3PbI_3$/Ag	0.06			250	T_0	Unencap, 25 °C	[206]
PI	ITO/PEDOT/$MAPb(I_xBr_{1-x})_3$/PCBM/C_{60}/Ag	0.031	10.87	50	250	T_{30}	Air	[98]
PI	ITO/Cu-NiO_x/$MAPb(I_xBr_{1-x})_3$/PCBM/C_{60}/Ag	0.031	11.9	50	250	T_{95}	Air	[98]
PI	ITO/CuO_x/$MAPbI_3$/C60:BCP/Ag	0.1	15.2	300	250	T_{90}	Air	[85]
PI	ITO/PEDOT/$MAPbI_3$/C60:BCP/Ag	0.1	13.5	300	250	T_{40}	Air	[85]
MC	FTO/TiO_2-c/TiO_2/$CH_3NH_3PBI_3$/ZrO_2-m/NiO-ns/C	0.6	14.2	50	250	T_{60}	N_2	[79]

(continued)

Table 13.4 (continued)

Type[a]	Configuration	Area (cm^2)	Eff (%)	Scan rate (mV/s)	Time (h)	T_x	Conditions	Refs.
PI	ITO/PEDOT/$CH_3NH_3PbI_3$/$PC_{61}BM$/CBL/Ag,	0.12	15.5	150	336	T_{70}	Air	[154]
MC	FTO/TiO_2/$MAPbI_3$/Spiro-MeOTA/Au	0.16	6.2	60	384	T_{95}	Air, 15–20%RH	[207]
MC	FTO/TiO_2/$CsPbi_3$/Spiro-MeOTA/Au	0.16	6.5	60	384	T_{10}	Air, 15–20%RH	[207]
MC	FTO/TiO_2/$CH_3NH_3PbI_3$/carbon	0.125	6.8		400	T_{160}	Unencap, Air, RT	[201]
PC	FTO/TiO_2-c/TiO_2/$CH_3NH_3PbI_{3-x}Cl_x$/DMC: Spiro-MeOTAD-F4-TCNQ/Au	0.16	8.9	200	430	T_{100}	Vacuum	[202]
PC	FTO/TiO_2-c/TiO_2/$CH_3NH_3PbI_{3-x}Cl_x$/DMC: Spiro-MeOTAD:F4-TCNQ/Au	0.16	9.7	200	430	T_{200}	Air	[202]
PC	FTO/TiO_2-c/TiO_2/$CH_3NH_3PbI_{3-x}Cl_x$/Spiro-MeOTAD/Au	0.16	7.3	200	480	T_{45}	Air	[202]
PC	FTO/TiO_2-c/TiO_2/$CH_3NH_3PbI_{3-x}Cl_x$/Spiro-MeOTAD/Au	0.16	6.5	200	480	T_{40}	Vacuum	[202]
MC	FTO/TiO_2-c/TiO_2/$CH_3NH_3PBI_3$/TTF-1/Au		11.03		500	T_{80}	Unencap, 25 °C, 40% RH	[208]
MC	FTO/TiO_2-c/TiO_2/$CH_3NH_3PBI_3$/Spiro-MeOTAD/Au		11.4		500	T_0	Unencap, 25 °C, 40% RH	[208]
MC	FTO/ZnO NRs/$CH_3NH_3PBI_3$/Spiro-MeOTAD/Ag	0.20	5		500	T_{13}		[110]
MC	FTO/TiO_2/$CH_3NH_3PbI_3$/Spiro-MeOTAD/Au	0.16	9.7		500	T_{100}	Unencap, 25 °C	[209]
MC	FTO/TiO_2/$MAPb(I_xBr_{1-x})_3$/PTAA/Au	0.16	12.3		528	T_{100}	Unencap, 25 °C, 35–55%RH	[210]
MC	FTO/TiO_2/$CH_3NH_3PBI_3$/Spiro-MeOTAD/Ag	6	15.2		576	T_{70}	Unencap	[118]
MC	FTO/TiO_2/$CH_3NH_3PBI_3$/Spiro-MeOTAD/Al2O3/Ag	6	12.9		576	T_{90}	Unencap	[118]
PC	FTO/SnO_2/$CH_3NH_3PBI_3$/Spiro-MeOTAD/Ag	0.04	13		700	T_{90}	25 °C	[179]
PC	FTO/TiO_2/$CH_3NH_3PBI_3$/Spiro-MeOTAD/Ag	0.04	13		700	T_{65}	25 °C	[179]
MC	FTO/TiO_2-c/TiO_2/$CH_3NH_3PBI_3$/C	0.12	7.4		800	T_{100}	Unencap, 25 °C	[211]
PC	FTO/TiO_2-c/TiO_2/$CH_3NH_3PbI_{3-x}Cl_x$/DMC: Spiro-MeOTAD:F4-TCNQ/Au	0.16	9.0	200	840	T_{101}	Vacuum	[202]

(continued)

Table 13.4 (continued)

Type[a]	Configuration	Area (cm^2)	Eff (%)	Scan rate (mV/s)	Time (h)	T_x	Conditions	Refs.
PC	FTO/TiO_2-c/TiO_2/$CH_3NH_3PbI_{3-x}Cl_x$/DMC: Spiro-MeOTAD:F4-TCNQ/Au	0.16	8.3	200	840	T_{172}	Air	[202]
PC	FTO/TiO_2-c/TiO_2/$CH_3NH_3PbI_{3-x}Cl_x$/Spiro-MeOTAD/Au	0.16	7.5	200	890	T_{45}	Air	[202]
PC	FTO/TiO_2-c/TiO_2/$CH_3NH_3PbI_{3-x}Cl_x$/Spiro-MeOTAD/Au	0.16	5.7	200	890	T_{50}	Vacuum	[202]
MC	FTO/TiO_2-c/TiO_2/$CH_3NH_3PBI_3$/PCBTDPP/Au	0.11	3.04		1000	T_{100}	Unencap, 25 °C	[212]
MC	FTO/TiO_2-c/TiO_2/$CH_3NH_3PBI_3$/P3HT/Au	0.11	0.76		1000			[212]
MC	FTO/TiO_2-c/TiO_2/$CH_3NH_3PbI_3$/PCBTDPP/Au	0.09	9.2		1000	T_{100}	Unencap, 25 °C, 20% RH	[213]
MC	FTO/TiO_2-c/TiO_2/$CH_3NH_3PbI_3$/P_3HT/Au	0.09	7.6		1000	T_{95}	Unencap, 25 °C, 20% RH	[213]
MC	FTO/TiO_2-c/TiO_2/$CH_3NH_3PbI_3$/Spiro-MeOTAD/Au	0.09	6.3		1000	T_{30}	Unencap, 25 °C, 20% RH	[213]
MC	FTO/TiO_2-c/TiO_2/Al_2O_3/$CH_3NH_3PbI_3$/NiO/C	0.16	15.03		1000	T_{80}	Unencap, 25 °C, 40% RH	[114]
MC	FTO/TiO_2-c/TiO_2/Al_2O_3/$CH_3NH_3PbI_3$/NiO/C	0.16	15.03		1000	T_{95}	Unencap, 60 °C, 10% RH	[114]
PI	FTO/NiMgLiO/$CH_3NH_3PbI_3$/PCBM/Ti(Nb)Ox/Ag	>1		70, 20, 10, 5	1000	T_{100}	25 °C, 20'%RH	[167]
MC	FTO/TiO_2/$CH_3NH_3PbI_3$/FeS_2-np/Au		12.56	X	1000	T_{93}	Unencap, Air	[214]
MC	FTO/TiO_2/$CH_3NH_3PbI_3$/Spiro-MeOTA/Au		14.20	x	1000	T_{63}	Unencap, Air	[214]
MC	FTO/TiO_2-c/TiO_2/$Cs_{0.2}FA_{0.8}PbI_{2.84}Br_{0.16}$/ Spiro-MeOTAD/Au	0.16	17.35	50	1000	T_{90}	Unencap, Ambient	[166]
MC	Glass-SAM-Ag-SAM/PCBM/$FAPbI_3$/PTAA: F4TCNQ/Ag	0.122	16.2	150	1000	T_{70}	Air	[155]
MC	FTO/TiO_2-c/TiO_2/Al_2O_3/NiO/$CH_3NH_3PbI_3$/Carbon	0.16	15.03		1000	T_{80}	Encap., 60 °C	[114]
MC	FTO/TiO_2-c/TiO_2/Al_2O_3/NiO/$CH_3NH_3PbI_3$/Carbon	0.16	15.03		1000	T_0	Encap., RT	[114]

(continued)

Table 13.4 (continued)

Type[a]	Configuration	Area (cm^2)	Eff (%)	Scan rate (mV/s)	Time (h)	T_x	Conditions	Refs.
PI	ITO/SAM:Ag:SAM/PCBM/MAPbI3/PTAA/Ag		14.48	240	1000			[155]
PI	FTO/NiO/$CH_3NH_3PBI_3$/ZnO/Al	0.1	16.1	20	1440	T_{95}	Unencap, 25 °C, 30–50%RH	[187]
PI	FTO/PEDOT/$CH_3NH_3PBI_3$/PCBM/Al	0.1	13.5	20	1440	T_0	Unencap, 25 °C, 30–50%RH	[187]
PC	FTO/TiO_2/$CH_3NH_3PbI_{3-x}Cl_x$/NiOx/Ni	0.1	7.28		1440			[191]
PC	FTO/TiO_2/$CH_3NH_3PbI_{3-x}Cl_x$/Spiro-MeOTAD/Ag	0.1	8.24		1440			[191]
PI	FTO/NiO/$CH_3NH_3PbI_{3-x}Cl_x$/PCBM:PN4 N/Ag	0.1	10.97	10–100	1440	T_{60}	Air	[81]
PI	FTO/NiO:DEA/$CH_3NH_3PbI_{3-x}Cl_x$/PCBM:PN4 N/Ag	0.1	15.90	10–100	1440	T_{88}	Air	[81]
MC	FTO/TiO_2/$CH_3NH_3PbI_3$/carbon	0.12	3.7		2000	T_{40}	Unencap, Air, RT	[201]
PC	FTO/TiO_2/$CH_3NH_3PBI_3$/Au		10		2160	T_{66}	25 °C, 30%RH	[215]
MC	FTO/TiO_2-/TiO_2/$MAPbI_3ZrO_2$/C	0.16	10	25	2160	T_{100}	Encap, 45 °C	[122]
MC	FTO/TiO_2-c/TiO_2/$CH_3NH_3PBI_3$/C	0.06			2500	T_{100}	Unencap, 25 °C, 70%RH	[206]
MC	FTO/TiO_2-c/TiO_2/$CH_3NH_3PBI_3$/C	0.06			2500	T_{100}		
MC	FTO/TiO_2-NRs/$CH_3NH_3PbI_{3-x}Cl_x$/Spiro-MeOTAD/Au	10.8	10.5	40	2500	T_0	Encap.	[111]
MC	FTO/TiO_2-Planar/$CH_3NH_3PbI_{3-x}Cl_x$/Spiro-MeOTAD/Au	10.8	5.8	40	2500	T_{100}	Encap.	[111]
MC	FTO/TiO_2-np/$CH_3NH_3PbI_{3-x}Cl_x$/Spiro-MeOTAD/Au	10.8	7.9	40	2500	T_{50}	Encap.	[111]
MC	FTO/TiO_2/$MAPbI_3$:FEAI/Spiro-MeOTAD/Ag	0.16	18	5	2880	T_{92}	Air	[158]
MC	FTO/TiO_2/$MAPbI_3$/Spiro-MeOTAD/Ag	0.16	15.4	5	2880	T_{79}	Air	[158]
PI	FTO/PEDOT:V_2O_5/$MAPbI_{3-x}Br_x$/CIL/Ag	0.04	16.09	50–1000	9000		Encap.	[19]

ISOS Protocols [108]: ISOS-D refers to Dark (storage) conditions

[a]*PI* Planar Inverted; *PC* Planar Conventional; *MC* Mesoscopic Conventional

Table 13.5 Summary of perovskite solar cells stability carried out under light irradiation conditions (artificial and outdoor)

Type[a]	Configuration	Area (cm^2)	Eff (%)	Scan rate (mV/s)	Time (h)	T_x	Conditions	Refs.
MI	FTO/NiO/$CH_3NH_3PBI_3$/PCBM/BCP/Ag		10.4		10 min		1 sun	[216]
MI	FTO/NiO-m/Al_2O_3/$CH_3NH_3PBI_3$/PCBM/BCP/Ag		11.6		10 min		1 sun	[216]
PI	ITO/PEDOT/$MAPbI_3$/PCBM/Al				1		1 sun	[103]
MC	FTO/TiO_2-c/TiO_2-m/$MAPbI_3$/spiro-OMeTAD/Au	0.045		125	5	T_{20}	Unencap., Dry Air/Light, 1 sun. w-LED, UV Filter	[135]
MC	FTO/TiO_2-c MeNH3PbI_3/spiro-OMeTAD/Au	0.045		125	5	T_5	Unencap., Dry Air/Light, 1 sun. w-LED, UV Filter	[135]
MC	FTO/TiO_2-c/Al_2O_3-m/MeNH3PbI3/spiro-OMeTAD/Au	0.045		125	5	T_0	Unencap., Dry Air/Light, 1 sun. w-LED, UV Filter	[135]
MC	FTO/TiO_2-c/TiO_2-m/$MeNH_3PI_3$/spiro-OMeTAD/Au	0.045	9.30	125	12	T_{100}	Encap., 1 sun w-LED, UV Filter. N_2Dry	[135]
MC	FTO/TiO_2-c/TiO_2-m/$MeNH_3PI_3$/spiro-OMeTAD/Au	0.045	9.42	125	12	T_{100}	Encap., 1 sun w-LED, UV Filter Dry air. Encap., 1 sun	[135]
MC	FTO/TiO_2-c/TiO_2-m/$MeNH_3PI_3$/spiro-OMeTAD/Au	0.045	8.70	125	12	T_0	w-LED, UV Filter N_2, 85%RH. Encap., 1 sun.	[135]
MC	FTO/TiO_2-c/TiO_2-m/$MeNH_3PI_3$/spiro-OMeTAD/Au	0.045	9.30	125	12	T_0	w-LED, UV Filter Dry Air. Encap., 1 sun	[135]
MC	FTO/TiO_2-c/TiO_2-m/$MeNH_3PI_3$/spiro-OMeTAD/Au	0.045	8.54	125	12	T_0	w-LED, UV Filter Dry Air 85%RH	[135]
MC	FTO/TiO_2-c/TiO_2/$CH_3NH_3PBI_3$/Spiro-MeOTAD/Au	0.10			17	T_{25}	Unencap., 45%RH, 1 sun	[183]
MC	FTO/TiO_2-c/TiO_2/$CH_3NH_3PBI_3$/TSHBC/Au	0.10	12.8		17	T_{55}	Unencap., 45%RH, 1sun	[183]
MC	FTO/TiO_2-c/TiO_2/$CH_3NH_3PBI_3$/ TSHBC-Graphene/Au	0.10	14		17	T_{70}	Unencap., 45%RH, 1 sun	[183]

(continued)

Table 13.5 (continued)

Type[a]	Configuration	Area (cm^2)	Eff (%)	Scan rate (mV/s)	Time (h)	T_x	Conditions	Refs.
MC	FTO/TiO_2-m/$MAPI_3$/spiro-OMeTAD/Au				60		70 sun	[217]
MC	FTO/TiO_2/$FAPbI_3$/spiro-OMeTAD/MoOx/Metal		16.3	110	70		<50% RH, 65 °C, N_2, 1sun	[218]
MC	FTO/TiO_2-c/Al_2O_3/$CH_3NH_3PbI_{3-x}Cl_x$/SWNT/PC/Ag	0.063	11.2		96	T_{95}	Encap.	[203]
MC	FTO/TiO_2-c/Al_2O_3/$CH_3NH_3PbI_{3-x}Cl_x$/ SWNT/PMMA/Ag	0.063	11.1		96	T_{90}	Encap.	[203]
MC	FTO/TiO_2-c/Li-doped TiO_2-m/$Cs_x(MA_{0.17}FA_{0.83})_{(100-x)}Pb(I_{0.83}Br_{0.17})_3$/ Spiro-OMeTAD/Au	0.16	17.4	10	100	T_{56}	N_2, RT, 1 sun	[20]
PI	TO/PEDOT/$MAPbI_3$/PCBM/Al:ZnO/ITO/MgF_2	0.12, 0.39	10.46		120		100, 1 sun w-LED	[219]
MC	FTO/TiO_2/$MAPbI_3$/spiro-OMeTAD/MoO_x/Metal	0.06		200	150	T_{30}	1 sun	[91]
MC	FTO/TiO_2-c/$CH_3NH_3PBI_3$/TiO2/ZrO_2/C	0.283	11.5	25	168	T_{100}	Encap., measured at noon	[122]
PI	ITO/SAM:Ag:SAM/PCBM/$MAPbI_3$/PTAA/Ag		14.48	240	200		1 sun	[155]
MC	FTO/TiO_2/$FA_{0.9}Cs_{0.1}PbI_3$/spiro-OMeTAD/MoO_x/ Metal		17.3		200		<50% RH, 65 °C, N_2, 1 sun	[218]
	Encap.							[113]
PI	TO/PEDOT/$MAPbI_3$/PCBM/Al:ZnO/ITO/MgF_2	0.12, 0.39	12.20		225		35, 1 sun w-LED	[219]
MC	FTO/TiO_2-c/TiO_2/$CH_3NH_3PBI_3$/Spiro-MeOTAD/Au		12.75		240	T_{92}	Unencap., 25 °C, 1sun	[220]
MC	FTO/TiO_2-c/TiO_2/$CH_3NH_3PBI_3$/FA-MeOPh/Au		11.86		240	T_{75}	Unencap., 25 °C, 1sun	[220]
MC	FTO/TiO_2-c/TiO_2/$CH_3NH_3PBI_3$/TPA-MePh/Au		10.79		240	T_{58}	Unencap., 25 °C, 1sun	[220]
MC	FTO/TiO_2-c/Li-doped TiO_2-m/$Cs_x(MA_{0.17}FA_{0.83})_{(100-x)}Pb(I_{0.83}Br_{0.17})_3$/ Spiro-OMeTAD/Au	0.16	21.1	10	250	T_{100}	Encap., N_2, RT, 1 sun	[20]
MC	FTO/TiO_2/$MAPbI_3$/spiro-OMeTAD/Carbon	0.152	13.6	100	720		1 sun	[194]

(continued)

Table 13.5 (continued)

Type[a]	Configuration	Area (cm^2)	Eff (%)	Scan rate (mV/s)	Time (h)	T_x	Conditions	Refs.
MC	FTO/TiO_{2-c}/TiO_2/Al_2O_3/NiO/$CH_3NH_3PBI_3$/Carbon	0.16	15.03		1000	T_{40}	Encap., 25 °C, 40% RH, 1sun w-LED	[114]
PI	FTO/NiMgLiO/$MAPbI_3$/PCBM/Ti(Nb)O_x/Ag	0.09/1.02	16.2	70, 20, 10, 5	1000	T_{90}	Encap., 100 mW/cm^2 UV filter	[167]
MC	FTO/TiO_{2-c}/Al_2O_3/CH3$NH_3PbI_{3-x}Cl_x$/ Spiro-MeOTAD/Au	0.09	12		1000	T_{50}	Encap., 40 °C, 1 sun, No UV filter	[157]
MC	FTO/TiO_{2-c}/TiO_2/$CH_3NH_3PBI_3$/ZrO_2/C	0.16	9	25	1050	T_{100}	Unencap., 45 °C, 1 sun w-LED, Ar	[122]
MC	FTO/TiO_2/$(FAPbI_3)_{0.85}(MAPbBr_3)_{0.15}$/ Spiro-OMeTAD/Au	0.36	14.5	20	1008		ISOS-O, encapsulated, 25 °C	[133]
MC	FTO//TiO_2/ZrO_2/$(5\text{-}AVA)_xMA_{1-x}PbI_3$/C		11.6	3	1000		Unencap., RT, 1 sun	[119]
MC	FTO//TiO_2/ZrO_2/$MAPbI_3$/C		7.2	3	1000		Unencap., RT, 1 sun	[119]
PI	FTO/PEDOT:V_2O_5/$MAPbI_{3-x}Br_x$/CIL/Ag	0.046	16.09	50–1000	4000		RT, 1 sun	[19]

ISOS Protocols [108]: ISOS-L refers to Laboratory conditions (artificial light) and ISOS-O refers to Outdoor conditions

[a]*PI* Planar Inverted; *PC* Planar Conventional; *MC* Mesoscopic Conventional; *MI* Mesoscopic Inverted

modify device performance and enhance stability. For example, γ-butyrolactone-dimethylsulphoxide mixtures followed by toluene drop-casting permits fabrication of dense, uniform and hysteresis-free perovskite layers with enhanced device performance [73]. Another study described the addition of hydroiodic acid, followed by treatment with isopropyl alcohol (IPA) to manufacture $CsPbI_3$-based PSCs. While the resulting device was not very efficient, this example still demonstrated that "solvent engineering" is a valid means of enhancing device performance and especially stability [161].

Encapsulation and mechanical stability. Good mechanical stability is compulsory for devices using portable electronics, especially in the context of flexible and wearable PSCs. The effects of bending are unfortunately a major issue, although several encouraging approaches have recently been described. For example, fiber-like PSCs can deform with a bending radius of 1 mm [162, 163], which is suitable for the human wrist. This device even had a PCE efficiency which was constant after more than 1000 bending cycles. After that period, a drop in PCE of only 7% was measured, which could be attributed to the formation of cracks in the transparent TiO_x conducting oxide layer [162, 163].

13.3 Long-Term Stability of PSCs

The investigation of factors affecting the long-term stability of PSCs is a relatively new area for the photovoltaic research community. Although the PCE of some PSCs have reached 22% efficiency, there are still many questions about different aspects and working mechanisms to be answered before the rational control and enhancement of device lifetimes becomes possible. Studies on the long-term stability of PSCs have evolved from initial findings of lifetimes in the minutes-to-hours range in the absence of illumination, to hundred-to-thousands of hours for current devices under conditions of continuous irradiation, variable weather and ambient outdoors conditions. In contrast to other emerging photovoltaic technologies, PSCs are based on mixed ionic-electronic conductors (MIEC) and their ionic components, which induce the hysteretic behaviour observed from IV-curves. As already discussed in Sect. 13.1, the extent of hysteresis is thought to depend on the steady-state regime of the solar cell [71]. This encompasses many different factors and device configurations. For example, special care is needed while recording IV-curves; this is especially true for the scanning speed and direction (forward or backward) [164]. Also, as already detailed in Sect. 13.1.1 (Best practices for measuring PSC), it is important to carefully determine the steady-state conditions (SSC) used for accurate determination of PSC properties. It is also important to note that the maximum power point method (MPP) for investigation of PSCs can guarantee the correct interpretation of the solar cell parameters. The MPP value is obtained by applying a constant voltage to the cell near the maximum power point, followed by monitoring the observed power output until a constant value is observed [165]. The protocols followed for many degradation studies were

initially developed for DSSCs and OPVs. These encompass the ISOS testing and stability procedures [53, 108], and are endorsed by the photovoltaic research community. Those protocols consider temperatures between −40 and 85 °C, although most real studies are undertaken in warmer surroundings (85 °C) [53, 108]. In the following sections, we describe the different stability tests carried out on PSCs in the absence of light (shelf, ISOS-D protocol, Table 13.4), and under different irradiation conditions, (ISOS-L protocol, Table 13.5). For purposes of comparison, we have included a column containing the experimental scan rates and active areas for each cell. We noticed that following the initial reports in 2014 describing PSC hysteresis, many other publications have appeared which detail other methods of reducing or avoiding this effect [71, 164, 165]. Nowadays, an increasing number of publications additionally state the scanning direction. The scan rates which were initially used for *IV* measurement have also dropped from 200–300 mV/s to the <50 mV/s range (Tables 13.4 and 13.5). Nevertheless, it is important to remember that decreasing the scan rate to low mV/s for determination of the *IV* curve cannot guarantee optimal device performance. Kamat et al. have shown that very slow scan rates can still underestimate the solar cell performance [55, 56, 64]. Thus, it is recommended to ensure that the optimal solid-state conditions (SSC) have been determined for each device. In Tables 13.4 and 13.5, we have included a column which provides the remaining PCE (as a percentage) after a specific duration of stability analysis, at which point the stability test will have been completed (T_x). For example, and as already explained, a PSC which had retained 80% of its original PCE after 1000 h of operation would have a T_{80} at 1000 h, i.e. only 20% degradation would have occurred.

Since studies on the long-term stability of PSC are scarce, we have therefore divided the following sections into two parts: measurements in the absence of light (usually by virtue of being stored in the dark) and measurements carried out under illumination. In general terms, these are the ISOS-D and ISOS-L protocols (see Tables 13.4 and 13.5, respectively.). Some earlier studies also report measurements which were conducted outdoors (ISOS-O). While still included in Table 13.5, nowadays such data is very infrequently reported.

13.3.1 Stability of PSC in the Absence of Light (ISOS-D)

The most frequently reported long-term stability test for PSC involves storage in the absence of light. Variables such as encapsulation, temperature, relative humidity or atmosphere may affect the final measurement outcome, and hence are also included in the test. Generally, in the absence of light, maintained at room temperature (or below) and under low relative humidity conditions (usually <30–40%), PSCs are stable for long periods of time. Under these conditions, encapsulation is not necessary and the devices may be used in either dry air or nitrogen.

As the data in Table 13.4 indicates, the most studied halide perovskite is $CH_3NH_3PbI_3$, followed by $CH_3NH_3PbI_{3-x}Cl_x$. Mixed cation halide perovskites also show exceptional stabilities. The addition of caesium cations to $FAPbI_3$ produces $Cs_{0.2}FA_{0.8}PbI_{2.84}Br_{0.16}$, which, under ambient conditions, displays greater stability than does simple $FAPbI_3$. After 1000 h illumination in air, this material still shows T_{90} [166].

Two examples using $MAPbI_3$, the transparent FTO electrode and in combination with other additives are also known. In one, a planar, inverted device containing Ni–Mg–LiO mixed salts, and which was configured as FTO/NiMgLiO/$MAPbI_3$/PCBM/Ti(Nb)Ox/Ag, possesses a T_{100} [167]. The associated measurements were carried out at 25 °C and 20% relative humidity. In another instance, the use of an aliphatic, fluorinated, amphiphillic compound, FEAI in a FTO/TiO_2/$MAPbI_3$:FEAI/Spiro-MeOTAD/Ag cell having a normal mesoscopic configuration was explored for effects on device stability. Using an extended stability test duration of 2880 h in the absence of illumination under air, the PSC almost kept its original PCE value, T_{92} [158]. To our knowledge, the greatest stability in the absence of light was measured for a PSC device having a planar, inverted configuration and whose ETL was functionalized with a so-called chemical inhibition layer (CIL). In this case, the CIL consisted of an amide-mediated titanium sub-oxide system. Hence, the entire system was configured as FTO/PEDOT:V_2O_5/$MAPbI_{3-x}Br_x$/CIL/Ag. In a stability test conducted after illumination for 9000 h, the modified device maintained T_{80}. For comparison, in the absence of the CIL treatment and after only 200 h of irradiation it gave T_{70} [19]. The same authors also reported the complete absence of hysteresis in the *IV*-curves, even after the stability test.

13.3.2 Stability of PSCs Under Light Irradiation (ISOS-L)

Although still infrequent, long-term stability measurements carried out on PSCs under conditions of moderate illumination have indicated stabilities in the 100–1000 h range. Such initial results are inspiring to the PSC research community and are promising for further developments throughout diverse solar cell research. Recently, Li et al. undertook outdoor stability measurements on $MAPbI_3$-based PSCs having PCE values in the 13% range and using high intensity light. Those devices were kept outdoor for 168 h (7 days), and their PCE values determined only once per day [122]. Other stability experiments undertaken by the same authors were according to the ISOS-L-2 protocol [108] (encapsulated sample, 80–85 °C, 1 sun LED white light, no UV light) and over 2160 h (90 days). After that period of time, the device still showed an encouraging final PCE of $\sim$10% [122]. In addition, Saliba et al. recently reported the use of "triple cation"-based (Cs/MA/FA) PSCs having 21.1% PCEs and, after 250 h of LED illumination (as opposed to UV light), good device lifetime [20]. In our own laboratory, we have constructed devices from mixed PSCs and having UV filter/FTO/TiO_2/$(FAPbI_3)_{0.85}(MAPbBr_3)_{0.15}$/Spiro-OMeTAD/Au configurations. Our measurements indicated

stabilities in excess of 1000 h under real outdoor conditions for these devices. Determination of the response from these PSCs under different light irradiation conditions suggests a highly ionic and electronic character of the perovskite concerned, with an increase in the ionic component under low-intensity light conditions [133].

13.4 Some Methods to Enhance Device Stability

Many methods have been proposed and published to enhance PSC lifetime and stability. In this section, we have selected a few examples, being the best ones those that have made an important improvement due to the enhanced stability observed on devices made by large-scale fabrication applying low-cost printing methods.

13.4.1 The Application of Oxides as Charge Extraction Layers

Transition metal oxides (TMOs) are standard materials applied nowadays in many optoelectronic devices such as thin-film photovoltaics (TFPVs), thin-film transistors (TFTs) or organic light emitting diodes (OLEDs) [168]. Attention is now directed into their manufacture which should include large-scale, large-volume, flexible and disposable/reusable devices. This is especially true for 3rd and 4th generation solar cells like, OPVs, HSCs, DSSCs or PSCs, where large-scale, large-volume fabrication requires low-cost fabrication and the possibility to be competitive with current Si-based photovoltaic technologies. As ideal candidates to act as barrier layers in PSCs, they should meet the following requirements: (a) good compatibility with the active layer, (b) optical transparency, (c) good conductivity, (d) good charge transport properties and (e) good processablility. They also to confer moisture resistant properties required for the fabrication of stable PSCs. Comparison between interlayers made of TMOs and the classical organic semiconductors (i.e. PEDOT:PSS) have resulted in devices with similar or enhanced power conversion efficiency and superior lifetimes. In PSCs TMOs have been applied as electron transport materials (ETM) or hole transport materials (HTM). As ETMs the most common oxide is the TiO_2, but others like ZnO [148, 169–175], WO_3 [112, 176–178], SnO_2 [179], and graphene oxide [180–184] are also being applied in PSCs. Complex TMOs such as $ZnSnO_4$ [136] or $SrTiO_3$ [182, 185, 186] are also examples of recently applied oxides with enhanced conductivity and optical quality if compared to their homologues basic oxides. As HTM NiO is the most applied oxide [75–83], followed by CuO_x [84–86], MoO_x [87–91], V_2O_5 [19, 92–95], or GeO_2 [96], which are now breaking ground. A major problem in these oxides is the high resistive properties of the bare oxides, so new examples applying doped Oxides like

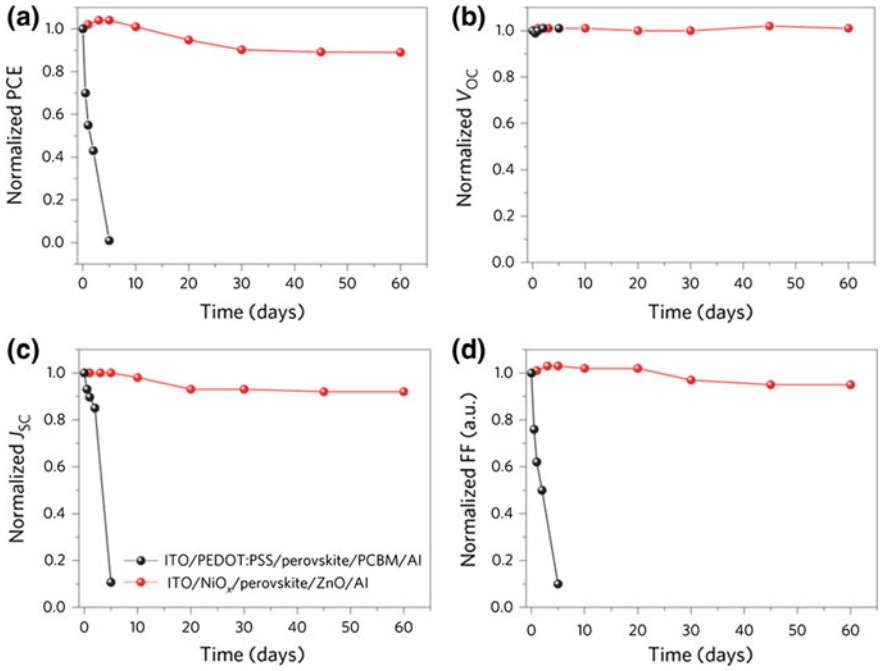

Fig. 13.5 Planar and inverted perovskite solar cells of the type ITO/NiO/halide perovskite/PCBM/Al (*black*) and ITO/NiO/halide perovskite/ZnO/Al (*red*), as a function of storage time in air at 25 °C and 30–50 RH %. Reprinted by permission from Macmillan Publishers Ltd: Nat. Nano [187], copyright 2016

Cu-doped NiO and CrO_x [97–100], are of high interest. The application of doped oxides permits conductivity properties to be tuned, as well as the work function and band alignment of the oxide thin film.

You et al. reported the application of a solution-processed PSCs applying p-type NiO and n-type ZnO nanoparticles as hole and electron transport layers, respectively, [187]. The final stability of the devices was enhanced against water and oxygen in comparison of devices applying PEDOT (Fig. 13.5). The PSC has the inverted planar configuration with a p–i–n structure of the type ITO/NiO/halide perovskite/ZnO/Al. Authors report on the isolation capability of the ZnO layer from the Al electrode which enhances device stability by preventing the degradation of Al. T_{90} was observed after 60 days of storage in the dark in air at room temperature which is much larger than devices applying PEDOT:PSS which were completely degraded after only 6 days [187]. The application of TMOs in conjunction with metal electrodes like Au, Ag or Al has been the basis of a study carried out by Sanehira et al. where MoO_x was applied as a thin layer in between the halide perovskite and the metal electrode. Authors found that the application of the MoO_x maintained the PCE of the original device (without oxide layer), but most important, they demonstrated that unencapsulated devices analysed under constant

irradiation conditions in air displayed significant stability enhancement. MoO_x is reported to inhibit the decomposition of the electrode by the halide perovskite [91].

Despite clear advantages on the application of TMOs, there are several issues that must be overcome for the technology to reach large-area fabrication by printing methods. Some of these issues are the low conductivity that characterizes oxide layers and the difficult to deposit very thin and homogeneous films (without pinholes or defects). In this respect, the application of doped TMOs has emerged as a solution to solve these problems. Doped oxides offer the possibility to tune the TMOs conductivity in very thin dense films that can also be deposited by solution processing techniques with good quality and homogeneity. Some doped oxides applied in PSC are Cu-doped CrO_x [100] or Cu-doped NiO [98, 188].

A remarkable work has been recently reported by Han et al. who applied doped oxides as charge carrier layers: $Ti_{0.95}Nb_{0.05}O_x$ was used as the ETL and $Li_{0.05}Mg_{0.15}Ni_{0.8}O$ as the HTL [167]. The conductivity of the oxides can be tuned by

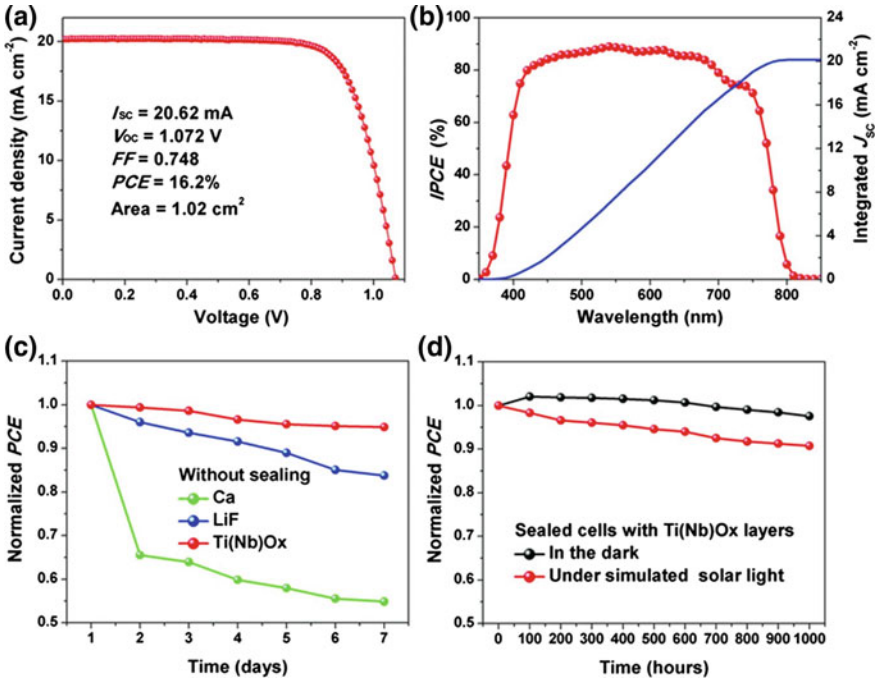

Fig. 13.6 Performance and stability of large-area (>1 cm^2) PSCs applying doped oxides as charge extraction layers. The devices have a configuration FTO/$Li_{0.05}Mg_{0.15}Ni_{0.8}O$/$MAPbI_3$/PCBM/$Ti_{0.95}Nb_{0.05}O_x$/Ag. **a** *J-V* curve of the champion cell endowed with antireflection film. **b** The corresponding IPCE spectrum (*red*) and integrated J_{sc} (*blue*). **c** The stability of the cells without sealing, based on different electron extraction layers of Ca (4 nm), LiF (1.5 nm), and $Ti_{0.95}Nb_{0.05}O_x$ (10 nm) between PCBM and the Ag contact. The cells were kept in a dry cabinet (<20% humidity) in the dark and measured in ambient air. **d** Stability of sealed cells kept in the dark or under simulated solar light (AM 1.5; 100 mW cm^{-2}; using a 420-nm UV light cut-off filter; surface temperature of the cell, 45–50 °C; bias potential, 0 V). From Ref. [167]. Reprinted with permission from AAAS

modifying the amount of "x", optimizing at the same time their alignment. The metal ions employed can also be chosen so their lattice mismatch is as low as possible. The application of these doped oxides in inverted planar PSC with configuration FTO/$Li_{0.05}Mg_{0.15}Ni_{0.8}O$/$MAPbI_3$/PCBM/$Ti_{0.95}Nb_{0.05}O_x$/Ag resulted in power conversion efficiencies of 16.2% with very good long-term stability in the dark (shelf) but also under continuous irradiation (1 sun, UV filter, 45–50 °C). The device showed exceptional stability reaching T_{95} and T_{90} after 1000 h of analysis stored in the dark and under 1 sun illumination, respectively, (Fig. 13.6). Doping metal oxides with transition metals prevents or reduces ion movement and eliminates defects (such as oxygen vacancies or metal interstitials), improving device lifetime. The latter proves the excellent stability of PSCs when doped oxides are applied. Moreover, the oxides synthesis method (sol-gel) is compatible with large-area (>1 cm^2) fabrication methods, which give a bright future for the scale up of PSCs and their possible commercialization.

13.4.2 *The Triple-Layer Junction: A Hole Conductor-Free PSC*

An example of a PSC architecture compatible with scalable and low-cost green materials is the device developed by Prof. Han, called the triple junction PSCs (Fig. 13.7). This PSC can be fully printed and eliminates the use of expensive hole transport layers and precious metals (Au or Ag) as the back electrode, which is replaced by low-cost carbon-based materials. The schematic representation of the triple-layer perovskite junction is shown in Fig. 13.7a. The device consists of a mesoporous layer of TiO_2 acting as the ETL, and a mesoporous layer of ZrO_2 used

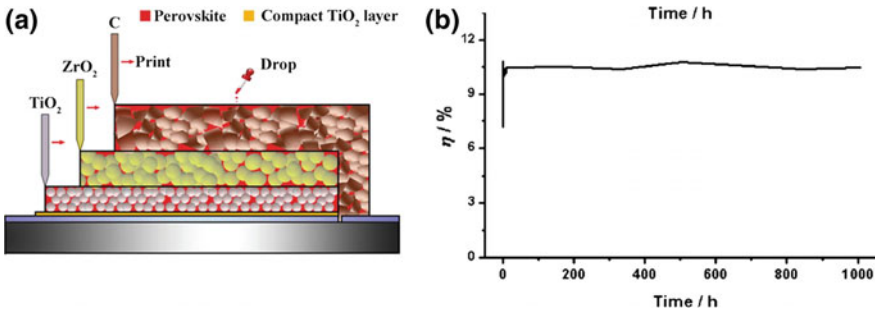

Fig. 13.7 The triple-layer perovskite junction. **a** Schematic drawing showing the cross section of the triple-layer perovskite-based fully printable mesoscopic solar cell. **b** Stability test under full AM 1.5 simulated sunlight in ambient air over 1008 h with an unsealed device, the perovskite being protected by the carbon layer acting as back contact. **c** Energy band diagram of the triple-layer device. Reproduced from Ref. [119] with permission from The Royal Society of Chemistry

as scaffold. These layers have a thickness of ~1 and 2 μm, respectively, and are deposited on a FTO-covered glass. The third layer is made of a porous carbon-based paste deposited on top of the ZrO_2 layer. The triple layer is infiltrated with the halide perovskite by drop-casting from solution.

The initial PCE of this triple junction PSC was 6.64% [35] but the application of a perovskite with mixed cations containing methylammonium (MA) and 5-aminovaleric acid (5-AVA), $(5\text{-AVA})_xMA_{1-x}PbI_3$, permitted the increase in efficiency of up to 12.84% [119]. The application of 5-AVA resulted in lower defects and better pore filling with a longer excitation lifetime and increased quantum yield. The PCS of this triple junction PSC is currently 15% efficiency as recently reported by the authors [35]. This type of PSC uses carbon back electrode instead of the expensive precious metals such as Au or Ag. The carbon layer works not only as a contact electrode; it also prevents moisture ingress because of its hydrophobic nature. Indoor and outdoor analyses of this solar cells reveal one of the most stable devices to date under long-term light-soaking, as well as heat exposure over three months at 80–85 °C [122]. Moreover, this solar cell can be fabricated in large areas, with 41 cm^2 active area and 15–16% efficiency [189].

This triple junction PSC can be considered the closest to commercialization for several reasons:

(a) Eliminates the use of expensive hole transport materials and expensive metal electrodes.
(b) Large-area fabrication is possible by screen-printing methods.
(c) The stability analyses demonstrate more than 1000 h under continuous (indoor) illumination in air without the need of encapsulation (Fig. 13.7b).
(d) The outdoor stability of the solar cell demonstrates more than 7 days (168 h).

13.4.3 Functionalization of Interfaces to Enhance PSCs Stability

The functionalization of PSC interfaces to enhance device efficiency is well documented; yet, very few research reports describe the complete synthesis of materials, interface modification, efficiency enhancement and also device stability analyses. In this respect, an interesting work carried out by Back et al. reports on the modification of the TiO_x layer by the application of an amine-mediated metal oxide system (Fig. 13.8). A planar PSC in the inverted configuration ITO/PEDOT:PSS/VO_x/$MAPbI_{3-x}Br_x$/$PC_{60}BM$/metal electrode (Ag or Al) was made by applying a chemical inhibition layer made of TiOx and diethanol amine. In this case the solar cell is also "sandwiched" between two TMOs layers as ETL and HTL. Authors report that the degradation mechanism of the device was mainly due to the corrosion of the metal electrodes due to the ionic defects of the perovskite layer. Thus, the application of the TiO_2-amine interlayer protected the degradation of the

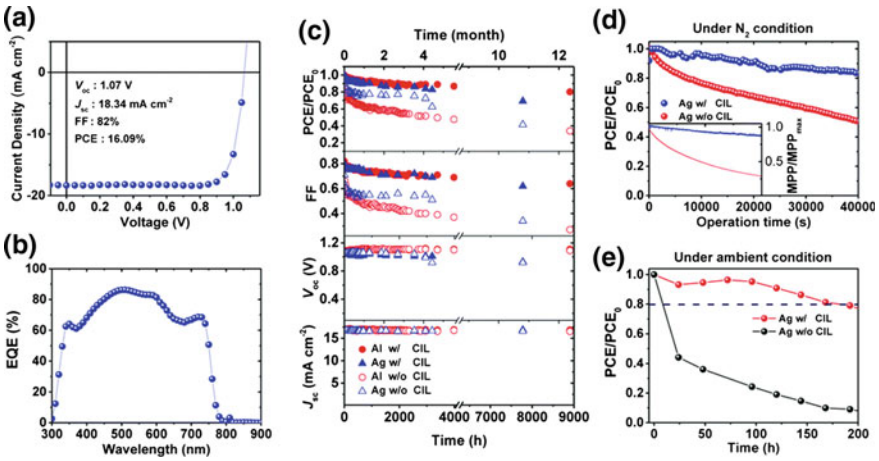

Fig. 13.8 J–V, EQE and lifetime measurements. **a** and **b** J–V curves and IPCE spectra for the optimized p–i–n PHJ perovskite solar cells with CILs measured under AM 1.5G. **c** The photovoltaic performances of p–i–n PSCs using CIL/Al, CIL/Ag, Al, and Ag electrodes, as a function of the storage time under N_2. **d** The device performances of p–i–n PSCs using CIL/Ag and Ag electrodes, as a function of the J–V sweep operation time under N_2. The inset also represents the device performance, as a function of MPP tracking time under N_2. **e** The device performances of p–i–n PSCs using CIL/Ag and Ag electrodes, as a function of the storage time in ambient conditions. Reproduced from Ref. [19] with permission from The Royal Society of Chemistry

electrodes increasing device stability. The device was analysed under storage in the dark in N_2, maintaining T_{90} after 4000 h of testing and T_{80} after 200 h under ambient conditions without encapsulation [19].

Other example of interface functionalization is the easy method to enhance PSC stability by the application of a thiol-functionalized cationic surfactant as cation buffer layer which also protects the Ag metal electrode by its interaction via Ag-S bonds [154]. The modification of PEDOT:PSS layer was also carried out by the addition of poly(4-styrenesulfonic acid) (PSSH). In this case the efficiency of the final device was improved due to the electrostatic interaction between the sulfonyl functional groups in PEDOT:PSS and perovskite precursor ions as shown in Fig. 13.8 [153].

13.4.4 Mix Cations to Reduce Ion Migration

The photo and moisture instability of the halide perovskite solar cells has been related to the weak interaction between the perovskite cations with the surrounding halides. The reason for the poor stability resides in the eight equivalent orientations of the organic cation along the diagonals in the unit cell and the instability of the organic cation. Thus, the combination of different cations in the halide perovskite is

a relatively new strategy to enhance device efficiency and stability. For example, the partial substitution of Cs^+ for $HC(NH_2)_2^+$ in $HC(NH_2)_2PbI_3$ has been reported by Lee et al. [146]. This partial cation substitution results in an enhancement of the PCE of the final solar cell, as well as its photo and moisture stability. The effect has been attributed to (a) the enhanced interaction between $HC(NH_2)_2^+$ and iodide due to contraction of cubo-octahedral volume and (b) to the reduction in trap density upon incorporation of the Cs^+ which increases V_{oc} and FF leading to PCEs of 16.5% [146]. Another example is the addition of Cs ions in mixtures of Cs/MA or Cs/FA which has demonstrated to enhance device stability by strengthen the thermal and moisture resistance and structural integrity of the halide perovskite [20, 23]. The difference in size between the FA and the Cs seems to be beneficial in the fabricating black perovskite, thus reducing the amount of the yellow phase. The latter is not observed with mixtures of FA/MA since MA has a similar radius to FA and the yellows phase is still observed. Thus, the application of mixed cation perovskites has recently emerged as promising candidates for the application in PSC. Saliba et al. reported on the application of triple cation halide perovskite of the type $Cs_x(MA_{0.17}FA_{0.83})_{(100-x)}Pb(_{I0.83}Br_{0.17})_3$. The PCE reported by the authors is one of the highest applying mixed cations, 21%, and the stability of the PSC is of T_{85} after 250 h under continuous irradiation conditions. The authors demonstrated higher reproducibility of the final device parameters, the thermal stability of the mixed cation perovskite and its stability towards solvents or temperature variations [20]. A similar response was observed with the mixed cations halide perovskite of the type $Cs_{0.2}FA_{0.8}PbI_{2.84}Br_{0.16}$, Cs and FA perovskites show the undesirable formation of small amounts of the yellow phase, while the mixture forms the desired black perovskite. PCEs as high as 17% were obtained applying this perovskite with devices showing non or negligible hysteresis and high stability in air [166].

13.5 Conclusions

PSCs are the basis of a promising photovoltaic technology and have already resulted in tremendous advances in terms of PCE and device lifetime. This technology is rapidly developing towards the capacity for large-area printing, which, in turn may make possible its introduction into the market place within a few years. Table 13.6 summarizes some of the most promising PSCs, either giving PCE values greater than 18% in the research laboratory, or high PCE values when used in large-area devices (>1 cm^2). The table also indicates those studies for which long-term stability has been documented.

In general, we conclude that PSCs can display long-term stability, either when stored in the absence of light (in the dark), or encapsulated, or if evaluated in an inert atmosphere. Stabilization of unsealed PSCs in air is only possible if the relative humidity of the environment (i.e. air or inert atmosphere) is below *ca.* 30%. Although good long-term stability during illumination has been reported, it will still be necessary to compare the technology and measurement methods used in different

Table 13.6 Summary of perovskite solar cells with PCEs above 18% and some examples of large area (>1 cm^2) devices

Type[a]	TE[b]/BL[c]	Perovskite	BL	E[d]	Area (cm^2)	Stability ISOS/Time (h)/T_x	Scan rate (mV/s)	PCE (%)	V_{oc} (V)	J_{sc} (mA/cm^2)	FF	Refs.
PI	FTO/NiMgLiO/	$MAPbI_3$	PCBM/Ti(Nb)O_x	Ag	1.02	L/1000/T_{90}	5	15	1.09	20.96	0.66	[167]
MC	FTO/TiO_2	$MAPbI_3$:FEAI	Spiro-MeOTAD	Ag	0.16	D/2880/T_{92}	5	18	1.06	21.2	0.79	[158]
PI	ITO/PEDOT	$CH_3NH_3PbI_3$	$PC_{71}BM$	Ca/Al	0.16	D/1080/T_{90}	10–500	18.0	1.03	20.6	0.85	[221]
PI	ITO/PTAA	$CH_3NH_3PbI_3$	PCBM/C_{60}/BCP	Ag	0.072		130	18.1	1.07	22.0	0.77	[222]
PI	ITO/PEDOT	$CH_3NH_3PbI_3$	$PC_{61}BM$	Au	0.09	L/1000/T_{50}	x	18.1	1.1	209	0.79	[157]
PI	ITO/PEDOT	$MAPbI_3$	PCBM	Au	0.16		10	18.2	1.1	20.9	0.79	[74]
PI	FTO/NiMgLiO	$MAPbI_3$	PCBM/Ti(Nb)O_x	Ag	0.09		5	18.39	1.085	20.418	0.83	[167]
PC	FTO/SnO_2	$(FAPbI_3)_{0.85}(MAPbBr_3)_{0.15}$	spiro-OMeTAD	Au	0.16		10	18.4	1.14	21.3	0.74	[21]
PI	ITO/MoO_3/PEDOT	$CH_3NH_3PbI_3$	C_{60}/BCP	LiF/Ag				18.8	0.97	22.6	0.83	[180]
MC	FTO/TiO2-c/TiO_2-ms	$(FAPbI_3)_{12x}(MAPbBr_3)_x$	spiro-OMeTAD	Au	0.096		10	19	1.12	22.5	0.75	[22]
MC	FTO/TiO_2.c/Li-TiO_2-ms	$Cs_x(MA_{0.17}FA_{0.83})_{(100-x)}Pb(I_{0.83}Br_{0.17})_3$	spiro-OMeTAD	Au	0.16	L/100/T_{56}	10	19.20	1.132	22.69	0.74	[20]
PC	ITO–PEIE/Y-TiO_2-c	$MAPbI_{3-x}Cl_x$	spiro-OMeTAD	Au	0.1			19.3	1.13	22.75	0.75	[223]
MC	FTO/TiO_2-c/TiO_2-ms	$MAPbI_3$	spiro-OMeTAD	Ag	0.125		60	19.7	1.09	23.83	0.76	[224]
MC	FTO/TiO_2-c/TiO_2-ms	$FAPbI_3$	PTAA	Au				20.2	1.06	24.7	0.77	[225]
MI	FTO/NiO-ms	$(FAPbI_3)_{0.85}(MAPbBr_3)_{0.15}$	PCBM/LiF	Al				20.2	1.06	24.7	0.77	[225]
MC	FTO/TiO_2-c/TiO_2-ms	FA0.81MA0.15PbI2.51Br0.45	spiro-OMeTAD	Au	1		50	20.6	1.14	23.28	0.76	[226]

(continued)

Table 13.6 (continued)

Type[a]	TE[b]/BL[c]	Perovskite	BL	E[d]	Area (cm^2)	Stability ISOS/Time (h)/T_x	Scan rate (mV/s)	PCE (%)	V_{oc} (V)	J_{sc} (mA/cm^2)	FF	Refs.
MC	FTO/TiO_2-c/TiO_2-ms	$FA_{0.83}MA_{0.17}(PbI_{0.83}Br_{0.17})_3$	spiro-OMeTAD	Au	0.16		10	20.8	1.14	23	0.75	[227]
MC	FTO/TiO_2.c/$LiTiO_2$-ms	$Cs_x(MA_{0.17}FA_{0.83})_{(100-x)}Pb(I_{0.83}Br_{0.17})_3$/	Spiro-OMeTAD	Au	0.16	L/250/T_{100}	10	21.17	1.14	23.5	0.78	[20]
PI	FTO/NiMgLiO	$MAPbI_3$	PCBM/Ti(Nb)O_x	Ag	0.09		70	22.35 (High hysteresis)	1.27	20.42	0.85	[167]

[a]*PI* Planar Inverted; *PC* Planar Conventional; *MC* Mesoscopic conventional; *MI* Mesoscopic Inverted
[b]*TE* Transparent Electrode
[c]*BL* Barrier Layer
[d]*E* back Electrode
[e]*ETL* Electron Transport Layer
[f]*PCE* Power Conversion Efficiency

laboratories before reaching conclusions. For example, exchange of materials between different laboratories for measurements under different preferred experimental conditions and greater inter-laboratory collaboration are needed. The number of measurements conducted outdoors is still limited, and substantial input in this area from the research community is needed. The increase in research and development work on PSC technology is uncovering novel properties and unexpected results. It is envisaged that many more interesting properties and working mechanisms will be defined in the near future and some of them will help to achieve the stability required for both practical and novel applications. Many questions remain outstanding; however, the number and range of important contributions and the advances in PSC technology that are being made are in step with the commercial aspirations.

Acknowledgements To the Spanish MINECO through the Severo Ochoa Centers of Excellence Program under Grant SEV-2013-0295 for the Postdoctoral contract to A.P. and postdoctoral contract to A.M; for the grant ENE2013-48816-C5-4-R, ENE2016-79282-C5-2-R and the Nanoselect Excelence Network MAT2015-68994-REDC. To the Agència de Gestiód'Ajuts Universitaris i de Recerca for the support to the consolidated Catalonia research group 2014SGR-1212 and the Xarxa de Referència en Materials Avançats per a l'Energia (Xarmae). To the COST Action StableNextSol project MP1307. To CONACYT (México) for the PhD scholarship awarded to Y.R. This work is being carried out under the materials science PhD degree for A:M of the Universitat Autonoma de Barcelona. To the CERCA Programme / Generalitat de Catalunya. To the Agencia Estatal de Investigación (AEI) and Fondo Europeo de Desarrollo Regional (FEDER) under contract ENE2015-74275-JIN.

References

1. https://ec.europa.eu/energy/en/topics/energy-strategy/2050-energy-strategyEES
2. Jacoby M (2016) The future of low-cost solar cells. C&EN 94(18):30–35
3. Kojima A, Teshima K, Shirai Y, Miyasaka T (2009) Organometal halide perovskites as visible-light sensitizers for photovoltaic cells. J Am Chem Soc 131(17):6050–6051. doi:10.1021/ja809598r
4. NREL C. http://www.nrelgov/ncpv/images/efficiency_chartjpg. Accessed 13 June 2016
5. Wells HLZ (1893) Anorg Chem 3:195–210
6. Moller CK (1957) A phase transition in caesium plumbochloride. Nature 180(4593):981–982
7. Weber D (1978) $CH_3NH_3PbX_3$, ein Pb(II)-System mit kubischer Perowskitstruktur/ $CH_3NH_3PbX_3$, a Pb(II)-system with cubic perovskite structure. Zeitschrift für Naturforschung B 33. doi:10.1515/znb-1978-1214
8. Reller A, Williams T (1989) Perovskites-chemical chameleons, vol 12. Chemical Society, London, ROYAUME-UNI
9. Manser JS, Saidaminov MI, Christians JA, Bakr OM, Kamat PV (2016) Making and breaking of lead halide perovskites. Acc Chem Res 49(2):330–338. doi:10.1021/acs.accounts.5b00455
10. Stoumpos CC, Malliakas CD, Kanatzidis MG (2013) $MAPbI_3$ structural changes at 55 °C. Inorg Chem 52:9019–9038

11. Conings B, Drijkoningen J, Gauquelin N, Babayigit A, D'Haen J, D'Olieslaeger L, Ethirajan A, Verbeeck J, Manca J, Mosconi E, Angelis FD, Boyen HG (2015) $MAPbI_3$ moisture and temp issues. Adv Energy Mater 5. doi:10.1002/aenm.201500477
12. Misra RK, Aharon S, Li B, Mogilyansky D, Visoly-Fisher I, Etgar L, Katz EA (2015) $MAPbI_3$ moisture and temp issues. J Phys Chem Lett 6:326–330
13. Hok ET, Slotcavage DJ, Dohner ER, Bowring AR, Karunadasa HI, McGehee MD (2015) MAPbI3 influence of light and halide segregation. Chem Sci 6:613–617
14. Moller CK (1958) $CsPbI_3$ band gap and annealing at 300 °C. Nature 182:1436
15. Zhao Y, Liang C, Zhang H, Li D, Tian D, Li G, Jing X, Zhang W, Xiao W, Liu Q, Zhanga F, He Z (2015) Anomalously large interface charge in polarityswitchable photovoltaic devices: an indication of mobile ions in organic–inorganic halide perovskites. Energy Environ Sci 8:1256–1260
16. Eames C, Frost JM, Barnes PRF, O'Regan BC, Walsh A, Islam MS (2015) Ionic transport in hybrid lead iodide perovskite solar cells. Nat Commun 6:7497
17. Yuan Y, Huang J (2016) Ion migration in organometal trihalide perovskite and its impact on photovoltaic efficiency and stability. Acc Chem Res 49:286–293
18. Yang T-Y, Gregori G, Pellet N, Gratzel M, Maier J (2015) The significance of ion conduction in a hybrid organic-inorganic lead-iodide-based perovskite photosensitizer. Angew Chem Int Ed 54:7905–7910
19. Back H, Kim G, Kim J, Kong J, Kim TK, Kang H, Kim H, Lee J, Lee S, Lee K (2016) Achieving long-term stable perovskite solar cells via ion neutralization. Energy Environ Sci 9(4):1258–1263. doi:10.1039/c6ee00612d
20. Saliba M, Matsui T, Seo J-Y, Domanski K, Correa-Baena J-P, Nazeeruddin MK, Zakeeruddin SM, Tress W, Abate A, Hagfeldtd A, Gratzel M (2016) Cesium-containing triple cation perovskite solar cells: improved stability, reproducibility and high efficiency. Energy Environ Sci 9:1989–1997
21. Baena JPC, Steier L, Tress W, Saliba M, Neutzner S, Matsui T, Giordano F, Jacobsson TJ, Kandada ARS, Zakeeruddin SM, Petrozza A, Abate A, Nazeeruddin MK, Gratzel M, Hagfeldt A (2015) Highly efficient planar perovskite solar cells through band alignment engineering. Energy Environ Sci 8:2928–2934
22. Jeon NJ, Noh JH, Yang WS, Kim YC, Ryu S, Seo J, Seok SI (2015) Compositional engineering of perovskite materials for high performance solar cells. Nature 517:476–480
23. Saliba M, Orlandi S, Matsui T, Aghazada S, Cavazzini M, Correa-Baena J-P, Gao P, Scopelliti R, Mosconi E, Dahmen K-H, Angelis FD, Abate A, Hagfeldt A, Pozzi G, Graetzel M, Nazeeruddin MK (2016) PSC with Novel HTl 20.2% Ref 50. Nat Energy 1:15017
24. Bi D, Tress W, Dar MI, Gao P, Luo J, Renevier C, Schenk K, Abate A, Giordano F, Baena JPC, Decoppet JD, Zakeeruddin SM, Nazeeruddin MK, Gratzel M, Hagfeldt A (2016) Efficienct luminescent solar cells based on tailored mixed cation perovskites. Sci Adv 2(1): e150117170
25. Li Z, Yang M, Park J-S, Wei S-H, Berry JJ, Zhu K (2016) Structural stability of Cs/FA perovskites. Chem Mater 28:284–292
26. Li B, Li Y, Zheng C, Gao D, Huang W (2016) Advancements in the stability of perovskite solar cells: degradation mechanisms and improvement approaches. RSC Adv 6(44):38079–38091. doi:10.1039/c5ra27424a
27. Niu G, Guo X, Wang L (2015) Review of recent progress in chemical stability of perovskite solar cells. J Mater Chem A 3(17):8970–8980. doi:10.1039/c4ta04994b
28. Yan W, Ye S, Li Y, Sun W, Rao H, Liu Z, Bian Z, Huang C (2016) Hole-transporting materials in inverted planar perovskite solar cells. Adv Energy Mater 1–18. doi:10.1002/aenm.201600474
29. Meng L, You J, Guo T-F, Yang Y (2016) Recent advances in the inverted planar structure of perovskite solar cells. Acc Chem Res 49(1):155–165. doi:10.1021/acs.accounts.5b00404

30. Ye M, Hong X, Zhang F, Liu X (2016) Recent advancements in perovskite solar cells: flexibility, stability and large scale. J Mater Chem A 4(18):6755–6771. doi:10.1039/c5ta09661h
31. Wang D, Wright M, Elumalai NK, Uddin A (2016) Stability of perovskite solar cells. Sol Energy Mater Sol Cells 147:255–275. doi:10.1016/j.solmat.2015.12.025
32. Shahbazi M, Wang H (2016) Progress in research on the stability of organometal perovskite solar cells. Sol Energy 123:74–87. doi:10.1016/j.solener.2015.11.008
33. Mali SS, Hong CK (2016) P-i-n/n-i-p type planar hybrid structure of highly efficient perovskite solar cells towards improved air stability: synthetic strategies and the role of p-type hole transport layer (HTL) and n-type electron transport layer (ETL) metal oxides. Nanoscale 8(20):10528–10540. doi:10.1039/c6nr02276f
34. Berhe TA, Su WN, Chen CH, Pan CJ, Cheng JH, Chen HM, Tsai MC, Chen LY, Dubale AA, Hwang BJ (2016) Organometal halide perovskite solar cells: degradation and stability. Energy Environ Sci 9(2):323–356. doi:10.1039/c5ee02733k
35. Rong Y, Liu L, Mei A, Li X, Han H (2015) Beyond efficiency: the challenge of stability in mesoscopic perovskite solar cells. Adv Energy Mater 5(20). doi:10.1002/aenm.201501066
36. Guo X, Niu G, Wang L (2015) Chemical stability issue and its research process of perovskite solar cells with high efficiency. Acta Chim Sinica 73(3):211–218. doi:10.6023/a14100687
37. Dennler G (2007) The value of values. Mater Today 10(11):56. doi:10.1016/S1369-7021(07)70290-0
38. Ito S, Matsui H, K-i Okada, S-i Kusano, Kitamura T, Wada Y, Yanagida S (2004) Calibration of solar simulator for evaluation of dye-sensitized solar cells. Sol Energy Mater Sol Cells 82(3):421–429. doi:10.1016/j.solmat.2004.01.030
39. Ito S, Nazeeruddin MK, Liska P, Comte P, Charvet R, Péchy P, Jirousek M, Kay A, Zakeeruddin SM, Grätzel M (2006) Photovoltaic characterization of dye-sensitized solar cells: effect of device masking on conversion efficiency. Prog Photovolt Res Appl 14(7):589–601. doi:10.1002/pip.683
40. Kroon JM, Wienk MM, Verhees WJH, Hummelen JC (2002) Accurate efficiency determination and stability studies of conjugated polymer/fullerene solar cells. Thin Solid Films 403–404:223–228. doi:10.1016/S0040-6090(01)01589-9
41. Shrotriya V, Li G, Yao Y, Moriarty T, Emery K, Yang Y (2006) Accurate measurement and characterization of organic solar cells. Adv Funct Mater 16(15):2016–2023
42. Snaith HJ (2012) The perils of solar cell efficiency measurements. Nat Photonics 6(6):337–340
43. Hodes G (2012) Photoelectrochemical cell measurements: getting the basics right. J Phys Chem Lett 3(9):1208–1213. doi:10.1021/jz300220b
44. Dennler G, Scharber MC, Brabec CJ (2009) Polymer-fullerene bulk-heterojunction solar cells. Adv Mater 21(13):1323–1338. doi:10.1002/adma.200801283
45. Snaith HJ (2012) How should you measure your excitonic solar cells? Energy Environ Sci 5(4):6513–6520
46. Greenham NC, Peng X, Alivisatos AP (1996) Charge separation and transport in conjugated-polymer/semiconductor-nanocrystal composites studied by photoluminescence quenching and photoconductivity. Phys Rev B 54(24):17628–17637
47. Gratzel M (2001) Photoelectrochemical cells. Nature 414(6861):338–344
48. Corazza M, Krebs FC, Gevorgyan SA (2014) Predicting, categorizing and intercomparing the lifetime of OPVs for different ageing tests. Sol Energy Mater Sol Cells 130:99–106. doi:10.1016/j.solmat.2014.06.031
49. Corazza M, Krebs FC, Gevorgyan SA (2015) Lifetime of organic photovoltaics: linking outdoor and indoor tests. Sol Energy Mater Sol Cells 143:467–472. doi:10.1016/j.solmat.2015.07.037
50. Timmreck R, Meyer T, Gilot J, Seifert H, Mueller T, Furlan A, Wienk MM, Wynands D, Hohl-Ebinger J, Warta W, Janssen RAJ, Riede M, Leo K (2015) Characterization of tandem organic solar cells. Nat Photonics 9(8):478–479. doi:10.1038/nphoton.2015.124 http://www.nature.com/nphoton/journal/v9/n8/abs/nphoton.2015.124.html#supplementary-information

51. Bahro D, Koppitz M, Colsmann A (2016) Tandem organic solar cells revisited. Nat Photonics 10(6):354–355. doi:10.1038/nphoton.2016.96
52. Timmreck R, Meyer T, Gilot J, Seifert H, Mueller T, Furlan A, Wienk MM, Wynands D, Hohl-Ebinger J, Warta W, Janssen RAJ, Riede M, Leo K (2016) Reply to 'Tandem organic solar cells revisited'. Nat Photon 10(6):355–355. doi:10.1038/nphoton.2016.99
53. Roesch R, Faber T, von Hauff E, Brown TM, Lira-Cantu M, Hoppe H (2015) Procedures and practices for evaluating thin-film solar cell stability. Adv Energy Mater 5(20):n/a–n/a. doi:10.1002/aenm.201501407
54. von Hauff E, Lira-Cantu M, Brown TM, Hoppe H (2015) Emerging thin-film photovoltaics: stabilize or perish. Adv Energy Mater 5(20):n/a–n/a. doi:10.1002/aenm.201501924
55. Christians JA, Manser JS, Kamat PV (2015) Best practices in perovskite solar cell efficiency measurements. Avoiding the error of making bad cells look good. J Phys Chem Lett 6 (5):852–857. doi:10.1021/acs.jpclett.5b00289
56. Zimmermann E, Wong KK, Müller M, Hu H, Ehrenreich P, Kohlstädt M, Würfel U, Mastroianni S, Mathiazhagan G, Hinsch A, Gujar TP, Thelakkat M, Pfadler T, Schmidt-Mende L (2016) Characterization of perovskite solar cells: towards a reliable measurement protocol. APL Mater 4(9):091901. doi:10.1063/1.4960759
57. Smestad GP, Krebs FC, Lampert CM, Granqvist CG, Chopra KL, Mathew X, Takakura H (2008) Reporting solar cell efficiencies in solar energy materials and solar cells. Sol Energy Mater Sol Cells 92(4):371–373
58. Zimmermann E, Ehrenreich P, Pfadler T, Dorman JA, Weickert J, Schmidt-Mende L (2014) Erroneous efficiency reports harm organic solar cell research. Nat Photonics 8(9):669–672. doi:10.1038/nphoton.2014.210
59. Yang X, Yanagida M, Han L (2013) Reliable evaluation of dye-sensitized solar cells. Energy Environ Sci 6(1):54–66. doi:10.1039/C2EE22998F
60. Beard MC, Luther JM, Nozik AJ (2014) The promise and challenge of nanostructured solar cells. Nat Nano 9(12):951–954. doi:10.1038/nnano.2014.292
61. Gratzel M (2014) The light and shade of perovskite solar cells. Nat Mater 13(9):838–842. doi:10.1038/nmat4065
62. Perovskite fever (2014) Nat Mater 13(9):837–837. doi:10.1038/nmat4079
63. Solar cell woes (2014) Nat Photonics 8(9):665–665. doi:10.1038/nphoton.2014.212
64. Hishikawa Y, Shimura H, Ueda T, Sasaki A, Ishii Y (2016) Precise performance characterization of perovskite solar cells. Curr Appl Phys 16(8):898–904. doi:10.1016/j.cap.2016.05.002
65. Krebs FC, Gevorgyan SA, Gholamkhass B, Holdcroft S, Schlenker C, Thompson ME, Thompson BC, Olson D, Ginley DS, Shaheen SE, Alshareef HN, Murphy JW, Youngblood WJ, Heston NC, Reynolds JR, Jia S, Laird D, Tuladhar SM, Dane JGA, Atienzar P, Nelson J, Kroon JM, Wienk MM, Janssen RAJ, Tvingstedt K, Zhang F, Andersson M, Inganäs O, Lira-Cantu M, de Bettignies R, Guillerez S, Aernouts T, Cheyns D, Lutsen L, Zimmermann B, Würfel U, Niggemann M, Schleiermacher HF, Liska P, Grätzel M, Lianos P, Katz EA, Lohwasser W, Jannon B (2009) A round robin study of flexible large-area roll-to-roll processed polymer solar cell modules. Sol Energy Mater Sol Cells 93(11):1968–1977. doi:10.1016/j.solmat.2009.07.015
66. Madsen MV, Gevorgyan SA, Pacios R, Ajuria J, Etxebarria I, Kettle J, Bristow ND, Neophytou M, Choulis SA, Stolz Roman L, Yohannes T, Cester A, Cheng P, Zhan X, Wu J, Xie Z, Tu WC, He JH, Fell CJ, Anderson K, Hermenau M, Bartesaghi D, Jan Anton Koster L, Machui F, González-Valls I, Lira-Cantu M, Khlyabich PP, Thompson BC, Gupta R, Shanmugam K, Kulkarni GU, Galagan Y, Urbina A, Abad J, Roesch R, Hoppe H, Morvillo P, Bobeico E, Panaitescu E, Menon L, Luo Q, Wu Z, Ma C, Hambarian A, Melikyan V, Hambsch M, Burn PL, Meredith P, Rath T, Dunst S, Trimmel G, Bardizza G, Müllejans H, Goryachev AE, Misra RK, Katz EA, Takagi K, Magaino S, Saito H, Aoki D, Sommeling PM, Kroon JM, Vangerven T, Manca J, Kesters J, Maes W, Bobkova OD, Trukhanov VA, Paraschuk DY, Castro FA, Blakesley J, Tuladhar SM, Alexander Röhr J, Nelson J, Xia J, Parlak EA, Tumay TA, Egelhaaf HJ, Tanenbaum DM, Mae Ferguson G,

Carpenter R, Chen H, Zimmermann B, Hirsch L, Wantz G, Sun Z, Singh P, Bapat C, Offermans T, Krebs FC (2014) Worldwide outdoor round robin study of organic photovoltaic devices and modules. Sol Energy Mater Sol Cells 130:281–290. doi:10.1016/j.solmat.2014.07.021

67. Rösch R, Tanenbaum DM, Jørgensen M, Seeland M, Bärenklau M, Hermenau M, Voroshazi E, Lloyd MT, Galagan Y, Zimmermann B, Würfel U, Hösel M, Dam HF, Gevorgyan SA, Kudret S, Maes W, Lutsen L, Vanderzande D, Andriessen R, Teran-Escobar G, Lira-Cantu M, Rivaton A, Uzunoğlu GY, Germack D, Andreasen B, Madsen MV, Norrman K, Hoppe H, Krebs FC (2012) Investigation of the degradation mechanisms of a variety of organic photovoltaic devices by combination of imaging techniques—the ISOS-3 inter-laboratory collaboration. Energy Environ Sci 5(4):6521–6540. doi:10.1039/c2ee03508a
68. Tanenbaum DM, Hermenau M, Voroshazi E, Lloyd MT, Galagan Y, Zimmermann B, Hösel M, Dam HF, Jørgensen M, Gevorgyan SA, Kudret S, Maes W, Lutsen L, Vanderzande D, Würfel U, Andriessen R, Rösch R, Hoppe H, Teran-Escobar G, Lira-Cantu M, Rivaton A, Uzunolu GY, Germack D, Andreasen B, Madsen MV, Norrman K, Krebs FC (2012) The ISOS-3 inter-laboratory collaboration focused on the stability of a variety of organic photovoltaic devices. RSC Adv 2(3):882–893. doi:10.1039/c1ra00686j
69. Teran-Escobar G, Tanenbaum DM, Voroshazi E, Hermenau M, Norrman K, Lloyd MT, Galagan Y, Zimmermann B, Hösel M, Dam HF, Jorgensen M, Gevorgyan S, Kudret S, Maes W, Lutsen L, Vanderzande D, Würfel U, Andriessen R, Rösch R, Hoppe H, Rivaton A, Uzunoglu GY, Germack D, Andreasen B, Madsen MV, Bundgaard E, Krebs FC, Lira-Cantu M (2012) On the stability of a variety of organic photovoltaic devices by IPCE and in situ IPCE analyses—the ISOS-3 inter-laboratory collaboration. Phys Chem Chem Phys 14(33):11824–11845. doi:10.1039/c2cp40821j
70. Andreasen B, Tanenbaum DM, Hermenau M, Voroshazi E, Lloyd MT, Galagan Y, Zimmernann B, Kudret S, Maes W, Lutsen L, Vanderzande D, Würfel U, Andriessen R, Rösch R, Hoppe H, Teran-Escobar G, Lira-Cantu M, Rivaton A, Uzunoglu GY, Germack DS, Hösel M, Dam HF, Jorgensen M, Gevorgyan SA, Madsen MV, Bundgaard E, Krebs FC, Norrman K (2012) TOF-SIMS investigation of degradation pathways occurring in a variety of organic photovoltaic devices—the ISOS-3 inter-laboratory collaboration. Phys Chem Chem Phys 14(33):11780–11799. doi:10.1039/c2cp41787a
71. Unger EL, Hoke ET, Bailie CD, Nguyen WH, Bowring AR, Heumuller T, Christoforo MG, McGehee MD (2014) Hysteresis and transient behavior in current-voltage measurements of hybrid-perovskite absorber solar cells. Energy Environ Sci 7(11):3690–3698. doi:10.1039/C4EE02465F
72. Tress W, Marinova N, Moehl T, Zakeeruddin SM, Nazeeruddin MK, Gratzel M (2015) Understanding the rate-dependent J-V hysteresis, slow time component, and aging in $CH_3NH_3PbI_3$ perovskite solar cells: the role of a compensated electric field. Energy Environ Sci 8(3):995–1004. doi:10.1039/C4EE03664F
73. Jeon NJ, Noh JH, Kim YC, Yang WS, Ryu S, Seok SI (2014) Solvent engineering for high-performance inorganic–organic hybrid perovskite solar cells. Nat Mater 13(9):897–903. doi:10.1038/nmat4014. http://www.nature.com/nmat/journal/v13/n9/abs/nmat4014.html#supplementary-information
74. Heo JH, Han HJ, Kim D, Ahn TK, Im SH (2015) Hysteresis-less inverted $CH_3NH_3PbI_3$ planar perovskite hybrid solar cells with 18.1% power conversion efficiency. Energy Environ Sci 8(5):1602–1608. doi:10.1039/C5EE00120J
75. Yin X, Que M, Xing Y, Que W (2015) High efficiency hysteresis-less inverted planar heterojunction perovskite solar cells with a solution-derived NiOx hole contact layer. J Mater Chem A 3(48):24495–24503. doi:10.1039/c5ta08193a
76. Wang H, Zeng X, Zhang W, Chen W (2014) The roles of different NiO compact blocking layers in P-type sensitized solar cells. In: Progress in electromagnetics research symposium, 2014, pp 1178–1181

77. Wang H, Zeng X, Huang Z, Zhang W, Qiao X, Hu B, Zou X, Wang M, Cheng YB, Chen W (2014) Boosting the photocurrent density of p-type solar cells based on organometal halide perovskite-sensitized mesoporous NiO photocathodes. ACS Appl Mater Interfaces 6 (15):12609–12617. doi:10.1021/am5025963
78. Trifiletti V, Roiati V, Colella S, Giannuzzi R, De Marco L, Rizzo A, Manca M, Listorti A, Gigli G (2015) NiO/$MAPbI_3$-xClx/PCBM: a model case for an improved understanding of inverted mesoscopic solar cells. ACS Appl Mater Interfaces 7(7):4283–4289. doi:10.1021/am508678p
79. Liu Z, Zhang M, Xu X, Bu L, Zhang W, Li W, Zhao Z, Wang M, Cheng YB, He H (2015) P-Type mesoscopic NiO as an active interfacial layer for carbon counter electrode based perovskite solar cells. Dalton Trans 44(9):3967–3973. doi:10.1039/c4dt02904f
80. Xu X, Liu Z, Zuo Z, Zhang M, Zhao Z, Shen Y, Zhou H, Chen Q, Yang Y, Wang M (2015) Hole selective NiO contact for efficient perovskite solar cells with carbon electrode. Nano Lett 15(4):2402–2408. doi:10.1021/nl504701y
81. Bai Y, Chen H, Xiao S, Xue Q, Zhang T, Zhu Z, Li Q, Hu C, Yang Y, Hu Z, Huang F, Wong KS, Yip HL, Yang S (2016) Effects of a molecular monolayer modification of NiO nanocrystal layer surfaces on perovskite crystallization and interface contact toward faster hole extraction and higher photovoltaic performance. Adv Func Mater 26(17):2950–2958. doi:10.1002/adfm.201505215
82. Park JH, Seo J, Park S, Shin SS, Kim YC, Jeon NJ, Shin H-W, Ahn TK, Noh JH, Yoon SC, Hwang CS, Seok SI (2015) Efficient $CH_3NH_3PbI_3$ perovskite solar cells employing nanostructured p-Type NiO electrode formed by a pulsed laser deposition. Adv Mater 27 (27):4013–4019. doi:10.1002/adma.201500523
83. Zhu Z, Bai Y, Zhang T, Liu Z, Long X, Wei Z, Wang Z, Zhang L, Wang J, Yan F, Yang S (2014) High-performance hole-extraction layer of sol–gel-processed NiO nanocrystals for inverted planar perovskite solar cells. Angew Chem Int Ed 53(46):12571–12575. doi:10.1002/anie.201405176
84. Rao H, Ye S, Sun W, Yan W, Li Y, Peng H, Liu Z, Bian Z, Li Y, Huang C (2016) A 19.0% efficiency achieved in CuOx-based inverted $CH_3NH_3PbI_3$-xClx solar cells by an effective Cl doping method. Nano Energy 27:51–59. doi:10.1016/j.nanoen.2016.06.044
85. Sun W, Li Y, Ye S, Rao H, Yan W, Peng H, Liu Z, Wang S, Chen Z, Xiao L, Bian Z, Huang C (2016) High-performance inverted planar heterojunction perovskite solar cells based on a solution-processed CuOx hole transport layer. Nanoscale 8(20):10806–10813. doi:10.1039/c6nr01927g
86. Zuo C, Ding L (2015) Solution-processed Cu_2O and CuO as hole transport materials for efficient perovskite solar cells. Small 11(41):5528–5532. doi:10.1002/smll.201501330
87. Zhao Y, Nardes AM, Zhu K (2014) Effective hole extraction using MoOx-Al contact in perovskite $CH_3NH_3PbI_3$ solar cells. Appl Phys Lett 104(21):213906. doi:10.1063/1.4880899
88. Hou F, Su Z, Jin F, Yan X, Wang L, Zhao H, Zhu J, Chu B, Li W (2015) Efficient and stable planar heterojunction perovskite solar cells with an MoO_3/PEDOT:PSS hole transporting layer. Nanoscale 7(21):9427–9432. doi:10.1039/c5nr01864a
89. Kim B-S, Kim T-M, Choi M-S, Shim H-S, Kim J-J (2015) Fully vacuum-processed perovskite solar cells with high open circuit voltage using MoO_3/NPB as hole extraction layers. Org Electron 17:102–106. doi:10.1016/j.orgel.2014.12.002
90. Liu P, Liu X, Lyu L, Xie H, Zhang H, Niu D, Huang H, Bi C, Xiao Z, Huang J, Gao Y (2015) Interfacial electronic structure at the $CH_3NH_3PbI_3$/MoOx interface. Appl Phys Lett 106(19)193903. doi:10.1063/1.4921339
91. Sanehira EM, Villers BJTd, Schulz P, Reese MO, Ferrere S, Zhu K, Lin LY, Berry JJ, Luther JM (2016) Influence of electrode interfaces on the stability of perovskite solar cells: reduced degradation using MoOx/Al for hole collection. ACS Energy Lett 1:38–45
92. Logan S, Donaghey JE, Zhang W, McCulloch I, Campbell AJ (2015) Compatibility of amorphous triarylamine copolymers with solution-processed hole injecting metal oxide bottom contacts. J Mater Chem C 3(17):4530–4536. doi:10.1039/c4tc02593h

93. Xiao M, Gao M, Huang F, Pascoe AR, Qin T, Cheng Y-B, Bach U, Spiccia L (2016) Efficient perovskite solar cells employing inorganic interlayers. ChemNanoMat 2(3):182–188. doi:10.1002/cnma.201500223
94. Guo CX, Sun K, Ouyang J, Lu X (2015) Layered V_2O_5/PEDOT nanowires and ultrathin nanobelts fabricated with a silk reelinglike process. Chem Mater 27(16):5813–5819. doi:10.1021/acs.chemmater.5b02512
95. Sun H, Hou X, Wei Q, Liu H, Yang K, Wang W, An Q, Rong Y (2016) Low-temperature solution-processed p-type vanadium oxide for perovskite solar cells. Chem Commun (Cambridge, England) 52(52):8099–8102. doi:10.1039/c6cc03740b
96. Lou Y-H, Li M, Wang Z-K (2016) Seed-mediated superior organometal halide films by GeO_2 nano-particles for high performance perovskite solar cells. Appl Phys Lett 108 (5):053301. doi:10.1063/1.4941416
97. Hossain MI, Alharbi FH, Tabet N (2015) Copper oxide as inorganic hole transport material for lead halide perovskite based solar cells. Sol Energy 120:370–380. doi:10.1016/j.solener.2015.07.040
98. Kim JH, Liang P-W, Williams ST, Cho N, Chueh C-C, Glaz MS, Ginger DS, Jen AKY (2015) High-performance and environmentally stable planar heterojunction perovskite solar cells based on a solution-processed copper-doped nickel oxide hole-transporting layer. Adv Mater 27(4):695–701. doi:10.1002/adma.201404189
99. Kim J, Lee HR, Kim HP, Lin T, Kanwat A, Yusoff ARb Mohd, Jang J (2016) Effects of UV-ozone irradiation on copper doped nickel acetate and its applicability to perovskite solar cells. Nanoscale 8(17):9284–9292. doi:10.1039/c6nr01308b
100. Qin P-L, Lei H-W, Zheng X-L, Liu Q, Tao H, Yang G, Ke W-J, Xiong L-B, Qin M-C, Zhao X-Z, Fang G-J (2016) Copper-doped chromium oxide hole-transporting layer for perovskite solar cells: interface engineering and performance improvement. Adv Mater Interfaces n/a–n/a. doi:10.1002/admi.201500799
101. Burschka J, Pellet N, Moon SJ, Humphry-Baker R, Gao P, Nazeeruddin MK, Grätzel M (2013) Sequential deposition as a route to high-performance perovskite-sensitized solar cells. Nature 499(7458):316–319. doi:10.1038/nature12340
102. Shao S, Abdu-Aguye M, Qiu L, Lai L-H, Liu J, Adjokatse S, Jahani F, Kamminga ME, ten Brink GH, Palstra TTM, Kooi BJ, Hummelen JC, Antonietta Loi M (2016) Elimination of the light soaking effect and performance enhancement in perovskite solar cells using a fullerene derivative. Energy Environ Sci 9(7):2444–2452. doi:10.1039/C6EE01337F
103. Nie W, Blancon J-C, Neukirch AJ, Appavoo K, Tsai H, Chhowalla M, Alam MA, Sfeir MY, Katan C, Even J, Tretiak S, Crochet JJ, Gupta G, Mohite AD (2016) Light-activated photocurrent degradation and self-healing in perovskite solar cells. Nat Commun 7. doi:10.1038/ncomms11574
104. Ripolles TS, Baranwal AK, Nishinaka K, Ogomi Y, Garcia-Belmonte G, Hayase S (2016) Mechanisms of charge accumulation in the dark operation of perovskite solar cells. Phys Chem Chem Phys 18(22):14970–14975. doi:10.1039/c6cp01427e
105. Zarazua I, Bisquert J, Garcia-Belmonte G (2016) Light-induced space-charge accumulation zone as photovoltaic mechanism in perovskite solar cells. J Phys Chem Lett 7(3):525–528. doi:10.1021/acs.jpclett.5b02810
106. Almora O, Zarazua I, Mas-Marza E, Mora-Sero I, Bisquert J, Garcia-Belmonte G (2015) Capacitive dark currents, hysteresis, and electrode polarization in lead halide perovskite solar cells. J Phys Chem Lett 6(9):1645–1652. doi:10.1021/acs.jpclett.5b00480
107. Kim H-S, Mora-Sero I, Gonzalez-Pedro V, Fabregat-Santiago F, Juarez-Perez EJ, Park N-G, Bisquert J (2013) Mechanism of carrier accumulation in perovskite thin-absorber solar cells. Nat Commun 4. doi:10.1038/ncomms3242
108. Reese MO, Gevorgyan SA, Jørgensen M, Bundgaard E, Kurtz SR, Ginley DS, Olson DC, Lloyd MT, Morvillo P, Katz EA, Elschner A, Haillant O, Currier TR, Shrotriya V, Hermenau M, Riede M, Kirov KR, Trimmel G, Rath T, Inganäs O, Zhang F, Andersson M, Tvingstedt K, Lira-Cantu M, Laird D, McGuiness C, Gowrisanker S, Pannone M, Xiao M, Hauch J, Steim R, Delongchamp DM, Rösch R, Hoppe H, Espinosa N, Urbina A,

Yaman-Uzunoglu G, Bonekamp JB, Van Breemen AJJM, Girotto C, Voroshazi E, Krebs FC (2011) Consensus stability testing protocols for organic photovoltaic materials and devices. Sol Energy Mater Sol Cells 95(5):1253–1267. doi:10.1016/j.solmat.2011.01.036
109. Matteocci F, Cinà L, Lamanna E, Cacovich S, Divitini G, Midgley PA, Ducati C, Di Carlo A (2016) Encapsulation for long-term stability enhancement of perovskite solar cells. Nano Energy 30:162–172. doi:10.1016/j.nanoen.2016.09.041
110. Bi D, Boschloo G, Schwarzmuller S, Yang L, Johansson EMJ, Hagfeldt A (2013) Efficient and stable $CH_3NH_3PbI_3$-sensitized ZnO nanorod array solid-state solar cells. Nanoscale 5 (23):11686–11691. doi:10.1039/c3nr01542d
111. Fakharuddin A, Di Giacomo F, Palma AL, Matteocci F, Ahmed I, Razza S, D'Epifanio A, Licoccia S, Ismail J, Di Carlo A, Brown TM, Jose R (2015) Vertical TiO_2 nanorods as a medium for stable and high-efficiency perovskite solar modules. ACS Nano 9(8):8420–8429. doi:10.1021/acsnano.5b03265
112. Mahmood K, Swain BS, Kirmani AR, Amassian A (2015) Highly efficient perovskite solar cells based on a nanostructured WO3-TiO2 core-shell electron transporting material. Journal of Materials Chemistry A 3(17):9051–9057. doi:10.1039/c4ta04883k
113. Huang S, Li Z, Kong L, Zhu N, Shan A, Li L (2016) Enhancing the stability of $CH_3NH_3PbBr_3$ quantum dots by embedding in silica spheres derived from tetramethyl orthosilicate in "Waterless" toluene. J Am Chem Soc 138(18):5749–5752. doi:10.1021/jacs.5b13101
114. Cao K, Zuo Z, Cui J, Shen Y, Moehl T, Zakeeruddin SM, Grätzel M, Wang M (2015) Efficient screen printed perovskite solar cells based on mesoscopic TiO_2/Al_2O_3/NiO/carbon architecture. Nano Energy 17:171–179. doi:10.1016/j.nanoen.2015.08.009
115. Corani A, Li MH, Shen PS, Chen P, Guo TF, El Nahhas A, Zheng K, Yartsev A, Sundström V, Ponseca CS (2016) Ultrafast dynamics of hole injection and recombination in organometal halide perovskite using nickel oxide as p-type contact electrode. J Phys Chem Letters 7(7):1096–1101. doi:10.1021/acs.jpclett.6b00238
116. Dubey A, Kantack N, Adhikari N, Reza KM, Venkatesan S, Kumar M, Khatiwada D, Darling S, Qiao Q (2016) Room temperature, air crystallized perovskite film for high performance solar cells. J Mater Chem A 4(26):10231–10240. doi:10.1039/C6TA02918C
117. Li H, Cao K, Cui J, Liu S, Qiao X, Shen Y, Wang M (2016) 14.7% efficient mesoscopic perovskite solar cells using single walled carbon nanotubes/carbon composite counter electrodes. Nanoscale 8(12):6379–6385. doi:10.1039/c5nr07347b
118. Dong X, Fang X, Lv M, Lin B, Zhang S, Ding J, Yuan N (2015) Improvement of the humidity stability of organic-inorganic perovskite solar cells using ultrathin Al_2O_3 layers prepared by atomic layer deposition. J Mater Chem A 3(10):5360–5367. doi:10.1039/c4ta06128d
119. Mei A, Li X, Liu L, Ku Z, Liu T, Rong Y, Xu M, Hu M, Chen J, Yang Y, Grätzel M, Han H (2014) A hole-conductor-free, fully printable mesoscopic perovskite solar cell with high stability. Science 345(6194):295–298. doi:10.1126/science.1254763
120. Cheng N, Liu P, Bai S, Yu Z, Liu W, Guo SS, Zhao XZ (2016) Application of mesoporous SiO2 layer as an insulating layer in high performance hole transport material free $CH_3NH_3PbI_3$ perovskite solar cells. J Power Sources 321:71–75. doi:10.1016/j.jpowsour.2016.04.124
121. Liu T, Hu Q, Wu J, Chen K, Zhao L, Liu F, Wang C, Lu H, Jia S, Russell T, Zhu R, Gong Q (2016) Mesoporous PbI_2 scaffold for high-performance planar heterojunction perovskite solar cells. Adv Energy Mater 6(3):n/a–n/a. doi:10.1002/aenm.201501890
122. Li X, Tschumi M, Han H, Babkair SS, Alzubaydi RA, Ansari AA, Habib SS, Nazeeruddin MK, Zakeeruddin SM, Grätzel M (2015) Outdoor performance and stability under elevated temperatures and long-term light soaking of triple-layer mesoporous perovskite photovoltaics. Energy Technol 3(6):551–555. doi:10.1002/ente.201500045
123. Chen J, Rong Y, Mei A, Xiong Y, Liu T, Sheng Y, Jiang P, Hong L, Guan Y, Zhu X, Hou X, Duan M, Zhao J, Li X, Han H (2016) Hole-conductor-free fully printable

mesoscopic solar cell with mixed-anion perovskite $CH_3NH_3PbI_{(3-x)}(BF_4)_x$. Adv Energy Mater 6(5):n/a–n/a. doi:10.1002/aenm.201502009
124. Liu T, Liu L, Hu M, Yang Y, Zhang L, Mei A, Han H (2015) Critical parameters in TiO_2/ZrO_2/Carbon-based mesoscopic perovskite solar cell. J Power Sources 293:533–538. doi:10.1016/j.jpowsour.2015.05.106
125. Huang L, Xu J, Sun X, Du Y, Cai H, Ni J, Li J, Hu Z, Zhang J (2016) Toward revealing the critical role of perovskite coverage in highly efficient electron-transport layer-free perovskite solar cells: an energy band and equivalent circuit model perspective. ACS Appl Mater Interfaces 8(15):9811–9820. doi:10.1021/acsami.6b00544
126. Li M-H, Yum J-H, Moon S-J, Chen P (2016) Inorganic p-type semiconductors: their applications and progress in dye-sensitized solar cells and perovskite solar cells. Energies 9 (5):331
127. Kim H, Lim KG, Lee TW (2016) Planar heterojunction organometal halide perovskite solar cells: roles of interfacial layers. Energy Environ Sci 9(1):12–30. doi:10.1039/c5ee02194d
128. Tiep NH, Ku Z, Fan HJ (2016) Recent advances in improving the stability of perovskite solar cells. Adv Energy Mater 6(3):n/a–n/a. doi:10.1002/aenm.201501420
129. Lira-Cantu M, Krebs FC (2006) Hybrid solar cells based on MEH-PPV and thin film semiconductor oxides (TiO_2, Nb_2O_5, ZnO, CeO_2 and CeO_2–TiO_2): performance improvement during long-time irradiation. Sol Energy Mater Sol Cells 90(14):2076–2086. doi:10.1016/j.solmat.2006.02.007
130. Lira-Cantu M, Norrman K, Andreasen JW, Krebs FC (2006) Oxygen release and exchange in niobium oxide MEHPPV hybrid solar cells. Chem Mater 18(24):5684–5690. doi:10.1021/cm061429d
131. Norrman K, Alstrup J, Jørgensen M, Lira-Cantu M, Larsen NB, Krebs FC (2006) Three-dimensional chemical and physical analysis of the degradation mechanisms in organic photovoltaics. In: Proceedings of SPIE—the international society for optical engineering, 2006. doi:10.1117/12.680403
132. Etgar L, Gao P, Xue Z, Peng Q, Chandiran AK, Liu B, Nazeeruddin MK, Grätzel M (2012) Mesoscopic $CH_3NH_3PbI_3$/TiO_2 heterojunction solar cells. J Am Chem Soc 134(42):17396–17399. doi:10.1021/ja307789s
133. Reyna Y, Salado M, Kazim S, Pérez-Tomas A, Ahmad S, Lira-Cantu M (2016) Performance and stability of mixed $FAPbI_3(0.85)MAPbBr_3(0.15)$ halide perovskite solar cells under outdoor conditions and the effect of low light irradiation. Nano Energy 30:570–579. doi:10.1016/j.nanoen.2016.10.053
134. Raifuku I, Ishikawa Y, Ito S, Uraoka Y (2016) Characteristics of perovskite solar cells under low-illuminance conditions. J Phys Chem C 120(34):18986–18990. doi:10.1021/acs.jpcc.6b05298
135. Bryant D, Aristidou N, Pont S, Sanchez-Molina I, Chotchunangatchaval T, Wheeler S, Durrant JR, Haque SA (2016) Light and oxygen induced degradation limits the operational stability of methylammonium lead triiodide perovskite solar cells. Energy Environ Sci 9 (5):1655–1660. doi:10.1039/c6ee00409a
136. Palazon F, Akkerman QA, Prato M, Manna L (2016) X-ray lithography on perovskite nanocrystals films: from patterning with anion-exchange reactions to enhanced stability in air and water. ACS Nano 10(1):1224–1230. doi:10.1021/acsnano.5b06536
137. Koocher NZ, Saldana-Greco D, Wang F, Liu S, Rappe AM (2015) Polarization dependence of water adsorption to $CH_3NH_3PbI_3(001)$ surfaces. J Phys Chem Lett 6(21):4371–4378. doi:10.1021/acs.jpclett.5b01797
138. Liu G, Wong WSY, Nasiri N, Tricoli A (2016) Ultraporous superhydrophobic gas-permeable nano-layers by scalable solvent-free one-step self-assembly. Nanoscale 8 (11):6085–6093. doi:10.1039/C5NR09000H
139. Chen H, Hou Y, Halbig CE, Chen S, Zhang H, Li N, Guo F, Tang X, Gasparini N, Levchuk I, Kahmann S, Ramirez Quiroz CO, Osvet A, Eigler S, Brabec CJ (2016) Extending the environmental lifetime of unpackaged perovskite solar cells through interfacial design. J Mater Chem A. doi:10.1039/C6TA03755K

140. Leijtens T, Giovenzana T, Habisreutinger SN, Tinkham JS, Noel NK, Kamino BA, Sadoughi G, Sellinger A, Snaith HJ (2016) Hydrophobic organic hole transporters for improved moisture resistance in metal halide perovskite solar cells. ACS Appl Mater Interfaces 8(9):5981–5989. doi:10.1021/acsami.5b10093
141. Adhikari N, Dubey A, Gaml EA, Vaagensmith B, Reza KM, Mabrouk SAA, Gu S, Zai J, Qian X, Qiao Q (2016) Crystallization of a perovskite film for higher performance solar cells by controlling water concentration in methyl ammonium iodide precursor solution. Nanoscale 8(5):2693–2703. doi:10.1039/C5NR06687E
142. Zhou W, Zhao Y, Shi C, Huang H, Wei J, Fu R, Liu K, Yu D, Zhao Q (2016) Reversible healing effect of water molecules on fully crystallized metal-halide perovskite film. J Phys Chem C 120(9):4759–4765. doi:10.1021/acs.jpcc.5b11465
143. Eperon GE, Habisreutinger SN, Leijtens T, Bruijnaers BJ, van Franeker JJ, deQuilettes DW, Pathak S, Sutton RJ, Grancini G, Ginger DS, Janssen RAJ, Petrozza A, Snaith HJ (2015) The importance of moisture in hybrid lead halide perovskite thin film fabrication. ACS Nano 9(9):9380–9393. doi:10.1021/acsnano.5b03626
144. You J, Yang Y, Hong Z, Song T-B, Meng L, Liu Y, Jiang C, Zhou H, Chang W-H, Li G, Yang Y (2014) Moisture assisted perovskite film growth for high performance solar cells. Appl Phys Lett 105(18):183902. doi:10.1063/1.4901510
145. Philippe B, Park B-W, Lindblad R, Oscarsson J, Ahmadi S, Johansson EMJ, Rensmo H (2015) Chemical and electronic structure characterization of lead halide perovskites and stability behavior under different exposures—a photoelectron spectroscopy investigation. Chem Mater 27(5):1720–1731. doi:10.1021/acs.chemmater.5b00348
146. Lee J-W, Kim D-H, Kim H-S, Seo S-W, Cho SM, Park N-G (2015) Formamidinium and cesium hybridization for photo- and moisture-stable perovskite solar cell. Adv Energy Mater 5(20):n/a–n/a. doi:10.1002/aenm.201501310
147. Kulbak M, Cahen D, Hodes G (2015) How important is the organic part of lead halide perovskite photovoltaic cells? Efficient $CsPbBr_3$ cells. J Phys Chem Lett 6(13):2452–2456. doi:10.1021/acs.jpclett.5b00968
148. Yang J, Siempelkamp BD, Mosconi E, De Angelis F, Kelly TL (2015) Origin of the thermal instability in $CH_3NH_3PbI_3$ thin films deposited on ZnO. Chem Mater 27(12):4229–4236. doi:10.1021/acs.chemmater.5b01598
149. Dualeh A, Gao P, Seok SI, Nazeeruddin MK, Grätzel M (2014) Thermal behavior of methylammonium lead-trihalide perovskite photovoltaic light harvesters. Chem Mater 26 (21):6160–6164. doi:10.1021/cm502468k
150. Borchert J, Boht H, Franzel W, Csuk R, Scheer R, Pistor P (2015) Structural investigation of co-evaporated methyl ammonium lead halide perovskite films during growth and thermal decomposition using different PbX_2 (X = I, Cl) precursors. J Mater Chem A 3(39):19842–19849. doi:10.1039/C5TA04944J
151. Ito S, Tanaka S, Manabe K, Nishino H (2014) Effects of surface blocking layer of Sb_2S_3 on nanocrystalline TiO_2 for $CH_3NH_3PbI_3$ perovskite solar cells. J Phys Chem C 118 (30):16995–17000. doi:10.1021/jp500449z
152. Zhao X, Shen H, Zhang Y, Li X, Zhao X, Tai M, Li J, Li J, Lin H (2016) Aluminum-doped zinc oxide as highly stable electron collection layer for perovskite solar cells. ACS Appl Mater Interfaces 8(12):7826–7833. doi:10.1021/acsami.6b00520
153. Back H, Kim J, Kim G, Kyun Kim T, Kang H, Kong J, Ho Lee S, Lee K (2016) Interfacial modification of hole transport layers for efficient large-area perovskite solar cells achieved via blade-coating. Sol Energy Mater Sol Cells 144:309–315. doi:10.1016/j.solmat.2015.09.018
154. Chang C-Y, Chang Y-C, Huang W-K, Lee K-T, Cho A-C, Hsu C-C (2015) Enhanced performance and stability of semitransparent perovskite solar cells using solution-processed thiol-functionalized cationic surfactant as cathode buffer layer. Chem Mater 27(20):7119–7127. doi:10.1021/acs.chemmater.5b03137
155. Chang C-Y, Chang Y-C, Huang W-K, Liao W-C, Wang H, Yeh C, Tsai B-C, Huang Y-C, Tsao C-S (2016) Achieving high efficiency and improved stability in large-area ITO-free

perovskite solar cells with thiol-functionalized self-assembled monolayers. J Mater Chem A 4(20):7903–7913. doi:10.1039/c6ta02581a
156. Yao K, Wang X, Y-x Xu, Li F, Zhou L (2016) Multilayered perovskite materials based on polymeric-ammonium cations for stable large-area solar cell. Chem Mater 28(9):3131–3138. doi:10.1021/acs.chemmater.6b00711
157. Leijtens T, Eperon GE, Pathak S, Abate A, Lee MM, Snaith HJ (2013) Overcoming ultraviolet light instability of sensitized TiO_2 with meso-superstructured organometal tri-halide perovskite solar cells. Nat Commun 4:2885. doi:10.1038/ncomms3885
158. Bi D, Gao P, Scopelliti R, Oveisi E, Luo J, Grätzel M, Hagfeldt A, Nazeeruddin MK (2016) High-performance perovskite solar cells with enhanced environmental stability based on amphiphile-modified $CH_3NH_3PbI_3$. Adv Mater 28(15):2910–2915. doi:10.1002/adma.201505255
159. Li X, Ibrahim Dar M, Yi C, Luo J, Tschumi M, Zakeeruddin SM, Nazeeruddin MK, Han H, Grätzel M (2015) Improved performance and stability of perovskite solar cells by crystal crosslinking with alkylphosphonic acid ω-ammonium chlorides. Nat Chem 7(9):703–711. doi:10.1038/nchem.2324
160. Wang H-H, Chen Q, Zhou H, Song L, Louis ZS, Marco ND, Fang Y, Sun P, Song T-B, Chen H, Yang Y (2015) Improving the TiO_2 electron transport layer in perovskite solar cells using acetylacetonate-based additives. J Mater Chem A 3(17):9108–9115. doi:10.1039/C4TA06394E
161. Luo P, Xia W, Zhou S, Sun L, Cheng J, Xu C, Lu Y (2016) Solvent engineering for ambient-air-processed, phase-stable $CsPbI_3$ in perovskite solar cells. J Phys Chem Lett 3603–3608. doi:10.1021/acs.jpclett.6b01576
162. Zuo C, Bolink HJ, Han H, Huang J, Cahen D, Ding L (2016) Advances in perovskite solar cells. Adv Sci 3(7):n/a–n/a. doi:10.1002/advs.201500324
163. Kim BJ, Kim DH, Lee Y-Y, Shin H-W, Han GS, Hong JS, Mahmood K, Ahn TK, Joo Y-C, Hong KS, Park N-G, Lee S, Jung HS (2015) Highly efficient and bending durable perovskite solar cells: toward a wearable power source. Energy Environ Sci 8(3):916–921. doi:10.1039/C4EE02441A
164. Snaith HJ, Abate A, Ball JM, Eperon GE, Leijtens T, Noel NK, Stranks SD, Wang JT-W, Wojciechowski K, Zhang W (2014) Anomalous hysteresis in perovskite solar cells. J Phys Chem Lett 5(9):1511–1515. doi:10.1021/jz500113x
165. Noel NK, Abate A, Stranks SD, Parrott ES, Burlakov VM, Goriely A, Snaith HJ (2014) Enhanced photoluminescence and solar cell performance via lewis base passivation of organic-inorganic lead halide perovskites. ACS Nano 8(10):9815–9821. doi:10.1021/nn5036476
166. Yi C, Luo J, Meloni S, Boziki A, Ashari-Astani N, Gratzel C, Zakeeruddin SM, Rothlisberger U, Gratzel M (2016) Entropic stabilization of mixed A-cation ABX3 metal halide perovskites for high performance perovskite solar cells. Energy Environ Sci 9:656–662
167. Chen W, Wu Y, Yue Y, Liu J, Zhang W, Yang X, Chen H, Bi E, Ashraful I, Grätzel M, Han L (2015) Efficient and stable large-area perovskite solar cells with inorganic charge extraction layers. Science 350(6263):944–948. doi:10.1126/science.aad1015
168. Yu X, Marks TJ, Facchetti A (2016) Metal oxides for optoelectronic applications. Nat Mater 15(4):383–396. doi:10.1038/nmat4599
169. Zhou H, Shi Y, Wang K, Dong Q, Bai X, Xing Y, Du Y, Ma T (2015) Low-temperature processed and carbon-based $ZnO/CH_3NH_3PbI_3/C$ planar heterojunction perovskite solar cells. J Phys Chem C 119(9):4600–4605. doi:10.1021/jp512101d
170. Xu X, Zhang H, Shi J, Dong J, Luo Y, Li D, Meng Q (2015) Highly efficient planar perovskite solar cells with a TiO_2/ZnO electron transport bilayer. J Mater Chem A 3(38):19288–19293. doi:10.1039/C5TA04239A
171. Shalan AE, Elseman AM, Rasly M, Moharam MM, Lira-Cantu M, Rashad MM (2015) Concordantly fabricated heterojunction $ZnO\text{-}TiO_2$ nanocomposite electrodes via a

co-precipitation method for efficient stable quasi-solid-state dye-sensitized solar cells. RSC Adv 5(125):103095–103104. doi:10.1039/c5ra21822e
172. Qiu W, Buffière M, Brammertz G, Paetzold UW, Froyen L, Heremans P, Cheyns D (2015) High efficiency perovskite solar cells using a PCBM/ZnO double electron transport layer and a short air-aging step. Org Electron 26:30–35. doi:10.1016/j.orgel.2015.06.046
173. Kim J, Kim G, Kim TK, Kwon S, Back H, Lee J, Lee SH, Kang H, Lee K (2014) Efficient planar-heterojunction perovskite solar cells achieved via interfacial modification of a sol-gel ZnO electron collection layer. J Mater Chem A 2(41):17291–17296. doi:10.1039/C4TA03954H
174. Dong X, Hu H, Lin B, Ding J, Yuan N (2014) The effect of ALD-Zno layers on the formation of $CH_3NH_3PbI_3$ with different perovskite precursors and sintering temperatures. Chem Commun 50(92):14405–14408. doi:10.1039/C4CC04685D
175. Kumar MH, Yantara N, Dharani S, Graetzel M, Mhaisalkar S, Boix PP, Mathews N (2013) Flexible, low-temperature, solution processed ZnO-based perovskite solid state solar cells. Chem Commun 49(94):11089–11091. doi:10.1039/C3CC46534A
176. Li Z (2015) Stable perovskite solar cells based on WO_3 nanocrystals as hole transport layer. Chem Lett 44(8):1140–1141. doi:10.1246/cl.150445
177. Zhang J, Shi C, Chen J, Wang Y, Li M (2016) Preparation of ultra-thin and high-quality WO_3 compact layers and comparison of WO_3 and TiO_2 compact layer thickness in planar perovskite solar cells. J Solid State Chem 238:223–228. doi:10.1016/j.jssc.2016.03.033
178. Zhang J, Shi C, Chen J, Ying C, Wu N, Wang M (2016) Pyrolysis preparation of WO_3 thin films using ammonium metatungstate DMF/water solution for efficient compact layers in planar perovskite solar cells. J Semiconductors 37(3):Unsp 033002. doi:10.1088/1674-4926/37/3/033002
179. Song J, Zheng E, Bian J, Wang X-F, Tian W, Sanehira Y, Miyasaka T (2015) Low-temperature SnO_2-based electron selective contact for efficient and stable perovskite solar cells. J Mater Chem A 3(20):10837–10844. doi:10.1039/c5ta01207d
180. Sung H, Ahn N, Jang MS, Lee J-K, Yoon H, Park N-G, Choi M (2016) Solar cells: transparent conductive oxide-free graphene-based perovskite solar cells with over 17% efficiency (Adv Energy Mater 3/2016). Adv Energy Mater 6(3):1501873. doi:10.1002/aenm.201670014
181. Acik M, Darling SB (2016) Graphene in perovskite solar cells: device design, characterization and implementation. J Mater Chem A 4(17):6185–6235. doi:10.1039/c5ta09911k
182. Wang C, Tang Y, Hu Y, Huang L, Fu J, Jin J, Shi W, Wang L, Yang W (2015) Graphene/$SrTiO_3$ nanocomposites used as an effective electron-transporting layer for high-performance perovskite solar cells. RSC Adv 5(64):52041–52047. doi:10.1039/C5RA09001F
183. Cao J, Liu Y-M, Jing X, Yin J, Li J, Xu B, Tan Y-Z, Zheng N (2015) Well-defined thiolated nanographene as hole-transporting material for efficient and stable perovskite solar cells. J Am Chem Soc 137(34):10914–10917. doi:10.1021/jacs.5b06493
184. Wu Z, Bai S, Xiang J, Yuan Z, Yang Y, Cui W, Gao X, Liu Z, Jin Y, Sun B (2014) Efficient planar heterojunction perovskite solar cells employing graphene oxide as hole conductor. Nanoscale 6(18):10505–10510. doi:10.1039/C4NR03181D
185. Bera A, Wu K, Sheikh A, Alarousu E, Mohammed OF, Wu T (2014) Perovskite oxide $SrTiO_3$ as an efficient electron transporter for hybrid perovskite solar cells. J Phys Chem C 118(49):28494–28501. doi:10.1021/jp509753p
186. Hu Y, Wang C, Tang Y, Huang L, Fu J, Shi W, Wang L, Yang W (2016) Three-dimensional self-branching anatase TiO_2 nanorods with the improved carrier collection for $SrTiO_3$-based perovskite solar cells. J Alloy Compd 679:32–38. doi:10.1016/j.jallcom.2016.04.049
187. You J, Meng L, Song T-B, Guo T-F, Yang Y, Chang W-H, Hong Z, Chen H, Zhou H, Chen Q, Liu Y, De Marco N (2016) Improved air stability of perovskite solar cells via solution-processed metal oxide transport layers. Nat Nano 11(1):75–81. doi:10.1038/nnano.2015.230. http://www.nature.com/nnano/journal/v11/n1/abs/nnano.2015.230.html#supplementary-information

188. Jung JW, Chueh C-C, Jen AKY (2015) A low-temperature, solution-processable, Cu-doped nickel oxide hole-transporting layer via the combustion method for high-performance thin-film perovskite solar cells. Adv Mater 27(47):7874–7880. doi:10.1002/adma.201503298
189. Zhao Y, Zhu K (2016) Organic-inorganic hybrid lead halide perovskites for optoelectronic and electronic applications. Chem Soc Rev 45(3):655–689. doi:10.1039/c4cs00458b
190. Wang W, Yuan J, Shi G, Zhu X, Shi S, Liu Z, Han L, Wang H-Q, Ma W (2015) Inverted planar heterojunction perovskite solar cells employing polymer as the electron conductor. ACS Appl Mater Interfaces 7(7):3994–3999. doi:10.1021/am506785k
191. Abdollahi Nejand B, Ahmadi V, Shahverdi HR (2015) New physical deposition approach for low cost inorganic hole transport layer in normal architecture of durable perovskite solar cells. ACS Appl Mater Interfaces 7(39):21807–21818. doi:10.1021/acsami.5b05477
192. Liu C, Wang K, Du P, Meng T, Yu X, Cheng SZD, Gong X (2015) High performance planar heterojunction perovskite solar cells with fullerene derivatives as the electron transport layer. ACS Appl Mater Interfaces 7(2):1153–1159. doi:10.1021/am506869k
193. You J, Hong Z, Yang Y, Chen Q, Cai M, Song T-B, Chen C-C, Lu S, Liu Y, Zhou H, Yang Y (2014) Low-temperature solution-processed perovskite solar cells with high efficiency and flexibility. ACS Nano 8(2):1674–1680. doi:10.1021/nn406020d
194. Yu Z, Chen B, Liu P, Wang C, Bu C, Cheng N, Bai S, Yan Y, Zhao X (2016) Stable organic–inorganic perovskite solar cells without hole-conductor layer achieved via cell structure design and contact engineering. Adv Funct Mater n/a–n/a. doi:10.1002/adfm.201504564
195. Ma Q, Huang S, Wen X, Green MA, Ho-Baillie AWY (2016) Hole transport layer free inorganic $CsPbIBr_2$ perovskite solar cell by dual source thermal evaporation. Adv Energy Mater 6(7). doi:10.1002/aenm.201502202
196. Huang L, Hu Z, Xu J, Sun X, Du Y, Ni J, Cai H, Li J, Zhang J (2016) Efficient planar perovskite solar cells without a high temperature processed titanium dioxide electron transport layer. Sol Energy Mater Sol Cells 149:1–8. doi:10.1016/j.solmat.2015.12.033
197. Liu T, Zuo L, Ye T, Wu J, Xue G, Fu W, Chen H (2015) Low temperature processed ITO-free perovskite solar cells without a hole transport layer. RSC Adv. 5(115):94752–94758. doi:10.1039/c5ra20125j
198. Zhang Y, Hu X, Chen L, Huang Z, Fu Q, Liu Y, Zhang L, Chen Y (2016) Flexible, hole transporting layer-free and stable $CH_3NH_3PbI_3$/PC61BM planar heterojunction perovskite solar cells. Org Electron 30:281–288. doi:10.1016/j.orgel.2016.01.002
199. Tsai K-W, Chueh C-C, Williams ST, Wen T-C, Jen AKY (2015) High-performance hole-transporting layer-free conventional perovskite/fullerene heterojunction thin-film solar cells. J Mater Chem A 3(17):9128–9132. doi:10.1039/c5ta01343g
200. Zhu Q, Bao X, Yu J, Zhu D, Qiu M, Yang R, Dong L (2016) Compact layer free perovskite solar cells with a high-mobility hole-transporting layer. ACS Appl Mater Interfaces 8(4):2652–2657. doi:10.1021/acsami.5b10555
201. Liu Z, Shi T, Tang Z, Sun B, Liao G (2016) Using a low-temperature carbon electrode for preparing hole-conductor-free perovskite heterojunction solar cells under high relative humidity. Nanoscale 8(13):7017–7023. doi:10.1039/c5nr07091k
202. Jung M-C, Raga SR, Ono LK, Qi Y (2015) Substantial improvement of perovskite solar cells stability by pinhole-free hole transport layer with doping engineering. Sci Rep 5:9863. doi:10.1038/srep09863. http://www.nature.com/articles/srep09863#supplementary-information
203. Habisreutinger SN, Leijtens T, Eperon GE, Stranks SD, Nicholas RJ, Snaith HJ (2014) Carbon nanotube/polymer composites as a highly stable hole collection layer in perovskite solar cells. Nano Lett 14(10):5561–5568. doi:10.1021/nl501982b
204. Li H, Fu K, Hagfeldt A, Grätzel M, Mhaisalkar SG, Grimsdale AC (2014) A simple 3,4-ethylenedioxythiophene based hole-transporting material for perovskite solar cells. Angew Chem Int Ed 53(16):4085–4088. doi:10.1002/anie.201310877
205. Xiao J, Han L, Zhu L, Lv S, Shi J, Wei H, Xu Y, Dong J, Xu X, Xiao Y, Li D, Wang S, Luo Y, Li X, Meng Q (2014) A thin pristine non-triarylamine hole-transporting material

layer for efficient CH3NH3PbI3 perovskite solar cells. RSC Adv 4(62):32918–32923. doi:10.1039/c4ra05199h
206. Zhou H, Shi Y, Dong Q, Zhang H, Xing Y, Wang K, Du Y, Ma T (2014) Hole-conductor-free, metal-electrode-free $TiO_2/CH_3NH_3PbI_3$ heterojunction solar cells based on a low-temperature carbon electrode. J Phys Chem Lett 5(18):3241–3246. doi:10.1021/jz5017069
207. Kulbak M, Gupta S, Kedem N, Levine I, Bendikov T, Hodes G, Cahen D (2016) Cesium enhances long-term stability of lead bromide perovskite-based solar cells. J Phys Chem Lett 7(1):167–172. doi:10.1021/acs.jpclett.5b02597
208. Liu J, Wu Y, Qin C, Yang X, Yasuda T, Islam A, Zhang K, Peng W, Chen W, Han L (2014) A dopant-free hole-transporting material for efficient and stable perovskite solar cells. Energy Environ Sci 7(9):2963–2967. doi:10.1039/c4ee01589d
209. Kim H-S, Lee C-R, Im J-H, Lee K-B, Moehl T, Marchioro A, Moon S-J, Humphry-Baker R, Yum J-H, Moser JE, Grätzel M, Park N-G (2012) Lead Iodide perovskite sensitized all-solid-state submicron thin film mesoscopic solar cell with efficiency exceeding 9%. Sci Rep 2:591. doi:10.1038/srep00591. http://www.nature.com/articles/srep00591#supplementary-information
210. Noh JH, Im SH, Heo JH, Mandal TN, Seok SI (2013) Chemical management for colorful, efficient, and stable inorganic-organic hybrid nanostructured solar cells. Nano Lett 13(4):1764–1769. doi:10.1021/nl400349b
211. Zhang F, Yang X, Wang H, Cheng M, Zhao J, Sun L (2014) Structure engineering of hole-conductor free perovskite-based solar cells with low-temperature-processed commercial carbon paste as cathode. ACS Appl Mater Interfaces 6(18):16140–16146. doi:10.1021/am504175x
212. Cai B, Xing Y, Yang Z, Zhang W-H, Qiu J (2013) High performance hybrid solar cells sensitized by organolead halide perovskites. Energy Environ Sci 6(5):1480–1485. doi:10.1039/c3ee40343b
213. Kwon YS, Lim J, Yun H-J, Kim Y-H, Park T (2014) A diketopyrrolopyrrole-containing hole transporting conjugated polymer for use in efficient stable organic-inorganic hybrid solar cells based on a perovskite. Energy Environ Sci 7(4):1454–1460. doi:10.1039/c3ee44174a
214. Koo B, Jung H, Park M, Kim J-Y, Son HJ, Cho J, Ko MJ (2016) Pyrite-based Bi-functional layer for long-term stability and high-performance of organo-lead halide perovskite solar cells. Adv Funct Mater n/a–n/a. doi:10.1002/adfm.201601119
215. Liu Y, Ji S, Li S, He W, Wang K, Hu H, Ye C (2015) Study on hole-transport-material-free planar $TiO_2/CH_3NH_3PbI_3$ heterojunction solar cells: the simplest configuration of a working perovskite solar cell. J Mater Chem A 3(28):14902–14909. doi:10.1039/c5ta03693c
216. Chen W, Wu Y, Liu J, Qin C, Yang X, Islam A, Cheng Y-B, Han L (2015) Hybrid interfacial layer leads to solid performance improvement of inverted perovskite solar cells. Energy Environ Sci 8(2):629–640
217. Law C, Miseikis L, Dimitrov S, Shakya-Tuladhar P, Li X, Barnes PRF, Durrant J, O'Regan BC (2014) Performance and stability of lead perovskite/TiO_2, Polymer/PCBM, and dye sensitized solar cells at light intensities up to 70 suns. Adv Mater 26(36):6268–6273. doi:10.1002/adma.201402612
218. Eperon GE, Stranks SD, Menelaou C, Johnston MB, Herz LM, Snaith HJ (2014) Formamidinium lead trihalide: a broadly tunable perovskite for efficient planar heterojunction solar cells. Energy Environ Sci 7(3):982–988. doi:10.1039/C3EE43822H
219. Bush KA, Bailie CD, Chen Y, Bowring AR, Wang W, Ma W, Leijtens T, Moghadam F, McGehee MD (2016) Thermal and environmental stability of semi-transparent perovskite solar cells for tandems enabled by a solution-processed nanoparticle buffer layer and sputtered ITO electrode. Adv Mater 28(20):3937–3943. doi:10.1002/adma.201505279
220. Choi H, Park S, Paek S, Ekanayake P, Nazeeruddin MK, Ko J (2014) Efficient star-shaped hole transporting materials with diphenylethenyl side arms for an efficient perovskite solar cell. J Mater Chem A 2(45):19136–19140. doi:10.1039/c4ta04179h

221. Wu C-G, Chiang C-H, Tseng Z-L, Nazeeruddin MK, Hagfeldt A, Gratzel M (2015) High efficiency stable inverted perovskite solar cells without current hysteresis. Energy Environ Sci 8(9):2725–2733. doi:10.1039/C5EE00645G
222. Bi C, Wang Q, Shao Y, Yuan Y, Xiao Z, Huang J (2015) Non-wetting surface-driven high-aspect-ratio crystalline grain growth for efficient hybrid perovskite solar cells. Nat Commun 6:7747. doi:10.1038/ncomms8747
223. Zhou H, Chen Q, Li G, Luo S, T-b Song, Duan H-S, Hong Z, You J, Liu Y, Yang Y (2014) Interface engineering of highly efficient perovskite solar cells. Science 345(6196):542–546. doi:10.1126/science.1254050
224. Ahn N, Son D-Y, Jang I-H, Kang SM, Choi M, Park N-G (2015) Highly reproducible perovskite solar cells with average efficiency of 18.3% and best efficiency of 19.7% fabricated via lewis base adduct of Lead(II) iodide. J Am Chem Soc 137(27):8696–8699. doi:10.1021/jacs.5b04930
225. Yang WS, Noh JH, Jeon NJ, Kim YC, Ryu S, Seo J, Seok SI (2015) High-performance photovoltaic perovskite layers fabricated through intramolecular exchange. Science 348 (6240):1234–1237. doi:10.1126/science.aaa9272
226. Li X, Bi D, Yi C, Décoppet J-D, Luo J, Zakeeruddin SM, Hagfeldt A, Grätzel M (2016) A vacuum flash–assisted solution process for high-efficiency large-area perovskite solar cells. Science 353(6294):58–62. doi:10.1126/science.aaf8060
227. Correa-Baena J-P, Anaya M, Lozano G, Tress W, Domanski K, Saliba M, Matsui T, Jacobsson TJ, Calvo ME, Abate A, Grätzel M, Míguez H, Hagfeldt A (2016) Unbroken perovskite: interplay of morphology, electro-optical properties, and ionic movement. Adv Mater 28(25):5031–5037. doi:10.1002/adma.201600624